



UNIL | Université de Lausanne

Unicentre
CH-1015 Lausanne
<http://serval.unil.ch>

Year: 2024

Processes and timescales of melt segregation within felsic magma reservoirs (Adamello batholith, Italy)

Grocolas Thomas

Grocolas Thomas, 2024, Processes and timescales of melt segregation within felsic magma reservoirs (Adamello batholith, Italy)

Originally published at : Thesis, University of Lausanne

Posted at the University of Lausanne Open Archive <http://serval.unil.ch>

Document URN : [urn:nbn:ch:serval-BIB_DB3F21560D533](http://nbn:ch:serval-BIB_DB3F21560D533)

Droits d'auteur

L'Université de Lausanne attire expressément l'attention des utilisateurs sur le fait que tous les documents publiés dans l'Archive SERVAL sont protégés par le droit d'auteur, conformément à la loi fédérale sur le droit d'auteur et les droits voisins (LDA). A ce titre, il est indispensable d'obtenir le consentement préalable de l'auteur et/ou de l'éditeur avant toute utilisation d'une oeuvre ou d'une partie d'une oeuvre ne relevant pas d'une utilisation à des fins personnelles au sens de la LDA (art. 19, al. 1 lettre a). A défaut, tout contrevenant s'expose aux sanctions prévues par cette loi. Nous déclinons toute responsabilité en la matière.

Copyright

The University of Lausanne expressly draws the attention of users to the fact that all documents published in the SERVAL Archive are protected by copyright in accordance with federal law on copyright and similar rights (LDA). Accordingly it is indispensable to obtain prior consent from the author and/or publisher before any use of a work or part of a work for purposes other than personal use within the meaning of LDA (art. 19, para. 1 letter a). Failure to do so will expose offenders to the sanctions laid down by this law. We accept no liability in this respect.



UNIL | Université de Lausanne

Faculté des géosciences et de l'environnement

Institut des Sciences et de la Terre

Processes and timescales of melt segregation within felsic magma reservoirs (Adamello batholith, Italy)

Thèse de doctorat

Présentée à la Faculté des géosciences et de l'environnement de l'Université de Lausanne

par

Thomas Grocolas

Master en Sciences de la Terre et des Planètes

Université de Lorraine, Nancy, France

En vue de l'obtention du grade de Docteur en Sciences de la Terre

Jury composé de

Rozenblat, Céline	Professeure, Université de Lausanne	Présidente du jury
Müntener, Othmar	Professeur, Université de Lausanne	Directeur de thèse
Blundy, Jon	Professeur, University of Oxford	Examineur
Costa, Fidel	Professeur, IPG Paris	Examineur
Klein, Benjamin	Chercheur post-doctoral, Université de Lausanne	Examineur
Ulmer, Peter	Professeur, ETH Zürich	Examineur

Lausanne, 2024

IMPRIMATUR

La Faculté des géosciences et de l'environnement de l'Université de Lausanne, vu le rapport du jury d'examen, autorise l'impression de la thèse de doctorat rédigée par

Thomas Gilles GROCOLAS

intitulée

***PROCESSES AND TIMESCALES OF MELT SEGREGATION WITHIN
FELSIC MAGMA RESERVOIRS (ADAMELLO BATHOLITH, ITALY).***

sans se prononcer sur les opinions exprimées dans cette thèse.

Directeur

Monsieur le Professeur Othmar Müntener

Lausanne, le 01.11.2024



Professeur Torsten Vennemann, Doyen





UNIL | Université de Lausanne

Unicentre

CH-1015 Lausanne

<http://serval.unil.ch>

Year: 2024

Processes and timescales of melt segregation within felsic magma reservoirs (Adamello batholith, Italy)

Thomas Grocolas

Thomas Grocolas, 2024, Processes and timescales of melt segregation within felsic magma reservoirs (Adamello batholith, Italy)

Originally published at: Thesis, University of Lausanne

Posted at the University of Lausanne Open Archive.

<http://serval.unil.ch>

Droits d'auteur

L'Université de Lausanne attire expressément l'attention des utilisateurs sur le fait que tous les documents publiés dans l'Archive SERVAL sont protégés par le droit d'auteur, conformément à la loi fédérale sur le droit d'auteur et les droits voisins (LDA). À ce titre, il est indispensable d'obtenir le consentement préalable de l'auteur et/ou de l'éditeur avant toute utilisation d'une œuvre ou d'une partie d'une œuvre ne relevant pas d'une utilisation à des fins personnelles au sens de la LDA (art. 19, al. 1 lettre a). À défaut, tout contrevenant s'expose aux sanctions prévues par cette loi. Nous déclinons toute responsabilité en la matière.

Copyright

The University of Lausanne expressly draws the attention of users to the fact that all documents published in the SERVAL Archive are protected by copyright in accordance with federal law on copyright and similar rights (LDA). Accordingly it is indispensable to obtain prior consent from the author and/or publisher before any use of a work or part of a work for purposes other than personal use within the meaning of LDA (art. 19, para. 1 letter a). Failure to do so will expose offenders to the sanctions laid down by this law. We accept no liability in this respect.

Acknowledgements

Many people have helped me along the way of my PhD, both on scientific and personal levels. Although I cannot acknowledge everyone who has made this 4-year journey enjoyable and enriching, there are some without whom this work would not have been possible. First, I want to express my gratitude to my supervisor, Othmar Müntener, who has offered me the opportunity to work in a cutting-edge lab with inspiring people; betting on a not-yet-funded PhD position revealed as one of my best choices! Thank you for granting me the freedom to tackle many scientific questions during my PhD, and your confidence in my ability to achieve it in the allocated time. I really appreciated our scientific discussions; I learnt a lot from your extensive geological culture. I would like to thank Eli Bloch for introducing me to the complicated world of sol-gel synthesis and diffusion experiments, and for encouraging me to refresh my memory regarding crystallography. Lukas Baumgartner also brought insights into the preparation of experimental runs, and, most importantly, reintroduced me to fluid-rock interactions. The calculation of volatile melt-fluid equilibria would have taken much longer without your knowledge on expected crustal fluid compositions. I would like to thank my field and conference partner, Ben Klein, with whom I really enjoyed discussing some aspects of this work, and from whom I learnt a lot. I also wish to express my gratitude to Peter Ulmer; who better to introduce me to the geology of the Adamello batholith? To continue with Zürich, I would like to offer particular thanks to Manuel Pimenta Silva, the one and only other Adamello PhD student! I really enjoyed the field, conferences and discussions, and I really look forward to continuing collaborating. A special mention goes to Christophe Jossevel, whose samples from the Western Adamello helped me starting my PhD on the right track despite Covid. I am grateful to Martin Robyr, Alexey Ulyanov, Anne-Sophie Bouvier, Stéphane Escrig and Nordine Bouden for their assistance with electron microprobe, laser ablation ICP-MS and ion probe analysis. Special thanks go to Alexey who accepted to teach me the LA-ICP-MS method and its associated counting statistics and uncertainties in details, and allowed me to use it whenever I needed. Martin also allowed me to use more than my fair share of

electron microprobe time during the first two years of my PhD and did not mind helping me fixing the machine even on weekends. Anne-Sophie and Stéphane assisted me on the SIMS and NanoSIMS, respectively, from analysis of Ti concentrations in quartz, volatiles in apatite, depth profiling in plagioclase, and line scanning in plagioclase and quartz. I am also extremely grateful to the SIMS team in Nancy who allowed me to use their machine with the record for the shortest waiting time, and especially Nordine for his assistance during analysis of sulphur isotopes in apatite. I would also like to thank Antoine, Aman, Delphine, María and Philip for making office 4639 such an enjoyable place to work and socialise, and Alexia, Aurore, Jack and Marko for also bringing their touch of support, help and good humour throughout the course of my PhD. Some of my professors back in Nancy played a determining role in the completion of this work, by teaching me the rudiment of geology and by igniting my interest in igneous petrology. I am thinking in particular about Pierre Bouilhol and Lydéric France; I would not be writing these lines if not for them. I am grateful to Jon Blundy, Fidel Costa, Ben Klein and Peter Ulmer for having accepted to evaluate this PhD thesis, and for having inspired my work along these years through their many interesting papers. Although they had a hard time understanding what I was actually doing during these four years, I thank my parents for their continuous support throughout my entire education. Finally, I wish to thank my wife, Marion, for her unwavering encouragement and support. You have largely contributed to the completion of this PhD thesis, but also to shape the person I am today; for that I am extremely grateful.

Abstract

The final differentiation of intermediate to felsic magmas plays a fundamental role for magmatic systems, linking crystallising plutons, volcanic activity, volatile exsolution and ore deposits. However, our understanding of the nature of these links is limited by the scarcity of outcrops exhibiting clear relationships between the plutonic roots that feed its volcanic counterpart. Recent advances on the topic of melt extraction processes and timescales benefited from improvements of analytical techniques enabling (1) high-precision zircon dating and (2) *in situ* measurements of trace and volatile element concentrations in minerals and glassy melt inclusions. The time constrains determined from zircon petrochronology and diffusion modelling are currently used to document the time required for eruptible magma to assemble, while the determination of volatile concentrations helps constraining the melt physical properties and the occurrence of a potential magmatic fluid. Diffusion modelling and volatile characterisation have widely been employed on quenched volcanic rock samples due to the absence of chemical re-equilibration related to cooling, whereas its application has been limited in plutonic rocks.

This study reconstructs the chemical and thermal evolution undergone by the Western Adamello and Re di Castello tonalites (Adamello batholith, Italy), Alpine calc-alkaline intrusions formed during the collision of the European and Adriatic plates, with the aim to precisely document the tonalite petrography in order to retrieve melt segregation timescales. In this scope, a detailed petrographic study is first performed and is based on thorough field and thin section observations, bulk rock and mineral chemistry, and mass balance modelling. This allowed the characterisation of a peritectic reaction consuming amphibole and crystallising biotite, and the quantification of crystal accumulation and melt segregation. Finally, the calculated volumes of segregated and extracted melt within the Western Adamello are then confronted to the scarcity of Alpine volcanism.

Precisely determining timescales using diffusion chronometry requires a robust knowledge of cation diffusion rates in minerals. Although diffusion coefficients of Sr and Ba in plagioclase were determined decades ago, recent studies performing diffusion experi-

ments demonstrated that the experimental setup of these previous studies might not be adequate to capture diffusion rates. New experiments have been performed using polished plagioclase crystals and sol-gel-derived source powders whose stable assemblage and compositions were thoroughly characterised. The retrieved diffusion coefficients for Sr and Ba after annealing are similar, and differ by ~ 2 and 0.5 orders of magnitude, respectively, from previous studies. Such differences are well-explained by the presence of a stable assemblage containing Ba-feldspar in the previous Ba experiments, whereas no Sr-bearing silicate was present in the source powders of previous studies. This hindered the incorporation of Sr in plagioclase and instead resulted in a reaction between Sr oxide and plagioclase.

Measured compositional profiles in minerals from the Western Adamello and Re di Castello lithologies revealed the presence of Sr and Ba zoning in plagioclase core-mantle and mantle-rim, Ti zoning in quartz rim, and Ba and Sr zoning in alkali feldspar. All these features, except the core-mantle plagioclase zoning, are related to the cooling of the pluton, which was inferred from diffusion modelling. The modelled cooling rates are fast (~ 150 °C Myr⁻¹ for the first two million years) for both locations and overlap with (1) the mineral ³⁹Ar/⁴⁰Ar ages determined by previous studies and (2) the thermal model reproducing the Western Adamello tonalite cooling path. After subtracting the cooling component from the measured plagioclase core-mantle profiles, plagioclase residence times before rim crystallisation could be modelled and range from ~ 20 to ~ 110 kyr. Such timescales ($\sim 10^4$ - 10^5 yr) are similar to high-precision zircon ages from the Adamello batholith and other plutons, and probably represent the ideal time to form a thermally stable magma reservoir able to segregate interstitial melt.

Finally, in order to evaluate the volatile budget and its potential role in the crystal-melt segregation process, the volatile content of apatite has been documented. Apatite-biotite pairs have been measured and cooling rates were determined based on F and Cl zoning in apatite to demonstrate that volatile re-equilibration during cooling was limited and, therefore, that apatite can indeed be used to reconstruct the equilibrium melt volatile composition. Coupling apatite volatile content with the plagioclase hygrometer helped concluding that the parental tonalitic melt was H₂O-saturated prior to apatite saturation. Based on partitioning and thermodynamic modelling, the melt and fluid volatile compositions as well as apatite crystallisation pressure could be inferred. Calculations of the average flux of fluid exsolution and the conditions required for diking and eruptions reveal that melt segregation in the Adamello batholith results from a combination of magma recharge and fluid-driven filter pressing.

Résumé

La différenciation des magmas intermédiaires à felsiques joue un rôle fondamental dans l'évolution des systèmes magmatiques, liant les réservoirs magmatiques à l'activité volcanique, l'exsolution de volatils et la formation de gisements métallogéniques. Cependant, la nature de ces relations est mal connue, principalement à cause de la faible abondance d'affleurements montrant des relations claires entre le réservoir magmatique en profondeur et le volcanisme de surface. Des études récentes traitant des processus et du temps nécessaire à la séparation entre cristaux et magma ont bénéficié de l'amélioration des techniques analytiques permettant (1) la datation de zircon à haute résolution et (2) l'analyse *in situ* des concentrations en éléments traces et volatils de minéraux et inclusions magmatiques. Les contraintes de temps déterminées à partir de la datation de zircon et de la modélisation de profils de diffusion sont utilisées afin de documenter le temps nécessaire à un réservoir magmatique d'accumuler du magma, tandis que déterminer les concentrations en éléments volatils permet de contraindre les propriétés physiques du magma et d'identifier la présence d'un fluide de faible densité. La modélisation de profils de diffusion et l'analyse des éléments volatils ont largement été employées dans des échantillons de roche volcanique du fait de l'absence de rééquilibre chimique lié au refroidissement, alors que son application dans les roches plutoniques est limitée.

Cette étude reconstruit l'évolution chimique et thermique suivie par les tonalites de Western Adamello et Re di Castello (batholithe de l'Adamello, Italie), des intrusions calco-alcalines Alpines formées durant la collision des plaques Européenne et Adriatique, dans le but de quantifier l'accumulation de cristaux et la séparation de magma et de calculer le temps nécessaire à ce processus. Dans ce cadre, une étude pétrographique a été réalisée et basée sur des observations détaillées de terrain et lames minces, des analyses chimiques en roche totale et des minéraux ainsi que des bilans de masse. Cela a permis la caractérisation d'une réaction péritectique consommant l'amphibole et formant de la biotite ainsi que la quantification de l'accumulation de cristaux et la séparation de magma. Enfin, les volumes calculés de magma ségrégués et extraits au sein de la tonalite de Western Adamello sont

confrontés à la rareté du volcanisme Alpin.

La datation relative basée sur la diffusion d'éléments dans les minéraux requiert une connaissance solide des vitesses de diffusion des éléments. Bien que des coefficients de diffusion du Sr et Ba dans les plagioclases ont été déterminés dans le passé, des études expérimentales récentes ont démontré que la configuration utilisée dans ces études n'est probablement pas adéquate pour extraire des vitesses de diffusion. De nouvelles expériences ont été réalisées à partir de cristaux polis de plagioclase et de sources en éléments traces dont les assemblages minéralogiques et les compositions ont été déterminés au préalable. Les coefficients de diffusion du Sr et Ba sont similaires entre eux mais différent de ceux des études précédentes respectivement d'un ordre de grandeur 2 et 0,5. Cette différence est expliquée par la présence de feldspath riche en Ba dans la source des études antérieures, alors qu'aucun silicate de Sr n'est présent dans les expériences de diffusion du Sr. Cela empêche l'incorporation du Sr dans le plagioclase et résulte plutôt en une réaction entre l'oxyde de Sr et le plagioclase.

Les profils chimiques mesurés dans les minéraux des lithologies de Western Adamello et Re di Castello ont révélé (1) la présence d'une forte zonation en Sr et Ba entre cœurs et manteaux et entre manteaux et bordures des plagioclases, (2) une zonation en Ti à la bordure des quartz et (3) une zonation en Sr et Ba dans les feldspaths alcalins. Toutes ces observations, exceptée la zonation entre cœurs et manteaux des plagioclases, sont liées au refroidissement du pluton qui est quantifié à partir de la modélisation des profils de diffusion. Les vitesses de refroidissement modélisées sont rapides (~ 150 °C Myr⁻¹ pour les deux premiers millions d'années) pour les deux zones d'étude et coïncident avec (1) les âges ³⁹Ar/⁴⁰Ar obtenus par différentes études et (2) le modèle thermique reproduisant le refroidissement de la tonalite de Western Adamello. Après le retrait de la composante de refroidissement aux profils cœurs-manteaux des plagioclases, les temps de résidence des plagioclases avant la cristallisation de la bordure ont été modélisés et sont compris entre ~ 20 et ~ 110 kyr. Ces temps ($\sim 10^4$ - 10^5 yr), similaires aux âges de haute précision mesurés sur des zircons provenant de l'Adamello et d'autres batholithes représentent probablement le temps idéal pour former un réservoir magmatique thermiquement stable et capable de ségréguer du magma interstitiel.

Enfin, afin d'évaluer les teneurs en volatils des systèmes tonalitiques et le rôle potentiel de ces éléments lors de la séparation entre cristaux et magma, les concentrations en volatils dans les apatites ont été déterminées. L'analyse de paires apatite-biotite et la préservation de zonations en F et Cl dans les apatites ont permis de démontrer que le rééquilibre des volatils pendant le refroidissement était limité et, par conséquent, que l'apatite peut

être utilisée dans le but de calculer la composition en volatils du magma à l'équilibre. L'association entre la composition en volatils des apatites et l'hygromètre basé sur la composition des plagioclases permet de conclure que le magma tonalitique parent était saturé en H₂O au moment de la saturation en apatite. À partir de coefficients de partage et de modélisation thermodynamique, la composition en volatils du magma et du fluide ainsi que la pression de cristallisation des apatites ont été déterminées. Le calcul du flux moyen d'exsolution de fluide ainsi que des conditions nécessaires pour le déclenchement d'éruptions révèlent que la ségrégation de magma dans le batholithe de l'Adamello résulte d'une combinaison entre réinjection de magma et cisaillement lié à l'exsolution de fluide.

Contents

1	Introduction	1
1.1	Upper crustal silicic magma reservoirs	1
1.1.1	Why is it important?	1
1.1.2	Forming intermediate to felsic melts	2
1.1.3	Transport and emplacement mechanisms	5
1.2	Evolution of silicic magma reservoirs	7
1.2.1	Crystallisation	7
1.2.2	Volatile evolution	8
1.2.3	Crystal-melt segregation	10
1.3	Timescales of melt segregation	11
1.3.1	Methods	11
1.3.2	Timescales of magmatic processes	14
1.3.3	Some complications and considerations	17
1.4	Rationale	20
1.5	Geological background	21
1.5.1	The Western Alps	21
1.5.2	The Adamello batholith	23
2	The role of peritectic biotite for the chemical and mechanical differentiation of felsic plutonic rocks (Western Adamello, Italy)	31
2.1	Abstract	31
2.2	Introduction	32
2.3	Geological setting	34
2.4	Field relationships and petrography	36
2.4.1	Tonalite	38
2.4.2	Hornblende-biotite-gabbro	40
2.4.3	Leucotonalite	42
2.4.4	Granite	43
2.5	Analytical techniques	44
2.5.1	Quantitative evaluation of minerals by scanning electron microscopy (QEMSCAN)	44
2.5.2	Bulk rock chemistry	44
2.5.3	Mineral chemistry	45
2.6	Results	47
2.6.1	Bulk rock major and trace element geochemistry	47

2.6.2	Mineral chemistry	49
2.6.3	Temperature constraints	56
2.7	Discussion	58
2.7.1	Melt versus cumulate	58
2.7.2	Tonalite liquid line of descent	60
2.7.3	Crystal-melt segregation model	64
2.7.4	Importance of peritectic biotite in crystallising felsic plutonic rocks	69
2.7.5	Phase relationships in pseudoternary projections	72
2.7.6	Implications for melt extraction in the WAT	75
2.8	Conclusions	77
2.9	Acknowledgements	78
3	Diffusion of Sr and Ba in plagioclase: Composition and silica activity dependencies, and application to volcanic rocks	81
3.1	Abstract	81
3.2	Introduction	82
3.3	Methods	84
3.3.1	Source powder	84
3.3.2	Plagioclase crystals	86
3.3.3	Experiments	87
3.3.4	Analytical techniques	88
3.3.5	Diffusion modelling	90
3.4	Results	91
3.4.1	Diffusion interface	91
3.4.2	Time-series experiments	92
3.4.3	Major element activities	95
3.4.4	Diffusion anisotropy	97
3.4.5	Temperature dependence	97
3.5	Discussion	98
3.5.1	Comparison with previous studies	98
3.5.2	Charge balance and the effect of silica activity	100
3.5.3	Application to natural samples	103
3.6	Conclusions	107
3.7	Acknowledgements	108
4	Cooling rates and crystal residence times in plutonic rocks determined by diffusion chronometry (Adamello batholith, Italy)	111
4.1	Abstract	111
4.2	Introduction	112
4.3	Geological settings	114
4.4	Methods	116
4.4.1	Backscattered electron imaging	116
4.4.2	Cathodoluminescence imaging	117
4.4.3	Electron probe microanalysis	117
4.4.4	Laser ablation inductively coupled plasma mass spectrometry	117

4.4.5	Secondary ion mass spectrometry	118
4.4.6	Nanoscale secondary ion mass spectrometry	119
4.4.7	Diffusion modelling	119
4.5	Results	123
4.5.1	Petrography	123
4.5.2	Alkali feldspar	124
4.5.3	Quartz	125
4.5.4	Plagioclase	127
4.6	Thermometry	129
4.7	Diffusion calculations	132
4.7.1	Cooling rates	132
4.7.2	Residence times	139
4.8	Comparison with volcanic timescales	141
4.8.1	Which diffusion coefficients?	141
4.8.2	Similarity with zircon timescales	144
4.8.3	Volcanic and plutonic timescales	146
4.9	Conclusions	147
5	Apatite as a tool to quantify the volatile budget of felsic magma reservoirs (Adamello batholith, Italy)	149
5.1	Abstract	149
5.2	Introduction	150
5.3	Geological settings	153
5.4	Methods	154
5.4.1	Mineral separation and imaging	154
5.4.2	Electron probe microanalysis	154
5.4.3	Secondary ion mass spectrometry	155
5.4.4	Laser ablation inductively coupled plasma mass spectrometry	156
5.4.5	Bulk F content	157
5.5	Results	157
5.5.1	Petrographic observations	157
5.5.2	Apatite chemistry	159
5.5.3	Biotite-apatite pairs	164
5.6	Magmatic volatile preservation	165
5.6.1	Bulk rock	166
5.6.2	Apatite	167
5.7	Composition of melts	169
5.7.1	Apatite crystallisation temperature	169
5.7.2	Initial F and H ₂ O melt contents	172
5.7.3	Calculation of melt composition	172
5.8	Composition of fluids	176
5.8.1	Melt-fluid partition coefficients	177
5.8.2	Modelling the fluid Cl budget	177
5.8.3	Calculation of fluid compositions	178
5.8.4	Re di Castello	180

Contents

5.9	Modelling the crystal-melt-fluid system	180
5.9.1	Model setup	180
5.9.2	Model results	181
5.10	Comparison with fluid inclusion studies	184
5.11	Impact of exsolving fluids on melt segregation	186
5.12	Reconstruction of plumbing system	187
5.13	Conclusions	190
6	General conclusions and perspectives	195
6.1	K-bearing phase in granitoids: Biotite vs. alkali feldspar	196
6.2	Role of source powders and mineral stability on diffusion experiments	198
6.3	Diffusion timescales in plutonic rocks: Assembly processes vs. eruption triggering	199
6.4	The volatile archive of apatite in plutonic rocks	201
6.5	Final remarks	203
A	Supplementary Materials	205
A.1	Supplementary Material to Chapter 2	205
A.1.1	Supplementary Text	205
A.1.2	Supplementary Figures	207
A.2	Supplementary Material to Chapter 3	239
A.2.1	Supplementary Figures	239
A.2.2	Supplementary Tables	256
A.3	Supplementary Material to Chapter 4	260
A.3.1	Supplementary Text	260
A.3.2	Supplementary Figures	261
A.3.3	Supplementary Tables	275
A.4	Supplementary Material to Chapter 5	322
A.4.1	Supplementary Text	322
A.4.2	Supplementary Figures	324
A.4.3	Supplementary Tables	333
	Bibliography	364

Chapter 1

Introduction

1.1 Upper crustal silicic magma reservoirs

1.1.1 Why is it important?

Volcanic activity is intimately tied to drastic climate changes through Earth's history potentially leading to local biological disturbances to global mass extinctions, and agricultural and economic crises (Oppenheimer et al., 2011; Self, 2006; Sigl et al., 2015). Examples include the Deccan Traps flood basalt province coinciding with the end-Cretaceous mass extinction (Schoene et al., 2019; Vogt, 1972), and the Tambora eruption in 1815 which has led to global crop failures and widespread outbreaks of epidemic typhus during the following decade (Oppenheimer, 2003). In addition, more than 800 million people live in the vicinity of an active volcano and could be physically impacted by potential eruptions that are directly fed by deeper magma reservoirs. Volcanic eruptions represent the culmination of a long series of processes happening in the Earth's lithosphere, starting with melting of a source region, magma accumulation in crustal reservoirs, and transport of segregated melt between source and storage regions and to the surface. The large number of active volcanoes worldwide could suggest that these processes are effective and operate at very high rates. However, a paradigm emerged a decade ago whereby the ascent of magma to the surface is hindered by several processes and is surprisingly complex. For example, the building of a magma reservoir requires large volumes of magma to counterbalance the relatively cold country rock and overcome instant solidification (e.g., Annen, 2009). The longevity of magma chambers is directly a function of the host rock temperature and, therefore, upper crustal reservoirs need larger melt supplies to be thermally sustained. Additionally, the exponential increase of magma viscosity during crystallisation-differentiation (Marsh, 1981; Shaw, 1972) calls for larger energy sources to efficiently segregate and transport interstitial

1. Introduction

melt. Interestingly, the most dangerous volcanic eruptions are systematically associated with silicic ($\text{SiO}_2 > 65 \text{ wt.}\%$), highly viscous, upper crustal magma reservoirs leading to explosive eruptions. Mitigating future volcanic hazards necessitates adequate warning of a pending eruption which, in turn, requires detailed understanding of the fundamental processes driving volcanic activity.

In addition to being associated to dangerous volcanic hazards, upper crustal volatile-rich magma reservoirs often host economically important ore deposits, such as porphyry copper deposits (Audéat, 2019; Blundy et al., 2015; Hedenquist and Lowenstern, 1994; Richards, 2011; Sillitoe, 2010). Upon exsolution of a magmatic volatile phase primarily composed of H_2O , fluid-mobile metals preferentially incorporate the fluid phase and eventually precipitate to form metal-enriched zones. The processes leading to metal concentration and precipitation are directly related to the melting source, the host rock encountered during magma ascent, and the magma crystallisation-differentiation path. The intimate relationship between magma reservoir processes, fluid exsolution and the formation of ore deposits underscores the need for a better characterisation of intermediate to felsic magma emplacement and differentiation.

1.1.2 Forming intermediate to felsic melts

The Earth's crust represents the product of a continuous differentiation process, whereby partial melts segregated and extracted from the mantle buoyantly rise and form the outermost layer of our planet. Interestingly, the composition of middle to upper crustal igneous rocks is in disequilibrium with the mantle, which implies that these crustal portions must originate from the differentiation of mantle-derived precursors. Three processes may lead to these silica-rich rocks: (1) fractionation of primary basaltic to andesitic magmas; (2) melting of pre-existing crustal lithologies; and (3) erosion of rocks of similar compositions (Rudnick and Fountain, 1995; Taylor and McLennan, 1995). In this manuscript, the latter process is not considered as it has proven less significant than magmatic processes (Hawkesworth and Kemp, 2006) and is beyond the scope of this study.

Through arc magmatism...

The geochemical similarity between arc-derived magmatic rocks and continental crust has fostered the hypothesis that arc magmatism above subduction zone has played a pivotal role in creating continental crust (Kelemen, 1995; Ringwood, 1974; Rudnick and Fountain, 1995; Taylor, 1967; Taylor and McLennan, 1985, 1995). Although this continent signature may arise from the recycling of subducted, continentally-derived sediments, the occurrence

of isotopically depleted arc lavas indicates little to no contribution from a recycled component and confirm that continental crust is mainly extracted from the Earth's mantle by arc magmatic processes (Fig. 1.1a) (Kelemen et al., 2003). Primitive melts in equilibrium with mantle peridotite typically have values of Mg-number [$\text{Mg\#} = 100 \times \text{molar Mg}/(\text{Mg} + \text{Fe}^{2+})$] from 70 to 75 mol.% (e.g., Green and Ringwood, 1970). Their composition varies with the melting pressure and temperature conditions as well as the H_2O content of the system, and ranges from picritic at high pressure (>2 GPa) to andesitic at lower pressure (<1 GPa) conditions (Baker et al., 1994; Bartels et al., 1991; Grove et al., 2003; Tatsumi et al., 1994; Ulmer, 1988). Upon ascent in the mantle, early differentiation can result from pervasive melt-rock interaction and reaction, whereby the primitive melt-mantle equilibrium is shifted towards more silicic melt compositions leading to clinopyroxene dissolution and olivine crystallisation (e.g., Bouilhol et al., 2009; Kelemen et al., 1995; Mitchell and Grove, 2016). Although dacitic melts are locally found within mantle xenoliths (Bénard et al., 2018), the most important part of melt differentiation occurs through crystallisation and/or melt-rock reaction within the crustal column (e.g., Sparks et al., 2019). Experimental liquid lines of descent at intermediate to high pressure in dry and hydrous systems unequivocally demonstrate that fractionation in the deep crust is the main process controlling the evolution from mafic to silicic volcanic and plutonic rocks (Alonso-Perez et al., 2009; Blatter et al., 2013, 2017; Marxer et al., 2022, 2023; Melekhova et al., 2015; Müntener and Ulmer, 2006, 2018; Nandedkar et al., 2014; Sisson et al., 2005; Ulmer et al., 2018; Villiger et al., 2007). These experimental studies show that differentiation of primitive melts is controlled by the pressure and temperature of crystallisation, the melt H_2O content, and the oxygen fugacity ($f\text{O}_2$) of the system. One of the other conclusions drawn from these works is the large amount of crystallisation needed (>65 %) to reach quartz saturation, which has important implications for continental crust composition, magma fluxes, and formation of upper crustal silica-rich magma reservoirs. In addition to reproducing dacitic to rhyolitic melt compositions, experimental cumulate and liquid lines of descent are strikingly similar to the differentiation sequences of juvenile exposed deep arc sections (Bouilhol et al., 2015; Burg et al., 1998; DeBari and Coleman, 1989; Greene et al., 2006; Jagoutz et al., 2007; Müntener and Ulmer, 2018), confirming the direct connection between mantle-derived melts and upper crustal magma reservoirs.

...and anatexis melting

The genesis of large volumes of granitoid may also result from the partial melting of pre-existing crust (Fig. 1.1b), either through (1) supplying H_2O to rocks at temperatures

1. Introduction

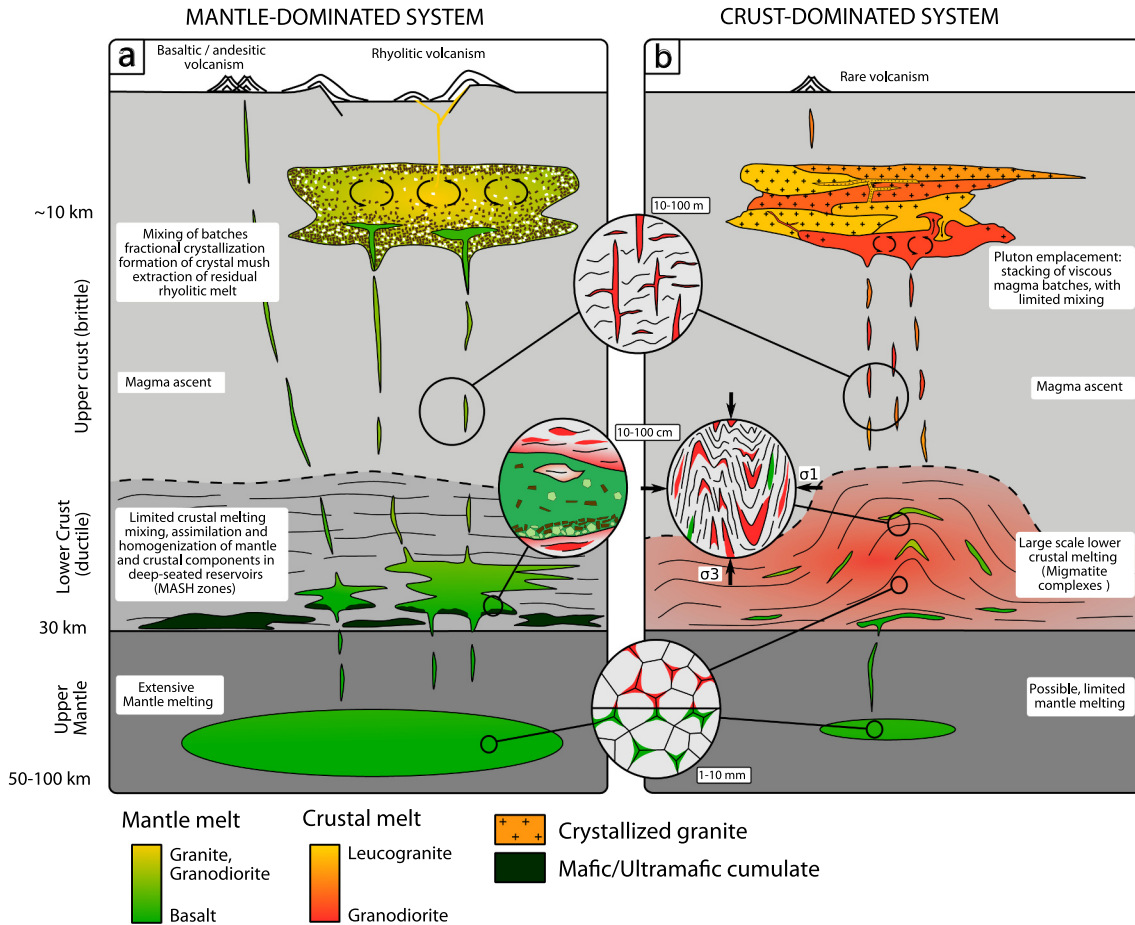


Figure 1.1. Schematic models of the petrogenesis of granitoids. **a**, The basaltic melt fractionation model, whereby the main driver is mantle melting and crystallisation-differentiation of the mantle-derived primary melt. This magma intrudes the pre-existing crust and evolves through a combination of processes involving closed-system (crystallisation) and open-system (assimilation, mixing) processes leading to silica-enrichment. In such mantle-derived systems, continuous magma replenishment usually leads to the development of interconnected magma reservoirs and volcanic eruptions. **b**, The crustal melting model, whereby most of the granitic magmas originate from partial melting of crustal material caused by a thermal anomaly or decompression during exhumation. In such crust-dominated systems, the ambient temperature is close the granite solidus, therefore limiting the interactions between the different magma batches and the volcanism. Figure from [Moyen et al. \(2021\)](#).

above their H_2O -saturated solidi, (2) heat supply increase, and/or (3) dehydration-melting reactions. Because free H_2O is scarce in the middle to lower continental crust (e.g., [Yardley and Valley, 1997](#)), and the effect of heat supply most likely triggers local partial melting, dehydration-melting of mica- and/or amphibole-bearing rocks represents the major process providing large volumes of crustal-derived melt ([Clemens and Vielzeuf, 1987](#); [Powell, 1983](#); [Thompson, 1983](#); [Thompson and Connolly, 1995](#)). This view has recently been challenged by considering the fluids exsolved during high-pressure differentiation of arc magmas potentially leading to fluid-present melting of pre-existing crustal lithologies ([Collins et al., 2020](#)). Regardless, the composition of the partial melts depends on the protolith nature,

the amount of melting, and the melting pressure and temperature conditions, and can either be tonalitic, trondhjemitic, granodioritic or granitic (Gardien et al., 1995; Le Breton and Thompson, 1988; Patiño Douce and Harris, 1998; Rapp et al., 1991; Rapp and Watson, 1995; Vielzeuf and Holloway, 1988). In detail, the proportion of crustal-derived granitoids is largely dominated by granitic compositions since the amount of melting required to form tonalitic to granodioritic crustal melts (>30 %) is rarely attained in nature. Recently, calculations based on previous experimental works highlighted that (1) the amount of restite needed is similar to twice higher than the volume of cumulate required to form a given volume of granitoid from a basaltic source, demonstrating the limited efficiency of crustal melting to generate granitoid bodies, and (2) the compositional diversity of restites does not cover the mafic to ultramafic compositions found in arc sections (Jagoutz and Klein, 2018). Although the occurrence of peraluminous felsic plutonic and volcanic rocks with a crustal signature (e.g., Ledru et al., 2001) illustrates that generating and segregating crustal melts can be achieved, batholiths and large-scale eruptions are mostly dominated by mantle-derived material. Despite this apparent difficulty, exhumation and/or heating of large and fertile crustal portions often lead to the genesis of granitic bodies exceeding 1,000 km³ (e.g., France-Lanord and Le Fort, 1988; Ledru et al., 2001; McFadden et al., 2010; Searle et al., 2009; Solar and Brown, 2001; Zhang et al., 2004), highlighting the importance of crustal reworking in generating silicic magmas.

1.1.3 Transport and emplacement mechanisms

The emplacement mechanism and geometry of magma reservoirs depends on the physical properties of the magma and the intruded crust, such as melt and surrounding crust temperatures, viscosities and densities, the presence of pre-existing or active crustal structures, or the magma injection rate. The transport of segregated melts has initially been classified into active, or forceful, and passive mechanisms, whereby the former refers to a melt actively creating space by deforming the host rock, and the latter instead encompasses magmas passively occupying the available space (Hutton, 1988). Amongst the active mechanisms, transport of magma as buoyant, slow-rising diapirs (Fig. 1.2a) emerged as a historical paradigm (e.g., Bateman, 1985; Courrioux, 1987; Cruden, 1990). However, it was later observed and modelled that diapirs preferentially form in a ductile environment (Weinberg and Podladchikov, 1994), as opposed to the brittle nature of the middle to upper crust favouring melt transport as self-propagating dikes (Clemens and Mawer, 1992; Clemens et al., 1997), or along pre-existing faults (Petford et al., 1993) or shear zones (Fig. 1.2b) (Brown and Solar, 1998; Grocott et al., 1994; Hutton, 1982, 1988;

1. Introduction

Hutton et al., 1990; Vigneresse, 1995; Weinberg et al., 2004, 2009). Pervasive porous flow has also been recognised as an efficient mechanism for melt transport in the upper mantle and the lower crust (Fig. 1.2c), whereby basaltic melt ascends along and react with grain boundaries, ultimately creating low-permeability feeder zones (e.g., Bouilhol et al., 2009; Daczko et al., 2016; Kelemen et al., 1992, 1995; Nicolas, 1986). Additionally, the ascent and emplacement of plutons usually result from a combination of “active” and “passive” processes which are intimately related and form a positive feedback loop (Paterson and Fowler Jr, 1993). Indeed, heat transfer from the hot magma typically weakens and deforms the host rock, therefore allowing more magma to ascent.

Upper crustal magma reservoirs are generally assembled incrementally, whereby small volumes of relatively hot magma are consecutively injected in a colder host rock. This mechanism is confirmed by the presence of textural, chemical and isotopic heterogeneities within plutonic bodies, and high-precision zircon geochronology (e.g., Coleman et al., 2004; de Saint Blanquat et al., 2011; Glazner et al., 2004; Leuthold et al., 2012; Miller et al., 2007; Schaltegger et al., 2009). Based on these petrographic and dating techniques, three emplacement geometries have been recognised, encompassing (1) radial growth (Fig. 1.2d), hereafter termed “ballooning” (e.g., Bateman, 1985; Brack, 1985; John and Blundy, 1993; Paterson and Vernon, 1995), (2) vertical growth of stacking horizontal sills (Fig. 1.2e) (e.g., de Saint-Blanquat et al., 2006; Leuthold et al., 2012; Michel et al., 2008), and (3) horizontal growth of stacking vertical dikes (Fig. 1.2f) (e.g., Allibon et al., 2011; Floess and Baumgartner, 2015). The final geometry of a pluton depends on a combination of parameters, including the intruding crust anisotropy and rheology, the far-field stress, and buoyancy (Anderson, 1951; Corry, 1988; Menand, 2011; Parsons et al., 1992). For example, a dike geometry preferentially forms when the least compressive stress is horizontal and/or the host rock exhibits a vertical foliation. A ballooning emplacement mechanism is defined as the radial expansion of a magma reservoir in a rather isotropic crust (Paterson and Vernon, 1995). Although it has been demonstrated that granitoids can be emplaced following these three mechanisms, field observations on exposed arc crustal sections suggest that horizontal fabrics generally dominate in the lower crust and progressively shift to vertical fabrics in the upper crust (Burg et al., 2006; Kidder et al., 2003; Klein and Jagoutz, 2021; Saleeby, 1990).

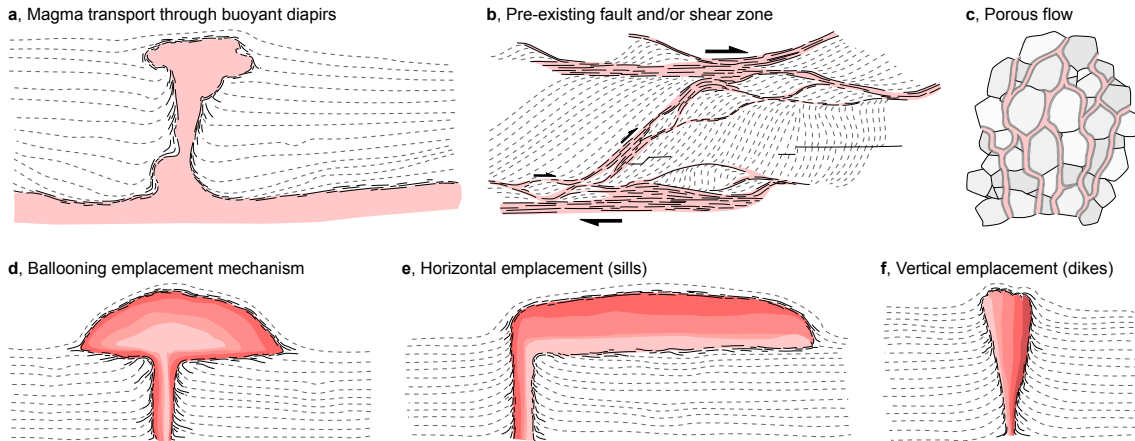


Figure 1.2. Schematic models of magma transport (**a–c**) and emplacement (**d–f**) mechanisms. **a**, Magma transport through diapirism, whereby buoyant magma rises into the crust as a large-volume, continuous batch. Figure inspired from [Cofrade et al. \(2023\)](#). **b**, Magma transport through anastomosing shear zones connected by minor oblique zones, here forming an S-C-style geometry. Figure modified from [Fossen and Cavalcante \(2017\)](#). **c**, Magma transport through porous flow, whereby magma percolates at grain boundaries and locally dissolves crystal rims and crystallises. This mechanism is ubiquitous for low-viscosity mafic melts and occurs in sub-arc and mid-ocean ridge mantle-to-crust transition. **d**, Magma emplacement through ballooning, whereby magma recharge results in a radial expansion of the magma reservoir. **e**, Magma emplacement as horizontal sills resulting in a vertical growth of the magma reservoir. This mechanism typically occurs in the lower crust or in a crust having a pre-existing horizontal anisotropy. Figure inspired from [Leuthold et al. \(2014\)](#). **f**, Magma emplacement as vertical dikes resulting in a horizontal growth of the magma reservoir. This mechanism typically occurs in the upper crust or in a crust having a pre-existing vertical anisotropy.

1.2 Evolution of silicic magma reservoirs

1.2.1 Crystallisation

Upon emplacement, magma usually has a low crystallinity and is dominated by the liquid phase; such a crystal-poor state is hereafter termed a “melt,” as opposed to a “mush.” This melt may carry some crystals originating from the crystallisation of the parental melt at greater depths, termed “antecrysts,” or from the crosscut host rock, termed “xenocrysts.” As the magma intrudes the colder middle to upper crust, the low crystal fraction allows cooling through convection, but with crystallisation, the heat dissipation mechanism progressively shifts toward conduction ([Marsh, 1989](#); [Tait and Jaupart, 1992](#)). In response to decreasing temperature, the crystallinity of the magma increases and, therefore, the physical properties (e.g., viscosity, permeability, density) of the system are modified (e.g., [Lange, 1994](#); [Shaw, 1972](#); [Sparks and Huppert, 1984](#)). Between 40 and 60 % crystallinity, a continuous framework of touching minerals is formed, hereafter termed the “rheological lock-up”; the rheological behaviour of the magma reservoir drastically changes from a liquid to a solid ([Cashman et al., 2017](#); [Marsh, 1981](#)). The relationship between temperature

1. Introduction

and crystallinity is a function of the melt composition and crystallisation pressure (Marxer and Ulmer, 2019; Marxer et al., 2022; Piwinski, 1968). In the case of a fluid-saturated intermediate to felsic melt intruding the upper crust, typical of calc-alkaline batholiths, the melt evolution is controlled by the plagioclase-amphibole cotectic and the melt fraction decreases relatively slowly until it reaches biotite and quartz (\pm alkali feldspar) saturation (Johnson and Rutherford, 1989; Marxer and Ulmer, 2019; Nandedkar et al., 2014; Piwinski, 1968). At this point, the crystallinity dramatically decreases over a small temperature interval before reaching a haplogranitic composition leading to extensive albite-rich plagioclase, quartz and alkali feldspar crystallisation. Furthermore, melt crystallisation leads to the release of latent heat, resulting in an apparent slower temperature, and therefore crystallinity, decrease. Thermal modelling highlights that the release of latent heat of crystallisation increases the lifespan of a magma reservoir by a factor of ~ 2 for a latent heat linearly correlated to the melt fraction (Lee et al., 2015). This assumption of a linear distribution of latent heat across the liquidus-solidus interval is reasonable for simple systems, but is incorrect for magma undergoing cotectic crystallisation or peritectic reactions leading to disproportionate release of latent heat (Lange et al., 1994).

1.2.2 Volatile evolution

Magmatic volatiles (e.g., H_2O , CO_2 , HCl , H_2S , SO_2) dramatically affect the magma density, viscosity and compressibility, thereby exerting a critical influence on the eruptability of magma reservoirs and the eruption style of volcanoes (Cassidy et al., 2018; Degruyter et al., 2017; Gardner, 2009). In calc-alkaline systems, primitive magmas contain significant amounts of dissolved volatiles originating from the dehydrating slab (e.g., Plank and Langmuir, 1993; Schmidt and Poli, 1998). Owing to the relationship between volatile solubility and pressure (e.g., Behrens, 1995; Fogel and Rutherford, 1990; Hamilton et al., 1964; Mitchell et al., 2017; Papale et al., 2006), and to the incompatible character of volatiles, melts can reach saturation with respect to a volatile phase during decompression, termed “first boiling,” or during isobaric cooling and crystallisation, termed “second boiling” (Candela, 1997; Sparks, 1978; Tait et al., 1989). Extensive experimental work has led to well-calibrated models predicting the solubilities of CO_2 and H_2O as a function of temperature, pressure, and melt composition (Botcharnikov et al., 2006; Holtz et al., 1995; Khitarov et al., 1968; Liu et al., 2005; Shishkina et al., 2014; Webster et al., 1999). No experimental study has focused on the solubilities of other species such as HCl and H_2S since they are limited by saturation with a solid or immiscible liquid phase (e.g., Carroll and Webster, 1994; Jugo et al., 2005).

The fluid saturation level of a magma can either be directly observed in passively degassing volcanic fields, or inferred from the H₂O and CO₂ contents of melt inclusions or crystal phases whose partitioning is known (e.g., pyroxenes, apatite). Furthermore, constraining the composition of the exsolved magmatic volatile phase recently emerged as an important tool to quantify the dynamic changes prior to volcanic eruptions (e.g., Aiuppa et al., 2010; Carn et al., 2016; de Moor et al., 2016; Werner et al., 2011), and the conditions of formation of ore deposits (e.g., Catchpole et al., 2015; Harris and Golding, 2002; Rusk et al., 2008; Shelton, 1983). Determining the composition of a magmatic (to hydrothermal) volatile phase can be achieved through monitoring of passively degassing active volcanoes (e.g., Aiuppa et al., 2008; Bini et al., 2022; Bluth et al., 1993; Krueger, 1983; Shinohara, 2013), investigating mineral-hosted fluid inclusions (e.g., Audéat et al., 1998), or measuring the volatile content of melt inclusions or crystal phases whose partitioning with a fluid phase is known (e.g., Lowenstern, 1995; Métrich and Wallace, 2008).

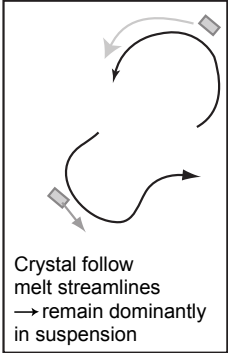
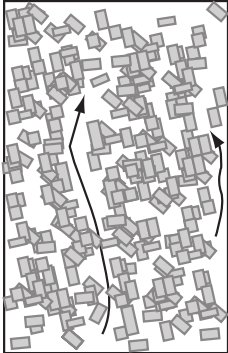
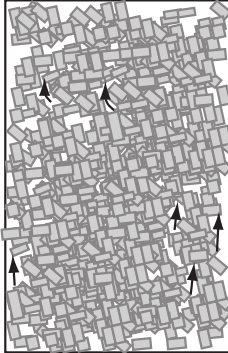
State of magma	High melt fraction Convective magma	Intermediate melt fraction Rigid crystal mush	Low melt fraction Rigid crystal mush
Silicic systems			
Mechanism for in situ crystal-melt separation	Crystal settling	Compaction with crystal repacking	Compaction with deformation of crystals
Rate of separation	Relatively fast, but disturbed by convection	Relatively slow	Very slow
Expected efficiency of crystal-melt separation	Limited	Optimal	Limited

Figure 1.3. Conceptual model of crystal-melt dynamics at different melt fractions. At high melt fraction, crystals are essentially kept in suspension by thermal convection. Locally, crystal may segregate at the base of the melt flow. As the crystal fraction approaches the mechanical lock-up (~40-60 %), crystal-melt segregation operates through compaction and crystal repacking. At even higher crystal fractions (>85 %), the low permeability hinders further crystal rearrangement, and the only mechanism allowing more melt to be segregated is crystal deformation. Figure from Bachmann and Huber (2019).

1.2.3 Crystal-melt segregation

Separating the interstitial melt from its crystalline framework represents a crucial step in generating a volcanic eruption and might be achieved through different processes as a function of the magma reservoir crystallinity. In the melt-dominated regime, where the crystallinity is lower than the rheological lock-up, the segregation of crystals from the melt operates through crystal settling (Fig. 1.3). This gravitational process typically follows Stokes' Law and is largely controlled by the size and shape of the crystals, the density contrast between the melt and the crystals, and the viscous drag (Martin and Nokes, 1989; Philpotts and Ague, 2009; Shaw, 1965; Vernon and Paterson, 2006). Therefore, crystal settling is particularly efficient in mafic magmatic systems where the melt viscosity is low, resulting in a reduced viscous drag (e.g., Boudreau and McBirney, 1997; Schmidt et al., 2012). However, this mechanism does not account for potential convection, yet important in crystal-poor systems, resulting in enhanced interaction between crystals (Faroughi and Huber, 2015; Martin et al., 1987; Nield and Bejan, 2006). Additionally, the efficiency of melt segregation is usually limited by the entrapment of significant amounts of melt (Bachmann and Huber, 2019; Lee and Morton, 2015).

The commonly endorsed paradigm states that a magma reservoir spends most of its lifespan as a crystal-rich mush (Cashman et al., 2017). Beyond the rheological lock-up, the magma reservoir behaves as a solid body, and the mechanisms allowing interstitial melt to separate from the crystals usually involve deformation of the crystal framework (Fig. 1.3). Two compaction regimes have been defined based on the deformation intensity: (1) compaction driven by a rearrangement of the crystal matrix, termed "mechanical compaction"; and (2) compaction driven by crystal deformation, termed "viscous compaction" (Holness et al., 2017; Philpotts and Ague, 2009). The efficiency of mechanical compaction is directly a function of the shape and size distribution of the crystals (Philpotts et al., 1998), with non-sphericity and grain size variation increasing the maximum packing fraction (Donev et al., 2004; Torquato et al., 2000). The occurrence of polymineralic orthocumulates is a direct manifestation of this mechanical compaction and is widespread in the rock record (e.g., Barnes et al., 2019; Deering and Bachmann, 2010; Schaen et al., 2018; Vernon, 2004). To further increase melt segregation beyond the maximum packing fraction, additional stress is required to exceed the plastic deformation threshold and reshape the crystals through viscous compaction. Experimental works have been performed to quantify the stresses required to deform crystals (Rybacki and Dresen, 2004), but natural observations are scarce due to the healing of these structures during protracted period at high temperature (Holness, 2018; Vernon, 2004; Webber et al., 2015). The required stresses to drive

these two compaction mechanisms may originate from local stress fields, magma recharge within the reservoir, and/or gas-driven filter-pressing (Barnes et al., 2016a; Bergantz et al., 2015; Holness et al., 2018; Sisson and Bacon, 1999; Vernon, 2004; Žák et al., 2007). Indeed, magma recharge and volatile exsolution are ubiquitous in crustal reservoirs and lead to local pressurisation and local shear stress. Several studies suggest that local shearing of a crystal-rich mush can lead to melt segregation (Bergantz et al., 2015; Caricchi et al., 2007; Kohlstedt and Holtzman, 2009; Pistone et al., 2013; Rabinowicz and Vigneresse, 2004). In addition, tectonic forces can also provide the required overpressure to efficiently remobilise the interstitial melt (Buck et al., 2006; Petford et al., 2000). In their review, Bachmann and Huber (2019) suggest that, taken individually, these processes are insufficient to reproduce segregation and extraction of large volumes of interstitial melt over the expected timescales of magma reservoir remobilisation prior to eruption. Instead, it is most likely a combination of these energy sources that controls the process of crystal-melt separation in magma reservoirs.

1.3 Timescales of melt segregation

Granitoids represent a fossilised telltale of the complex physical and chemical history of silicic magma reservoirs and therefore constitute a useful tool to reconstruct the time integrated thermal evolution of a building crust and provide additional constraints regarding volcanic hazards. The two principal techniques enabling the timescales of magmatic processes to be inferred are radiometric dating and intracrystalline diffusion modelling (Costa et al., 2020). Although timescales of volatile degassing and magma decompression exist in the literature (e.g., Ferguson et al., 2016), the focus of this manuscript lies on the mixing-to-eruption timescales and magma reservoir lifespans.

1.3.1 Methods

Radiometric dating

The decay of radiogenic isotopes through time represents a robust tool to accurately determine the absolute age of crystal growth and, thus, magmatic processes. Therefore, the minimum required temporal resolution must resolve timescales on the order of the magmatic process of interest. The methods able to obtain crystallisation ages with a total uncertainty smaller than 100 kyr are high-precision U-Pb zircon dating (e.g., Miller et al., 2007; Schaltegger et al., 2009; Schoene et al., 2010) and U-Th-Ra dating of bulk rocks, mineral separates and zircon (Claiborne et al., 2010; Condomines et al., 2003; Cooper

1. Introduction

and Reid, 2008; Hawkesworth et al., 2004; Reid, 2003). Upon crystallisation, U, Th and Ra are fractionated as a function of the partitioning between the host mineral and the equilibrium melt, leading to a deviation from the secular equilibrium and the start of the isotopic re-equilibration. Most studies take advantage of the relatively short half-lives of the decay of ^{238}U to ^{230}Th (75,000 years) and ^{230}Th to ^{226}Ra (1,600 years) to access timescales of hundreds to hundreds of thousands of years (Bourdon et al., 2003), encompassing typical timescales of magma reservoir processes. The ages are interpreted to represent crystal residence times before eruption. However, analysis of bulk mineral separates usually represents averaged ages between different crystal populations and zones, rendering their interpretation difficult (Cooper, 2019). High-precision U-Pb dating of single zircon grains through chemical abrasion isotope dilution thermal ionisation mass spectrometry (CA-ID-TIMS) allows determination of timescales operating in long-lived, older magmatic systems at a temporal resolution of $\sim 10,000$ years (e.g., Miller et al., 2007; Schaltegger et al., 2009; Schoene et al., 2010). Most high-precision CA-ID-TIMS studies analyse ≤ 10 whole grains per sample, and then calculate the timespan of zircon crystallisation. To robustly interpret high-precision U-Pb zircon ages and infer magma reservoir lifespan, autocrystic zircons must be distinguished from xenocrysts and antecrysts (e.g., Miller et al., 2007; Samperton et al., 2015), and the temperature of zircon saturation in the parental melt must be inferred. This is typically done by combining age distribution spectra with calculated zircon saturation (Watson and Harrison, 1983) and magma emplacement temperatures.

Intracrystalline diffusion

Diffusion chronometry uses re-equilibration of chemical disequilibria within volcanic and plutonic minerals to constrain timescales of magmatic processes (Fig. 1.4a-d) such as mixing-to-eruption times or cooling rates (e.g., Costa and Dungan, 2005; Davidson et al., 2007; Devoir et al., 2021; Ginibre et al., 2007; Ubide and Kamber, 2018). The extent of chemical disequilibrium is constrained through *in situ* quantification of zoning patterns using different analytical techniques depending on the desired spatial resolution and the concentration level of the elements of interest. These compositional gradients can result from: (1) interface-controlled crystal growth during melt differentiation, in which case the resulting gradient is smooth (e.g., Pearce, 1987; Shea et al., 2015); (2) diffusion-controlled crystal growth leading to sharp, oscillatory zoning (e.g., Faure et al., 2003, 2007; Welsch et al., 2014); and (3) open-system processes such as rejuvenation associated with reverse zoning (e.g., Bachmann et al., 2002; Cooper and Kent, 2014; Saunders et al., 2012; Sparks

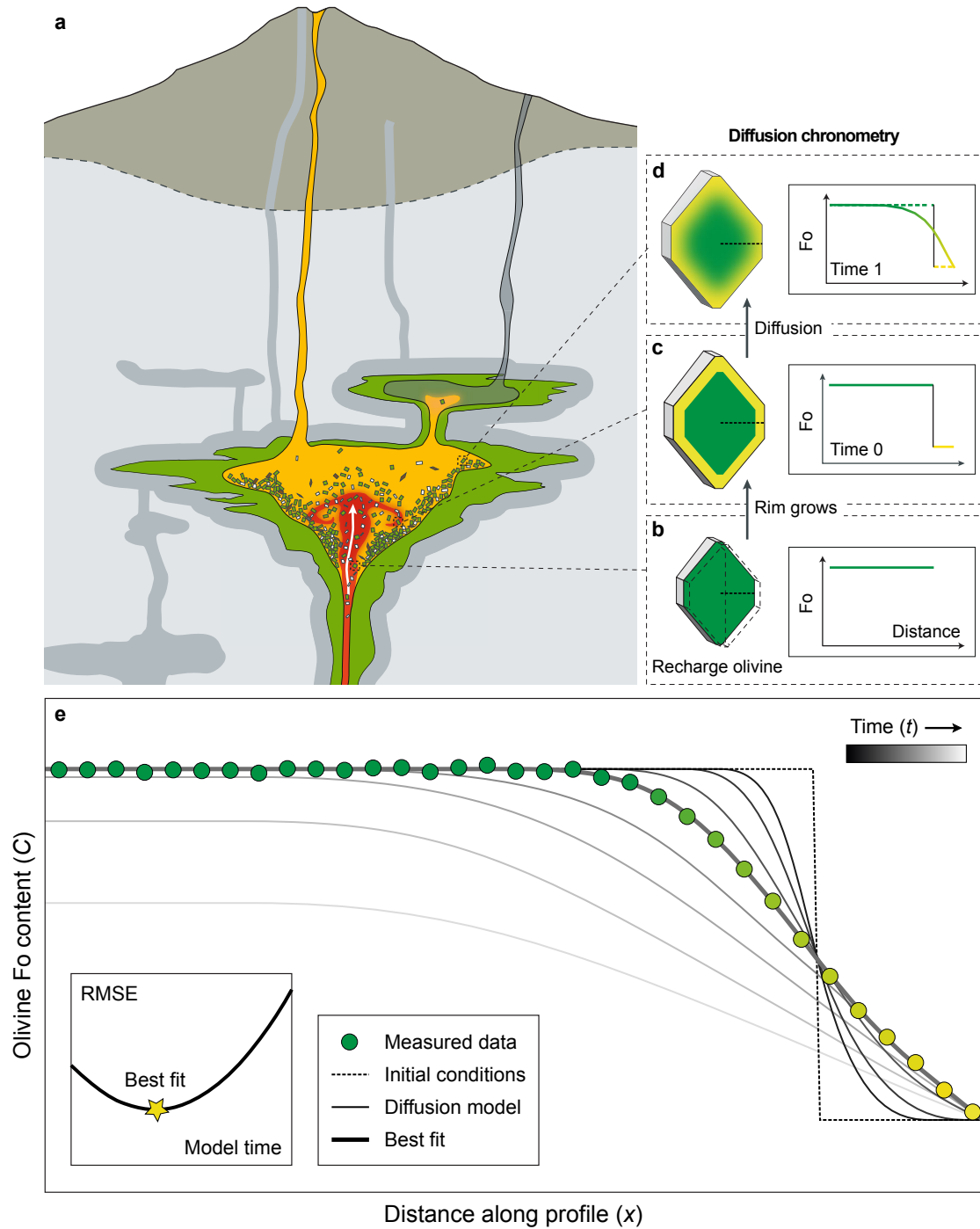


Figure 1.4. Crystal zoning re-equilibration through diffusion in a magma reservoir. **a**, Schematic of a subvolcanic magma reservoir undergoing magma recharge leading to different crystal populations. **b**, Forsterite-rich olivine crystallises as a response to mafic magma recharge and has a flat forsterite (Fo) profile. **c**, As crystallisation-differentiation operates, a more differentiated, Fo-poor olivine rim grows on the Fo-rich core. **d**, At the onset of the rim growth, the magmatic clock starts and the Fo content of the olivine core and rim chemically re-equilibrates through diffusion. **e**, Modelling of diffusion re-equilibration as a function of time. When the initial conditions prior to diffusion, boundary conditions and diffusion coefficient of the element of interest are known, the diffusion time can be calculated by solving the diffusion equation and minimising deviation from the measured data. Figure modified from [Costa et al. \(2020\)](#).

1. Introduction

et al., 1977). Therefore, the development of compositional zoning in minerals causes high-temperature diffusion of chemical species during magma storage as the system tends to re-equilibrate (Fig. 1.4e). If the storage temperature, the diffusivities (D) and concentrations (C) of the species of interest are known, one is able to calculate diffusion time (t) using Fick's second law of diffusion defined by Eq. 1.1:

$$\frac{\partial C}{\partial t} = D \frac{\partial^2 C}{\partial x^2} \quad (1.1)$$

where x is the distance along the measured profile. The determination of robust diffusion coefficients represents a key requirement to successfully model and retrieve diffusion timescales. Diffusion coefficients are typically experimentally determined by annealing a crystal in contact with a powder doped in the element of interest for a pre-defined amount of time (e.g., Cherniak and Watson, 1994). In addition to temperature, other parameters are routinely investigated, such as pressure (e.g., Bloch et al., 2015; Van Orman et al., 2001), crystal orientation (e.g., Cherniak and Watson, 1994; Dohmen et al., 2016; Giletti and Casserly, 1994), oxygen fugacity (e.g., Jollands et al., 2016a), water fugacity (e.g., Costa and Chakraborty, 2008; Farver and Yund, 1991; Yund and Snow, 1989), major element activity (Bloch et al., 2019, 2022; Zhukova et al., 2014), diffusant concentration (Jollands et al., 2020, 2023), and reveal the complexity of diffusion mechanisms in some minerals. The initial temperature, determined using geothermometers or phase equilibria, exerts a strong influence on the retrieved timescale, owing to the temperature dependence of diffusion coefficients. As such, a detailed petrographic study defining the crystallisation temperature and the initial concentrations of the crystal of interest must be undertaken prior to modelling diffusion profiles.

1.3.2 Timescales of magmatic processes

Retrieved timescales using U-Pb and U-Th-Ra dating

High-precision U-Pb CA-ID-TIMS dating of zircon has been performed for numerous intermediate to felsic magma reservoirs, ranging from rather small magmatic systems to large-volume magma bodies beneath caldera-forming volcanic systems (Fig. 1.5). The retrieved timescales are systematically comprised between $>10^4$ and 10^6 years regardless of the size of the magmatic system (e.g., Broderick et al., 2015; Coleman et al., 2004; Schaen et al., 2021; Schoene et al., 2012; Szymanowski et al., 2023; Tavazzani et al., 2023; Wotzlaw et al., 2014). In addition, no clear difference emerges between timescales obtained on volcanic products and plutonic rocks. These timescales represent the timespan of zircon

saturation and crystallisation in the melt and are interpreted as reflecting the magma reservoir lifespan prior to eruption or complete solidification. This indicates that zircon crystals in individual samples can record much of the magma reservoir history (Cooper, 2019). Interestingly, these timescales are similar to the time necessary for upper crustal silicic magma reservoirs to reach thermal maturation based on thermal modelling (Annen, 2009; Caricchi et al., 2014a; Karakas et al., 2017; Weber et al., 2020).

Dating of single accessory minerals (mostly zircon) from recent volcanic products using the decay of ^{238}U to ^{230}Th yields ages ranging from $\sim 10^4$ to $>10^5$ years (Fig. 1.5), the latter corresponding to the re-equilibration of the isotopic system (e.g., Claiborne et al., 2010; Cooper and Kent, 2014; Cooper, 2015; Schmitt et al., 2010; Shane et al., 2012). These ages are, unsurprisingly, similar to the high-precision U-Pb zircon ages. However, ^{238}U - ^{230}Th ages of mineral separates are usually lower than the corresponding ^{238}U - ^{230}Th zircon ages, with more than 50 % of the mean ^{238}U - ^{230}Th bulk crystal ages younger than 10^4 years (Cooper, 2015). Finally, ^{230}Th - ^{226}Ra ages of mineral separates are usually younger than the maximum time before isotopic re-equilibration ($\sim 10^4$ years) and sometimes yield different ages compared to the corresponding ^{238}U - ^{230}Th ages (Cooper et al., 2001; Cooper, 2015; Volpe and Hammond, 1991). Although the interpretation of such discordant ages is difficult (Cooper and Reid, 2003; Sims et al., 2013), this provides evidence for multistage crystallisation in magma reservoirs highlighting their dynamic nature.

Retrieved timescales using diffusion chronometry

Diffusion studies take advantage of the large occurrence of olivine in mafic erupted products and the availability of experimentally determined diffusion coefficients for major, minor and trace elements. These works typically use olivine, pyroxenes and/or plagioclase phenocrysts exhibiting normal or reverse rim zoning interpreted as rejuvenation prior to mush remobilisation and eruption. Mixing-to-eruption timescales have been calculated for many active volcanoes erupting mafic materials (e.g., Etna, Eyjafjallajökull, Kīlauea, Piton de la Fournaise, mid-ocean ridges) and are comprised between $\sim 10^{-1}$ and $\sim 10^0$ years (Fig. 1.5) (e.g., Albert et al., 2019; Kahl et al., 2011, 2023; Lynn et al., 2017; Moore et al., 2014; Mourey et al., 2023; Pankhurst et al., 2018; Rae et al., 2016). In addition, longer timescales ($\sim 10^0$ - 10^1 years) are obtained based on Mg# zoning in clinopyroxene from Stromboli (Petroni et al., 2018) and Sr zoning in plagioclase from different mid-ocean ridge segments (Zellmer et al., 2011). These timescales are confirmed by monitoring signals (e.g., degassing fluxes, seismic data) at restless volcanoes, thus improving volcanic hazard forecasting through petrology (e.g., Rasmussen et al., 2018; Saunders et al., 2012).

1. Introduction

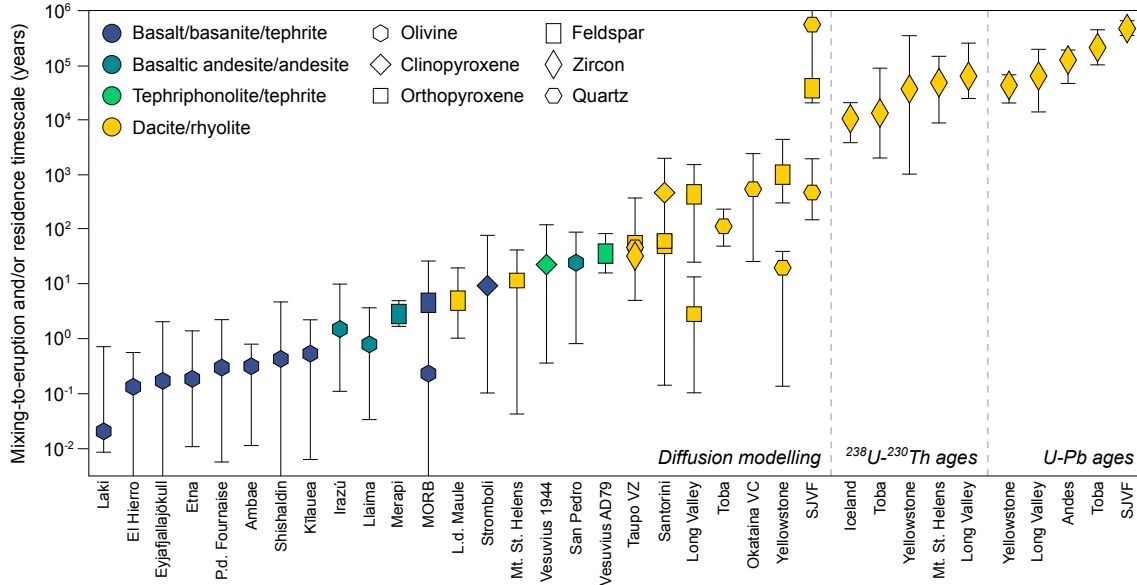


Figure 1.5. Compilation of mixing-to-eruption magmatic timescales and crystal residence times that have been obtained from different magmatic systems worldwide using diffusion modelling and zircon dating. Symbol shapes represent different minerals and symbol colours correspond to magma compositions. Mixing-to-eruption timescales increase from a few weeks to years in mafic systems to decadal to centennial timescales for felsic melt compositions. Longer diffusion timescales obtained for the San Juan Volcanic Field (SJVF) using the slow Ti-in-quartz diffusion coefficients (Jollands et al., 2020) and Mg-in-sanidine might instead represent residence times prior to eruption. The mineral ^{238}U - ^{230}Th and zircon U-Pb ages span 10^4 to 10^6 years and are usually interpreted as residence times prior to eruption. Figure modified from Costa et al. (2020). Additional magmatic systems used in this compilation include: Andes (Schaen et al., 2021); Iceland (Carley et al., 2011); Long Valley (Chamberlain et al., 2014b; Reid et al., 1997); Mount St. Helens (Claiborne et al., 2010; Cooper and Reid, 2003); San Juan Volcanic Field (SJVF) (Brückel et al., 2023; Schmitz and Bowring, 2001); Yellowstone caldera (Vazquez and Reid, 2002; Wotzlaw et al., 2014); Younger Toba Tuff (Reid and Vazquez, 2017; Szymanowski et al., 2023; Vazquez and Reid, 2004).

The impact of explosive, caldera-forming, silicic eruptions on Earth’s climate, evolutionary biology, and human society (e.g., Oppenheimer et al., 2011; Self, 2006; Sigl et al., 2015) led scientists to deeply investigate the timescales linked to these catastrophic events to potentially mitigate future volcanic hazards. The diverse mineralogy of most silicic volcanic rocks allows application of diffusion on a range of minerals and elements, such as Ba, Sr and Mg in feldspars, Ti in quartz, and Mg# in pyroxenes. Similar to mafic systems, these studies largely focused on crystals showing normal or reverse zoning close to their outermost rim. The reported timescales between magma recharge and eruption are, however, longer than for mafic volcanoes and range from $\sim 10^0$ and $\sim 10^3$ years (Fig. 1.5) (e.g., Chamberlain et al., 2014a; Druitt et al., 2012; Flaherty et al., 2018; Lubbers et al., 2022; Rubin et al., 2017; Saunders et al., 2012; Till et al., 2015). In addition, some studies also investigated Ti-in-quartz diffusion profiles measured in crystal mantles to cores from historical eruptions (e.g., Bishop Tuff, Taupo volcanic zone, Younger Toba

Tuff) and report similar timescales ($\sim 10^1$ - 10^3 years) as the ones modelled from outermost crystal rims (Gualda et al., 2012; Matthews et al., 2012; Wark et al., 2007). These results contrast with the longevity of magmatic systems inferred from high-precision U-Pb zircon ages (e.g., Szymanowski et al., 2023) and thermal modelling (e.g., Annen, 2009) and potentially highlight extensive remobilisation and dissolution of major phases through the magma reservoir lifespan. However, recent natural and experimental studies attempting to revisit Ti diffusion in quartz concluded that diffusion operates at slower rates than previously thought (Audétat et al., 2021, 2023; Jollands et al., 2020). Discussions and comparisons of the different diffusion coefficients are still ongoing (e.g., Boro et al., 2021; Brückel et al., 2023; Wang et al., 2023), but the slower diffusion rates reconcile the quartz diffusion timescales with high-precision zircon ages, quartz growth rates (Bindeman, 2003; Christensen and DePaolo, 1993), and thermal modelling. Since quartz represents the most studied phase in felsic systems, this has profound implications for the interpretation of diffusion timescales calculated for these explosive eruptions.

1.3.3 Some complications and considerations

Zircon ages

The interpretation of timescales obtained from high-precision U-Pb zircon dating has several caveats. The first consideration lies in the analysed material; whole grain ages produced by CA-ID-TIMS analysis are inevitably biased toward the second half of the zircon crystallisation interval, regardless of the zircon growth rate (Curry et al., 2021; Klein and Eddy, 2023). In addition, zircon grains are often found included within other silicate phases, which are termed “armoured zircon,” therefore hindering further growth and displacing the zircon whole grain age toward older ages (Clarke et al., 2022; Klein and Eddy, 2023). Nucleation and growth rates also lead to different age distributions but are poorly constrained and difficult to evaluate for each magmatic system. Finally, to interpret an age distribution as representing the lifespan of a magma reservoir, every analysed grain must have crystallised from the same parental magma and at the emplacement level. To determine the zircon crystallisation conditions, the zircon saturation temperature is routinely calculated based on the equilibrium melt composition (e.g., Watson and Harrison, 1983) and must be compared to the magma temperature upon emplacement. However, evaluating the equilibrium state between zircon and melt might be difficult, especially in plutonic rocks, and the temperature of magma emplacement is typically based on numerous assumptions and associated with relatively large uncertainties. Furthermore, the zircon saturation temperature is potentially crossed multiple times in dynamic magmatic systems,

1. Introduction

hence forming zoned crystals with a protracted crystallisation history, sometimes starting prior to emplacement when zircon saturation is reached at greater depths (Gaynor et al., 2022; Miller et al., 2007).

The occurrence of apparent discordant ages between ^{238}U - ^{230}Th and ^{230}Th - ^{226}Ra obtained on the same mineral separates has been a matter of debate (Cooper and Reid, 2003, 2008; Cooper, 2015; Sims et al., 2013; Turner et al., 2003). The most straightforward explanation is based on the open-system nature of most magmatic systems, whereby some crystals reside for prolonged times within magma reservoirs and may coexist with younger crystals originating from magma recharge events (Cooper and Reid, 2003; Sims et al., 2013). In such a scenario, the bulk ^{238}U - ^{230}Th ages would represent a mixing between an old component with an apparent maximum age of 350,000 years corresponding to the isotopic equilibrium, and a younger component. On the other hand, younger ages obtained using the ^{230}Th - ^{226}Ra system result from the same mixing between old crystals with an apparent maximum age controlled by the isotopic equilibrium ($\sim 10,000$ years) and younger crystals. Altogether, this highlights the dynamic and open-system nature of most magmatic systems, and the difficulty to interpret accessory phase and bulk major phase ages.

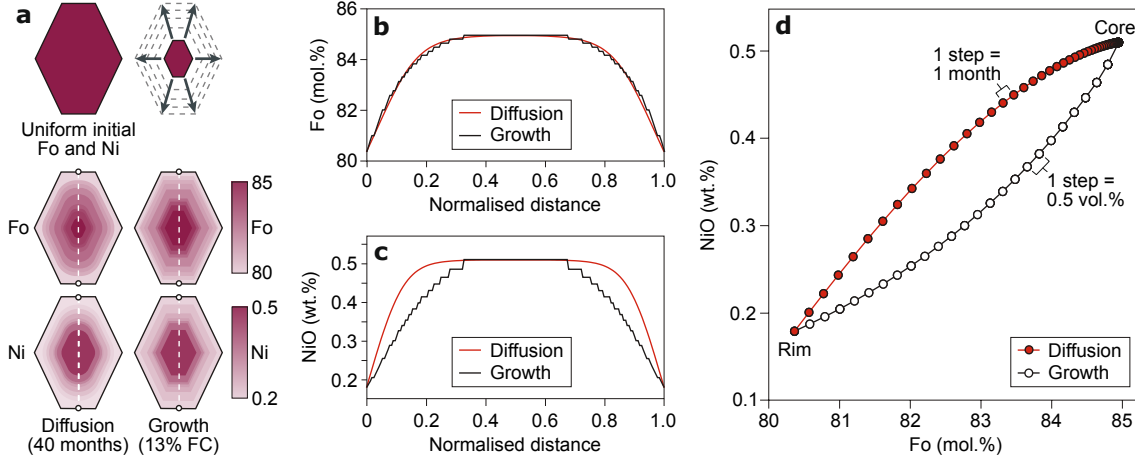


Figure 1.6. Comparison of the effects of diffusion re-equilibration and crystal growth. **a**, Modelled concentration gradients obtained after growth (13 % fractional crystallisation) or diffusion (40 months at 1,200 °C) in olivine. **b**, One-dimension Fo zoning patterns in olivine resulting from growth and diffusion re-equilibration. Note the very similar profiles for both mechanisms. **c**, One-dimension Ni zoning patterns in olivine resulting from growth and diffusion re-equilibration. Note the different effects of diffusion and growth on the olivine Ni zoning. **d**, The difference between growth and diffusion in olivine can be appreciated on a plot of Fo vs. Ni, where crystal growth has a concave shape, whereas the diffusion trend is convex. Figure modified from Costa et al. (2020).

Crystal growth versus diffusion re-equilibration

Chemical gradients within minerals usually result from a combination of crystal growth and diffusion re-equilibration at variable temperature conditions (Fig. 1.6). Therefore, assuming that zoning patterns are the result of diffusion alone represents a simplification of natural systems. This is especially the case for fast-diffusing elements incorporated in crystals with slow growth rates and short residence times. Distinguishing between crystal growth and diffusion as well as ascertaining the amount and rate of crystal growth requires careful petrographic observations. Multi-element concentration profiles allow distinction between growth- and diffusion-dominated chemical gradients, resulting in different curve tendency when plotting two elements with contrasting diffusivities and partitioning (e.g., de Maisonneuve et al., 2016; Gordeychik et al., 2020; Shea et al., 2015). For example, Costa et al. (2020) modelled the effect of diffusion and fractional crystallisation on the Fo and Ni zoning pattern of an olivine (Fig. 1.6). The two resulting Fo profiles are undistinguishable, while diffusion and growth have different effects on the Ni compositional zoning. In another case, Till et al. (2015) used fast-diffusing and slow-diffusing elements to unravel the origin of sanidine zoning. The measured concentration profiles from elements having contrasting diffusivities (Sr, Ba and Mg) resemble smoothed step-function with similar widths, ruling out diffusion from an initial step function. Instead, the authors have considered the time required for the Sr concentration profile (fast-diffusing element) to diffusively diverge from the Ba concentration profile (slow-diffusing element). This method allows to place an upper limit on the timescales between the start of rim growth and the time of eruption.

Uncertainties of diffusion timescales

Previous studies demonstrated that the uncertainty of modelled diffusion timescales is controlled by the temperature (Fig. 1.7) and the parameters describing diffusion coefficients (Costa et al., 2008; Costa and Morgan, 2010), that is the pre-exponential factor ($\log_{10}D_0$) and the activation energy (E_a). Diffusion coefficient parameters are usually extracted from experimental data and typically follow an Arrhenius law following Eq. 1.2:

$$\log_{10} D = \log_{10} D_0 - \frac{E_a}{2.303RT} \quad (1.2)$$

where R is the universal gas constant ($\text{J mol}^{-1} \text{K}^{-1}$) and T is the temperature (K). Since the slope and intercept of a linear regression are related to each other, the uncertainties associated with E_a and $\log_{10}D_0$ are strongly covariant (Mutch et al., 2021; Wu et al., 2022). Previous studies attempting to quantify the uncertainty associated with diffusion

1. Introduction

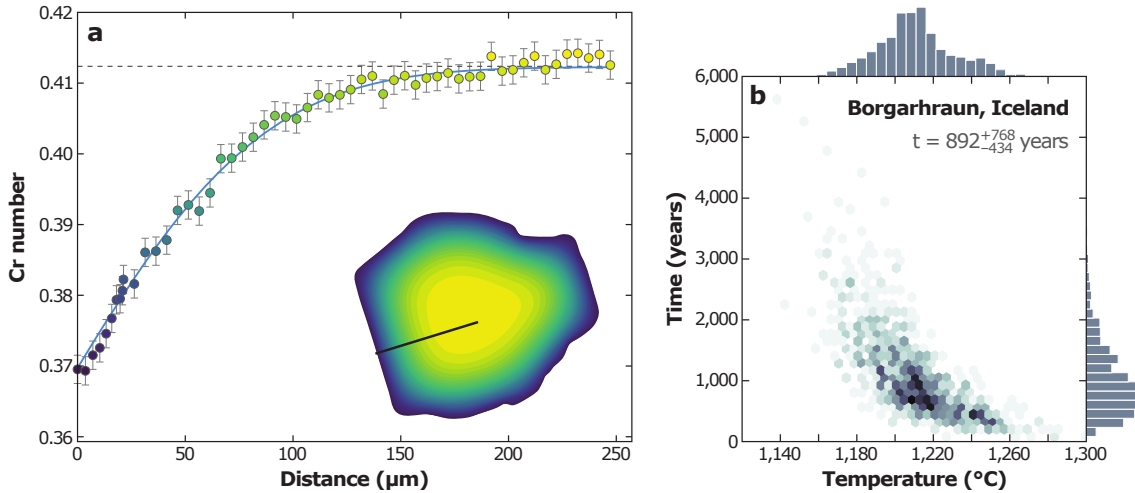


Figure 1.7. Example of error propagation during modelling of diffusion re-equilibration of a spinel from Borgarhraun (Iceland). **a**, One-dimension spinel Cr-number [Cr# = molar Cr/(Cr + Al)] profile measured by electron probe microanalysis. The blue curve represents the modelled best fit to the measured data, while the dashed line corresponds to the initial concentrations. **b**, Temperature-time density plot highlighting the importance of considering the temperature uncertainty when calculating timescales through diffusion modelling. Figure from [Mutch et al. \(2019\)](#).

modelling assumed an independent uncertainty structure of the diffusion parameters, leading to significant uncertainty overestimations ([Hartley et al., 2016](#); [Ruprecht and Plank, 2013](#)).

Crystallisation temperatures are typically determined using geothermometers and/or phase equilibria modelling and have uncertainties commonly ranging from ~ 20 to ~ 50 °C. Additionally, most studies investigating mixing-to-eruption timescales assume a constant temperature through diffusion re-equilibration. Although the effect of such an assumption cannot be quantified, it probably represents a negligible part of the uncertainty budget since the temperature uncertainty most likely encompasses potential thermal oscillations.

In addition, [Wu et al. \(2022\)](#) include the quality of the curve fitting as part of their uncertainty budget. In the application of their diffusion model, they highlight that the curve fitting may account for up to ~ 80 % of the uncertainty budget. However, they systematically use a step-like initial profile which does not account for the potential coeval crystal growth. It is unclear which parameter would affect most the total uncertainty, and whether these two potential sources of uncertainty would be covariant.

1.4 Rationale

As demonstrated in the previous sections, constraining the physicochemical evolution of intermediate to felsic magma reservoirs and its associated timescales represents a scientific

and societal challenge. Diffusion chronometry, coupled with detailed petrographic observations, has proved to be a robust approach to unravel mixing-to-eruption timescales. Yet, its design is quite recent as most studies have been conducted in the past ten years and only focus on volcanic rocks (e.g., Chamberlain et al., 2014a; Rubin et al., 2017; Shea et al., 2015; Till et al., 2015). In addition, the potential impact of an exsolved magmatic volatile phase on the magma chemical budget and melt segregation process is poorly constrained from the rock record. Consequently, the volatile budget and crystal-melt segregation timescales of now-frozen magma reservoirs require more complete understanding.

The work presented in the manuscript focuses on the Adamello batholith located in the southernmost part of the Eastern Central Alps (Italy), the largest exposure of the calc-alkaline magmatism across the Alps. A critical feature of this incrementally built batholith lies in the detailed petrographic characterisation and dating of each magmatic unit (e.g., Blundy and Sparks, 1992; Callegari and Brack, 2002; Schoene et al., 2012; Ulmer et al., 1983). New field, structural, petrological and geochemical data from host tonalite, crystal accumulation zones, and segregated felsic melt from the central and southern Adamello, in conjunction with a new set of plagioclase diffusion coefficients, are used to (1) identify a biotite-producing peritectic reaction controlling the final differentiation of the crystallising melt, (2) quantify the amount of segregated melt within a magma reservoir, (3) infer the timescales of melt segregation and associated cooling rates, and (4) constrain the volatile budget in the crystal-melt-fluid system.

1.5 Geological background

1.5.1 The Western Alps

General overview

The Alps of Western Europe (Fig. 1.8) are part of the Mesozoic to Cenozoic collisional Alpine orogenic system extending over 8,000 km from the Atlas Mountains to the Himalayas. It developed as a result of the convergence between the African-Adriatic and European continental margins leading to the closure of the Piemonte-Liguria oceanic domain and subsequent continental underplating (e.g., Handy et al., 2010; Schmid et al., 2004; Stampfli et al., 1998).

At 170 Ma, spreading of the Piemonte and Liguria (hereafter termed “Neotethys”) oceans, separated by a transform fault, started and separated Europe from Africa in the west, and from the Adria microplate, corresponding to the present-day Austroalpine domain, in the east (Dewey et al., 1973; Laubscher and Bernoulli, 1977). Simultaneously,

1. Introduction

rifting and continental break-up took place within the European plate, leading to the formation of the Valais ocean and the separation of the Briançonnais unit (Müntener et al., *in prep*; Ribes et al., 2020). This is in contrast with previous studies whereby the Valais ocean was interpreted to start opening after the Neotethys ocean (e.g., Handy et al., 2010). Spreading ceased at ~ 150 Ma as a result of stress redistribution caused by opening of the southern North Atlantic (Müntener and McCarthy, 2024). Important geodynamic regime modifications occurred in Late Cretaceous with the onset of the southward subduction of the Piemont and Valais parts of the Neotethys ocean beneath the African and, later, Adriatic plates, followed by the subduction of the Liguria ocean (e.g., Lahondère and Guerrot, 1997; Michard et al., 2002; Puga et al., 2011). These tectonic events coincide with the first stage of subduction in the Betic Cordillera (Elter and Pertusati, 1973; Michard et al., 2002). Subduction triggered magmatism through slab dehydration and fluid-assisted mantle wedge melting, evidenced by the occurrence of calc-alkaline plutonic bodies along the Periadriatic fault system (Fig. 1.8), such as the Adamello batholith (43–32 Ma), the Bregaglia pluton (32–30 Ma), and the Traversella pluton (31 Ma). The entry of the negatively buoyant European continental crust into the subduction trench at 35 Ma coupled with anticlockwise rotation of the Ligurian plate resulted in the typical Alpine arcuate shape (Ceriani et al., 2001; Schmid and Kissling, 2000). Although several studies based on magmatism (von Blanckenburg and Davies, 1995), seismic tomography (Piomallo and Faccenna, 2004) and sediment record (Sinclair, 1997) showed that slab break-off occurred at 30 Ma, the presence of collision-related plutons along the Periadriatic fault (e.g., Müntener et al., 2021) older than the inferred slab break-off casts doubt on such conclusions (Handy et al., 2021).

The missing volcanic arc

The current shape of the Alps preserves no clear evidence of island-arc magmatism, while collisional calc-alkaline magmatism is mostly found as small intrusive bodies along the Periadriatic fault system (e.g., Del Moro et al., 1983; Hürlimann et al., 2016) and as andesitic clasts in sediments shed from the Alpine orogeny (Lu et al., 2018; Ruffini et al., 1997). Additionally, McCarthy et al. (2018) demonstrated that no zircon older than 45 Ma occurs in sediments deposited between the initiation of subduction and the Quaternary. This result has been interpreted to reflect the absence of magmatism associated with subduction initiation, as detrital zircons represent the output of rapidly remobilised volcanic deposits (Cawood et al., 2012; Condie and Aster, 2009; Hawkesworth et al., 2010). Slab-derived fluid-mobile elements largely control mantle wedge partial melting and arc magmatism

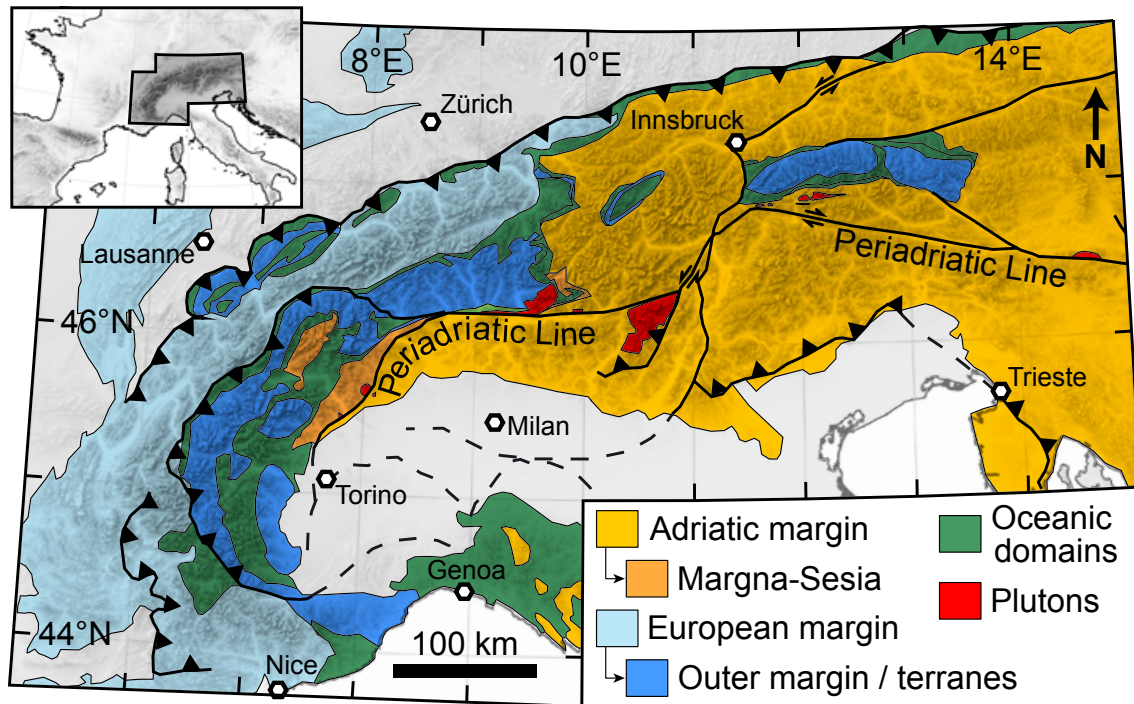


Figure 1.8. Tectonic map of European Alps showing the main paleogeographic units and the Alpine magmatism. Note that dikes along the Periadriatic Line are not represented. The ocean domains include the Valaisan and Piemont-Liguria domains, as discussed in the main text. Figure from [McCarthy et al. \(2018\)](#).

and volcanism (e.g., [Ballhaus and Frost, 1994](#); [Poli, 2015](#)). Therefore, the subduction of a dry oceanic lithosphere would potentially lead to a nearly amagmatic closure of the Neotethys ocean. Several studies stressed that the Piemont-Liguria ocean was highly serpentinised ([Barrett and Spooner, 1977](#); [Lagabrielle and Cannat, 1990](#); [Lagabrielle and Lemoine, 1997](#)), leading to a rheological interface and, hence, the development of large detachments to accommodate the Alpine convergence. This decoupling behaviour resulted in serpentinite stacking in the accretionary wedge, subduction of a dry oceanic lithosphere and, ultimately, limited subduction-related volcanism ([McCarthy et al., 2018](#)).

1.5.2 The Adamello batholith

Geographic setting

The Adamello batholith is located in the Brescian Alps of Northern Italy between the regions of Trentino-Alto Adige and Lombardy, some 150 km northeast of Milano and 100 km northwest of Verona (Fig. 1.9). It is exposed over an area of 675 km² with up to 3 km of vertical relief, making it the largest of the Tertiary intrusions encountered along the Periadriatic fault system in the Alps. Moreover, the Adamello batholith is the only Periadriatic pluton that was emplaced South of the fault system. The dextral Tonale

1. Introduction

Line to the north, which is part of the Periadriatic lineament, and the Giudicarie Line to the southeast with sinistral transpressive displacement pinch the Adamello batholith and merge at the northeastern edge of the batholith near the locality of Dimaro.

Host rock

The Adamello intruded the anchizone to metamorphic Permo-triassic cover series of the South Alps and the polymetamorphic pre-Permian basement (Fig. 1.9) (Laubscher, 1985). The Permo-triassic cover records continuous subsidence, starting from graben formation and alluvial deposits in the Permian, to generalised subsidence associated with the precipitation of evaporites followed by the formation of shallow marine carbonate platforms and deep marine pelagic sedimentation during the Triassic. Equivalent sequences were deposited along the shelf of the Neotethys ocean and are found in the Northern Calcareous Alps in Austria and in the Dolomites. The pre-Permian basement records a main pre-Alpine metamorphic event at 430-350 Ma (Mottana et al., 1985) associated with pressure-temperature conditions of 570-610 °C and 700-900 MPa estimated from the metamorphic paragenesis composed of garnet, biotite, muscovite, staurolite, kyanite, ilmenite and plagioclase (Diella et al., 1992). This Variscan event is followed by rapid uplift and subsequent greenschist facies retrogression at ~300 Ma.

Petrology

The Adamello batholith is separated into four superunits exhibiting intrusive contacts, namely Re di Castello, Adamello, Avio and Presanella. The Re di Castello superunit is subdivided into the Corno Alto, and the southern and northern Re di Castello based on lithological and compositional distinctions (Fig. 1.9). The Corno Alto, located in the eastern margin and in contact with the Avio superunit in the north, intruded the Variscan basement at 43.66 Ma, making it the oldest Adamello intrusion (Schaltegger et al., 2019). It mainly consists of granodiorite and trondhjemite having large plagioclase phenocrysts, variable amounts of quartz and alkali feldspar, and magmatic biotite and muscovite (Callegari and Dal Piaz, 1973). The well-studied southern Re di Castello displays the largest compositional diversity ranging from ultramafic cumulates, gabbro, diorite, tonalite, granodiorite, and leucotonalite (Bianchi et al., 1970; Blundy and Sparks, 1992; Brack, 1985; Colbertaldo, 1940; John and Blundy, 1993; Kagami et al., 1991; Ulmer et al., 1983) that were emplaced between 42.5 and 41.7 Ma (Broderick et al., 2015; Hansmann and Oberli, 1991; Schaltegger et al., 2009; Schoene et al., 2012; Verberne, 2013). The northern part largely comprises medium-grained, amphibole- and biotite-bearing tonalite and small vol-

umes of granite (Bianchi et al., 1970) emplaced around 39.8 Ma (Hansmann and Oberli, 1991), as well as mafic satellite bodies (Zantedeschi et al., 1989). The Re di Castello superunit is crosscut by metre- to kilometre-scale, basaltic to dacitic post-plutonic dikes dated between 41.7 Ma for the least differentiated to 38.6 Ma for the most evolved compositions (Hürlimann et al., 2016).

The Adamello superunit is subdivided into the Western Adamello tonalite and Central Adamello leucotonalite based on textural distinctions. The Western Adamello, incrementally built between 37.6 and 36.4 Ma (Floess, 2013), is composed of a homogeneous coarse-grained tonalite with plurimillimetric amphibole and columnar biotite phenocrysts. From the southern contact with the Re di Castello superunit, locally displaying schlieren-rich zones (Callegari and Dal Piaz, 1973), to the northeast, the relative proportion of biotite increases compared to amphibole. Two zones can be distinguished based on structural and

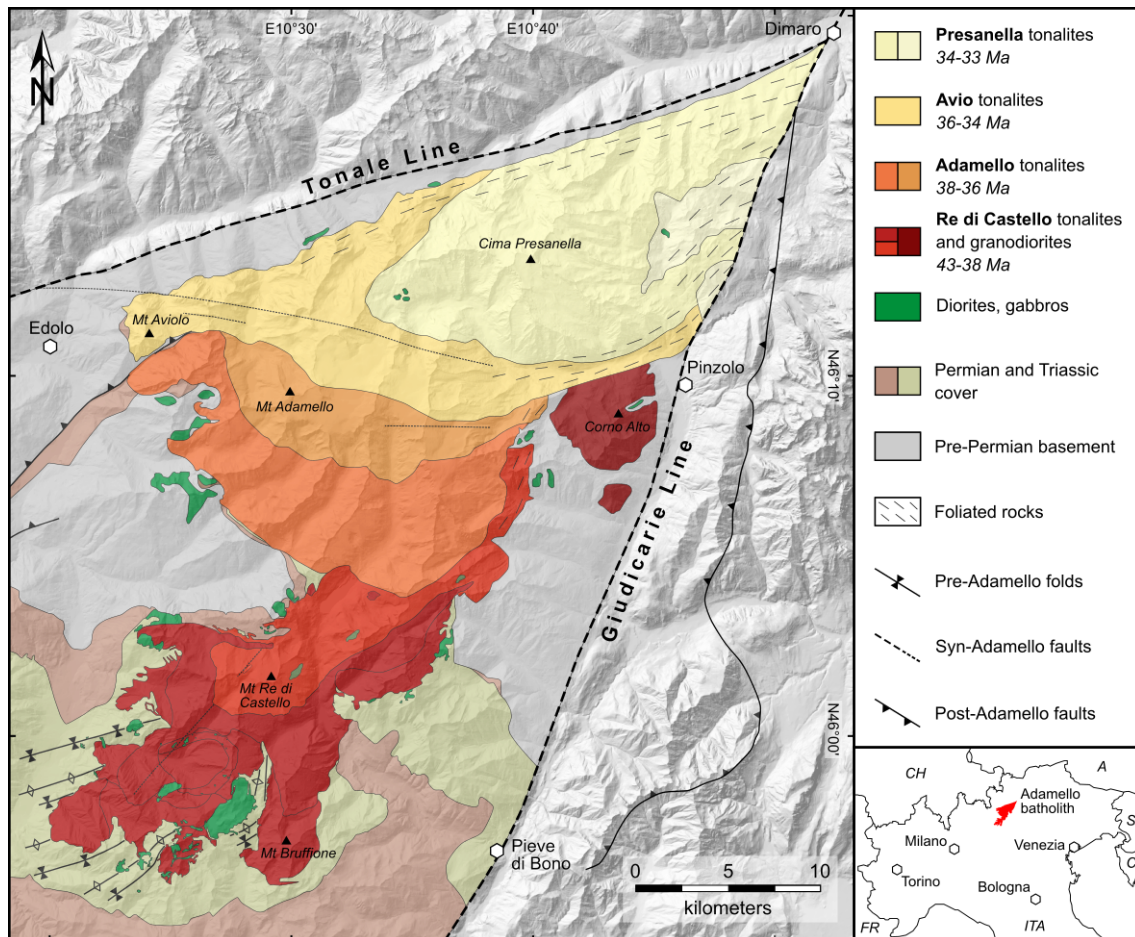


Figure 1.9. Simplified geological map of the Adamello batholith, wedged between the Tonale and Giudicarie Lines, illustrating the approximate ages (Schaltegger et al., 2019), the distinction into superunits (Callegari and Brack, 2002), and the rock types. The colours both represent the superunit subdivision and the age zoning. Figure modified from Schaltegger et al. (2009).

1. Introduction

compositional arguments (Floess, 2013; Floess and Baumgartner, 2015): (1) the southern external zone interpreted as a feeder conduit and associated with a metamorphic contact aureole; and (2) the internal zone representing magma batch accumulation. The transition to the Central Adamello leucotonalite is characterised by the progressive decrease of the amphibole abundance from >10 vol.% in the Western Adamello to ~1 vol.% in the Central Adamello (Callegari and Dal Piaz, 1973). In addition, small (<500 m) gabbroic bodies occur in the metasediments close to the southern edge of the Western Adamello tonalite (Zanettin, 1956).

The Avio superunit was built between 36.2 and 34.5 Ma (Schaltegger et al., 2019) and consists of fine-grained, locally garnet-bearing quartz-diorite and biotite-bearing tonalite (Callegari and Brack, 2002). Toward the contact with the younger Presanella superunit, the tonalite is slightly foliated and can contain amphibole. According to Stipp et al. (2004), the syn-to-post-magmatism dextral shearing along the Tonale Line led to the development of a foliation crosscutting the contact with the host rock.

The heterogeneous Presanella superunit, emplaced between 34.5 and 33.1 Ma (Schaltegger et al., 2019), is composed of medium-grained tonalite whose foliation is controlled by biotite and anhedral to euhedral amphibole, schlieren-rich zones, fine-grained mafic enclaves, and crosscutting mica-rich aplitic dikes (Callegari and Dal Piaz, 1973). The main tonalite exhibits variable textures close to the contact with the Avio superunit, suggesting magma mixing and mingling (Bianchi et al., 1970; Callegari and Brack, 2002). Similar to the Avio superunit, the syn-to-post-magmatic dextral shearing of the Periadriatic fault system led to deformation and the late development of a foliation (Grujic et al., 2011; Stipp et al., 2004).

Geochemistry

The Adamello batholith comprises a wide range of plutonic rock types from ultramafic cumulates to evolved granitoids, and subvolcanic rocks from high-Mg basalts to dacitic dikes defining a typical subduction-related calc-alkaline trend (Bianchi et al., 1970; Blundy and Sparks, 1992; Del Moro et al., 1983; Hürlimann et al., 2016; John and Blundy, 1993; Macera et al., 1983; Thompson et al., 2002; Ulmer et al., 1983; Verberne, 2013). In detail, the plutonic rocks define a calc-alkaline to high-K calc-alkaline differentiation trend as demonstrated by the intermediate to high K_2O concentrations (1-7 wt.%) and the decreasing Mg# (55-10 mol.%) with increasing SiO_2 contents (57-77 wt.%) of the Adamello granitoids. Furthermore, rare nepheline-normative, mafic dikes occur in the Blumone complex and probably result from hydrous cumulate re-melting in hot subvolcanic plumbing

systems (Pimenta Silva et al., 2023).

The progressive increase of the $^{87}\text{Sr}/^{86}\text{Sr}_i$ ratio and $\delta^{18}\text{O}$ value and decrease of the ϵNd_i value from the Re di Castello superunit (43-39 Ma) to the Presanella superunit (35-33 Ma) was interpreted as the relative increase of assimilation with time (Bigazzi et al., 1986; Del Moro et al., 1985; Dupuy et al., 1982; Kagami et al., 1991; Schaltegger et al., 2019; Taylor Jr, 1980). It was argued that, for the Re di Castello superunit, assimilation increased with differentiation. It contrasts with the study of Zantedeschi et al. (1989) where trace element and isotopic ratios were used to argue that mafic enclaves and host tonalite were cogenetic, and that most of the Sr isotopic signature was already acquired by the mafic magmas. The absence of further assimilation with differentiation is confirmed by a recent study showing constant plagioclase $^{87}\text{Sr}/^{86}\text{Sr}$ ratios with differentiation and highlighting that crustal contamination predominantly occurred before the Adamello magmas reached plagioclase saturation (Pimenta Silva et al., 2024).

Conditions of emplacement

Prior to and upon emplacement during the Alpine orogeny, the ambient pressure of the host rock is 250-300 MPa. The most robust pressure estimates rely on the metamorphic assemblage of marbles and metapelites from the pre-Permian basement and Triassic shales that underwent contact metamorphism upon magma intrusion (Floess, 2013; Floess and Baumgartner, 2013; Stipp et al., 2002; Ulmer, 1982). The presence of andalusite and Ca-poor garnet in metapelites from the Western Adamello contact aureole were used to constrain an emplacement pressure of 250-300 MPa (Floess and Baumgartner, 2013). Similar pressure estimates were made based on the metamorphic assemblage of hornfels (Riklin, 1983) from the Re di Castello superunit. Additionally, John and Blundy (1993) inferred an emplacement pressure of ~ 300 MPa based on the normative composition of aplitic dikes from the southern Re di Castello superunit. Other studies reported pressures ranging from 250 to 550 MPa based on the Al-in-hornblende barometry (Brack, 1985; Matile, 1996). However, these estimates must be taken with caution since the Al-in-hornblende barometer requires presence of a buffer assemblage (Hammarstrom and Zen, 1986; Mutch et al., 2016; Schmidt, 1992) that is rarely found, for example, in the Western Adamello lithologies. The occurrence of spinel, olivine and pyroxene inclusions in the Monte Mattoni and Blumone ultramafic cumulates has been interpreted to reflect crystallisation-differentiation at lower crustal pressures (Blundy and Sparks, 1992; Nimis and Ulmer, 1998; Ulmer et al., 1983).

The temperature of the host rock prior to magma emplacement was constrained using (1) zircon fission track data from the pre-Permian basement yielding ages of ~ 100 Ma

1. Introduction

indicating cooling to below 250 ± 50 °C with no subsequent re-heating (Viola, 2000; Viola et al., 2001), and (2) the illite crystallinity of Permian sandstones indicating upper anchizonal conditions (Riklin, 1983). The temperature of the magma intruding the Alpine upper crust was determined using geothermometers and thermal modelling. The magma emplacement temperature inferred from modelling of the thermal evolution of the Western Adamello contact aureole ranges between 850 and 950 °C (Floess and Baumgartner, 2015). This can be further refined by considering the crystallisation path of the tonalite of Malga Listino (Re di Castello) determined by Marxer and Ulmer (2019). In their experiments, the liquidus temperature was constrained at 990 °C, while ~ 45 vol.% of the melt already crystallised at 850 °C. Although the tonalite of Malga Listino is slightly less evolved than the Western Adamello tonalite, this suggests that magma emplaced at temperatures ranging from 900 to >950 °C. Ulmer (1982) estimated an intrusion temperature of 800-900 °C for intermediate melts of the southern Re di Castello superunit based on the temperature-sensitive forsterite-monticellite solvus in marbles. The composition of coexisting amphibole and plagioclase pairs has been used to determine equilibrium temperatures of 1,050-1,100 °C for hornblende-gabbro (Blundy and Sparks, 1992) and 650-780 °C for tonalites and granodiorites from the southern Re di Castello (John and Blundy, 1993). Finally, the crystallisation temperatures of olivine, spinel and pyroxene inclusions from the Mattoni and Blumone ultramafic cumulates were calculated using various geothermometers and range from 950 to 1,150 °C (Nimis and Ulmer, 1998; Ulmer et al., 1983). Given the cumulate nature of these rocks, these temperatures probably represent maximum emplacement temperatures.

Chapter 2

The role of peritectic biotite for the chemical and mechanical differentiation of felsic plutonic rocks (Western Adamello, Italy)

Chapter published in the *Journal of Petrology*:

Grocolas, T. and Müntener, O. (2024). The role of peritectic biotite for the chemical and mechanical differentiation of felsic plutonic rocks (Western Adamello, Italy). *Journal of Petrology* 65, 1–28. <https://doi.org/10.1093/petrology/egae009>

2.1 Abstract

The volcanic-plutonic connection plays a fundamental role for magmatic systems, linking crystallising plutons, volcanic activity, volatile exsolution and ore deposits. Nonetheless, our understanding of the nature of these links is limited by the scarcity of continuous outcrops exhibiting clear relationships between the plutonic roots that feed its volcanic counterpart. One way to better characterise the volcanic–plutonic connection is to quantify the amount of melt segregation within crystallising tonalitic to granodioritic plutonic rocks, and to compare those with recent silicic eruptions. Here we investigate the processes of interstitial melt segregation in the calc-alkaline Western Adamello pluton (Italy). The Western Adamello tonalite exhibits a coarse-grained, equigranular texture and is mainly composed of hornblende partially replaced by biotite, plagioclase, quartz and al-

2. *Peritectic biotite and crystal-melt segregation*

kali feldspar. Within the tonalites, several types of schlieren textures, crystal accumulation zones and dikes are found, comprising: (1) hornblende-biotite-gabbros, spatially-related to (2) plagioclase- and quartz-rich leucotonalites; and (3) quartz-, albite- and alkali-feldspar-rich domains forming aplitic to pegmatitic dikes indicative of melt segregation and extraction. Hornblende, biotite and plagioclase phenocrysts have essentially the same compositional range in the tonalites, gabbros and leucotonalites. Together with field observations, this indicates that deformation-driven crystal-melt segregation controls the modal variation within the host tonalite. The calculated melt in equilibrium with the primitive amphiboles has the same trace element composition as the host tonalite to within 5-10 %, indicating that the tonalite did not experience substantial melt loss. Quantitative modal compositions and crystallisation-differentiation calculations suggest that the evolution of the tonalite is controlled by plagioclase and hornblende crystallisation followed by a biotite-forming peritectic reaction. This peritectic reaction can be written as $\text{melt}_1 + \text{amphibole} = \text{melt}_2 + \text{biotite} + \text{quartz} + \text{plagioclase}$ and decreases the remaining interstitial melt fraction from 40 to 15 % in a small temperature interval (~ 50 °C), therefore reducing the temperature window for large-scale melt segregation. The biotite-forming reaction initiates in weakly corundum-normative compositions in low to intermediate K calc-alkaline differentiation (e.g., Western Adamello and Peninsular Ranges batholith, California), whereas it seems absent in intermediate to high K, clinopyroxene-normative melts (e.g., Tuolumne intrusive suite, California). This difference is likely controlled by the initial aluminium saturation index and the differentiation path of the parental melt within the middle to lower crust. Textural observations and mass balance models indicate that 75-88 % plagioclase and quartz and 30-70 % interstitial melt was mechanically removed from the Western Adamello tonalite to form hornblende-biotite-gabbros, whereas the leucotonalites result from the accumulation of 40-80 % plagioclase and quartz. Of the emplaced 300-400 km³ of Western Adamello tonalite, only about 0.8-2.4 km³ represent rock types related to physical segregation processes, indicating limited melt extraction. Such crystal-melt segregation processes in tonalitic to granodioritic plutons are observed worldwide and facilitate the extraction of granitic liquids. This mechanism as observed in the Western Adamello tonalite potentially contributes to the accumulation of crystal-poor rhyolites and the segregation of metal-rich brines.

2.2 Introduction

Crystallisation and segregation between crystals and interstitial melt represents the main mechanism of differentiation from the magma reservoir to the crustal scale (e.g., [Bowen](#),

1928). Although the compositional trends leading to silicic liquids are well reproduced by fractionation experiments and its resulting liquid and cumulate lines of descent (e.g., Blatter et al., 2017; Marxer et al., 2022; Müntener and Ulmer, 2018; Sisson et al., 2005), the physicochemical processes and their associated timescales allowing large melt volumes to segregate within a magma reservoir remain unclear. During cooling, the physical state of magma reservoirs changes from a liquid-dominated magma (<50 vol.% crystals) to a mush state (>50 vol.% crystals) (Cashman et al., 2017; Marsh, 1981). There is a growing consensus that magma reservoirs reside dominantly in the mush state, in good agreement with recent studies using U-series disequilibria and trace element diffusion modelling (Cooper and Kent, 2014), and zircon saturation thermometry and high resolution dating (Barboni et al., 2016). At low crystallinity (<30-40 %), the phase separation is mainly driven by the density contrast between the crystal cargo and the interstitial melt (e.g., Shaw, 1965). Nevertheless, this crystal settling mechanism usually causes the entrapment of significant amount of melt resulting in a rather limited efficiency (Bachmann and Huber, 2019; Lee and Morton, 2015). Furthermore, crystal settling is largely stunted by the exponential increase of the melt viscosity as well as, to a lesser extent, chemical convection (Faroughi and Huber, 2015; Martin et al., 1987; Nield and Bejan, 2006). At higher crystallinity (>50 %), the reservoir has a well-developed crystal framework and behaves as a near-solid body. The separation between crystals and melt is therefore controlled by local stress fields, magma recharge within the reservoir, rapid decompression in ascent conduits, and gas-driven filter pressing (Barnes et al., 2016a; Bergantz et al., 2015; Holness, 2018; Sisson and Bacon, 1999; Vernon, 2004; Žák et al., 2007). Despite our improved physical understanding regarding segregation processes, none of these can reproduce the segregation of tens to thousands cubic kilometres of melt feeding eruptions in the order of years to decades (e.g., Lee and Morton, 2015).

In plutonic rocks, this segregation process is commonly observed at different scales ranging from centimetre-sized melt pockets of haplogranite composition to high-silica granite bodies covering several square kilometres (Bachl et al., 2001; Barnes et al., 2016a; Bouilhol et al., 2015; Glazner et al., 2020; Greene et al., 2006; Hacker et al., 2008; Jagoutz et al., 2009; Lee and Morton, 2015; Otamendi et al., 2009; Vernon and Paterson, 2008). Such interstitial melt segregation must be associated with geochemically complementary cumulates. Crystal accumulation in mafic plutonic systems is well-demonstrated by field studies, for example by mono-mineral rocks and igneous layering (e.g., Kelemen et al., 1997) but also geochemically with large offsets from liquid lines of descent (e.g., Jagoutz et al., 2011). However, the identification of silicic cumulates remains elusive because of

2. Peritectic biotite and crystal-melt segregation

the large variability of granitoid textures and the often small deviation from liquid lines of descent (LLD) caused by crystal accumulation in cotectic proportions (e.g., [Deering and Bachmann, 2010](#)). Several studies based on bulk rock composition modelling and zircon saturation temperatures show that granitoids have lost up to tens of percent of melt ([Barnes et al., 2019](#); [Deering and Bachmann, 2010](#); [Lee and Morton, 2015](#)), whereas only a few authors instead argue that granitic rocks predominantly represent actual melt compositions (e.g., [Coleman et al., 2012](#)).

The goal of this contribution is to demonstrate that the rocks from the Western Adamello constitute an exemplary case of a large granitoid body with a melt composition whose LLD is largely controlled by hornblende + plagioclase fractionation followed by a peritectic reaction involving biotite and amphibole. This peritectic reaction consumes melt components and coincides with physical separation mechanisms, such as *in situ* melt segregation and crystal accumulation forming granite, hornblende-biotite-bearing gabbro and leucotonalite. We present field data and phase relationships coupled with bulk rock and mineral major and trace element compositions to demonstrate that the crystal-rich domains and the extracted melts are cogenetic with the host tonalitic body and constitute the final stage of magma differentiation. We use amphibole compositions and known partition coefficients to show that tonalite has a very similar trace element composition as the calculated parental melt. This melt composition is used to reconstruct the tonalite LLD. The differentiation model is based on detailed thin section observations, chemical maps and phase proportions and includes the peritectic origin of biotite as well as the segregation of high-silica granite leaving behind cumulative leucotonalite and gabbro. The inferred mineral assemblage and peritectic reaction are similar to crystallisation experiments performed at 200 MPa by [Marxer and Ulmer \(2019\)](#) using a slightly less differentiated tonalite from the southern Adamello. Finally, we compare our data with the Peninsular Ranges batholith (Mexico and USA) and the Tuolumne intrusive suite (Sierra Nevada, USA) and argue that both the amphibole-involving peritectic reaction and the physical separation of plagioclase, quartz, amphibole and biotite during crystal-melt segregation represent the chemical and physical processes that drive differentiation from intermediate dacitic to rhyolitic compositions.

2.3 Geological setting

The Adamello batholith, located in the Brescian Alps of northern Italy, represents the largest and oldest Tertiary calc-alkaline intrusive body in the Alps and was formed during the collision of the European and Adriatic plates (e.g., [Callegari and Brack, 2002](#)).

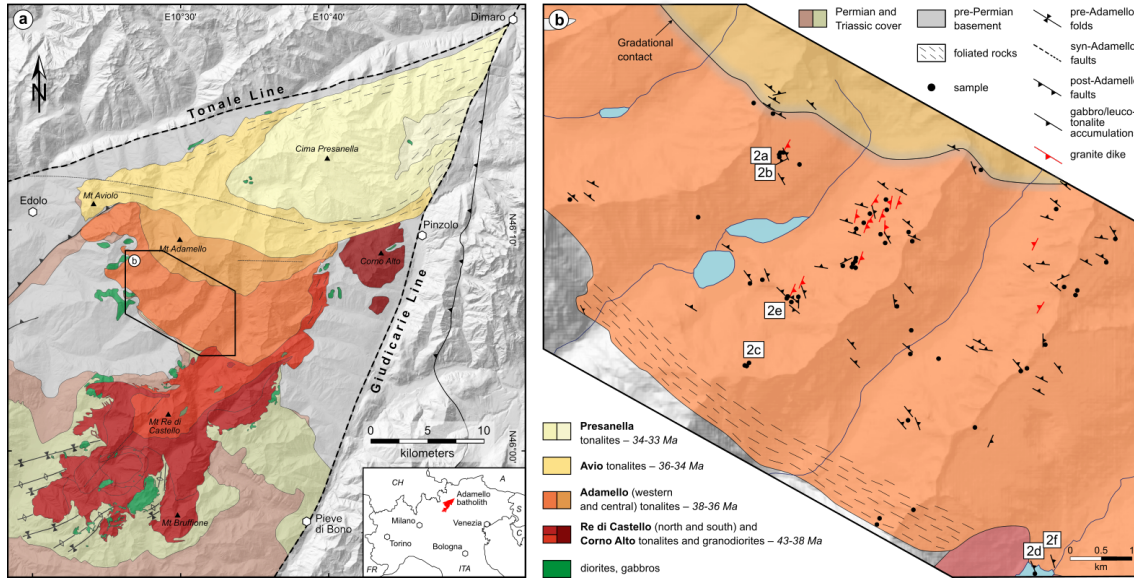


Figure 2.1. a, Simplified geological map of the Adamello batholith exhibiting the four superunits and corresponding lithologies (modified after [Schaltegger et al., 2009](#)). Location of field area is also represented. b, Geological map of the Western Adamello tonalite (modified after [Floess and Baumgartner, 2015](#)). Sample locations and orientation of magmatic structures are indicated, as well as the locations of the photographs shown in Fig. 2. Coordinates are reported using the WGS84 Coordinate System.

It is the only large Periadriatic intrusion that was emplaced south of the Alpine suture zone separating the metamorphic belt of the northeastern Alps from the Southern Alps. The Adamello pluton covers an area of $\sim 675 \text{ km}^2$ with more than 3 km of vertical relief. It is separated into four superunits exhibiting intrusive contacts, namely Re di Castello, Adamello, Avio and Presanella (Fig. 2.1a). These superunits are dominantly composed of quartz-diorite, tonalite and granodiorite, with only 1 % of hornblende and gabbro ([Ulmer et al., 1983](#)). The emplacement ages progressively decrease from South (42-38 Ma) to North (34-31 Ma) ([Del Moro et al., 1983](#); [Schaltegger et al., 2019](#)). Crustal contamination follows the same trend with a respective increase and a decrease of the $^{87}\text{Sr}/^{86}\text{Sr}$ and $^{143}\text{Nd}/^{144}\text{Nd}$ ratios towards the north, highlighting the upper crustal contribution variation with time ([Del Moro et al., 1983](#); [Kagami et al., 1991](#)). The Adamello superunit (Fig. 2.1b), located in the centre of the Adamello batholith, is separated into two distinctive zones which are the Western Adamello tonalite (WAT) and the Central Adamello leucotonalite (CAL) ([Bianchi et al., 1970](#)). The WAT is a coarse-grained, homogeneous tonalite with large abundances of amphibole and biotite phenocrysts ($\sim 20 \text{ vol.}\%$) whereas the CAL is more felsic and has distinctly lower amounts of mafic phases ($< 5 \text{ vol.}\%$). The contact between the WAT and the CAL is transitional over tens of metres with a progressive decrease of the mafic mineral content. The southeastern contact with the older North Re di Castello (RdC) unit is characterised by a sharp, contact-parallel, decimetre-to

2. Peritectic biotite and crystal-melt segregation

metre-sized fingering of the WAT within the RdC and is usually associated with schlieren-rich zones (Callegari and Dal Piaz, 1973). Satellite gabbroic to dioritic rocks are slightly older than the Adamello superunit (Callegari and Dal Piaz, 1973; Del Moro et al., 1983; Mayer et al., 2003). The WAT comprises an external zone of ~ 500 m at its southern edge exhibiting a steeply-dipping, contact-parallel magmatic foliation directly in contact with the pre-Permian basement and Triassic cover that underwent intense contact metamorphism (Floess, 2013). In contrast, the internal zone shows little to no foliation. Based on metamorphic reactions, Floess and Baumgartner (2015) modelled the thermal evolution of the contact aureole and demonstrated that the WAT was emplaced incrementally over a period of 1.2 Myr from 37.6 to 36.4 Ma (Floess, 2013) at a pressure of 250 to 300 MPa.

Fine-grained mafic enclaves (<1 vol.%) are commonly present within the WAT and, locally, form enclave swarms parallel to the external zone with concentrations reaching >50 vol.% (Blundy and Sparks, 1992). They are systematically associated with hornblende- and biotite-rich accumulation zones texturally identical to the host tonalitic body, an observation also well-described close to the contact with the RdC (Callegari and Dal Piaz, 1973), yet their relationship with the host granitoid has not been evaluated.

2.4 Field relationships and petrography

Five lithologies have been distinguished within the Western Adamello unit (Fig. 2.2). The most dominant is the tonalite which is monotonous with only slight variations of textures and phase modal proportions except in the external zone where heterogeneities in grain

Figure 2.2. Field observations of igneous rocks and structures from the Western Adamello area. **a**, Panoramic picture of a hornblende-biotite-gabbro dike in contact with the host tonalite (N46°07'35.6", E10°29'26.8"). Note that the contact of the gabbro dike with the tonalite is perpendicular to the picture view. **b**, Coarse-grained, hornblende- and biotite-bearing tonalite crosscut by a granite dike (N46°07'06.6", E10°30'25.3"). The strike and dip of the dike are also represented. **c**, Panoramic picture of a diapir-shaped hornblende-biotite-gabbro body (>10 m-wide) within the host tonalite surrounded by a high density of enclaves (N46°05'53.7", E10°28'56.6"). The inset focuses on the relationship between the enclave and the hornblende-biotite-gabbro. **d**, Host tonalite with hornblende-biotite-gabbro and leucotonalite exhibiting an undulating and irregular contact (N46°04'09.0", E10°32'18.6"). **e**, Contact between a coarse-grained, plagioclase- and quartz-rich leucotonalite dike and a porphyritic hornblende-biotite gabbro (N46°06'24.7", E10°29'30.2"). The strike and dip of the contact are also shown. **f**, Magmatic structures observed within the host tonalite, which comprise (1) accumulations of hornblende and biotite which form hornblende-biotite-gabbro, (2) accumulations of plagioclase (and quartz) forming the leucotonalite, and (3) a centimetre-sized granitic dike crosscutting, and locally parallel to, the gabbro and leucotonalite (N46°04'11.9", E10°32'32.6"). **g**, Detailed drawing of (f) with an emphasis on the magmatic structure and the granitic dike. Note the oscillating direction of the dike which indicates a ductile regime upon dike injection.

2.4. Field relationships and petrography

size and mafic phase abundances occur. Schlieren-shaped bodies and dikes of hornblende-biotite-bearing gabbros are present throughout the WAT and are intimately related to

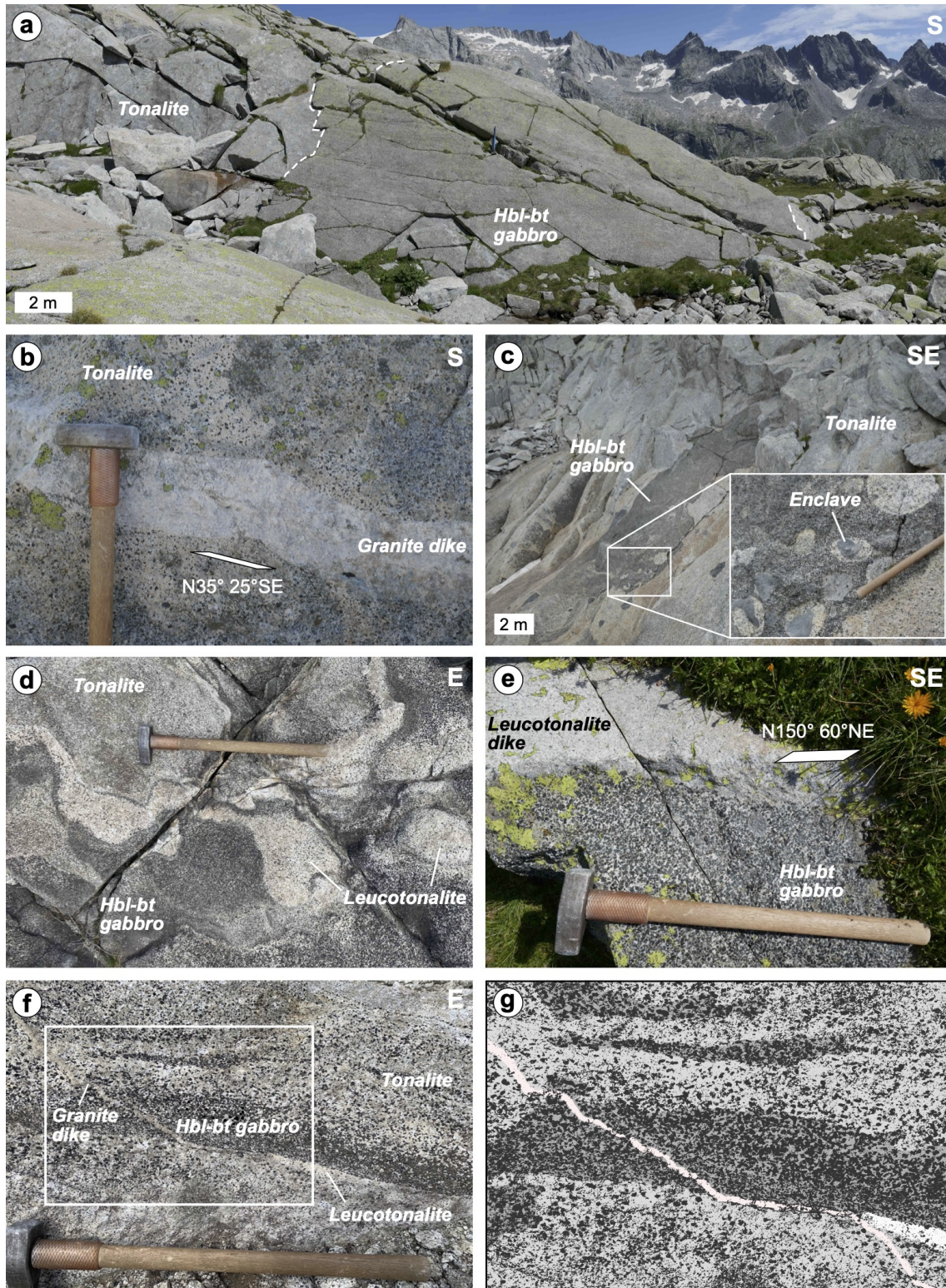


Figure 2.2. (Figure caption on previous page.)

2. Peritectic biotite and crystal-melt segregation

leucotonalites. Gabbros and leucotonalites are subparallel to the external zone. As described by [Blundy and Sparks \(1992\)](#), these hornblende- and biotite-rich zones also display an increase in mafic enclave proportions. Finally, the WAT is crosscut by dikes of granitic composition striking perpendicular to the gabbros and leucotonalites. Phase proportions of the tonalite, hornblende-biotite-gabbro, leucotonalite and granite are summarised in [Table 2.1](#).

2.4.1 Tonalite

The WAT is a coarse-grained tonalite ($\sim 60\text{-}70$ vol.% crystals >3 mm) with little to no foliation ([Fig. 2.2b,f](#)) mainly composed of hornblende (2-11 vol.%), biotite (6-15 vol.%), plagioclase (50-56 vol.%), quartz (22-30 vol.%) and alkali feldspar (2-5 vol.%) ([Fig. 2.3](#) and [Table 2.1](#)). The total proportion of hornblende and biotite is homogeneous around 17-22 vol.% but their relative abundance varies with progressive biotite enrichment relative to hornblende from south to north ([Fig. 2.3](#)). Similarly, the modal amounts of plagioclase and quartz increase towards the north from 50 to 56 vol.%, and from 22 to 30 vol.%, respectively.

Hornblende is present as subhedral to euhedral phenocrysts (3-10 mm) with no visible zoning enclosing submillimetric plagioclase, biotite, magnetite, zircon, and apatite inclusions ([Fig. 2.4a,b](#)). Two generations of biotite are observed based on their texture, size and location. The first type (Bt₁) comprises phenocrysts formed by a tightened stacking of sheets with a columnar shape very similar to the hornblendes and displays inclusions of quartz, zircon and apatite ([Figs. 2.3](#) and [2.4a,d](#)). At the microscopic scale, biotite replaces hornblende ([Fig. 2.4a](#)) and can present deformed cleavage planes ([Fig. 2.4d](#)). Smaller (1-3 mm), subhedral biotite is considered as the same biotite type. The second generation (Bt₂) is smaller (<1 mm), has a subhedral to anhedral shape, and is interstitial ([Fig. 2.4b](#)). Plagioclase crystals (>3 mm) are subhedral to euhedral and exhibit a normal or complex oscillatory zoning with rare altered, anorthite-rich cores ([Figs. 2.3](#) and [2.4f](#)).

Table 2.1. Modal proportions of the main phases in the Western Adamello determined by QEMSCAN or estimated from petrographic observations.

Rock type	Amphibole vol.%	Biotite vol.%	Plagioclase vol.%	Quartz vol.%	K-feldspar vol.%
Tonalite	2-11	6-15	50-56	22-30	2-5
Gabbro	3-40	8-45	18-36	13-18	0.5-4
Leucotonalite	0-2	1-6	44-70	16-41	3-8
Granite	<0.5	0.5-2	25-34	35-42	28-38

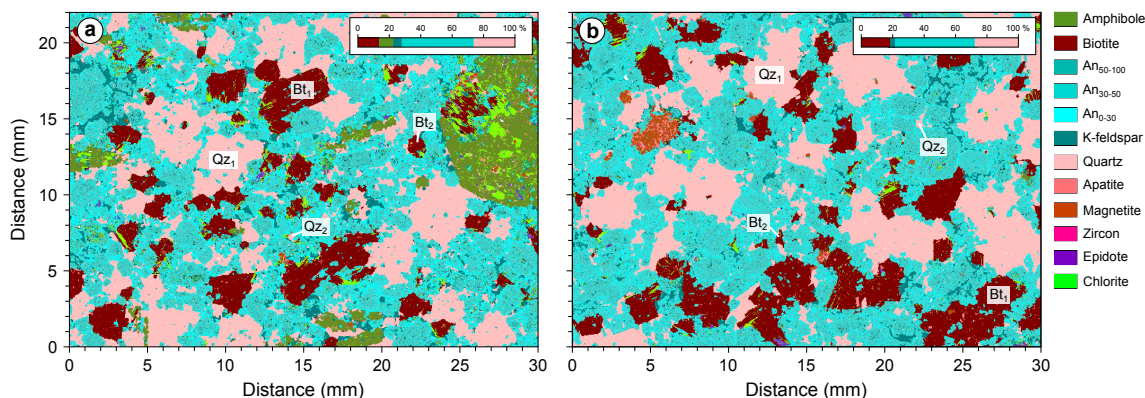


Figure 2.3. Thin section QEMSCAN maps of (a) an amphibole-rich tonalite (WA21-11; N46°07'00.1", E10°30'16.9") and (b) a biotite-dominated tonalite (CJ26; N46°07'57.1", E10°29'19.3") highlighting the two generations of quartz (Qz_1 and Qz_2) and biotite (Bt_1 and Bt_2). Note that the sum of amphibole and biotite proportions are approximately constant in both sections.

Myrmekite can occur at the rim of the plagioclase (Fig. 2.4f). In the same way, two types of quartz are identified with subhedral, rounded quartz phenocrysts (>3 mm) in contact with biotite phenocrysts (Qz_1), and smaller (<1 mm), interstitial quartz (Qz_2) in contact with plagioclase rims (Figs. 2.3 and 2.4c,f). Anhedronal alkali feldspar (0.1-2 mm) is systematically interstitial with no well-defined shape and surrounds the other phases (Fig. 2.3). The interstitial assemblage is therefore constituted of plagioclase (25-35 vol.%, including the rims), quartz (35-40 vol.%), alkali feldspar (30-35 vol.%) and biotite (~ 5 vol.%) and is identified based on the interstitial position of quartz, alkali feldspar and biotite, and on the albite-rich composition of plagioclase rims (Fig. 2.3). Reconstructed bulk chemistry based on phase proportions and mineral compositions of this interstitial assemblage corresponds to a haplogranite. Fe-Ti oxides (~ 0.5 mm) are dominated by subhedral, equant magnetite with smaller amounts of ilmenite. They are either interstitial or can be found enclosed in hornblende and plagioclase for some ilmenites, or in small aggregates along with apatite and zircon. Ilmenite is abundant in amphibole-rich, biotite-poor rocks. Apatite is euhedral and ranges from 100 to 500 μm and can be interstitial or enclosed in hornblende, biotite and plagioclase. Zircon is generally smaller than apatite (50-300 μm) and is usually included within hornblende and biotite (Fig. 2.4a) or, more rarely, interstitial. Rare titanite (100-300 μm) is found in interstitial position. Secondary phases such as epidote and chlorite partially replace hornblende and biotite, respectively, and are indicative of late-stage alteration by hydrothermal fluid upon cooling of the pluton. Locally, tonalites contain submillimetric miarolitic cavities illustrating the presence of exsolved fluids (Fig. 2.4a).

2. Peritectic biotite and crystal-melt segregation

2.4.2 Hornblende-biotite-gabbro

The WAT is locally composed of hornblende- and biotite-bearing gabbro zones sharing a similar porphyritic texture (Fig. 2.2a,c-g). The same mineralogy as the WAT is observed except that the proportion of coarse grains is higher (up to 85 vol.%), and the modal composition and crystal size distribution are different. Indeed, the gabbros are enriched in hornblende (3-40 vol.%) and biotite (8-45 vol.%) with a total abundance of 48-64 vol.%, whereas quartz (13-18 vol.%), alkali feldspar (0.5-4 vol.%) and especially plagioclase (18-36 vol.%) are less abundant (Figs. 2.2d-g and 2.4c,d, Table 2.1 and Supplementary Material 1).

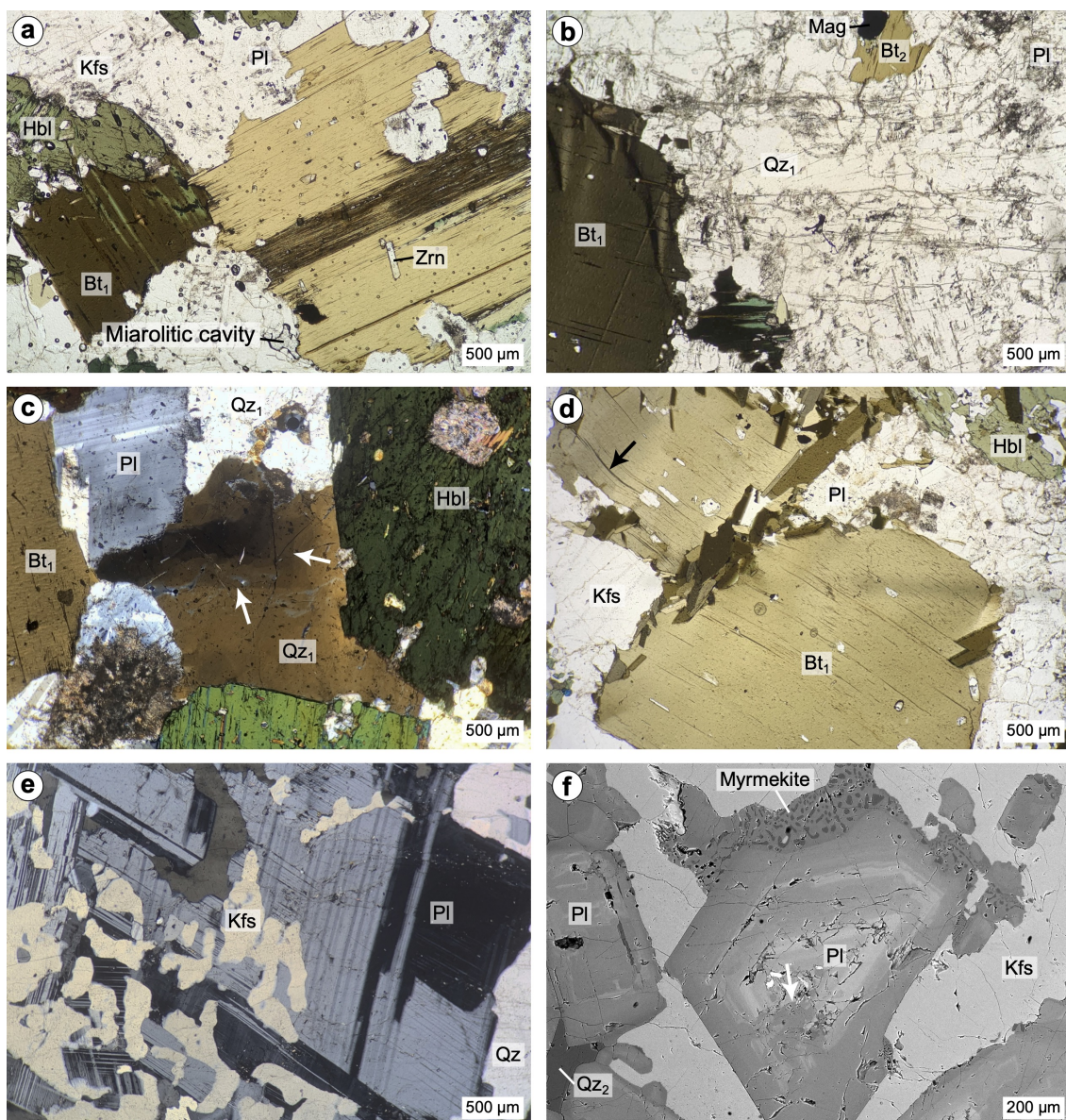


Figure 2.4. (Figure caption on next page.)

These hornblende-biotite-gabbros appear within the WAT as dikes, schlieren-shaped bodies and layered lenses striking $N132 \pm 52^\circ$ (2σ) which corresponds to a direction sub-parallel to the inferred WAT feeder conduit (Floess, 2013) (Fig. 2.1b). The gabbro dikes, ranging in thickness from 5 cm to <1 m, are usually accompanied by a leucotonalite dike (Fig. 2.2e). The contact between these two zones is sharp. Likewise, the boundary between the gabbro dikes and the host tonalite is usually sharp, but can be more gradational at the upper part of the contact (Fig. 2.2f,g). The schlieren-shaped gabbros are similar to the ones described in Blundy and Sparks (1992) and show centimetre-scale zones of hornblende and biotite enrichment within the WAT (Fig. 2.2g) to decametre-sized diapir-like bodies with decimetric mafic enclave inclusions (Fig. 2.2a,c). Finally, gabbros can develop a metre-scale, undulating layering between hornblende-biotite-rich zones and more plagioclase-rich zones (Fig. 2.2d). In this context, the hornblende-biotite-gabbro can also form larger zones of 5-30 cm. This layering is typically observed close to the contact with the older Re di Castello superunit.

Hornblende and biotite form a framework of touching minerals. Importantly, the cleavage plane deformation of biotite is much more pronounced in the gabbros relative to the WAT. Rare quartz crystals (Q_{Z1}) are 2-3 mm in size and interstitial between hornblende and biotite, consistent with a near absence of the interstitial haplogranitic assemblage. In addition, the first generation of quartz occasionally displays subgrain boundaries and undulose extinction. The minor phases also present some differences compared to the

Figure 2.4. Photomicrographs of thin sections in plane-polarised light (**a**, **b**, **d**), under crossed polars light (**c**, **e**), and backscattered electron (**f**) illustrating the mineralogy and textural features of the Western Adamello. **a**, Hornblende-bearing tonalite sample constituted of amphibole, biotite, plagioclase, quartz and alkali feldspar highlighting the peritectic transformation of amphibole phenocrysts into biotite ($N46^\circ04'34.4''$, $E10^\circ30'27.6''$). Zircon inclusions are abundant in biotite, and miarolitic cavities rarely occur in tonalite along grain boundaries. No particular systematics has been observed for the latter. **b**, Biotite-rich tonalite section with a large, slightly deformed biotite plate in contact with a quartz phenocryst ($N46^\circ07'65.4''$, $E10^\circ28'81.6''$). Magnetite is also present in the tonalite mineral assemblage. Note the difference in size between the two generations of biotite (Bt_1 and Bt_2). **c**, Hornblende-biotite-gabbro section showing hornblende and biotite phenocrysts ($N46^\circ06'41.3''$, $E10^\circ30'13.8''$). The white arrows highlight undulose extinction of quartz (Q_{Z1}) typical of intracrystalline deformation. Note the alteration of the plagioclase core. **d**, Biotite-rich gabbro exhibiting plastic deformation of biotite (Bt_1) cleavage planes emphasised by the black arrow ($N46^\circ07'38.2''$, $E10^\circ29'26.7''$). **e**, Granitic dike formed by plagioclase, quartz and alkali feldspar and exhibiting a coarse-grained texture ($N46^\circ07'17.1''$, $E10^\circ26'54.8''$). Graphic intergrowth texture between plagioclase and alkali feldspar is typically observed in the pegmatitic granite dikes. **f**, Leucotonalite thin section consisting of touching plagioclase phenocrysts surrounded by anhedral alkali feldspar oikocrysts and quartz reminiscent of interstitial melt and described as a synneusis (“swimming together”) texture (Vance, 1969) in the main text ($N46^\circ05'49.7''$, $E10^\circ32'16.0''$). Myrmekite consisting of quartz and albitic plagioclase occurs at plagioclase rims. The white arrow highlights the resorbed, anorthite-rich plagioclase core.

2. Peritectic biotite and crystal-melt segregation

WAT. Coexisting ilmenite and magnetite are sometimes associated with apatite clusters. It is important to note that magnetite and ilmenite proportions are inversely correlated, especially in the biotite-rich gabbros. Titanite ($\sim 500 \mu\text{m}$) is only observed in one sample and is associated with hornblende.

2.4.3 Leucotonalite

The hornblende-biotite-gabbros are spatially related to medium-grained, distinctly felsic zones dominated by feldspar and quartz that can locally be porphyritic because of the variable amounts of mafic phases (Fig. 2.2d-g). A similar mineralogy to the WAT is observed, albeit with drastically different mineral proportions. Indeed, the abundance of hornblende (0-2 vol.%) and biotite (1-6 vol.%) is reduced to a total of 2-7 vol.%, whereas plagioclase (44-70 vol.%) and quartz (16-41 vol.%) represent between 84 and 94 vol.% of these rocks (Fig. 2.4f, Table 2.1 and Supplementary Material 1). Finally, alkali feldspar only constitutes 3-8 vol.% of the leucotonalites.

Plagioclase-rich leucotonalitic zones, usually associated with hornblende-biotite-gabbros, occur as dikes or layers to larger zones directly in contact with other gabbro dikes and layers. These leucotonalites strike $N148 \pm 39^\circ$ (2σ) which coincides with the hornblende-biotite-gabbros and the main direction of the WAT feeder conduit (Fig. 2.1b). The leucotonalite dikes have a thickness ranging from a few centimetres up to a metre and display sharp contacts with the accompanying hornblende-biotite-gabbro and the host WAT. Leucotonalite, as mentioned previously, can form schlieren layering with the hornblende-biotite-gabbro or larger, undulating layer zones also in contact with the gabbro (Fig. 2.2d,f). The leucotonalite layers related to the gabbro interlayering are thin ($< 3 \text{ cm}$) while the larger zones range from 5 to 30 cm (Fig. 2.2e).

Plagioclase is the dominating phase of the leucotonalites, and displays similar features compared to the WAT and hornblende-biotite-gabbro except for abundant altered, anorthite-rich cores (Fig. 2.4f). Plagioclase crystals (3-6 mm) are subhedral to euhedral and are in contact with each other and form a continuous framework of touching crystals. Two quartz types are found in leucotonalites, that is quartz phenocrysts (Qz_1) and interstitial quartz (Qz_2) surrounding the other phases and in equilibrium with interstitial, oikocrystic alkali feldspar (Fig. 2.4f). Similar alkali feldspar oikocrysts are also found in the mafic enclaves (Blundy and Sparks, 1992). Such a structure of plagioclase (\pm quartz) phenocryst chains suspended in a matrix constituted of quartz and/or alkali feldspar is often referred to as a synneusis ('swimming together') structure (Vance, 1969). The difference in alkali feldspar fractions reflects the variable proportions of the inter-

stitial haplogranitic assemblage. Hornblende and biotite only occur as phenocrysts (>1 mm) and, except for a few biotite crystals, are absent from the interstitial assemblage. Accessory phases including apatite, magnetite, ilmenite and zircon are less represented in leucotonalites compared to the host WAT. These phases are either included within hornblende and biotite or in equilibrium with plagioclase phenocrysts, whereas they are never surrounded by interstitial alkali feldspar or quartz.

2.4.4 Granite

The granite displays a medium-grained, aplitic texture similar to the leucotonalites, but more often granite shows a well-developed pegmatitic texture with intergrowths of alkali feldspar with quartz or plagioclase (Fig. 2.4e). The mineral assemblage is typical of a granite with large amounts of plagioclase (25-34 vol.%), quartz (35-42 vol.%), and alkali feldspar (28-38 vol.%), and ≤ 2 vol.% of biotite and garnet (Fig. 2.4e, Table 2.1 and Supplementary Material 1). The latter is only present in dikes. Rare hornblende (<0.5 vol.%) antecrysts are inherited from the tonalite. Some aplitic dikes have mineral proportions forming a continuum between a leucotonalite and a granite with intermediate plagioclase (39-48 vol.%), quartz (30-39 vol.%), and alkali feldspar (17-18 vol.%) contents.

Aplitic and pegmatitic granites appear either as dikes intruding the host WAT (Fig. 2.2b) or as undulating dikelets originating from the host tonalite concordant or discordant to the gabbro-leucotonalite contact (Fig. 2.2f,g). The latter indicates that evolved melts are directly segregated from the host tonalite, while the thicker dikes instead represent larger volumes of extracted melt, probably from deeper levels. They strike on average $032 \pm 29^\circ$ (2σ) which is almost perpendicular to the average strike of the hornblende-biotite-gabbros and leucotonalites (Fig. 2.1b). The granitic dikes (2-40 cm thick) display sharp contacts with the WAT. The alkali feldspar-poor aplitic dikes are considered to be related to the granites because they present the same direction as the alkali feldspar-rich granites and are not found in contact with the gabbros or leucotonalites.

In aplitic granites, plagioclase, quartz and alkali feldspar (1-3 mm) are equigranular and subhedral except for euhedral, zoned plagioclases, texturally similar to plagioclase from the other rock types, which represent a second population. Biotite (0.2-3 mm) and hornblende (0.5-2 mm) are subhedral to euhedral and have the same characteristics as the ones from the host tonalite. Garnet (0.3-1.5 mm) occurs as subhedral, rounded shape crystal and usually displays radial fractures. Euhedral apatite, magnetite and zircon are included within biotite and hornblende or located at the grain boundaries. In pegmatitic granites, millimetre- to centimetre-sized plagioclase, quartz and perthitic alkali feldspar

2. *Peritectic biotite and crystal-melt segregation*

display a graphic intergrowth texture (Supplementary Material 1). Garnet shares the same features as the ones from aplitic granites. Apatite and zircon are smaller ($<250\ \mu\text{m}$) compared to the aplitic granites and display an anhedral shape, whereas magnetite is absent.

2.5 Analytical techniques

2.5.1 Quantitative evaluation of minerals by scanning electron microscopy (QEMSCAN)

Chemical mapping of 6 carbon-coated polished thin sections (2 tonalites, 2 hornblende-biotite-gabbros, 1 leucotonalite, 1 granite) was performed by automated mineral analysis and textural imaging using an FEI QEMSCAN Quanta 650F equipped with two Bruker QUANTAX energy-dispersive spectrometers at the University of Geneva. The acceleration voltage was set to 15 kV and the beam current to 10 nA. For each section, a high-resolution scan ($17 \times 17\ \text{mm}$ at $10\ \mu\text{m}$ grid) and a low-resolution scan ($30 \times 22\ \text{mm}$ at $30\ \mu\text{m}$ grid) were performed in order to obtain plagioclase composition zoning and more reliable modal compositions because of the coarse grain size, respectively. Three groups of different compositions were defined based on their anorthite contents (An_{0-30} , An_{30-60} , An_{60-100}).

2.5.2 Bulk rock chemistry

A total of 28 samples (5 tonalites, 5 hornblende-biotite-gabbros, 7 leucotonalites, 11 granites) from the Western Adamello were analysed for bulk rock major and trace elements. Rock samples were cut using a diamond saw to remove the altered crust. The fresh blocks were crushed using a hydraulic press and ground to a fine powder using a tungsten carbide mill for 3 min at $900\ \text{min}^{-1}$. A representative aliquot was heated at $1050\ ^\circ\text{C}$ in a Borel FP 1100-30 furnace for 2 h to determine the loss on ignition (LOI). The calcinated product was mixed with lithium tetraborate ($\text{Li}_2\text{B}_4\text{O}_7$) in the appropriate proportions (1:6), fused in a Pt crucible at $1200\ ^\circ\text{C}$ for 5 min in a PANalytical Claisse Eagon 2 furnace, poured into a Pt mould, and quenched in air. Bulk rock major element compositions were determined by X-ray fluorescence (XRF) using a PANalytical AXIOS^{mAX} spectrometer at the University of Lausanne. BHVO-2, JA-3, GH and RGM-2 standards were used for quality control. Uncertainties in XRF analyses are in the range of 0.4 % for a major component such as SiO_2 and 0.005 % for a minor component such as MnO. The same glass beads were crushed to only keep $\sim 4 \times 2\ \text{mm}$ pieces, mounted in epoxy, and analysed for their trace element concentrations using laser ablation inductively coupled plasma mass spec-

trometer (LA-ICP-MS). The measurements were performed using an Australian Scientific Instrument RESolution 193 nm Ar-F excimer laser interfaced to a sector field Thermo Scientific Element XR mass spectrometer at the University of Lausanne. The LA-ICP-MS system was optimised by linearly scanning the NIST SRM-612 glass standard at $10 \mu\text{m s}^{-1}$ in order to increase the spectrometer sensitivity ($^{139}\text{La}^+ > 2.5 \times 10^6$ cps) without significantly producing oxides ($^{248}\text{ThO}^+ / ^{232}\text{Th}^+ < 0.2 \%$) and doubly-charged ions ($\text{Ba}^{2+} / \text{Ba}^+ < 2.5 \%$). Three replicative measurements were done on each piece of glass bead with a laser pit diameter of $80 \mu\text{m}$ using a frequency of 10 Hz and an energy density of 6 J cm^{-2} . Helium (500 ml min^{-1}) was used as a carrier gas. Background, ablation and wash-out interval acquisition times were 70, 35 and 35 s, respectively. Dwell times range from 10 to 20 ms depending on the measured isotope. Absolute concentrations were calculated using CaO (measured by XRF) as internal reference, NIST SRM-612 as primary standard, and BCR-2G as secondary standard for quality control. Data reduction was performed with the LAMtrace software (Jackson, 2008). The average elemental abundances of the standards were taken from Pearce et al. (1997).

2.5.3 Mineral chemistry

Mineral major element compositions were determined on carbon-coated polished thin sections by field-emission gun electron probe microanalyses (FEG-EPMA) using a JEOL JXA-8530F HyperProbe equipped with five wavelength dispersive spectrometers at the University of Lausanne. The acceleration voltage was set to 15 kV, the beam current to 10 nA, and the beam size ranged from 1 to $5 \mu\text{m}$. Counting times were 30 s on the peak and 15 s on the background. Measurements were corrected with the PRZF method (Armstrong, 1995) and standardised using synthetic glasses and natural minerals.

Trace element concentrations were determined on the same polished thin sections using a sector field Thermo Scientific Element XR and a triple quadrupole Perkin Elmer NexION 5000 mass spectrometers coupled with an Australian Scientific Instrument RESolution 193 nm Ar-F excimer laser at the University of Lausanne. A similar optimisation procedure was followed, except that the target values for sensitivity ($^{139}\text{La}^+ > 1.9 \times 10^6$ cps) and doubly-charged ions ($\text{Ba}^{2+} / \text{Ba}^+ < 3.0 \%$) and oxides ($^{248}\text{ThO}^+ / ^{232}\text{Th}^+ < 0.4 \%$) production were different for the Perkin Elmer NexION 5000 mass spectrometer, as well as the carrier gases ($\text{He} = 1,000 \text{ ml min}^{-1}$, $\text{N}_2 = 1 \text{ ml min}^{-1}$). The laser pit diameter was chosen according to the grain size and mineral texture and alteration and varied between 30 and $80 \mu\text{m}$. Repetition rate was set to 10 Hz independent of the analysed phase, while the energy density varied between 6 J cm^{-2} for amphibole, biotite and Ca-rich plagioclase

2. Peritectic biotite and crystal-melt segregation

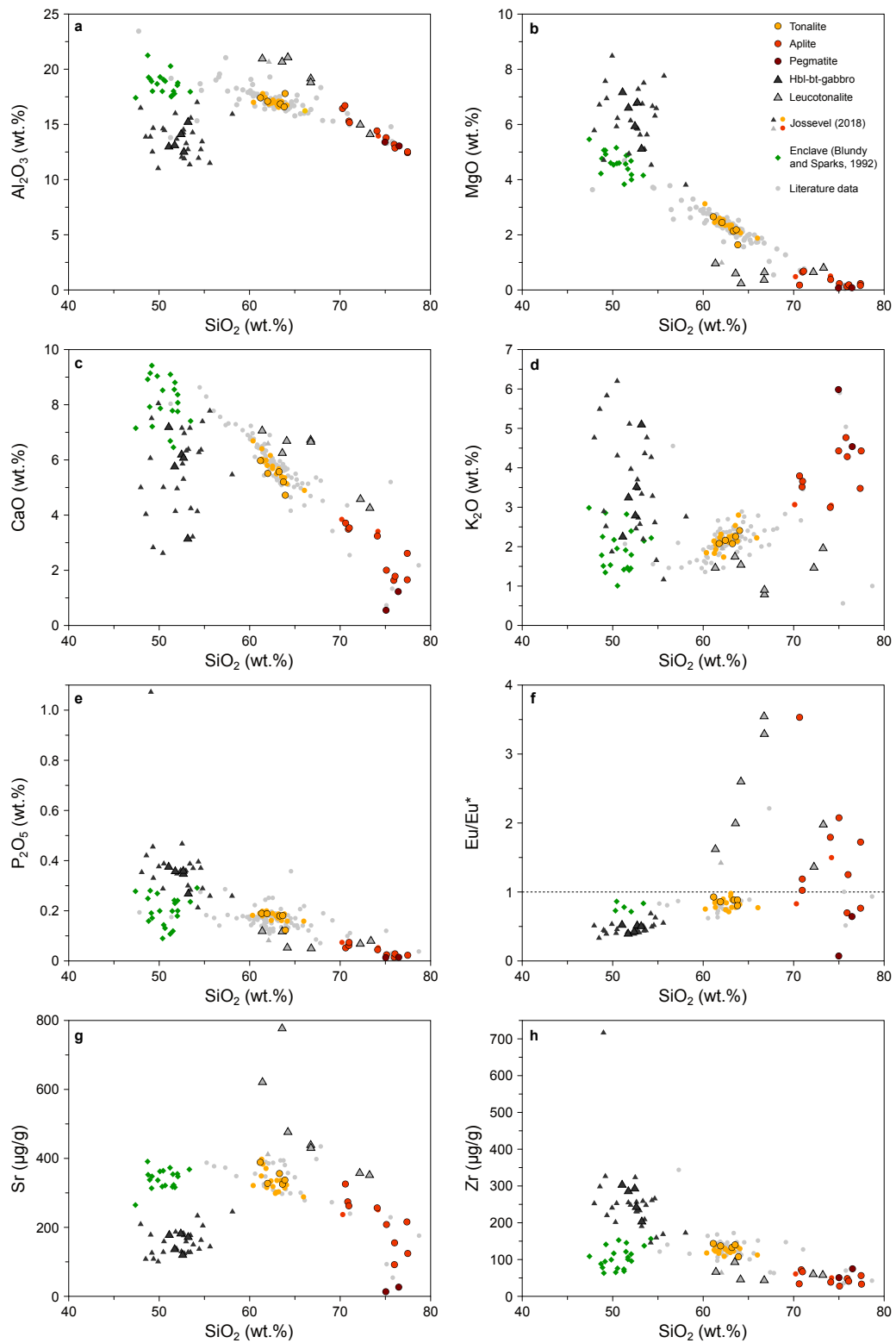


Figure 2.5. Major element bulk rock analyses of the Western Adamello lithologies. **a**, SiO_2 vs. Al_2O_3 . **b**, SiO_2 vs. MgO . **c**, SiO_2 vs. CaO . **d**, SiO_2 vs. K_2O . **e**, SiO_2 vs. P_2O_5 . **f**, SiO_2 vs. Eu/Eu^* . **g**, SiO_2 vs. Sr . **h**, SiO_2 vs. Zr . Mafic enclave compositions (Blundy and Sparks, 1992) are shown for comparison. Literature data are from Blundy and Sparks (1992), Del Moro et al. (1983), Dupuy et al. (1982), Floess (2013), Ji et al. (2019), Macera et al. (1983).

(i.e., andesine to anorthite), to 10 J cm^{-2} for low-absorbing phases, that is Na-rich plagioclase, alkali feldspar and quartz. Background, ablation and wash-out interval acquisition times were 70, 35 and 35 s, respectively. Dwell times range from 10 to 20 ms depending on the measured isotope. Absolute concentrations were calculated using CaO or Al_2O_3 (measured by EPMA) as internal reference, NIST SRM-612 as primary standard, and BCR-2G as secondary standard for quality control. The same data reduction scheme as for the bulk rock was applied to the mineral analyses.

2.6 Results

2.6.1 Bulk rock major and trace element geochemistry

The collected samples encompass a wide range of bulk rock compositions (Supplementary Material 1) reflecting the differences in texture and mineral proportions of the four studied lithologies. Such a compositional range is well demonstrated by the variation in SiO_2 from the mafic enclaves (48.7-53.4 wt.%), hornblende-biotite-gabbros (48.0-58.1 wt.%), the tonalites (60.3-66.0 wt.%), the leucotonalites (61.4-73.3 wt.%), to the granites (70.3-77.5 wt.%) (Fig. 2.5). The silica content is correlated with MgO, Al_2O_3 , CaO, K_2O , TiO_2 , Fe_2O_3 , P_2O_5 and the $\text{Na}_2\text{O}/\text{K}_2\text{O}$ ratio except for the gabbros and, to a lesser degree, the leucotonalites that exhibit larger scatter (Fig. 2.5). The hornblende-biotite-gabbros display low Al_2O_3 (11.0-17.1 wt.%) and CaO (2.6-8.0 wt.%) contents as well as

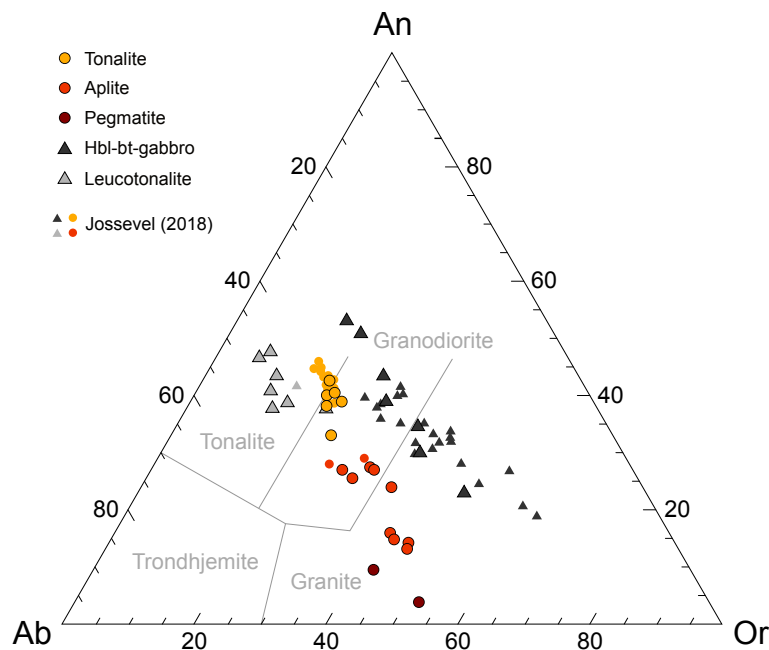


Figure 2.6. Normative An-Ab-Or ternary diagram (Barker, 1979; O'Connor, 1965) showing that the leucotonalites have abundant normative plagioclase but are not trondhjemites *sensu stricto*.

2. Peritectic biotite and crystal-melt segregation

low $\text{Na}_2\text{O}/\text{K}_2\text{O}$ ratios (0.24-1.24), and high MgO (3.8-8.5 wt.%) and K_2O (1.2-6.2 wt.%) values. In contrast, the leucotonalites show an opposite behaviour with high Al_2O_3 (14.2-21.1 wt.%) contents and $\text{Na}_2\text{O}/\text{K}_2\text{O}$ ratios (1.40-4.80) coupled with low K_2O (0.80-1.96 wt.%) values, in good agreement with modal variability. Furthermore, the granites present an inflection point at 76-77 wt.% SiO_2 where CaO decreases and K_2O increases at constant SiO_2 values. In the normative An-Ab-Or ternary diagram (Barker, 1979; O'Connor, 1965), the tonalites plot between the tonalite and granodiorite fields and the granites actually range from granodioritic to granitic compositions (Fig. 2.6). The leucotonalites are also located within the tonalite field but with higher normative plagioclase contents than the tonalite. The leucotonalites are distinguished from trondhjemites by their lower $\text{Na}_2\text{O}/\text{CaO}$ ratios.

Bulk rock trace element variations of tonalites and granites display trends of increasing Rb contents (62 to 145 $\mu\text{g}/\text{g}$) and decreasing Sr (397 to 123 $\mu\text{g}/\text{g}$) and Zr (143 to 29 $\mu\text{g}/\text{g}$) contents with differentiation, which is followed by the same inflection-point leading to higher Rb (up to 429 $\mu\text{g}/\text{g}$) and lower Sr (down to 12 $\mu\text{g}/\text{g}$) values corresponding to pegmatitic granites (Fig. 2.5f). However, hornblende-biotite-gabbros have higher Rb (37-272 $\mu\text{g}/\text{g}$), Ba (115-1,167 $\mu\text{g}/\text{g}$) and Zr (145-718 $\mu\text{g}/\text{g}$) values and lower Sr concentrations (99-246 $\mu\text{g}/\text{g}$), in contrast to the high Sr contents (215-734 $\mu\text{g}/\text{g}$) of leucotonalites. Other compatible elements such as V and Cr behave similarly with a linear decrease from the most primitive tonalite (145 $\mu\text{g}/\text{g}$ V, 20 $\mu\text{g}/\text{g}$ Cr) to the most differentiated granite (7 $\mu\text{g}/\text{g}$ V, 5 $\mu\text{g}/\text{g}$ Cr) and include the ilmenite-rich gabbros (294 $\mu\text{g}/\text{g}$ V, 40 $\mu\text{g}/\text{g}$ Cr), while magnetite-rich gabbros (up to 478 $\mu\text{g}/\text{g}$ V, 81 $\mu\text{g}/\text{g}$ Cr) and the leucotonalites (down to 28 $\mu\text{g}/\text{g}$ V, 5 $\mu\text{g}/\text{g}$ Cr) remain off this trend.

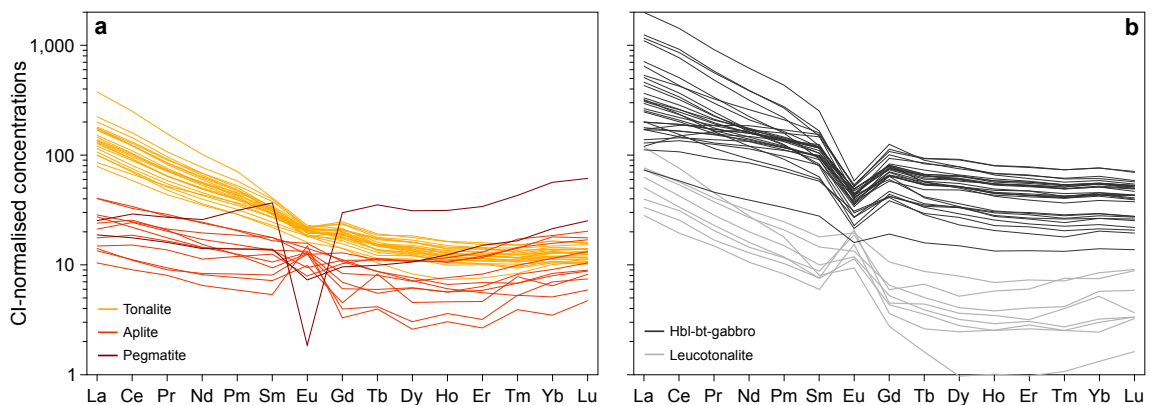


Figure 2.7. Bulk rock chondrite-normalised REE contents of the Western Adamello lithologies. **a**, Tonalite and granite samples. **b**, Hornblende-biotite-gabbro and leucotonalite samples. Normalisation values are from Sun and McDonough (1989). The represented data are from this study and Jossevel (2018). *CI*, CI-chondrite.

Chondrite normalised rare earth element (REE) patterns show fractionated light REE (LREE) segments ($\text{La}_N/\text{Sm}_N = 0.69\text{-}14.63$) and rather flat heavy REE (HREE) segments ($\text{Dy}_N/\text{Lu}_N = 0.42\text{-}1.44$) (Fig. 2.7). The most REE-enriched samples are hornblende-biotite-gabbros whereas the granites and especially the leucotonalites are REE-depleted (Fig. 2.7). The WAT represents a transition in terms of REE concentrations. The Eu anomaly [$\text{Eu}/\text{Eu}^* = \text{Eu}_N/(\text{Sm}_N \times \text{Gd}_N)^{1/2}$] of the tonalites is slightly negative and rather homogeneous ($\text{Eu}/\text{Eu}^* = 0.70\text{-}0.98$), whereas the granites are more heterogeneous ($\text{Eu}/\text{Eu}^* = 0.63\text{-}1.79$), with four samples having highly positive Eu anomalies probably reflecting plagioclase accumulation, and one enriched pegmatite with a strongly negative Eu anomaly ($\text{Eu}/\text{Eu}^* = 0.06$) most likely caused by late fractionation of plagioclase (Figs. 2.5f and 2.7a). Hornblende-biotite-gabbros have strong negative Eu anomalies (0.33-0.69) and leucotonalites positive Eu anomalies (1.36-3.56) (Figs. 2.5f and 2.7b).

In summary, the tonalites and the granites exhibit a trend of increasing incompatible and decreasing compatible elements with increasing SiO_2 contents. On the other hand, the hornblende-biotite-gabbros and the leucotonalites are off these trends because of the enrichment in hornblende, biotite, magnetite and ilmenite (e.g., REEs, Mg, Fe, Ba, Zr, Ti), or plagioclase (e.g., Ca, Al, Sr, Eu), respectively.

2.6.2 Mineral chemistry

In this section, we present the major and trace element chemistry of the main phases constituting the four lithologies of the Western Adamello (Figs. 2.8-2.11). The complete dataset is presented in the Supplementary Material of Grocolas and Müntener (2024).

Amphibole

Amphibole is only present in tonalites, hornblende-biotite-gabbros, and leucotonalites and has identical compositions within these lithologies. Unless stated otherwise, the following description accounts for amphiboles from every rock type. Amphibole is mostly Mg-hornblende with a few pargasitic or edenitic cores (Fig. 2.8a). Their Mg-number [$\text{Mg}\# = 100 \times \text{molar Mg}/(\text{Mg} + \text{Fe}^{2+}); \text{Fe}^{3+}$ calculated following Leake et al. (1997)] is usually used as a proxy for differentiation and decreases from 70.6 to 50.5 mol.% (Fig. 2.8b). During differentiation, amphibole Si content increases from 6.4 to 7.0 atoms per formula unit (a.p.f.u.) while their $(\text{Na} + \text{K})^A$ content decreases from 0.60 to 0.25 a.p.f.u. (Fig. 2.8b). Within all analysed amphiboles, Al^{IV} is rather high (0.96-1.47 a.p.f.u.) and is correlated with $(\text{Na} + \text{K})^A$ illustrating the effect of temperature on the edenite exchange (Fig. 2.8a). On the other hand, Al^{IV} is uncorrelated to Ti and Al^{VI} , implying that

2. Peritectic biotite and crystal-melt segregation

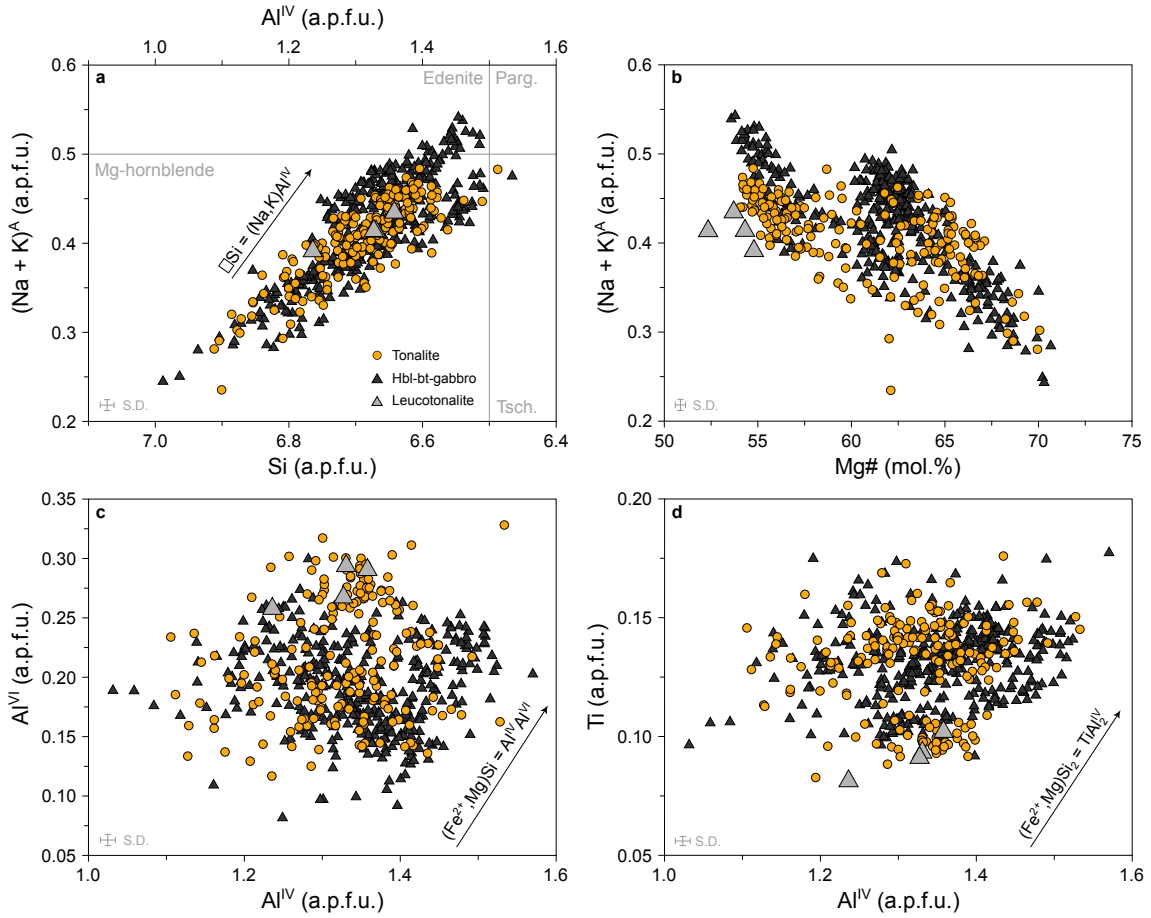


Figure 2.8. Major element compositions of Western Adamello amphiboles. **a**, Si vs. A-site ($\text{Na}^{\text{A}} + \text{K}^{\text{A}}$) amphibole classification diagram of [Leake \(1978\)](#). Tetrahedral Al (Al^{IV}) depends on Si content and is also represented. The black arrow illustrates the trajectory of the ideal edenite exchange vector [$\square\text{Si} = (\text{Na}, \text{K})\text{Al}^{\text{IV}}$] followed by the analysed amphiboles. **b**, Mg# vs. $(\text{Na} + \text{K})^{\text{A}}$. **c**, Al^{IV} vs. octahedral Al (Al^{VI}). The arrow represents the trajectory of the ideal Al-Tschermak exchange vector [$(\text{Fe}^{2+}, \text{Mg})\text{Si} = \text{Al}^{\text{IV}}\text{Al}^{\text{VI}}$]. **d**, Al^{IV} vs. Ti. The arrow illustrates the trajectory of the ideal Ti-Tschermak exchange vector [$(\text{Fe}^{2+}, \text{Mg})\text{Si}_2 = \text{TiAl}_2^{\text{IV}}$]. *S.D.*, standard deviation, corresponding to the mean 2σ .

the temperature-dependant Ti-Tschermak and the pressure-dependant Al-Tschermak exchanges only played a minor role during amphibole crystallisation (Fig. 2.8c,d). With differentiation, amphibole TiO_2 (0.8-1.2 wt.%), Sr (11-40 $\mu\text{g/g}$), Zr (12-68 $\mu\text{g/g}$) and $(\text{Gd}/\text{Yb})_{\text{N}}$ (0.76-2.02) contents and Eu anomaly (0.25-0.65) decrease whereas Li (3.2-17.9 $\mu\text{g/g}$) and Ba (9.0-48.6 $\mu\text{g/g}$) contents increase (Fig. 2.9). Chondrite normalised REE patterns of hornblende exhibit strongly fractionated LREE segments ($\text{La}_{\text{N}}/\text{Sm}_{\text{N}} = 0.05\text{-}0.75$) and rather flat HREE segments (0.75-1.45). Evolved amphiboles (i.e., with lower Mg#) have more fractionated LREE segments with lower LREE values, larger Eu anomalies, and more fractionated HREE segments (Fig. 2.9b,c). This behaviour is probably caused by the co-crystallisation of a LREE-rich phase such as plagioclase and, to a lesser extent, apatite.

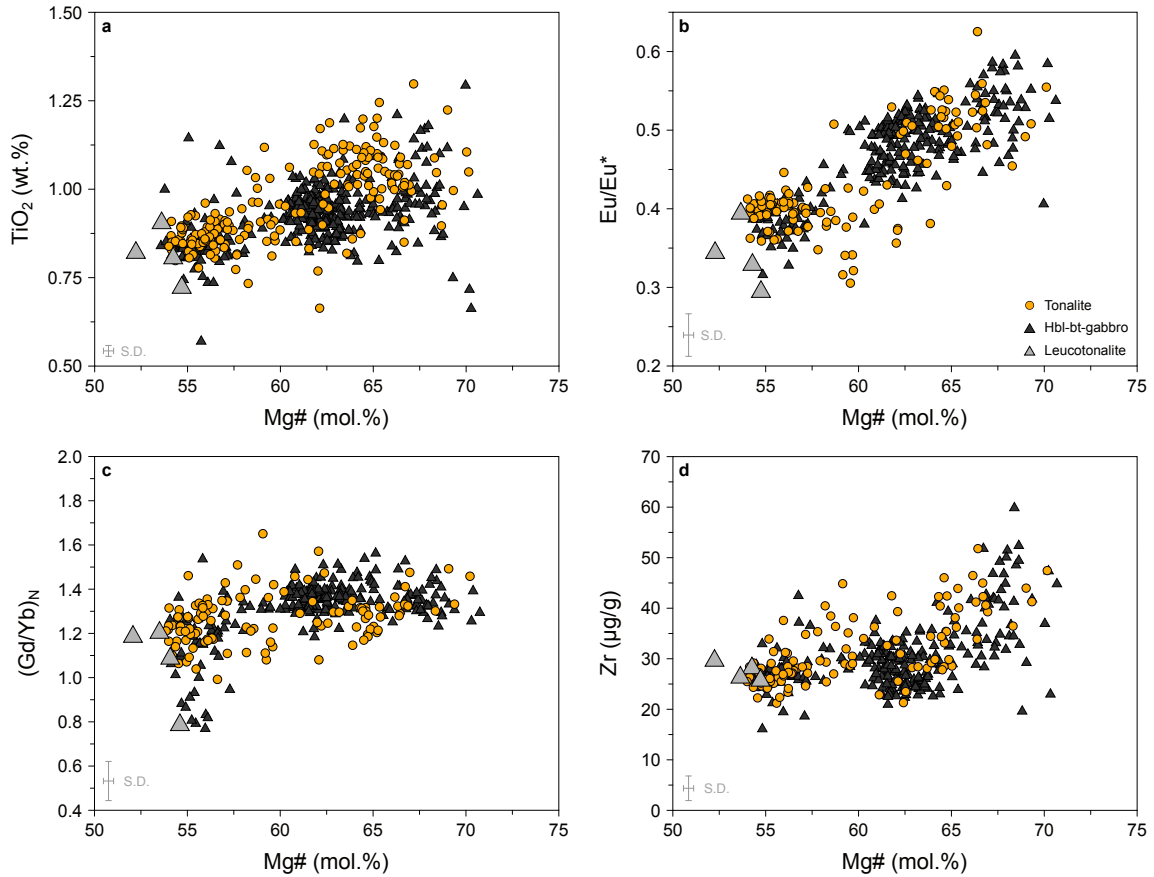


Figure 2.9. Major and trace element compositions of the Western Adamello amphiboles illustrating their chemical evolution as a function of Mg#. **a**, Mg# vs. TiO₂. **b**, Mg# vs. Eu/Eu*. **c**, Mg# vs. (Gd/Yb)_N. **d**, Mg# vs. Zr. *S.D.*, standard deviation, corresponding to the mean 2 σ .

Biotite

Biotite is present within the four described lithologies and display similar compositions in tonalite, hornblende-biotite-gabbro and leucotonalite. The texturally different biotites from granites show distinct trace element concentrations. Biotites from tonalite, gabbro, leucotonalite and aplitic granite exhibit the same range of Mg# (49-64 mol.%), as opposed to the more restricted values of biotite Mg# in the pegmatitic granite (50-56 mol.%) with the higher values corresponding to biotite texturally similar to peritectic biotite in tonalite (Fig. 2.10). Biotite from the tonalite, gabbro, leucotonalite and aplitic granite has MnO contents increasing from 0.20 to 0.67 wt.% with differentiation whereas biotite in pegmatitic granite displays significantly higher MnO concentrations (0.53-1.05 wt.%) (Fig. 2.10a). The Na₂O concentration decreases from 0.25 to 0.07 wt.% with decreasing Mg#, except for some biotites from hornblende-biotite-gabbro having higher, probably inherited Na₂O values (up to 0.56 wt.%) from consumed amphibole. The correlation and the slope between Al^{tot} and (Si + R²⁺) indicate that Tschermak, Ti-Tschermak, or Al-oxy substitu-

2. Peritectic biotite and crystal-melt segregation

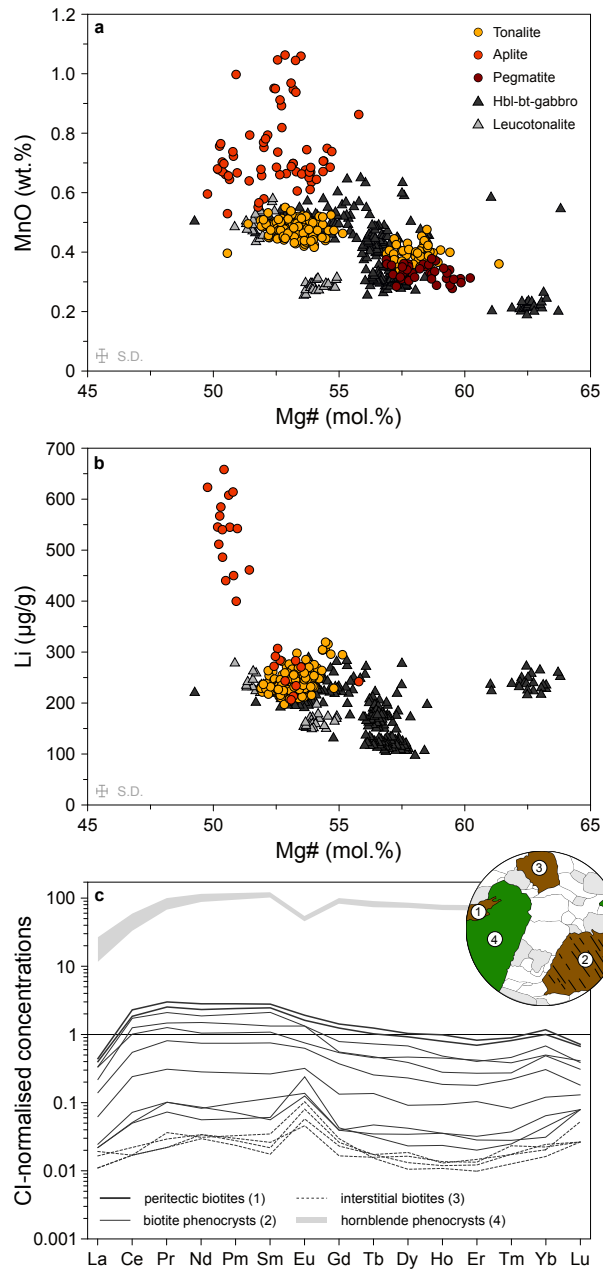


Figure 2.10. Major and trace element compositions of Western Adamello biotite. **a**, Mg# vs. MnO. **b**, Mg# vs. Li. **c**, Chondrite-normalised REE contents of some Western Adamello biotites. Different types of biotite are represented as a function of their texture, size and relationship with other phases. Some Western Adamello amphiboles are represented for comparison. The top right panel illustrates the three different biotite types and is derived from a tonalite thin section. Normalisation values are from [Sun and McDonough \(1989\)](#). CI, CI-type chondrite; S.D., standard deviation, corresponding to the mean 2σ .

tion controls biotite composition. Trace element concentrations in biotite from granite are significantly different from the ones originating from tonalite, gabbro and leucotonalite. Biotite in granite display high Li values (399-657 µg/g) compared to the other rock types (101-312 µg/g) (Fig. 2.10b). Ba and V contents from the same biotites from granite decrease with differentiation. Interstitial biotite in granite displays lower concentrations

(Ba = 69-1,203 $\mu\text{g/g}$, V = 364-648 $\mu\text{g/g}$) than large biotite phenocrysts (Ba = 1,062-4,874 $\mu\text{g/g}$, V = 156-338 $\mu\text{g/g}$). Chondrite normalised REE patterns present an identical range of REE concentrations for the four rock types with rather low REE concentrations ($\Sigma\text{REE} < 1 \mu\text{g/g}$), flat LREE and HREE segments and positive Eu anomalies ($\text{Eu}/\text{Eu}^* = 1.5\text{-}23$) (Fig. 2.10c). However, some biotite replacing amphibole but also large phenocrysts exhibit negative to slightly positive Eu anomalies ($\text{Eu}/\text{Eu}^* = 0.48\text{-}1.28$) and fractionated LREE (Fig. 2.10c). These features are similar to hornblende REE patterns albeit with lower absolute REE concentrations. This signature is interpreted as inherited from hornblende.

Plagioclase

Within all rock types, plagioclase compositions span a wide range of anorthite content [$\text{An} = 100 \times \text{molar Ca}/(\text{Ca} + \text{Na} + \text{K})$] from An_{19} to An_{91} (Fig. 2.11a). The intermediate-to-high-An values ($>\text{An}_{50}$) are related to plagioclase cores and dominantly occur in leucotonalite ($>7 \text{ vol.}\%$) and tonalite (4-5 vol.%), rarely in hornblende-biotite-gabbro (0-2 vol.%) and is rare ($<0.4 \text{ vol.}\%$) in granitic samples. The andesine-type plagioclase ($\text{An}_{30\text{-}50}$) is the most represented within tonalites (25-34 vol.%) and leucotonalites ($>40 \text{ vol.}\%$), while gabbros and granites are dominated by plagioclase with lower An contents ($<\text{An}_{30}$). Beside its variable distribution within the four lithologies, the plagioclase compositions are similar in tonalites, gabbros and leucotonalites, while it reveals a more evolved character in granites (Fig. 2.11a). Plagioclase from the first three rock types

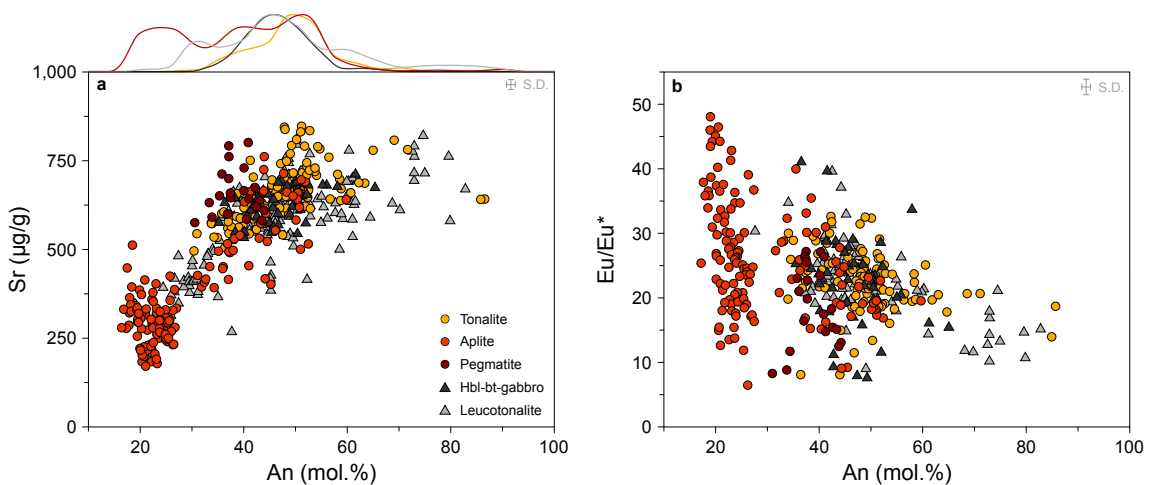


Figure 2.11. Major and trace element compositions of Western Adamello plagioclase illustrating their chemical evolution. **a**, An content vs. Sr. The lines on the top of the diagram represent Kernel density estimations of the plagioclase An contents from the Western Adamello four lithologies. **b**, An content vs. Eu/Eu^* . Note the similar plagioclase compositions for the four lithologies, except pegmatitic granites having more differentiated plagioclase compositions. *S.D.*, standard deviation, corresponding to the mean 2σ .

2. Peritectic biotite and crystal-melt segregation

is systematically zoned, with predominantly normally zoned crystals and minor reverse zoning. Three plagioclase populations are identified based on their An content (Figs. 2.3 and 2.4). (1) High-An ($>An_{65}$) compositions corresponding to plagioclase cores that are highly resorbed and fractured. The inner core is strongly resorbed while the preserved outer core is mostly euhedral. (2) Plagioclase with intermediate composition (An_{40-65}) is related to core, mantle, and may extend to the rim, and constitutes >50 vol.% of plagioclase phenocrysts. (3) Low-An ($<An_{40}$) plagioclase compositions correspond to crystal rims (<100 μm), interstitial grains and plagioclase from the pegmatitic granites. Aplitic granite dikes have plagioclase compositions covering the whole compositional spectrum (An_{26-90}). With decreasing An content, the Fe (145-2,425 $\mu\text{g/g}$), Mg (5-38 $\mu\text{g/g}$), Ti (7-30 $\mu\text{g/g}$), Sr (390-850 $\mu\text{g/g}$) and $(La/Sm)_N$ (3-64) values of plagioclase from every rock type decrease, while the Eu anomaly is rather constant in high-An plagioclase ($Eu/Eu^* = 11-20$) and then increases in more differentiated grains (7-49) (Fig. 2.11). This highlights that the WAT was relatively rapidly cooled, as diffusive reequilibration would result in a positive correlation between An and Sr (e.g., Blundy and Shimizu, 1991). It contrasts with the incompatible behaviour of Li (0-7 $\mu\text{g/g}$), Rb (0-0.5 $\mu\text{g/g}$) and Pb (13-45 $\mu\text{g/g}$). Barium also follows an incompatible trend (from 30 to 200 $\mu\text{g/g}$ Ba) but low-An plagioclase ($<An_{40}$) from the pegmatitic granites have distinctly lower Ba contents (<40 $\mu\text{g/g}$) reflecting the co-crystallisation of alkali feldspar.

Alkali feldspar

Alkali feldspars are texturally and compositionally similar within the four described lithologies. They display a restricted range of orthoclase [$Or = 100 \times \text{molar K}/(\text{K} + \text{Na} + \text{Ca})$] content from Or_{88} to Or_{98} that is uncorrelated to their large array of BaO contents (0-1.31 wt.%). The highest BaO concentration is determined in the cores and decreases towards the contact with other phases. A correlation between Ba and Sr is observed with a decrease from 600 to 120 $\mu\text{g/g}$ Sr from core to rim (Fig. 2.12). In contrast, the Cs contents slightly increase with Ba from 1.5 to 8 $\mu\text{g/g}$ and reach >30 $\mu\text{g/g}$ in the most evolved crystals from pegmatitic granites. Alkali feldspars from tonalite, gabbro and leucotonalite exhibit low Li concentrations (2-14 $\mu\text{g/g}$) whereas in granite they have distinctly higher Li values (4-40 $\mu\text{g/g}$) with the highest values corresponding to alkali feldspar from pegmatitic granites. Chondrite normalised REE patterns exhibit fractionated LREE segments ($La_N/Sm_N = 11-23$), slightly fractionated HREE segments ($Dy_N/Lu_N = 0.71-0.98$) and strongly positive Eu anomalies (>40).

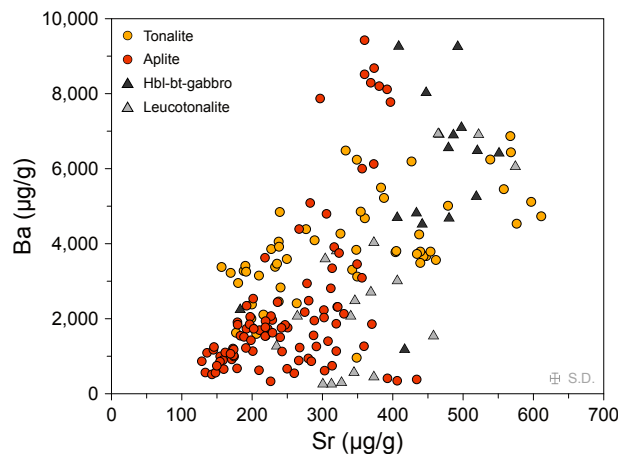


Figure 2.12. Trace element compositions of Western Adamello alkali feldspar illustrating their chemical evolution as Sr vs. Ba contents for the four main lithologies. *S.D.*, standard deviation.

Quartz

The two previously defined quartz populations exhibit different trace element chemistry regardless of their host rock. The quartz phenocrysts present in tonalite, hornblende-biotite-gabbro and leucotonalite (Q_{z1}) have higher Ti contents (39.7-53.9 $\mu\text{g/g}$) whereas interstitial quartz in tonalite (Q_{z2}) and pegmatite display distinctly lower Ti concentrations (21.0-30.8 $\mu\text{g/g}$) (Fig. 2.13). Conversely, Ge is more abundant in interstitial quartz (1.0-2.8 $\mu\text{g/g}$) compared to phenocrysts (1.0-1.5 $\mu\text{g/g}$). The other measured elements are present in similar amounts in the two quartz generations. The Li (2.5-12.2 $\mu\text{g/g}$) and Sr (0.02-0.37 $\mu\text{g/g}$) contents are positively correlated to Al (25.0-103.7 $\mu\text{g/g}$).

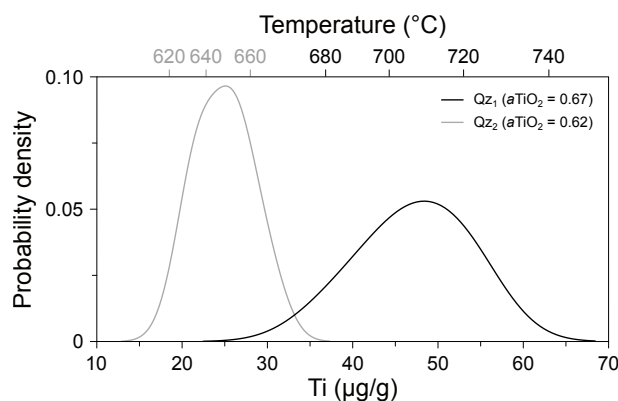


Figure 2.13. Titanium contents of quartz for the two types of quartz (Q_{z1} and Q_{z2}) as described in the main text and represented as Kernel density estimations. The calculated temperatures are also reported in black for Q_{z1} ($a\text{TiO}_2 = 0.67$) and grey for Q_{z2} ($a\text{TiO}_2 = 0.62$). Note the temperature difference between the two generations of quartz.

2.6.3 Temperature constraints

In this section, we use calibrated thermobarometers based on bulk rock and mineral chemistry to assess the crystallisation conditions of the four studied lithologies. A summary of the calculated temperatures for the four studied lithologies is reported in Table 2.2. [Marxer and Ulmer \(2019\)](#) performed crystallisation experiments on a tonalite from Malga Listino (Re di Castello superunit) and derived a temperature-dependent parameterisation for CaO based on the experimental LLD. The calculated temperatures for tonalite range from 922 to 973 °C. For the high-silica granites ($\text{SiO}_2 \geq 75$ wt.%), which are thought to represent liquid compositions, the calculated temperatures range from 697 to 749 °C. The combined uncertainty from the measurements and experimental calibration ranges from 48 °C for the tonalites to 64 °C for the granites.

The hornblende chemistry revealed that the temperature-dependent edenite exchange controlled their chemical evolution (Fig. 2.8a), whereas the Ti- and Al-Tschermak substitutions were minor (Fig. 2.8c,d). We applied the pressure-dependent amphibole-plagioclase thermometer of [Holland and Blundy \(1994\)](#) whose typical uncertainty is 35-40 °C by measuring touching amphibole-plagioclase pairs. The pressure conditions have been previously inferred to be 250-300 MPa based on the contact aureole metamorphic assemblage ([Floess and Baumgartner, 2015](#)). Pressure estimates using amphibole barometry resulted in pressures of 320-410 MPa ([Mutch et al., 2016](#)), slightly higher than the estimates of [Floess and Baumgartner \(2015\)](#). However the application of this barometer is strictly valid only for a buffer assemblage composed of plagioclase, biotite, quartz, alkali feldspar, magnetite, epidote, apatite and ilmenite or titanite (e.g., [Hammarstrom and Zen, 1986](#); [Mutch et al., 2016](#); [Schmidt, 1992](#)), potentially explaining the slight discrepancy between amphibole barometry and contact aureole barometry. As the magma was probably undersaturated with respect to quartz during amphibole crystallisation, we employed the edenite-richterite thermometer. The resulting temperatures range from 724 to 865 °C.

The incorporation of Ti in quartz depends on different intensive parameters such as melt temperature, chemistry and the kinetics of crystal growth ([Huang and Audétat, 2012](#); [Thomas et al., 2010, 2015](#); [Wark and Watson, 2006](#); [Wark et al., 2007](#)). To accurately calculate the crystallisation temperature of quartz, the TiO_2 activity (a_{TiO_2}) must be known. To do so, we model the TiO_2 chemical potential (μ_{TiO_2}) evolution during melt evolution using *Perple_X* ([Connolly, 2005, 2009](#)) coupled with recently published thermodynamic solution models ([Holland et al., 2018](#)) developed to reproduce mafic to felsic LLD. The calculations successfully reproduce the phase proportions observed in the Western Adamello tonalite and modal data of hydrous crystallisation experiments ([Marxer](#)

and Ulmer, 2019). The reader is referred to the Supplementary Material 1 for further discussion concerning the model benchmark. To calculate a_{TiO_2} from μ_{TiO_2} , we use Eq. 2.1:

$$a_{\text{TiO}_2} = \exp\left(-\frac{G_{\text{TiO}_2}^{P,T} - \mu_{\text{TiO}_2}^{P,T}}{RT}\right) \quad (2.1)$$

where $\mu_{\text{TiO}_2}^{P,T}$ (J mol⁻¹) is the chemical potential of rutile, $G_{\text{TiO}_2}^{P,T}$ (J) is the Gibbs free energy of rutile calculated at the temperatures (K) and pressures (Pa) used in *Perple_X*, and R is the gas constant (J mol⁻¹ K⁻¹). At the onset of quartz crystallisation, the calculated a_{TiO_2} in the melt is 0.62 and increases to 0.67 with increasing crystal fraction which are reasonable values for intermediate to felsic magmas (e.g., Ghiorso and Gualda, 2013). The crystallisation temperatures of the quartz phenocrysts and interstitial quartz are then calculated using the parametrisation of Wark and Watson (2006). Given the uncertainty on the experimental fit and the analytical conditions, the uncertainty of the calculated temperature ranges from 11 to 14 °C. The calculated temperatures of the quartz phenocrysts (Qz₁) are 689-731 °C with an average of 715 ± 26 °C (2σ) (Fig. 2.13) which corresponds, within error, to quartz saturation temperatures of an experimental study on tonalite at 200 MPa (Marxer and Ulmer, 2019). In contrast, the interstitial quartz (Qz₂) crystallised between 618 and 660 °C with an average of 640 ± 24 °C (2σ) (Fig. 2.13), corresponding to the H₂O-saturated solidus (Johannes and Holtz, 2012, e.g.,). Magnetite and ilmenite were measured for potential application of the Fe-Ti oxide geothermometer (e.g., Ghiorso and Sack, 1991), but the TiO₂ content of magnetite was very low (<0.1 wt.%), pointing to chemical reequilibration under subsolidus conditions.

Table 2.2. Summary of calculated temperatures. The dataset is available in the Supplementary Material 1.

Rock type	CaO-in-melt (°C) Marxer and Ulmer (2019)	2σ	Amp-Pl (°C) Holland and Blundy (1994)	2σ	Ti-in-quartz (°C) Wark and Watson (2006)	2σ
Hbl-bt gabbro	-	-	795 (46)	67	712 (3)	10
Leucotonalite	-	-	791 (4)	76	638 ^b (4)	19
Tonalite	948 (22) ^a	24	779 (53)	62	716 (8)	32
Granite	766 (6)	76	-	-	641 (18)	26

^aThe number in brackets indicates the number of analyses

^bCrystallisation temperature of interstitial quartz

2.7 Discussion

In this section, we use (1) bulk rock and mineral chemistry to distinguish the rocks that experienced crystal accumulation from the rocks considered as crystallised melt, (2) textural observations and mass balance to reconstruct the tonalitic parental melt evolution and quantify the crystal-melt segregation process, and (3) existing bulk rock data from other plutonic bodies to highlight the importance of the biotite-forming peritectic reaction and the widespread occurrence of *in situ* leucotonalitic cumulates and melt segregates within the Western Adamello tonalites and batholiths in general.

2.7.1 Melt versus cumulate

Crystal accumulation within plutonic mafic systems principally arises from the density and viscosity contrast between crystals and interstitial melt. However, the identification of such a process in differentiated systems is challenging given the propensity of silica-rich granitoids to accumulate crystals in cotectic proportions. The primary definition of cumulate, regardless of the involved process, is largely based on its texture, that is a framework of touching minerals that were accumulated through crystallisation-differentiation and usually trapped some proportions of interstitial melt (Irvine, 1982). Although cumulate composition is controlled by the accumulated phase chemistry and usually plots off their parental LLD, two scenarios complicate the interpretation of Si-rich felsic systems. The first one is related to the accumulation of crystals in cotectic proportions resulting in a melt-like composition, whereas the second is associated with the inefficiency of crystal-melt separation allowing for large amounts of melt entrapment. As such, distinguishing between a cumulate and a melt origin can be difficult, especially for silica-rich compositions, but careful field and textural observations (e.g., Bachl et al., 2001; Barnes et al., 2001; Paterson, 2009; Turnbull et al., 2010; Vernon and Paterson, 2008; Walker Jr et al., 2007) coupled with bulk rock and mineral chemistry (e.g., Barnes et al., 2016a; Deering and Bachmann, 2010; Lee and Morton, 2015; Schaen et al., 2017, 2018) usually allow to identify crystal accumulation processes.

Within the Western Adamello, the hornblende-biotite-gabbros and the leucotonalites are identified as cumulates based on their respective textures. Indeed, the gabbros exhibit a framework of touching hornblende and biotite macrocrysts that are texturally and geochemically identical to the ones from the main WAT (Figs. 2.4, 2.8 and 2.9). In contrast, the interstitial crystals are smaller and form a granitic assemblage reminiscent of a frozen, pore-filling melt. The leucotonalites share similar characteristics as the gabbros. It includes synnesis of touching plagioclase phenocrysts (Fig. 2.4f) and a surrounding in-

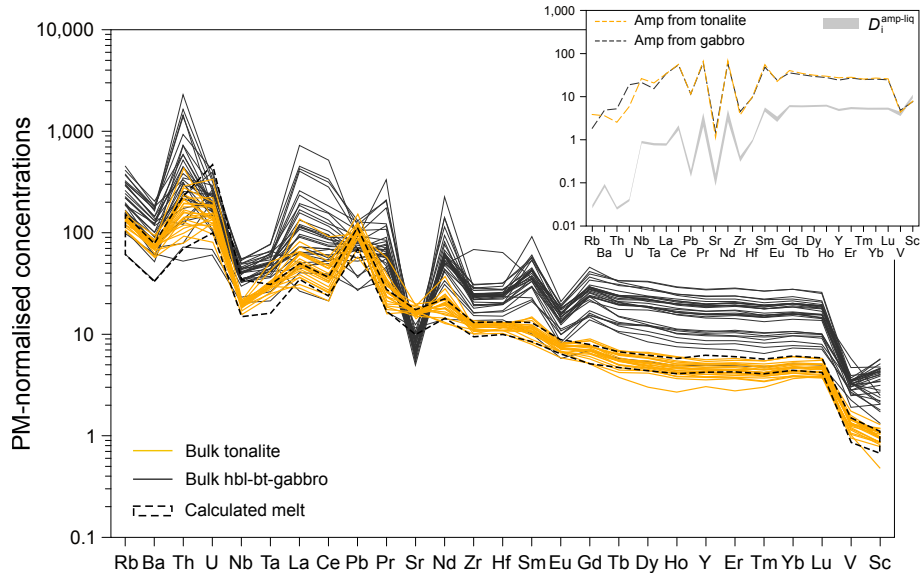


Figure 2.14. Primitive mantle normalised trace element patterns of bulk tonalite and hornblende-biotite-gabbros, as well as primitive hornblendes and their calculated parental melts. The distribution coefficients are from [Nandedkar et al. \(2016\)](#) and [Sisson \(1994\)](#). The most primitive hornblende compositions found in the tonalite and in the gabbro and the distribution coefficients are represented in the top right panel. Normalisation values are from [Sun and McDonough \(1989\)](#). *PM*, primitive mantle.

terstitial assemblage composed of quartz, alkali feldspar and Na-rich plagioclase rims (Fig. 2.4e,f). Such a network of euhedral crystals coupled with interstitial phases are commonly interpreted as crystal accumulation ([Irvine, 1982](#); [Miller and Miller, 2002](#); [Schaen et al., 2018](#); [Vance, 1969](#); [Vernon and Paterson, 2008](#)). In addition, the similar textures as well as the field relationship with the host WAT indicate that the hornblende-biotite-gabbros and leucotonalites represent cumulates that are cogenetic with the main tonalite. In fact, mineral compositions in the gabbros and the leucotonalites are identical to the main tonalite, and the bulk chemical composition is controlled by modal abundance.

On the other hand, the graphic intergrowth texture present within the pegmatitic granites (dikes and small pockets) is typical of an H_2O -saturated granitic melt undergoing liquidus undercooling ([Deveineau et al., 2020](#); [London et al., 1989](#)). These pegmatites are often associated with aplitic borders, a feature observed within the Western Adamello rock record and characteristic of different undercooling compared to the pegmatitic core ([London, 2014](#)). Locally, these dikes contain plagioclase crystals identical to those from the tonalite and the leucotonalite, suggesting that (1) the dikes represent segregated interstitial melt directly derived from the WAT (Fig. 2.2f,g), and (2) the melt segregation process is imperfect. This is well demonstrated by the positive Eu anomaly of some granitic dikes (Fig. 2.7a).

The cumulus or melt character of the main tonalite is difficult to identify given its

2. Peritectic biotite and crystal-melt segregation

coarse-grained texture without any clear crystal alignment or touching biotites or hornblendes. In a melt-like plutonic rock, the most primitive crystals are in equilibrium with the bulk rock chemistry. We thus explore this hypothesis and compare the calculated melt in equilibrium with the most primitive hornblendes with the tonalite bulk rock chemistry. We used tonalite and gabbro hornblendes with Mg# >60 mol.% combined with trace element distribution coefficients between melt and amphibole from [Nandedkar et al. \(2016\)](#) and [Sisson \(1994\)](#). All the WAT samples have trace element contents within the range of the calculated melts in equilibrium with hornblende (Fig. 2.14). As such, the tonalite did not experience extensive crystal accumulation and/or melt loss and probably preserves a melt composition. Indeed, accumulation of >5 % amphibole would result in MREE and HREE concentrations exceeding the calculated melts. Although high-An plagioclase ($\sim\text{An}_{65-70}$) forms the liquidus phase, it only represents a minor amount of the final crystal assemblage. Additionally, some high An-plagioclase ($\sim\text{An}_{80-90}$) crystallised prior to emplacement and accounts for <0.1 vol.% of the rock. Therefore, the influence on bulk rock chemistry is negligible (e.g., CaO <0.01 wt.%, Al_2O_3 <0.01 wt.%, Sr <1 $\mu\text{g/g}$, La <1 $\mu\text{g/g}$) and does not significantly influence our calculations.

To summarise, most of the WAT preserved a melt-like composition and experienced less than about 5 % melt loss, whereas the gabbros and leucotonalites correspond to *in situ* cumulates resulting from crystal accumulation within the crystallising WAT. Finally, granites represent highly differentiated melts directly extracted from the main tonalite carrying a few percent of tonalite-derived antecrysts.

2.7.2 Tonalite liquid line of descent

As shown above, the majority of the tonalites have characteristics of melt and can therefore be used to reconstruct the tonalitic parental LLD. The selected sample (CJ26) is a biotite-rich tonalite which is chemically representative of the Western Adamello tonalite (63.1 wt.% SiO_2), has a negative REE slope ($\text{La}_N/\text{Lu}_N = 7.4$), and no significant Eu anomaly ($\text{Eu}/\text{Eu}^* = 0.98$). The tonalite LLD is modelled for major and some trace elements following the method of [Jagoutz \(2010\)](#) using a rearrangement of the mass balance equation. The model assumes fixed cumulate composition subtraction, although composition may vary with crystallisation, rather than mineral-melt distribution coefficients for major element modelling. To obtain the most robust LLD, the textural observations and the QEMSCAN analysis of sample CJ26 are used so that the order of phase appearance and proportions are respected throughout the model. The different mineral assemblages, their proportions and major element compositions are reported in Table 2.3.

The first phase to crystallise is a high-An ($\sim\text{An}_{65}$) plagioclase alongside, or rapidly followed by, ilmenite and apatite. Indeed, hornblende is in equilibrium with plagioclase rims having lower An contents ($\sim\text{An}_{50}$), and ilmenite and apatite are the only phases present

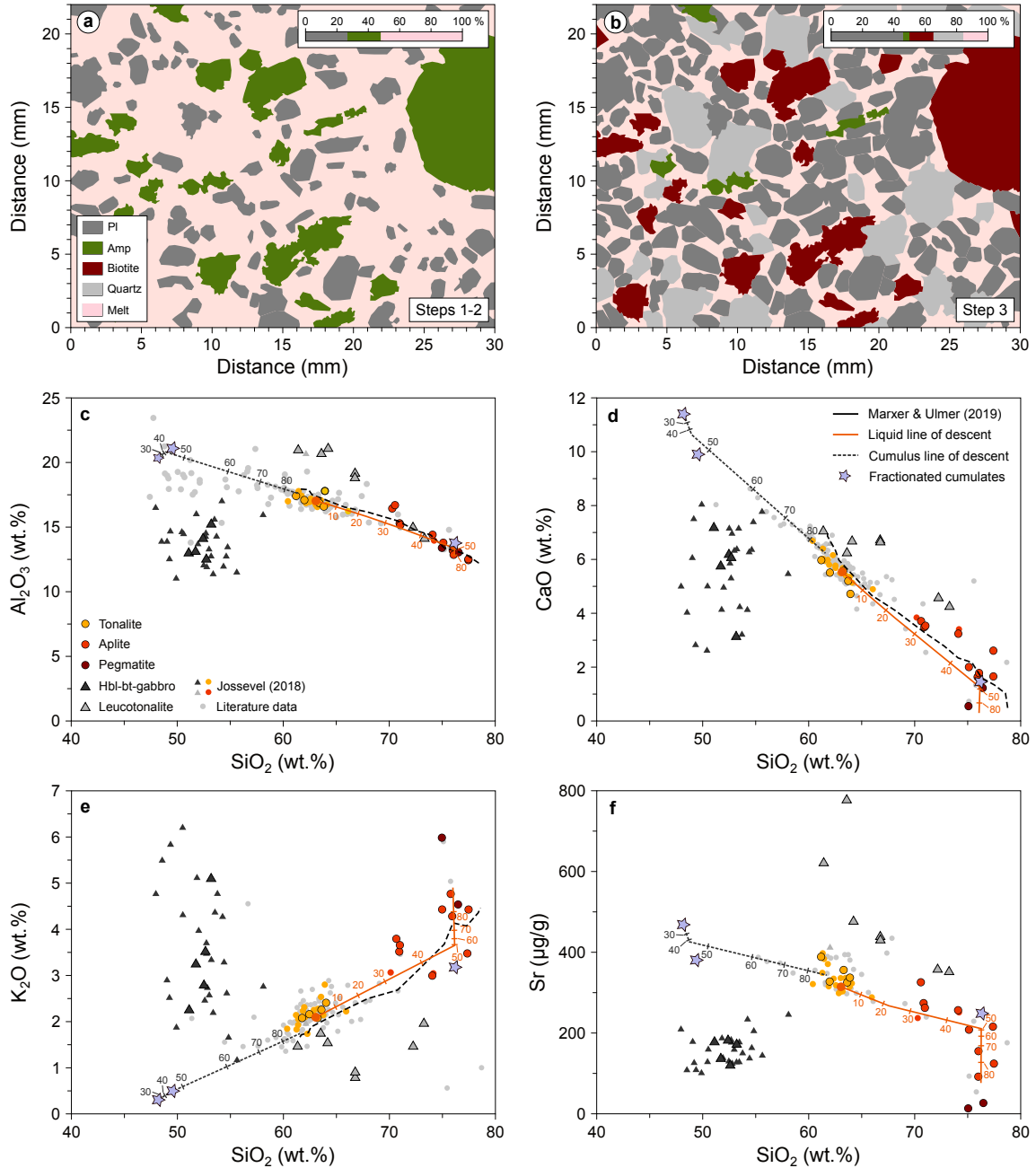
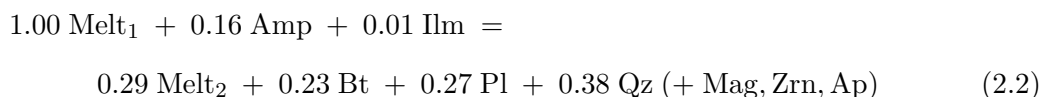


Figure 2.15. Sketches and results of the melt differentiation model. **a**, Simple illustration of the two first steps of the LLD model. **b**, Simple illustration of the third step of the LLD model corresponding to the biotite-forming peritectic reaction. **c**, SiO₂ vs. Al₂O₃. **d**, SiO₂ vs. CaO. **e**, SiO₂ vs. K₂O. **f**, SiO₂ vs. Sr. The orange line illustrates the LLD, while the bluish line represents the bulk CLD. The three grey stars are the composition of the three different fractionated mineral assemblages described in the text. Small lines indicate 10 % fractionation steps. The initial melt composition is represented by the orange plain circle. The experimental LLD from [Marxer and Ulmer \(2019\)](#) is also shown for comparison. The literature data are the same as in [Fig. 2.5](#).

2. Peritectic biotite and crystal-melt segregation

as inclusions within plagioclase cores. However, liquidus crystallisation of plagioclase only represents a few percent. As such, the first modelled crystal assemblage is composed of plagioclase (An₅₇), apatite, ilmenite, hornblende (Mg# = 64 mol.%), magnetite and zircon, and crystallises 24 % of the melt (Fig. 2.15a). It results in a decrease in MgO, FeO, Al₂O₃, TiO₂, CaO, Sr, Eu/Eu* and Zr, and an increase in SiO₂ (~68 wt.%), K₂O and Rb in the residual melt (Fig. 2.15 and Supplementary Material 1). The second crystal assemblage is the same as the first one, except that the plagioclase is An₄₇ to account for the strong crystal zoning, hornblende has a more evolved composition (Mg# = 56 mol.%), and biotite starts crystallising (<5 % of the crystallising assemblage) (Fig. 2.15a). The LLD follows the same trends as for the first crystallising assemblage, albeit with slightly different slopes in Harker diagrams especially visible for Sr (Fig. 2.15f). This second crystal assemblage also represents 24 % of the total system. After 48 % crystallisation, the evolving melt has >76 wt.% SiO₂, and reproduces the Western Adamello granites having rather low K₂O concentrations (~3.5-4 wt.%). By applying the CaO-in-melt thermometer of [Marxer and Ulmer \(2019\)](#), the modelled melt temperature is ~735 °C after 48 % crystallisation, which is in excellent agreement with the amphibole-plagioclase temperatures of the most differentiated hornblendes (~740 °C).

The textural observations indicate that biotite mainly forms by a peritectic reaction (Figs. 2.3 and 2.4a,c). Additionally, the samples exhibiting the highest magnetite (and lowest ilmenite) contents correspond to biotite-rich tonalites, suggesting that ilmenite is probably consumed at the expense of magnetite. Plagioclase continuously crystallises along its solid solution, and quartz phenocrysts and interstitial apatite and zircon are present in equilibrium with biotite. To quantify the third crystallising assemblage comprising the biotite-forming peritectic reaction, we used the modal proportion difference between two quantitatively mapped tonalite thin sections (WA21-11 and CJ26) having similar compositions but distinct hornblende and biotite contents. These different modal proportions provide a snapshot of the biotite peritectic reaction. The calculated assemblage can be written following Eq. 2.2:



where plagioclase, quartz, apatite, magnetite and zircon co-crystallise but do not represent peritectic products (Fig. 2.15b). This is in good agreement with the experimentally produced biotite peritectic reaction of [Marxer and Ulmer \(2019\)](#): 1.00 Melt₁ + 0.15 Amp

= 0.27 Melt₂ + 0.25 Bt + 0.24 Pl + 0.39 Qz. A bulk “cumulate” is then calculated from this reaction (and the co-crystallising phases) and geochemically resembles a granite (76 wt.% SiO₂, 14 wt.% Al₂O₃, 3 wt.% CaO), but does not contain alkali feldspar. The melt K₂O content increases and approaches the concentration of the most differentiated pegmatitic granites, whereas SiO₂ (~75-76 wt.%) remains roughly constant, as indicated by the observed turning-point (Fig. 2.15e). On the other hand, MgO (<0.5 wt.%), CaO (<0.5 wt.%) and Al₂O₃ (~13 wt.%) only slightly decrease (Fig. 2.15c,d), and Sr decreases sharply from 200 to <50 µg/g (Fig. 2.15f). This step involving the hornblende-consuming reaction crystallises 37 % of the system and, by applying the CaO-in-melt thermometer of [Marxer and Ulmer \(2019\)](#) on our modelled melt, ranges from 740 to 690 °C. Consequently, the total crystal cargo of the system reaches 85 %, leaving only 15 % interstitial melt with a haplogranitic composition. The biotite-producing reaction decreases the interstitial melt fraction over a small temperature interval – a common feature of peritectic reactions (e.g., [Blatter et al., 2017](#); [Marxer and Ulmer, 2019](#)). Experimental data indicate a temperature of 725 °C and a similar strong decrease of the melt fraction from 45 to 15 vol.% in a <50 °C interval ([Marxer and Ulmer, 2019](#)). Such a narrow temperature window is in good agreement with the calculated Ti-in-quartz temperatures (690-730 °C) and the model-derived CaO-in-melt temperatures (690-740 °C). The final phases to crystallise correspond to the haplogranitic assemblage identified as the interstitial quartz and alkali feldspar as well as the low-An (~An₃₀) plagioclase rims. The QEMSCAN analyses and thin section observations revealed that it constitutes between 12 and 16 % of the tonalites, which is well-reproduced by the LLD model. This last crystallisation step is not modelled because its modal composition largely depends, in addition to pressure, temperature and melt H₂O content, on the melt composition ([Blundy and Cashman, 2001](#)). Nonetheless, the crystal assemblage would be constituted of 34 % quartz, 25 % alkali feldspar and 41 % plagioclase according to the QEMSCAN analyses, which is similar to the calculated normative compositions. Such CIPW proportions correspond to the H₂O-saturated granite minimum at ~250-300 MPa reached at 680 °C ([Blundy and Cashman, 2001](#)), which is in reasonable agreement with the lowest CaO-in-melt temperature of a pegmatitic granite (696 °C). The calculated crystallisation temperatures of quartz intergrown with alkali feldspar are slightly lower (618-660 °C) and probably represent the transition between magmatic and hydrothermal conditions.

After 100 % crystallisation, the modal proportions of sample CJ26 are reproduced and the initial melt composition is matched by the bulk composition, implying that the LLD model reproduces the textural and geochemical data. This mass balance model

2. Peritectic biotite and crystal-melt segregation

Table 2.3. Crystallising assemblages and their major element compositions used in the differentiation model.

Step No.	Modelled crystallising assemblages	Proportions wt.%							
Step 1	Amp ₁ + Pl ₁ + Ap + Ilm + Mag + Zrn	24							
Step 2	Amp ₂ + Pl ₂ + Ap + Ilm + Mag + Zrn	24							
Step 3 ^a	Melt ₁ + Amp + Ilm = Melt ₂ + Bt + Qz + Pl ₃ + Ap + Mag + Zrn	37-40							

Step No.	Temperature °C	SiO ₂ wt.%	TiO ₂ wt.%	Al ₂ O ₃ wt.%	FeO wt.%	MgO wt.%	CaO wt.%	Na ₂ O wt.%	K ₂ O wt.%
Step 1	950-825	48.14	1.09	20.30	8.86	4.51	10.74	2.98	0.29
Step 2	825-725	49.51	1.30	21.07	8.05	3.62	9.30	4.00	0.50
Step 3 ^a	725-700	76.23	0.06	13.85	1.70	0.67	1.62	2.13	3.20

^aIncludes peritectic reaction and co-crystallising phases

reconstructs the tonalite LLD from a parental andesitic melt to an evolved interstitial rhyolitic melt and reasonably matches the tonalite and granite compositions from Western Adamello. However, the modelled cumulate line of descent cannot explain the composition of the hornblende-biotite-gabbros and leucotonalites (Fig 2.15).

2.7.3 Crystal-melt segregation model

The field and textural relationships suggest that the Western Adamello tonalite underwent *in situ* crystal accumulation and melt segregation and extraction as illustrated by the gabbroic and leucotonalitic cumulates associated with the granitic dikelets and dikes, respectively. Based on the simple hypothesis that hornblende-biotite-gabbros have lost plagioclase to the leucotonalites, we used the calculated LLD and cumulate line of descent (CLD) to model the chemical evolution of the crystal-melt segregation process occurring within the crystallising tonalite (Fig. 2.16). The first part of the model (Part 1) consists of removing plagioclase, and quartz when it crystallises, at every step along the CLD, and adding it at every step of the LLD (Fig. 2.16a). This operation leads, on the one hand, to a strong K₂O increase along the CLD starting at the onset of biotite crystallisation. On the other hand, the modified LLD is progressively enriched in the plagioclase-forming elements (i.e., CaO, Na₂O, Al₂O₃), but not in SiO₂ given that quartz appears after ~50 % crystallisation while the interstitial melt displays >75 wt.% SiO₂. Potassium continuously decreases as the melt proportion relatively decreases. This model reproduces the

leucotonalite compositions but only the low-K₂O (<4 wt.%) hornblende-biotite-gabbros.

The different processes leading to crystal accumulation and melt segregation are inefficient and hindered by several physical factors. As such, we consider, in a second step (Part 2), different fractions of trapped melt between the crystals that accumulate along the CLD (Fig. 2.16b). This model considering trapped melt fractions results in an increase in incompatible elements (e.g., SiO₂, K₂O), and especially at low to intermediate crystal proportions and high trapped melt fractions compared to the previous models. For example, at 50 % crystallinity, the difference between 0 and 50 % trapped melt results in a difference of 0.8 wt.% K₂O and 8 wt.% SiO₂ for the hornblende-biotite gabbros. This effect is due to the differential impact of trapped melt at different crystallinity levels. Overall, this model combining plagioclase and quartz loss in equal proportions and the presence of trapped melt reproduces the observed increase of K₂O in the hornblende-biotite-gabbros, and approaches the observed modal variability of gabbros. However, the modelled K₂O contents remain lower compared to the bulk rock compositions and the gabbro modal proportions exhibit higher proportions of quartz relative to plagioclase.

Based on these observations, we refined and developed a third model (Part 3) that integrates the preferential loss of plagioclase with respect to quartz (Fig. 2.16c). Because quartz loss is only effective after quartz saturation, the resulting CLD is shifted to higher SiO₂ contents starting from the onset of quartz crystallisation, that is after 48 % crystallisation. Two models encompassing the gabbroic and leucotonalitic compositions are presented in Fig. 2.16c and Table 2.4. Part 3a accounts for the low-SiO₂ end of the gabbroic spectrum and has 95 % and 80 % of plagioclase and quartz removal, respectively, and 30 % trapped melt. The leucotonalitic counterpart is correspondingly enriched in these phases. Part 3b has less crystal and interstitial melt loss with 80 % plagioclase and 70 % quartz removal, and 70 % trapped melt in the gabbros, which leads to smaller corresponding plagioclase and quartz gain in the leucotonalite. The same conclusions can be drawn using Al₂O₃, CaO, Sr and Zr (Supplementary Material 1). Overall, Parts 3a and 3b reproduce the leucotonalite and hornblende-biotite-gabbro crystal proportions and chemical compositions and emphasise that plagioclase and quartz do not accumulate in cotectic proportions. It appears that the composition of hornblende-biotite-gabbros is controlled (1) by the amount of trapped melt in the first half of the CLD (i.e., before the biotite-forming peritectic reaction), and (2) by the proportions of plagioclase and quartz segregation after the onset of quartz crystallisation.

It is important to note that the hornblende-biotite-gabbros are reproduced after the onset of the peritectic reaction. This corresponds to a crystallinity of about 40-60 %.

2. Peritectic biotite and crystal-melt segregation

Indeed, at such crystal fraction, the crystal matrix likely forms a continuous framework that has a finite rigidity, therefore promoting compaction and filter pressing as the most efficient processes leading to crystal-melt segregation. Compaction is thought to operate at two different degrees, the first one agglomerating the crystals with significant trapped

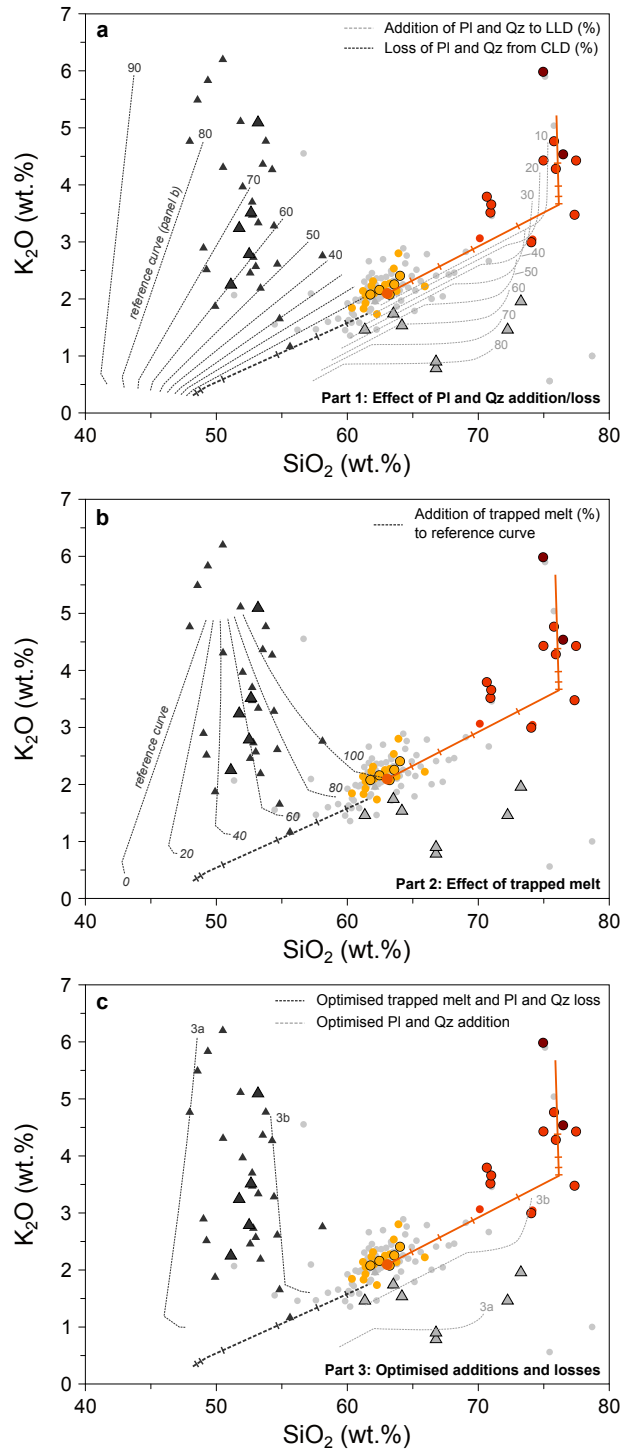


Figure 2.16. (Figure caption on next page.)

melt fraction (“mechanical compaction” of [Holness et al., 2018](#)), and the second one deforming the agglomerating crystals (“viscous compaction” of [Holness et al., 2018](#)) allowing more interstitial melt (\pm crystals) to escape ([Holness, 2018](#); [Holness et al., 2018](#); [Philpotts and Ague, 2009](#)). The field relationships and texture of the associated hornblende-biotite-gabbro and leucotonalite dikes represent examples of crystal accumulation through mechanical compaction, whereas the deformed biotite and quartz crystals in some gabbros provide evidence of viscous compaction. Such a phenomenon occurs at high crystal fractions close to the maximum packing (>70 % crystals) and requires a relatively high differential stress (>10 MPa) to deform centimetre-sized crystals ([Rybacki and Dresen, 2004](#)). Viscous compaction is usually difficult to observe in the plutonic rock record and can potentially lead to the additional extraction of 10-20 % melt. In contrast, the diapir-shaped gabbros and thick gabbro-leucotonalite layering are associated with abundant mafic enclaves and represent irregular segregation zones with a shape controlled by mafic melt injection. Such mafic melt injections would locally reduce the viscosity enabling the system to reach a critical state where deformation induced crystal-melt segregation is efficient. However, the volume, and thus the amount of shear stress, of magma recharge tends to be smaller with differentiation, thus providing only limited additional energy (e.g., [Dufek and Bergantz, 2005](#)). Finally, the observation of miarolitic cavities suggests that late-stage fluids exsolved during the differentiation of the tonalite. The exsolution of a fluid phase results in volume expansion of the magma reservoir and might trigger, or at least aid, melt segregation, although this process is thought to have a limited impact because of the positive buoyancy of the fluid phase (e.g., [Parmigiani et al., 2016](#)).

Based on the estimated volumes of the Western Adamello (300-400 km³), hornblende-

Figure 2.16. Illustration of a two-step model (crystal loss or addition followed by trapped liquid) plotted as SiO₂ vs. K₂O. **a**, Part 1: Effects of plagioclase and quartz addition and loss on the compositional evolution of liquids (LLD) and cumulates (CLD). Dashed green lines illustrate the compositional effects of 10 to 90 % removal of quartz + plagioclase to the CLD. The reference curve (80 %) is used for the trapped melt model in panel **b**. Dashed grey lines illustrate the compositional effects 10 to 90 % addition of quartz + plagioclase to the LLD. For example, 50 % of plagioclase + quartz addition to the LLD means that 50 % of total plagioclase and 50 % of total quartz are added to the LLD. Quartz is removed or added only when it is part of the mineral assemblage, otherwise only plagioclase is removed or added. **b**, Part 2: Effects of trapped melt on the CLD. The green dashed lines correspond to different proportions of added trapped melt to a reference curve. The reference corresponds to 80 % plagioclase and 80 % quartz loss from the CLD (see Part 1). The trapped melt composition corresponds to the interstitial melt composition at the step of interest. **c**, Optimised addition and loss of plagioclase and quartz, and addition of trapped melt covering covering the whole range of hornblende-biotite-gabbro and leucotonalite compositions and highlighting non-cotectic proportions of plagioclase and quartz. The proportions of plagioclase and quartz loss or addition as well as trapped melt proportions are discussed in the main text.

2. Peritectic biotite and crystal-melt segregation

Table 2.4. Proportions of phase added and removed along the liquid and cumulate lines of descent for the crystal-melt segregation model. A range of values is given for models testing multiple inputs.

	Cumulate line of descent			Liquid line of descent	
	Pl loss	Qz loss	Trapped melt	Pl gain	Qz gain
	wt.%	wt.%	wt.%	wt.%	wt.%
Part 1	0-90	0-90	0	0-80	0-80
Part 2	80	80	0-100	0-80	0-80
Part 3a	95	80	30	48	32
Part 3b	80	70	70	22	18

biotite-gabbros (0.2-0.5 vol.%, 0.6-2.0 km³), leucotonalites (0.05-0.1 vol.%, 0.15-0.40 km³) and granites (0.1-0.2 vol.%, 0.3-0.8 km³), it is possible to estimate the volumes of accumulated crystals, trapped melt and extracted melt. If the crystal-melt segregation process would be perfect, the extracted melt and accumulated crystal volumes would be equal to the volume of the gabbro and leucotonalite (0.75-2.4 km³) and the granite volume (0.3-0.8 km³), respectively. Nevertheless, we demonstrated that some amount of interstitial melt is trapped between the accumulating crystals. By considering the proportions of trapped melt in the hornblende-biotite-gabbros (10-25 %) and in the leucotonalites (20-60 %), the volume of trapped melt reaches 0.09-0.74 km³. This calculation places the efficiency of melt segregation from 52 to 77 %, highlighting the imperfect nature of the crystal-melt segregation within the Western Adamello tonalite. The systematic incorporation of a few plagioclase and quartz crystals in granite as well as the high proportions of trapped melt in leucotonalite indicate that plagioclase and quartz probably inhibit complete phase separation. The efficiency of compaction highly depends on the particle size and shape (e.g., [Philpotts et al., 1998](#)), but it is also controlled by the melt viscosity and the density contrast between crystals and melt. The separation of small crystals from a low density, highly viscous melt is extremely slow. A typical H₂O-saturated granitic melt at 200-300 MPa has a high viscosity ($\sim 10^5$ Pa s) and relatively low density ($\sim 2,200$ - $2,300$ kg m⁻³; [Lange and Carmichael, 1990](#)). The density contrast with plagioclase ($\Delta\rho = 400$ kg m⁻³) and quartz ($\Delta\rho = 300$ kg m⁻³) is smaller than with amphibole ($\Delta\rho = 700$ - $1,200$ kg m⁻³) and biotite ($\Delta\rho = 700$ - $1,200$ kg m⁻³), and the plagioclase and quartz crystals are on average smaller than amphibole and biotite. Altogether, this indicates that separation of the interstitial melt from plagioclase and quartz is expected to be less efficient than from amphibole and biotite.

2.7.4 Importance of peritectic biotite in crystallising felsic plutonic rocks

In this section, we investigate the role of crystallising biotite and the potential links to leucotonalite and high-silica granite production in felsic plutonic rocks. We evaluate field relationships and bulk rock chemistry of the Peninsular Ranges batholith (Mexico and USA) and the Tuolumne intrusive suite (Sierra Nevada, USA), and compare them with the Western Adamello data (Figs. 2.17 and 2.18).

Peninsular Ranges batholith

The Peninsular Ranges batholith (PRB) (Fig. 2.17a) mainly consists of tonalites and granodiorites emplaced in a Cretaceous (126-98 Ma) continental arc associated with the subduction of the Farallon plate beneath North America. The PRB is composed of two units, the eastern PRB and the western PRB, based on different Sr, Nd and O isotopic signatures, even though compositional differences also occur (Kistler et al., 2003). Bulk rock data of the PRB (Lee et al., 2007) exhibit a LLD starting from a tonalitic parental melt evolving toward a K₂O-rich granite (Fig. 2.17b). In detail, the eastern PRB tonalite-granodiorite is more heterogeneous than the western part, perhaps best illustrated by the wide range of K₂O contents spanning almost 3 wt.% K₂O. Despite this heterogeneity, we model a simplified LLD for the PRB because the observed mineral assemblages in the eastern and western PRB are similar. The same mass balance calculations as described above have been employed to model the PRB parental melt evolution. To identify a potential parental tonalitic melt, we calculated the K₂O composition of the melt in equilibrium with the most primitive amphibole using distribution coefficients of Nandedkar et al. (2016) (Fig. 2.17c). Some of the PRB tonalites have similar compositions as the calculated melt, indicating that a melt composition has been preserved by at least some tonalites. The initial melt has ~63 wt.% SiO₂ and 1.9 wt.% K₂O and has similar mineral assemblages as the Western Adamello tonalite. Mineral proportions of the rocks constituting the PRB were reported by Morton et al. (2014) and were used to model the PRB LLD. They show that the tonalite and granodiorite hornblende content decreases with increasing biotite and quartz indicating a similar biotite-forming peritectic reaction.

Magmatic structures are described throughout the entire Peninsular Ranges batholith (Fig. 2.17a). These encompass (1) melanocratic hornblende-biotite-rich gabbrodiorite schlieren alternating with (2) leucocratic plagioclase-quartz leucotonalite schlieren, both having similar textures as the host tonalite, as well as (3) pegmatite dikes of granite composition (Morton, 1969; Morton et al., 2014). Bulk rock analyses of the schlieren are lacking in the PRB rock record. We infer, however, based on field descriptions and modal

2. Peritectic biotite and crystal-melt segregation

mineralogy (Morton, 1969; Morton et al., 2014), that the hornblende-biotite-gabbros have intermediate K_2O contents (2-5 wt.%) and rather low SiO_2 contents (<55 wt.%), and that the leucotonalite schlieren have higher SiO_2 (60-70 wt.%) and lower K_2O contents (<2 wt.%). Because bulk rock data for the different magmatic structures are not available, no mass balance model has been employed but we infer that plagioclase and melt loss along the CLD on one hand, and plagioclase and quartz addition to the LLD on the other, would explain the presence of hornblende-biotite-gabbros and leucotonalites, respectively.

Tuolumne intrusive suite

The Tuolumne intrusive suite (TIS) (Fig. 2.17d) is mainly composed of granodiorite emplaced in a Cretaceous (95-85 Ma) continental arc along the western margin of North America. It is separated into five units based on rock textures: the Kuna Crest granodiorite, the equigranular and porphyritic Half Dome granodiorites, the Cathedral Peak granodiorite, and the porphyritic Johnson leucogranite (e.g., Bateman and Chappell, 1979; Coleman et al., 2004). The host granodiorites from the different units exhibit comparable compositions, except the Kuna Crest granodiorite that is less differentiated (SiO_2 <65 wt.%) and some Cathedral Peak granodiorite samples having lower K_2O contents (<3 wt.%) forming a LLD towards granitic compositions (Fig. 2.17e). We modelled one LLD following the same procedure as for the WAT and the PRB using mineral proportions from Solgadi and Sawyer (2008). The parental melt has been calculated using the most primitive amphibole from the equigranular Half Dome granodiorite, and the partition coefficients of Nandedkar et al. (2016) (Fig. 2.17f). The initial melt has ~67 wt.% SiO_2 and 3.2 wt.% K_2O with a first mineral assemblage mainly composed of plagioclase, amphibole and biotite, resulting in a calculated interstitial melt of 75 wt.% SiO_2 and 4.2 wt.% K_2O . Unlike the WAT and the PRB, the K_2O -bearing phase responsible for the final differentiation of the TIS is alkali feldspar which makes up to 20 vol.% of the Cathedral Peak granodiorite (Solgadi and Sawyer, 2008). The second fractionating assemblage is made of plagioclase, quartz, alkali feldspar and minor biotite, leading to an increase of K_2O in the interstitial melt. This crystallisation path involving the formation of alkali feldspar at relatively high melt fraction represents one endmember of the spectrum of granitoid crystallisation paths, as opposed to the peritectic biotite and quartz crystallisation.

Field observations indicate abundant magmatic structures (Fig. 2.17d) such as (1) hornblende- and biotite-rich schlieren of gabbroic composition often intermingled with plagioclase-rich (leucotonalite) and/or alkali-feldspar-rich accumulations, (2) hornblende- and biotite-rich ladder dikes (Glazner et al., 2021), and (3) leucogranite dikes (Ardill

et al., 2020). The gabbro-leucotonalite layers display similar field relationships as the accumulation zones within the Western Adamello. Bulk rock major and trace element chemistry are comparable as illustrated by the large variability of K_2O of the hornblende-biotite-rich schlieren (1.9-5.2 wt.%) at lower SiO_2 values (48.3-63.9 wt.%), and the lower K_2O contents (0.8-4.6 wt.%) of the leucotonalites relative to granodiorite and granitic

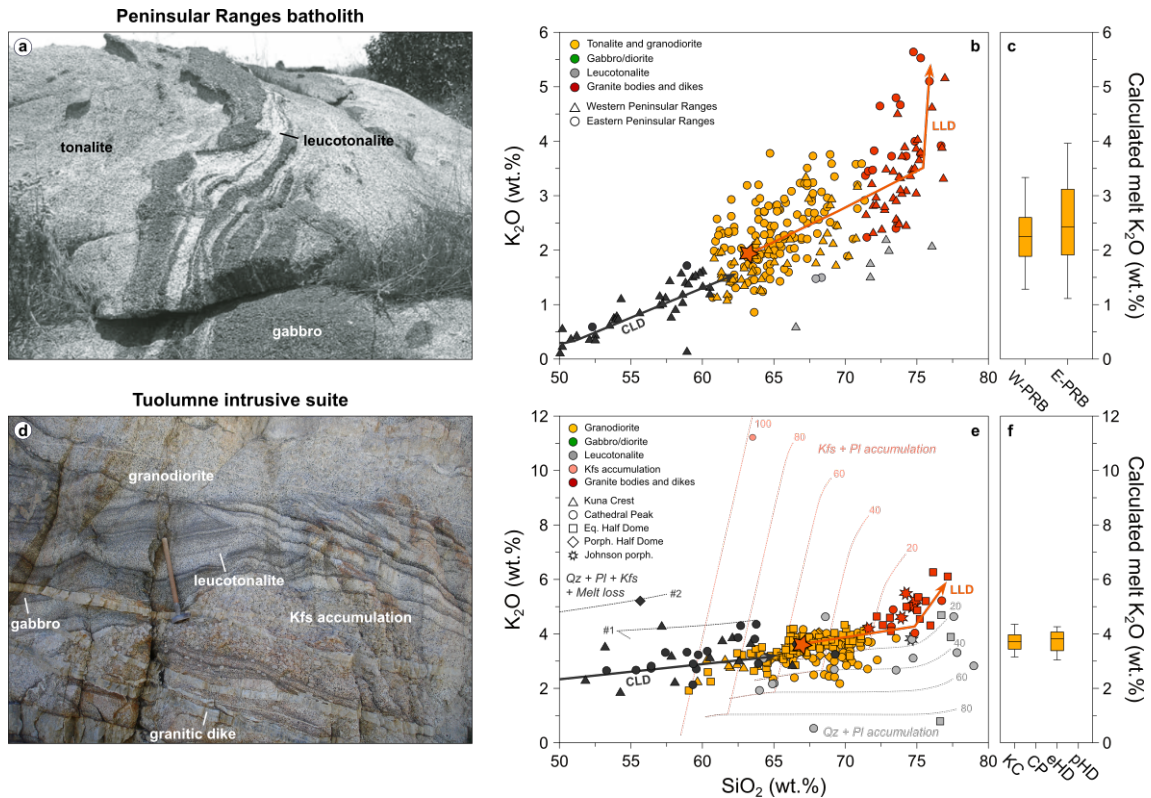


Figure 2.17. Textural and geochemical comparison with different batholiths from the western United States. **a**, Peninsular Ranges batholith field relationships observed in the southwestern Lakeview Mountains pluton. Typical interlayered melanocratic hornblende-biotite-gabbro schlieren and leucocratic plagioclase- and quartz-rich leucotonalite schlieren within the host tonalite. Modified after Morton et al. (2014). **b**, SiO_2 vs. K_2O diagram illustrating the LLD and CLD. The developed model follows the same logic as the Western Adamello model. Bulk rock data are from Lee et al. (2007). **c**, Box plots of the K_2O contents of the calculated melt in equilibrium with the most primitive amphiboles reported in the western and eastern Peninsular Ranges batholith (W-PRB and E-PRB, respectively). Amphibole compositions are from Jiang and Lee (2017). **d**, Tuolumne intrusive suite field relationships observed in the Sawmill canyon (Photo: O. Müntener). Typical hornblende-biotite-gabbro and leucotonalite schlierens are in contact with a alkali feldspar accumulation zones, the whole comprised in the host granodiorite. **e**, SiO_2 vs. K_2O diagram illustrating the LLD, CLD and the crystal-melt segregation model. The developed model follows the same logic as the Western Adamello model and is further explained in the main text. Bulk rock data are from Ardill et al. (2020), Bateman and Chappell (1979), Bateman et al. (1984), Burgess and Miller (2008), Coleman et al. (2012), Glazner et al. (2020), Gray et al. (2008), Oppenheim et al. (2021), Paterson et al. (2008) and Solgadi and Sawyer (2008). **f**, Box plots of the K_2O contents of the calculated melt in equilibrium with the most primitive amphiboles reported in the Kuna Crest granodiorite (KC) and equigranular Half Dome granodiorite (eHD). Amphibole compositions are from Barnes et al. (2016b) and Werts et al. (2020).

2. *Peritectic biotite and crystal-melt segregation*

dikes. The main difference resides in the alkali feldspar accumulation zones having K_2O contents up to 11 wt.%. The same crystal-melt segregation model is developed for the TIS, which is based on the modelled liquid and CLD, and consists of three different steps: (1) different amounts of plagioclase, quartz and alkali feldspar are lost, and interstitial melt is added, along the CLD to reproduce the hornblende-biotite-gabbros; (2) these plagioclase and quartz crystals are then added to the LLD; and (3) alkali feldspar crystals, alongside small amounts of plagioclase and quartz, are also added to the evolving melt. Rock types showing mineral accumulations (i.e., hornblende-biotite-gabbros, leucotonalites and alkali feldspar accumulations) are well-reproduced using this mass balance model (Fig. 2.17e). The gabbroic compositions are the consequence of plagioclase, quartz, alkali feldspar and melt segregation in different proportions, with Model 1 corresponding to moderate crystal and melt segregation (70 % plagioclase, 40 % quartz and alkali feldspar, 50 % melt), and Model 2 to high crystal and melt segregation (85 % plagioclase, 70 % quartz, 50 % alkali feldspar, 70 % melt).

Based on hornblende chemistry and zircon saturation temperatures, [Barnes et al. \(2019\)](#) proposed that each TIS unit experienced crystal accumulation and therefore represents cumulates. Bulk rock major element chemistry suggests that some granodiorites from Cathedral Peak have accumulated plagioclase and/or hornblende, resulting in lower K_2O values. Nonetheless, a large part of the granodiorites follows a trend of increasing K_2O (3-4 wt.%) with SiO_2 (65-70 wt.%) probably indicating crystallisation without substantial melt loss. By applying a recent calibration of zircon saturation in tonalite ([Marxer and Ulmer, 2019](#)) and following the reasoning of [Barnes et al. \(2019\)](#), we find that the majority of the TIS granodiorite did not experience significant melt loss (mostly <15 %). Additionally, amphibole composition is in trace element equilibrium with most of their host granodiorite, which further supports such an hypothesis. In summary, the TIS granodiorites represent melt that underwent extensive alkali feldspar crystallisation coupled with crystal-melt segregation forming hornblende-biotite-gabbros, leucotonalites and alkali feldspar-rich layers.

2.7.5 Phase relationships in pseudoternary projections

Tonalites and granites along with gabbroic and leucotonalitic cumulates are plotted on the clinopyroxene-olivine-quartz (Cpx-Ol-Qz+Or) pseudoternary diagram to illustrate the control of phase equilibria on the LLD (Fig. 2.18). Normative mineral compounds were calculated from bulk rock compositions following the approach presented by [Grove \(1993\)](#) and the modifications proposed by [Blatter et al. \(2017\)](#). Experimental and natural studies

demonstrated that the early evolution of basaltic to andesitic melts are controlled by the olivine + clinopyroxene cotectic followed by the two-pyroxene cotectic. Amphibole forms through a distributary peritectic reaction consuming clinopyroxene and/or orthopyroxene (e.g., [Sisson and Grove, 1993](#)). The experimental tonalite LLD ([Marxer and Ulmer, 2019](#)) maps out the two-pyroxene cotectic as well as the clinopyroxene + melt₁ = amphibole + melt₂ reaction, but also highlights a second, amphibole-consuming peritectic reaction driving the residual melt towards the quartz apex (Fig. 2.18b).

The Western Adamello tonalite is slightly more evolved than the starting material used by [Marxer and Ulmer \(2019\)](#). Except for one sample with higher normative clinopyroxene, the majority of Western Adamello tonalites has a weakly negative clinopyroxene component and are therefore corundum-normative (Fig. 2.18a,c). Amphibole is the first ferromagnesian phase to crystallise and drives the interstitial melt towards higher normative quartz, and corundum, contents. As liquids evolve down-temperature, amphibole reacts and is replaced by biotite, consistent with the peritectic reaction amphibole + melt₁ = biotite + melt₂. The onset of this reaction is probably controlled by the composition of the evolving melt. Indeed, the residual melt becomes corundum- and quartz-normative

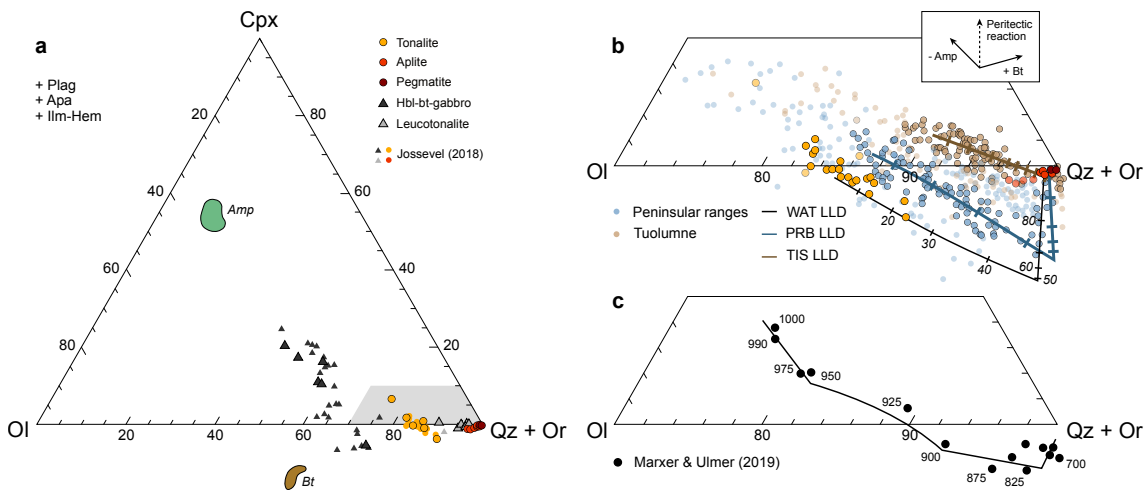


Figure 2.18. Clinopyroxene (Cpx)-olivine (Ol)-quartz + orthoclase (Qz + Or) pseudoternary diagrams represented from the plagioclase apex ([Grove, 1993](#)) illustrating the experimental LLD of a tonalite at 200 MPa ([Marxer and Ulmer, 2019](#)) and the LLD of the Western Adamello tonalite, Peninsular Ranges batholith and Tuolumne intrusive suite. **a**, Pseudoternary Ol-Cpx-Qz+Or projection of Western Adamello samples with amphibole and biotite compositions. **b**, Enlargement of the quartz + orthoclase apex showing the Western Adamello along with the Peninsular Ranges batholith and Tuolumne intrusive suite compositions. The three modelled LLD with 10 % fractionation steps are also represented for comparison. Three vectors are displayed to highlight the effects of biotite crystallisation, amphibole consumption and peritectic reaction on the melt composition. The shaded symbols represent cumulate compositions identified based on their major and trace element contents. **c**, Enlargement of the quartz + orthoclase apex with the tonalite experimental LLD and the associated run temperatures ([Marxer and Ulmer, 2019](#)). *Amp*, amphibole; *Hem*, hematite; *Opx*, orthopyroxene. Other abbreviations as in the text and previous figures.

2. Peritectic biotite and crystal-melt segregation

(i.e., SiO₂-rich, CaO-poor) causing a disequilibrium with amphibole. The resulting dissolution of amphibole combined with the crystallisation of biotite having highly negative clinopyroxene and quartz components pushes derivative biotite-saturated melts to higher, although still negative, clinopyroxene-normative compositions approaching the quartz + orthoclase apex, and thus the granite minimum, and crystallising quartz + plagioclase + alkali feldspar ± biotite. Accumulation of trace amounts of amphibole and/or biotite in leucotonalite results in a small shift from the quartz + orthoclase apex towards the olivine corner (Fig. 2.18b).

The Peninsular Ranges batholith exhibits comparable phase relationships as the Western Adamello tonalite. The difference resides in the lower MgO and higher CaO contents of the PRB parental melt which shifts derivative melt compositions towards the quartz apex (Fig. 2.18c). The first modelled fractionating mineral assemblage consists of amphibole and plagioclase and drives the melt to increasing corundum-normative contents until saturation with biotite and quartz. We infer from the data that the same ‘turning-point’ corresponding to the biotite-forming peritectic reaction controls the evolution of the interstitial melt composition towards the Qz + Or component.

In contrast, the TIS exhibits different phase relationships compared to the WAT and the PRB. First the TIS granodiorites display higher normative clinopyroxene and quartz components reflecting higher initial CaO and SiO₂ contents (Fig. 2.18). After emplacement, the dacitic to rhyodacitic melts can be modelled by first crystallising amphibole, plagioclase and biotite, enhancing their normative quartz component. Further differentiation results in the crystallisation of plagioclase, quartz, alkali feldspar and minor amounts of biotite, presumably without reaction with amphibole (e.g., [Solgadi and Sawyer, 2008](#)). Indeed, the CaO contents of the TIS residual melts are higher compared to the WAT and PRB and we infer that amphibole remains in equilibrium with the interstitial melt, therefore suppressing peritectic biotite formation and favouring cotectic alkali feldspar as the K₂O-bearing phase. Early alkali feldspar crystallisation (735-760 °C) has been documented in the TIS based on textures and titanite compositions ([Moore and Sisson, 2008](#)) and might suppress the biotite peritectic reaction.

The differences exhibited by the Western Adamello tonalite and the Tuolumne intrusive suite are related to the degree of peraluminosity of their parental melt which most likely reflects contrasting crystallisation-differentiation paths before emplacement in the upper crust. Extensive olivine, orthopyroxene and/or garnet fractionation keeps the melt clinopyroxene-normative, whereas clinopyroxene (and amphibole) fractionation drives the evolving melt towards peraluminous compositions. Petrology of ultramafic enclaves from

the southern Adamello (Ulmer et al., 1983) and the bulk rock dataset of the Adamello batholith (Müntener et al., 2021) reveal that the early differentiation of Adamello melts is controlled by olivine and followed by clinopyroxene. In contrast, the occurrence of garnet-bearing websterite cumulates has been used to argue for garnet fractionation in the Sierra Nevada lower crust (Lee et al., 2006). This is consistent with a slight increase of the MnO/MgO ratio with differentiation in the Sierra Nevada, supporting early garnet fractionation (Klein and Müntener, 2023). Garnet is a stable phase in hydrous, andesitic magmas at >800 - $1,000$ MPa (Alonso-Perez et al., 2009; Blatter et al., 2023; Müntener et al., 2001; Ulmer et al., 2018), and contributes at keeping the melt metaluminous. However, liquidus olivine and (extensive) clinopyroxene are usually related to the crystallisation of hydrous basaltic melts at ≥ 700 MPa (Müntener and Ulmer, 2018; Nandedkar et al., 2014), which drives the melt towards corundum-normative compositions before garnet saturation. Collectively, this information suggest that the primitive melt H₂O content and the fractionation pressure exert a major control on the final differentiation of felsic melts.

2.7.6 Implications for melt extraction in the WAT

The biotite-forming peritectic reaction controls the late evolution of weakly peraluminous, corundum-normative, intermediate to felsic melts and lowers the melt fraction from ~ 40 to ~ 15 wt.% over only a 50 °C temperature window (Marxer and Ulmer, 2019). This is also true for the WAT modelled LLD as the CaO content, and thus temperature (Marxer and Ulmer, 2019), sharply decreases from ~ 740 °C at the onset of the peritectic reaction (~ 50 wt.% crystals) to ~ 700 °C when the melt reaches a haplogranitic composition (~ 85 wt.% crystals). The crystal-melt segregation within the Western Adamello only occurs after the onset of the peritectic reaction consistent with achieving a critical crystallinity from a magma to a mush behaviour. This rapid decrease of melt fraction probably exerts an important control on segregation of interstitial melt. Enhanced crystallisation with peritectic reactions is associated with substantial release of latent heat of crystallisation. Therefore, despite an increase in crystallinity of ~ 35 % over a small temperature interval, enthalpy significantly decreases during peritectic reactions and buffers temperature (e.g., Blatter et al., 2017; Ussler III and Glazner, 1992). This process slows down cooling and extends the time spent at the biotite peritectic reaction and the window for melt segregation and extraction.

Two “storage models” are currently debated to describe the thermal state of magma reservoirs. The first model argues for a near- to subsolidus storage of upper crustal magma

2. Peritectic biotite and crystal-melt segregation

reservoirs based on U-series disequilibria and Sr diffusion in plagioclase (Cooper and Kent, 2014), whereas the second instead favours a storage at higher temperatures inferred from zircon high-resolution geochronology and trace element data (Barboni et al., 2016). Regardless of the storage model, the thermal evolution of magma reservoirs is controlled by the average flux of magma input and the volume of a single injection. Different thermal models have shown that, depending on these two parameters, upper crustal magma reservoirs are stored between $\sim 700\text{--}720$ °C for relatively low average fluxes and $\sim 750\text{--}770$ °C for higher average magma fluxes (e.g., Weber et al., 2020). The WAT has a total volume of ~ 400 km³ and has been emplaced in ~ 1.2 Myr (Floess, 2013) which corresponds to an average normalised flux of $\sim 3.3 \times 10^{-6}$ km³ km⁻² yr⁻¹. The calculated magma inputs are typical of plutonic bodies and are predicted to be stored at temperatures $< 710\text{--}720$ °C (e.g., Weber et al., 2020) and crystallinities > 80 wt.% (Marxer and Ulmer, 2019). This is in good agreement with the developed crystal-melt segregation model showing that the extracted granite compositions are reached after ≥ 80 wt.% crystallisation. Such high crystal fractions, which are directly linked to the average magma flux and storage temperature, probably hampers the segregation of large volumes of interstitial melt. Indeed, the largest

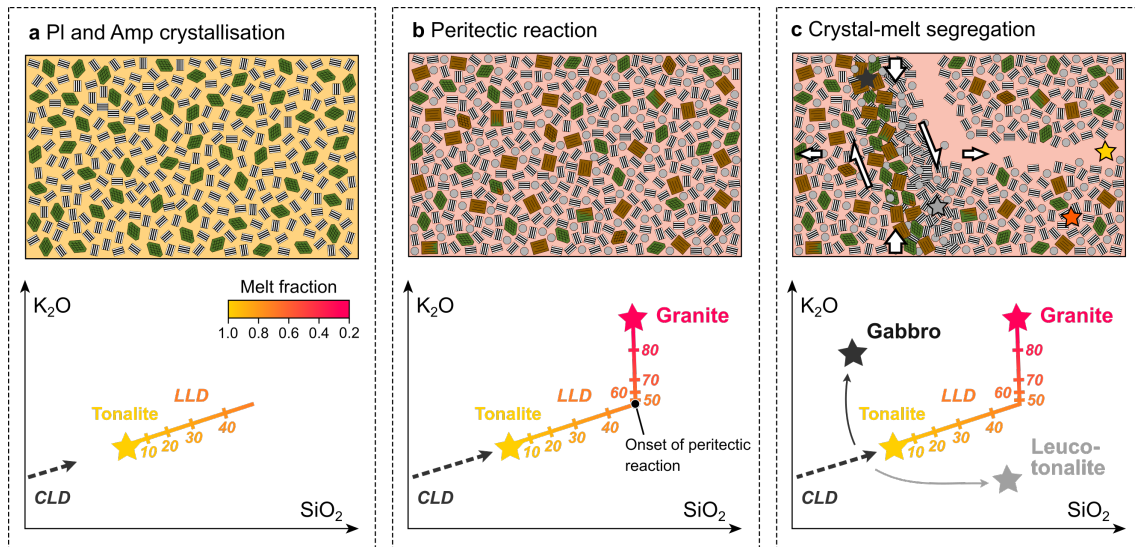


Figure 2.19. Schematic model of the physicochemical evolution of the Western Adamello tonalite illustrated with SiO₂ vs. K₂O. The interstitial melt evolution is qualitatively represented as well as the four principal phases (i.e., amphibole, biotite, plagioclase, quartz) and their proportions. Tick marks along the LLD indicate 10 % fractionation steps. **a**, Amphibole- and plagioclase-dominated crystallisation from the liquidus to ~ 50 % crystallinity. **b**, The onset of the biotite-forming peritectic reaction results in a sharp increase of the crystallinity as well as the melt K₂O content at constant melt SiO₂ content. **c**, The mush undergoes crystal-melt segregation resulting in the formation of cumulative hornblende-biotite-gabbro and leucotonalite and the segregation and extraction of the interstitial granitic melt. A physical mechanism is proposed whereby the cumulative rocks result from shearing of the crystal mush while the granitic melts are segregated subparallel to the shear planes and then extracted.

granitic dike observed within the WAT is ~ 1 m wide and ~ 200 m long. We emphasise that the biotite peritectic reaction, by rapidly consuming the interstitial melt, coupled with the rather low temperature storage of the WAT, probably hinders large rhyolitic melt volumes to be extracted.

2.8 Conclusions

The Western Adamello tonalite records the physicochemical evolution of an upper crustal magma reservoir leading to the formation of crystal-poor granitic liquids. Field observations, bulk rock and mineral analyses coupled with known distribution coefficients suggest that the most primitive amphiboles are in equilibrium with the bulk tonalite composition, indicating that the WAT largely kept its original melt composition. Field and microtextural observations along with LLD modelling emphasise that crystallisation-differentiation of the tonalite is controlled by an amphibole-consuming, biotite-forming peritectic reaction and ultimately produces the granitic magmas after at least 50 % crystallisation. The weakly peraluminous character of the parental andesitic melt controls the onset of this peritectic reaction. Indeed, the Western Adamello magmas are relatively CaO-poor and weakly corundum-normative, while other intermediate to felsic melts such as the Tuolumne intrusive suite granodiorites are CaO-rich and have a positive clinopyroxene component which instead results in the formation of cotectic alkali feldspar. In contrast to the tonalites and granites, the WAT gabbros and leucotonalites accumulated large proportions of hornblende and biotite, and plagioclase and quartz, respectively, and represent *in situ* cumulates formed by dynamic segregation of crystals (Fig. 2.19). These cumulate rocks do not follow the modelled CLD and instead constitute ‘cumulative unmixing’ between amphibole-biotite and plagioclase-quartz taking place during the extraction of the granitic interstitial melts. We demonstrate through quantitative mass balance models that crystal-melt segregation operates after ≥ 50 % crystallisation and that > 30 % of the interstitial melt remains trapped between the accumulating hornblende and biotite crystals. This process is probably hindered by the combination of the high viscosity of the interstitial melt, the small density difference between plagioclase and interstitial melt, and by the rapid decrease of the melt fraction during the biotite-forming peritectic reaction. Our observations and models connect peritectic biotite formation with physical segregation of cumulates and melts and extraction of crystal-poor rhyolite. The studied tonalitic pluton ($300\text{--}400$ km³) essentially kept its original melt composition with volumetrically limited ($1.0\text{--}3.2$ km³) crystal accumulation and melt segregation. This view contrasts with other studies working on granitoids (e.g., Barnes et al., 2019; Deering and Bachmann, 2010)

2. Peritectic biotite and crystal-melt segregation

but is consistent with the scarcity of volcanic rocks in the Adamello batholith ([Müntener et al., 2021](#)).

2.9 Acknowledgements

We thank Ben Klein, Luka Wanner and Damien Roy for assistance in the field, Benita Putlitz with the sample preparation, Antoine de Haller for QEMSCAN analysis, Alexey Ulianov for precious help with LA-ICP-MS analysis, and Ben Klein and Lukas Baumgartner for discussion. We are grateful to an anonymous reviewer, Antonio Castro and especially Jon Blundy for very helpful reviews.

Chapter 3

Diffusion of Sr and Ba in plagioclase: Composition and silica activity dependencies, and application to volcanic rocks

Chapter submitted in *Earth and Planetary Science Letters*:

Grocolas, T., Bloch, E. M., Bouvier, A.-S. and Müntener, O. (in review). Diffusion of Sr and Ba in plagioclase: Composition and silica activity dependencies, and application to volcanic rocks. *Earth and Planetary Science Letters*.

3.1 Abstract

Strontium and barium diffusion chronometry in plagioclase is routinely applied to mafic and felsic magmatic systems. This technique can be used to determine the timescales of magma reservoir assembly and the cooling rates of plutons and volcanic rocks, which has emerged as a useful method to assess volcanic hazards. Here we report diffusion experiments that aim to constrain the diffusivities of Sr and Ba in oligoclase and labradorite at 1 atm pressure, between 900 and 1,200 °C, and assessing diffusion in different crystallographic orientations. In all of the reported experiments, silica activity (a_{SiO_2}) is buffered by varying stable phase assemblages in the diffusant source powder. The experimental products were analysed by secondary ion mass spectrometry (SIMS) depth profiling and laser ablation inductively coupled mass spectrometry (LA-ICP-MS) line scanning. There

3. Diffusion of Sr and Ba in plagioclase

is no resolvable dependence of Sr and Ba diffusion in plagioclase upon $a\text{SiO}_2$ or crystal orientation. However, Sr and Ba diffusivities are found to vary as functions of the plagioclase anorthite content. As such, we parameterise the diffusivity of Sr and Ba in plagioclase as a function of temperature and anorthite content as follows:

$$\log_{10}D_{\text{Sr}} \text{ (m}^2\text{/s)} = -1.65 (\pm 0.24) X_{\text{An}} - 3.03 (\pm 1.16) - \left[\frac{368,142 (\pm 27,141)}{2.303RT} \right],$$
$$\log_{10}D_{\text{Ba}} \text{ (m}^2\text{/s)} = -1.43 (\pm 0.20) X_{\text{An}} - 4.65 (\pm 0.96) - \left[\frac{337,037 (\pm 22,969)}{2.303RT} \right],$$

where X_{An} is the plagioclase anorthite content (mole fraction), T is the temperature (K), and R is the gas constant ($\text{J mol}^{-1} \text{K}^{-1}$). The diffusion rate of Sr in plagioclase determined in this study is ~ 1.5 -2 orders of magnitude slower than previously determined, whereas Ba diffusion is similar to previous studies. This is most likely due to the Ba-feldspar stability at the experimental conditions employed by previous studies, whereas Sr-feldspar was absent from the source powder stable assemblage. By applying the diffusivities determined in this study to plagioclase crystals from the Cerro Galán ignimbrite (Argentina) and Santorini caldera (Greece), we find timescales of $\sim 10^5$ years, with a good agreement between results from Sr and Ba diffusion modelling. Therefore, our data reconcile experimental diffusion data with measured Sr and Ba profiles in plagioclase and suggest that, at least regarding the Cerro Galán ignimbrite and Santorini caldera, plagioclase records the time needed to differentiate magma reservoirs and assemble large volumes of eruptible magma.

3.2 Introduction

In the last two decades, plagioclase [solid-solution from albite ($\text{NaAlSi}_3\text{O}_8$) to anorthite ($\text{CaAl}_2\text{Si}_2\text{O}_8$)] has emerged as a valuable tool for studying magma reservoir dynamics (e.g., [Ginibre et al., 2002](#)), magma water budget ([Waters and Lange, 2015](#)), ternary feldspar thermometry (e.g., [Fuhrman and Lindsley, 1988](#); [Putirka, 2005](#)), melt inclusions ([Blundy and Cashman, 2005](#); [Philpotts, 1981](#)), and timescales of magmatic processes (e.g., [Costa et al., 2003](#)). These studies take advantage of the capability of plagioclase to crystallise in mafic to felsic systems and, therefore, to record magmatic processes such as crystallisation-differentiation, magma recharge and mixing. The majority of applications of diffusion chronometry in plagioclase makes use of chemical zoning in anorthite [$\text{An} = 100 \times \text{molar Ca}/(\text{Ca} + \text{Na})$], Sr, Mg and Ba contents to infer magma residence time preceding volcanic eruptions (e.g., [Costa et al., 2010](#); [Druitt et al., 2012](#); [Flaherty et al., 2018](#); [Lubbers et al., 2022](#); [Zellmer et al., 1999](#)). The diffusion kinetics of many species within plagioclase

class have been experimentally determined for a wide range of temperatures, host mineral compositions and crystal orientations (Behrens et al., 1990; Cherniak and Watson, 1992, 1994; Cherniak, 1995, 2002, 2003; Faak et al., 2013; Giletti and Casserly, 1994; Giletti and Shanahan, 1997; Grove et al., 1984; Johnson and Rossman, 2013; LaTourrette and Wasserburg, 1998; Liu and Yund, 1992; Van Orman et al., 2014; Yund and Snow, 1989). In addition to these parameters, Faak et al. (2013) investigated the effect of silica activity on the diffusivity (D) of Mg in plagioclase; $a\text{SiO}_2$ is a variable that is routinely controlled in diffusion experiments on silicate minerals over the last ten years (e.g., Bloch et al., 2022; Zhukova et al., 2014).

Despite the development of a large database regarding the diffusivities of Sr, Ba and Mg in plagioclase, discrepancies between studies persist. Most of the previous studies report diffusion anisotropy in plagioclase (Supplementary Material 2), which is coherent with its triclinic crystal system. However, Giletti and Casserly (1994), Giletti and Shanahan (1997), LaTourrette and Wasserburg (1998) and Faak et al. (2013) instead propose that Sr, Rb and Mg diffuse isotropically in plagioclase, in contrast to the strong Sr diffusion anisotropy reported by Cherniak and Watson (1994). Additionally, Cherniak (2002) showed that Ba diffusivity is weakly anisotropic in oligoclase, whereas it is isotropic in labradorite. The plagioclase structure changes along its solid-solution, therefore varying the element compatibility in its crystallographic sites as a function of the plagioclase major element composition (e.g., Dohmen and Blundy, 2014). This phenomenon is expected to influence diffusivity and has been observed for all elements except in the study of Faak et al. (2013) where Mg diffusivity appears to be insensitive to the plagioclase composition. Another discrepancy resides in the higher diffusion rate of Sr parallel to the b -axis in andesine compared to oligoclase reported by Cherniak and Watson (1994). Finally, Faak et al. (2013) investigated the effect of the source $a\text{SiO}_2$ and propose that it represents an important variable controlling the diffusion rate of Mg in plagioclase.

In this study, we investigate the diffusion of Sr and Ba in oligoclase (An_{28}) and labradorite (An_{67}) between 900 and 1,200 °C and at 1-atm pressure, along the a , b and c crystallographic axes, and under conditions where the silica activity is buffered by varying stable phase assemblages in the diffusant source powder. We compare the diffusion coefficients determined in previous studies with the new diffusivities inferred from our experiments, and explain the apparent discrepancies by the stability of the powder assemblages. Finally, we apply our new experimental data to natural plagioclase Sr and Ba diffusion profiles, and retrieve similar diffusion timescales ($\sim 10^5$ yr) from modelling these two elements independently.

3.3 Methods

3.3.1 Source powder

Experiments were performed using a variety of powder diffusant sources, which were designed to impose varying $a\text{SiO}_2$ while also providing a stable phase assemblage in order to avoid surface reactions during the experiments. The bulk composition of the powders resides in the $\text{SiO}_2\text{-Al}_2\text{O}_3\text{-CaO-Na}_2\text{O}$ system and were synthesised using a mixture consisting of natural plagioclase crystals and either synthetic cristobalite (SiO_2) and mullite

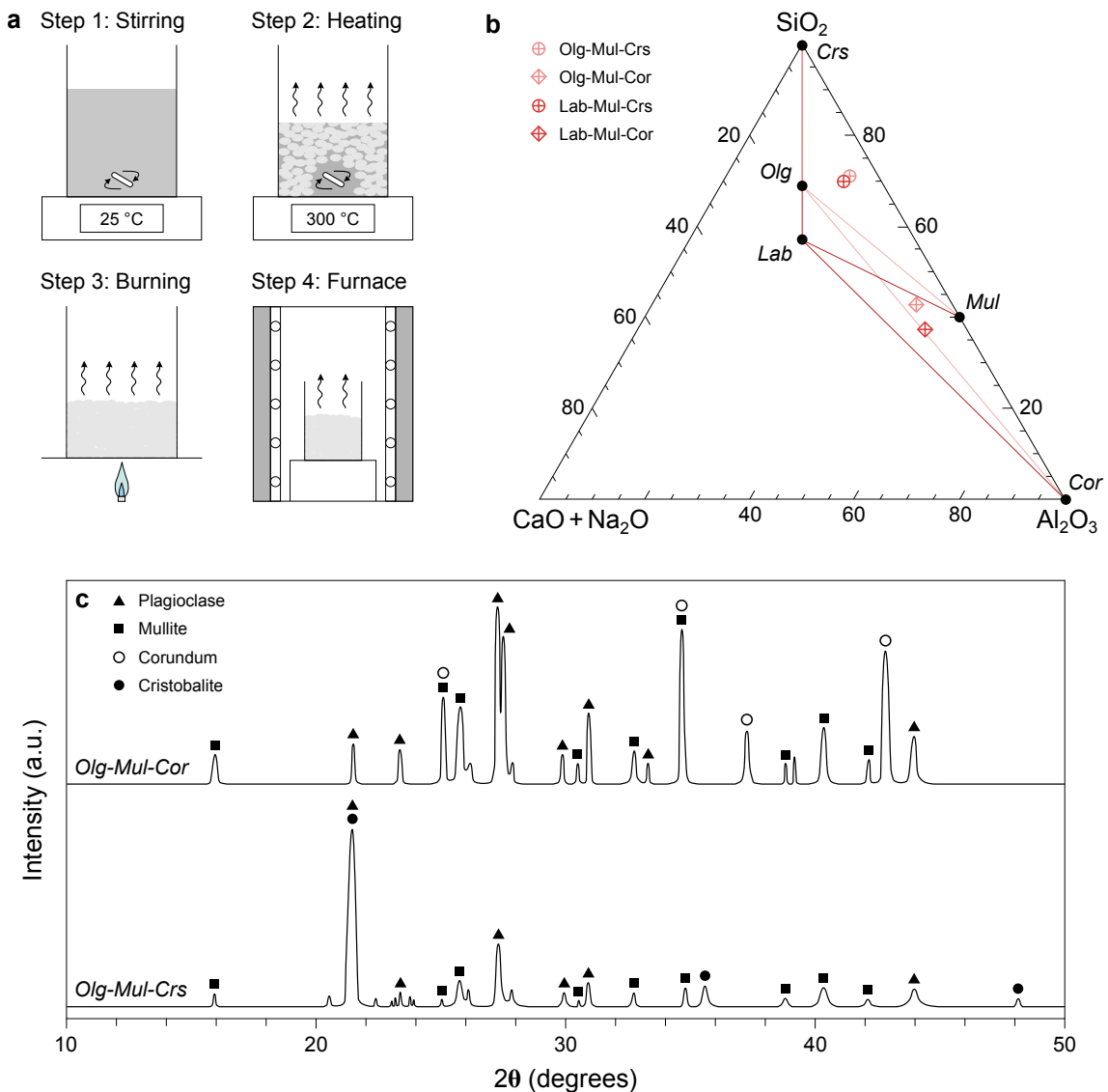


Figure 3.1. Source powder synthesis and composition. **a**, Description of the four-step procedure used for the synthesis of the individual phases present in the source powders based on the sol-gel method. **b**, $\text{SiO}_2\text{-Al}_2\text{O}_3\text{-CaO + Na}_2\text{O}$ ternary diagram highlighting the two buffer assemblages and the composition of the four source powders synthesised using the sol-gel method. **c**, X-ray diffraction spectra from Olg-Mul-Crs and Olg-Mul-Cor powder sources used in the oligoclase experiments.

[$3\text{Al}_2\text{O}_3 \cdot 2\text{SiO}_2$] for the high- $a\text{SiO}_2$ experiments, or synthetic corundum (Al_2O_3) and mullite for the low- $a\text{SiO}_2$ experiments (Fig. 3.1). Cristobalite, mullite and corundum were individually synthesised following a sol-gel method where (1) cristobalite was made by mixing tetraethyl orthosilicate [$\text{Si}(\text{OC}_2\text{H}_5)_4$] with ethanol, deionised water and HCl, (2) corundum consisted of a mixing of aluminium nitrate nonahydrate [$\text{Al}(\text{NO}_3)_3 \cdot 9\text{H}_2\text{O}$] and deionised water, and (3) mullite was synthesised by mixing tetraethyl orthosilicate, aluminium nitrate nonahydrate, deionised water, ethanol and HCl. Mullite was doped in Sr and Ba by adding strontium nitrate [$\text{Sr}(\text{NO}_3)_2$] and barium nitrate [$\text{Ba}(\text{NO}_3)_2$] (Supplementary Material 2). Each mixture was homogenised using a magnetic stirrer for ~ 15 min at room temperature and then dried down on a hotplate at $300\text{ }^\circ\text{C}$ for $\sim 2\text{-}3$ h under continuous stirring (Fig. 3.1a). The gelled products were then heated in a Pt crucible using a Bunsen burner to burn off most of the residual organic components. The remaining powders were then ground in an agate mortar, packed in Pt crucibles, and then annealed at $1,300\text{ }^\circ\text{C}$ in a furnace for a minimum of 48 h. During this final annealing step, any remaining organic components were removed from the mixtures, and the crystal phase

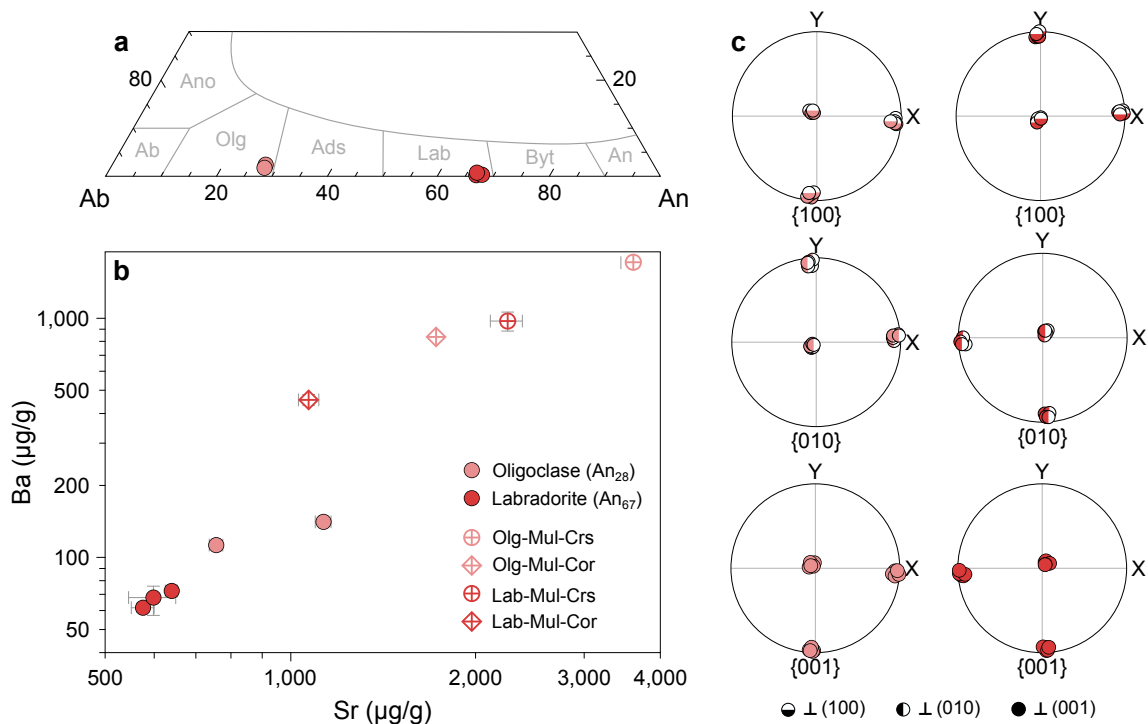


Figure 3.2. Crystal compositions and orientations. **a**, Feldspar ternary diagram focused on the plagioclase endmembers highlighting the plagioclase compositions used in this study. The solvus corresponds to temperature and pressure conditions of $1,000\text{ }^\circ\text{C}$ and 1 bar and was drawn from Ghiorso (1984). **b**, Sr ($\mu\text{g/g}$) vs. Ba ($\mu\text{g/g}$) for the plagioclase crystals and source powders used in this study. **c**, Electron backscatter diffraction (EBSD) pole figures for the oriented oligoclase and labradorite crystals. *Ano*, anorthoclase; *Ab*, albite; *Olg*, oligoclase; *Ads*, andesine; *Lab*, labradorite; *Byt*, bytownite; *An*, anorthite.

3. Diffusion of Sr and Ba in plagioclase

formed. In addition, gem quality plagioclase crystals with the same composition as the starting materials (i.e., An₂₈ or An₆₇) were ground to powder. They were then mixed with varying combinations of cristobalite and mullite, or corundum and mullite (Supplementary Material 2), pressed into pellets, and annealed at 1,300 °C. The annealed pellets were then ground, analysed by X-ray powder diffraction (Supplementary Material 2) using an ARL Thermo X'tra diffractometer housed in the Institute of Earth Sciences at the University of Lausanne, and again pressed into pellets, annealed at 1,300 °C, ground into powder, and analysed by X-ray diffraction (Fig. 3.1c). The purpose of this second annealing is to ensure that the mixed powders are completely equilibrated. The trace element compositions of these source powders are reported in Fig. 3.2 and in the Supplementary Material 2.

In addition to the experiments described above, several experiments were performed following the design of Cherniak and Watson (1992, 1994) and Cherniak (2002). In these experiments, the source powders for Sr and Ba were made separately and consisted of mixtures of SiO₂, Al₂O₃ and SrO or BaO powders, plus finely ground plagioclase (An₆₇). The proportions between the oxide mixtures are the same as reported in Cherniak (2002), and are available in the Supplementary Material 2. The mixture was homogenised through grinding, annealed in a Pt crucible at 970 °C for ~48 h, and then reground. Finally, these two powders were analysed by X-ray diffraction (Supplementary Material 2).

3.3.2 Plagioclase crystals

A total of five plagioclase specimens (Fig. 3.2) between 1 and 2 cm in length were used in these diffusion experiments. These include three labradorites from Lake View, Oregon, USA (NMGE 416.040), procured from the Natural History Museum of Geneva (NMGE), and two oligoclase crystals from Uluguru Mountains, Morogoro Region, Tanzania, purchased from an online vendor. The major and trace element compositions of these crystals are reported in Fig. 3.2 and the Supplementary Material 2. To determine the crystal orientations, a part (~8 mm³) of each crystal was cut, mounted in epoxy, polished stepwise using 9, 6, 3, 1, and 0.5 µm diamond paste followed by a colloidal silica solution. They were analysed using a Tescan Mira II scanning electron microscope (SEM) equipped with a Symmetry electron backscatter diffraction (EBSD) detector housed in the Institute of Earth Sciences at the University of Lausanne. The oriented crystals (Fig. 3.2c) were cut into cubes of ~2 × 2 × 2 mm with faces perpendicular to the *a*, *b* and *c* crystallographic axes. The cubes were embedded into thermoplastic acrylic in 2.5 cm discs, which were then polished using the same method as for EBSD analyses, such that each cube had a

single polished face to study diffusion parallel to the a -, b - and c -axis, respectively. Following removal from the acrylic, the crystals were thoroughly cleaned via sonication in isopropanol, then sonicated again in deionised water, and then pre-annealed at 1,050 °C for \sim 48 h.

During the pre-annealing, the crystals were placed in contact with Sr- and Ba-free powders with the same stable phase assemblages as the Sr- and Ba-doped powders designed for in-diffusion experiments. The purpose of pre-annealing is to equilibrate the crystal defect concentrations under conditions close to the in-diffusion experiments. After this pre-annealing step, the crystals were again mounted in acrylic, polished stepwise using diamond paste down to 0.5 μ m abrasive followed by colloidal silica in order to erase any possible out-diffusion of Sr and Ba that may have occurred during pre-annealing, and lastly cleaned via sonication in isopropanol and deionised water.

3.3.3 Experiments

Diffusion experiments were carried out at a pressure of 1 atm in Borel box furnaces in the hydrothermal experimental laboratory at the University of Lausanne. Temperature was monitored using a type-B thermocouple located at \sim 1 cm of the sample, yielding

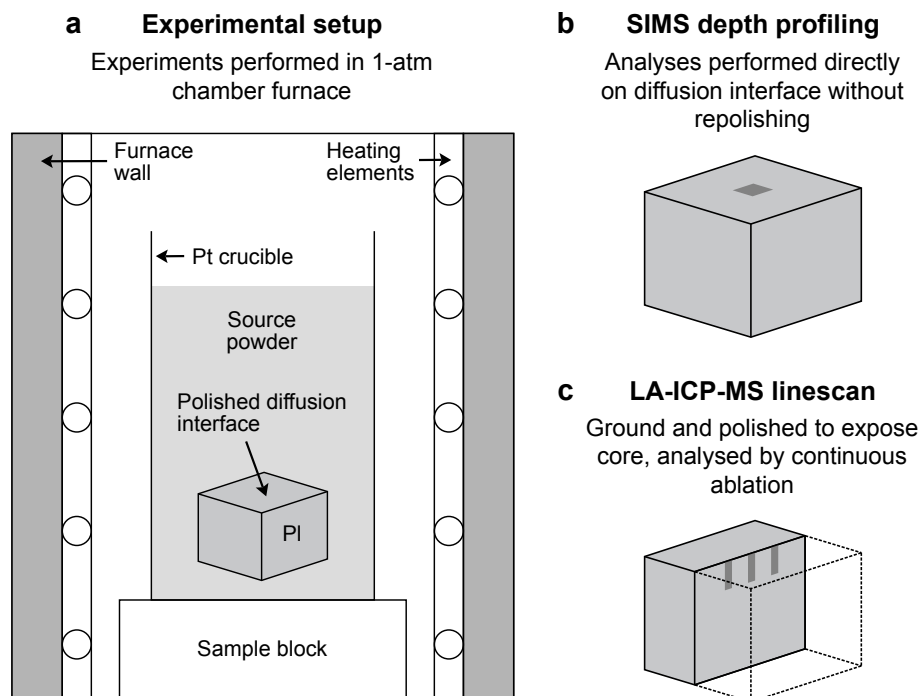


Figure 3.3. Experimental setup and preparation for analyses. **a**, Experimental design. Oriented and polished plagioclase crystals were packed into a Pt crucible where they were completely surrounded with source powder throughout the diffusion experiment. **b**, Preparation of plagioclase crystals for SIMS depth-profiling analyses. **c**, Preparation of plagioclase crystals for LA-ICP-MS line-scanning analyses.

3. Diffusion of Sr and Ba in plagioclase

temperature uncertainties of ~ 0.5 %. Oriented and polished plagioclase crystals were surrounded by source powder and packed into small Pt crucibles (Fig. 3.3a). Experimental conditions are reported in Table 3.1. After the experiments were completed, the source powder was completely removed and samples were cleaned by sonication in isopropanol and then in deionised water. Samples intended for secondary ion mass spectrometry (SIMS) depth profiling were not re-polished after diffusion anneals (Fig. 3.3b). Samples designated for laser ablation inductively coupled plasma mass spectrometry (LA-ICP-MS) were cut perpendicular to the polished diffusion interface using a diamond wire saw, mounted in epoxy and repolished stepwise using diamond paste down to 1 μm abrasive (Fig. 3.3c). The two diffusion experiments using oxide mixtures as diffusant sources, following the design of Cherniak and Watson (1992, 1994) and Cherniak (2002) as described above, were performed at 1,075 °C in the same apparatus as the other experiments. In these runs, the source powder was largely solidified and was removed via sonication in isopropanol, and then in deionised water.

3.3.4 Analytical techniques

Electron probe microanalysis

Plagioclase major element compositions were determined on carbon-coated polished mounts by field-emission gun electron probe microanalyses (FEG-EPMA) using a JEOL JXA-8530F HyperProbe equipped with five wavelength dispersive spectrometers at the University of Lausanne. The accelerating voltage was set to 15 kV, the beam current to 10 nA, and the beam size was 5 μm . Counting times were 30 s on the peak and 15 s on the background. Measurements were corrected with the PRZF method (Armstrong, 1995) and standardised using natural anorthite for Ca, Al and Si, and natural albite for Na.

Secondary ion mass spectrometry

Depth profiling analyses were performed using the Cameca 1280HR SIMS instrument housed in the SwissSIMS laboratory at University of Lausanne. Samples were mounted in indium and coated with ~ 35 nm of Au prior to SIMS analysis. A typical indium mount contained 7-10 plagioclase cubes and a piece of NIST SRM-610. The measured positive secondary ions were ^{30}Si , ^{86}Sr , ^{137}Ba and ^{138}Ba . The choice to measure both ^{137}Ba and ^{138}Ba arises from the presence of possible isobaric interferences. Samples were held at +5 kV and sputtered with an $^{16}\text{O}^{2-}$ primary ion beam (PIB) which was accelerated at -10 kV and generated using a Hyperion-II RF plasma source. The primary ion beam was focused to a ~ 10 μm spot and then rastered over a 125×125 μm area. A combination

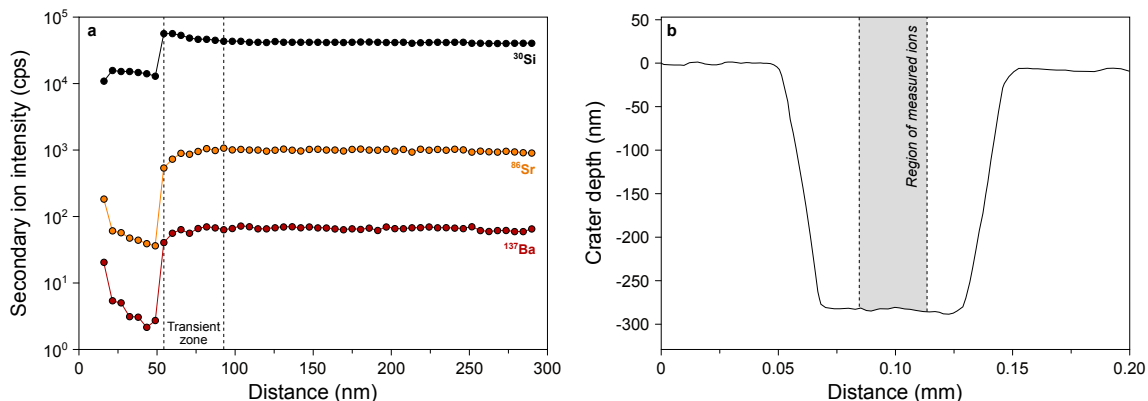


Figure 3.4. Raw data from SIMS depth profiling analysis of the blank labradorite. **a**, Counts per second of every ion measured throughout the analysis as a function of depth. The start and end of the transient zone is also represented. **b**, Depth measurement of crater following depth profiling analysis.

of electronic and field gating was used such that the only secondary ions originating from the $\sim 35 \times 35 \mu\text{m}$ region at the centre of the rastered area entered the mass spectrometer (Fig. 3.4). In order to compensate for charging throughout the analyses, we applied an energy recentring routine using ^{30}Si at the beginning of each cycle.

The locations of the crystal surface and the end of the transient zone (Williams and Baker, 1981) were identified using the signal of the non-diffusing species ^{30}Si (Fig. 3.4a). The first 30-50 nm consist of a low ^{30}Si signal corresponding to the Au layer, and are followed by 50-250 nm of transient zone where the ^{30}Si signal is slowly decreasing due to an initially non-steady state of PIB ion implantation during sputtering (Williams and Baker, 1981). The location of the polished crystal surface is inferred to correspond to the peak of the ^{30}Si signal, while the stabilisation of this signal represents the end of the transient zone (Ganguly et al., 1998).

Subsequent to the SIMS depth profiling, the depth of each crater was measured using a Bruker ContourGT-K white-light microscope in order to assess the depth and topography of the resulting crater (Fig. 3.4b). We also checked that the bottom of the craters had sufficiently low topographical variation to ensure that the sampling depth was uniform throughout the measurements. Any craters with more than 25 nm topography were not used to extract diffusion data.

Laser ablation inductively coupled plasma mass spectrometry

Two different LA-ICP-MS methods were used, both employing the Perkin Elmer NexION 5000 ICP-MS coupled with an Australian Scientific Instruments RESolution 193 nm Ar-F excimer laser at University of Lausanne. The LA-ICP-MS system was optimised by linearly scanning the NIST SRM-612 glass standard at $10 \mu\text{m s}^{-1}$ in order to increase the

3. Diffusion of Sr and Ba in plagioclase

spectrometer sensitivity ($^{139}\text{La}^+ > 2.0 \times 10^6$ cps) without significantly producing oxides ($^{248}\text{ThO}^+ / ^{232}\text{Th}^+ < 0.5\%$) and doubly-charged ions ($\text{Ba}^{2+} / \text{Ba}^+ < 3.0\%$). Repetition rate was set to 10 Hz and the energy density was 6 J cm^{-2} . Helium ($1,000 \text{ ml min}^{-1}$) and N_2 (1 ml min^{-1}) were used as carrier gases. The measured isotopes were ^{29}Si , ^{86}Sr , and ^{137}Ba . Both methods were using slits to shape the laser beam as a $7.5 \times 100 \mu\text{m}$ rectangular area with the long axis parallel to the diffusion interface. The first method consisted of punctual analyses along a transect perpendicular to the diffusion interface. Background, ablation and wash-out interval acquisition times were 70, 35 and 35 s, respectively. Dwell times were 10 ms for ^{29}Si , and 30 ms for ^{86}Sr and ^{137}Ba . Absolute concentrations were calculated using CaO as internal reference, NIST SRM-612 as primary standard, and BCR-2G as secondary standard for quality control. Data reduction was performed with the LAMtrace software (Jackson, 2008). The average elemental abundances of the standards were taken from Pearce et al. (1997). The second method utilised the scanning mode, whereby the stage was moved at a constant rate of $1 \mu\text{m s}^{-1}$. Background and wash-out interval acquisition times were 70 and 35 s, respectively. Absolute concentrations and quality control followed the same procedure as the spot analyses. Data reduction was performed with the Iolite 4 software (Paton et al., 2011), employing a step forward function for the background and a polynomial function for the primary standard.

3.3.5 Diffusion modelling

Following our experimental design, the expected solution to the diffusion equation would correspond to diffusion into a semi-infinite medium of plane-sheet geometry, with a homogeneous initial concentration and a fixed surface concentration according to Eq. 3.1:

$$\frac{C_S - C(x, t)}{C_S - C_\infty} = \text{erf} \left(\frac{x}{2\sqrt{Dt}} \right) \quad (3.1)$$

where C_S is the fixed surface concentration, $C(x, t)$ is the concentration at point x and time t , C_∞ is the homogeneous initial concentration, and D is the diffusion coefficient (Crank, 1975). Profiles were modelled by pairing Eq. 3.1 with a least-squares optimisation routine, and uncertainties were quantified by manually varying the model parameters (i.e., C_S , C_∞ , D) to estimate minimum and maximum values that could still produce acceptable fits to the data.

3.4 Results

All of the diffusion profiles measured in this study exhibit a typical error-function shape (Fig. 3.5a-l) that can be modelled using Eq. 3.1. At the same time, we note that a second, slower mechanism cannot be ruled out by the data presented here, given the long transient zones observed in these depth profiling analyses (Figs. 3.4 and 3.5). In the following, we present the results of the Sr and Ba in-diffusion experiments for different αSiO_2 , crystal orientations and temperatures. The details of the experimental conditions and modelled diffusion coefficients are reported in Table 3.1.

3.4.1 Diffusion interface

After recovery of the experimental products, the topography of the diffusion interface was inspected using a Bruker ContourGT-K white light interferometer to check for reaction between the powder source and the crystal (Figs. 3.5 and 3.6). Additionally, a blank sample was analysed for comparison. Relative topography is almost absent (<15 nm) for the blank samples as well as experiments with annealing temperatures $<1,150$ °C (Fig. 3.6a,b). On the other hand, crystals annealed at $\geq 1,150$ °C exhibit a higher relative topography at the diffusion interface (~ 20 nm) (Fig. 3.6c). This effect is enhanced for long-duration experiments with annealing time >100 h. The experiment performed at $1,200$ °C and analysed with SIMS (LHSC_6) presents a typical “reacted” profile with an unstable signal for all analysed masses (Fig. 3.5m-o). Conversely, the two long, high-temperature experiments analysed via LA-ICP-MS (OHSC_8, LHSC_5) exhibit a typical error-function diffusion profile, probably due to the lower spatial resolution of LA-ICP-MS analyses (Supplementary Material 2). Therefore, these crystals presenting surface degradation will be presented but not used for further diffusion parameterisation. In addition, the experiments using oxides as diffusant sources, in proportion similar to the experiments of Cherniak and Watson (1992, 1994) and Cherniak (2002), also display degradation of the diffusion interface (Fig. 3.6d,e), similar to the high-temperature experiments using sol-gel-derived powders. This degradation indicates that a reaction likely took place at the surface of the crystals during the diffusion experiments. The areas that are not completely altered present a relatively high topography of ~ 35 - 40 nm. Similar results were reported by Jollands et al. (2020) whereby experiments aimed at replicating the Ti-in-quartz diffusion experiments of Cherniak et al. (2007), using the highly-concentrated powder sources employed in that study, led to a large degree of surface reaction [see Fig. S3 of Jollands et al. (2020)].

3. Diffusion of Sr and Ba in plagioclase

Table 3.1. Summary of experimental conditions and retrieved diffusion coefficients of Sr and Ba in plagioclase. All experiments were conducted at 1-atm pressure. The plagioclase composition (oligoclase and labradorite; O or L) and orientation (parallel to the a -, b - and c -axis; A, B or C), and $a\text{SiO}_2$ (low $a\text{SiO}_2$ and high $a\text{SiO}_2$; LS or HS) can be found in the run number. Mineral abbreviations as in the text.

Run No.	Powder assemblage	T ($^{\circ}\text{C}$)	Time (s)	$\log_{10}D_{Sr}$	\pm	$\log_{10}D_{Ba}$	\pm
OHSC_1 ^a	Olg-Mul-Crs	1,000	3.6060×10^5	-18.44	0.14	-18.75	0.20
OHSC_2 ^a	Olg-Mul-Crs	1,000	7.8918×10^5	-18.82	0.22	-19.03	0.19
OHSC_3 ^a	Olg-Mul-Crs	950	1.6193×10^6	-18.94	0.25	-19.16	0.25
OHSC_4 ^a	Olg-Mul-Crs	900	4.8115×10^6	-19.58	0.20	-19.79	0.24
OHSC_5 ^a	Olg-Mul-Crs	1,100	5.6340×10^4	-17.34	0.13	-17.70	0.08
OHSC_6 ^a	Olg-Mul-Crs	1,000	2.6670×10^5	-18.58	0.22	-18.89	0.24
OHSC_7 ^a	Olg-Mul-Crs	1,000	2.5806×10^5	-18.87	0.15	-18.92	0.18
OHSC_8 ^b	Olg-Mul-Crs	1,100	5.3582×10^6	-16.93	0.06	-17.02	0.10
OHSA_1 ^a	Olg-Mul-Crs	1,000	3.6060×10^5	-18.77	0.17	-18.87	0.20
OHSB_1 ^a	Olg-Mul-Crs	1,000	3.6060×10^5	-18.54	0.21	-18.61	0.17
OLSA_1 ^a	Olg-Mul-Cor	1,000	3.6060×10^5	-18.78	0.16	-18.86	0.19
OLSB_1 ^a	Olg-Mul-Cor	1,000	3.6060×10^5	-18.79	0.16	-18.93	0.28
OLSC_1 ^a	Olg-Mul-Cor	1,000	3.6060×10^5	-18.72	0.25	-18.82	0.27
LHSC_2 ^a	Lab-Mul-Crs	1,100	2.5584×10^5	-18.10	0.18	-18.25	0.12
LHSC_3 ^a	Lab-Mul-Crs	1,100	2.5584×10^5	-17.86	0.09	-18.20	0.12
LHSC_4 ^a	Lab-Mul-Crs	950	8.2595×10^6	-19.72	0.21	-19.74	0.25
LHSC_5 ^b	Lab-Mul-Crs	1,200	6.2785×10^6	-16.12	0.10	-16.41	0.12
LHSC_7 ^a	Lab-Mul-Crs	1,100	1.7106×10^5	-18.51	0.14	-18.64	0.14
LHSC_8 ^a	Lab-Mul-Crs	1,100	5.9958×10^5	-18.09	0.26	-18.24	0.17
LHSC_9 ^a	Lab-Mul-Crs	1,150	6.1158×10^5	-17.45	0.19	-17.52	0.10
LHSC_10 ^a	Lab-Mul-Crs	1,000	1.8310×10^6	-19.23	0.24	-19.31	0.26
LHSC_12 ^a	Lab-Mul-Crs	1,150	8.1180×10^4	-17.68	0.20	-17.85	0.22
LHSA_1 ^a	Lab-Mul-Crs	1,100	2.5584×10^5	-17.81	0.07	-18.24	0.09
LHSB_1 ^a	Lab-Mul-Crs	1,100	2.5584×10^5	-18.22	0.15	-18.59	0.23
LLSA_2 ^a	Lab-Mul-Cor	1,100	2.6112×10^5	-18.72	0.13	-18.77	0.16
LLSB_1 ^a	Lab-Mul-Cor	1,100	2.5584×10^5	-18.32	0.12	-18.47	0.18
LLSC_1 ^a	Lab-Mul-Cor	1,100	2.5584×10^5	-18.12	0.17	-18.26	0.21

^aSIMS depth profiling

^bLA-ICP-MS line scanning

3.4.2 Time-series experiments

Time-series experiments for Sr and Ba diffusion in oligoclase and labradorite were carried out at 1,000 $^{\circ}\text{C}$ and 1,100 $^{\circ}\text{C}$, respectively, and were conducted to observe diffusion parallel

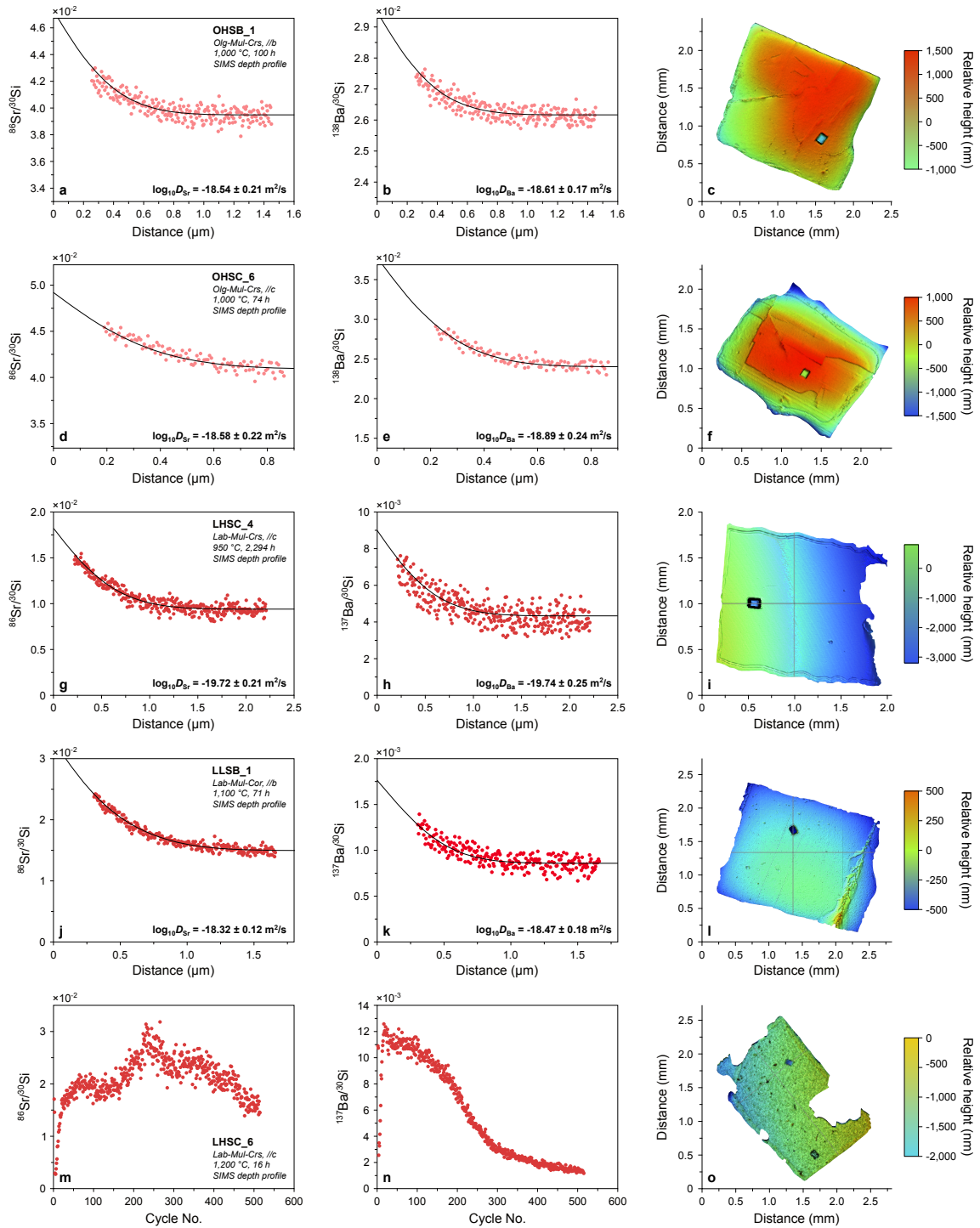


Figure 3.5. Representative Sr and Ba diffusion profiles produced in this study and the associated topography of the experimental run. Samples were analysed by SIMS depth profiling. The stable phase assemblage of the Sr and Ba source powders and analytical technique used for each experiment are labelled, along with temperature and duration of the experiments. Model fits are solid lines obtained using Eq. 3.1 from the main text. Note that profiles m and n were not fitted due to reaction at the diffusion interface visible on panel o. Mineral abbreviations as in the main text.

3. Diffusion of Sr and Ba in plagioclase

to the c -axis (Fig. 3.7a,b). The duration of these experiments was 74, 100 and 219 h for oligoclase, and 48, 71 and 167 h for labradorite. No resolvable dependence of Sr and Ba diffusivity in plagioclase was observed upon experiment duration, satisfying an important permissive criterion for the interpretation that these profiles represent volume diffusion. The mean Sr and Ba diffusivities in oligoclase at 1,000 °C ($\log_{10}D_{\text{Sr}} = -18.23 \pm 0.24 \text{ m}^2$

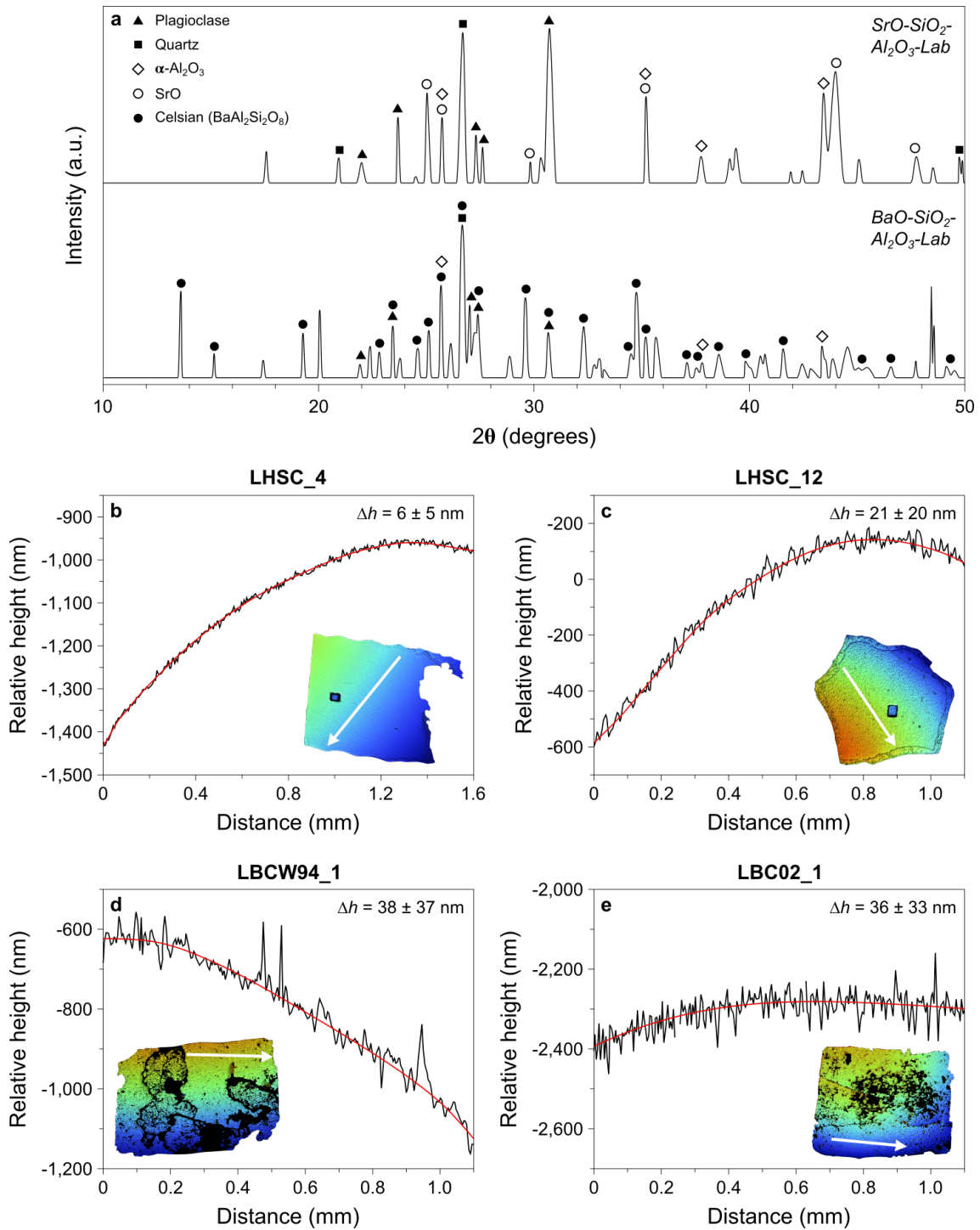


Figure 3.6. (Figure caption on next page.)

s^{-1} , $\log_{10}D_{\text{Ba}} = -18.31 \pm 0.23 \text{ m}^2 \text{ s}^{-1}$) and labradorite at 1,100 °C ($\log_{10}D_{\text{Sr}} = -18.61 \pm 0.26 \text{ m}^2 \text{ s}^{-1}$, $\log_{10}D_{\text{Ba}} = -18.70 \pm 0.20 \text{ m}^2 \text{ s}^{-1}$) highlight the similar diffusion rate of Sr and Ba both in oligoclase and labradorite.

3.4.3 Major element activities

The synthesised source powders, comprising either corundum (Cor) or cristobalite (Crs) alongside mullite (Mul) and oligoclase (Olg) or labradorite (Lab), were designed to buffer $a\text{SiO}_2$ following Eq. 3.2:



Calculations of $a\text{SiO}_2$ were made using the internally consistent database of [Holland and Powell \(2011\)](#). Across the range of experimental temperatures imposed in this study (900-1,200 °C), $a\text{SiO}_2$ of the Olg-Mul-Cor and Lab-Mul-Cor source powders ranges from 0.04 to 0.05 (low $a\text{SiO}_2$), whereas $a\text{SiO}_2$ of the Olg-Mul-Crs and Lab-Mul-Crs source powders is constrained to a value of 1 (high $a\text{SiO}_2$). Although the source powders were designed to buffer $a\text{SiO}_2$, it is, however, possible that the rather low experimental temperatures (1,000-1,100 °C) do not allow for a complete activity buffering. To evaluate this possibility, EPMA spot analyses were performed on two experimental runs with distinctive buffering powders. The plagioclase crystal surrounded by a silica-saturated buffering powder exhibits a decrease of Na and increase of Ca towards the rim, while Si and Al remain constant. Decomposing the measured plagioclase compositions in the anorthite, albite and $\square\text{Si}_4\text{O}_8$ theoretical components results in a decrease of the albite component, and an increase of the anorthite and $\square\text{Si}_4\text{O}_8$ components towards the crystal border (Fig. 3.8a). On the other hand, the crystal surrounded by a silica-undersaturated buffering powder

Figure 3.6. Mineralogy of the source powders (LBCW94_1 and LBC02_1) following the synthesis method of [Cherniak and Watson \(1992, 1994\)](#) and [Cherniak \(2002\)](#), and topography variations of the diffusion interfaces. **a**, X-ray diffraction spectra from SrO-SiO₂-Al₂O₃-Lab (LBCW94_1) and BaO-SiO₂-Al₂O₃-Lab (LBC02_1) powder sources synthesised following the method of [Cherniak and Watson \(1992, 1994\)](#) and [Cherniak \(2002\)](#). **b**, Topography profile of the LHSC_4 experiment alongside a topography map and the location of the profile. **c**, Topography profile of the LHSC_12 experiment alongside a topography map and the location of the profile. **d**, Topography profile of the LBCW94_1 experiment following the experimental design of [Cherniak and Watson \(1992, 1994\)](#) alongside a topography map and the location of the profile. **e**, Topography profile of the LBC02_1 experiment following the experimental design of [Cherniak \(2002\)](#) alongside a topography map and the location of the profile. Δh represents the relative topography, or height variation, calculated as the mean deviation from the best fit (red line) with an uncertainty corresponding to 2σ .

3. Diffusion of Sr and Ba in plagioclase

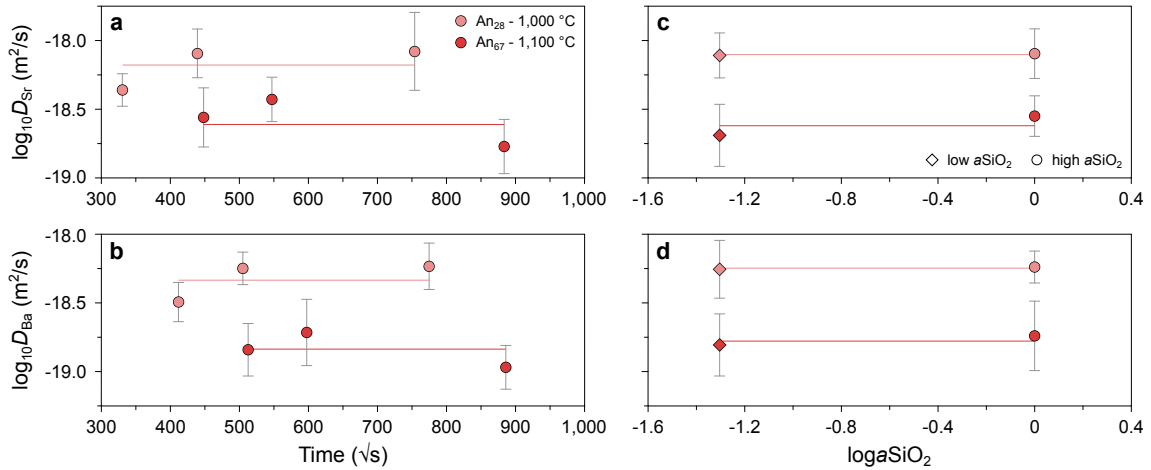


Figure 3.7. Results of time-series experiments and for different $a\text{SiO}_2$. **a**, Sr diffusion coefficients determined at 1,000 °C for oligoclase and 1,100 °C for labradorite as a function of time. **b**, Ba diffusion coefficients determined at 1,000 °C for oligoclase and 1,100 °C for labradorite as a function of time. **c**, Sr diffusion coefficients determined at 1,000 °C for oligoclase and 1,100 °C for labradorite as a function of $\log a\text{SiO}_2$. **d**, Ba diffusion coefficients determined at 1,000 °C for oligoclase and 1,100 °C for labradorite as a function of $\log a\text{SiO}_2$.

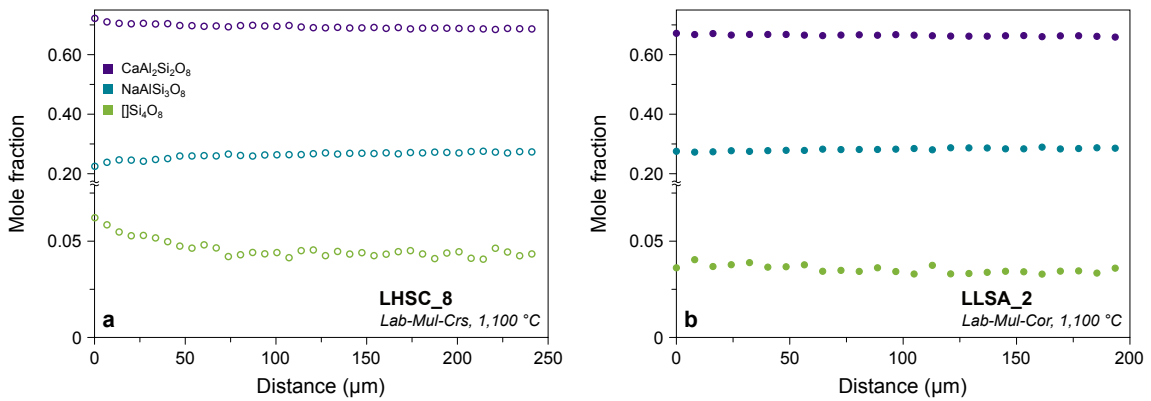


Figure 3.8. Plagioclase theoretical component profiles. **a**, Chemical profiles of the experimental run LHSC.8 represented as anorthite, albite and $\square\text{Si}_4\text{O}_8$ components. The high- $a\text{SiO}_2$ powder source results in an increase of the $\square\text{Si}_4\text{O}_8$ component towards the crystal rim. **b**, Chemical profiles of the experimental run LLSA.2 represented as anorthite, albite and $\square\text{Si}_4\text{O}_8$ components. The low- $a\text{SiO}_2$ powder source results in a flat profile for all components.

essentially shows flat anorthite, albite and $\square\text{Si}_4\text{O}_8$ profiles (Fig. 3.8b). Therefore, we conclude that $a\text{SiO}_2$ was indeed imposed by the synthesised buffering assemblage during the experiments, which resulted in the creation of vacancies in the metal site. Based on the calculated diffusivities, there is, within uncertainty, no resolvable dependence of Sr and Ba diffusion both in oligoclase and labradorite upon $a\text{SiO}_2$ (Fig. 3.7c,d). As such, silica activity is not considered to play a significant role during diffusion of Sr and Ba in plagioclase.

3.4.4 Diffusion anisotropy

In this study, diffusion parallel to the three crystallographic axes of plagioclase was investigated. Experiments parallel to the a - and b -axis were performed at 1,000 °C for oligoclase and 1,100 °C for labradorite, while those along the c -axis were carried out at 900-1,150 °C for oligoclase and 950-1,200 °C for labradorite. The retrieved diffusion profiles exhibit no clear differences as a function of the crystallographic orientation for both Sr and Ba, suggesting that Sr and Ba diffusion in plagioclase is isotropic within uncertainty. This is consistent with the experimental studies of [Cherniak \(2002\)](#) and [Giletti and Casserly \(1994\)](#), whereas [Cherniak and Watson \(1994\)](#) report slower diffusion of Sr parallel to the b -axis by ~ 0.7 log units for labradorite, and no anisotropy for oligoclase. However, they only performed three experiments parallel to the b -axis, amongst which one yielded similar diffusivities, within uncertainty, to the experiments parallel to the c -axis.

3.4.5 Temperature dependence

Because there is no resolvable dependence of Sr or Ba diffusion in plagioclase on $a\text{SiO}_2$ or crystallographic orientation, the diffusion coefficients determined in this study were used to define a single Arrhenius trend for each plagioclase composition (Fig. 3.9). To parameterise the diffusion of Sr and Ba, we use all the retrieved diffusivities except those associated with interface degradation. The data were fitted, and the error envelopes calculated employing a Monte Carlo scheme involving 2,000 resampling iterations (Fig. 3.9a,b). The error envelopes encompass data within one standard deviation. Taking this approach, the diffusivities of Sr and Ba in oligoclase are described by Eqs. 3.3 and 3.4:

$$\log_{10}D_{\text{Sr}} \text{ (m}^2 \text{ s}^{-1}\text{)} = -4.15 (\pm 1.27) - \left[\frac{352,212 (\pm 31,273)}{2.303RT} \right], \quad (3.3)$$

$$\log_{10}D_{\text{Ba}} \text{ (m}^2 \text{ s}^{-1}\text{)} = -4.62 (\pm 1.10) - \left[\frac{345,740 (\pm 27,206)}{2.303RT} \right], \quad (3.4)$$

while Sr and Ba diffusivities in labradorite are described by Eqs. 3.5 and 3.6:

$$\log_{10}D_{\text{Sr}} \text{ (m}^2 \text{ s}^{-1}\text{)} = -4.72 (\pm 1.50) - \left[\frac{352,805 (\pm 39,470)}{2.303RT} \right], \quad (3.5)$$

$$\log_{10}D_{\text{Ba}} \text{ (m}^2 \text{ s}^{-1}\text{)} = -6.58 (\pm 1.75) - \left[\frac{309,437 (\pm 45,779)}{2.303RT} \right], \quad (3.6)$$

where T is the temperature (K) and R is the universal gas constant ($\text{J mol}^{-1} \text{K}^{-1}$). Our experimental data highlight the strong dependence of Sr and Ba diffusivities on plagioclase composition, which systematically increase with decreasing anorthite content. This

3. Diffusion of Sr and Ba in plagioclase

behaviour has been observed for many other cations in plagioclase, including K, Mg, Pb and the rare earth elements (REE) (Cherniak, 1995, 2003; Giletti and Shanahan, 1997; LaTourrette and Wasserburg, 1998; Van Orman et al., 2014). Activation energies (E_a) for Sr and Ba diffusion are similar within error for oligoclase and labradorite. Therefore, activation energies are considered constant across plagioclase composition, and $\log_{10}D_0$ a linear function of the plagioclase composition. As such, we parameterise Sr and Ba diffusion in plagioclase following Eqs. 3.7 and 3.8, respectively:

$$\log_{10}D_{\text{Sr}} (\text{m}^2 \text{s}^{-1}) = -1.65 (\pm 0.24) X_{\text{An}} - 3.03 (\pm 1.16) - \left[\frac{368,142 (\pm 27,141)}{2.303RT} \right], \quad (3.7)$$

$$\log_{10}D_{\text{Ba}} (\text{m}^2 \text{s}^{-1}) = -1.43 (\pm 0.20) X_{\text{An}} - 4.65 (\pm 0.96) - \left[\frac{337,037 (\pm 22,969)}{2.303RT} \right], \quad (3.8)$$

where X_{An} is the anorthite mole fraction. The data set was fit with a least-squares optimisation routine using MATLAB, and the uncertainties associated with the calculation of $\log_{10}D_0$ and the activation energy were determined using a Monte Carlo scheme involving 2,000 resampling iterations. Similar parameterisations have been proposed for diffusion of Mg and Sr in plagioclase whereby the pre-exponential factor was linearly dependent on plagioclase composition, while activation energy was kept constant (Costa et al., 2003; Van Orman et al., 2014).

3.5 Discussion

3.5.1 Comparison with previous studies

The data in this study show significantly slower diffusion of Sr in plagioclase than observed in previous studies. Within the range of parameters investigated in this study and by Cherniak and Watson (1994) and Giletti and Casserly (1994), the new Sr diffusivities differ by ~ 1 -2 log units compared to the previous studies (Fig. 3.9c). On the other hand, we determined similar to slightly faster (~ 0.5 log unit) Ba diffusion rates compared to Cherniak (2002) (Fig. 3.9d). We report higher activation energies by up to 70 kJ mol⁻¹ and slightly weaker compositional dependence for Sr diffusion in plagioclase compared to previous studies. For Ba diffusion, the retrieved activation energies and compositional dependence are identical within error to the ones reported by Cherniak (2002).

The diffusion experiments on Sr in labradorite performed parallel to the b -axis by Cherniak and Watson (1994) are ~ 0.5 log unit slower than parallel to the c -axis, whereas they report no anisotropy for other plagioclase compositions and Ba diffusion (Fig. 3.9c,d).

Similar to [Giletti and Casserly \(1994\)](#) and [Cherniak \(2002\)](#), we find no dependence of Sr and Ba diffusion in plagioclase on crystal orientation, pointing to an ostensibly near-isotropic diffusion process for Sr and Ba in plagioclase. The most likely explanation for the observed isotropic diffusion behaviour is the similar size of open channels parallel to the a -, b - and c -axis in plagioclase (Fig. 3.10a-c). Similar arguments were used to explain the strong diffusion anisotropy of Ti in zircon, whereby fast diffusion only occurs parallel to the c -axis where open channels are present ([Bloch et al., 2022](#)).

The diffusion interfaces of the recovered experiments present higher degrees of degradation at higher experimental temperature. However, insofar as the experimental design

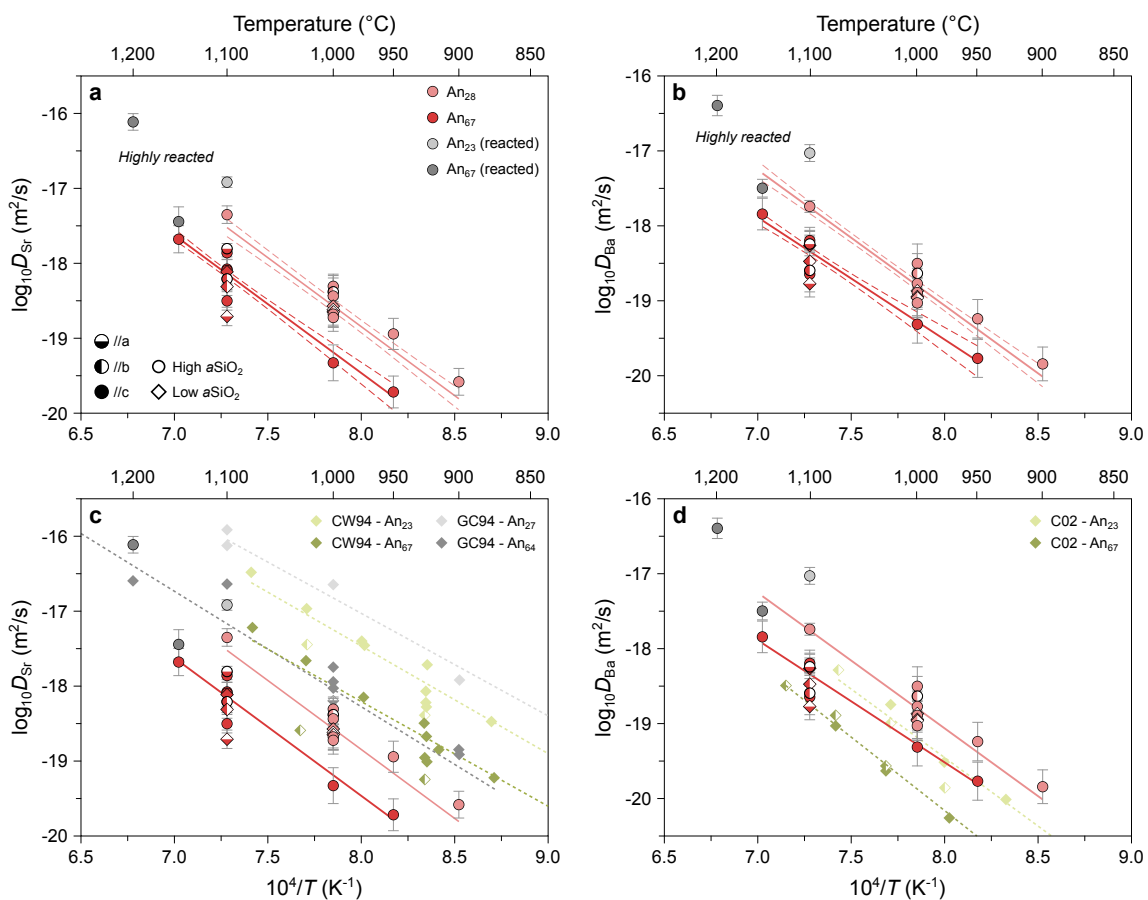


Figure 3.9. Arrhenius plots for the experiments performed in this study and comparison with literature data. **a**, Diffusion coefficients determined for Sr diffusion in oligoclase (An₂₈) and labradorite (An₆₇) as a function of temperature, crystal orientation and $aSiO_2$. **b**, Diffusion coefficients determined for Ba diffusion in oligoclase (An₂₈) and labradorite (An₆₇) as a function of temperature, crystal orientation and $aSiO_2$. The solid lines are the best fit to the data, and the dashed lines indicate the associated uncertainty envelopes (one standard deviation) calculated using a Monte Carlo scheme involving 2,000 resampling iterations. The reacted experiments are indicated and are excluded from the fit. **c**, Comparison of the Sr diffusion coefficients with the studies of [Cherniak and Watson \(1994\)](#) and [Giletti and Casserly \(1994\)](#). **d**, Comparison of the Ba diffusion coefficients with the study of [Cherniak \(2002\)](#). *CW94*, [Cherniak and Watson \(1994\)](#); *C02*, [Cherniak \(2002\)](#); *GC94*, [Giletti and Casserly \(1994\)](#).

3. Diffusion of Sr and Ba in plagioclase

of Cherniak and Watson (1992, 1994) and Cherniak (2002) is accurately reproduced, the surface degradation observed in these studies is slightly higher than the high-temperature experiments performed using sol-gel-derived source powders. Therefore, the difference between the results presented in this study and the diffusion coefficients reported elsewhere (Cherniak and Watson, 1992, 1994; Cherniak, 2002) cannot be explained by surface reactions alone. Similarly, both Cherniak and Watson (1992, 1994) and Cherniak (2002) used Rutherford backscatter spectrometry (RBS), a low-penetration spectrometric technique, to analyse their experimental products, which rules out the analysing technique as the source of discrepancy.

Interestingly, the XRD patterns of the source powders reproduced from Cherniak and Watson (1992, 1994) and Cherniak (2002) reveal the presence of Ba-feldspar ($\text{BaAl}_2\text{Si}_2\text{O}_8$) in the Ba-doped powder, whereas Sr-feldspar ($\text{SrAl}_2\text{Si}_2\text{O}_8$) is absent from the Sr-doped powder (Fig. 3.6a). Previous studies investigating the thermodynamic properties of Sr- and Ba-feldspars demonstrated that Ba-feldspar crystallises from room temperature to $>1,500\text{ }^\circ\text{C}$ (Lin and Foster, 1968), whereas Sr-feldspar starts forming at $\sim 1,150\text{ }^\circ\text{C}$ (Ptáček et al., 2016), which is higher than the experimental temperatures used by Cherniak and Watson (1992, 1994). One possibility is that Ba diffusivities as reported by Cherniak (2002) represent coupled diffusion between $\text{Ca}_x\text{Na}_{1-x}\text{Al}_{1+x}\text{Si}_{3-x}\text{O}_8$ and $\text{BaAl}_2\text{Si}_2\text{O}_8$ components. The similar diffusivities reported in this study and by Cherniak (2002) most likely indicate that Ba diffusion in plagioclase is independent of Ba concentration in the source powder, as long as Ba-feldspar is a stable phase in Ba-rich ($>1\text{ wt.}\%$) source powders.

On the other hand, Sr only occurs as Sr oxide in the reproduced source powder of Cherniak and Watson (1992, 1994), and no Sr-feldspar formed. As such, the in-diffusion of Sr in plagioclase is hindered in the experiments of Cherniak and Watson (1992, 1994). Therefore, we speculate that the measured diffusion profiles presented in those studies instead represent SrO-plagioclase reaction fronts whose mechanism and rate are different from a solid-state diffusion process. A similar conclusion can be drawn from the experiments of Giletti and Casserly (1994), whereby the evaporated Sr chloride at the diffusion interface probably led to a disequilibrium with the plagioclase crystal.

3.5.2 Charge balance and the effect of silica activity

Plagioclase is composed of tetrahedral sites occupied by Si^{4+} and Al^{3+} , and metal sites occupied by Ca^{2+} and Na^+ (Fig. 3.10). The organisation and symmetry of plagioclase tetrahedral and metal sites are dependent on its composition and the ambient temperature; plagioclase structure can vary from the most disordered C2/m to the most ordered $\text{P}\bar{1}$,

with $\text{C}\bar{1}$, $\text{I}\bar{1}$ and $\text{X}\bar{1}$ in between (e.g., [Carpenter and McConnell, 1984](#)). Divalent trace elements in plagioclase such as Sr^{2+} (1.26 Å) and Ba^{2+} (1.42 Å) [cation radii from [Shannon \(1976\)](#)] have cation radii close to the ideal metal site cation (~ 1.18 Å) ([Jensen, 1973](#)), which implies that they are preferentially incorporated into the metal site. Meanwhile, Mg^{2+} (0.89 Å) has a smaller radius which is intermediate between metal site cations and tetrahedral site cations. Some studies investigating the substitution of Mg^{2+} and Fe^{2+} in lunar plagioclase ([Longhi et al., 1976](#)) and the synthesis of plagioclase in the CaO-MgO-SiO₂ system ([Peters et al., 1995](#); [Sclar and Benimoff, 1980](#)) conclude that Mg^{2+} is more

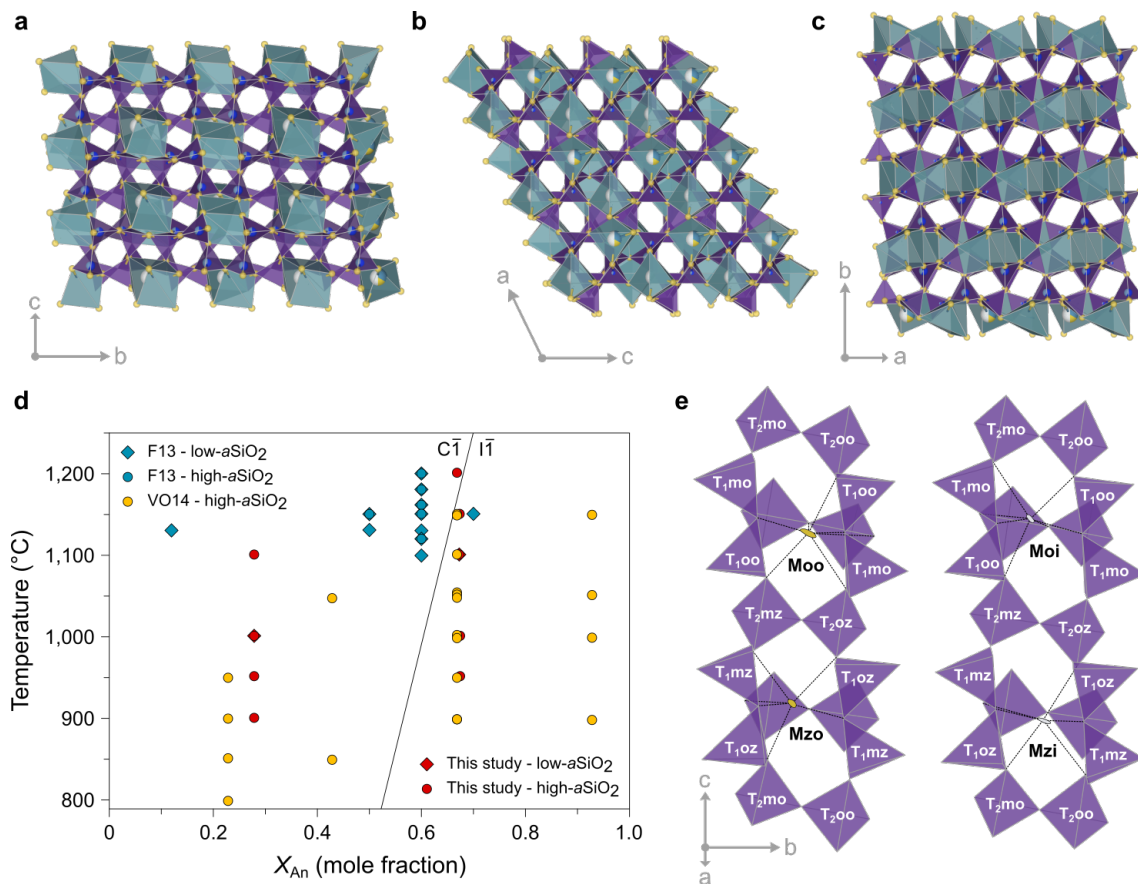
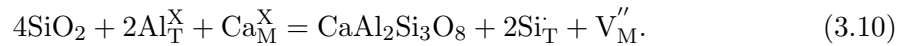
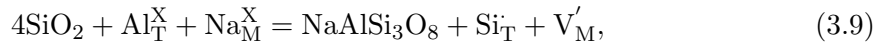


Figure 3.10. Potential cation diffusion mechanism in plagioclase. **a**, Projection of the plagioclase structure onto the b - c plane, illustrating the open channels parallel to the crystallographic a -axis. **b**, Projection of the plagioclase structure onto the a - c plane, illustrating the open channels parallel to the crystallographic b -axis. **c**, Projection of the plagioclase structure onto the a - b plane, illustrating the open channels parallel to the crystallographic c -axis. Blue dodecahedra represent $^{[\text{VIII}]}\text{Ca}^{2+}$ and $^{[\text{VIII}]}\text{Na}^+$, purple tetrahedral represent $^{[\text{IV}]}\text{Si}^{4+}$ and $^{[\text{IV}]}\text{Al}^{3+}$, and yellow spheres represent O^{2-} . Images were drawn using the software package VESTA ([Momma and Izumi, 2011](#)) and labradorite crystal ([Wenk et al., 1980](#)). **d**, Plagioclase X_{An} (mole fraction) vs. temperature (°C) for the experimental data of [Faak et al. \(2013\)](#) and [Van Orman et al. \(2014\)](#). The $\text{C}\bar{1}$ - $\text{I}\bar{1}$ phase transition was drawn using the equation from [Carpenter and McConnell \(1984\)](#). **e**, The environment around the Mo and Mz sites of a labradorite crystal having an $\text{I}\bar{1}$ structure ([Jin et al., 2018](#)) viewed along a^* . The left part highlights the bonding environment around the Moo and Mzo sites, while the right part highlights the bonding environment around the Moi and Mzi sites.

3. Diffusion of Sr and Ba in plagioclase

likely to occupy the tetrahedral site. Similarly, [Faak et al. \(2013\)](#) proposed, based on Mg diffusion experiments, that the tetrahedral site represents the preferred site occupancy of Mg^{2+} . On the other hand, the lattice strain model developed by [Blundy and Wood \(1994\)](#) shows a good agreement with experimentally-determined partition coefficients with the assumption that Mg^{2+} occupies the metal site.

The equilibrium substitution sees Sr^{2+} and Ba^{2+} (and Mg^{2+}) exchanging for Ca^{2+} on the metal site, which is the most stable configuration as no charge balance is required. Although the reported diffusion coefficients of Sr and Ba in plagioclase are similar within error, Ba diffusion rate is systematically slower than Sr, in agreement with the larger ionic radius of Ba^{2+} (1.42 Å) compared to Sr^{2+} (1.26 Å), resulting in a larger energy barrier to substitute for Ca^{2+} . An exchange for Na^+ compensated by a substitution of Si^{4+} by Al^{3+} is also possible. In addition, there are two mechanisms that allow for coupled substitution of Mg^{2+} : (1) Mg^{2+} and Si^{4+} are balanced by two Al^{3+} ; and (2) two Mg^{2+} incorporate the tetrahedral and metal sites and are balanced by Na^+ and Al^{3+} . In addition, diffusion can occur through vacancies in the metal and tetrahedral sites whereby vacancies can be created by metal and/or tetrahedral cations jumping into interstitial positions. Yet another possibility relates to the free silica in the high- $a\text{SiO}_2$ experiments resulting in the incorporation of an excess Si^{4+} in the tetrahedral site compensated by a vacancy in the metal site. This can be described for anorthite (Eq. 3.9) and albite (Eq. 3.10) endmembers using the Kröger-Vink notation ([Kröger and Vink, 1956](#)):



The development of such vacancies in the metal site has been proposed by [Faak et al. \(2013\)](#) to explain the higher diffusivities of Mg at high $a\text{SiO}_2$. On the other hand, Sr and Ba diffusion in plagioclase shows no clear dependence on $a\text{SiO}_2$ and is therefore likely insensitive to the formation of $\square\text{Si}_4\text{O}_8$ -type vacancies. As such, we further propose that $\square\text{Si}_4\text{O}_8$ -type vacancies only form in some ‘differentiated’ M-sites.

The thermal conditions of the experimental runs performed in this study and by [Faak et al. \(2013\)](#) and [Van Orman et al. \(2014\)](#) place the plagioclase crystals either in the $\text{C}\bar{1}$ or $\bar{1}\bar{1}$ structural domains (Fig. 3.10d). In the $\text{C}\bar{1}$ symmetry, plagioclase is composed of four tetrahedral sites ($\text{T}_{1\text{o}}$, $\text{T}_{1\text{m}}$, $\text{T}_{2\text{o}}$, $\text{T}_{2\text{m}}$) and two metal sites (M_1 , M_2) with Ca^{2+} being dominant in the M_2 site ([Fitz Gerald et al., 1986](#); [Jin and Xu, 2017](#)). As such, we propose that (1) this ordering is probably related to the smaller size of the M_2 site where large cations (Na^+ , Sr^{2+} , Ba^{2+}) are hardly incorporated, and (2) $\square\text{Si}_4\text{O}_8$ -type vacancies

preferentially form in this M_2 site. On the other hand, the $I\bar{1}$ symmetry exhibits eight different tetrahedral sites (T_{100} , T_{1m0} , T_{10z} , T_{1mz} , T_{200} , T_{2m0} , T_{20z} and T_{2mz}) and four different metal sites (M_{00} , M_{0i} , M_{z0} and M_{zi}) (Fig. 3.10e). Previous studies observed that vacancies preferentially form in the M_{zi} -site with a site occupancy $\sim 50\%$ lower than in the M_{z0} -site which is due to the switching of Al and Si tetrahedra beneath the metal site related to the $C\bar{1}$ - $I\bar{1}$ phase transition (Jin et al., 2018). Furthermore, the lower Na^+/Ca^{2+} ratio in the M_{zi} -site compared to the other metal sites (Angel et al., 1990; Jin et al., 2018; Wenk et al., 1980; Wenk and Kroll, 1984) highlights the hindered incorporation of large cations in this site. As a result, high- $aSiO_2$ environments probably lead to a preferential development of $\square Si_4O_8$ -type vacancies in these M_2 ($C\bar{1}$ symmetry) and M_{zi} ($I\bar{1}$ symmetry) sites where Mg^{2+} can quickly diffuse whereas larger Sr^{2+} and Ba^{2+} do not enter these sites. A similar mechanism has been advocated by Bloch et al. (2019) to explain the dependence of Co diffusion in olivine upon $aSiO_2$ while Ca diffusion was insensitive to $aSiO_2$.

3.5.3 Application to natural samples

The similarity between the diffusion rates of Sr and Ba in plagioclase experimentally determined in this study contrasts with previous studies (Cherniak and Watson, 1994; Cherniak, 2002; Giletti and Casserly, 1994) that showed a difference ranging from 2 to 2.5 orders of magnitude depending on the temperature for these two elements (Fig. 3.9c,d). This discrepancy holds important implications for estimating timescales of magma storage and evolution (Lubbers et al., 2022; Mutch et al., 2019; Zellmer et al., 1999). Here, we discuss the different experimentally derived diffusivities and apply them to detailed plagioclase compositional profiles from well-studied localities.

Because of the dependence of cation diffusion rate and plagioclase-melt partitioning on the anorthite content of plagioclase (e.g., Bindeman et al., 1998; Cherniak and Watson, 1992, 1994; Cherniak, 2002; Dohmen and Blundy, 2014; Giletti and Casserly, 1994; Nielsen et al., 2017; Van Orman et al., 2014; Sun et al., 2017), diffusive re-equilibration of trace elements progresses towards a compositional profile in equilibrium with the plagioclase anorthite content (Costa et al., 2003; Dohmen et al., 2017; Zellmer et al., 1999). Equilibrium, or “quasi steady-state,” profiles were modelled using partition coefficients from Bindeman et al. (1998). Additionally, to model cation diffusion in zoned plagioclase, one has to consider the variation of the chemical potential of the cation with the anorthite content following Eq. 3.11 (Costa et al., 2003):

$$\frac{\partial C_i}{\partial t} = D_i^t \frac{\partial^2 C}{\partial x^2} - \frac{D_i^t C_i}{RT} A_i \frac{\partial^2 X_{An}}{\partial x^2}, \quad (3.11)$$

3. Diffusion of Sr and Ba in plagioclase

where C is the concentration of the cation i , t is time (s), D is the diffusion coefficient ($\text{m}^2 \text{s}^{-1}$), x is the distance (m), R is the gas constant ($\text{J mol}^{-1} \text{K}^{-1}$), T is the temperature (K), A is a thermodynamic parameter related to the partitioning of cation i between plagioclase and melt, and X_{An} is the anorthite content (mole fraction).

Most of the compositional profiles used in this study were measured in plagioclase crystals hosted in a rhyolite from the Cerro Galán caldera (CGC), Argentina (Lubbers et al., 2022). In detail, the rock samples from the Cerro Galán caldera hosting the plagioclase crystals used to perform our test is a crystal-rich (~ 50 vol.%) rhyolitic ignimbrite, locally called “white pumice,” containing plagioclase, quartz, biotite, Fe-Ti-oxides, sanidine, apatite and zircon (Lubbers et al., 2022; Wright et al., 2011). The most reliable pre-eruptive temperature estimate was obtained by combining the crystallinity of the Cerro Galán ignimbrite with the rheological lock-up temperature of intermediate to felsic melts (750 ± 20 °C; Lubbers et al., 2022). The studied plagioclase profiles were measured from the crystal mantle to rim and are typified by two to three zones as part of larger scale oscillatory zoning (Lubbers et al., 2022).

The initial Sr and Ba concentrations prior to diffusion were inferred using the covariation between trace elements and the plagioclase anorthite content. During crystallisation, Sr and Ba behaves as compatible elements in plagioclase which results in a positive correlation between these elements and the anorthite content (e.g., Dohmen and Blundy, 2014). At the onset of diffusion, the slope of this correlation decreases and, if a quasi-steady state is reached, might be reversed (Dohmen et al., 2017). In order to account for potential diffusion, we only used the steepest slopes in the trace element-anorthite content diagrams from Lubbers et al. (2022). The boundary conditions are set such that the plagioclase rim remains in equilibrium with the interstitial melt, and the core is allowed to diffuse (e.g., Costa et al., 2003). The uncertainties associated with the diffusion experiments and the diffusion temperature are propagated using a Monte Carlo approach. The uncertainty structure of $\log_{10}D_0$ and E_a is strongly covariant (Mutch et al., 2021; Wu et al., 2022) and must be considered during the resampling process, which otherwise would lead to overestimated total uncertainties. For this model, we assume that $\log_{10}D_0$ and E_a follow a linear trend without any uncertainty envelope, which slightly underestimate the total uncertainty. First, the temperature and the three constants describing Sr and Ba diffusion in plagioclase (Eqs. 3.7 and 3.8) are sampled following a Gaussian distribution around the mean. Then, the time associated with the best fit is calculated by numerically solving Eq. 3.11 using the explicit finite-difference method (Crank, 1975). Finally, after repeating this operation 2,000 times, the mean diffusion time and its associated uncertainty are

calculated (Fig. 3.11).

The calculated equilibrium profiles highlight that Sr and Ba did not reach this quasi steady-state profile (Fig. 3.11). As such, we use Eqs. 3.7 and 3.8 to model Sr and Ba diffusion and calculate timescales ranging from $52.9_{-25.4}^{+41.2}$ to 168_{-85}^{+137} kyr using Sr, and from $41.0_{-19.7}^{+27.2}$ to 193_{-91}^{+141} kyr using Ba for the Cerro Galán ignimbrite. These calculated times using our new Sr and Ba diffusion coefficients are the same within uncertainty for individual grains, therefore confirming the robustness of these diffusion coefficients. To rigorously compare our experimentally determined diffusivities, the data of Giletti and Casserly (1994), Cherniak and Watson (1992, 1994) and Cherniak (2002) were parameterised using a Monte-Carlo approach, and are described following Eqs. 3.12, 3.13 and 3.14, respectively:

$$\log_{10}D_{\text{Sr}} (\text{m}^2 \text{s}^{-1}) = -3.76 (\pm 0.08) X_{\text{An}} - 4.52 (\pm 0.21) - \left[\frac{270,607 (\pm 4,286)}{2.303RT} \right], \quad (3.12)$$

$$\log_{10}D_{\text{Sr}} (\text{m}^2 \text{s}^{-1}) = -2.30 (\pm 0.02) X_{\text{An}} - 4.12 (\pm 0.08) - \left[\frac{304,382 (\pm 1,773)}{2.303RT} \right], \quad (3.13)$$

$$\log_{10}D_{\text{Ba}} (\text{m}^2 \text{s}^{-1}) = -1.27 (\pm 0.14) X_{\text{An}} - 5.47 (\pm 0.44) - \left[\frac{331,858 (\pm 10,077)}{2.303RT} \right]. \quad (3.14)$$

By combining these equations with the diffusion model highlighted above, the retrieved timescales are ~ 2 - 2.5 orders of magnitude shorter ($0.11_{-0.04}^{+0.06}$ to $0.42_{-0.16}^{+0.24}$ kyr) for Sr diffusion using the diffusivities of Giletti and Casserly (1994), and ~ 1.5 - 2 orders of magnitude shorter ($0.61_{-0.27}^{+0.41}$ to $2.08_{-0.87}^{+1.31}$ kyr) using Cherniak and Watson (1992, 1994), whereas residence times are ~ 3 times longer for Ba diffusion (128_{-61}^{+82} to 610_{-274}^{+378} kyr) using Cherniak (2002). Owing to the complete Mg re-equilibration in the plagioclase crystals from the Cerro Galán ignimbrite (Mutch et al., 2022), no comparison between Mg and Sr or Ba could be performed.

One plagioclase profile was measured in a rhyodacite from the Santorini caldera, Greece (Druitt et al., 2012) was used to apply our new diffusion coefficients. The host rock is a rhyodacitic pumice from the Minoan eruption that contains plagioclase, orthopyroxene, clinopyroxene, magnetite, ilmenite and apatite (Druitt et al., 2012). The pre-eruptive temperature (855-900 °C; Druitt et al., 2012) was constrained using the composition of touching ilmenite-magnetite pairs. The modelled plagioclase profile has an An-rich inner core (An₆₅₋₇₀) followed by a core within intermediate An contents (An₄₅₋₅₀) and an An-poor rim (\sim An₄₀). Determination of the initial trace element concentrations, boundary conditions, and calculation of uncertainties follow the same procedure as described above. The calculated equilibrium profiles for the Santorini plagioclase reveal that Sr did not

3. Diffusion of Sr and Ba in plagioclase

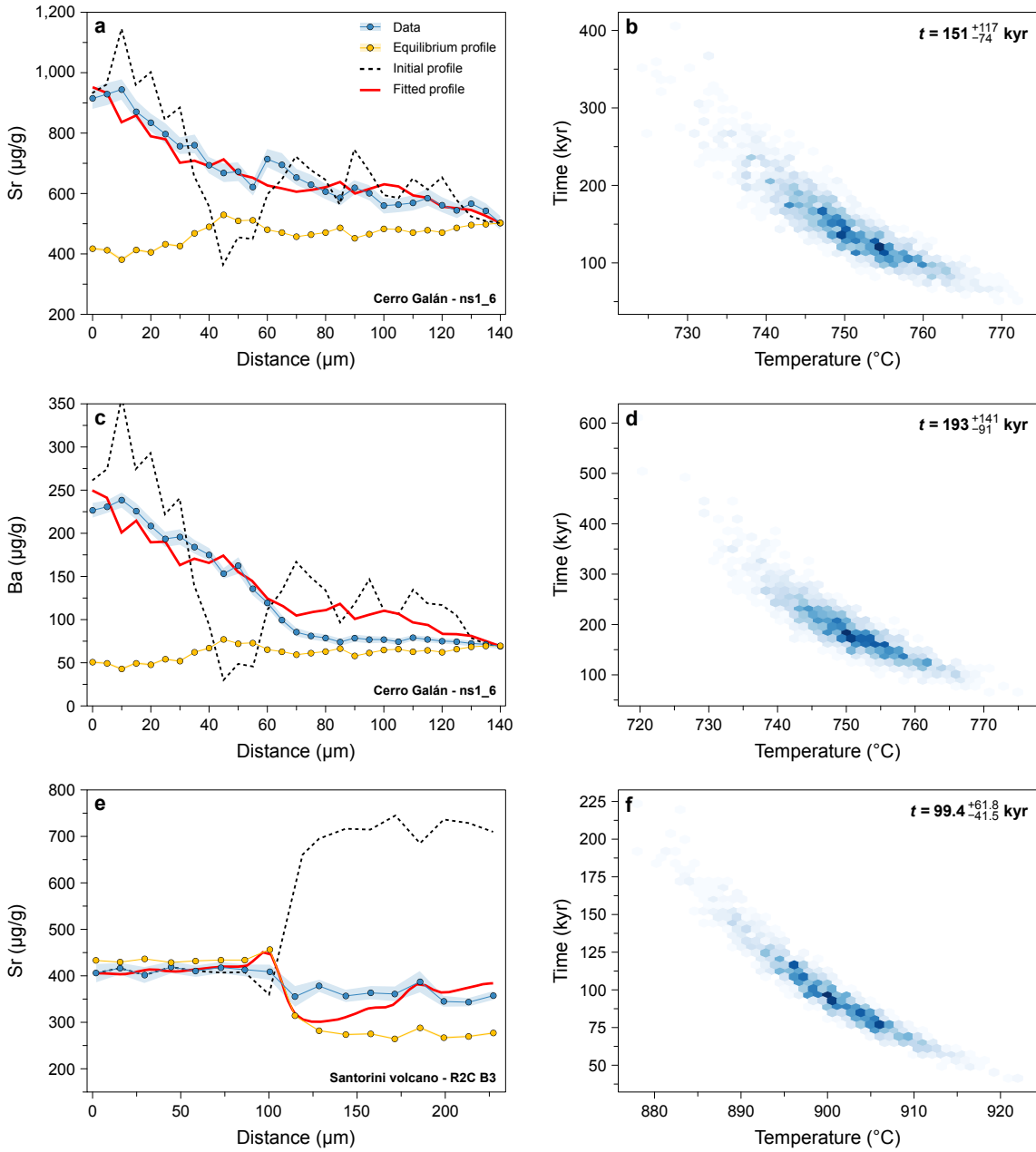


Figure 3.11. Application of the parameterised Sr and Ba diffusion coefficients determined in this study to natural data. (a, c, e) Plagioclase Sr and Ba diffusion profiles from the Cerro Galán ignimbrite (Lubbers et al., 2022) and Santorini caldera (Druitt et al., 2012) alongside the initial profiles, the equilibrium profiles, and the fitted profiles. (b, d, f) Results of the Monte Carlo simulation represented as temperature ($^{\circ}\text{C}$) vs. time (kyr). See main text for explanations regarding diffusion modelling and Monte Carlo resampling.

reach the quasi-steady state profile (Fig. 3.11), whereas Ba completely re-equilibrated (Supplementary Material 2). We use Eqs. 3.7 and 3.11 to model Sr diffusion and calculate timescales of $99.4^{+61.8}_{-41.5}$ kyr for the Santorini rhyodacitic pumice.

Therefore, using Sr and Ba diffusivities from previous studies can yield timescale differences of ~ 2 -2.5 orders of magnitude, whereas the Sr and Ba diffusion coefficients de-

terminated in this study lead to the same calculated timescales within uncertainty. The recalculated timescales for the Cerro Galán and Santorini calderas ($\sim 10^5$ yr) are significantly longer than previous estimates and are, eventually, linked to the differentiation of the magma reservoir and assembly of eruptible magma, rather than magma mixing prior to eruption. Although speculative, such differentiation timescales are in good agreement with physical melt segregation models derived from hindered settling velocities and compaction rates which require 10^4 - 10^6 yr to form >500 km³ of eruptible magma (McKenzie, 1985; Rabinowicz and Vigneresse, 2004).

The diffusion experiments performed in this study were done under anhydrous conditions, while natural magmatic and metamorphic systems usually have higher water fugacity ($f_{\text{H}_2\text{O}}$). Previous experimental studies indicate that increasing pressure and $f_{\text{H}_2\text{O}}$ may lead to faster cation diffusivities in some systems (e.g., Costa and Chakraborty, 2008; Holzapfel et al., 2009; Yund and Snow, 1989). However, Giletti and Shanahan (1997) report similar K diffusivities in plagioclase at 1 atm and at 100 MPa under hydrothermal conditions, suggesting that Sr and Ba diffusion might be rather insensitive to $f_{\text{H}_2\text{O}}$ if Sr and Ba diffusion mechanisms are similar to K. Therefore, future studies should vary pressure and $f_{\text{H}_2\text{O}}$ to clarify their effect on the diffusion of Sr and Ba in plagioclase.

3.6 Conclusions

The diffusion coefficients of Sr and Ba in plagioclase were experimentally determined as a function of temperature, anorthite content, crystal orientation and $a\text{SiO}_2$. Our results demonstrate that diffusion of Sr and Ba in plagioclase at 1 atm operates at a very similar rate, and is mainly controlled by the plagioclase anorthite content and the temperature, in agreement with previous studies investigating the diffusion of these two cations. However, Sr diffusion coefficients in plagioclase are ~ 1.5 -2 orders of magnitude slower than what has been measured previously, while Ba diffusion coefficients are ~ 0.5 order of magnitude faster. Such a discrepancy is most likely due to the different thermal stability of Sr- and Ba-feldspar in the source powders. For the investigated range of temperatures, the stability of Ba-feldspar in the source powder probably allows for Ba diffusion coupling, explaining the similar diffusion coefficients between different studies using different experimental approaches and analytical methods. In contrast, the absence of Sr-feldspar most likely leads to reaction with the plagioclase crystal at the diffusion interface. Furthermore, the independence of Sr and Ba diffusion upon $a\text{SiO}_2$ contrasts with the $a\text{SiO}_2$ -dependence of Mg diffusion in plagioclase. This difference is probably caused by the preferential formation of $\square\text{Si}_4\text{O}_8$ -type vacancies in plagioclase Mzi-sites, only occupied by smaller cations

3. Diffusion of Sr and Ba in plagioclase

like Mg^{2+} , at silica saturated conditions. Application to natural diffusion profiles in plagioclase reveals timescale discrepancies of 2.5-3.5 orders of magnitude between Sr and Ba by using the previously determined diffusion coefficients, whereas the diffusivities determined in this study yield consistent crystal residence timescales of ~ 100 kyr for the Cerro Galán and Santorini calderas. Such timescales may be interpreted as crystal residence time prior to eruption, rather than mixing-to-eruption timescales, in good agreement with the measured profiles located in plagioclase cores to mantles. If Sr and Ba diffusion indeed operates at similar slow rates, this opens new perspectives to study magmatic processes in volcanic and plutonic rocks using plagioclase, such as determining crystal residence time prior to melt segregation and extraction, and magma reservoir cooling rates.

3.7 Acknowledgements

We thank Sumit Chakraborty and Nick Greber for providing plagioclase crystals, Alfons Berger and Goran Andjić for assistance with EBSD analysis, Alexey Ulianov for precious help with LA-ICP-MS analysis, and Sumit Chakraborty for fruitful discussions. We are grateful to Andreas Audétat and Jim Van Orman for very helpful reviews.

Chapter 4

Cooling rates and crystal residence times in plutonic rocks determined by diffusion chronometry (Adamello batholith, Italy)

Chapter in preparation for submission in *Contributions to Mineralogy and Petrology*

4.1 Abstract

The thermal evolution of upper crustal magma reservoirs exerts the main control on the physical properties of the magma, therefore regulating the eruptability of magma chambers. Constraining the temperature evolution of these reservoirs through time thus constitutes an important scientific and societal challenge in order to mitigate future volcanic hazards. Diffusion chronometry emerged as a valuable tool to track the timescales of magmatic processes and is now routinely applied on erupted volcanic products to infer crystal residence times and mixing-to-eruption timescales. Despite some attempts to apply such a technique on plutonic rocks, their slow cooling prevented a robust interpretation of the retrieved timescales. Here we investigate the cooling rates and crystal-melt segregation timescales in the Western Adamello tonalite (WAT) and Re di Castello (RdC) units of the Adamello batholith (Italy). The WAT is mainly composed of tonalite displaying *in situ* crystal accumulations forming hornblende-biotite-gabbro and leucotonalite, and melt segregation as aplitic and pegmatitic granite. The studied area from the RdC exhibits

4. Cooling rates and crystal residence times

a concentric structure mainly composed of tonalite, granodiorite, and aplitic and pegmatitic granite. The Laione granodiorite from the RdC contains (1) partly resorbed, high-An plagioclase cores in contact with a crystal mantle having intermediate An contents surrounded by a thin, low-An rim, (2) Ba-zoned alkali feldspar oikocrysts hosting (3) small ($<100\ \mu\text{m}$) quartz exhibiting a normal Ti zoning. Western Adamello leucotonalitic dikes and domains contain similar plagioclase cores, mantles and rims. After determining the crystallisation temperatures of plagioclase mantle and rim, alkali feldspar and quartz, and the initial conditions prior to diffusion re-equilibration, the cooling rates of the WAT and RdC was inferred using diffusion modelling. The retrieved cooling paths are typified by an exponential decrease of the temperature and correspond, within uncertainty, to cooling rates calculated using thermal modelling and by previous studies using $^{39}\text{Ar}/^{40}\text{Ar}$ ages of minerals with different closure temperatures. Crystal-melt segregation timescales were then calculated based on the diffusion modelling of plagioclase core-to-mantle profiles and the retrieved cooling rates. The calculated timescales range from $\sim 10^4$ to $\sim 10^5$ yr, which most likely corresponds to the plagioclase core-to-mantle residence time prior to crystallisation of the low-An rim. Interestingly, these crystal residence times are similar to the zircon crystallisation timespan recorded in the same Adamello units, and to the crystal residence times obtained on historical volcanic eruptions using diffusion chronometry and high-precision zircon dating. Consequently, these timescales ($\sim 10^4$ - 10^5 yr) probably represent the ideal time to form a thermally stable magma reservoir able to segregate interstitial melt.

4.2 Introduction

Almost one billion people live close to an active volcanic area. Forecasting of volcanic unrest is therefore very important and requires understanding of the fundamental processes leading to an eruption and their associated timescales. Volcanic eruptions are triggered by several, not mutually exclusive processes including magma replenishment, second boiling and buoyancy (e.g., [Caricchi et al., 2014a](#); [Degruyter and Huber, 2014](#); [Sparks et al., 1977](#)). Reconstructing the mechanisms that operate in Earth's crustal reservoirs is intimately linked to precisely constraining the thermal evolution of these magma bodies. Indeed, the thermal budget of crustal reservoirs exerts the main control on the physical properties of the magma, therefore regulating the eruptability of magma chambers. Additionally, constraining timescales associated with the assembly of eruptible magma, magma mixing prior to eruption, and melt extraction within volcanic conduits is crucial to quantify the lifespan of magma reservoirs and mitigate volcanic hazards.

The view regarding the thermal and physical conditions of magma storage has shifted toward a consensus whereby magma reservoirs are composed of a volumetrically dominant (>50 vol.%), interconnected crystal network, hereafter referred to as “mush,” whereas crystal-poor domains (“melt”) are rare (Cashman et al., 2017; Marsh, 1981). Recently, two studies quantifying the thermal conditions of magma storage using zircon dating and diffusion modelling demonstrated that magma reservoirs predominantly reside at temperatures slightly above the solidus, typically between 700 and 750 °C (Barboni et al., 2016; Cooper and Kent, 2014). In detail, this magma storage temperature is a direct function of the melt recharge rate, which is commonly divided into an instantaneous and a long-term, average magma flux (Caricchi et al., 2014a). Some studies attempted to precisely constrain the storage temperature as a function of the melt recharge rate (e.g., Caricchi et al., 2014b; Weber et al., 2020), which is critical since the investigated temperature window (700-750 °C) typically corresponds to dramatic rheologic changes within evolved magma reservoirs. Slightly peraluminous felsic melts undergo a biotite-forming peritectic reaction (Grocolas and Müntener, 2024), while metaluminous felsic melts are instead dominated by alkali feldspar crystallisation (e.g., Johnson and Rutherford, 1989). These two crystallisation processes substantially decrease melt fractions with modest decreases in temperature, marking a severe change in magma’s mobility and dynamics. As such, accurately constraining the storage temperature of magma reservoirs and their cooling rates is essential to evaluate the eruptability potential, calculate crystal residence time, and retrieve crystal-melt segregation timescales.

The time parameter associated with volcanic eruption is commonly determined using high-resolution U-Pb zircon dating (e.g., Miller et al., 2007; Walker Jr et al., 2007), U-series disequilibria (e.g., Condomines et al., 2003; Cooper and Reid, 2008), crystal size distribution coupled to crystal growth rate (Higgins, 2006; Marsh, 1988; Randolph and Larson, 1971), and diffusion chronometry (Costa et al., 2020). The latter is now routinely applied and, by measuring elements having different diffusivities in different minerals, holds the potential to reconstruct the temporal evolution of a crustal reservoir from assembly to eruption. Most of the studies using diffusion chronometry interpret their results as rejuvenation timescales based on the presence of reverse zoning at crystal rims (e.g., Morgan et al., 2006). The calculated timescales of magma recharge prior to eruption at basaltic volcanoes generally span a few weeks to a few years, whereas decadal to millennial timescales are typical of volcanoes erupting evolved material (Cooper, 2019; Costa et al., 2020). On the other hand, U-series disequilibria and zircon U-Pb systems typically yield ages ranging from 10^4 to $>10^6$ yr, which are usually interpreted as crystal

4. Cooling rates and crystal residence times

residence times (e.g., [Barboni and Schoene, 2014](#); [Chambers et al., 2020](#); [Cooper, 2015](#); [Karakas et al., 2019](#); [Klein and Jagoutz, 2021](#); [Leuthold et al., 2012](#); [Samperton et al., 2015](#); [Schaen et al., 2021](#)). Similar diffusion profiles are often preserved in plutonic rocks, but diffusion re-equilibration during protracted cooling complicates the interpretation of calculated timescales ([Tavazzani et al., 2020](#)).

The goal of this contribution is to determine timescales of melt segregation and extraction within a slowly-cooled, upper crustal plutonic body, the Western Adamello batholith. We present field relationships and detailed textural observations coupled with thermometry and multi-mineral compositional profiles and maps to demonstrate that quartz, alkali feldspar and plagioclase rims capture the cooling history of the pluton, while plagioclase cores within in situ cumulates record residence times prior to crystal accumulation and melt segregation. We first precisely characterise mineral zoning and recognise three diffused zones in plagioclase recording its complex history, while quartz and alkali feldspar are only composed of two zones. Detailed thermometry using experimentally calibrated geothermometers and crystallisation experiments combined with diffusion equations allowed to reproduce the diffusion profiles and calculate cooling rates and crystal-melt segregation timescales. Finally, we compare the retrieved cooling rates and timescales with a thermal model, local $^{39}\text{Ar}/^{40}\text{Ar}$ ages and high-resolution zircon U-Pb ages to verify the accuracy of the employed methods, as well as with worldwide timescale data, and emphasise that diffusion timescales obtained in plutonic rocks are comparable to zircon derived timescales and document magma reservoir differentiation and assembly of eruptible magma prior to melt extraction.

4.3 Geological settings

The Adamello batholith, located in the Brescian Alps of northern Italy, represents the largest and oldest Tertiary calc-alkaline intrusive body in the Alps and was formed during the collision of the European and Adriatic plates (e.g., [Callegari and Brack, 2002](#)). The excellently exposed Adamello pluton covers a 675 km² area with up to 3 km of vertical relief and is usually separated into four superunits; Re di Castello, Adamello, Avio and Presanella (Fig. [4.1](#)). These superunits are composed at 99 % of quartz-diorite, tonalite and granodiorite, the remaining 1 % being hornblendite and gabbro ([Ulmer et al., 1983](#)), and have an emplacement age progressively decreasing from South (42-38 Ma) to North (34-31 Ma) ([Del Moro et al., 1983](#); [Schaltegger et al., 2019](#)).

The Western Adamello unit is part of the Adamello superunit (Fig. [4.1](#)) and is a coarse-grained, homogeneous tonalite with large abundances of amphibole and biotite

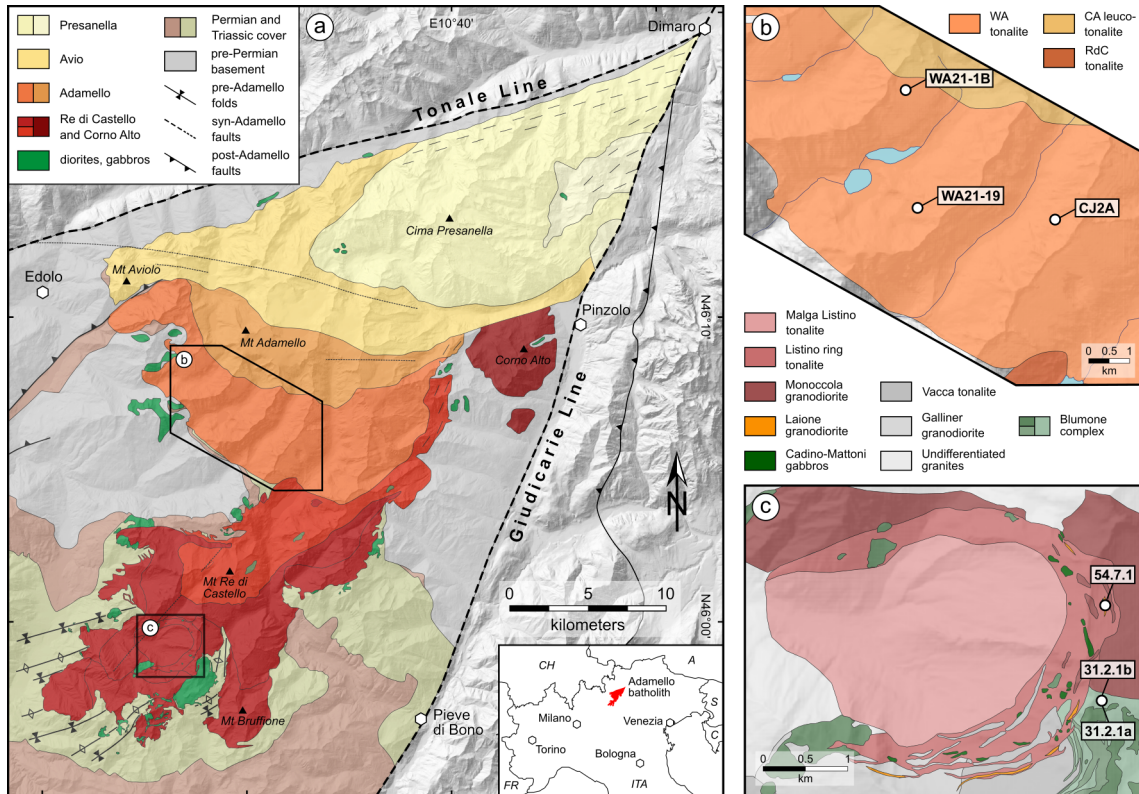


Figure 4.1. a, Simplified geological map of the Adamello batholith exhibiting the four superunits and corresponding lithologies (modified after [Schaltegger et al., 2009](#)). Location of field areas are also represented. b, Geological map of the Western Adamello tonalite and location of the studied samples (modified after [Floess and Baumgartner, 2015](#)). c, Geological map of the Listino ring complex and vicinity and location of the studied samples (modified after [Verberne, 2013](#)). Coordinates are reported using the WGS84 Coordinate System. CA, Central Adamello; RdC, Re di Castello; WA, Western Adamello.

phenocrysts (~ 20 vol.%). The WAT comprises an external zone of ~ 500 m at its southern border exhibiting a steeply-dipping, contact-parallel foliation interpreted as a feeder zone ([Floess and Baumgartner, 2015](#)). During differentiation, the WAT underwent a hornblende-consuming peritectic reaction producing biotite, and crystal-melt segregation forming cumulative hornblende-biotite-gabbro and leucotonalite, and extracted melt zones represented by granitic dikes ([Grocolas and Müntener, 2024](#)). The thermal evolution of the contact aureole has been used to demonstrate that the WAT was emplaced incrementally from northeast to southwest over a period of 1.2 Myr from 37.6 to 36.4 Ma at a pressure of ~ 250 MPa ([Floess, 2013](#); [Floess and Baumgartner, 2015](#)). For a detailed petrography of the Western Adamello tonalite (WAT), the reader is referred to [Grocolas and Müntener \(2024\)](#) and Chapter 2.

The Listino ring complex (LRC) and Lago della Vacca (LdV) suite are located in the southern part of the Re di Castello superunit and form a 5-km semi-circular zone of intensely foliated tonalites (Fig. 4.1) emplaced through a ballooning mechanism ([John and](#)

4. Cooling rates and crystal residence times

[Blundy, 1993](#); [Verberne, 2013](#)). The Monoccola granodiorite (MGD) is the most outward lithology of the LRC and is a medium- to coarse-grained, homogeneous granodiorite. It contains plagioclase, amphibole, biotite and quartz phenocrysts, while alkali feldspar is interstitial and surrounds the phenocrysts. A weak, inward foliation is present close to the contact with the Listino ring tonalite (LRT). The LRT is a medium-grained, rather homogeneous tonalite with abundant plagioclase phenocrysts. A similar magmatic inward foliation occurs and is defined by plagioclase, acicular amphibole, and biotite. The Laione granodiorite (LGD) is a hypabyssal, plagioclase-phyric granodiorite that forms small bodies (10-30 m large) included within the LRT displaying sharp contacts with the host tonalite ([Verberne, 2013](#)). It contains alkali feldspar oikocrysts and plagioclase phenocrysts texturally similar to the plagioclase crystals from the LRT. In addition, the Lago della Vacca suite also contains small LGD bodies displaying similar sharp contacts with the host diorites. The tonalite of Malga Listino (TML) constitutes the core of the LRC and is a homogeneous, medium-grained tonalite deprived of foliation except close to the contact with the LRT. It texturally resembles the MGD but with less modal quartz and biotite. Finally, granitic dikes (up to 1 m wide), originating from the LRT and MGD, radially crosscut all the LRC units. These dikes are composed of plagioclase, alkali feldspar, quartz and minor garnet and display either an aplitic texture or a pegmatitic texture with aplitic rims. The emplacement age decreases from 41.7 Myr for the outward MGD to 41.2 Myr for the inward TML ([Verberne, 2013](#)).

4.4 Methods

4.4.1 Backscattered electron imaging

Zoning patterns in plagioclase and alkali feldspar were determined on carbon-coated polished thin sections using backscattered electron (BSE) images acquired with a Tescan Mira II LMU field-emission gun scanning-electron microscope (SEM) equipped with an Oxford energy dispersive chemical detector at the University of Lausanne. The acceleration voltage was set to 10 kV and the beam current between 5 and 10 nA. Changes in BSE brightness are related to differences in the mean atomic number of pixels. In plagioclase, the major component affecting the BSE brightness is the anorthite [$An = 100 \times \text{molar Ca}/(\text{Ca} + \text{Na} + \text{K})$] content, while alkali feldspar brightness is largely controlled by the Ba content if the orthoclase [$Or = 100 \times \text{molar K}/(\text{Ca} + \text{Na} + \text{K})$] content remains constant, which is typically the case in slowly-cooled plutonic rocks.

4.4.2 Cathodoluminescence imaging

Zoning patterns in quartz were imaged on carbon-coated polished thin sections using a cathodoluminescence (CL) detector attached to a CamScan MV2300 SEM at the University of Lausanne. The acceleration voltage was set to 10 kV and the beam current to ~ 10 nA. Initial, low-quality images containing numerous quartz crystals were first acquired so that a large number of crystals could be evaluated for their zoning patterns prior to single crystal images. Changes in luminescence in quartz have been ascribed to Ti variations (Wark and Spear, 2005), but differences in Al contents can also play a role.

4.4.3 Electron probe microanalysis

Mineral major element compositions were acquired on carbon-coated polished thin sections by field-emission gun electron probe microanalyses (EPMA) using a JEOL JXA-8530F HyperProbe equipped with five wavelength dispersive spectrometers (WDS) at the University of Lausanne. The acceleration voltage was set to 15 kV, the beam current to 10 nA, and the beam size ranged from 1 to 5 μm . Counting times were 30 s on the peak and 15 s on the background. Measurements were corrected with the PRZF method (Armstrong, 1995), and standardised using synthetic glasses and natural minerals.

X-ray compositional maps of alkali feldspar were carried out using an acceleration voltage of 10 kV and a beam current of 150 nA, with dwell times of 20 ms for major elements (Si, Al, Ca, Na, K), and 200 ms for Ba. The pixel size ranged from 1 to 2 μm to compromise between spatial resolution and acquisition time. Detailed profiles of ~ 50 individual points across grains were used to standardise elemental maps. The raw, X-ray compositional maps were converted to quantitative concentrations using a linear standardisation scheme and performed using XMapTools (Lanari et al., 2014).

4.4.4 Laser ablation inductively coupled plasma mass spectrometry

Trace element composition profiles of plagioclase and alkali feldspar were determined using a Perkin Elmer NexION 5000 ICP-MS coupled with an Australian Scientific Instruments RESolution 193 nm Ar-F excimer laser at the University of Lausanne. The LA-ICP-MS system was optimised by linearly scanning the NIST SRM-612 glass standard at $10 \mu\text{m s}^{-1}$ in order to increase the spectrometer sensitivity ($^{139}\text{La}^+ > 2.0 \times 10^6$ cps) without significantly producing oxides ($^{248}\text{ThO}^+ / ^{232}\text{Th}^+ < 0.5\%$) and doubly-charged ions ($\text{Ba}^{2+} / \text{Ba}^+ < 3.0\%$). The repetition rate was set to 10 Hz and the energy density was 6 J cm^{-2} . Helium (1 l min^{-1}) and N_2 (1 ml min^{-1}) were used as carrier gases. The measured isotopes were ^{25}Mg , ^{27}Al , ^{42}Ca , ^{49}Ti , ^{57}Fe , ^{86}Sr , ^{137}Ba , ^{139}La , ^{151}Eu and ^{208}Pb .

4. Cooling rates and crystal residence times

The data were acquired using slits to shape the laser beam as a $7.5 \times 50 \mu\text{m}$ rectangular area with the long axis parallel to the diffusion interface. The scanning mode was used, whereby the stage was moved at a constant rate of $1 \mu\text{m s}^{-1}$. Background and wash-out interval acquisition times were 70 and 35 s, respectively. Dwell times were 10 ms for ^{27}Al and ^{42}Ca , 20 ms for ^{25}Mg , ^{57}Fe , ^{139}La , ^{151}Eu and ^{208}Pb , and 30 ms for ^{49}Ti , ^{86}Sr and ^{137}Ba . Each five unknown measurement, NIST SRM-612 and BCR-2G were measured using the scanning mode. Absolute concentrations were calculated using CaO as internal reference, NIST SRM-612 as primary standard, and BCR-2G as secondary standard for quality control. Data reduction was performed with the Iolite 4 software (Paton et al., 2011), employing a step forward function for the background and a polynomial function for the primary standard. The average elemental abundances of the standards were taken from Pearce et al. (1997). The scanning depth was then checked using a white-light interferometer and ranged from 0.5 to $1 \mu\text{m}$.

The trace element compositions of amphibole, plagioclase, alkali feldspar, quartz and zircon follows the same procedure as described by Grocolas and Müntener (2024) and are reported in the Supplementary Material 3.

4.4.5 Secondary ion mass spectrometry

Thin sections from the Laione granodiorite and Western Adamello leucotonalite were cut using a diamond wire saw and pressed in indium. The mounts were cleaned with ethanol and coated with gold ($\sim 35 \text{ nm}$) before being loaded into the sample chamber at least 24 h before analysis. Titanium concentrations in quartz from the Laione granodiorite were measured using a Cameca IMS 1280-HR secondary ion mass spectrometer (SIMS) at the University of Lausanne. The vacuum of the sample chamber was kept at $\sim 6 \times 10^{-9}$ mbar. Secondary ions of ^{27}Al , ^{30}Si and ^{48}Ti produced by a primary O^{2-} beam of $\sim 3 \text{ nA}$ were measured using the axial electron multiplier for ^{27}Al and ^{48}Ti , and a Faraday cup (FC2) for ^{30}Si . The field aperture was set at $5,000 \mu\text{m}$ and the energy window at 50 eV. The analysed area was pre-sputtered for 1 min followed by 6 min of data collection over an area of $\sim 6 \times 6 \mu\text{m}$. Entrance ($\sim 80 \mu\text{m}$) and exit ($\sim 400 \mu\text{m}$) slits were adjusted to get a mass resolving power (MRP) of $\sim 3,000$. Secondary ion intensities were normalised to ^{30}Si and Ti contents and quantified using one natural quartz standard with known Ti concentrations (Audétat et al., 2015).

4.4.6 Nanoscale secondary ion mass spectrometry

High-resolution profiles of Ti in quartz and Sr in plagioclase for both investigated lithologies were determined using a Cameca NanoSIMS 50L at the University of Lausanne. Areas of interest were sputtered with a primary $^{16}\text{O}^-$ beam focused to a spot size of ~ 900 nm. Following an implantation phase required to reach a significant emission of secondary ions, 35×35 μm images with 256×256 pixels resolution were rapidly collected. Based on the obtained ion images, locations for profiles were defined perpendicular to the crystal zoning. These profiles were acquired by continuously scanning the target segment for a total of 20 cycles. Secondary ions of ^{46}Ti , ^{47}Ti , ^{48}Ti , ^{28}Si and ^{29}Si for quartz, and ^{27}Al , ^{28}Si , ^{40}Ca , ^{86}Sr and ^{88}Sr for plagioclase were measured using electron multipliers. The reported data correspond to the cumulated counts of the cycles free of any spikes caused by the presence of small inclusions. To remove the effect of local variation in the ionisation and extraction processes, the data are reported as $^{48}\text{Ti}/^{28}\text{Si}$ for quartz (Seitz et al., 2018), while the major element zoning of plagioclase only allow to use the measured counts of ^{86}Sr or ^{88}Sr . Absolute concentrations were calculated using the quartz Ti concentrations measured by SIMS coupled with the CL greyscale intensity, and the plagioclase Sr concentrations measured by LA-ICP-MS.

4.4.7 Diffusion modelling

When a crystal exhibits a chemical gradient, Fick's second law (Fick, 1855) can be used to describe the homogenisation of this chemical gradient and calculate the thermal evolution undergone by the host crystal:

$$\frac{\partial C}{\partial t} = D \frac{\partial^2 C}{\partial x^2}, \quad (4.1)$$

where C is the concentration of element i , t is time, D is the diffusion coefficient of element i at time t , and x is the position along the modelled profile. This equation can be solved using the explicit finite-difference method and treated as tracer systems, whereby diffusion of each element occurs solely in response to its own concentration gradient (Crank, 1975).

This is described by Eq. 4.2:

$$\frac{C_i^{t+1} - C_i^t}{\Delta t} = \frac{1}{\Delta x^2} [D_i^t (C_{i+1}^t - 2C_i^t + C_{i-1}^t)]. \quad (4.2)$$

By precisely determining the initial conditions, boundary conditions and diffusion coefficients, temperature–time paths can be retrieved by fitting a model to the concentration gradient. To model cooling paths, temperature was changed at every time step and followed an exponential function, and diffusion coefficients were recalculated following Eq.

4. Cooling rates and crystal residence times

4.3:

$$\log_{10}D_i = \log_{10}D_0 - \left(\frac{E_a}{2.303RT} \right), \quad (4.3)$$

where $\log_{10}D_0$ ($\text{m}^2 \text{s}^{-1}$) and E_a (J mol^{-1}) are the parameters describing the diffusion of element i , R is the universal gas constant ($\text{J mol}^{-1} \text{K}^{-1}$), and T is the temperature (K). The presented model assumes that crystal overgrowths have formed sufficiently fast to be treated as instantaneous compared to diffusion timescales (e.g., [Devoir et al., 2021](#)).

Ti in quartz and Ba in alkali feldspar

Because the initial chemical profiles are erased after the onset of diffusion, two different initial concentrations were used for diffusion modelling of Ti in quartz and Ba in alkali feldspar. The first one was a simple step-function while the second one accounts for a potential growth zone between two plateaus. The boundary conditions were fixed as diffusion did not operate further than $\sim 5\text{-}10 \mu\text{m}$. Finally, the diffusion coefficients used for Ti-in-quartz diffusion were taken from [Cherniak et al. \(2007\)](#), [Jollands et al. \(2020\)](#), and [Aud  tat et al. \(2021, 2023\)](#), while Ba diffusion in alkali feldspar was modelled using the data from [Cherniak \(2002\)](#). A rigorous comparison between these studies is done and the retrieved timescales are discussed as a function of the diffusion coefficients.

Sr and Ba in plagioclase

Trace element partitioning in plagioclase is strongly dependent on temperature and plagioclase composition ([Bindeman et al., 1998](#); [Dohmen and Blundy, 2014](#); [Mutch et al., 2022](#); [Nielsen et al., 2017](#); [Sun et al., 2017](#)), and follows an Arrhenius relationship as defined by Eq. 4.4:

$$RT \ln K_{D_i} = A_i \cdot X_{\text{An}} + B_i, \quad (4.4)$$

where K_{D_i} is the partition coefficient between plagioclase and melt for element i , X_{An} is the molar anorthite (An) content [molar $\text{Ca}/(\text{Ca} + \text{Na} + \text{K})$], and both A and B are constants (J mol^{-1}) and are different for each element. Likewise, Sr and Ba diffusion in plagioclase is a function of An content and temperature ([Cherniak and Watson, 1992, 1994](#); [Giletti and Casserly, 1994](#); [Grocolas et al., in review](#); [LaTourrette and Wasserburg, 1998](#); [Costa et al., 2003](#); [Van Orman et al., 2014](#)). Therefore, a modified solution to the diffusion equation has been developed by [Costa et al. \(2003\)](#) to incorporate the dependence on An content (Eq. 4.5):

$$\frac{\partial C_i}{\partial t} = D_i^t \frac{\partial^2 C}{\partial x^2} - \frac{D_i^t C_i}{RT} A_i \frac{\partial^2 X_{\text{An}}}{\partial x^2}. \quad (4.5)$$

This solution to the diffusion equation leads to a quasi-steady state profile that depends on the measured plagioclase An content, assumed to remain constant through time (Grove et al., 1984), where the chemical gradient of element i never reaches complete homogenisation (Costa et al., 2003; Dohmen and Blundy, 2014; Faak et al., 2013). We then solve this equation using the explicit finite-difference method (Eq. 4.6):

$$\begin{aligned} \frac{C_i^{t+1} - C_i^t}{\Delta t} = & \left[D_i^t \left(\frac{C_{i+1}^t - 2C_i^t + C_{i-1}^t}{\Delta x^2} \right) + \left(\frac{D_{i+1}^t - D_i^t}{\Delta x} \right) \left(\frac{C_{i+1}^t - C_i^t}{\Delta x} \right) \right] \\ & - \frac{A_i}{RT} \left[D_i^t \left(\frac{C_{i+1}^t - C_i^t}{\Delta x} \cdot \frac{X_{\text{An},i+1}^t - X_{\text{An},i}^t}{\Delta x} \right) + C_i^t \left(\frac{D_{i+1}^t - D_i^t}{\Delta x} \cdot \frac{X_{\text{An},i+1}^t - X_{\text{An},i}^t}{\Delta x} \right) \right. \\ & \left. + D_i^t C_i^t \left(\frac{X_{\text{An},i+1}^t - 2X_{\text{An},i}^t + X_{\text{An},i-1}^t}{\Delta x^2} \right) \right]. \quad (4.6) \end{aligned}$$

Before modelling diffusion profiles, the first step involves determining the quasi-steady state profiles by fixing the rim trace element composition to the measured rim composition (Costa et al., 2003). The quasi-steady state profile is then calculated inward by using partition coefficients (Dohmen and Blundy, 2014), and compared to the measured trace element profile; matching profiles occur when diffusion went to completion. In such cases, the calculated timescale and/or cooling rate only represent minimum values.

Finally, to infer initial profiles, two methods have been applied in the literature. The first one consists in using the correlation between the plagioclase An content and the trace element of interest (Druitt et al., 2012), and highly relies on the degree of diffusion of this element. It is therefore important to distinguish original magmatic trace element contents from concentrations modified by diffusion. The second method is based on the reset of the diffused profile using partitioning (Lubbers et al., 2022; Mutch et al., 2021). The observed trace element profile is divided by the partition coefficient to obtain the equilibrium melt compositions from which a simplified series of discrete melt compositions is generated. The initial trace element profile is then calculated by multiplying this simplified equilibrium melt profile with the K_D . In the following, we use the first method because it is based on less assumptions, and the correlation between the plagioclase An content and trace elements prior to diffusion has been previously evaluated based on analyses in homogeneous plagioclase cores and mantles from the same samples (Grocolas and Müntener, 2024).

Analysis and model uncertainties

Analytical uncertainties using conventional spectrometric techniques are mainly associated with counting statistics and standardisation. For LA-ICP-MS scanning analyses,

4. Cooling rates and crystal residence times

uncertainties were determined by calculating the relative standard deviation of the measured concentrations obtained from the analysis of BCR-2G from its known concentrations (Pearce et al., 1997). The typical standard deviation is in the range of $\sim 2-6$ % for Sr and Ba. A similar operation was done to calculate the uncertainties on SIMS measurements, but compositional variations between acquisition cycles were also considered, and errors were propagated to give typical uncertainties for Ti concentrations in quartz of $\sim 2-3$ %. Finally, the high-resolution Ti profiles in quartz and Sr profiles in plagioclase are not associated with any uncertainty as we report the NanoSIMS data as cumulated counts.

Several parameters used during diffusion modelling are associated with an uncertainty which must be considered when calculating timescales. In addition to the initial profile, the uncertainty budget is largely controlled by the initial temperature, the parameters of the diffusion coefficients ($\log_{10}D_0$ and E_a), and the curve fitting including the measurement uncertainties (Costa et al., 2008; Wu et al., 2022). In this study, we only consider uncertainties related to the geometry of the initial profile (for quartz and alkali feldspar), temperature, and diffusion coefficients. In normally zoned crystals, the impact of crystal growth on the initial conditions is probably more important than the uncertainty on the curve fitting, especially when the profile shape is well-resolved. To evaluate the total uncertainty, a Monte Carlo approach was employed for each profile where 1,500 trials were performed. The uncertainty structure of $\log_{10}D_0$ and E_a is strongly covariant (Mutch et al., 2021; Wu et al., 2022) and must be considered during the resampling process, which otherwise would lead to overestimated total uncertainties. For this model, we assume that $\log_{10}D_0$ and E_a follow a linear trend without any uncertainty envelope, which slightly underestimate the total uncertainty. For modelling cooling rates, the initial temperature and diffusion parameters were sampled following a Gaussian distribution around the mean, and profiles were modelled using Eqs. 4.2 and 4.5, and fitted with a least-square optimisation routine. In addition to the abovementioned parameters, the calculated crystal-melt segregation timescales also account for the uncertainties associated with the cooling rates. The Monte Carlo model randomly samples the exponential factor controlling the cooling rate around the mean and considers a standard deviation of 20 %. The uncertainties related to the calculated cooling rates and crystal-melt segregation timescales are reported as the two-fold standard deviation.

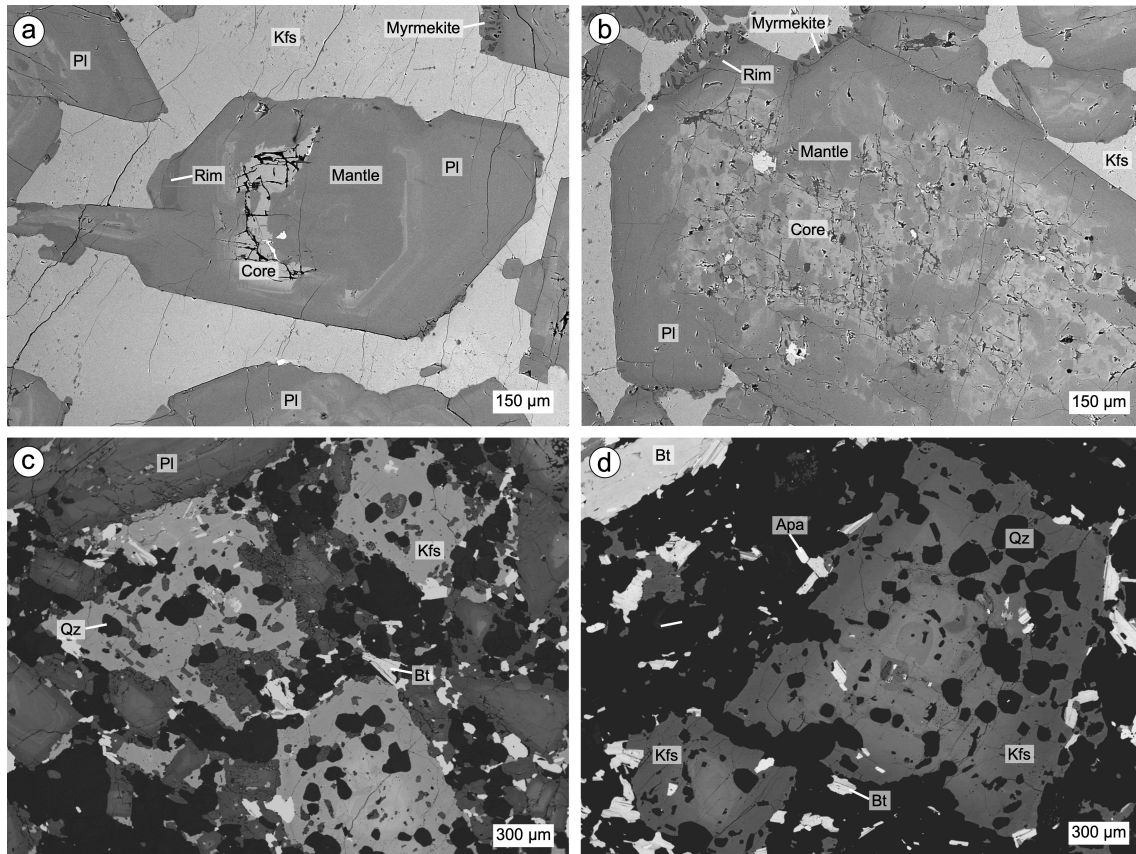


Figure 4.2. Backscatter electron images of representative crystal zoning of the studied lithologies. **a**, Subhedral to euhedral plagioclase crystal from Western Adamello leucotonalite exhibiting a dissolved inner core and resorbed outer core, a homogenous mantle, and a discontinuous dark rim. Plagioclase crystals are surrounded by a single anhedral alkali feldspar oikocryst. Myrmekite occurs at some plagioclase rims (N46°05'49.7", E10°32'16.0"). **b**, Subhedral to euhedral plagioclase crystal from Western Adamello leucotonalite having a large, patchy zoned, bright core, a homogeneous mantle, and a discontinuous rim with local myrmekite. Interstitial alkali feldspar surrounds plagioclase (N46°06'26.6", E10°29'26.8"). **c**, Laione granodiorite constituted of plagioclase phenocrysts, anhedral to subhedral alkali feldspar oikocrysts with inclusions of small, subhedral quartz, biotite and plagioclase, and a fine-grained matrix composed of the same small quartz crystals, plagioclase and biotite (N45°58'52.5", E10°27'35.7"). **d**, Laione granodiorite highlighting the presence of some biotite phenocrysts, the occurrence of apatite in the matrix assemblage, and the zoning pattern of alkali feldspar oikocrysts (N45°58'52.5", E10°27'35.7").

4.5 Results

4.5.1 Petrography

The samples used in this study come from the Western Adamello and the Re di Castello superunits, which are part of the Adamello batholith. They consist of three leucotonalites from the Western Adamello, and three Laione granodiorites from the Listino ring and Blumone (Lago della Vacca) complexes (Fig. 4.1). Leucotonalites from the Western Adamello are relatively fine-grained leucocratic rocks mainly composed of plagioclase and quartz with interstitial, oikocrystic alkali feldspar, and minor amphibole and/or biotite

4. Cooling rates and crystal residence times

phenocrysts (Fig. 4.2a,b). Field observations coupled with phase relationships and chemistry suggest that these leucotonalites represent *in situ* accumulations of plagioclase and quartz in non-cotectic proportions from the main tonalitic melt (Grocolas and Müntener, 2024). In these rocks, plagioclase is normally zoned and can be subdivided into three main zones: (1) relatively rare calcium-rich ($>An_{70}$) cores with partial resorption textures, probably caused by near-adiabatic ascent from lower portions of the crust; (2) volumetrically dominant core-to-mantle intermediate compositions (An_{40-60}); and (3) a thin ($<150\ \mu\text{m}$), sodium-rich ($\sim An_{30}$) rim that can locally be absent (Fig. 4.2a,b). Leucotonalite from the Western Adamello typically has a plagioclase-dominated bulk rock composition with high Sr contents (215-734 $\mu\text{g/g}$) and a wide range of positive Eu anomalies [$\text{Eu}/\text{Eu}^* = \text{Eu}_N/(\text{Sm}_N \times \text{Gd}_N)^{1/2}$; 1.36-3.56] (Fig. 4.3).

The Laione granodiorite from the Listino ring and Blumone complexes is a porphyritic granodiorite containing large (0.5-5 mm), inclusion-free, oscillatory-zoned plagioclase phenocrysts, and large (0.5-3 mm) alkali feldspar oikocrysts (Fig. 4.2c,d). The latter contains inclusions of subhedral quartz crystals (50-150 μm) often forming small aggregates, small ($<100\ \mu\text{m}$) subhedral biotite, and small ($<100\ \mu\text{m}$) plagioclase crystals elongated parallel to the alkali feldspar grain boundaries. The matrix is composed of small ($<150\ \mu\text{m}$) plagioclase and biotite, and the same subhedral quartz crystals as those included in alkali feldspar. The same three plagioclase zones as in the Western Adamello leucotonalite are also identified in the Laione granodiorite, albeit with thinner ($<30\ \mu\text{m}$) rims. Subhedral amphibole phenocrysts (1-3 mm) rarely occur. Euhedral apatite and zircon (50-250 μm) are present in the matrix or as inclusions within interstitial biotite, while rare titanite crystals (50-150 μm) are only present in the matrix. The Laione granodiorite samples from the Listino ring and Blumone complexes have homogeneous bulk rock compositions with SiO_2 (65.7-69.6 wt.%) inversely correlated to Sr (454-375 $\mu\text{g/g}$), high Ba (630-875 $\mu\text{g/g}$) contents and no significant Eu anomaly (0.87-1.12) (Fig. 4.3). These values of Eu anomaly coupled with the compositional homogeneity of the Laione granodiorite are typical of plutonic rocks that did not undergo significant melt extraction and crystal accumulation.

4.5.2 Alkali feldspar

Alkali feldspar oikocrysts from the Laione granodiorite have a restrictive range of Or contents from Or_{85} to Or_{92} inversely correlated to BaO (2.77-0.34 wt.%). They have Ba-poor (BaO <1 wt.%) rims and Ba-rich (BaO >1.5 wt.%) cores correlated to the brightness of the BSE images. Different types of zoning are observed; it comprises patchy, Ba-poor

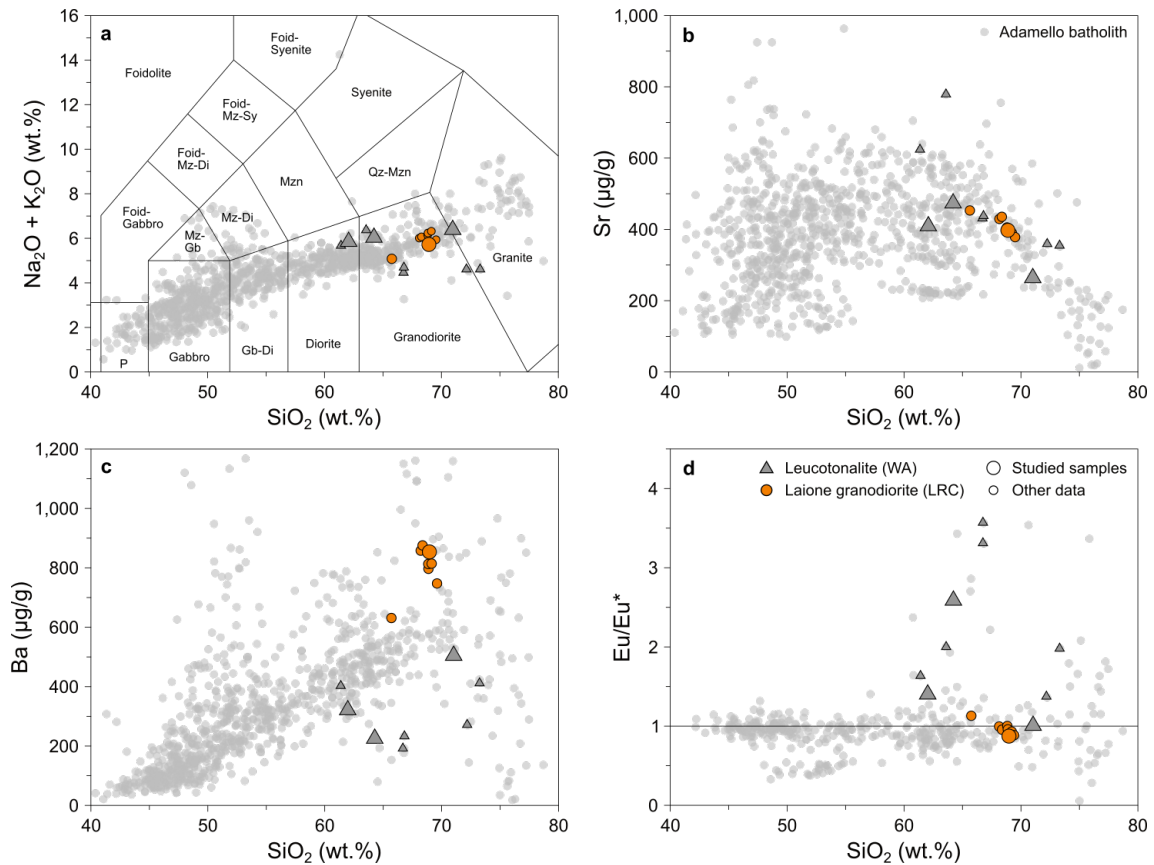


Figure 4.3. Major and trace element bulk rock compositions of the Western Adamello leucotonalite and Laione granodiorite. **a**, Total alkali silica [SiO_2 (wt.%) vs. $\text{Na}_2\text{O} + \text{K}_2\text{O}$ (wt.%)] diagram (Middlemost, 1994). **b**, SiO_2 (wt.%) vs. Sr ($\mu\text{g/g}$). **c**, SiO_2 (wt.%) vs. Ba ($\mu\text{g/g}$). **d**, SiO_2 (wt.%) vs. Eu/Eu^* . The larger symbols correspond to the samples investigated in this study, and the smaller symbols represent other samples from the same lithologies. The data from the Adamello batholith are from the compilation of Müntener et al. (2021).

zones in the centre of the Ba-rich core and around some quartz inclusions, and local, laterally discontinuous sawtooth zoning (Fig. 4.4a,b). The transition from Ba-rich core to Ba-poor rim is usually gradational, but it can laterally evolve toward a sharp contact (Fig. 4.4b). This complex zoning records the thermal and chemical history of these alkali feldspars where multiple episodes of growth and dissolution occurred, probably in response to magma recharge.

4.5.3 Quartz

Small, subhedral to euhedral quartz from the Laione granodiorite present in the matrix and as inclusions within alkali feldspar oikocrysts systematically exhibit a gradational transition from a bright core to darker rims in CL images (Fig. 4.4c,d). Quartz often has well-defined crystal faces, contrasting with the boundary between the crystal core and rim which is diffuse and has a rounded shape. This may arise either from (1) the growth of a

4. Cooling rates and crystal residence times

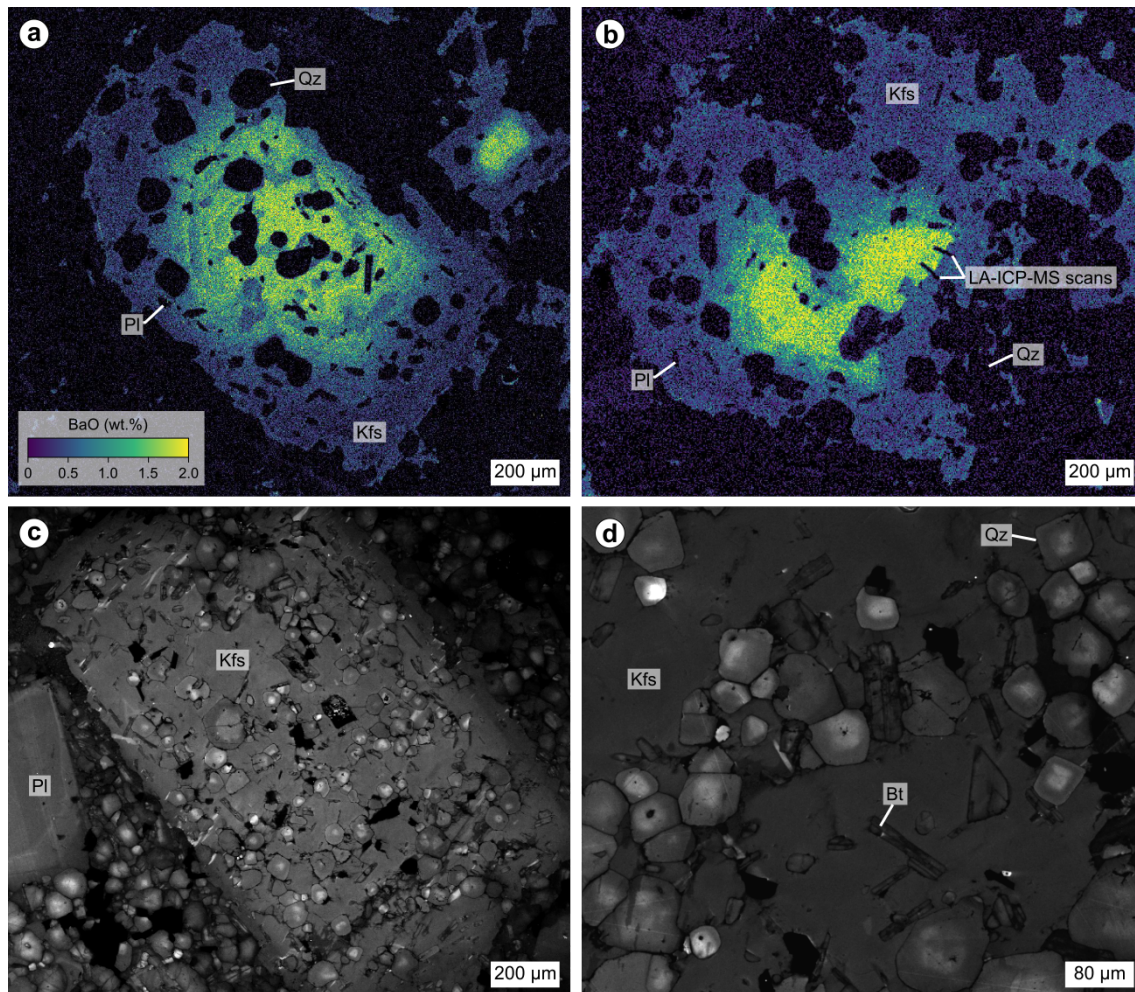


Figure 4.4. Compositional zoning observed in the Laione granodiorite minerals. **a**, X-ray Ba map of an alkali feldspar oikocryst highlighting the Ba-rich core and Ba-poor external domain connected either by normal or oscillatory zoned mantle. Ba-poor patches occur in the core and mantle, and discontinuous Ba-poor halos surround quartz inclusions. **b**, X-ray Ba map of an alkali feldspar oikocryst showing the lateral transition from a normal, smooth zoning to a normal, sharp zoning. LA-ICP-MS line scans were done in this sharp transition to infer cooling rates. **c**, Cathodoluminescence (CL) image of an alkali feldspar oikocryst highlighting the systematic normal zoning of interstitial quartz and quartz inclusions. **d**, Similar CL image focusing on the normal zoning of quartz crystals included in an alkali feldspar oikocryst.

bright core at emplacement pressure followed by the growth of a darker rim coupled with diffusion re-equilibration, or (2) the growth of a bright core at higher pressure followed by decompression leading to partial dissolution of the quartz core, and growth of a darker rim followed by diffusion re-equilibration. The relative brightness of quartz CL images is usually ascribed to the variations of the Ti and/or Al contents (e.g., [Götze et al., 2001](#); [Pamukçu et al., 2016](#); [Spear and Wark, 2009](#); [Tavazzani et al., 2020](#); [Wark and Spear, 2005](#)). The small, subhedral to euhedral quartz from the Laione granodiorite have Al contents ranging from 23 to 49 $\mu\text{g/g}$ with no relationship with the CL greyscale intensity. On the other hand, the quartz Ti concentrations are linked to the CL brightness, with

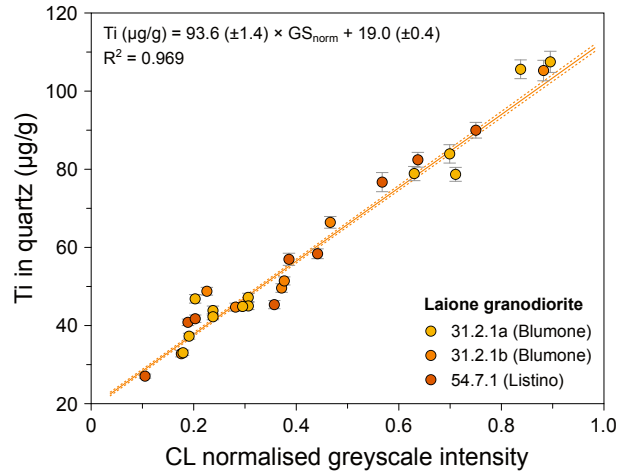


Figure 4.5. Calibration of the cathodoluminescence greyscale intensity of quartz to the Ti concentrations measured by SIMS based on quartz from three Laione granodiorite samples. The data were fit using a Monte Carlo scheme coupled to a root-mean square optimisation.

the quartz bright cores having high Ti concentrations (79-110 $\mu\text{g/g}$) while the dark rims have lower Ti contents (28-52 $\mu\text{g/g}$). This correlation is used to calibrate the quartz Ti concentrations from the CL greyscale intensity (Fig. 4.5) and NanoSIMS intensity ratios.

4.5.4 Plagioclase

Three plagioclase zones have been recognised in the Western Adamello leucotonalite. The first zone corresponds to bright, subhedral to euhedral cores (<1 vol.%) presenting resorption surfaces, patchy zones, and sometimes having their inner core completely dissolved (Fig. 4.2a). They have An contents ranging from An_{67} to An_{87} , while their Sr and Ba contents are relatively high (600-800 $\mu\text{g/g}$) and low (17-43 $\mu\text{g/g}$), respectively (Fig. 4.6). The second zone is volumetrically dominant (>80 vol.%) and corresponds to relatively dark, subhedral to euhedral mantle (Fig. 4.2a,b). No zoning is observed within single grains, but they span a wide range of An contents from An_{39} to An_{62} . With decreasing An, plagioclase Sr and Ba contents decrease from 880 to 500 $\mu\text{g/g}$, and from ~ 100 to ~ 50 $\mu\text{g/g}$, respectively (Fig. 4.6). Finally, the last zone is represented by thin (10-80 μm), discontinuous rims with low BSE intensity which accounts for ~ 15 -20 vol.% of the total plagioclase volume (Fig. 4.2a,b). This zone exhibits a sharp decrease of the Sr (480-390 $\mu\text{g/g}$) and Ba (57-38 $\mu\text{g/g}$) contents with decreasing An (An_{32-36}) (Fig. 4.6) and probably represent the last crystallisation product of the Western Adamello tonalite (Grocolas and Müntener, 2024). Compositional profiles measured across the two first zones reveal a negative correlation of Sr and Ba with the An content, and a vertical correlation at the An content minimum and maximum values (Fig. 4.6a,b). This is typical of diffused profiles in

4. Cooling rates and crystal residence times

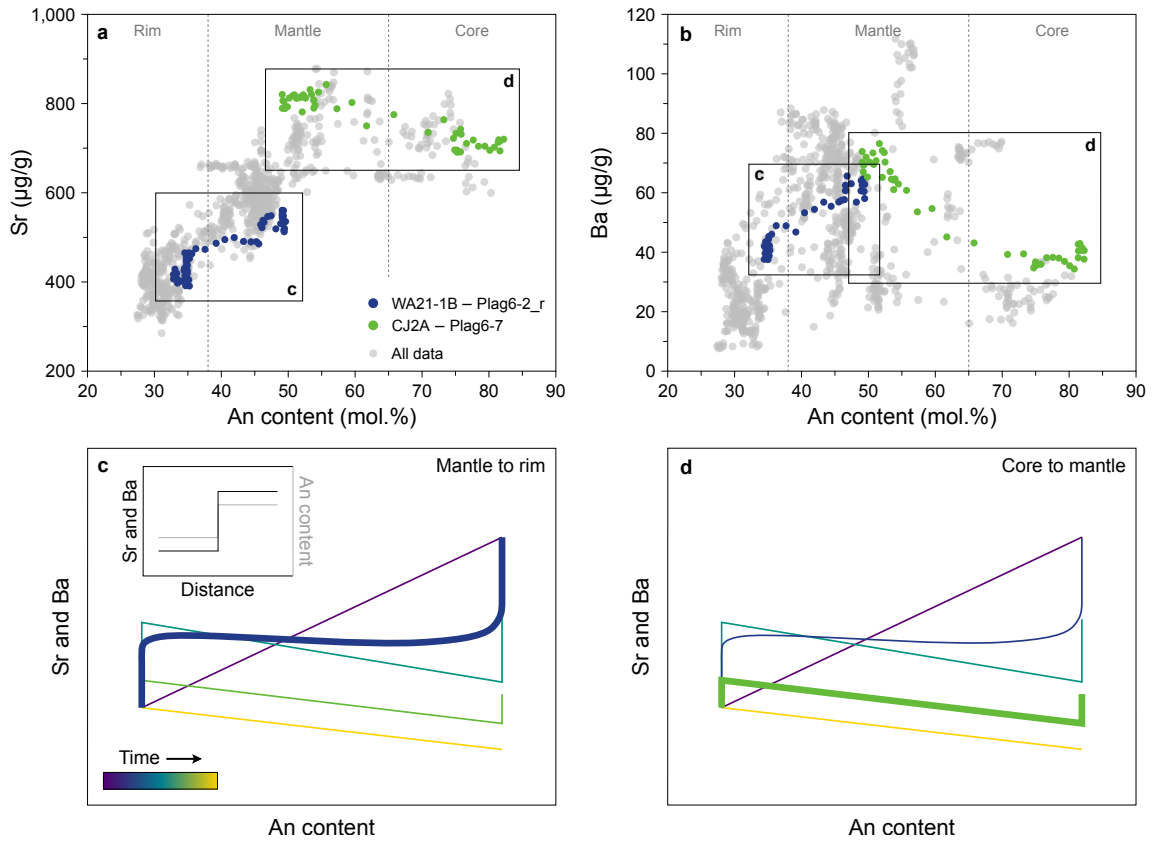


Figure 4.6. Plagioclase compositions and extent of diffusion re-equilibration. **a**, Plagioclase An content (mol.%) vs. Sr ($\mu\text{g/g}$). The grey data points represent all the data measured through LA-ICP-MS line scanning, and the coloured data points highlight two representative examples of a core-to-mantle profile and a mantle-to-rim profile. **b**, Plagioclase An content (mol.%) vs. Ba ($\mu\text{g/g}$). The two highlighted profiles are the same as in (a). **c**, Theoretical Sr- and Ba-in-plagioclase diffusion model for a mantle-to-rim profile plotted as plagioclase An content vs. trace elements. The inset represents the initial conditions for the trace elements and An content as a function of the distance. The diffusion model highlights that the mantle-to-rim profiles only slightly re-equilibrated through diffusion. For these profiles, the initial conditions can be directly inferred from the plagioclase An content. **d**, Theoretical Sr- and Ba-in-plagioclase diffusion model for a core-to-mantle profile plotted as plagioclase An content vs. trace elements. Note the larger extent of diffusion re-equilibration undergone by these profiles. The initial conditions for the inner part of these profiles are determined using the correlation between the plagioclase An content and the trace elements from Grocolas and Müntener (2024).

plagioclase that almost reached complete re-equilibration (Fig. 4.6d). On the other hand, profiles measured across the mantle-rim transition exhibit a vertical correlation at $\sim\text{An}_{50}$, followed by a horizontal transition from $\sim\text{An}_{50}$ to $\sim\text{An}_{35}$, and another vertical trend at $\sim\text{An}_{35}$ (Fig. 4.6a,b). This type of relation between the plagioclase An content and trace elements is also caused by diffusion re-equilibration, albeit for shorter times than profiles from the core-mantle transition (Fig. 4.6c). Interestingly, spot analysis of plagioclase from the Western Adamello, measured in large homogeneous zones, shows a slightly different trend with higher Sr and Ba contents at high An contents, and a more continuous negative

correlation at lower An contents (Grocolas and Müntener, 2024). This either reflects a less significant diffusion imprint or the complete absence of diffusion in this dataset. Therefore, we use the correlation between the plagioclase An content and the trace elements from the data of Grocolas and Müntener (2024) to infer the initial conditions for diffusion modelling of the core-mantle profiles.

Plagioclase from the Laione granodiorite exhibits very similar textures and compositions as plagioclase from the Western Adamello leucotonalite. The three zones are also observed, except that (1) the An-rich (An_{64-89}) cores are fewer than in the Western Adamello, (2) the volumetrically dominant mantles are heterogeneous and systematically present an oscillatory zoning with the An content ranging from An_{39} to An_{65} indicating multiple events of magma recharge, and (3) plagioclase rims are thinner ($<30\ \mu\text{m}$) and can reach lower An contents (An_{21-40}), which could be related to different crystallisation pressure, melt H_2O content, or fractional crystallisation (e.g., Yoder, 1969). In addition, similar relationships between the plagioclase An content and trace elements are observed, where most of the core-mantle profiles completely re-equilibrated, while the mantle-rim profiles only underwent partial re-equilibration. Similar to the Western Adamello, spot analysis data of plagioclase homogeneous zones from the Listino ring complex reveal a horizontal trend at high An contents (Supplementary Material 3) indicating that diffusion did not operate at the same level as the data reported in this study. As such, the correlation between the plagioclase An content and trace elements observed from spot analysis is used to infer the initial conditions of the diffusion modelling.

4.6 Thermometry

In this section, we use calibrated thermometers based on mineral chemistry to assess the temperature conditions at the onset of diffusion for alkali feldspar, quartz and plagioclase. The amphibole chemistry from the Western Adamello tonalite and Listino ring complex reveals that the temperature-dependent edenite exchange controlled their chemical evolution (Supplementary Material 3) (Grocolas and Müntener, 2024). As such, we applied the pressure-dependent amphibole-plagioclase thermometer of Holland and Blundy (1994) to determine the plagioclase crystallisation temperature, whose typical uncertainties associated with the thermometer calibration and *in situ* analyses are $\sim 35-40\ ^\circ\text{C}$. The measurements were done within $<100\ \mu\text{m}$ of the amphibole-plagioclase boundary and encompass a wide range of plagioclase compositions (An_{36-72}). We used the same pressure (250 MPa) as in the Perple-X and Ti-in-quartz thermometer models (Blundy and Sparks, 1992; Floess and Baumgartner, 2015). As the magma was probably undersaturated with respect to

4. Cooling rates and crystal residence times

quartz upon amphibole saturation and crystallisation, we employed the edenite-richterite thermometer. The resulting equilibrium temperatures range from 724 to 865 °C for the Western Adamello, and from 746 to 885 °C for the Listino ring complex (Fig. 4.7a). The calculated temperatures are correlated with the plagioclase An content with a residual error of ~15 °C. As such, we either use (1) the temperature calculated directly from the amphibole-plagioclase touching pairs, or (2) the observed correlation between the calculated temperature and the plagioclase An content when no amphibole was in equilibrium with plagioclase. The uncertainty on the initial temperature for diffusion modelling was kept to 15 °C.

The crystallisation temperature of quartz is inferred by using the temperature dependence of Ti incorporation into the quartz crystal lattice (Huang and Audétat, 2012; Thomas et al., 2010, 2015; Wark and Watson, 2006). To accurately determine the crystallisation temperature of quartz, the TiO_2 activity (a_{TiO_2}) must be constrained. To do so, we model the TiO_2 chemical potential (μ_{TiO_2}) evolution during the differentiation of the Laione granodiorite using Perple_X (Connolly, 2005, 2009) coupled with recently published thermodynamic solution models (Holland et al., 2018) developed to reproduce felsic liquid lines of descent. The calculations successfully reproduce the phase proportions observed in the Laione granodiorite, as well as the modal proportions of hydrous

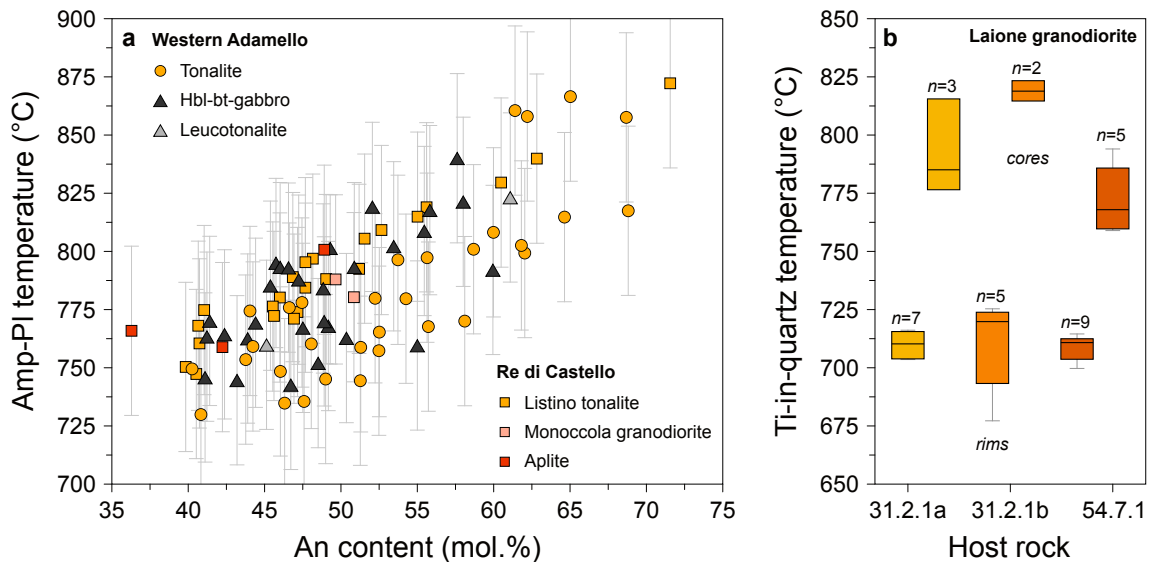


Figure 4.7. Thermometry used to infer the initial temperature of the diffusion modelling. **a**, Amphibole-plagioclase temperatures (°C) vs. plagioclase An content (mol.%) for various lithologies from the Western Adamello and southern Re di Castello. The amphibole-plagioclase temperatures were calculated using the edenite-richterite thermometer of Holland and Blundy (1994) and a pressure of 250 MPa. **b**, Ti-in-quartz temperatures (°C) for the three studied Laione granodiorite samples represented as box-and-whiskers. The calculated temperatures were calculated following Wark and Watson (2006) and were distinguished between Ti-rich cores and Ti-poor rims. *Amp*, amphibole; *Pl*, plagioclase.

crystallisation experiments (Marxer and Ulmer, 2019). The reader is referred to the study of Grocolas and Müntener (2024) for further discussion concerning the model benchmark. To calculate a_{TiO_2} from μ_{TiO_2} , we use Eq. 4.7:

$$a_{\text{TiO}_2} = \exp\left(-\frac{G_{\text{TiO}_2}^{P,T} - \mu_{\text{TiO}_2}^{P,T}}{RT}\right) \quad (4.7)$$

where P is the pressure (Pa), T is the temperature (K), $\mu_{\text{TiO}_2}^{P,T}$ is the chemical potential of rutile (J mol^{-1}), $G_{\text{TiO}_2}^{P,T}$ is the Gibbs free energy of rutile (J), and R is the universal gas constant ($\text{J mol}^{-1} \text{K}^{-1}$). In a first step, a pressure of 250 MPa is assumed based on the different barometry results obtained throughout the Adamello batholith (e.g., Blundy and Sparks, 1992; Floess and Baumgartner, 2015). The Perple_X modelling reveals that, at the onset of quartz crystallisation (~ 715 °C), the calculated melt a_{TiO_2} is 0.57 and decreases to 0.52 with increasing crystallinity. The crystallisation temperatures of the quartz cores and rims are then calculated using the parameterisation of Wark and Watson (2006). Given the uncertainties on the experimental fit and the analytical conditions, the uncertainty of the calculated temperatures ranges from 11 to 14 °C. The calculated temperatures for the quartz bright cores are 797 ± 47 °C (2σ), while the darker rims display lower temperatures (717 ± 36 °C) (Fig. 4.7b). The thermometer of Huang and Audétat (2012) gives the same results within uncertainty. The calculated temperatures for the quartz rims are in good agreement with the temperatures modelled using Perple_X, whereas the temperatures calculated from the core compositions are ~ 80 °C higher. The stability field of quartz is expanded at higher pressure and at lower $f_{\text{H}_2\text{O}}$. However, quartz typically saturates beyond the rheological lock-up where efficient magma transport from higher pressures is hindered. Alternatively, the Laione granodiorite could represent remobilised crystal mushes from the Listino ring complex that are reheated during emplacement of the tonalite of Malga Listino. This thermal event could potentially lower $f_{\text{H}_2\text{O}}$, resulting in extensive quartz crystallisation. Regardless, both methods yield similar crystallisation temperatures for quartz rims and suggest that diffusion re-equilibration of Ti in quartz started at 715 ± 15 °C. Given the textural relationship between the zoned quartz and alkali feldspar oikocrysts, and the absence of robust thermometer to determine alkali feldspar crystallisation conditions, we assume that diffusion in alkali feldspar started operating at 710 ± 15 °C.

4.7 Diffusion calculations

In this section, we model diffusion in quartz, alkali feldspar and plagioclase to extract cooling rates and crystal-melt segregation timescales. This is done by using (1) the initial concentrations inferred from the measured, diffused profiles for quartz and alkali feldspar, and the correlation between the An content and trace elements observed from spot analysis for plagioclase, and (2) the initial temperatures calculated using the Ti concentration in quartz and the equilibrium between amphibole and plagioclase touching pairs.

4.7.1 Cooling rates

Laione granodiorite

Quartz and alkali feldspar represent the final crystallising phases of metaluminous and peraluminous intermediate to felsic melts (e.g., [Johnson and Rutherford, 1989](#)). Textural relationships and phase proportions suggest that quartz Ti-poor rims and alkali feldspar Ba-poor zones from the Laione granodiorite probably crystallised at a melt fraction comprised between 15 and 30 vol.%, before the interstitial melt reached a haplogranitic composition. However, given the high number of inclusions within alkali feldspar and the high nucleation-to-growth ratio of quartz from the Laione granodiorite, it is unlikely that these crystal rims experienced prolonged residence time at suprasolidus temperatures. As such, we model the diffused profiles of Ti in quartz and Ba in alkali feldspar by lowering the temperature exponentially with time to infer the cooling rate of the Laione granodiorite. This is done using the diffusion coefficients of [Cherniak et al. \(2007\)](#), [Jollands et al. \(2020\)](#) and [Audétat et al. \(2021, 2023\)](#) for Ti-in-quartz diffusion, and [Cherniak \(2002\)](#) for the diffusion of Ba in alkali feldspar.

The two different initial conditions used to model diffusion in alkali feldspar (Fig. [4.8a](#)) and quartz (Fig. [4.9a](#)) yield very close cooling rates with a temperature difference of <20 °C after 1 Myr of diffusion (Figs. [4.8](#) and [4.9](#)). As such, only the initial conditions using a step-function profile will be further used and discussed for clarity. The diffusion of Ba in alkali feldspar results in relatively slow cooling rates with ~0.7-10 Myr needed to cool by 100 °C, with no clear distinction between samples from the Listino ring and the Blumone complexes (Fig. [4.8](#)). These calculated cooling rates are slower than the cooling rates inferred from ³⁹Ar/⁴⁰Ar mineral ages of the Re di Castello superunit ([Schaltegger et al., 2019](#)) by a factor of 2 to 10.

The cooling rates obtained from diffusion of Ti in quartz span ~3.5 orders of magnitude as a function of the diffusion coefficients used for modelling (Fig. [4.9](#)). No clear difference

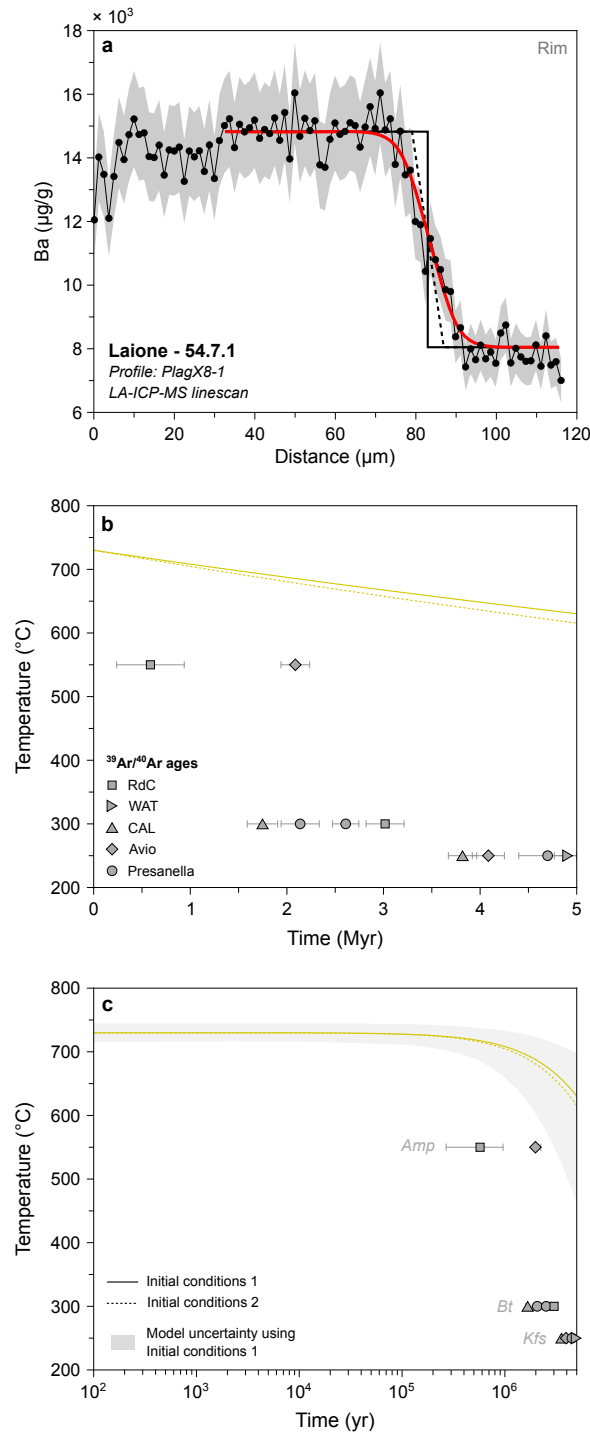


Figure 4.8. Results of Ba-in-alkali-feldspar diffusion modelling used to infer cooling rates. **a**, Ba (µg/g) vs. distance (µm). The black dotted line and continuous line represent the two initial conditions tested in the model, and the red line corresponds to the best fit to the data (black). **b**, Temperature (°C) evolution through time (Myr) associated with the best fits using the two different initial conditions. The ³⁹Ar/⁴⁰Ar ages obtained on amphibole, biotite and K-feldspar, which have different closure temperatures, are represented for comparison (Schaltegger et al., 2019). **c**, Temperature (°C) evolution through time (yr) in logarithmic scale. The grey zones represent the uncertainty envelopes modelled using a Monte Carlo scheme. *Amp*, amphibole; *Bt*, biotite; *Kfs*, K-feldspar.

4. Cooling rates and crystal residence times

is observed between the Laione granodiorite sampled in the Listino ring complex and samples from the Blumone complex. The time required for quartz crystals to cool by 100 °C is ~ 0.5 -2.5 kyr using the diffusion coefficients of Cherniak et al. (2007), ~ 26 -130 kyr using Audétat et al. (2023), ~ 0.8 -4.1 Myr using Jollands et al. (2020), and ~ 1.8 -9.0 Myr using Audétat et al. (2021) (Fig. 4.9). The cooling rates obtained using the diffusion coefficients of Audétat et al. (2021, 2023) and Jollands et al. (2020) are comprised within one order of magnitude of the $^{39}\text{Ar}/^{40}\text{Ar}$ cooling rates (Fig. 4.9b-d). On the other hand, the diffusivities of Cherniak et al. (2007) yield cooling rates >2 orders of magnitude faster than the $^{39}\text{Ar}/^{40}\text{Ar}$ data.

Such fast cooling rates are unrealistic for kilometre-scale magmatic systems which usu-

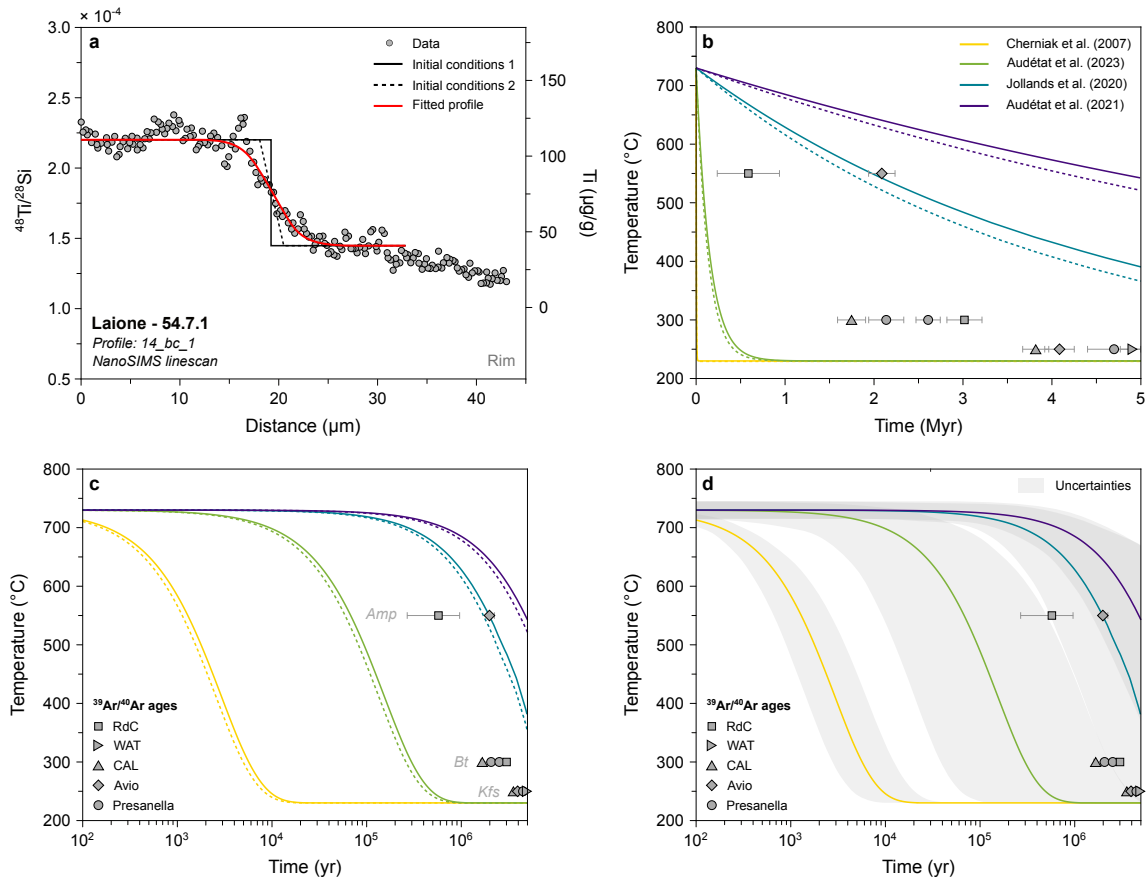


Figure 4.9. Results of Ti-in-quartz diffusion modelling used to infer cooling rates. **a**, $^{48}\text{Ti}/^{28}\text{Si}$ and Ti ($\mu\text{g/g}$) vs. distance (μm). The black dotted line and continuous line represent the two initial conditions tested in the model, and the red line corresponds to the best fit to the data (grey). **b**, Temperature ($^{\circ}\text{C}$) evolution through time (Myr) associated with the best fits using the two different initial conditions. The $^{39}\text{Ar}/^{40}\text{Ar}$ ages obtained on amphibole, biotite and K-feldspar, which have different closure temperatures, are represented for comparison (Schaltegger et al., 2019). **c**, Temperature ($^{\circ}\text{C}$) evolution through time (yr) in logarithmic scale, with the best fits using the two different initial conditions represented. **d**, Same figure as **c**, but with the grey zones representing the uncertainty envelopes modelled using a Monte Carlo scheme. *Amp*, amphibole; *Bt*, biotite; *Kfs*, K-feldspar.

ally have cooling rates ranging from ~ 20 to ~ 200 $^{\circ}\text{C Myr}^{-1}$ (e.g., [Annen et al., 2006](#); [Floess and Baumgartner, 2015](#); [Long et al., 2005](#); [Spears and Parrish, 1996](#)). As such, we do not further consider the results obtained from the diffusion models using data from [Cherniak et al. \(2007\)](#). Furthermore, the modelled time-temperature paths using Ba diffusion in alkali feldspar are similar to the Ti-in-quartz cooling rates calculated using the diffusivities of [Audézat et al. \(2021\)](#) and [Jollands et al. \(2020\)](#). By considering the uncertainties associated with each modelled time-temperature path, the cooling rates modelled using diffusion in alkali feldspar are all comprised within the quartz cooling rates calculated using the diffusion coefficients of [Jollands et al. \(2020\)](#). As such, we only consider the quartz models based on the experiments of [Jollands et al. \(2020\)](#) for simplicity, although we recognise that the models using the diffusivities of [Audézat et al. \(2021\)](#) yield similar results within error.

Western Adamello

Low-An ($\sim \text{An}_{30}$) plagioclase from the Western Adamello crystallised in equilibrium with quartz and alkali feldspar and is part of the final crystal assemblage of the tonalitic melt ([Grocolas and Müntener, 2024](#)). As such, we model the observed profiles of Sr and Ba in plagioclase and retrieve cooling rates associated with each profile. We employ the diffusion coefficients of [Giletti and Casserly \(1994\)](#), [Cherniak and Watson \(1992, 1994\)](#) and [Grocolas et al. \(in review\)](#) for diffusion of Sr, and [Cherniak \(2002\)](#) and [Grocolas et al. \(in review\)](#) for diffusion of Ba in plagioclase. As mentioned above, the measured mantle-rim profiles are far from quasi-steady state and, therefore, cooling rates can be calculated.

The diffusion of Sr and Ba in plagioclase from the Western Adamello results in cooling rates spanning ~ 2 - 3 orders of magnitude as a function of the diffusion coefficients used for modelling (Fig. 4.10). The time required for plagioclase crystals to cool by 100 $^{\circ}\text{C}$ is ~ 27 - 870 yr using the diffusion coefficients of [Giletti and Casserly \(1994\)](#), ~ 0.3 - 9.1 kyr using [Cherniak and Watson \(1992, 1994\)](#), and ~ 0.04 - 1.4 Myr using [Grocolas et al. \(in review\)](#) and [Cherniak \(2002\)](#). Unlike the data from the Laione granodiorite, cooling rates obtained from Sr and Ba diffusion modelling in plagioclase using the diffusivities of [Grocolas et al. \(in review\)](#) and [Cherniak \(2002\)](#) overlap with the cooling rates of the Western Adamello tonalite inferred from $^{39}\text{Ar}/^{40}\text{Ar}$ mineral ages (Fig. 4.10b-d).

The cooling rates calculated using the Sr diffusion coefficients of [Giletti and Casserly \(1994\)](#) and [Cherniak and Watson \(1992, 1994\)](#) are unreasonably fast for large granitoid bodies. Additionally, as discussed in [Grocolas et al. \(in review\)](#), the presence of Ba-feldspar in the source powder of the diffusion experiments of [Cherniak \(2002\)](#) probably resulted

4. Cooling rates and crystal residence times

in coupled diffusion, whereas the experiments of [Cherniak and Watson \(1992, 1994\)](#) most likely record the reaction rate of Sr oxide with plagioclase. Similarly, the precipitation of pure Sr at the surface of the plagioclase crystal in the experiments of [Giletti and Casserly \(1994\)](#) probably led to significant degradation of the diffusion interface. As such, we only consider the results of diffusion modelling using the plagioclase diffusivities of [Grocolas et al. \(in review\)](#) and [Cherniak \(2002\)](#).

Critical assumptions are associated with the employed initial conditions prior to diffusion, and the initial concentrations profiles are close to the measured mantle-rim plagioclase profiles. To evaluate the robustness of the inferred cooling rates, a numerical model

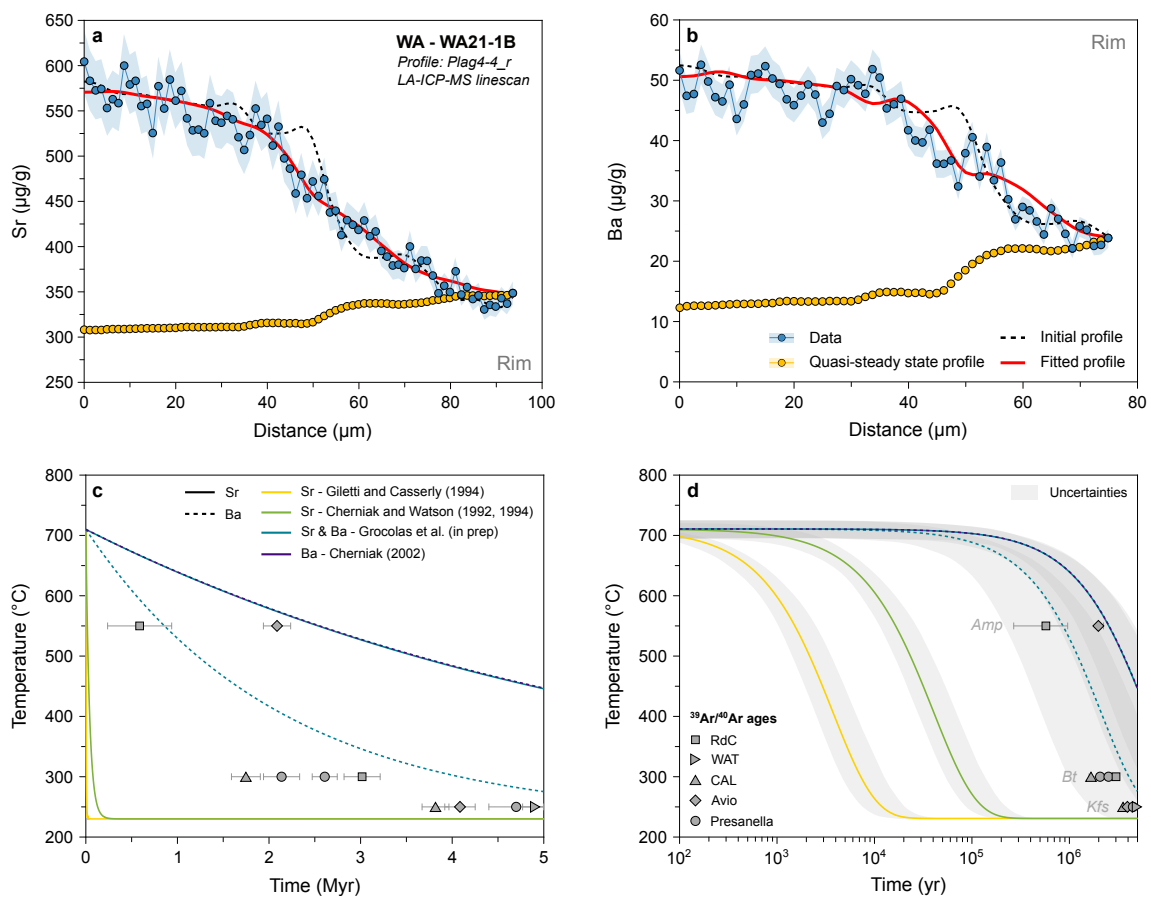


Figure 4.10. Results of Sr- and Ba-in-plagioclase diffusion modelling used to infer cooling rates. **a**, Sr ($\mu\text{g/g}$) vs. distance (μm). The black dotted line represents the initial conditions, the red line corresponds to the best fit to the data (blue), and the yellow data points are for the calculated quasi-steady state profile. **b**, Ba ($\mu\text{g/g}$) vs. distance (μm). **c**, Temperature ($^{\circ}\text{C}$) evolution through time (Myr) associated with the best fits using different diffusion coefficients for Sr and Ba diffusion in plagioclase ([Cherniak and Watson, 1992, 1994](#); [Cherniak, 2002](#); [Giletti and Casserly, 1994](#); [Grocolas et al., in review](#)). The $^{39}\text{Ar}/^{40}\text{Ar}$ ages obtained on amphibole, biotite and K-feldspar, which have different closure temperatures, are represented for comparison ([Schaltegger et al., 2019](#)). **d**, Temperature ($^{\circ}\text{C}$) evolution through time (yr) in logarithmic scale. The grey zones represent the uncertainty envelopes modelled using a Monte Carlo scheme. *Amp*, amphibole; *Bt*, biotite; *Kfs*, K-feldspar.

reproducing the thermal evolution of the Western Adamello tonalite was developed. Based on the results of Floess and Baumgartner (2015), the magma reservoir was constructed as the horizontal stacking of vertical, 20-m-thick dikes with a flow time of 70 yr and no-flow time of 3,000 yr, which corresponds to a magma flux of $2 \times 10^{-4} \text{ km}^3 \text{ yr}^{-1}$. The temperature evolution was calculated by numerically solving the heat equation using the explicit finite-difference method, and is representative of a point located 3 km away from the southwestern contact. For further explanations regarding the method, the reader is referred to Supplementary Material 3. The developed model overlaps with the cooling rates calculated using plagioclase diffusion (Fig. 4.11). The observed temperature-time slope slightly differs from the diffusion cooling rate, which is probably due to the exponential temperature decrease that was imposed during diffusion modelling. Regardless, this indicates that diffusion of Sr and Ba in plagioclase mantle-rim operated continuously and recorded the cooling of the pluton.

Discussion

The retrieved cooling rates for the Laione granodiorite, both from the Listino ring and Blumone complexes, are systematically slower than those from the Western Adamello, and slower than those inferred from $^{39}\text{Ar}/^{40}\text{Ar}$ mineral ages (Fig. 4.11). However, the samples from the Re di Castello superunit used for $^{39}\text{Ar}/^{40}\text{Ar}$ dating were collected in the northern Re di Castello, 8 and 15 km away from the Laione granodiorite samples. Cooling rate is primarily a function of the average magma flux (e.g., de Saint Blanquat et al., 2011; de Silva and Gosnold, 2007; Glazner et al., 2004) and, therefore, can vary within a batholith if the magma flux changes over time. The Western Adamello covers an area of $\sim 105 \text{ km}^2$ and, by assuming that the $\sim 3 \text{ km}$ of vertical relief represents the reservoir thickness, a volume of $\sim 315 \text{ km}^3$. Floess (2013) demonstrated via high-precision U-Pb zircon dating that the Western Adamello tonalite emplaced incrementally over a time period of $\sim 1.2 \text{ Myr}$. The resulting average magma flux is $\sim 2.5 \times 10^{-4} \text{ km}^3 \text{ yr}^{-1}$ for the Western Adamello. Similar calculations can be done for the Listino ring (Verberne, 2013) and Blumone (Schoene et al., 2012) complexes, and both resulted in an average magma flux of $\sim 1.3 \times 10^{-4} \text{ km}^3 \text{ yr}^{-1}$. Given the uncertainties on the volumes, these rates can be considered similar, which is unexpected in order to reconcile the differences in cooling rates experienced by the Western Adamello leucotonalite and Laione granodiorite. This difference in cooling rate can either arise from (1) the parameters describing Ba diffusion in alkali feldspar, or (2) the emplacement mechanism of these two units.

The experiments of Cherniak (2002) yielded an activation energy of 455 kJ mol^{-1} for Ba

4. Cooling rates and crystal residence times

diffusion in sanidine, which is higher than the ones inferred for Ba diffusion in plagioclase (303-377 kJ mol⁻¹) (Cherniak, 2002; Grocolas et al., in review). Such a large difference is unexpected given the very similar crystal structure of the sanidine crystals used by Cherniak (2002) with the oligoclase crystals used by Cherniak (2002) and Grocolas et al. (in review). This observation probably rules out the difference in the crystal structure between sanidine and oligoclase as the main control of activation energy for diffusion. Using a lower activation energy would yield faster diffusion coefficients at low temperatures and, therefore, faster cooling rates. This would bring the calculated cooling rates for the Laione granodiorite closer to the ones obtained for the Western Adamello leucotonalite, and reconcile the modelled cooling rates with the calculated magma fluxes.

The second possible explanation might be related to the different emplacement mechanisms of the Western Adamello and southern Re di Castello, possibly leading to different cooling rates for similar magma fluxes. The Western Adamello tonalite was emplaced incrementally from South to North by repeated intrusions of ~10-m-thick vertical dikes over a time period of ~1.2 Myr (Floess, 2013; Floess and Baumgartner, 2015). This is based on the tonalite vertical foliation in the southernmost part of the Western Adamello, and modelling of the thermal budget leading to the observed metamorphic assemblage in the contact aureole. On the other hand, the magmatic foliation parallel to the circular structure of the Listino ring and Blumone complexes and the progressive younging towards the centre of the structure are commonly attributed to a ballooning emplacement

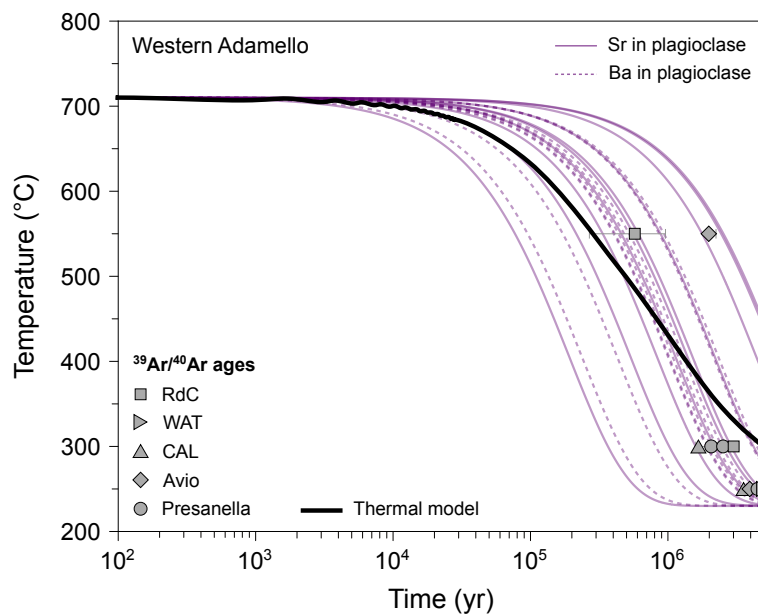


Figure 4.11. Compilation of the cooling rates obtained from Sr- and Ba-in-plagioclase diffusion modelling on crystals from Western Adamello leucotonalites compared to cooling rates inferred from thermal modelling and mineral ³⁹Ar/⁴⁰Ar ages (Schaltegger et al., 2019).

mechanism (John and Blundy, 1993; Schoene et al., 2012; Verberne, 2013). In the ballooning model, magma batches are injected into the upper crust and radially expand, leading to magmatic foliation parallel to the concentric structure slowly disappearing toward the centre of the pluton (Bateman, 1985; John and Blundy, 1993; Paterson and Vernon, 1995). These contrasting emplacement symmetries have different cooling regimes. Indeed, Caricchi et al. (2014b) modelled the thermal evolution of magma reservoirs with ballooning and vertical emplacement mechanisms and, by comparing the thermal structures after 100 kyr, they concluded that (1) a concentric growth like the southern Re di Castello leads to an isotropic heat redistribution, whereas (2) plutons emplaced by stacking of vertical dikes like the Western Adamello tonalite exhibit an ellipsoidal thermal structure with faster cooling rates in the horizontal direction. As such, the difference in calculated cooling rates between the Western Adamello and the Lago della Vacca complex might be related to the different emplacement mechanisms, although the unexpected high activation energy for diffusion of Ba in alkali feldspar (Cherniak, 2002) may also lead to slightly faster cooling rates.

4.7.2 Residence times

Xenocrysts and antecrysts are commonly found in plutonic and volcanic rocks and are indicative of open, dynamic systems. The plagioclase cores having high-An (An_{70-90}) compositions as well as resorption surfaces found in the Western Adamello leucotonalite have been previously interpreted as antecrysts sampled in deeper parts of the crust during magma ascent (Grocolas and Müntener, 2024). Similar observations and conclusions can be done for the high-An plagioclase cores occurring in the Laione granodiorite. As such, the diffusion re-equilibration between the plagioclase cores ($\sim An_{70-90}$) and mantles ($\sim An_{40-65}$) can be used to infer the plagioclase mantle residence time within the tonalitic and granodioritic mushes before the onset of cooling (Fig. 4.12). Given the usually sharp contact between the host tonalite and the lithologies resulting from crystal-melt segregation, these residence times can be interpreted as the maximum time plagioclase crystals remained in the tonalitic mush before crystal-melt segregation and subsequent cooling.

Diffusion modelling of Sr and Ba in plagioclase core to mantle yielded timescales ranging from 13_{-11}^{+27} to 132_{-80}^{+140} kyr for the Western Adamello leucotonalite, and 36_{-21}^{+37} to 63_{-53}^{+121} kyr for the Laione granodiorite using the diffusion coefficients of Grocolas et al. (in review) (Fig. 4.13). In detail, modelling of Sr and Ba in plagioclase yields the same timescales within uncertainty, with a difference ranging from 2 to 53 %. Interestingly, the lowest initial temperatures coincide with the rheological lock-up temperature (Marxer and Ul-

4. Cooling rates and crystal residence times

mer, 2019) and correspond to the shortest calculated timescales (<20 kyr) (Fig. 4.13). The other calculated times between plagioclase mantle crystallisation and the rheological lock-up range from ~ 40 to ~ 110 kyr. Within this time interval, the calculated cooling rates vary from ~ 300 to $\sim 1,000$ $^{\circ}\text{C Myr}^{-1}$ based on the minimum and maximum values of initial temperature and residence time. The calculated residence times above the rheological lock-up ($\sim 10^4$ - 10^5 yr) are comparable to the thermal model developed in this study (Supplementary Material 3) and those from previous studies (e.g., Annen et al., 2006; Caricchi et al., 2014a). These models highlight that the long-term ($>10^5$ yr) thermal evolution of magma reservoirs is a first-order function of the time-averaged rate of magma input. For relatively high magma fluxes ($\sim 10^{-2}$ $\text{km}^3 \text{yr}^{-1}$), thermal models predict that eruptible magma (i.e., above the rheological lock-up) continuously accumulates within the magma reservoir, whereas for lower magma input such as in the Adamello batholith

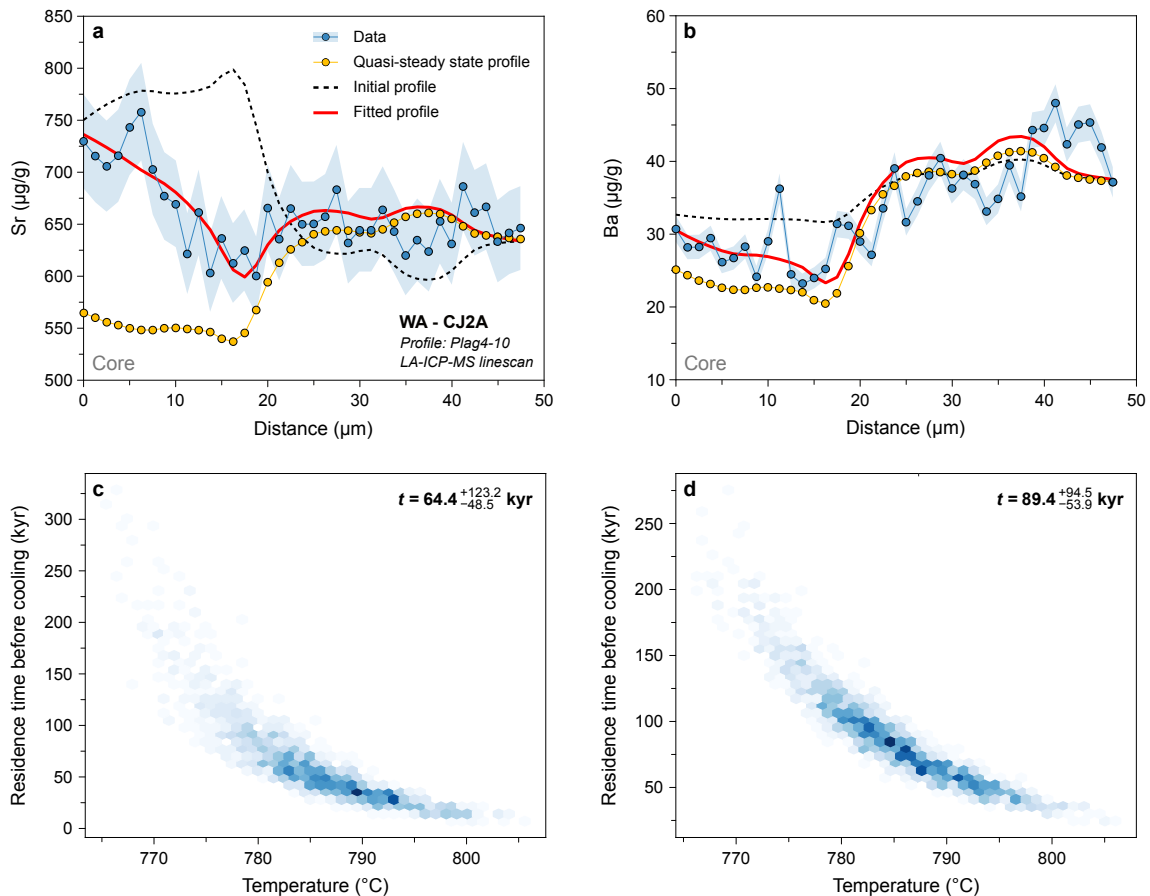


Figure 4.12. Results of Sr- and Ba-in-plagioclase diffusion modelling used to infer crystal-melt segregation timescales. **a**, Sr ($\mu\text{g/g}$) vs. distance (μm). The black dotted line represents the initial conditions, the red line corresponds to the best fit to the data (blue), and the yellow data points are for the calculated quasi-steady state profile. **b**, Ba ($\mu\text{g/g}$) vs. distance (μm). **c**, **d**, Results of the Monte Carlo simulation for Sr and Ba diffusion, respectively, represented as temperature ($^{\circ}\text{C}$) vs. time (kyr). See main text for explanations regarding diffusion modelling and Monte Carlo resampling.

($\sim 10^{-4} \text{ km}^3 \text{ yr}^{-1}$), eruptible magma is only sporadically present for time periods of $\leq 10^5$ yr (Annen, 2009; Caricchi et al., 2021). In addition, Karakas et al. (2017) demonstrated that in transcrustal magmatic systems, the development of extensive lower crustal mush zones modifies the thermal budget of the upper crust. The required magma fluxes to sustain shallow magma reservoirs is therefore reduced, allowing systems like the Adamello batholith to store mobile magma for tens of thousands of years.

4.8 Comparison with volcanic timescales

In this section, we compare diffusion timescales obtained in (1) well-studied volcanic rocks using different diffusivities, (2) with magma chamber lifespans as determined by high-precision zircon U-Pb dating, and (3) with the crystal-melt segregation timescales obtained in the Adamello batholith.

4.8.1 Which diffusion coefficients?

Explosive rhyolitic eruptions from caldera-forming systems have been widely studied, owing to their influence on populations and climate. Diffusion chronometry has the potential to record timescales associated with magmatic system assembly, pre-eruptive magma recharge, and magma ascent, while high-precision zircon U-Pb chronology tracks the mag-

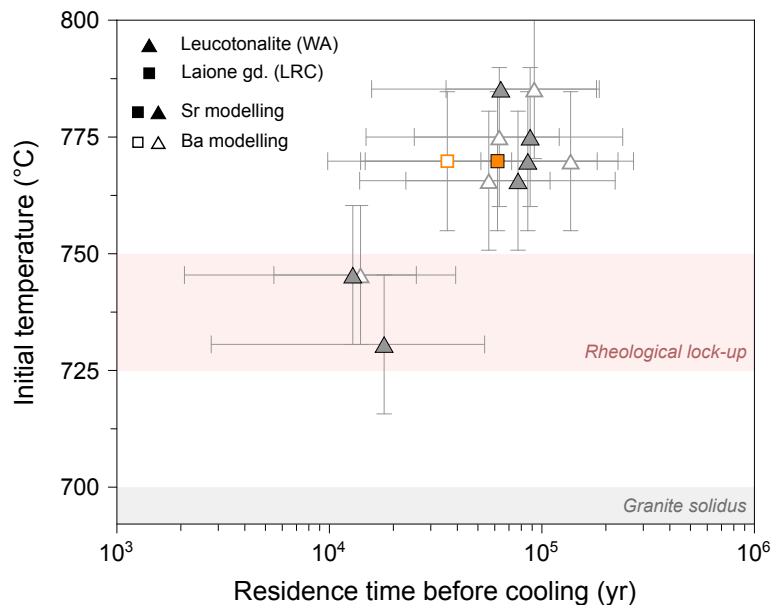


Figure 4.13. Compilation of the crystal-melt segregation timescales obtained by diffusion modelling of Sr and Ba in plagioclase from the Western Adamello leucotonalite and Laione granodiorite represented as initial temperature ($^{\circ}\text{C}$) vs. residence time before cooling (yr). The rheological lock-up for a tonalitic starting material (Marxer and Ulmer, 2019) and the granite solidus (Johannes and Holtz, 2012) are represented for comparison.

4. Cooling rates and crystal residence times

matic system assembly and differentiation (e.g., [Bachmann and Huber, 2016](#)). Numerous studies focused on reversely zoned crystal rims, typically in sanidine and pyroxenes, and reported timescales that range from 10^1 to 10^2 years, most likely representing the timespan between rejuvenation and eruption (e.g., [Chamberlain et al., 2014a](#); [Cooper and Kent, 2014](#); [Saunders et al., 2012](#); [Till et al., 2015](#)). On the other hand, timescales inferred from diffusion in crystal core and/or mantle are much longer (10^4 - 10^6 yr) (Fig. 4.14), similar to magma reservoir lifespans obtained from high-precision zircon U-Pb dating (e.g., [Chambers et al., 2020](#); [Rout and Wörner, 2018](#); [Rout et al., 2021](#); [Schoene et al., 2012](#); [Szymanowski et al., 2017](#)).

The usual correlation between quartz Ti concentrations and CL greyscale intensities

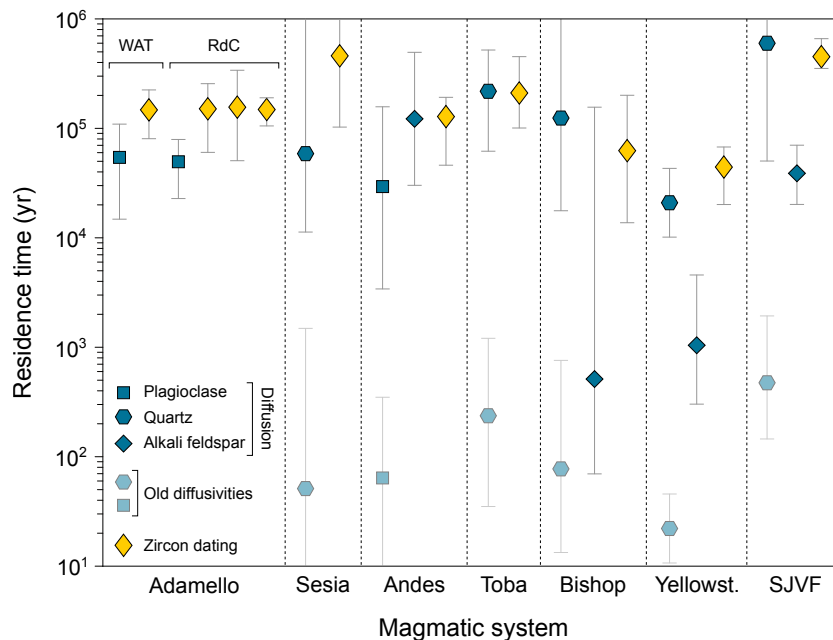


Figure 4.14. Compilation of crystal residence time prior to eruption (or cooling) obtained for different silicic volcanoes worldwide through diffusion modelling, or high-precision U-Pb zircon dating, and comparison with the timescales obtained in this study. Symbols represent different minerals, colours represent the technique employed to infer timescales, and the symbol is positioned at the average value. Ti-in-quartz and Sr-in-plagioclase timescales were recalculated using the diffusion coefficients of [Jollands et al. \(2020\)](#) and [Grocolas et al. \(in review\)](#), respectively. The reader is referred to the main text for a more extensive discussion. Residence times inferred from diffusion in quartz, plagioclase and alkali feldspar generally span 10^4 to 10^6 yr, similar to the zircon crystallisation timespan. Shorter timescales are systematically associated with analysis the crystal rims and instead represent mixing-to-eruption timescales. Magmatic systems used in this compilation include: Adamello batholith (this study [Broderick et al., 2015](#); [Floess, 2013](#); [Schoene et al., 2012](#); [Verberne, 2013](#)); Sesia magmatic system ([Karakas et al., 2019](#); [Tavazzani et al., 2020, 2023](#)); Cerro Galán caldera ([Lubbers et al., 2022](#)), Risco Bayo-Huemul plutonic complex ([Schaen et al., 2021](#)), and Taápaca volcano ([Rout et al., 2021](#)), Andes; Younger Toba Tuff ([Reid and Vazquez, 2017](#); [Szymanowski et al., 2023](#); [Wang et al., 2023](#)); Bishop Tuff ([Chamberlain et al., 2014b,a](#); [Gualda et al., 2012](#)); Yellowstone (Yellowst.) caldera ([Shamloo and Till, 2019](#); [Till et al., 2015](#); [Wotzlaw et al., 2014](#)); San Juan Volcanic Field (SJVF) ([Brückel et al., 2023](#); [Schmitz and Bowring, 2001](#)).

largely contributed to broaden the use of Ti diffusion re-equilibration in quartz to retrieve timescales of magmatic processes. However, recent advances showed that Ti diffusion rates in quartz might be slower by ~ 2 -3 orders of magnitude than previously thought (Audétat et al., 2021, 2023; Cherniak et al., 2007; Jollands et al., 2020). Likewise, Grocolas et al. (in review) demonstrated that Sr and Ba diffusion in plagioclase operated at comparable rates, ~ 2 -3 orders of magnitude slower than previously determined by Gilletti and Casserly (1994) and Cherniak and Watson (1992, 1994) for Sr, and similar to the Ba diffusion rates defined by Cherniak (2002). In the following, we reiterate our comparisons of the different diffusion coefficients by compiling well-studied caldera-forming eruptions for which the location of the measured profiles is clearly documented. All the compiled profiles were located in the crystal core and/or mantle except the Ba- and Mg-in-sanidine profiles reported for the Bishop Tuff (Chamberlain et al., 2014a) and Yellowstone caldera (Till et al., 2015). In these cases, the modelled timescales most likely represent the timespan between rejuvenation and eruption and, therefore, are unsurprisingly fast ($\sim 10^3$ yr). This contrasts with the core-to-rim Ba profiles measured in sanidine from the Laacher See (Germany) and Taápaca (Chile) volcanoes that yielded timescales on the order of 10^4 - 10^5 yr (Fig. 4.14), which instead represent crystal residence times prior to eruption (Rout and Wörner, 2018; Rout et al., 2021).

Measured Ti-in-quartz profiles from the compiled dataset usually display reverse zoning and are located in the mantle part of millimetre-sized quartz phenocrysts (e.g., Brückel et al., 2023; Shamloo and Till, 2019; Tavazzani et al., 2020; Wang et al., 2023), except for the Bishop Tuff where the profiles represent the outermost ~ 100 - 200 μm of the crystals (Chamberlain et al., 2014a). Modelled Ti-in-quartz profiles yield timescales ranging from $\sim 10^2$ yr by using the diffusivities of Cherniak et al. (2007), to $\sim 10^5$ yr by employing diffusion coefficients from Jollands et al. (2020) and Audétat et al. (2021) (Fig. 4.14). In addition to the profiles being located in the crystal mantle, another argument favouring the slower diffusivities lies in the time necessary to grow these quartz phenocrysts. Quartz growth rates determined both on natural samples and experimentally are comprised between 10^{-15} and 10^{-17} m s^{-1} (Acosta et al., 2020; Bindeman, 2003; Christensen and DePaolo, 1993), which results in a required time to grow a 300 - μm quartz rim of 10^4 - 10^6 yr. The calculated quartz growth times are 2 to 4 orders of magnitude longer than the diffusion times calculated with the faster diffusion coefficients of Cherniak et al. (2007), which are therefore precluded for further discussion.

Modelling of diffusion in plagioclase has been more limited, probably owing to its relation to the plagioclase major element composition and partitioning usually leading to

4. Cooling rates and crystal residence times

larger uncertainties in defining initial conditions (e.g., [Dohmen et al., 2017](#)). Nevertheless, some studies attempted to infer mixing-to-eruption and/or crystal residence times using Mg and Sr diffusion in plagioclase from Santorini ([Druitt et al., 2012](#)) and the Cerro Galán ignimbrite ([Lubbers et al., 2022](#)). In these studies, compositional profiles were measured in normally- or oscillatory-zoned plagioclase crystals either from crystal core to mantle, across the mantle, or from mantle to rim. No clear feature related to pre-eruptive magma recharge (e.g., reverse zoning at the rim) was documented. They report timescales in the range of 10^1 - 10^2 yr using the diffusion coefficients of [Giletti and Casserly \(1994\)](#), with surprisingly no clear difference between profiles measured in the crystal cores and in the rims. On the other hand, recalculated diffusion timescales using the Sr and Ba diffusion coefficients of [Grocolas et al. \(in review\)](#) are 3 orders of magnitude longer (10^4 - 10^5 yr), overlapping with the crystal residence times inferred from Ba diffusion in sanidine from Taápaca volcano (Fig. 4.14) ([Rout et al., 2021](#)). Although there is no available experiment constraining plagioclase growth rate that thoroughly evaluates the attainment of equilibrium, several studies have demonstrated that feldspars grew at a similar rate as quartz (e.g., [Swanson, 1977](#)). Therefore, the diffusion timescales calculated using the fast diffusivities are ~ 2 orders of magnitude shorter than the time required to grow a 300- μm -large plagioclase crystal. For these reasons, only the diffusion timescales using the Sr and Ba diffusivities of [Grocolas et al. \(in review\)](#) will be discussed further. Altogether, this suggests that the timescales obtained from diffusion in feldspar and quartz represent crystal residence time rather than mixing-to-eruption time, except for profiles measured in the outermost part of crystal rims.

4.8.2 Similarity with zircon timescales

High-precision chemical abrasion–isotopic dilution–thermal ionisation mass spectrometry (CA-ID-TIMS) dating is typically associated with uncertainties of ~ 20 kyr and therefore represents the ideal analytical technique to resolve magmatic processes operating over timescales of 10^4 - 10^6 yr (e.g., [Schaltegger et al., 2009](#)). Moreover, dating of young (< 1 Ma) zircons using conventional *in situ* techniques (e.g., LA-ICP-MS, SIMS) also yields ages with reasonable uncertainties (< 50 kyr) (e.g., [Chamberlain et al., 2014b](#)). We compiled high-precision U-Pb zircon ages for the same magmatic systems, and compare it with the crystal residence times inferred from diffusion modelling (Fig. 4.14). The crystal residence time before cooling in the Adamello batholith, interpreted as crystal-melt segregation timescales, ranges from $\sim 10^4$ to $\sim 10^5$ yr, while zircon records crystallisation timescales of $\sim 10^5$ yr ([Broderick et al., 2015](#); [Floess, 2013](#); [Schaltegger et al., 2009](#); [Schoene et al., 2012](#);

Verberne, 2013). Similar conclusions can be drawn from large-volume, caldera-forming rhyolitic eruptions, where diffusion timescales are usually similar to zircon crystallisation timespan, except for Ba- and Mg-in-sanidine diffusion timescales reported for the Bishop Tuff and Yellowstone that instead represent the time between rejuvenation and eruption (Chamberlain et al., 2014a; Till et al., 2015).

However, the zircon age distribution produced in magma reservoir and measured via CA-ID-TIMS is a function of the zircon saturation temperature and the reservoir cooling rate to the solidus, potentially leading to different interpretations between magmatic systems. If zircon saturation is reached at the emplacement depth, these grains are called “autocrysts” and their age distribution documents the magma reservoir lifespan. On the other hand, magmas emplaced at temperatures below the zircon saturation temperature may carry zircon crystals from lower parts of the crust genetically related (“antecrysts”) or unrelated (“xenocrysts”) to the parental magmas (Miller et al., 2007). This second end-member typically results in a zircon crystallisation history longer than the upper crustal magma body. In the Adamello batholith, a zircon saturation temperature of ~ 800 °C has been experimentally determined for a tonalite with ~ 61 wt.% SiO₂ (Marxer and Ulmer, 2019), which is consistent with the calculated Ti-in-zircon temperatures ranging from 660 to 810 °C in the Western Adamello (Supplementary Material 3). This is below the emplacement temperature of ~ 900 °C for the Western Adamello tonalite (Floess and Baumgartner, 2015; Grocolas and Müntener, 2024). Hence, zircons from the Western Adamello are autocrysts and their crystallisation ages most likely represent the duration between zircon saturation (~ 800 °C) and the solidus (~ 680 °C). The higher zircon saturation temperatures compared to the initial temperatures used for diffusion modelling (≤ 780 °C) might bridge the gap between the slightly different timescales using both methods.

Constraining the emplacement mechanism and temperature of parental magmas associated with volcanic eruptions is challenged by the rare exposure of their plutonic roots. As such, a rigorous comparison of zircon saturation temperatures with emplacement temperatures remains elusive, which prevents determination of the timing of zircon saturation. The zircon age spreads obtained via high-precision CA-ID-TIMS dating are therefore considered as maximum residence times since there is no robust method to differentiate antecrysts or xenocrysts from autocrysts. These maximum zircon residence times before eruption are similar within uncertainty to the diffusion timescales, but some exhibit higher values than those derived from diffusion modelling. This small difference may arise from the higher zircon saturation temperatures compared to the initial temperatures used in diffusion modelling. Regardless, these similar timescales demonstrate the ability of pla-

4. Cooling rates and crystal residence times

gioclase, quartz and alkali feldspar to record residence times prior to melt segregation and extraction. In addition, previous studies showed that diffusion in outermost crystal rims can also record mixing-to-eruption timescales (e.g., [Chamberlain et al., 2014a](#); [Till et al., 2015](#)), highlighting the importance of detailed petrographic observations prior to diffusion modelling.

4.8.3 Volcanic and plutonic timescales

The crystal-melt segregation timescales obtained through diffusion modelling in this study are, to our knowledge, the first determined in plutonic rocks. Interestingly, these plutonic timescales (10^4 - 10^5 yr) are comprised within the same range as the crystal residence times prior to volcanic eruption (10^4 - 10^6 yr) (Fig. 4.14). Such similarity raises questions regarding the nature of the trigger of these volcanic eruptions, as opposed to the scarcity of volcanic products originating from the Adamello batholith ([Lu et al., 2018](#)). Most studies suggest, based on thermal modelling, that the eruptability of a given magmatic system is largely controlled by the average magma flux ([Caricchi et al., 2021](#); [Degruyter and Huber, 2014](#)). This is well demonstrated by the contrasting magma fluxes inferred from the Adamello batholith and plutonic bodies in general ($\sim 10^{-4}$ km³ yr⁻¹), and the ones associated with caldera-forming eruptions which are typically ~ 2 orders of magnitude higher ([Costa, 2008](#)). In addition, the phenocrysts included in these volcanic rocks often present reverse zoning at the crystal rims, revealing the important role of mafic rejuvenation prior to eruption ([Bachmann et al., 2002](#); [Murphy et al., 2000](#); [Vazquez and Reid, 2004](#); [Wark et al., 2007](#)). In this thermal rejuvenation scenario, crystal-rich mushes are re-heated and subsequently undergo convection and homogenisation (e.g., [Couch et al., 2001](#)). On the other hand, the scarcity of such reverse zoning from the plutonic crystal record might indicate that magma recharge was inefficient during crystal-melt segregation. We propose that 10^4 - 10^6 yr represent the ideal time to assemble a thermally stable magma reservoir able to internally segregate interstitial melt and extract it to shallower depths. Our calculated timescales suggest that this thermal maturation time is independent on the average magma flux, which is supported by the thermal modelling of [Karakas et al. \(2017\)](#) whereby the development of extensive lower crustal mush zones controls the thermal budget of the upper crust. However, we stress that the average magma flux exerts a first-order control on the total amount of segregated melt and, therefore, the eruptability of a magmatic system.

4.9 Conclusions

The compositional zoning of plagioclase, quartz and alkali feldspar from the Western Adamello leucotonalite and Laione granodiorite record the thermal evolution of the Adamello batholith and was used to infer residence times and cooling rates. Microscopic observations coupled with mineral chemistry suggest that plagioclase crystals from both rocks are composed of high-An, inherited cores, volumetrically dominant mantles with intermediate An values, and thin, low-An rims. In addition to the plagioclase mantle-to-rim profiles, the Ti and Ba zoning present in quartz and alkali feldspar, respectively, are used to infer the cooling rates of the different units. Prior to diffusion modelling, the initial temperature was constrained using the compositions of amphibole-plagioclase pairs and the Ti concentration of quartz rims and yielded temperatures of 700-730 °C. From these temperatures, the modelled nonlinear cooling rates are relatively slow with a cooling of 100 °C attained in ~400 kyr in the Western Adamello, and >1 Myr for the Laione granodiorite, in agreement with thermal models and $^{39}\text{Ar}/^{40}\text{Ar}$ mineral ages determined in previous studies. Furthermore, the plagioclase core-to-mantle profiles were reproduced by using the calculated cooling rates and amphibole-plagioclase equilibrium temperatures of 730-780 °C. The extracted timescales are in the range of ~20-110 kyr, which corresponds to the time period between the crystallisation of the plagioclase mantle and the rim. Interestingly, these crystal residence times above the solidus are similar to (1) crystal residence times before caldera-forming eruptions and (2) zircon crystallisation timespan for the same plutonic and volcanic systems. Consequently, these timescales (10^4 - 10^6 yr) probably represent the ideal time to form a thermally stable magma reservoir able to segregate interstitial melt, regardless of the average magma fluxes. The latter instead control the total amount of segregated melt and, thus, the eruptability of a magma reservoir (e.g., [Caricchi et al., 2014a](#)).

Chapter 5

Apatite as a tool to quantify the volatile budget of felsic magma reservoirs (Adamello batholith, Italy)

Chapter in preparation for submission in *Geochimica et Cosmochimica Acta*

5.1 Abstract

The presence of dissolved and exsolved volatiles in melt plays a key role in the differentiation of magmas by controlling their chemical and physical properties. Volatile concentrations within the melt are commonly determined from glass inclusions which, however, may have experienced post-entrapment modification, or may not be present in the studied rocks. Alternatively, volatile-bearing minerals such as biotite, amphibole and apatite represent an invaluable tool to reconstruct the volatile history of their parental melt. Here we investigate the volatile evolution of differentiating magmas from emplacement to interstitial melt extraction within the Western Adamello tonalite (WAT) and Re di Castello (RdC) units of the Adamello batholith (Italy). The WAT is a tonalitic body displaying *in situ* crystal accumulations resulting in hornblende-biotite-gabbro and leucotonalite, and melt segregation forming aplitic and pegmatitic granite. The studied area from the RdC exhibits a concentric structure mainly composed of tonalite, granodiorite, and aplitic and pegmatitic granite. Apatite is a ubiquitous phase and exhibits a compositional trend of

5. Volatile budget of magma reservoirs

decreasing F, Cl and S with Eu anomaly, which is used as a differentiation proxy. Both locations are associated with low-CO₂ apatite (<300 µg/g) having variable δ³⁴S signatures (+1 to +10 ‰), whereas S contents are one order of magnitude higher in the RdC (600-2,000 µg/g) compared to the WAT (40-300 µg/g). Furthermore, some apatite cores are enriched in CO₂ (>1,000 µg/g), while apatite grains from a pegmatite sample from the WAT are S-rich compared to the host tonalite grains and have higher δ³⁴S values (+12 ‰). Variable F-Cl partitioning between apatite and host biotite and the preservation of volatile zoning in apatite linked to the cooling history of the pluton suggest that volatiles in apatite did not completely re-equilibrate. The equilibrium melt volatile content was calculated and yielded the same Cl decrease (~500-50 µg/g) with differentiation, indicative of fluid saturation. The melt H₂O and CO₂ contents, coupled to saturation curves, were used to retrieve crystallisation pressures of ~200-300 MPa for the low-CO₂ apatite, and ~400-700 MPa for high-CO₂ apatite, in good agreement with pressures inferred from metamorphic assemblages and amphibole chemistry. Furthermore, the calculated and modelled fluid composition reproduces (1) the δ³⁴S signature of apatite from pegmatite, suggesting that these grains incorporated a fluid component upon crystallisation, and the (2) composition of the intermediate density fluid inclusions. Such a low-density fluid, together with episodes of magma recharge, probably promoted melt segregation and extraction. Altogether, this highlights that apatite represents a valuable proxy to track the volatile budget of crystallising magma reservoirs, to recognise the economic potential of magma bodies, and to reconstruct the architecture of transcrustal magmatic systems.

5.2 Introduction

Magmatic volatiles play a key role in the chemical differentiation of magmas by controlling their liquid line of descent (Sisson and Grove, 1993; Zimmer et al., 2010) and have a direct impact on the physical properties of magma reservoirs, such as viscosity and buoyancy, which, in turn, determine the eruption style of volcanoes (Cashman, 2004; Cassidy et al., 2018; Edmonds, 2008; Parmigiani et al., 2016). The magma volatile budget depends on the parental melt volatile concentrations and liquid line of descent, and its pressure-temperature path, which defines the timing of volatile exsolution (e.g., Holtz et al., 1995; Iacono-Marziano et al., 2012; Liu et al., 2005; Webster, 1997). When the concentration of a volatile species exceeds its solubility, a high-volume, low-density fluid phase exsolves and can theoretically lead to the segregation and extraction of a similar volume of melt (Parmigiani et al., 2016; Pistone et al., 2015; Sisson and Bacon, 1999). In the middle to upper crust, such fluids are usually H₂O-dominated with relatively high

Cl and S concentrations that may result in the precipitation of critical metals (e.g., [Zajacz and Halter, 2009](#)). The abundances of volatiles dissolved in magmas are commonly inferred from petrological investigations through the analysis of volatiles present in melt inclusions (e.g., [Rose-Koga et al., 2021](#)), nominally-anhydrous and hydrous minerals (e.g., [Li et al., 2021](#); [Urann et al., 2022](#); [Wade et al., 2008](#)), calculations using mineral-based geohygrometers (e.g., [Waters and Lange, 2015](#)), and phase equilibrium experiments (e.g., [Foden and Green, 1992](#); [Krawczynski et al., 2012](#)). Some studies demonstrate that melt inclusions can be representative of the parental melt volatile composition, but they might not be present in the studied rocks, such as plutonic rocks, and usually experience different degree of post-entrapment modification with their host phase ([Bucholz et al., 2013](#); [Danyushevsky et al., 2002](#); [Gaetani et al., 2012](#)). This is well-demonstrated by the difference in volatile concentrations between melt inclusions that never exceed 8 wt.% H₂O ([Reubi and Müntener, 2022](#)) and calculated melts from nominally-anhydrous minerals that may reach ~20 wt.% H₂O ([Urann et al., 2022](#)). Geohygrometers and phase equilibrium experiments are useful to infer melt volatile contents but a detailed petrographic study is required to apply such techniques, and these only account for H₂O concentration.

An alternative method to track the melt volatile budget in the plutonic rock record is available through the accessory mineral apatite [Ca₅(PO₄)₃(F,Cl,OH)], which incorporates large amounts of volatiles (H₂O, CO₂, F, Cl, S) into its crystal structure (e.g., [McCubbin et al., 2015](#); [Riker et al., 2018](#); [Webster and Piccoli, 2015](#)). The volatiles are primarily located in the anion site with dominantly F⁻, Cl⁻ and OH⁻ anions, and rarer S²⁻ and CO₃²⁻ ([Piccoli and Candela, 2002](#)). However, the valence of S and C highly depends on the oxygen fugacity (fO_2), and S⁴⁺, S⁶⁺ and C⁴⁺ cations may be incorporated into the phosphate site ([Kim et al., 2017](#); [Konecke et al., 2017](#)). Additionally, apatite continuously crystallises during the differentiation of intermediate to silicic and carbonatitic melts ([Webster and Piccoli, 2015](#)), allowing investigation of the volatile budget of the evolving equilibrium melt. The recent parameterisation of the non-Nernstian partitioning of volatiles between apatite and melt ([Li and Costa, 2020](#)) resulted in a growing use of apatite to infer melt volatile concentrations. The applications comprise the reconstruction of plumbing systems by determining the crystallisation pressure of apatite ([Li et al., 2021](#)), and the determination of the fluid saturation level of the pre-eruptive melt in volcanic rocks based on the different partitioning behaviour of F, Cl and OH in the crystal-melt-fluid system ([Humphreys et al., 2021](#); [Keller et al., 2023](#); [Kendall-Langley et al., 2021](#); [Popa et al., 2021](#); [Sharpe et al., 2022](#); [Stock et al., 2016, 2018](#)).

The goal of this contribution is to demonstrate that apatite can be used as a proxy

5. Volatile budget of magma reservoirs

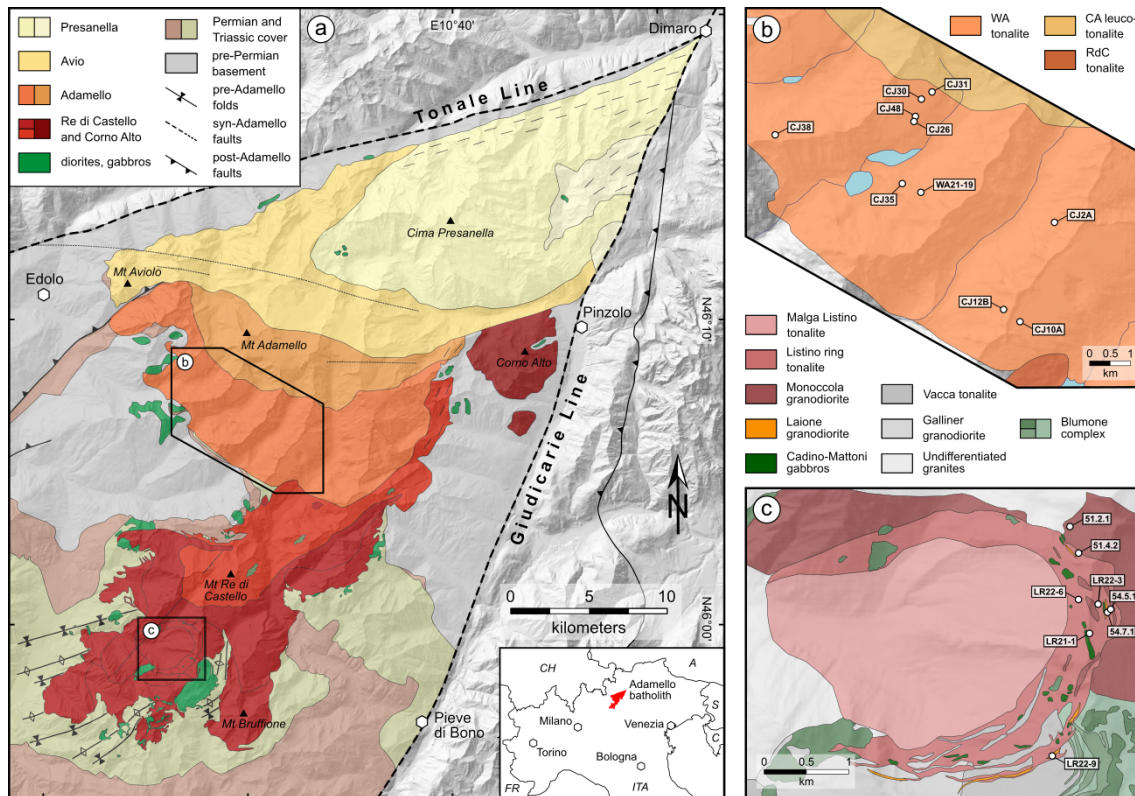


Figure 5.1. a, Simplified geological map of the Adamello batholith exhibiting the four superunits and corresponding lithologies (modified after [Schaltegger et al., 2009](#)). Location of field areas are also represented. b, Geological map of the Western Adamello tonalite and location of the studied samples (modified after [Floess and Baumgartner, 2015](#)). c, Geological map of the Listino ring complex and vicinity and location of the studied samples (modified after [Verberne, 2013](#)). Coordinates are reported using the WGS84 Coordinate System. CA, Central Adamello; RdC, Re di Castello; WA, Western Adamello.

to track the crystal-melt-fluid volatile budget of slowly-cooled plutonic rocks. We present phase relationships coupled with major, trace and volatile element chemistry of apatite to demonstrate that apatite from the Adamello batholith did not completely re-equilibrate during protracted cooling. Based on apatite volatile exchange coefficients and different geothermometers, the melt and fluid compositions in equilibrium with apatite were calculated. This demonstrates that the Adamello tonalites are CO_2 - and S-poor magmas whose differentiation leads to the exsolution of an H_2O -dominated fluid that incorporates most of the S and Cl. The calculated fluid compositions are then compared to fluid inclusion data to confirm the robustness of the employed methods. Finally, the Adamello plumbing system is discussed based on the occurrence of CO_2 -rich, inherited apatite cores sampling deeper levels of the crust.

5.3 Geological settings

The Adamello batholith, located in the Brescian Alps of northern Italy, represents the largest and oldest Tertiary calc-alkaline intrusive body in the Alps and was formed during the collision of the European and Adriatic plates (e.g., [Callegari and Brack, 2002](#)). The excellently exposed Adamello pluton covers an area of 675 km² with up to 3 km of vertical relief and is usually separated into four superunits; Re di Castello, Adamello, Avio and Presanella (Fig. 5.1a). These superunits are composed at 99 % of quartz-diorite, tonalite and granodiorite, the remaining 1 % being hornblende and gabbro ([Ulmer et al., 1983](#)), and have an emplacement age progressively decreasing from South (42-38 Ma) to North (34-31 Ma) ([Del Moro et al., 1983](#); [Schaltegger et al., 2019](#)).

The Western Adamello unit is part of the Adamello superunit (Fig. 5.1b) and is a coarse-grained, homogeneous tonalite with large abundances of amphibole and biotite phenocrysts (~20 vol.%). The WAT comprises an external zone of ~500 m at its southern border exhibiting a steeply-dipping, contact-parallel foliation interpreted as a feeder zone ([Floess and Baumgartner, 2015](#)). During differentiation, the WAT underwent a hornblende-consuming peritectic reaction producing biotite, and crystal-melt segregation forming cumulative hornblende-biotite-gabbro and leucotonalite, and extracted melt zones represented by granitic dikes ([Grocolas and Müntener, 2024](#)). The thermal evolution of the contact aureole has been used to demonstrate that the WAT was emplaced incrementally from northeast to southwest over a period of 1.2 Myr from 37.6 to 36.4 Ma at a pressure of ~250 MPa ([Floess, 2013](#); [Floess and Baumgartner, 2015](#)). For a detailed petrography of the Western Adamello tonalite (WAT), the reader is referred to [Grocolas and Müntener \(2024\)](#) and Chapter 2.

The Listino ring complex (LRC) is located in the southern part of the Re di Castello (RdC) superunit and forms a 5-km semi-circular zone of intensively foliated tonalites (Fig. 5.1c) emplaced with a ballooning mechanism ([John and Blundy, 1993](#); [Verberne, 2013](#)). The Monoccola granodiorite (MGD) is the outermost lithology of the LRC and is a medium- to coarse-grained, homogeneous granodiorite. It contains plagioclase, amphibole, biotite and quartz phenocrysts, while alkali feldspar is interstitial and surrounds the phenocrysts. A weak, inward foliation is present close to the contact with the Listino ring tonalite (LRT). The LRT is a medium-grained, rather homogeneous tonalite with abundant plagioclase phenocrysts. A similar magmatic inward foliation occurs and is defined by plagioclase, acicular amphibole, and biotite. The Laione granodiorite (LGD) is a hypabyssal, plagioclase-phyric granodiorite that forms small bodies (10-30 m large) included within the LRT displaying sharp contacts with the host tonalite ([Verberne, 2013](#)).

5. Volatile budget of magma reservoirs

It contains alkali feldspar oikocrysts and plagioclase phenocrysts texturally similar to the plagioclase crystals from the LRT. In addition, the Lago della Vacca suite also contains small LGD bodies displaying similar sharp contacts with the host diorites. The tonalite of Malga Listino (TML) constitutes the core of the LRC and is a homogeneous, medium-grained tonalite deprived of foliation except close to the contact with the LRT. It texturally resembles the MGD but with less modal quartz and biotite. Finally, granitic dikes (up to 1 m wide), originating from the LRT and MGD, radially crosscut all the LRC units. These dikes are composed of plagioclase, alkali feldspar, quartz and minor garnet and display either an aplitic texture or a pegmatitic texture with aplitic rims. The emplacement age decreases from 41.7 Myr for the outward MGD to 41.2 Myr for the inward TML (Verberne, 2013).

5.4 Methods

5.4.1 Mineral separation and imaging

A total of 18 rock samples (10 from Western Adamello, 8 from Re di Castello) were cut using a diamond saw to remove the altered crust and veins. The fresh blocks were crushed using a hydraulic press and ground to a fine powder using a tungsten carbide mill for 15 s at 700 min^{-1} . The powders were then sieved to retain the fractions of 90-125 μm and 125-250 μm . Both fractions were pre-panned, and amphibole, biotite, magnetite and titanite were removed using a Frantz magnetic separator. The mineral separation was further processed through a slightly diluted methylene iodide solution (3.15 g cm^{-3}) so that the only phases remaining were zircon, titanite and apatite. Finally, single apatite grains were hand-picked under a binocular microscope, mounted in epoxy with their *c*-axis perpendicular to the surface, and polished stepwise using 9, 6, 3, 1, and 0.5 μm diamond paste. Prior to any quantitative analysis, the epoxy mounts were carbon-coated and cathodoluminescence (CL) images of each apatite grain were acquired using a CamScan MV2300 scanning-electron microscope (SEM) with an acceleration voltage set at 10 kV.

5.4.2 Electron probe microanalysis

Apatite major element compositions were determined on both separated apatite grains and carbon-coated polished thin sections by field-emission gun electron probe microanalysis (EPMA) using a JEOL JXA-8530F HyperProbe equipped with five wavelength dispersive spectrometers at the University of Lausanne. Spot analysis of Si, La, Ce, Fe, Mg, Ca, Na, P, F and Cl were acquired using an acceleration voltage of 15 kV, a beam current of 10 nA,

and a beam size of 5 μm . The on-peak counting times were 60 s for F and Cl, 40 s for Fe, Mg, La and Ce, 30 s for Si, and 20 s for Ca, Na and P, and half the time for background. Standardisation was as follow: apatite for Ca, P, F, Cl; anorthite for Si, Ca; albite for Na; forsterite for Mg; fayalite for Fe; synthetic glasses for La and Ce. Measurements were corrected with the PRZF method ([Armstrong, 1995](#)). Detection limits for F, Cl, La and Ce are ~ 150 $\mu\text{g/g}$, ~ 40 $\mu\text{g/g}$, ~ 130 $\mu\text{g/g}$ and ~ 220 $\mu\text{g/g}$, respectively. Relative errors are <1 % for major elements in apatite (Ca and P), <2 % for F and Cl in Cl-rich (>0.10 wt.%) apatites, <8 % for Cl in Cl-poor (<0.10 wt.%) apatites, and <15 % for minor elements (Si, Fe, Mg, Na, La, Ce). Apatite backscattered electron (BSE) and CL images as well as semi-quantitative maps of P, Ce, F and Cl were acquired using an acceleration voltage of 10 kV, a beam current of 10 nA, and a beam size of 2 μm . The counting time was set to 80 ms per pixel.

5.4.3 Secondary ion mass spectrometry

The epoxy mounts containing the separated apatite crystals were cut using a Presi diamond wire saw and pressed in indium. The mounts were cleaned with ethanol and coated with gold before being loaded into the sample chamber at least 24 h before analysis. Volatile concentrations were measured for ~ 300 apatite grains using a Cameca IMS 1280-HR secondary ion mass spectrometer (SIMS) at the University of Lausanne. The vacuum of the sample chamber was kept at $\sim 6 \times 10^{-9}$ mbar. Secondary ions of ^1H , ^{12}C , ^{31}P , ^{32}S and ^{37}Cl produced by a primary O^{2-} beam of ~ 5.3 nA were measured in mono-collection using the axial electron multiplier. The field aperture was set at 2,000 μm and the energy window at 50 eV. The analysed area was pre-sputtered for 5 min over an area of $\sim 15 \times 15$ μm , after which the raster size was reduced to $\sim 8 \times 8$ μm for 7 min of data collection. Entrance (~ 150 μm) and exit (~ 400 μm) slits were adjusted to get a mass resolving power (MRP) of $\sim 3,000$. Secondary ion intensities were normalised to ^{31}P to quantify H_2O , CO_2 , S and Cl concentrations using calibration curves determined from 7 natural apatite standards: APS-25 ([Schettler et al., 2011](#)), Hormuz, YAM, Mud Tank, Madagascar, Big-1 and Durango-B ([Hammerli et al., 2021a,b](#)). Prior to SIMS analysis, the CO_2 content of some of these standards was determined by attenuated total reflection Fourier transform infrared (ATR-FTIR) spectrometry at the University of Bern (Supplementary Material 4). Each indium mount contained Hormuz, Mud Tank and Durango apatite standards that were measured every 5 analyses to correct for potential drift. Calibration curves show linear correlation between secondary ion intensities and volatile concentrations in the standards (Supplementary Material 4). However, we noticed that the calibration

5. Volatile budget of magma reservoirs

shifted every day of the session, especially for CO₂. Therefore calibration has been made on a daily basis. Detection limits could be determined by using 2 standards with very low but different volatile concentrations, and were ~ 300 $\mu\text{g/g}$ for H₂O, ~ 30 $\mu\text{g/g}$ for CO₂ and S, and < 200 $\mu\text{g/g}$ for Cl. Relative errors in the determined concentrations are ~ 5 - 7 % for H₂O and Cl, and ~ 10 % for CO₂ and S. The Cl concentrations measured by EPMA and SIMS are the same within error ($R^2 > 0.97$), whereas the calculated H₂O from stoichiometry based on the EPMA measurements can differ by up to 80 % from the H₂O measured by SIMS (Supplementary Material 4). This is possibly related to (1) the error that was propagated from the uncertainties in major element concentrations determined by EPMA, (2) the assumption of a stoichiometric anion site only composed of F, Cl and OH, and/or (3) to the presence of H⁺ cations in other crystallographic sites that could increase the apatite H₂O budget. Therefore, only H₂O concentrations determined by SIMS will be used further.

Sulphur isotope analysis of ~ 100 apatite grains previously analysed for volatile contents were also performed using a Cameca IMS 1280-HR SIMS housed at the Centre de Recherches Pétrographiques et Géo-chimiques (CRPG, Nancy). Secondary ions of ³²S and ³⁴S produced by a primary Cs⁺ beam of ~ 2 nA were measured in multi-collection using a Faraday cup and an electron multiplier, respectively. An electron gun produced low-energy electrons that flooded the target area of the Cs⁺ beam to avoid charging during the analysis. The field aperture was set at 3,000 μm and the energy window at 50 eV. The analysed area was pre-sputtered for 2 min over an area of $\sim 15 \times 15$ μm , after which the raster size was reduced to $\sim 8 \times 8$ μm for 5 min of data collection. To resolve the ¹H³¹P isobaric interference on the ³²S peak, entrance (~ 90 μm) and exit (~ 400 μm) slits were adjusted to get an MRP of $\sim 5,000$. The Durango-B apatite standard was measured five times every 20 analyses to correct from drift and instrumental mass fractionation. The sulphur isotope analyses are reported in the delta notation as $\delta^{34}\text{S}_{\text{V-CDT}}$, where V-CDT corresponds to the Vienna Canyon Diablo Troilite reference standard (Coplen and Krouse, 1998; Ding et al., 2001).

5.4.4 Laser ablation inductively coupled plasma mass spectrometry

Trace element concentrations were determined on the same polished epoxy mounts using a triple quadrupole Perkin Elmer NexION 5000 mass spectrometer coupled with an Australian Scientific Instrument RESOLUTION 193 nm Ar-F excimer laser at the University of Lausanne. The LA-ICP-MS system was optimised by linearly scanning the NIST SRM-612 glass standard at 10 $\mu\text{m s}^{-1}$ in order to increase the spectrometer sensitivity (¹³⁹La⁺ > 1.9

$\times 10^6$ cps) without significantly producing oxides ($^{248}\text{ThO}^+ / ^{232}\text{Th}^+ < 0.4\%$) and doubly-charged ions ($\text{Ba}^{2+} / \text{Ba}^+ < 3.0\%$). Helium ($1,000 \text{ ml min}^{-1}$) and N_2 (1 ml min^{-1}) were used as carrier gases. The laser pit diameter was chosen according to the grain size and mineral texture and alteration, and was varied between 20 and 30 μm . The repetition rate was set to 10 Hz and the energy density to 6 J cm^{-2} . Background, ablation and wash-out interval acquisition times were 70, 35 and 35 s, respectively. Dwell times ranged from 10 to 20 ms depending on the measured isotope. Absolute concentrations were calculated using CaO (measured by EPMA) as internal reference, NIST SRM-612 as primary standard, and BCR-2G as secondary standard for quality control. The data reduction was performed with the LAMtrace software (Jackson, 2008). The average elemental abundances of the standards were taken from Pearce et al. (1997).

5.4.5 Bulk F content

To quantify bulk F concentrations, the selected rock samples were cut using a diamond saw to remove the altered crust. The fresh blocks were crushed using a hydraulic press and ground to a fine powder using a tungsten carbide mill for 3 min at 900 min^{-1} . A representative aliquot of each sample and six international standards with different SiO_2 and F concentrations (BCR-2, G-2, GSP1, NIM-L, SY-3, RGM-1) was put into a Pt crucible and melted at $1,400^\circ\text{C}$ and 1 atm for 5 min in a Borel FP 1100-30 furnace. The recovered glasses were mounted in epoxy, polished stepwise using 9, 6, 3, 1, and 0.5 μm diamond paste, carbon-coated and analysed by field-emission gun EPMA using a JEOL JXA-8530F Hyperprobe at the University of Lausanne. Six spot analyses for each sample were performed and included measurements of Si, Al, Fe, Mg, Ca, F and Cl using an acceleration voltage of 15 kV, a beam current of 10 nA, and a beam size of 10 μm . The on-peak counting times were 30 s for all elements, and half the time for background. Standardisation was as follow: apatite for P, F, Cl; anorthite for Si, Al, Ca; albite for Na; forsterite for Mg; fayalite for Fe. Measurements were corrected with the PRZF method (Armstrong, 1995). Detection limit for F is $\sim 150 \mu\text{g/g}$. Relative errors are $< 10\%$ for high F concentrations ($> 2,000 \mu\text{g/g}$), and $< 50\%$ for low F concentrations ($< 300 \mu\text{g/g}$).

5.5 Results

5.5.1 Petrographic observations

Apatite represents an ubiquitous accessory phase in all the studied lithologies (Fig. 5.2). Tonalites and granodiorites contain 0.28 to 0.50 vol.% apatite which exhibits a wide range

5. Volatile budget of magma reservoirs

of size ($\sim 50\text{-}500\ \mu\text{m}$) and is usually present as inclusions within hornblende, biotite, quartz and plagioclase mantle and rim, and rarely in magnetite and zircon (Fig. 5.2c-f). Smaller grains ($<100\ \mu\text{m}$) occur in interstitial position and are usually associated with interstitial biotite, quartz and K-feldspar (Fig. 5.2e). In addition, the Laione granodiorite also contains apatite grains ($<100\ \mu\text{m}$) included within K-feldspar oikocrysts. In the Western Adamello, the lithologies that underwent crystal accumulations, namely the hornblende-biotite-gabbros and leucotonalites, display higher (0.62-0.88 vol.%) and lower (0.11-0.20 vol.%) apatite modal amounts, respectively. Regardless of the abundances, apatite exhibits the same textural relationships in the tonalites and granodiorites from the Western

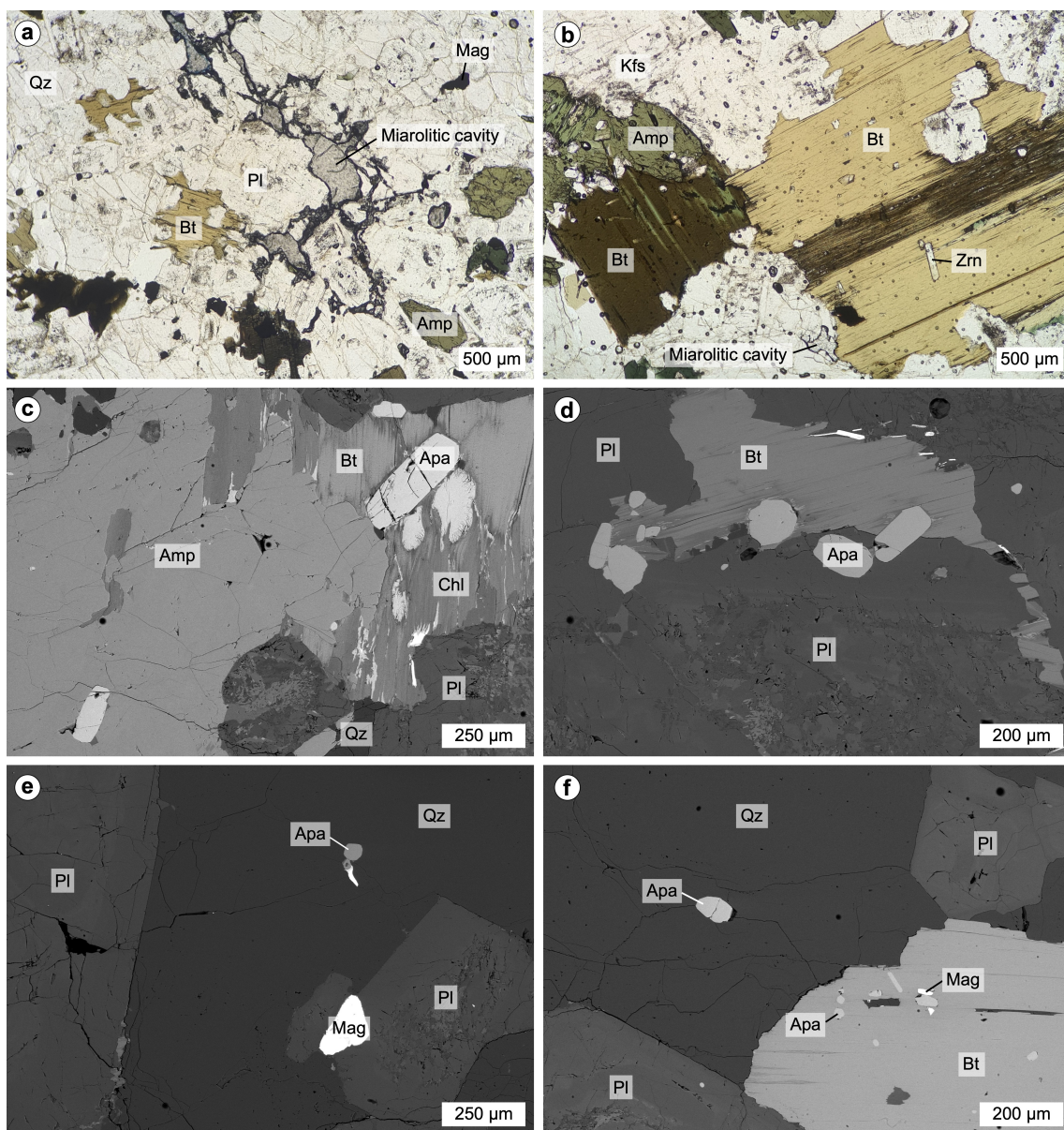


Figure 5.2. (Figure caption on next page.)

Adamello and Re di Castello units. Finally, the granitic dikes from both locations contain 0.02 to 0.16 vol.% apatite, with the lowest amounts corresponding to pegmatitic granites. In these rocks, apatite is texturally similar to the smallest grains from the other lithologies and is either included in or at the boundary of quartz, K-feldspar and plagioclase. In addition, rare tonalite-derived plagioclase cores may host larger ($>100\ \mu\text{m}$) apatite inclusions. These textural information, coupled with the continuous decrease of the bulk P_2O_5 content with differentiation (Grocolas and Müntener, 2024), suggest that apatite saturates close to the tonalite and granodiorite liquids and continuously crystallises to temperatures close to the solidus. Interestingly, miarolitic cavities are locally found in tonalitic samples from both locations. In detail, the Western Adamello tonalite contains small miarolitic cavities (100-300 μm) (Fig. 5.2b), while the Listino ring tonalite exhibits elongated miarolitic cavities ($>20 \times 1\ \text{mm}$) parallel to each other (Fig. 5.2a).

5.5.2 Apatite chemistry

Apatite volatile and trace element contents

Apatite crystals from both locations are dominantly F-rich apatites with X_{F} ranging from 39.3 to 91.5 mol.% in the WAT, and from 31.4 to 70.2 mol.% in the RdC, whereas their X_{Cl} (WAT: 13.0-0.3 mol.%; RdC: 8.1-1.3 mol.%) and X_{OH} (WAT: 54.3-8.0 mol.%; RdC: 61.5-27.8 mol.%) are lower and decrease with increasing X_{F} (Fig. 5.3). These compositions and correlations are similar to other apatites present in felsic plutonic rocks (Fig. 5.3a)

Figure 5.2. Photomicrographs of thin sections in plane-polarised light (**a, b**) and backscattered electron (**c-f**) highlighting the presence of miarolitic cavities and the widespread occurrence of apatite. **a**, Listino tonalite sample mainly constituted of amphibole, biotite, plagioclase and quartz exhibiting $>1\ \text{mm}$ long miarolitic cavities that connect and form $>1\ \text{cm}$ long channels (N45°57'44.3", E10°26'43.0"). Magnetite can be found at ground boundaries or included within amphibole and biotite. **b**, Western Adamello tonalite sample formed by amphibole, biotite, plagioclase, quartz and alkali feldspar highlighting the peritectic transformation of amphibole phenocrysts into biotite and the presence of small ($<500\ \mu\text{m}$) miarolitic cavities (N46°04'34.4", E10°30'27.6"). Zircon inclusions are abundant in biotite. **c**, Western Adamello hornblende-biotite-gabbro consisting of an amphibole phenocryst in contact with a chloritised biotite hosting large ($\sim 100\text{-}250\ \mu\text{m}$) apatite grains (N46°04'41.8", E10°30'53.6"). Quartz and altered plagioclase occur as interstitial phases. **d**, Western Adamello hornblende-biotite-gabbro sample highlighting the presence of plagioclase-hosted and biotite-hosted apatite grains (N46°04'41.8", E10°30'53.6"). Note the higher alteration of the plagioclase core compared to the plagioclase rim. **e**, Western Adamello hornblende-biotite-gabbro sample showing the occurrence of small ($\sim 50\ \mu\text{m}$) apatite grains enclosed in interstitial quartz (N46°04'41.8", E10°30'53.6"). **f**, Western Adamello tonalite sample highlighting the numerous euhedral apatite inclusions present in biotite and the subhedral characteristic of interstitial quartz hosted apatite grains (N46°07'57.1", E10°29'19.3"). *Amp*, amphibole; *Apa*, apatite; *Bt*, biotite; *Chl*, chlorite; *Kfs*, K-feldspar; *Mag*, magnetite; *Pl*, plagioclase; *Qz*, quartz; *Zrn*, zircon.

5. Volatile budget of magma reservoirs

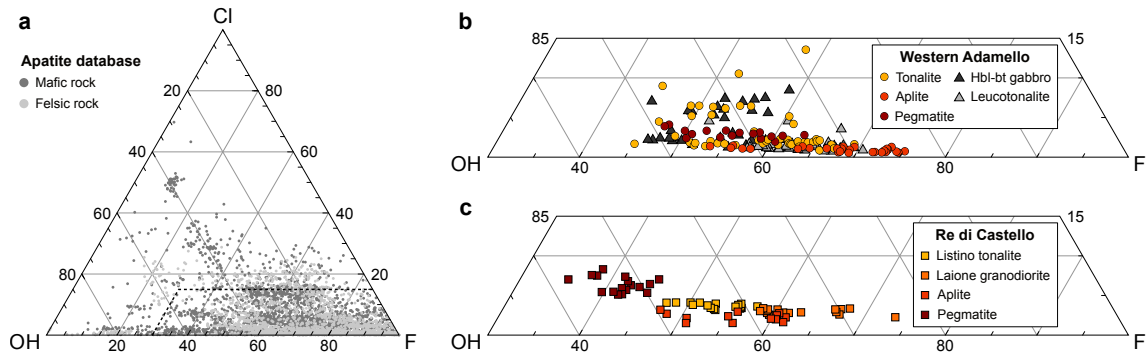


Figure 5.3. Halogen content of apatite in molar proportions plotted in the Cl-OH-F ternary diagram. **a**, Apatite compositions from igneous mafic and felsic rocks compiled from Georoc. The dashed line defines the zone plotted in (b) and (c). **b**, Halogen content of apatite grains from the Western Adamello unit. The highest Cl contents are associated with samples from the southern part of the unit. **c** Halogen content of apatite grains from the Re di Castello unit. Molar proportions were calculated using SIMS data only for the OH component.

(e.g., Kendall-Langley et al., 2021; Webster and Piccoli, 2015). Furthermore, the highest X_{Cl} values from WAT apatites are systematically associated with samples from the South of the unit, in agreement with the differentiation increase of the bulk tonalite from South to North (Floess, 2013).

Furthermore, the zoning pattern of apatite was evaluated on texturally-controlled grains from the WAT based on compositional maps and profiles measured in thin section. Fluorine and Cl maps and profiles reveal that the core and rim F and Cl concentrations as well as the profile shape is dependent on the petrographic position of apatite (Figs. 5.4 and 5.5). Apatite enclosed in plagioclase mantle ($>An_{55}$) exhibits flat Cl profiles and have the highest Cl contents (>0.25 wt.%), while grains closer to the plagioclase rim (An_{40-50}) show a continuous Cl decrease from core (0.18 wt.%) to rim (0.10 wt.%) (Fig. 5.5b). Finally, lower Cl contents are observed in biotite-hosted (0.04-0.15 wt.%) and interstitial (0.04-0.11 wt.%) apatites with the highest values associated with a plateau in the core (Fig. 5.5b). A sharp Ce zoning is only observed in a plagioclase-hosted apatite and is correlated to the BSE and CL brightness (Fig. 5.4c), in good agreement with previous studies emphasising the rare earth element control on CL brightness in apatite (e.g., Roeder et al., 1987). Apatite from tonalite- and granodiorite-derived lithologies usually display oscillatory zoning in CL (Fig. 5.4), while the majority of apatite originating from aplitic and pegmatitic granite displays no visible CL zoning.

Apatite crystals from the WAT and RdC systematically exhibit negative Eu anomalies [$Eu/Eu^* = Eu_N / (Sm_N \times Gd_N)^{1/2}$] ranging from 0.62 to 0.09 (Fig. 5.6). The lowest values correspond to apatite originating from leucotonalitic to granitic host rocks. In detail, one pegmatitic granite sample from the WAT has higher apatite Eu anomalies (0.27-0.52)

but is associated with (sub)solidus Ti-in-quartz temperatures ($<660\text{ }^{\circ}\text{C}$) (Grocolas and

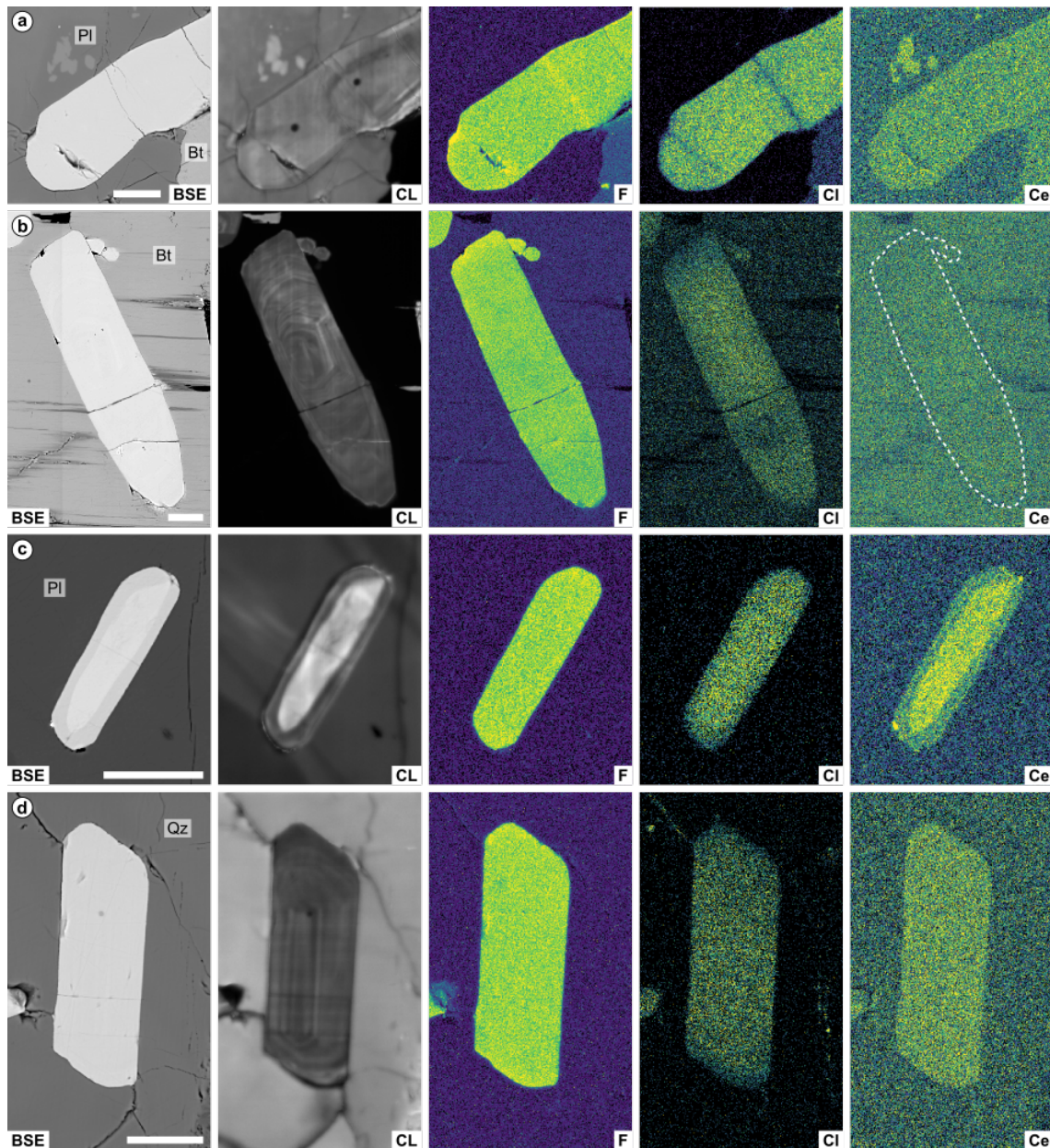


Figure 5.4. Backscattered electron (BSE), cathodoluminescence (CL) and X-ray maps highlighting the compositional zoning observed in apatite from different samples from the Western Adamello tonalite. **a**, Large ($>100\text{ }\mu\text{m}$) apatite grain pinched between a plagioclase and biotite phenocrysts ($\text{N}46^{\circ}04'34.4''$, $\text{E}10^{\circ}30'27.6''$). Note the modifications of the F and Cl contents along the two major cracks. **b**, Large ($>100\text{ }\mu\text{m}$) apatite grain enclosed in partly chloritised biotite exhibiting a typical oscillatory zoning in CL, and an F increase and Cl decrease toward the upper rim ($\text{N}46^{\circ}07'57.1''$, $\text{E}10^{\circ}29'19.3''$). **c**, Small ($\sim 15\text{ }\mu\text{m}$) apatite grain enclosed in plagioclase mantle having a bright core in BSE and CL imaging correlated to high Ce concentrations ($\text{N}46^{\circ}07'57.1''$, $\text{E}10^{\circ}29'19.3''$). Note the relative decrease in F and Cl decrease toward the rims. **d**, Small ($\sim 30\text{ }\mu\text{m}$) apatite grains hosted in an interstitial quartz exhibiting an oscillatory zoning in CL, and an F increase and Cl decrease toward the upper and lower rims ($\text{N}46^{\circ}07'65.4''$, $\text{E}10^{\circ}30'58.3''$). The white bar is $10\text{ }\mu\text{m}$.

5. Volatile budget of magma reservoirs

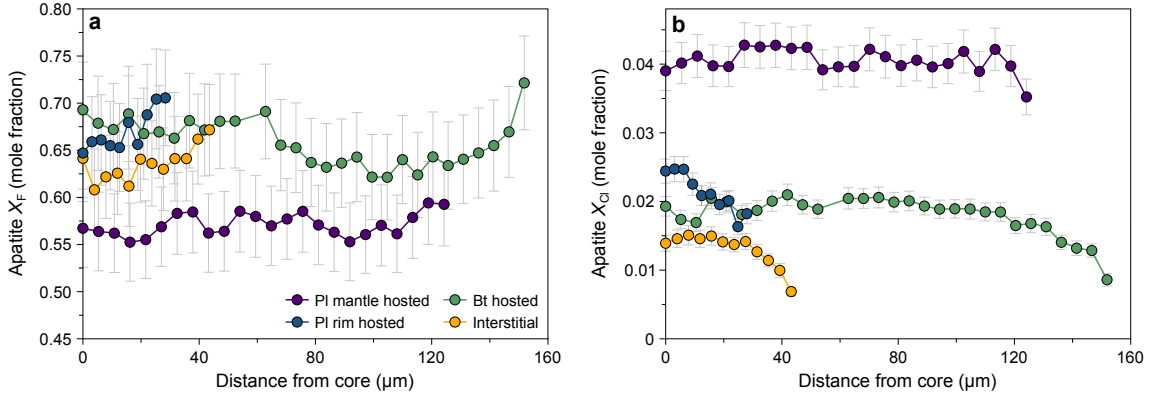


Figure 5.5. Fluorine (a) and chlorine (b) profiles measured in apatite grains from the Western Adamello tonalite having different textural positions. Note the higher Cl concentrations and flat Cl (and F) profiles in apatite included in early crystallising phases (i.e., plagioclase mantle) compared to the overall lower Cl concentrations and preserved Cl (and F) zoning in apatite hosted in low-temperature phases (i.e., plagioclase rim, biotite, interstitial).

Müntener, 2024). A possible explanation resides in the fast growth of feldspar in pegmatite, potentially leading to the formation of boundary layers enriched in slow-diffusing elements (e.g., P, heavy REE) and, therefore, kinetic fraction during apatite growth (e.g., Holycross and Watson, 2018). Therefore, the apatite Eu anomaly probably reflects the equilibrium melt evolution and, in the following, is considered as a differentiation proxy (e.g., Belousova et al., 2002; Kieffer et al., 2023). The apatite Cl content (WAT: 0.78-0.04 wt.%; RdC: 0.25-0.11 wt.%) decreases with the Eu anomaly, except for one pegmatitic granite sample from the RdC that has higher apatite Cl content (0.33-0.49 wt.%) (Fig. 5.6a,b). Such a trend is usually interpreted as representative of fluid saturation during crystallisation (Humphreys et al., 2021; Popa et al., 2021; Stock et al., 2018). Apatite from the WAT exhibits a wide range of S contents (<30-1,020 $\mu\text{g/g}$) with the highest values found in crystals rims and in grains originating from pegmatite (Fig. 5.6c). On the other hand, apatite grains from the RdC overall have higher S contents (110-1,400 $\mu\text{g/g}$) with most values comprised between ~ 300 and 800 $\mu\text{g/g}$ (Fig. 5.6d). The large majority of apatite crystals from both locations have low CO_2 contents (<30-500 $\mu\text{g/g}$) (Fig. 5.6e,f). Nevertheless, some grains have higher CO_2 concentrations (>800 $\mu\text{g/g}$) independent of the Eu anomaly. These CO_2 -rich apatite compositions either correspond to (1) S-rich apatite grains from pegmatitic granite or located at crystal rims, or (2) S-poor crystal cores originating from samples having numerous antecrystic high-An plagioclase cores. Therefore, such CO_2 -rich, S-poor crystal cores probably represent antecrysts that crystallised from an S-poor melt close to, or at, fluid saturation prior to emplacement in the upper crust. Such S depletion could be due to (1) sulphide saturation in the lower to middle crust, (2) S incorporation into an early exsolving fluid, and/or (3) low $f\text{O}_2$ conditions resulting in a hindered S incorporation

into apatite (Konecke et al., 2019; Parat and Holtz, 2004, 2005).

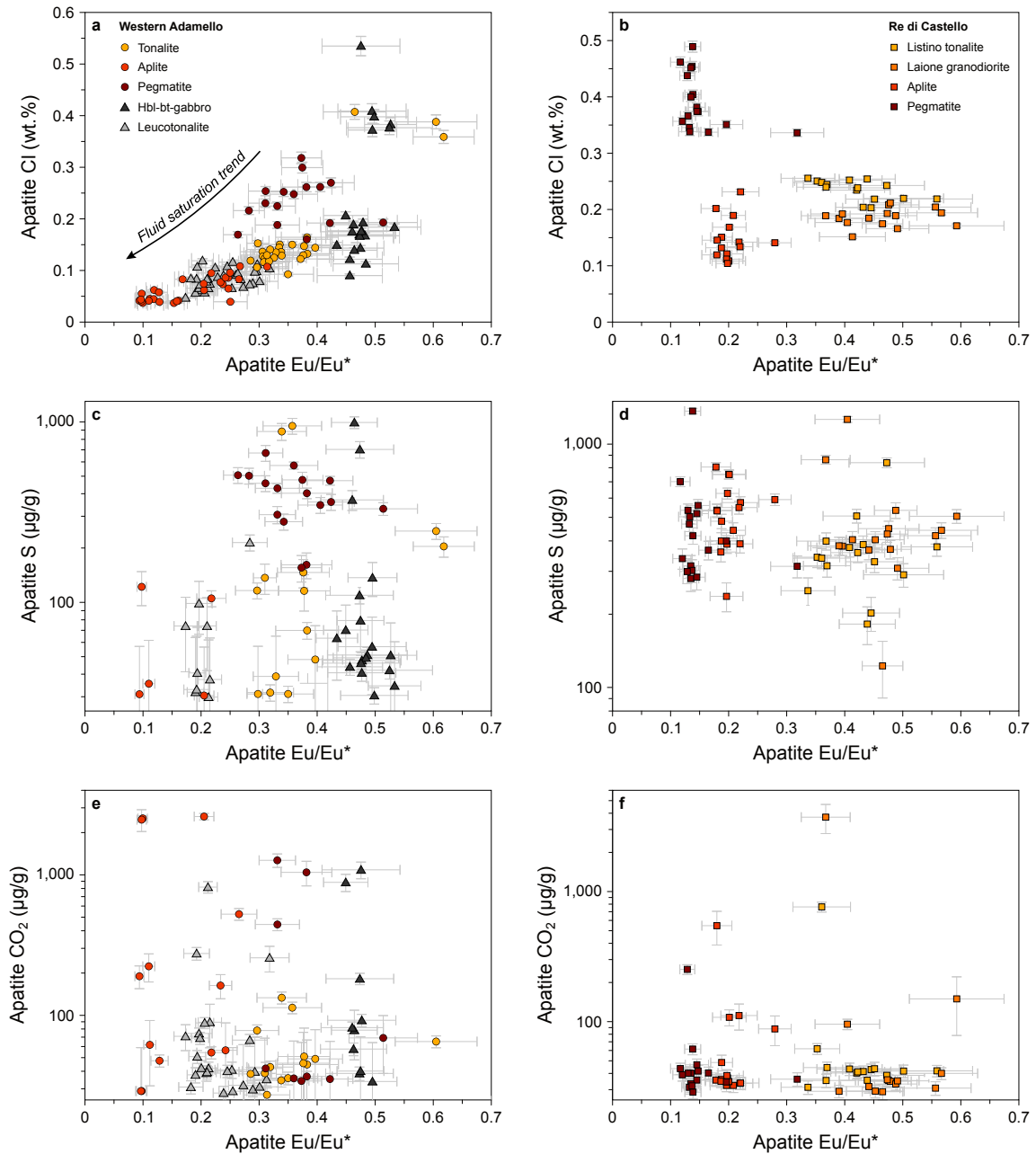


Figure 5.6. Volatile and trace element compositions of apatite from the Western Adamello (a, c, e) and Re di Castello (b, d, f) lithologies. a, b, Apatite Eu/Eu* vs. Cl (wt.%). Note the clear Cl decrease with decreasing the Eu anomaly in apatite from the Western Adamello, which is symptomatic of fluid saturation. c, d, Apatite Eu/Eu* vs. S (µg/g). The S content of Western Adamello apatite grains is one order of magnitude lower than in the Re di Castello unit, except for some crystal rims from Western Adamello tonalite and hornblende-biotite-gabbro, and apatite originating from pegmatitic granite. e, f, Apatite Eu/Eu* vs. CO₂ (µg/g). Most apatite grains have low CO₂ contents, except some crystal cores probably originating from higher pressure, and some S-rich apatite grains from pegmatitic granite.

5. Volatile budget of magma reservoirs

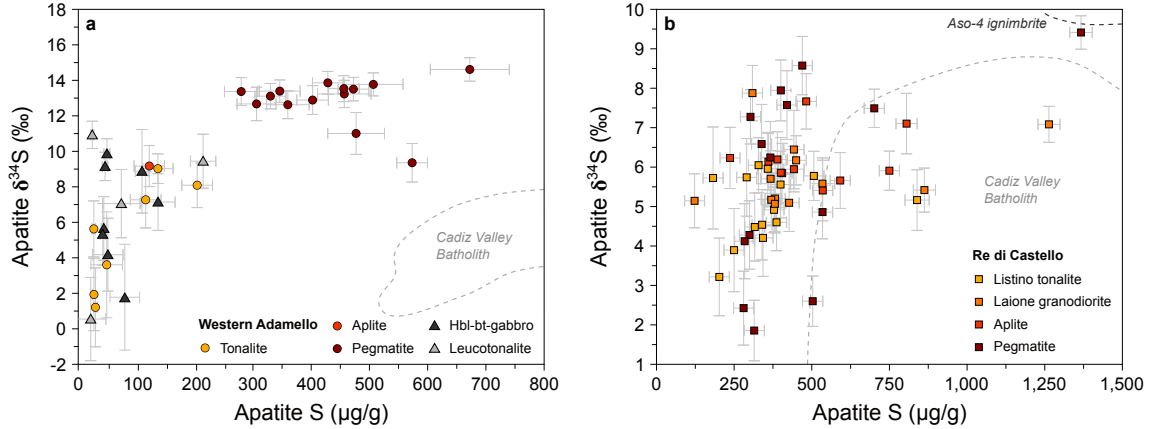


Figure 5.7. Sulphur elemental and isotopic composition of apatite from the Western Adamello (a) and Re di Castello (b) lithologies plotted as S (µg/g) vs. $\delta^{34}\text{S}$ (‰) relative to the Vienna Canyon Diabolo Troilite standard (Coplen and Krouse, 1998; Ding et al., 2001). The investigated lithologies have similar $\delta^{34}\text{S}$ signatures, except the Western Adamello pegmatite sample that exhibits higher $\delta^{34}\text{S}$ values. Data from the Cadiz Valley Batholith (USA) (Economos et al., 2017) and Aso-4 ignimbrite (Japan) (Keller et al., 2023) are represented for comparison.

Apatite sulphur isotope signatures

The apatite sulphur isotopic signature from the Adamello batholith almost span the entire range of volcanic arc compositions ($\delta^{34}\text{S} = 0\text{-}20$ ‰) (Hammerli et al., 2021a). Apatite from the Western Adamello tonalite, hornblende-biotite-gabbro, leucotonalite and aplitic granite has $\delta^{34}\text{S}$ values ranging from +0.5 to +12.2 ‰ that decrease with the apatite S content and, to some extent, with the apatite Eu anomaly (Fig. 5.7a). Amongst those grains, the CO₂-rich, S-poor apatite cores have the highest $\delta^{34}\text{S}$ values. On the other hand, the $\delta^{34}\text{S}$ values of apatite originating from the pegmatite sample are higher (+9.3 to +14.9 ‰) and also decrease with the apatite S concentration, albeit with a gentler slope. In the Re di Castello superunit, the apatite $\delta^{34}\text{S}$ ranges from +1.8 to +9.4 ‰ and displays a similar correlation with the apatite S content (Fig. 5.7b). Apatite grains from the Cadiz Valley Batholith (USA) (Economos et al., 2017) have similar $\delta^{34}\text{S}$ values and higher S concentrations, while the Aso-4 ignimbrite (Japan) (Keller et al., 2023) contains apatite with higher sulphur elemental and isotopic contents.

5.5.3 Biotite-apatite pairs

Fluorine and Cl contents of biotite-hosted apatite inclusions and host biotite were measured to determine the extent of volatile exchange and evaluate the amount of re-equilibration undergone by apatite during slow cooling of the pluton. Amphibole-apatite pairs were not analysed because of the difficulty to precisely measure amphibole F content by EPMA. In these three Western Adamello tonalite samples, host biotite F content ranges from 0.09

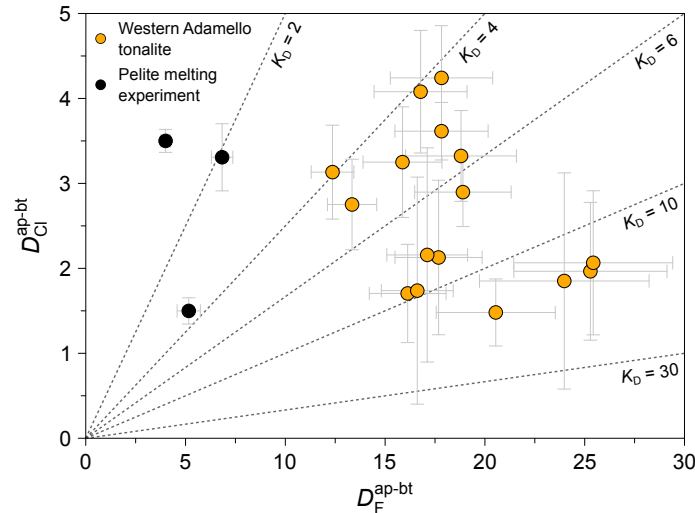


Figure 5.8. Partitioning of F-Cl between apatite and biotite from Western Adamello tonalite samples plotted as $D_F^{\text{ap/bt}}$ vs. $D_{\text{Cl}}^{\text{ap/bt}}$. The exchange coefficients (K_D) represent the ratio of the two partition coefficients. Note the wide range of K_D values covered by the measured data. The apatite-biotite equilibrium data from the pelite melting experiments at high pressure (2.5 GPa) of [Li and Hermann \(2017\)](#) are represented for comparison.

to 0.20 wt.% and is inversely correlated to Cl (0.03-0.11 wt.%), while apatite exhibits its typical negative correlation between Cl (0.43-0.06 wt.%) and F (2.14-2.76 wt.%). The calculated partition coefficients (D_i) between apatite and biotite for F and Cl range from 13 to 26 for D_F , and from 1.5 to 4.3 for D_{Cl} (Fig. 5.8). To assess the extent of volatile re-equilibration between these two phases, the ratio between the two calculated D s, corresponding to the exchange coefficients (K_D), is calculated. The calculated K_D s for the three samples span a wide range of values from 4 to 18 (14 K_D -units), while the K_D variation within sample varies from 4 to 17 (Fig. 5.8). The only experimental apatite-biotite F and Cl partitioning data, to our knowledge, come from the ultrahigh-pressure melting experiments of [Li and Hermann \(2017\)](#). In their experiments, D_{Cl} (1.5-3.5) is similar to our measured values whereas D_F is lower (4.0-6.8), resulting in K_D values ranging from 1.1 to 3.5. Such differences probably arise from the sedimentary starting materials and mantle pressures representative of a subducting slab used by [Li and Hermann \(2017\)](#), coupled with the high-Mg composition of their equilibrium biotite.

5.6 Magmatic volatile preservation

Several studies have highlighted that the investigation of volatile elements is challenging because of their natural behaviour and the difficulty to analyse them. Indeed, volatile elements (1) are extremely sensitive to the presence of a fluid and usually compatible into such a fluid phase (e.g., [Webster et al., 2009](#)), (2) tend to diffusive quickly ([Woods et al.,](#)

5. Volatile budget of magma reservoirs

2000), and (3) are challenging to measure by conventional techniques. In this section we discuss these aspects with an emphasis on bulk rock analysis and texturally-controlled apatite compositions.

5.6.1 Bulk rock

Upon emplacement, a magma reservoir formed by a hydrous melt is either fluid-saturated or fluid-undersaturated but, during differentiation, will eventually saturate with respect to an H₂O- and/or CO₂-dominated fluid phase. At the onset of fluid saturation, the general behaviour of the system changes and some melt-forming elements are preferentially incorporated into the fluid phase ($D_i^{\text{fluid-melt}} > 1$), therefore modifying the initial melt composition. Amongst the elements of interest in this study, H₂O, CO₂, S and Cl are largely compatible into magmatic fluids (e.g., Iveson et al., 2018; Webster et al., 2009; Zajacz et al., 2013), so bulk rock compositions do not necessarily reflect the original volatile budget of the parental melt. On the other hand, several studies have illustrated the tendency of F to remain in the melt during fluid exsolution (Baker and Alletti, 2012; Balcone-Boissard et al., 2010; Webster and Holloway, 1990). More specifically, Webster and Holloway (1990) reported low $D_{\text{F}}^{\text{fluid-melt}}$ values of ~ 0.3 between an F-rich (~ 2 wt.%) rhyodacitic melt and an aqueous fluid at 200 MPa and 800 °C. In addition, Webster et al. (2009) demonstrated that the measured $D_{\text{Cl}}^{\text{fluid-melt}}$ is positively correlated to the melt Cl content; therefore, the $D_{\text{F}}^{\text{fluid-melt}}$ values reported by Webster and Holloway (1990) probably represent maximum values. As such, the sampled rocks probably retained the F content of the melt they derive from.

Additionally, the possibility of F loss during melting of the rock powders has been tested through analysis of six standards that underwent the same procedure. The comparison between the known concentrations and the measured concentrations of six standards ($R^2 = 0.988$) yielded a difference of < 15 % for F contents of > 500 $\mu\text{g/g}$, whereas the very low concentrations (RGM-1; F = 342 $\mu\text{g/g}$) differed by 29 % (Supplementary Material 4). The measured glasses were slightly heterogeneous with a two-fold standard deviation, based on 6 analyses, of 15-30 % for F concentrations of < 500 $\mu\text{g/g}$, and up to 60 % for the RGM-1 standard. Therefore, our method to measure the F content of plutonic rocks most likely approaches the initial magmatic F concentrations and will further be used to calculate melt volatile concentrations.

5.6.2 Apatite

Several studies demonstrate that volatiles rapidly diffuse in melt (e.g., Behrens and Zhang, 2009; Zhang and Stolper, 1991), glassy melt inclusions present in volcanic rocks (e.g., Bucholz et al., 2013; Gaetani et al., 2012), and crystal lattices (e.g., Demers-Roberge et al., 2021; Mackwell and Kohlstedt, 1990). Recently, Huang et al. (2024) investigated the apatite composition from ore-forming plutonic rocks and found that apatite experienced volatile re-equilibration except zircon-hosted apatite. It is therefore important to evaluate the propensity of volatiles to diffuse out of apatite crystals in slowly-cooled plutonic systems. In this section, we address this potential issue by testing two different hypotheses where apatite volatile concentrations could have been modified.

Intra-crystalline diffusion of volatiles in apatite has been recently re-evaluated (Li et al., 2020), but little is known about volatile interdiffusion between apatite and other phases. In such a scenario, and if complete equilibrium is reached, volatile ratios between apatite and its host mineral should systematically be the same. The calculated K_{DS} between apatite and biotite for F and Cl range from 4 to 18, with a similar variation within sample, which precludes the complete re-equilibration hypothesis. Similarly, the incompatible behaviour of volatiles in nominally anhydrous minerals implies that apatite included within plagioclase and quartz probably behaves as a closed system and preserves its bulk grain volatile concentration, although diffusion along fast diffusion paths such as cracks and grain boundaries cannot be excluded.

In contrast to volcanic rocks, heat dissipation in plutonic rocks is a slow process and is accompanied by diffusive re-equilibration within minerals. Although volatile diffusion in apatite has been demonstrated to be a relatively slow process (Li et al., 2020), the extent of diffusion re-equilibration undergone by apatite must be addressed. The different shapes of the measured Cl profiles (Fig. 5.5b) suggest that apatite underwent different degrees of volatile re-equilibration. Interestingly, the flat Cl profiles are systematically associated to early-crystallising phases (i.e., plagioclase mantle), whereas apatite included within phases crystallising at lower temperature (e.g., plagioclase rim, biotite) or in an interstitial position exhibits a clear decrease in Cl toward crystal rims. This observation could be related to differential re-equilibration, whereby apatite grains hosted in early-crystallising phases started cooling at higher temperature and completely re-equilibrated, while zoned apatite only partly re-equilibrated. This hypothesis has been tested by modelling the cooling path of these zoned apatites using the explicit finite-difference method (Crank, 1975) and the diffusion coefficients of Li et al. (2020) (Fig. 5.9). Furthermore, diffusion was allowed to proceed at the crystal core and rim. Although the modelled cooling rates

5. Volatile budget of magma reservoirs

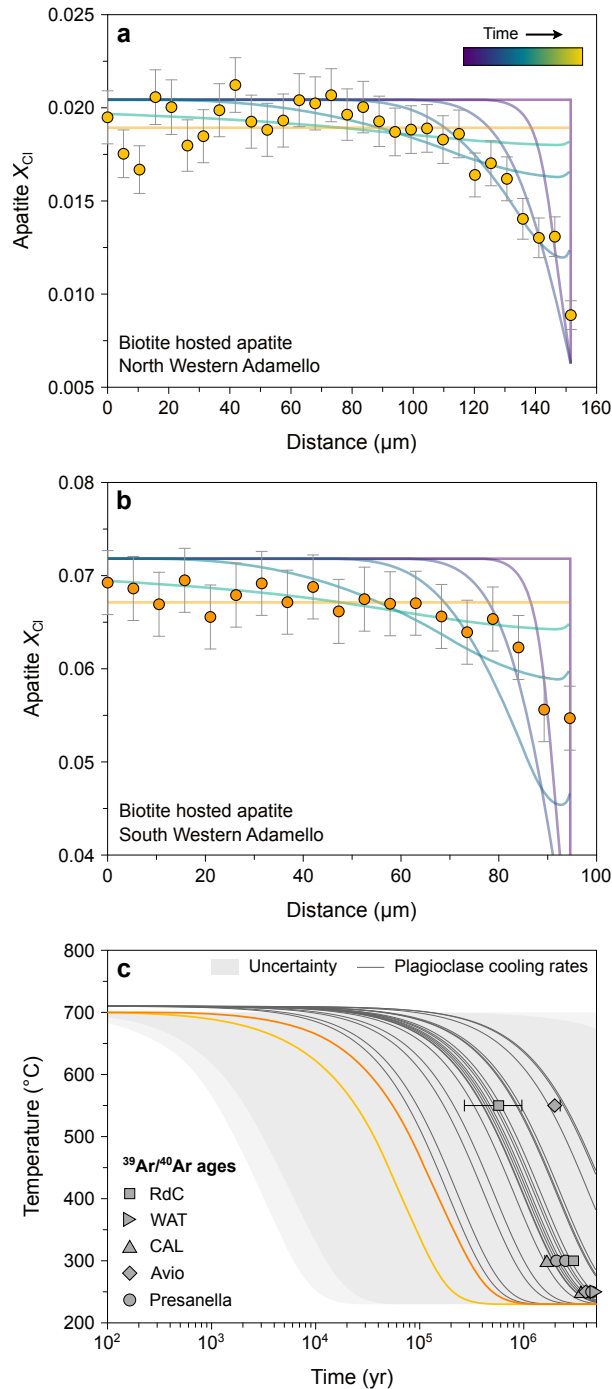


Figure 5.9. Results of halogen-in-apatite diffusion modelling used to infer cooling rates. **a**, Chlorine molar fraction (X_{Cl}) vs. distance (μm) of an apatite originating from a tonalite sample from the northern part of the Western Adamello (N46°07'57.1", E10°29'19.3"). **b**, Chlorine molar fraction (X_{Cl}) vs. distance (μm) of an apatite originating from a tonalite sample from the southern part of the Western Adamello (N46°04'34.4", E10°30'27.6"). **c**, Temperature ($^{\circ}\text{C}$) evolution through time (yr) associated with the best fits using the diffusion coefficients of Li et al. (2020). The $^{39}\text{Ar}/^{40}\text{Ar}$ ages obtained on minerals with different closure temperatures (Schaltegger et al., 2019) and the cooling paths inferred from plagioclase diffusion profiles (Chapter 4) are represented as comparison. The grey zones represent the uncertainty envelopes modelled using a Monte Carlo scheme.

are associated with large uncertainties, mainly because of the experimental uncertainties on F diffusivities (Li et al., 2020), they are comprised within the cooling rates obtained from local hornblende, mica and K-feldspar $^{39}\text{Ar}/^{40}\text{Ar}$ ages (Schaltegger et al., 2019), as well as Sr and Ba diffusion in plagioclase (Fig. 5.9c) (Chapter 4). Additionally, the modelled profiles reveal a progressive re-equilibration toward a completely flat profile, whereby the core Cl concentration slightly decreases before reaching equilibrium, while the outermost rim experiences an important Cl increase (Fig. 5.9a,b). This confirms that (1) diffusive re-equilibration during cooling is incomplete in apatite hosted in plagioclase rim and biotite, and (2) re-equilibrated apatite core compositions are very close to their initial F, Cl and OH contents. Indeed, the diffusion modelling reveals that, even after complete re-equilibration, the final core composition only differs by <10 % from its initial composition. Altogether, these observations demonstrate that apatite compositions from the Adamello batholith approach the parental melt volatile compositions and can be used to reconstruct the volatile evolution of the crystal-melt-fluid system.

5.7 Composition of melts

To calculate the equilibrium melt volatile composition using partitioning between apatite and melt (Li and Costa, 2020), the apatite crystallisation temperature must be determined as well as the melt F, Cl or H₂O composition. In the following, we first constrain the thermal evolution of the studied lithologies by using the apatite saturation temperature (Piccoli and Candela, 1994), the CaO-in-melt liquidus thermometer (Marxer and Ulmer, 2019), and the amphibole-plagioclase (Holland and Blundy, 1994) and Ti-in-quartz (Wark and Watson, 2006) thermometers. Then we parameterise apatite temperatures using texturally-controlled apatite compositions measured in thin sections. After determining the bulk F or melt H₂O contents using EPMA and the plagioclase hygrometer (Waters and Lange, 2015), respectively, we calculate the volatile composition of the melt in equilibrium with apatite.

5.7.1 Apatite crystallisation temperature

The calculated apatite saturation temperature (AST) is very sensitive to the P₂O₅ concentration (Piccoli and Candela, 1994), which can be shifted to higher values in apatite-rich cumulates. Detailed observations coupled with trace element modelling (Grocolas and Müntener, 2024) allowed to identify samples that kept a melt compositions suitable for AST calculation. The calculated AST are 857-911 °C for the Western Adamello tonalite

5. Volatile budget of magma reservoirs

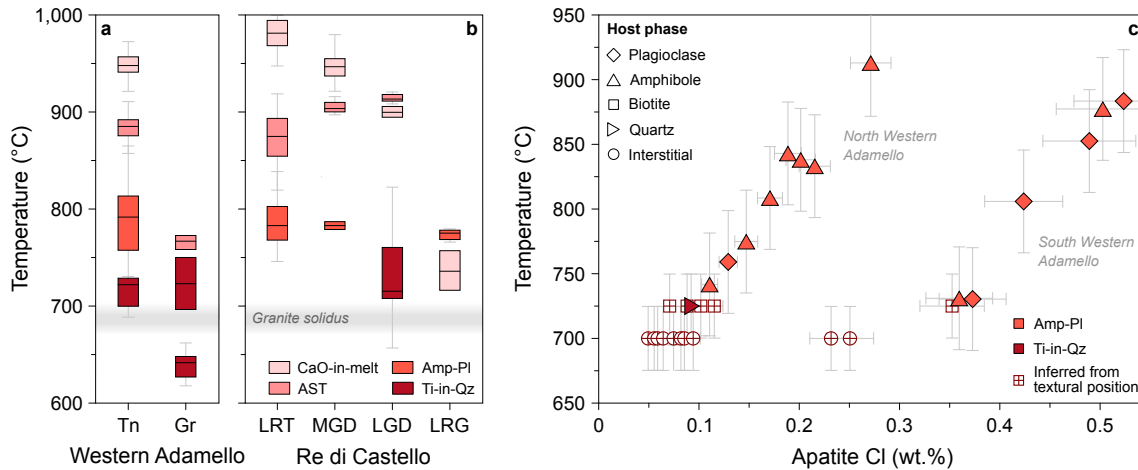


Figure 5.10. Calculation and parameterisation of apatite crystallisation temperature. Summary of temperature constraints obtained from various thermometers (Holland and Blundy, 1994; Marxer and Ulmer, 2019; Piccoli and Candela, 1994; Wark and Watson, 2006) applied on (a) the Western Adamello and (b) Re di Castello lithologies. c, Apatite Cl (wt.%) vs. apatite crystallisation temperature (°C) inferred from host phase crystallisation temperature either calculated using a geothermometer or inferred from the textural position of the host phase. Note the positive correlation between the apatite Cl content and its crystallisation temperature, and the difference between samples from the North and South of the Western Adamello unit.

and 848-919 °C for the Listino tonalite (Fig. 5.10a,b). The Monoccola and Laione granodiorites have similar AST of 877-916 °C and 908-919 °C, respectively. Finally, the calculated AST for the aplitic granite for both locations yield unreasonably high values ranging from 775 to 878 °C, probably owing to the presence of xenocrystic apatite. Errors in the calculated AST are ~ 7 °C, considering errors in the concentrations of SiO_2 (~ 0.4 % relative) and P_2O_5 (~ 0.5 % relative) from X-ray fluorescence (XRF) measurements. These results are in good agreement with crystallisation experiments of a tonalite at 200 MPa where apatite saturates at 900 °C (Marxer and Ulmer, 2019). The minimum AST of the parental melt associated with the antecrystic CO_2 -rich, S-poor apatite can be approximated by taking the highest AST calculated from the tonalitic melt (920 °C) as a minimum.

Sulphur-rich apatite from the pegmatitic granites probably crystallised at temperatures close or below the granite solidus. Based on Ti-in-quartz and CaO-in-melt thermometers, Grocolas and Müntener (2024) calculated the crystallisation temperatures of pegmatites from the Western Adamello and found temperatures ranging from 618 to 660 °C and 696 to 749 °C, respectively (Fig. 5.10a,b). The latter is sensitive to plagioclase accumulation and an addition of 5 % andesine would result in a temperature increase of ~ 30 °C. The application of the AST (758-772 °C) is also possible, although the effect of undercooling on apatite saturation and crystallisation is unknown. Amphibole-plagioclase and Ti-in-quartz temperatures probably represent the most reliable temperatures and will therefore

be used for further calculations.

To associate a temperature to each apatite grain, we use texturally-controlled apatite analysis coupled with amphibole-plagioclase (Holland and Blundy, 1994) or Ti-in-quartz (Wark and Watson, 2006) thermometry, as well as the crystallisation experiments of Marxer and Ulmer (2019) and the petrographic study of Grocolas and Müntener (2024) (Fig. 5.10c). It was demonstrated in these two studies that biotite and quartz phenocrysts crystallised at 725 ± 25 °C, while a temperature of 700 ± 25 °C was ascribed to alkali feldspar. As such, the apatite crystallisation temperature is parameterised as a function of its Cl content. Interestingly, the calculated and inferred crystallisation temperatures are correlated to the apatite Cl content, with a shift to higher Cl values for apatite originating from the southernmost Western Adamello (Fig. 5.10c). For the Re di Castello, where temperature constraints are fewer, we use the apatite saturation temperature from the Listino tonalite and Laione granodiorite and assume that apatite continuously crystallises until the system reaches the solidus, and parameterise it to the apatite Cl content. In detail, the apatite saturation temperature (900 °C) is ascribed to apatite with the highest Cl content, while the lowest Cl content is associated with near-solidus temperatures (700 °C). The temperature and Cl content are then assumed to evolve linearly. For the Re di Castello aplitic and pegmatitic granite, a temperature of 690 ± 20 °C is assumed.

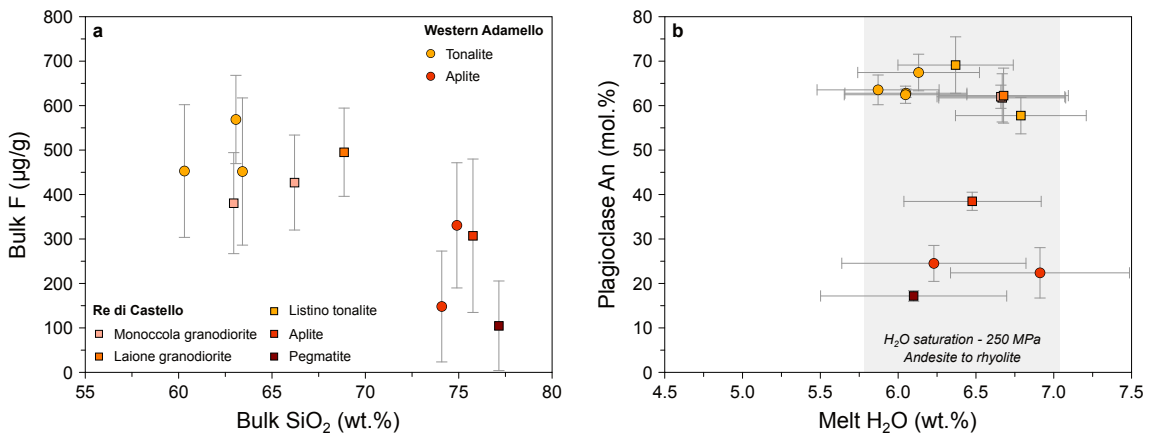


Figure 5.11. Determination of parental melt F and H₂O required to calculate absolute volatile concentrations using exchange coefficients. **a**, Bulk SiO₂ (wt.%) vs. F (µg/g) of the investigated lithologies. The bulk F content has been measured on melted powders by EPMA. **b**, Calculated melt H₂O (wt.%) vs. plagioclase An content (mol.%). The melt H₂O content has been calculated using the plagioclase hygrometer of Waters and Lange (2015). The error propagation accounts for the uncertainties on plagioclase and bulk rock composition, and plagioclase crystallisation temperature and pressure. The H₂O saturation surface was taken from Botcharnikov et al. (2015).

5.7.2 Initial F and H₂O melt contents

Measured bulk F concentrations in both Re di Castello and Western Adamello samples define a trend of decreasing F contents (570-100 µg/g) with increasing differentiation (SiO₂ = 60.3-77.2 wt.%) (Fig. 5.11a). In detail, tonalites from the WAT exhibit F contents of 438-574 ± 100 µg/g at ~60-63 wt.% SiO₂, which is slightly higher than the Monoccola (350-425 ± 70 µg/g F; ~63-66 wt.% SiO₂) and Laione (384 ± 120 µg/g F; ~69 wt.% SiO₂) granodiorites. Granites from both locations display similar compositions with a relatively large range of F contents (104-305 µg/g) at 74-77 wt.% SiO₂.

The melt H₂O content can be quantified using the plagioclase hygrometer of [Waters and Lange \(2015\)](#) which relies on plagioclase composition, crystallisation temperature and pressure, and bulk rock composition. Petrographic observations suggest that plagioclase starts crystallising at the liquidus in the studied tonalites and granodiorites. According to the CaO-in-melt thermometer experimentally developed by [Marxer and Ulmer \(2019\)](#), it corresponds to 922-973 °C for the Western Adamello tonalite, 948-1,000 °C for the Listino tonalite, 897-980 °C for the Monoccola granodiorite, and 894-936 °C for the Laione granodiorite. Errors in the calculated temperatures are ~50 °C, considering errors in the experimental regression and in the concentrations of CaO (~0.6 % relative) from XRF measurements. By combining these temperatures with pressures of 250-300 MPa ([Floess and Baumgartner, 2015](#)) and measured bulk rock and plagioclase compositions ([Grocolas and Müntener, 2024](#)), we find melt H₂O contents of 6.3 ± 0.3 wt.% for tonalites and granodiorites from both locations, and 6.5 ± 0.4 wt.% for aplitic and pegmatitic granites from both locations (Fig. 5.11b). These values correspond to H₂O saturation levels for intermediate to felsic melts at 250 MPa (e.g., [Botcharnikov et al., 2015](#)), indicating that these tonalites and granodiorites were fluid-saturated upon emplacement.

5.7.3 Calculation of melt composition

Using the determined apatite compositions and temperatures, we calculated the apatite exchange coefficients (K_D) for OH-F and OH-Cl. To calculate the absolute F, Cl and H₂O concentrations of the melts in equilibrium with apatite, we use (1) the calculated melt H₂O contents for both the CO₂-poor apatite compositions and S-rich apatite grains from the pegmatitic granites, and (2) the bulk F content for the CO₂-rich, S-poor apatites (Table 5.1).

To calculate the melt CO₂ concentrations, we employed the exchange coefficient from [Riker et al. \(2018\)](#) ($K_D = 0.629 \pm 0.08$), which has been experimentally determined for basaltic andesite compositions at 1,250 °C and 1 GPa. Substantially lower K_D values (0.04-

Table 5.1. Results of the crystal-melt-fluid fractionation model used to reproduce the volatile and isotopic compositions of the Western Adamello lithologies.

Partitioning	Range of values	Reference
<i>Apatite-melt</i>		
$K_D^{\text{OH/F}}$	0.01-0.001	Li and Costa (2020)
$K_D^{\text{OH/Cl}}$	0.02-0.07	Li and Costa (2020)
$K_D^{\text{Cl/F}}$	0.03-0.23	Li and Costa (2020)
$K_D^{\text{H}_2\text{O/CO}_2}$	0.629	Riker et al. (2018)
D_S	17-19	Parat and Holtz (2004, 2005)
<i>Melt-fluid</i>		
D_F	0.1-0.3	Webster et al. (2009)
D_{Cl}	160-380	
D_S	25-35	Ding et al. (2023)
$D_{\text{H}_2\text{O}}$	0.2	
D_{CO_2}	0.01	

0.08) have been inferred from melt inclusion and apatite equilibria at lower temperatures (950 °C) from Mount Erebus (Li et al., 2023). However, this has been done for a phonolitic melt composition in equilibrium with almost pure fluorapatite, and very low pressures (<200 MPa). Although the pressure and temperature conditions used by Riker et al. (2018) are probably too high for the investigated apatite grains, the extremely alkaline compositions of Mount Erebus reported by Li et al. (2023) preclude the use of their exchange coefficients.

Sulphur partitioning between apatite and melt has been demonstrated to vary with $f\text{O}_2$ (Konecke et al., 2019; Parat and Holtz, 2004, 2005). Arc-derived melts generally exhibit $f\text{O}_2$ values ranging from NNO to NNO+2 (e.g., Cottrell et al., 2021). The $f\text{O}_2$ has been evaluated using the biotite-feldspar-magnetite (Wones, 1972) and amphibole-only (Ridolfi et al., 2010) oxybarometers. To apply the oxybarometer based on biotite-feldspar-magnetite equilibria, average values for magnetite (Supplementary Material 4) and alkali feldspar (Grocolas and Müntener, 2024) were taken based on the absence of zoning in these phases. In addition, the alkali feldspar compositions were recalculated by adding the exsolved albite-rich plagioclase component to the measured alkali feldspar compositions ($\sim\text{Or}_{90}$), which resulted in an alkali feldspar composition of Or_{71} . Such recalculation resulted in a decrease of the calculated $f\text{O}_2$ by ~ 0.13 log-unit. To calculate oxygen fugacities from the oxybarometer of Wones (1972), the method of Li et al. (2019) was employed. As for the amphibole-only oxybarometer, the amphibole structural formulae were calculated using the method of Leake et al. (1997). The calculated $f\text{O}_2$ are similar using both methods, with an average ΔNNO value of 0.61 ± 0.24 obtained from the biotite-feldspar-magnetite oxybarometer, and 0.50 ± 0.58 for the amphibole-only oxybarometer (Supplementary Material 4).

5. Volatile budget of magma reservoirs

At such fO_2 , the sulphur speciation is dominated by the S^{6+} cation ($S^{6+}/\Sigma S > 0.6$) at high temperature (1,000 °C) and intermediate composition, but the S^{2-} cation dominates the sulphur budget ($S^{6+}/\Sigma S = 0.35-0.50$) at temperatures corresponding to apatite crystallisation (Supplementary Material 4) (Nash et al., 2019; O'Neill and Mavrogenes, 2022). The D_S values associated with the latter scenario range from 0.66 to 0.90 based on experiments performed at 300 MPa and using a very mafic starting material (Konecke et al., 2019). On the other hand, Parat and Holtz (2004, 2005) used a haplogranitic starting composition and performed crystallisation experiments at 200 MPa and NNO+3.6. For apatite S concentrations similar to the Western Adamello and Re di Castello, the calculated D_S values range from ~ 15 to ~ 19 . Since the low D_S values from Konecke et al. (2019) are derived from basaltic compositions and would yield melt S concentrations above sulphur saturation (Kleinsasser et al., 2022), which is not observed in the investigated samples, the D_S values from Parat and Holtz (2004, 2005) are used to calculate the melt S contents.

To keep the same differentiation proxy, the Eu anomaly of the melt in equilibrium with apatite has been calculated using the rare earth element partitioning between apatite and felsic, subalkaline melt of Brophy et al. (2011), Nagasawa (1970) and Watson and Green (1981).

Western Adamello

The melts in equilibrium with CO_2 -poor apatite from the Western Adamello were calculated using H_2O as a constant and define a trend of decreasing Cl (1,280-60 $\mu g/g$) and F ($\sim 350-90$ $\mu g/g$) with decreasing the melt Eu anomaly (1.20-0.18) (Fig. 5.12a,c). This volatile behaviour has previously been interpreted to reflect the preferential partitioning of Cl into the exsolving fluid phase, while F preferentially remains in the crystal-melt system (e.g., Webster et al., 2009). Therefore, this indicates that the tonalitic to granodioritic melts were fluid-saturated upon apatite saturation. The calculated melt S content ranges from <1 to ~ 60 $\mu g/g$ (Fig. 5.12e), which is below the sulphide (~ 190 $\mu g/g$) and anhydrite ($\sim 1,100$ $\mu g/g$) saturation levels (Kleinsasser et al., 2022), consistent with the absence of S-bearing phases in the studied samples. At low melt S concentrations (<5 $\mu g/g$), there is a correlation of decreasing melt S content with decreasing melt Eu anomaly, in line with the exsolution of a comparatively S-rich fluid phase. The highest melt S concentrations (10-60 $\mu g/g$) are associated with apatite from pegmatitic granite or crystal rims sampled in tonalite and hornblende-biotite-gabbro. These relatively S-rich melts exhibit a wide range of calculated CO_2 contents (70-14,500 $\mu g/g$), while the S-poor melts are systematically

CO₂-poor (30-1,980 µg/g). Such S-rich, tonalite- and gabbro-derived compositions might either be derived from (1) the addition of a fluid component upon crystallisation, or could represent (2) an initial fluid-undersaturated trend whereby the absence of a fluid phase

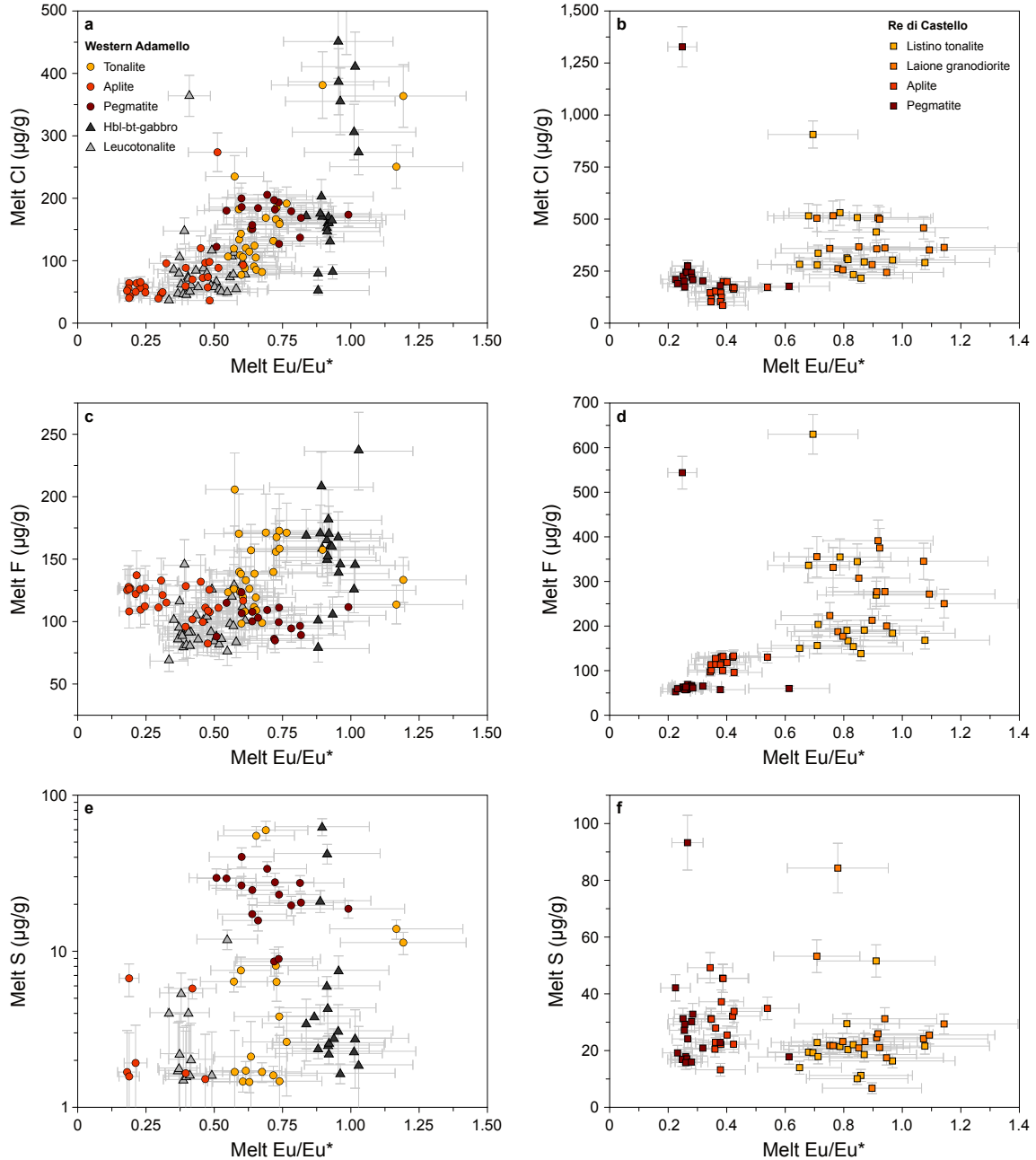


Figure 5.12. Volatile and trace element compositions of the calculated melt in equilibrium with apatite from the Western Adamello (a, c, e) and Re di Castello (b, d, f) lithologies. a, b, Melt Eu/Eu* vs. Cl (µg/g). Note the clear melt Cl decrease with decreasing the Eu anomaly in apatite from the Western Adamello and, to a lesser extent, the Re di Castello unit except for two CO₂-rich melt compositions. c, d, Melt Eu/Eu* vs. F (µg/g). The F content of the Re di Castello unit and, to some degree, the Western Adamello, melt compositions decreases with differentiation, except for the same two CO₂-rich compositions from the RdC. e, f, Melt Eu/Eu* vs. S (µg/g). The melt S contents reflect the apatite S contents.

5. Volatile budget of magma reservoirs

and the incompatible behaviour of S would result in an increase of the melt S content. However, the continuously decreasing melt Cl content with differentiation favours the former hypothesis. In such a scenario, the significance of calculating the composition of the melt in equilibrium with these pegmatite-hosted apatite grains remains unclear. Tracing the source of this pegmatitic dike would help clarifying this aspect; this will be achieved by analysing the Nd isotopes of the same apatite grains.

The CO₂-rich apatite cores from Western Adamello equilibrated with a melt having relatively high F contents (550-650 µg/g) and low S contents (<10 µg/g). Their melt Cl contents span a wide range of values (80-1,400 µg/g), with the lowest concentrations corresponding to apatite grains in granite and leucotonalite. The calculated melt H₂O and CO₂ contents are high and range from 6.9 to 8.7 wt.%, and from 1,900 to 7,600 µg/g, respectively.

Re di Castello

The calculated melts in equilibrium with apatite from Re di Castello span similar compositions as the Western Adamello melts, albeit with higher S contents. The Cl (530-120 µg/g) and F (410-45 µg/g) contents of the melt in equilibrium with CO₂-poor apatite decrease with decreasing melt Eu anomaly (1.15-0.22), with the highest Cl values corresponding to the Listino tonalite and Laione granodiorite, and the lowest to the pegmatitic granite (Fig. 5.12b,d). The calculated melt S contents from the Listino tonalite and Laione granodiorite (7-52 µg/g) is positively correlated to the melt Eu anomaly, while the calculated melt in equilibrium with apatite from granite spans a similar range of S contents (11-50 µg/g) but only covers a restricted range of Eu anomalies (0.23-0.52) (Fig. 5.12f). The melt CO₂ contents (40-2,800 µg/g) calculated from these CO₂-poor apatites exhibit the same range of values as the ones from Western Adamello.

The melt compositions calculated from the two CO₂-rich apatites from the Re di Castello superunit have high Cl (910-1,330 µg/g) and F (540-630 µg/g) contents. They have high CO₂ (2,200-7,200 µg/g) and H₂O (10.1-10.3 wt%) contents, while their S concentrations are rather low (17-19 µg/g).

5.8 Composition of fluids

To calculate the composition of the fluid in equilibrium with apatite and melt, the volatile partitioning between the melt and the fluid and the relative abundance of Cl⁻ compared to other Cl species in the fluid must be determined. In the following, we determine the F and S partition coefficients used to calculate the equilibrium fluid F and S composition, and

model the fluid total Cl concentration that is in equilibrium with apatite from the Western Adamello and Re di Castello, allowing a robust evaluation of the fluid Cl budget. The CO₂-rich, S-poor apatite compositions, most likely related to a deeper magma reservoir, are not discussed in this section.

5.8.1 Melt-fluid partition coefficients

Numerous studies have investigated the fluid-melt partitioning of F and S as a function of the melt composition, initial volatile concentration, temperature, pressure and fO_2 (e.g., Botcharnikov et al., 2004, 2015; Colin et al., 2020; Keppler, 2010; Lesne et al., 2011; Stelling et al., 2008; Webster, 1990, 1992; Zajacz et al., 2012). The experimental work of Webster (1990) revealed that, for felsic systems at 200 MPa, the F fluid-melt partitioning is strongly correlated to the melt F concentrations. However, at low melt F content (<1 wt.%), D_F is mainly controlled by temperature. Therefore, we use the available experimental data to parameterise D_F as a function of temperature, which results in D_F values ranging from ~ 0.35 at 950 °C to ~ 0.10 at 700 °C.

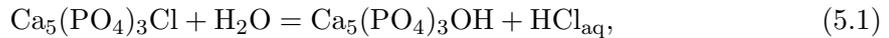
The fluid-melt partitioning of S has been demonstrated to be mainly dependent on fO_2 and melt composition (Colin et al., 2020; Fiege et al., 2015; Jégo and Dasgupta, 2013, 2014; Keppler, 2010; Lesne et al., 2011; Webster and Botcharnikov, 2011; Zajacz et al., 2012, 2013). A parameterisation of D_S based on numerous experimental works has been developed by Ding et al. (2023) and integrates the temperature, pressure, fO_2 and melt composition. By using the liquid line of descent model of Grocolas and Müntener (2024), an fO_2 of NNO+0.55, and the sulphur speciation model of O'Neill and Mavrogenes (2022), we find D_S values between 30 at 900 °C and 40 at 700 °C (Supplementary Material 4). However, melt oxidation during continuous crystallisation may instead lead to a decrease of D_S with differentiation. As such, we use a constant value of 30 ± 5 regardless of the temperature and melt composition.

5.8.2 Modelling the fluid Cl budget

Magmatic fluids are ubiquitous in hydrous magmatic systems and usually contain large amounts of chlorine (1-60 wt.% NaCl_{eq}) occurring either as chloride anions (Cl⁻) or associated to cations (e.g., NaCl, KCl, CaCl⁺) as a function of thermodynamic and chemical parameters (e.g., Helgeson et al., 1981; Sverjensky et al., 1997). Experimental studies investigating the partitioning of Cl between coexisting melt and fluid demonstrated that Cl is preferentially incorporated in the fluid phase (e.g., Iveson et al., 2018; Webster et al., 2009). However, these studies usually employ a chloridometer to quantify the concentra-

5. Volatile budget of magma reservoirs

tion of chloride ions in the fluid (Iveson et al., 2018; Mathez and Webster, 2005; Webster et al., 2009), thus ignoring the other Cl-bearing species. As such, we model the composition of the fluid in equilibrium with the mineral assemblage observed in the Western Adamello and Listino tonalites by writing dissolution and dissociation reactions (Supplementary Material 4) coupled to the thermodynamic database SUPCRTBL (Zimmer et al., 2016). The fluid total Al molality was constrained by assuming a sillimanite activity ($a_{\text{Al}_2\text{SiO}_5}$) of 0.5 for the temperature range of interest (700-900 °C), while the fluid HCl_{aq} molality was inferred from the apatite chemistry. This was done based on the following reaction (Eq. 5.1) and its equilibrium constant (Eq. 5.2):



$$\log K = \log a_{\text{Ca}_5(\text{PO}_4)_3\text{OH}} + \log a_{\text{HCl}_{\text{aq}}} - \log a_{\text{Ca}_5(\text{PO}_4)_3\text{Cl}} - \log a_{\text{H}_2\text{O}}. \quad (5.2)$$

By assuming that concentrations are equal to activities, and combining the measured apatite compositions with the equilibrium constant value obtained from the SUPCRTBL database, the fluid HCl_{aq} molality is inferred for a given temperature and pressure. The calculations reveal that the fluid HCl_{aq} content and the $\text{Cl}^-/\Sigma\text{Cl}$ ratio are very sensitive to the temperature. From 900 to 700 °C, the fluid HCl_{aq} molality decreases from $\sim 10^{-2}$ to $\sim 10^{-3}$ mol kg^{-1} , while the $\text{Cl}^-/\Sigma\text{Cl}$ ratio increases from ~ 1 to ~ 8 % (Supplementary Material 4). Finally, the fluid total Cl content is calculated by summing all the Cl species considered in the calculations.

5.8.3 Calculation of fluid compositions

Western Adamello

In the following, the fluid total Cl content is expressed as NaCl_{eq} , or fluid salinity, to allow comparison with fluid inclusion studies, whereby it is assumed that Cl only occurs as Cl^- anions associated with Na^+ cations. The calculated fluid compositions from apatite originating from the Western Adamello lithologies yield NaCl_{eq} values ranging from 4 to 12 wt.%, and define a positive correlation with the equilibrium melt Eu anomaly (Fig. 5.13a). This decrease in salinity with differentiation is well-documented (e.g., Cline and Bodnar, 1991; Hennings et al., 2017) and is typically ascribed to the preferential partitioning of Cl into the fluid phase, resulting in the initial exsolution of saline to hypersaline fluids. The fluid F content ranges from 6 to 53 $\mu\text{g/g}$ and generally decreases with the melt Eu anomaly (Fig. 5.13c). This is mainly due to the preferential affinity of F for the crystal-melt system (e.g., Webster et al., 2009). The calculated fluid S concentrations span more

than one order of magnitude, with the lowest concentrations ($\sim 30\text{-}200\ \mu\text{g/g S}$) associated with apatite probably derived from the differentiation of the tonalitic melt (Fig. 5.13e). On the other hand, the highest fluid S contents ($\sim 200\text{-}1,100\ \mu\text{g/g}$) were calculated from

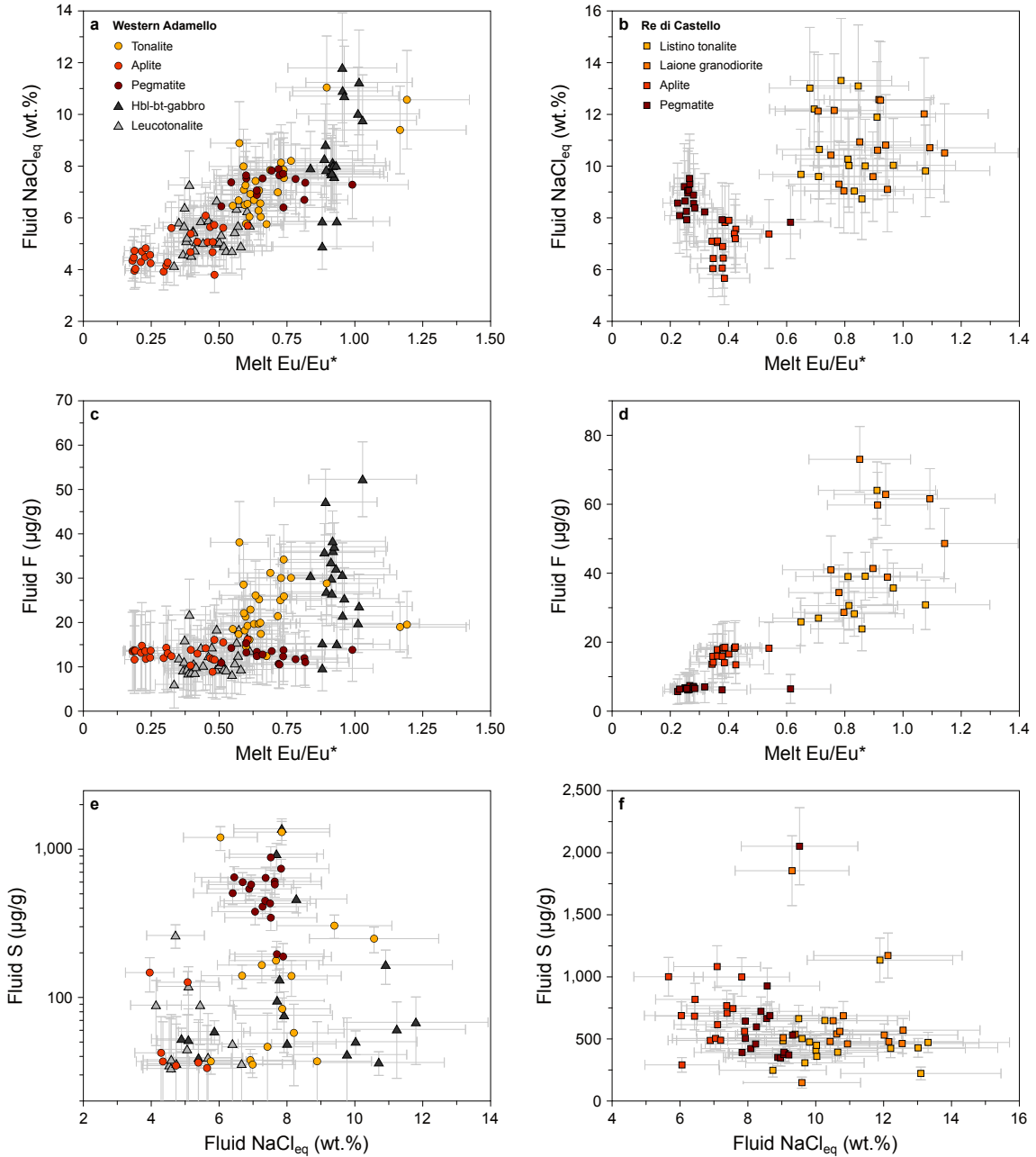


Figure 5.13. Fluorine, chlorine and sulphur composition of the calculated fluid in equilibrium with the calculated melt compositions from the Western Adamello (a, c, e) and Re di Castello (b, d, f) lithologies. a, b, Melt Eu/Eu* vs. fluid NaCl_{eq} (wt.%). Note the fluid NaCl_{eq} decrease with the equilibrium melt differentiation. c, d, Melt Eu/Eu* vs. fluid F (μg/g). A similar fluid F decrease with differentiation is observed. e, f, Fluid NaCl_{eq} (wt.%) vs. S (μg/g). The fluid S concentrations from the Western Adamello are one order of magnitude lower than in the Re di Castello unit. Note that the significance of the high-S fluid compositions from the Western Adamello pegmatite remains unclear (see text). The fluid compositions in equilibrium with the CO₂-rich apatite grains are not represented.

5. Volatile budget of magma reservoirs

apatite originating from crystal rims and pegmatitic granite. If these apatite grains indeed crystallised, at least partly, from a fluid, the significance of such values remains unclear.

5.8.4 Re di Castello

The modelled fluid compositions of the Re di Castello unit display NaCl_{eq} values ($\sim 6\text{-}14$ wt.%) very similar to the calculated fluids from the Western Adamello (Fig. 5.13b). A similar NaCl_{eq} decrease with differentiation is observed, except for the pegmatite-derived fluid compositions that have relatively high NaCl_{eq} contents ($\sim 8\text{-}10$ wt.%). The fluid F concentrations ($5\text{-}72$ $\mu\text{g/g}$) cover a similar range of values as the Western Adamello fluids and decrease with melt differentiation (Fig. 5.13d). Most of the calculated fluid compositions have S concentrations between 170 and 1,100 $\mu\text{g/g}$ and are uncorrelated to the fluid NaCl_{eq} (Fig. 5.13f). In addition, two fluid compositions have slightly higher S contents ($\sim 1,600\text{-}2,100$ $\mu\text{g/g}$) for intermediate NaCl_{eq} values ($\sim 9\text{-}10$ wt.%).

5.9 Modelling the crystal-melt-fluid system

As shown above, the apatite effectively records the melt volatile evolution and also tracks the presence of an exsolving magmatic volatile phase. In the following, we detail the methods used to model the volatile evolution of the crystal-melt-fluid system, and attempt to reproduce the calculated melt and fluid volatile compositions and the measured $\delta^{34}\text{S}$ signatures.

5.9.1 Model setup

To model the volatile evolution of the crystal-melt-fluid system, we employ a similar method as [Humphreys et al. \(2021\)](#) and [Stock et al. \(2018\)](#). The evolving melt composition is calculated using the fractional crystallisation equation ([Shaw, 1970](#)), and the equilibrium fluid composition is simply calculated using fluid-melt partitioning from the literature. The initial conditions were determined using the highest melt F, Cl and S values calculated from apatite compositions, and the H_2O and CO_2 concentrations corresponding to saturation at 250 MPa (e.g., [Burgisser et al., 2015](#)). Fractional crystallisation was applied to calculate the melt evolution at each step, and the excess H_2O and CO_2 was removed to keep the melt H_2O and CO_2 concentrations at the saturation level. The bulk crystal-melt partition coefficients for F, Cl and S were taken from [Callegaro et al. \(2020\)](#), [Dalou et al. \(2012\)](#), [Giesting and Filiberto \(2014\)](#), [Guggino \(2012\)](#), [Icenhower and London \(1997\)](#) and [Webster et al. \(2009\)](#). For H_2O , a value of 0.2 was chosen based on the difference between the

structural H₂O content of the tonalite and granodiorite samples (~1.2 wt.%, calculated from average biotite, amphibole and apatite compositions and mass balance) and H₂O saturation at 250 MPa (~6 wt.%). This value is in good agreement with different mineral-melt partitioning from the literature (e.g., Dalou et al., 2012; Hauri et al., 2006). A partitioning coefficient between melt and fluid of 0.01 was assumed for CO₂. As for the bulk fluid-melt partitioning, we use the same methods as discussed in a previous section, except for Cl whereby the partitioning was inferred from the relationship between the fluid and melt Cl contents that were calculated and modelled in previous sections. Since the parameterisation of the F fluid-melt partition coefficient is a function of temperature, each melt fraction is associated with a temperature following the temperature-melt fraction relationship of Grocolas and Müntener (2024). Because fluid is continuously exsolving, the final melt F, Cl and S composition is recalculated at each step by subtracting the amount of F, Cl and S incorporated into the fluid phase from the melt composition calculated using the fractional crystallisation equation.

The $\delta^{34}\text{S}$ evolution of the equilibrium melt and fluid for the Western Adamello and Re di Castello units was modelled using the Rayleigh fractionation equation. Several studies demonstrated that the S isotopic fractionation is strongly dependent on temperature and $f\text{O}_2$ (Fiege et al., 2014, 2015; Miyoshi et al., 1984; Taylor, 1986). For example, at relatively reducing $f\text{O}_2$ conditions ($<\text{NNO}+0.5$), the melt and fluid sulphur budgets are dominated by S^{2-} and H_2S , respectively (e.g., Burgisser et al., 2008), and the fractionation factor exceeds unity (Fiege et al., 2014). On the other hand, at oxidised $f\text{O}_2$ conditions ($>\text{NNO}+1$), the dominant sulphur species in the melt and fluid are SO_4^{2-} and SO_2 , respectively (e.g., Burgisser et al., 2008), and the fractionation factor is less than unity (Fiege et al., 2014). In addition, lower temperatures result in higher fractionation factors at low $f\text{O}_2$ and lower fractionation factors at high $f\text{O}_2$ (Supplementary Material 4). The $f\text{O}_2$ conditions of the Western Adamello and Listino tonalites have been estimated at $\sim\text{NNO}+0.5$, which corresponds to a $\text{S}^{6+}/\Sigma\text{S}$ ratio of 0.3-0.5 (e.g., O'Neill and Mavrogenes, 2022). The fractionation factors are then calculated based on the parameterisations of Fiege et al. (2015) for the $\text{H}_2\text{S}-\text{S}^{2-}$ and $\text{SO}_2-\text{SO}_4^{2-}$ pairs. The initial $\delta^{34}\text{S}$ compositions were inferred from the highest $\delta^{34}\text{S}$ values measured in tonalite-derived apatites, and are +11.9 ‰ for Western Adamello and +9.1 ‰ for Re di Castello.

5.9.2 Model results

In this section, we focus on the results of the S isotopic fractionation model because the volatile modelling was primarily made to verify the coherence of the crystallisation and ex-

5. Volatile budget of magma reservoirs

Table 5.2. Results of the crystal-melt-fluid fractionation model used to reproduce the volatile and isotopic compositions of the Western Adamello lithologies.

Melt fraction %	$\alpha^{\text{fluid-melt}}$	Melt S $\mu\text{g/g}$	Fluid S $\mu\text{g/g}$	Melt $\delta^{34}\text{S}$ ‰	Fluid $\delta^{34}\text{S}$ ‰
0.8	1.0031	6.50	111.8	11.88	15.00
0.7	1.0036	6.54	112.7	11.42	15.02
0.6	1.0041	6.48	112.1	10.82	14.98
0.5	1.0048	6.22	108.4	9.98	14.79
0.4	1.0050	5.65	99.7	9.22	14.29
0.3	1.0052	4.53	82.0	7.90	13.11
0.2	1.0053	2.59	50.2	4.69	10.04

solution model. The results of this model can, nevertheless, be found in the Supplementary Material 4. Prior to the rheological lock-up (i.e., <50 % crystallinity), the S content of the Western Adamello tonalitic melt remains constant ($\sim 5 \mu\text{g/g}$), while $\delta^{34}\text{S}$ slightly decreases (+12 to +10 ‰) (Fig. 5.14a and Table 5.2). With increasing differentiation, the evolving melt S content and $\delta^{34}\text{S}$ markedly decrease from ~ 5 to $\sim 1 \mu\text{g/g}$ and +10 to 0 ‰, respectively. At apatite saturation, the equilibrium fluid has relatively high S concentrations ($\sim 110 \mu\text{g/g}$) and $\delta^{34}\text{S}$ values (+15 ‰). With increasing crystallisation, the fluid S content rapidly decreases while $\delta^{34}\text{S}$ remains constant until the rheological lock-up. After >70 % crystallisation, the modelled fluid S and $\delta^{34}\text{S}$ composition overlaps with the measured

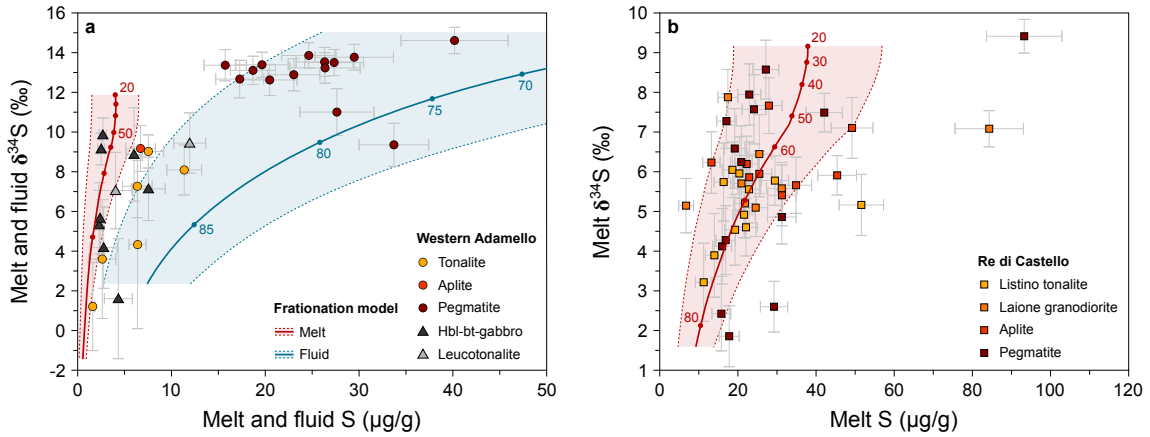


Figure 5.14. Modelling of the volatile and isotopic composition of the crystal-melt-fluid system plotted as melt (and fluid) S ($\mu\text{g/g}$) vs. melt (and fluid) $\delta^{34}\text{S}$ (‰) for the Western Adamello (a) and Re di Castello (b) superunits. The measured data are also represented. The modelling was done using a Rayleigh fractionation model and is represented as the evolution of the melt (red) and fluid (blue) compositions. The error envelopes account for different starting S contents, and the numbers correspond to the crystal fraction in the magma. Note that the model starts at 20 % crystallinity, which approximately corresponds to the magma crystallinity at the onset of apatite crystallisation. Most of the data are relatively well-reproduced by the melt evolution, while the modelled fluid evolution overlaps with the data from the Western Adamello pegmatite.

pegmatite-derived compositions. Interestingly, such crystal fractions have been identified as the window for melt segregation and extraction in the Western Adamello (Grocolas and Müntener, 2024). Therefore, one possible interpretation of the pegmatite-hosted apatite compositions is that they crystallised at the magmatic-hydrothermal transition and incorporated a fluid component. However, these apatite grains have similar Cl concentrations as apatite from tonalite, which is unexpected in a scenario whereby the pegmatite-derived apatites crystallised, at least partly, from a Cl-rich fluid. This could be explained by the difference in the partitioning behaviour of Cl and S. For example, the strong affinity of Cl for the fluid phase (e.g., Webster et al., 2009) and the competition with F to enter the apatite lattice might result in a limited Cl enrichment in apatite during crystallisation at the magmatic-hydrothermal transition. On the other hand, the highly oxidised conditions of most pegmatite-forming melts probably result in the predominance of the S^{6+} species that preferentially incorporates the phosphate crystallographic site (Konecke et al., 2017). This might result in a more compatible behaviour of S in apatite compared to Cl. Alternatively, these high- $\delta^{34}S$, S-rich apatite compositions might result from extreme differentiation in a highly oxidised environment, leading to an enhanced S^{6+} and ^{34}S incorporation into apatite. Although this could account for the high $\delta^{34}S$ values, the partitioning behaviour of S between apatite and melt of Parat and Holtz (2004, 2005) was determined at NNO+3.6, the highest fO_2 conditions observed in subduction-related magmas. Using higher D_S is therefore unreasonable. Finally, this pegmatitic granite could represent the coeval injection of an exotic melt into the active Western Adamello magma reservoir. In this case, the fractionation model reproducing these high S and $\delta^{34}S$ values would be a coincidence. Analysing and comparing the Nd or Sr isotopic composition of apatite from the tonalite-derived lithologies and the pegmatite would allow to distinguish between these two scenarios.

The same isotopic fractionation model has been applied to the Re di Castello lithologies, albeit with higher initial S concentrations ($38 \pm 20 \mu\text{g/g}$) and a lower melt initial $\delta^{34}S$ value (+9.1 ‰) (Fig. 5.14b). Similar to the Western Adamello model, the melt S concentration and $\delta^{34}S$ slowly decrease from 20 to 50 % crystallinity, and then decrease more rapidly until it reaches S concentrations of $\sim 10 \mu\text{g/g}$ and a $\delta^{34}S$ of +2 ‰ at 80 % crystallisation. Most of the calculated melt S contents and measured $\delta^{34}S$ values are reasonably reproduced by the fractionation model, except two compositions having higher S contents ($>80 \mu\text{g/g}$). Such a discrepancy may arise from a more heterogenous source or, alternatively, from the incorporation of a fluid component having high S concentrations. Regardless, this model highlights that the measured apatite compositions from the Re di

Castello, including the pegmatitic granite, most likely represent melt differentiation with no major fluid signature.

5.10 Comparison with fluid inclusion studies

The evolution of magmatic-hydrothermal fluids is commonly constrained through *in situ* analysis of fluid inclusions (e.g., [Audétat and Pettke, 2003](#); [Bodnar, 1995](#); [Reynolds and Beane, 1985](#); [Roedder, 1971](#)). These studies investigating the major and trace element signatures of fluid inclusions demonstrated that fluids from barren intrusions have lower metal concentrations than in mineralised systems and that the absolute metal concentration is linked to the fluid salinity ([Audétat and Pettke, 2003](#); [Audétat et al., 2008](#); [Bodnar, 1995](#)). This correlation was interpreted to be primarily caused by the formation of metal-complexing ligands with chloride in saline to hypersaline fluids. However, experimental studies focusing on the fluid-melt partitioning of Cu for a range of fluid S and Cl concentrations highlighted the variety of possible metal-complexing ligands involving Cl^- and S^{2-} anions ([Tattitch et al., 2015](#); [Zajacz et al., 2008](#)).

Experimental and natural fluid inclusion studies demonstrated that the fluid inclusion budget can either be (1) entirely represented by a single, intermediate density fluid, sometimes called a “supercritical fluid,” or (2) composed of low-density, NaCl-poor inclusions, hereafter termed as “vapour,” and comparatively high-density, NaCl-rich inclusions, hereafter referred to as “brine” ([Driesner and Heinrich, 2007](#); [Liebscher and Heinrich, 2007](#); [Shinohara, 1994](#)). The latter scenario occurs when fluid inclusions are entrapped at pressures below the miscibility gap between H_2O and NaCl (e.g., [Driesner and Heinrich, 2007](#)). To retrieve the initial fluid composition prior to exsolution, the transition from single- to two-phase fluid must have occurred in a closed system, and the distribution of the fluid inclusions of interest must be representative of the initial single-phase fluid. Evaluating these conditions and reconstructing the composition of the initial fluid is routinely done by a mass balance calculation between the vapour and brine phases for a large number of elements (e.g., [Audétat et al., 2008](#)).

In the following, we compare the S and NaCl_{eq} compositions of the fluid calculated from apatite with fluid inclusion data from barren and mineralised systems. The calculated fluid compositions from the Western Adamello tonalite-derived lithologies have low S concentrations ($\sim 25\text{--}110$ $\mu\text{g/g}$) and NaCl_{eq} contents ranging from 4 to 14 wt.% (Fig. 5.15). The fluid compositions in equilibrium with the Re di Castello apatites exhibit similar NaCl_{eq} ($\sim 6\text{--}16$ wt.%) and higher S ($\sim 170\text{--}2,000$ $\mu\text{g/g}$) contents compared to those calculated for the Western Adamello. These salinities are similar to the intermediate den-

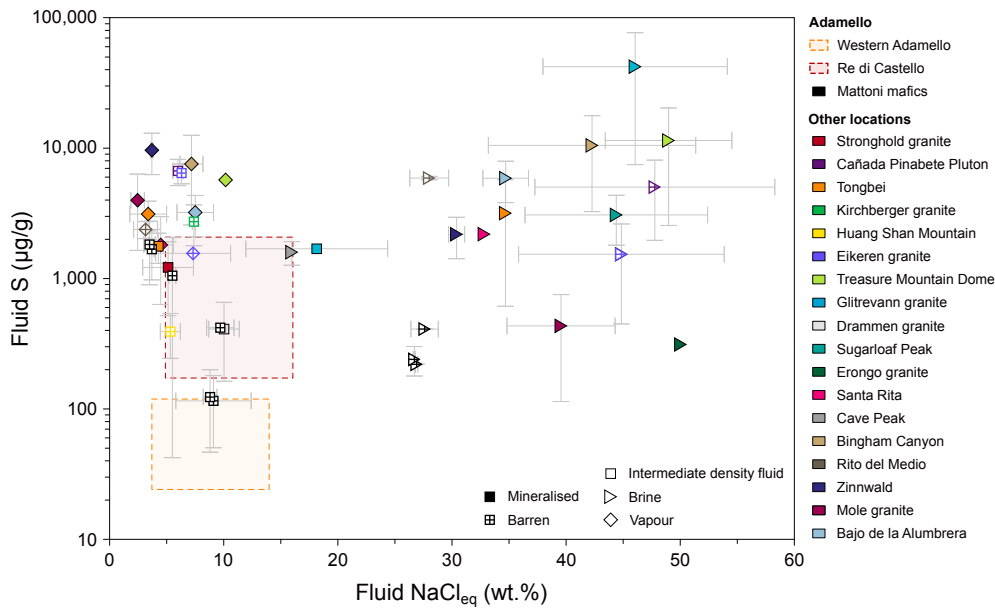


Figure 5.15. Comparison of the calculated fluid compositions from apatite with fluid inclusions data from the southern Re di Castello and other barren and mineralised systems, plotted as fluid NaCl_{eq} (wt.%) vs. S ($\mu\text{g/g}$). The symbol shapes account for the type of magmatic system, while each colour represents a given location. The apatite-derived fluid compositions are plotted as boxes encompassing the calculated range of compositions, and are similar to some intermediate density fluid inclusion compositions from barren and some mineralised systems.

sity fluid inclusion compositions from the Monte Mattoni and Cadino gabbros (southern Re di Castello) and other barren and mineralised systems (Fig. 5.15). This is in good agreement with the crystallisation pressure of tonalite-derived apatite (~ 250 MPa) being higher than the miscibility gap critical pressure (e.g., Driesner and Heinrich, 2007). Some NaCl_{eq} -rich vapour and a brine composition from Cave Peak (USA) also overlap with our calculated fluid compositions, while the other brine compositions exceed 25 wt.% NaCl_{eq} . The calculated fluid S contents are also similar to the intermediate density fluid inclusions from Monte Mattoni and Cadino (Hennings et al., 2017), as well as to intermediate density fluid inclusions from Huang Shan Mountain (China), Stronghold (USA) and Drammen (Norway) granites, and a vapour composition from Eikeren granite (Norway). Most of these fluid inclusion compositions were measured in barren systems, while mineralised systems tend to have higher fluid S concentrations, as outlined by Audétat et al. (2008). This comparison with fluid inclusion data highlights that (1) apatite composition can be used as a robust proxy to reconstruct the composition of the equilibrium magmatic fluid, and (2) since most magma reservoirs crystallise at pressures above the critical pressure of the H_2O - NaCl miscibility gap, apatite-derived fluid compositions represent actual compositions of single-phase, intermediate density fluid prior to immiscibility.

5.11 Impact of exsolving fluids on melt segregation

The developed model allows the quantification of the total amount of exsolved fluid and, by combining it with the average magma flux, calculation of the average rate of fluid exsolution. As previously discussed, the tonalitic parental melts from the Western Adamello and Listino ring complex were most likely H₂O-saturated upon emplacement in the upper crust. From this point to complete crystallisation, ~80 % H₂O, >95 % CO₂ and Cl, ~90 % S, and <10 % F is exsolved, which corresponds to ~3.9-4.4 wt.% of the bulk parental magma. By integrating it with the average magma fluxes inferred from high-precision zircon geochronology (Floess, 2013; Schoene et al., 2012; Verberne, 2013), the estimated total volumes of the Western Adamello (~300-400 km³) and Listino ring complex (~50-100 km³) units, and the parental melt density (~2,200-2,300 kg m⁻³), an average fluid flux of ~10⁷ kg yr⁻¹ is calculated. At 250 MPa and for the investigated temperature range (700-900 °C), the density of pure H₂O ranges from 440 to 570 kg m⁻³ (Helgeson and Kirkham, 1974), while addition of electrolytes slightly increases its density by <100 kg m⁻³ for concentrations relevant to this study (Helgeson et al., 1981). Considering the fluid density results in a volumetric average fluid flux of ~10⁻⁵-10⁻⁴ km³ yr⁻¹. This calculated fluid flux is at the lower bound of the measured degassing fluxes of modern volcanoes that range from ~10⁻⁴ to ~10⁻¹ km³ yr⁻¹ (Carn et al., 2017; Fischer et al., 2019).

Such low fluid flux is intimately linked to the relatively low magma flux in the Adamello batholith (Schaltegger et al., 2019) compared to active volcanic systems (e.g., Caricchi et al., 2014a). Despite the scarcity of volcanic products found in the vicinity of the Adamello batholith (Müntener et al., 2021), internal melt segregation has been widely documented in different units of the batholith (e.g., Grocolas and Müntener, 2024; Verberne, 2013). The granitic dike orientations perpendicular to the main stress direction in the vertically-emplaced Western Adamello (Grocolas and Müntener, 2024) and ballooning-related Listino ring complex (Brack, 1985; Verberne, 2013) suggest that melt segregation was primarily controlled by the local tectonic forces associated with magma emplacement. However, fluid exsolution and segregation forming oriented structures (Fig. 5.2b), probably linked to local shearing, might also contribute to melt segregation (e.g., Pistone et al., 2015; Sisson and Bacon, 1999). Indeed, the exsolution of a low-density fluid could theoretically lead to the extraction of a similar volume of material from the magma reservoir. This phenomenon was investigated by numerous studies and is controlled by the rate of melt supply and the viscosity of the surrounding crust (Caricchi et al., 2021; Degruyter and Huber, 2014). By comparing the surrounding crust deformation regime and the melt recharge rate, these studies derived a model predicting the main physical parameter caus-

ing diking and eruption. By using the inferred melt fluxes and volumes from the WAT and LRC, a critical overpressure of 20 MPa (Caricchi et al., 2021), a crust viscosity of 10^{19} - 10^{21} Pa s (Caricchi et al., 2021), and an upper crustal thermal diffusivity of 10^{-6} m² s⁻¹ (Whittington et al., 2009), we find that, for a relatively elastic crust, diking to eruption may occur and would be equally controlled by second boiling and magma recharge. On the other hand, a relatively viscous crust would lead to a large accommodation of the volume increase of the magma reservoir, inhibiting the system to reach the critical strain for eruption. It is therefore possible that continuously exsolving fluids, coupled to local stress related to magma recharge, contributed to the melt segregation and extraction in the Adamello batholith.

5.12 Reconstruction of plumbing system

Constraining the architecture of magma plumbing systems helps interpreting magmatic activity at the surface, monitoring data for eruption forecasting, and understanding the differentiation of the Earth's crust. Exposed crustal sections represent the most direct and accurate way to reconstruct magmatic systems, but these are scarce and located in remote regions (e.g., Burg, 2011; Greene et al., 2006). Alternatively, emplacement depths of magma reservoirs and pre-eruptive magma storage are routinely constrained using mineral-based geobarometry, melt inclusion, and/or geophysical techniques. However, most petrological and geophysical methods are associated with large uncertainties mostly due to geobarometer calibration and spatial resolution, respectively.

Mineral-based geobarometers are generally subdivided into mineral-only and mineral-melt geobarometers. The former gives the largest uncertainties (\sim 200-350 MPa) as the changes in partial molar volume of solid solutions are small with varying pressure (e.g., Putirka, 2008). Mineral-melt geobarometers are based on the pressure-dependent incorporation of some elements in a crystal lattice (e.g., Putirka et al., 1996), and are also associated with significant uncertainties (\sim 150-250 MPa). In addition, several other parameters must be considered: (1) some barometers require a buffer mineral assemblage to be applicable (e.g., Hammarstrom and Zen, 1986); (2) the equilibrium between crystals and melt can be difficult to assess and can evolve during magma ascent (Rutherford and Hill, 1993); (3) crystals are commonly zoned and, thus, in partial disequilibrium with the surrounding glass; and (4) volcanic eruptions can sample multiple crystal populations. The measurement of volatiles in melt inclusions, coupled to H₂O and CO₂ solubilities, represents a valuable tool to determine entrapment pressures. However, volatiles are generally subject to post-entrapment processes such as diffusive re-equilibration or bubble

5. Volatile budget of magma reservoirs

formation (e.g., [Buchholz et al., 2013](#)).

Geophysical methods identifying magma reservoirs are based on the inversion of signals transmitted through the crust and measured at the surface. Such geophysical imaging techniques typically include seismic tomography (e.g., [Dawson et al., 1990](#)) and magnetotelluric surveys (e.g., [Hill et al., 2009](#)), and allow examination of the temporal development of magmatic systems, magma movements, and estimates of melt sources and melt fractions. However, inversion of these geophysical data usually results in non-unique, relatively low-resolution images, and are rarely capable of distinguishing a crystal-dominated mush from completely consolidated igneous rocks. This primarily arises from the dependence of geophysical variables (elastic, magnetic, electric) on multiple physical parameters of magma reservoirs (temperature, melt fraction and connectivity, composition, exsolved gas).

In the following, we employ the H₂O and CO₂ composition of the calculated melt in equilibrium with apatite from the Western Adamello and Re di Castello units, and couple it with H₂O and CO₂ saturation curves calculated using the model of [Burgisser et al. \(2015\)](#). Most calculated melts have low CO₂ concentrations (<3,000 µg/g) at relatively high H₂O contents (6.0-6.7 wt.%), which corresponds to pressures ranging from 200 to 300 MPa at saturated conditions for dacitic to rhyolitic compositions (Fig. 5.16). These pressures correspond to an emplacement depth of 8-10 km and are in good agreement with the existing literature. Indeed, the widespread occurrence of andalusite in the Western Adamello contact aureole assemblage requires an emplacement pressure of 250-300 MPa ([Floess and Baumgartner, 2015](#)). Similarly, [Riklin \(1983\)](#) estimated an emplacement pressure of ≤220 MPa for the Re di Castello superunit based on the coexistence of andalusite and sillimanite within the contact aureole assemblage. [John and Blundy \(1993\)](#) modelled this metamorphic assemblage using the thermodynamic database of [Holland and Powell \(1990\)](#) and calculated a slightly higher pressure of 350 ± 50 MPa, within the same range of their Al-in-hornblende pressures (~350 ± 60 MPa).

A few apatite cores from the Western Adamello and Re di Castello units returned equilibrium melt compositions with high CO₂ (1,900-7,600 µg/g) and H₂O concentrations (6.9-10.3 wt.%). By considering the relatively large uncertainties associated with measurements and equilibrium melt calculation, such high volatile contents correspond to pressures ranging from 450 to 700 MPa at saturation conditions and for andesitic to dacitic compositions (Fig. 5.16). Although the H₂O content of the studied tonalites and granodiorites indicate that the tonalitic systems reached fluid-saturation prior to emplacement, it is difficult to evaluate the saturation level of these high-pressure melts. Therefore, the inferred pressures only represent minimum estimates. Interestingly, these pressures cover the range

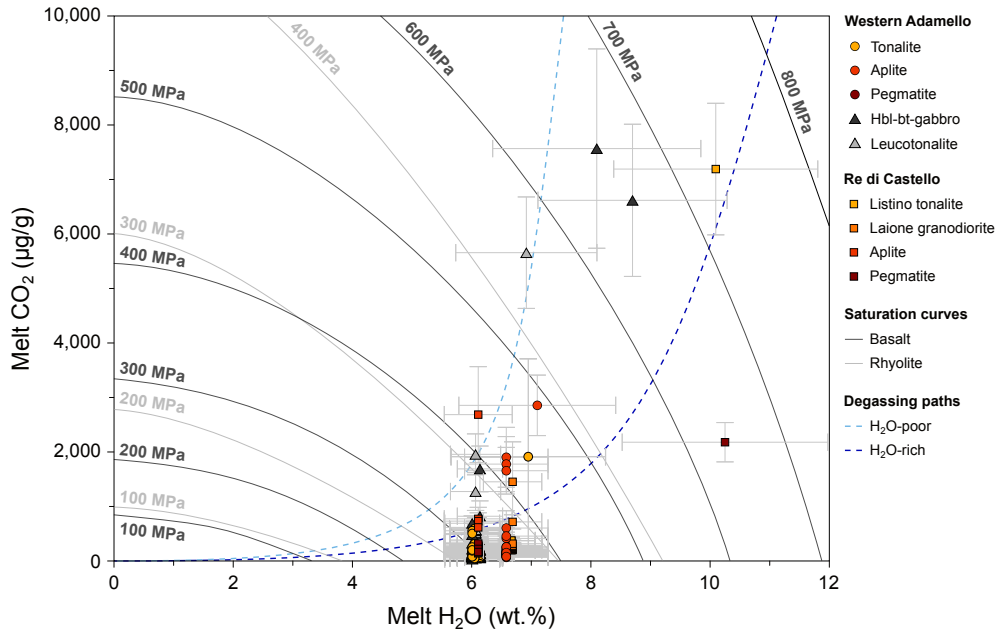


Figure 5.16. Calculated melt H₂O (wt.%) vs. CO₂ (µg/g) compositions used to infer the apatite crystallisation pressure. The melt compositions in equilibrium with the high-CO₂ apatite cores from both locations have high H₂O and CO₂ contents that correspond to minimum crystallisation pressures of 400-700 MPa for an intermediate composition. Isobars were calculated using the H₂O-CO₂ solubility model of Burgisser et al. (2015). Degassing paths were modelled to fit the calculated melt compositions, and the starting compositions correspond to pressures of ~800-1,000 MPa for a basaltic composition.

of calculated crystallisation pressures of phenocrystic amphibole present in post-plutonic andesitic to dacitic dikes in the Re di Castello superunit ($650-780 \pm 150$ MPa) (Hürlimann et al., 2016), suggesting that these apatite cores crystallised from a fluid-saturated melt.

To determine the source depth of the parental melt of these high-pressure apatite cores, we modelled degassing paths using the solubility model of Burgisser et al. (2015) for the Western Adamello and Re di Castello superunits. This method assumes that (1) fluid-saturation was reached early and maintained during differentiation, and (2) the calculated melts are cogenetic. Since this is uncertain, the inferred pressures only represent first-order estimates. The calculated melt compositions are bracketed by degassing paths with initial H₂O and CO₂ contents of 8.8-10.5 wt.% and ~16,000 µg/g, respectively (Fig. 5.16). This corresponds to pressures of ~800-900 MPa for a fluid-saturated basaltic liquid. Ulmer et al. (1983) and Blundy and Sparks (1992) interpreted the occurrence of hornblende-bearing gabbro to hornblendite at Monte Mattoni (Re di Castello superunit) as reflecting high-pressure crystallisation (800-1,000 MPa). More specifically, the crystallisation of hornblende prior to plagioclase returns a minimum crystallisation pressure of 700 MPa (Grove et al., 2003; Nandedkar et al., 2014). Similarly, Jossevel (2018) documents a hornblendite enclave having pargasitic crystal cores in the Western Adamello tonalite,

5. Volatile budget of magma reservoirs

comparable to the hornblendite unit at Monte Mattoni.

Overall, the calculated melts in equilibrium with apatite allowed reconstruction of the Adamello magmatic system with the identification of (1) the melt source in the lower crust (800-1,000 MPa), (2) a first step of apatite crystallisation in the middle to lower crust (400-650 MPa) which is related either to cooling of a mid-crust magma reservoir or to crystallisation during decompression, and (3) a second step of apatite crystallisation during cooling of the tonalitic melt (250-300 MPa). The occurrence of these CO₂-rich apatite cores having crystallised from a fluid-saturated (8 to >10 wt.% H₂O) dacitic melt in the middle to lower crust highlights the hydrous to superhydrous character of the parental to primitive melts of the Adamello batholith, as previously suggested by Müntener et al. (2021). Early fluid saturation in the lower crust leads to continuous fluid emission in the crustal column and, therefore, loss of fluid-mobile element such as Cl, Cu and S. This phenomenon would dramatically reduce the potential to form ore deposits and could explain the absence of mineralisation in the Adamello batholith.

5.13 Conclusions

The apatite compositions from the Adamello batholith have been used to quantify the volatile budget of the crystal-melt-fluid system as it evolves during differentiation (Fig. 5.17). Detailed petrography revealed that apatite saturates close to the tonalite and granodiorite liquids and continuously crystallises until the system reaches the solidus. Compositional profiles allowed the identification of different degrees of re-equilibration with more diffused profiles in early-crystallising phases. Modelling of these diffusion profiles resulted in cooling rates reasonably similar to the cooling paths inferred from plagioclase zoning. Together with the incomplete re-equilibration of apatite with host biotite, this suggests that apatite from the Adamello batholith records the volatile composition of its parental melt. Based on the volatile composition of apatite, three populations have been identified: (1) a volumetrically-dominant CO₂-poor population having low to intermediate S concentrations that crystallised from the tonalitic to granodioritic melts; (2) rare, CO₂-rich apatite cores with low to intermediate S contents that most likely crystallised from a CO₂-rich melt at higher pressures; and (3) S-rich, high- $\delta^{34}\text{S}$ apatite grains originating from a pegmatitic granite from the Western Adamello (Fig. 5.17) that either crystallised (1) at the magmatic-hydrothermal transition or (2) from an exotic, unrelated magma. The calculated melt compositions have decreasing F, Cl and S contents with differentiation, in good agreement with the partitioning of Cl into exsolving fluids. These equilibrium fluid compositions have salinities ranging from ~ 4 to ~ 16 wt.% NaCl_{eq}, which is similar to the

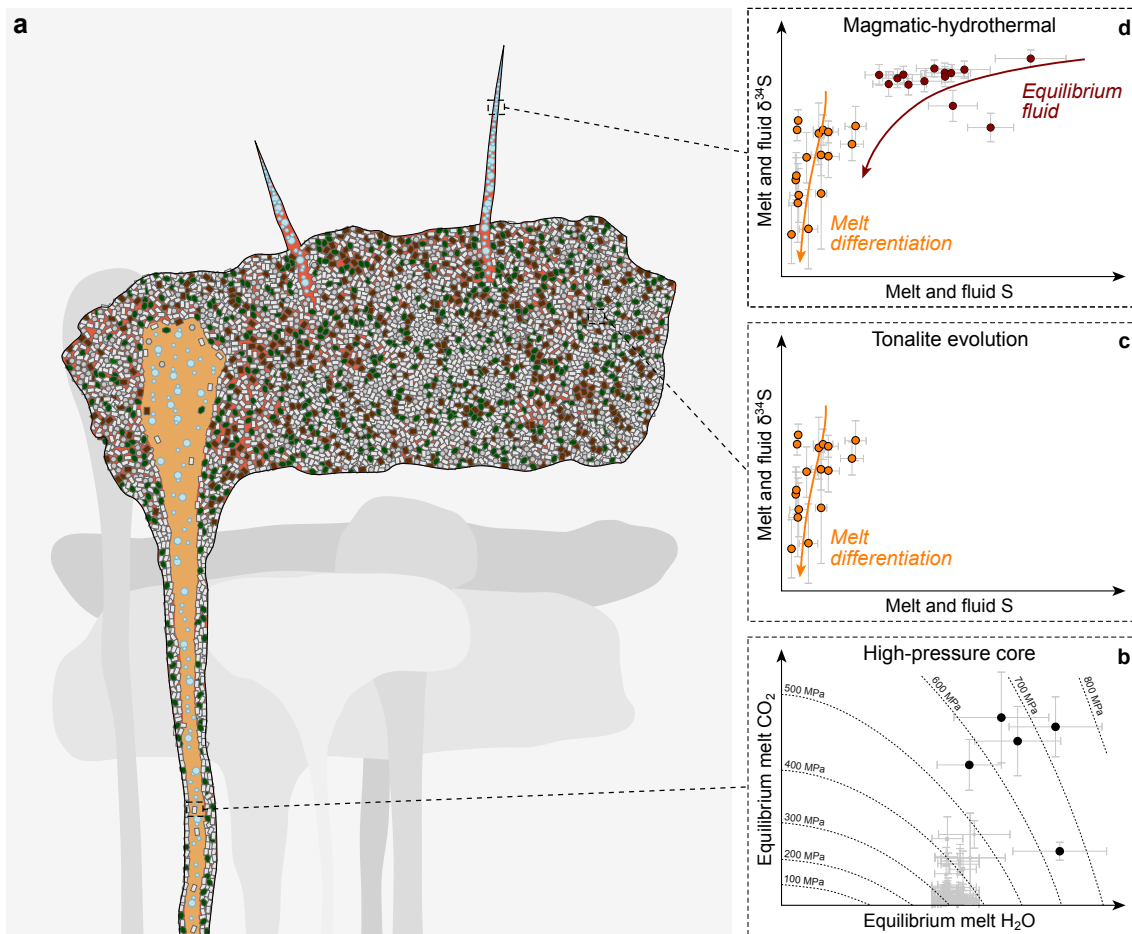


Figure 5.17. Summary of the main findings based on the volatile signature of apatite. **a**, Schematic model of the middle to upper crustal magmatic system of the Western Adamello and Listino ring complex units, showing a major reservoir in the upper crust undergoing fluid exsolution, melt extraction in its upper part and magma recharge in its lower part. **b**, Crystallisation of the high-CO₂ apatite cores at deeper levels of the crust, for example as a result of magma decompression, from an H₂O- and CO₂-rich parental melt. **c**, Evolution of the main tonalitic to granodioritic body materialised by a melt S and $\delta^{34}\text{S}$ decrease with increasing differentiation. **d**, A possible explanation of the high-S and $\delta^{34}\text{S}$ apatite from the Western Adamello pegmatite is the incorporation of a fluid component at the magmatic-hydrothermal transition that has high S concentrations coupled with high $\delta^{34}\text{S}$ values.

intermediate density fluid inclusions from barren and mineralised systems. Furthermore, modelling of the melt and equilibrium fluid S and $\delta^{34}\text{S}$ compositions revealed that the tonalite- and granodiorite-derived compositions are well-reproduced by differentiation of an initially high- $\delta^{34}\text{S}$ melt, while the pegmatite signatures are reproduced by the equilibrium fluid composition after 70-85 % crystallisation. Such high $\delta^{34}\text{S}$ initial values are probably inherited from the mantle source and/or the early differentiation path of the Adamello parental melts, as a difference in $\delta^{34}\text{S}$ would be expected between the Western Adamello and Re di Castello superunits if contamination was the dominating process controlling $\delta^{34}\text{S}$. Calculations of the average flux of fluid exsolution and the conditions

5. Volatile budget of magma reservoirs

for diking and eruptions reveal that melt segregation in the Adamello batholith results from a combination of magma recharge and fluid-driven filter pressing. Finally, by coupling the calculated melt H₂O and CO₂ contents with experimental saturation curves, the crystallisation pressure of the CO₂-rich apatite cores have been constrained between 400 and 650 MPa. Altogether, this suggests that apatite represents a reliable proxy to track the crystal-melt-fluid system and can be used to identify fluid saturation, evaluate the economic potential of magma reservoirs, and reconstruct the architecture of magmatic plumbing systems.

Chapter 6

General conclusions and perspectives

The aim of this thesis was to investigate the processes and timescales of crystal accumulation and associated melt segregation and extraction that operate in upper crustal magma reservoirs, with an emphasis on the plutonic rocks from the calc-alkaline Adamello batholith (Italy). A detailed field and petrographic study has been performed in order to document the liquid line of descent and crystallinity evolution with melt fraction, and quantify the amount of crystal accumulation and extracted interstitial melt. To precisely constrain the timescales of melt segregation and extraction, new Sr and Ba diffusivities in plagioclase have been determined through 1-atm diffusion experiments performed for a range of temperatures, plagioclase compositions, crystallographic orientations, and silica activities. Compositional zoning patterns of crystals originating from tonalites and granodiorites from the Adamello batholith, as well as from *in situ* cumulates were characterised using microanalytical techniques. Major and minor element distributions in plagioclase and alkali feldspar were determined using a combination of backscattered electron (BSE) imaging and electron probe microanalysis (EPMA). As for trace element profiles, these were characterised using laser ablation inductively coupled plasma mass spectrometry (LA-ICP-MS), secondary ion mass spectrometry (SIMS), and nanoscale secondary ion mass spectrometry (NanoSIMS). Modelling of diffusion re-equilibration was then conducted using appropriate initial conditions, boundary conditions and diffusion coefficients, including the ones determined in this study, to estimate cooling rates of the plutons and timescales of crystal-melt segregation. Finally, the volatile budget of the crystal-melt-fluid system has been investigated through *in situ* analysis of apatite using EPMA and SIMS. The results of this study and some suggestions for further work are summarised in this

chapter; more detailed conclusions are given in Chapters 2 to 5.

6.1 K-bearing phase in granitoids: Biotite vs. alkali feldspar

The occurrence of an amphibole-consuming, biotite-producing peritectic reaction in felsic melts has been inferred by [Marxer and Ulmer \(2019\)](#) through crystallisation experiments of the tonalite of Malga Listino (Re di Castello, Adamello batholith) at 200 MPa. In the investigated samples from the Western Adamello, which mainly consists of a coarse-grained medium-K tonalite, amphibole occurs as phenocryst locally replaced by biotite. Interestingly, such amphibole-consuming, biotite-producing reaction almost went to completion in the northern part of the Western Adamello, where the bulk tonalite is more differentiated and has a higher aluminium saturation index (ASI). Based on a compilation of bulk rock data from the metaluminous to slightly peraluminous Peninsular Ranges batholith (Mexico and USA) and metaluminous, alkali feldspar megacryst-bearing, K-rich Tuolumne Intrusive Suite (Sierra Nevada, USA), a relationship between the aluminium saturation index (ASI) and the dominating potassium-bearing phase has been proposed. During equilibrium crystallisation, peraluminous interstitial melts react with amphibole to form biotite and quartz (\pm plagioclase), whereas amphibole remains stable in metaluminous melts and alkali feldspar becomes the dominating potassium-bearing phase. In addition to ASI, lower H₂O and higher normative orthoclase compositions probably favour the crystallisation of alkali feldspar instead of biotite. Such a hypothesis is supported by experimental studies whereby alkali feldspar is virtually absent from slightly peraluminous, H₂O-rich systems ([Johannes and Holtz, 2012](#); [Marxer and Ulmer, 2019](#); [Piwinskii, 1968](#)), while alkali feldspar megacrysts occur in metaluminous environments and starts crystallising at temperatures as high as ~ 760 °C ([Johnson and Rutherford, 1989](#); [Moore and Sisson, 2008](#)) (Fig. 6.1).

Regardless of the prevailing crystallisation regime, this crystallisation step is systematically associated with a rapid decrease in crystallinity for a given temperature interval ([Johnson and Rutherford, 1989](#); [Marxer and Ulmer, 2019](#); [Piwinskii, 1968](#)), potentially counterbalanced by the large release of latent heat of crystallisation (e.g., [Blatter et al., 2017](#); [Ussler III and Glazner, 1992](#)). [Lee et al. \(2015\)](#) investigated the impact of latent heat of crystallisation on the crystallinity evolution using thermal modelling and demonstrated that although the latent heat of crystallisation slows the cooling rate, it does not completely compensate for the crystallinity decrease over such a small temperature window. Furthermore, the onset of the biotite peritectic reaction in the Adamello and the saturation of alkali feldspar in the Tuolumne Intrusive Suite ([Moore and Sisson, 2008](#))

6.1. K-bearing phase in granitoids: Biotite vs. alkali feldspar

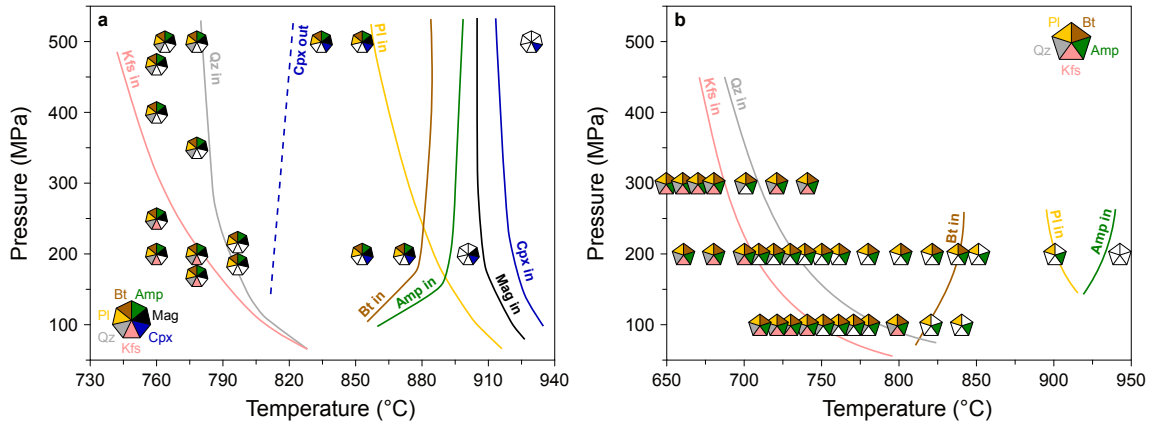


Figure 6.1. Pressure-temperature phase diagrams with phase assemblages and mineral saturation curves summarising the results of previous experimental studies. **a**, Result of equilibrium crystallisation experiments using a starting material having the Fish Canyon Tuff bulk composition and a fluid X_{H_2O} of 0.5. Figure modified after [Johnson and Rutherford \(1989\)](#). **b**, Result of equilibrium crystallisation experiments using a granodiorite from the Central Sierra Nevada with 15 wt.% H_2O as a starting material. Figure modified after [Piwinski \(1968\)](#). Each hexagon represents a single experiment and small coloured triangles illustrate the presence (coloured) and absence (empty) of stable mineral phases. *Amp*, amphibole; *Bt*, biotite; *Cpx*, clinopyroxene; *Kfs*, K-feldspar; *Mag*, magnetite; *Pl*, plagioclase; *Qz*, quartz.

correspond to temperatures close to the rheological lock-up, whereby crystals form a continuous framework of touching minerals ([Cashman et al., 2017](#); [Marsh, 1981](#)). This holds important implications for the ability of magma reservoirs to segregate interstitial melt, as a rapid crystallinity decrease would significantly reduce the window for crystal-melt segregation.

Future work should focus on determining the stability of biotite and alkali feldspar in intermediate to felsic magmas for a range of bulk compositions. This could be achieved by (1) systematically characterising the equilibrium assemblage of intermediate to felsic plutonic rocks worldwide, or (2) performing crystallisation experiments using metaluminous and slightly peraluminous felsic starting materials at middle to upper crustal conditions. Other parameters should be explored, such as the melt a_{H_2O} which could potentially stabilise a hydrous phase such as biotite relative to alkali feldspar ([Johnson and Rutherford, 1989](#)). Such studies should also document the relationship between crystal fraction and temperature to gain knowledge regarding the eruptive potential of a magma reservoir as a function of its initial bulk composition. Finally, direct measurements of latent heat using a calorimeter during melting and/or crystallisation experiments (e.g., [Lange et al., 1991, 1994](#)) would allow a robust quantification of the effect of latent heat of crystallisation close to the rheological lock-up.

6.2 Role of source powders and mineral stability on diffusion experiments

Recent experimental works investigating the diffusion rate of Ti in quartz (Audétat et al., 2021; Jollands et al., 2020) suggest that the high Ti concentration within the source powder of previous experimental studies (Cherniak et al., 2007) created a strong reaction between the crystal and its surrounding powder, therefore questioning the use of these diffusion coefficients. The existing data on Sr and Ba diffusivities in plagioclase (Cherniak and Watson, 1992, 1994; Cherniak, 2002) also employed similar concentrations levels (>30 wt.%) for Sr and Ba, suggesting that similar surface processes could occur in these experiments. Therefore, 1-atm diffusion experiments were performed, whereby oriented labradorite and oligoclase crystals were embedded in an Sr- and Ba-doped source powder consisting of an $a\text{SiO}_2$ -controlled, sol-gel-derived stable assemblage. The retrieved diffusion coefficients follow an Arrhenius relationship with similar diffusion rates for Sr and Ba. Interestingly, the new Ba diffusion coefficients (Grocolas et al., in review) are similar to the ones of Cherniak (2002), whereas Sr diffuses ~ 2 orders of magnitude slower than previously thought (Cherniak and Watson, 1992, 1994; Giletti and Casserly, 1994). In order to understand this discrepancy, the experiments of Cherniak and Watson (1992, 1994) and Cherniak (2002) were reproduced, with an emphasis on the assemblage present in the source powder. X-ray diffractometry (XRD) analysis revealed that the annealed Ba-doped source powder contained Ba-feldspar, a stable phase between room temperature and 1,500 °C at 1 atm, whereas the annealed Sr-doped source powder only contained the original Sr oxide since Sr-feldspar is only stable at temperatures above 1,150 °C. This highlights (1) the importance of precisely constraining the source of the diffused elements, and (2) the independence of Ba diffusion upon source concentration.

Future work should investigate the role of pressure and H_2O fugacity ($f\text{H}_2\text{O}$) on diffusion rates. Indeed, magmatic and metamorphic systems occur at higher pressures and usually have higher $f\text{H}_2\text{O}$. Experimental studies investigating the CaAl-NaSi interdiffusion in plagioclase at higher pressure and $f\text{H}_2\text{O}$ (Liu and Yund, 1992; Yund, 1986; Yund and Snow, 1989) retrieved interdiffusion coefficients three to four orders of magnitude higher than dry experiments performed at 1 atm (Grove et al., 1984) and 1.5 GPa (Yund, 1986) (Fig. 6.2). Similarly, Costa and Chakraborty (2008) performed experiments focusing on Si and O diffusion in olivine at high pressure and $f\text{H}_2\text{O}$, and others at atmospheric conditions. Their results show that diffusion operates three orders of magnitude faster at high pressure and $f\text{H}_2\text{O}$ for Si, and one order of magnitude faster for O, compared to diffusion

6.3. Diffusion timescales in plutonic rocks: Assembly processes vs. eruption triggering

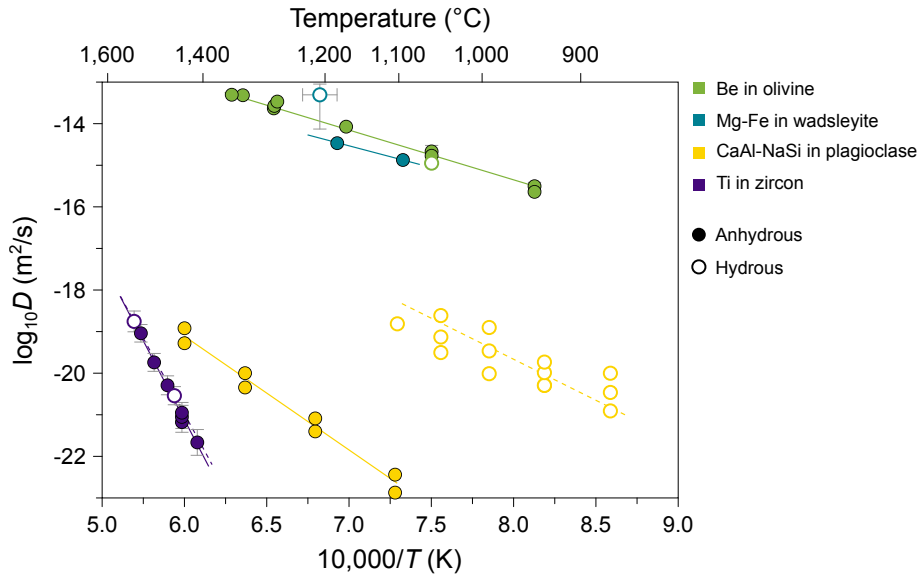


Figure 6.2. Compilation of experiments investigating the role of $f\text{H}_2\text{O}$ on the diffusion rates of Be in olivine (Jollands et al., 2016b), Mg-Fe in wadsleyite (Chakraborty et al., 1999; Kubo et al., 2004), CaAl-NaSi in plagioclase (Grove et al., 1984; Yund and Snow, 1989), and Ti in zircon (Cherniak and Watson, 2007). Note the difference in diffusivities between hydrous and anhydrous systems for Mg-Fe in wadsleyite and CaAl-NaSi in plagioclase, by ~ 1 and ~ 4 orders of magnitude, respectively.

at 1 atm. On the other hand, other studies using a similar approach found no clear evidence for pressure and H_2O dependence (Fig. 6.2) (e.g., Béjina et al., 1997; Cherniak and Watson, 2007; Jollands et al., 2016b). As such, it is critical to determine the impact of increasing pressure and $f\text{H}_2\text{O}$ on diffusion coefficients for each diffusion system, such as Sr and Ba in plagioclase.

6.3 Diffusion timescales in plutonic rocks: Assembly processes vs. eruption triggering

The Western Adamello and southern Re di Castello units contain plagioclase crystals recording three crystallisation events, with (1) resorbed high-An cores that probably formed at higher pressures, (2) volumetrically dominant crystal mantle with intermediate An contents, and (3) thin, low-An crystal rims that crystallised from the evolved interstitial melt. Additionally, Ba-zoned alkali feldspar oikocrysts hosting normally-zoned quartz occur in the Laione granodiorite from the Re di Castello unit. The cooling paths of the investigated lithologies was modelled based on the alkali-feldspar, quartz, and plagioclase mantle-to-rim compositional profiles using diffusion coefficients from the literature (Audétat et al., 2021, 2023; Cherniak and Watson, 1992, 1994; Cherniak, 2002; Cherniak et al., 2007; Giletti and Casserly, 1994; Jollands et al., 2020) and Chapter 3. The retrieved

6. General conclusions and perspectives

cooling paths overlap with the local $^{39}\text{Ar}/^{40}\text{Ar}$ ages from previous studies, therefore confirming the robustness of the newly-determined diffusion coefficients. On the other hand, using the diffusion coefficients of [Audétat et al. \(2023\)](#), [Cherniak and Watson \(1992\)](#), [Cherniak and Watson \(1994\)](#), [Cherniak et al. \(2007\)](#) and [Giletti and Casserly \(1994\)](#) results in a discrepancy of 1 to 3 orders of magnitude with the $^{39}\text{Ar}/^{40}\text{Ar}$ ages. Furthermore, the plagioclase core-to-mantle profiles were used to infer crystal residence times prior to melt segregation, and resulted in timescales ranging from $\sim 10^4$ to $\sim 10^5$ years, similar to the Western Adamello tonalite lifespan inferred from high-precision zircon geochronology ([Floess, 2013](#)). Interestingly, the retrieved crystal residence times are also similar to the lifespan of volcanic and plutonic systems inferred from zircon geochronology (e.g., [Schoene et al., 2012](#); [Wotzlaw et al., 2014](#)), and the crystal residence times of sanidine and quartz derived from diffusion modelling ([Brückel et al., 2023](#); [Rout et al., 2021](#); [Wang et al., 2023](#)). Such similarities suggest that these timescales of tens to hundreds of thousands of years represent the sweet spot for assembling a thermally stable magma reservoir able to internally segregate and externally injected interstitial melt.

Owing to the growing knowledge on cation diffusion mechanisms and rates in olivine, numerous authors attempted to extract timescales from olivine compositional profiles (e.g., [Chakraborty, 2010](#)). However, these studies usually focus on the outermost rim of olivine crystals and, therefore, the retrieved timescales only record the magmatic event directly preceding volcanic eruption and ignore the parental melt differentiation (e.g., [Hartley et al., 2016](#); [Lynn et al., 2017](#); [Pan and Batiza, 2002](#)). Since zircon is scarce in mafic magmas and only saturates at relatively high crystallinities in mafic systems ([Watson and Harrison, 1983](#)), diffusion represents the most viable option to retrieve the timespan between melt injection in the magma reservoir and the eruption event. Although diffusion re-equilibration operates at much faster rates in high-temperature mafic magmas compared to felsic systems, future work should focus on the history of crystal cores with an emphasis on slow-diffusing elements such as phosphorus ([Devoir et al., 2021](#); [Watson et al., 2015](#)). A recent study investigating the major element and phosphorus distribution in a Kīlauea olivine concluded that, despite diffusion re-equilibration operating for ~ 6 months at $1,225^\circ\text{C}$, phosphorus remained largely immobile ([Shea et al., 2015](#)). It was recognised that mixing-to-eruption timescales increase from weeks to years in mafic systems, to decadal to centennial in felsic systems ([Costa et al., 2020](#)). Focusing on the whole crystal record of mafic systems would shed light on the igneous differentiation timescales of the lower to middle crust.

6.4 The volatile archive of apatite in plutonic rocks

Owing to the recent parameterisation of the volatile partitioning between apatite and melt (Li and Costa, 2020), apatite became a powerful tool to characterise the volatile evolution of the crystal-melt-fluid system. The main applications comprise quantifying the volatile concentrations of the equilibrium melt (Li et al., 2021; Sharpe et al., 2022), identifying the presence of an exsolving fluid (Huang et al., 2024; Humphreys et al., 2021; Keller et al., 2023; Lormand et al., 2024; Popa et al., 2021; Stock et al., 2016, 2018), and reconstructing the architecture of magmatic plumbing systems (Li et al., 2021). Despite the growing literature taking advantage of the widespread occurrence of apatite in volcanic systems, only a few studies used apatite to access the volatile budget of plutonic

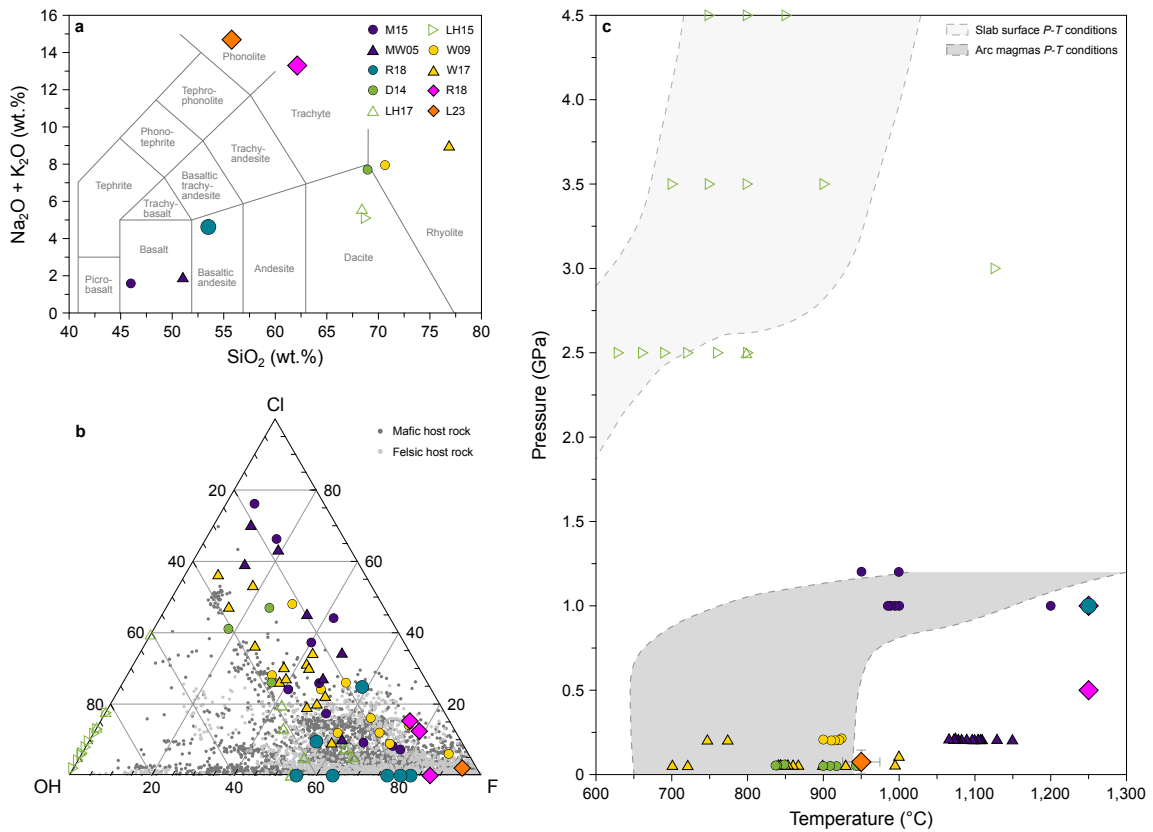


Figure 6.3. Compilation of available partitioning data of volatiles in apatite. **a**, Composition of the starting materials used in the experiments plotted in the total alkali silica diagram [SiO_2 (wt.%) vs. $\text{Na}_2\text{O} + \text{K}_2\text{O}$ (wt.%) of Le Bas et al. (1986). **b**, Halogen content of experimentally crystallised apatite plotted in the Cl-OH-F ternary diagram. Apatite compositions from igneous mafic and felsic rocks compiled from Georoc are represented for comparison. **c**, Experimental conditions plotted in a pressure-temperature diagram. Pressure-temperature conditions undergone by slab surfaces (Syracuse et al., 2010) and arc magmas (Klein and Jagoutz, 2021) are represented for comparison. The larger symbols highlight experiments determining H_2O - CO_2 exchange coefficients. *D14*, Doherty et al. (2014); *LH15*, Li and Hermann (2015); *LH17*, Li and Hermann (2017); *L23*, Li et al. (2023); *MW05*, Mathez and Webster (2005); *M15*, McCubbin et al. (2015); *R18*, Riker et al. (2018); *W09*, Webster et al. (2009); *W17*, Webster et al. (2017).

6. General conclusions and perspectives

rocks (e.g., Kendall-Langley et al., 2021). This is mainly due to the common idea that volatiles rapidly re-equilibrate in slowly-cooled plutonic rocks, which is supported by the post-entrapment re-equilibration occurring in melt inclusions (e.g., Bucholz et al., 2013; Gaetani et al., 2012). However, measured halogen profiles in apatite grains originating from the Western Adamello tonalite are well-reproduced through diffusion of an initial profile following similar cooling paths as highlighted in Chapter 4. Together with the incomplete re-equilibration with host biotite, this indicates that apatite from the Adamello batholith record the volatile evolution of the equilibrium melt. Therefore, the volatile compositions of the equilibrium melt and fluid were calculated, and revealed a Cl preferential incorporation into the exsolving fluid. The melt H₂O and CO₂ compositions, coupled with saturation curves, were used to identify early crystallisation in the middle crust, followed by extensive apatite formation in the upper crustal magma reservoir. In addition, the calculated fluid has similar a composition as intermediate density fluid inclusions, therefore emphasising the potential of apatite to quantify the volatile evolution of the crystal-melt-fluid system in plutonic rocks.

The main factor that is limiting the calculation of melt compositions from apatite chemistry is the scarcity of experiments investigating the volatile partitioning between apatite and melt. Indeed, the available data do not cover the whole range of apatite compositions, nor the temperature and pressure at which it is stable in nature (Fig. 6.3). This is especially the case for the H₂O-CO₂ exchange coefficients, whereby the literature only spans conditions relevant for low-pressure (<200 MPa), alkali-rich systems (Li et al., 2023), and high-pressure (1 GPa), basaltic to andesitic systems (Fig. 6.3) (Riker et al., 2018). Future work should explore other pressure conditions and system variables. Furthermore, as emphasised in Chapter 5, ensuring that slowly-cooled apatite did not experience complete re-equilibration is fundamental. Two techniques have been employed; it encompasses calculating exchange coefficients (K_D) of apatite-biotite pairs and modelling the diffusion re-equilibration of volatiles in apatite. Although the heterogeneity of the calculated K_D s favours the hypothesis of an uncomplete re-equilibration, comparing with equilibrium apatite-biotite pairs from experiments (e.g., Li and Hermann, 2017) spanning a wide range of conditions would strengthen this argument. Therefore, measuring apatite-biotite and apatite-amphibole pairs in existing experimental runs and/or performing new crystallisation experiments covering relevant P - T - fO_2 conditions of crustal magmatic systems are needed to properly assess the partitioning behaviour of halogens between hydrous phases.

6.5 Final remarks

The questions addressed in this thesis are linked to the eruptability of a magma reservoir with an emphasis on the rates of crystal-melt separation and the potential role of an exsolving magmatic volatile phase. To address these questions, a wide range of analytical, experimental and computational techniques has been employed. The application of these methods offers the opportunity to integrate the dimension of time to igneous petrology, and to consider the potential impacts of volatile elements on magmatic processes, allowing geologists to better understand the timescales of continental crust genesis, and its expression at the surface as volcanic eruptions. In order to interpret the results obtained using these modern techniques, it is, however, important to undertake a detailed petrographic study based on traditional field work and thin section observations. A comprehensive picture of the dynamics of magmatic systems can only be achieved through a multi-disciplinary approach that combines cutting-edge techniques with traditional petrography. This thesis might encourage future work to perform detailed petrographic observations on *a priori* well-known granitoids, precisely constrain the source powder assemblages in diffusion experiments, use diffusion to retrieve timescales in plutonic rocks, and investigate the volatile budget of plutonic rocks using apatite.

Appendix A

Supplementary Materials

A.1 Supplementary Material to Chapter 2

The full supplementary material to Chapter 2, which includes the mineral trace element chemistry, can be found online following <https://doi.org/10.1093/petrology/egae009>.

A.1.1 Supplementary Text

Perple_X modelling

To constrain the TiO_2 activity (a_{TiO_2}) of the tonalitic and granitic melts, we can model the tonalite liquid line of descent using the Perple_X software that calculate at every step the TiO_2 chemical potential (μ_{TiO_2}). To do so, we used Perple_X (Connolly, 2005, 2009) version 6.9.1 and the internally consistent end-member database of Holland et al. (2018). Calculations were undertaken in the chemical system $\text{Na}_2\text{O}-\text{CaO}-\text{K}_2\text{O}-\text{FeO}-\text{MgO}-\text{Al}_2\text{O}_3-\text{SiO}_2-\text{H}_2\text{O}-\text{TiO}_2$ (NCKFMASHT). Manganese is neglected from the calculations as it does not control the appearance of any phase and instead favours the formation of garnet. The activity-composition ($a-X$) relationships of Holland et al. (2018) for silicate melt, spinel, orthopyroxene, clinopyroxene, olivine and garnet, Holland and Powell (2003) for plagioclase and alkali feldspar, White et al. (2014) for biotite, Holland and Powell (2011) for epidote, White et al. (2000) for ilmenite, and Green et al. (2016) for amphibole. The oxygen fugacity (f_{O_2}) was buffered at NNO in the thermodynamic data file, and the H_2O content was set at 6 wt.% to ensure saturation.

We illustrate the advantage of using Perple_X in the Supplementary Figures by comparing our modelled melt differentiation with the experimentally determined liquid line of descent of an arc tonalite at 200 MPa (Marxer and Ulmer, 2019). Perple_X overpredicts

A. Supplementary Materials

the liquidus temperature by ~ 80 °C, but the modelled melt fractions reasonably match the experimental melt fractions once it reaches the liquidus at ~ 990 °C. From 950 °C, the *Perple_X* model overestimates the melt fraction by ~ 15 wt.% which can be due to the absence of clinopyroxene and is reflected in the higher melt MgO contents of the model compared to the experiments. Additionally, the Al_2O_3 content of the melt modelled by *Perple_X* is lower by ~ 1.5 wt.% which is a consequence of the plagioclase being the only liquidus phase at high temperature. Except for these two discrepancies, *Perple_X* faithfully reproduces (1) the crystal assemblages and modal amounts, (2) the major element trends, and (3) the biotite-producing peritectic reaction observed in the experimental liquid line of descent. Therefore, we believe that the calculated liquid line of descent fairly replicates its experimental counterpart and can be further used to calculate the $a\text{TiO}_2$ of the melt.

Liquid line of descent modelling

The crystallisation path of the parental tonalitic melt uses the method described in [Jagoutz \(2010\)](#) for major and trace elements and is based on cumulate subtraction rather than mineral-melt partition coefficients. The model assumes fixed cumulate compositions. Parental melt, cumulus and evolving melt compositions are related as follow:

$$C_L^{n-1} = \frac{C_L^{n-1} - (X \times C_C)}{1 - X}, \quad (\text{A1.1})$$

where C_L^n represents the concentration of a given element in the evolving melt at step n , C_L^{n-1} at step $n-1$, and C_C is the bulk cumulus composition. Crystallisation step is 1 % and is defined as follow:

$$X = \frac{X^{n-1} - (X^n)}{X^{n-1}}, \quad (\text{A1.2})$$

where X^n is the percentage of melt remaining at step n , and X^{n-1} at step $n-1$. C_C has been constrained by textural observations and mass balance, and C_L^0 represents the parental tonalitic melt composition.

A.1.2 Supplementary Figures

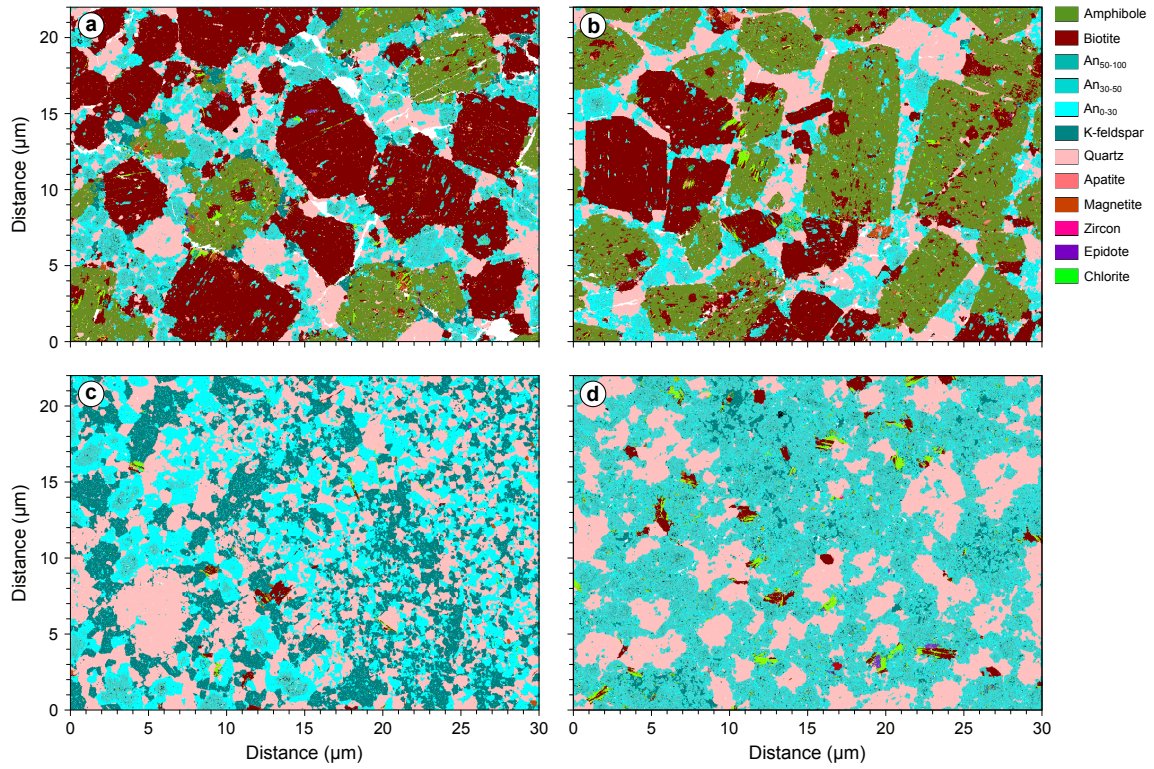


Figure A1.1. Thin section QEMSCAN maps of (a) a biotite-rich gabbro (CJ4B; N46°06'58.0", E10°30'53.9"), (b) a hornblende-rich gabbro (CJ15A; N46°05'55.4", E10°31'13.5"), (c) a granitic dike (WA21-20; N46°06'27.2", E10°29'27.6") and (d) a leucotonalite (WA21-25; N46°05'55.1", E10°28'59.3").

A. Supplementary Materials

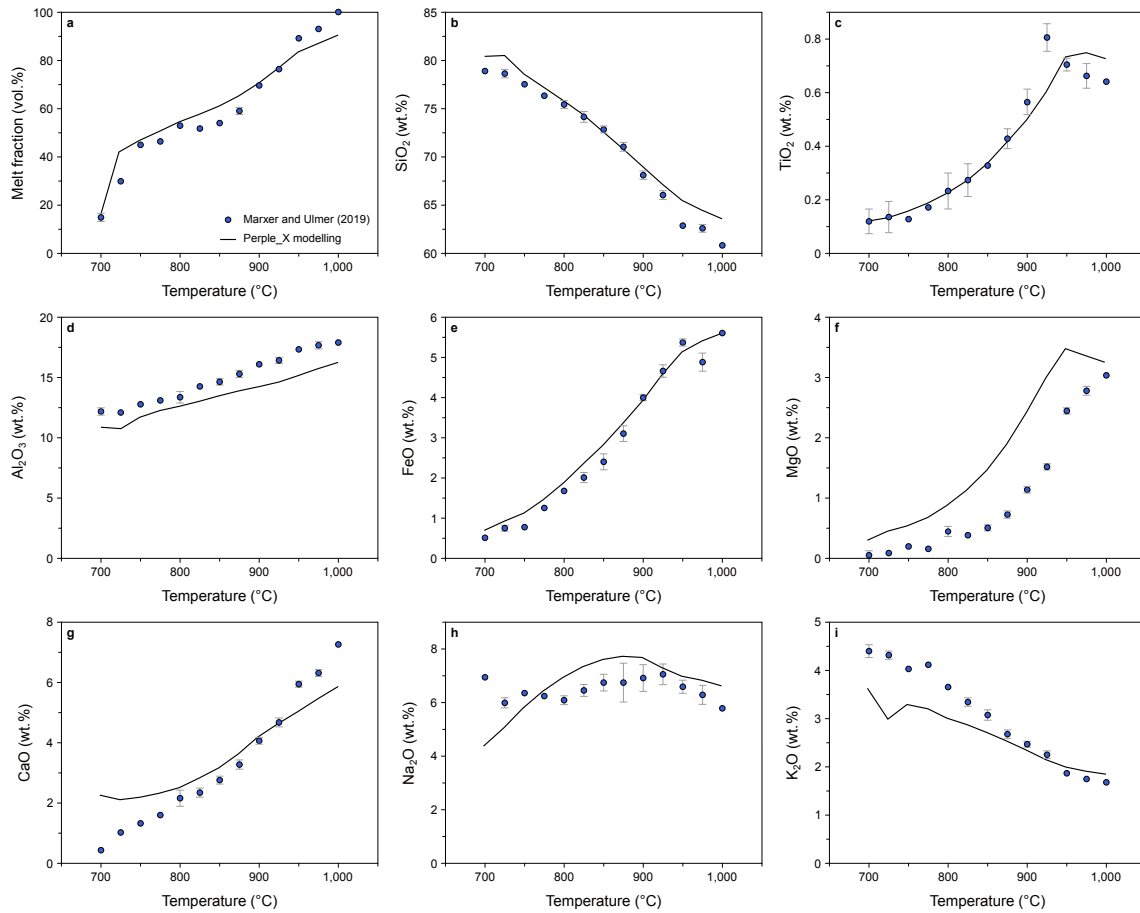


Figure A1.2. Temperature vs. melt fraction and oxides comparing the modelled liquid line of descent and the experimental liquid line of descent of Marxer and Ulmer (2019). The thermodynamic model is detailed in the Supplementary Text.

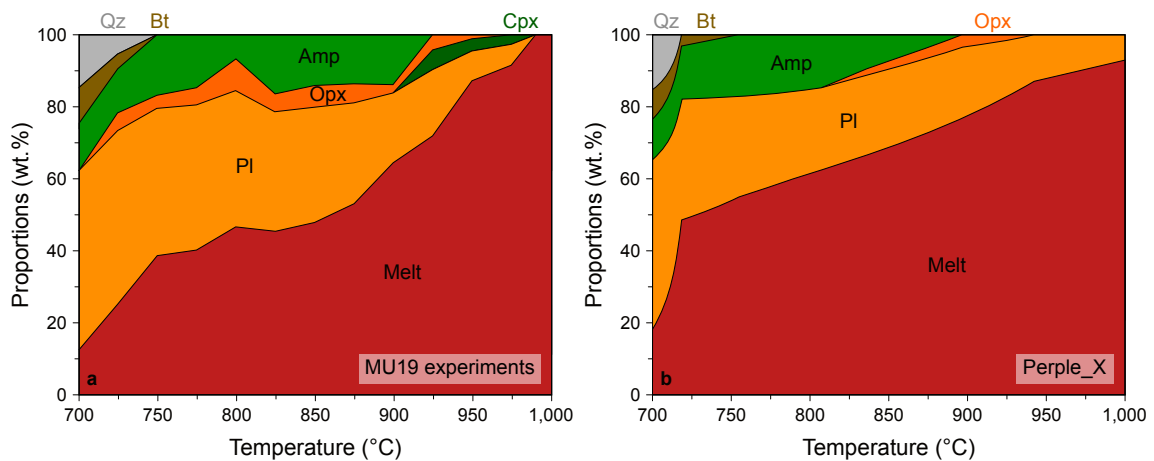


Figure A1.3. Temperature vs. mineral proportions comparing the modelled liquid line of descent and the experimental liquid line of descent of Marxer and Ulmer (2019).

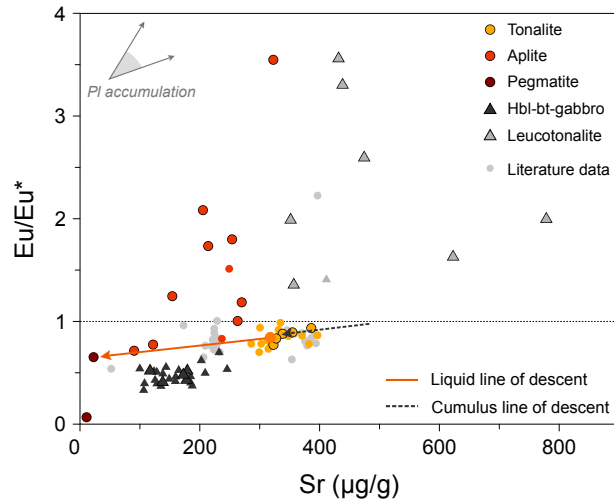


Figure A1.4. Results of the liquid line of descent model represented as Sr vs. Eu/Eu^* . Plagioclase accumulation in leucotonalite results in an increase of Sr and Eu/Eu^* , whereas plagioclase loss in hornblende-biotite-gabbro results in a strong depletion in Sr and a strongly negative Eu anomaly. The two vectors highlighting the direction of plagioclase accumulation are qualitative and represent a range depending on the accumulated plagioclase composition.

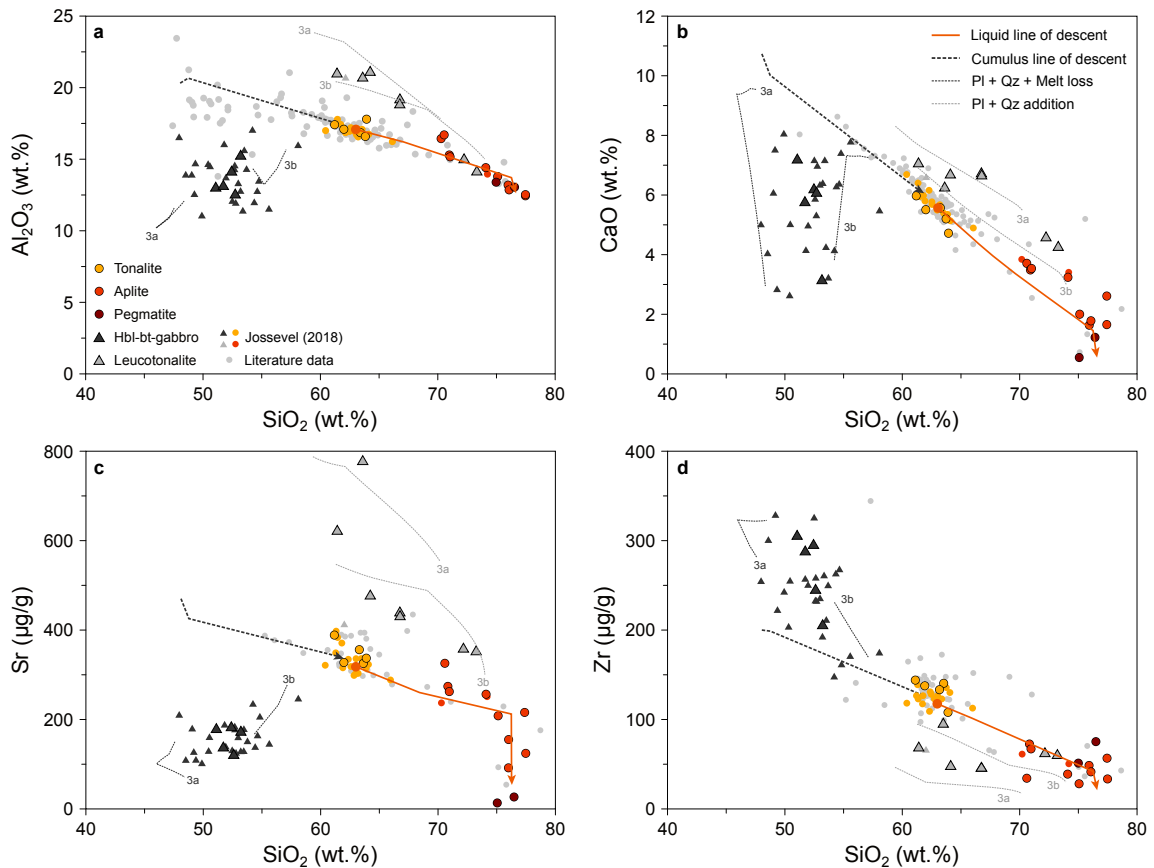


Figure A1.5. Results of the crystal-melt segregation model (Parts 3a and 3b) plotted as SiO_2 vs. (a) Al_2O_3 , (b) CaO, (c) Sr and (d) Zr. The model is detailed in the main text.

A. Supplementary Materials

Table A1.1. Bulk rock major and trace element analyses of the different Western Adamello lithologies. Sample names starting with “CJ” are from [Jossevel \(2018\)](#).

Sample	WA21-3	WA21-7	WA21-11	WA21-13	WA21-24	CJ1A	CJ1D	CJ2C
Rock type	Tonalite							
<i>Major elements (wt.%)</i>								
SiO ₂	63.93	63.68	62.04	63.29	61.17	62.55	62.59	62.94
TiO ₂	0.49	0.58	0.64	0.57	0.64	0.62	0.64	0.63
Al ₂ O ₃	17.80	16.60	16.85	16.93	17.35	17.13	17.08	16.87
Fe ₂ O ₃	4.26	5.19	5.69	5.09	5.85	5.64	5.65	5.57
MnO	0.10	0.12	0.13	0.11	0.13	0.13	0.12	0.13
MgO	1.64	2.16	2.40	2.12	2.61	2.35	2.35	2.33
CaO	4.71	5.20	5.49	5.57	5.96	5.75	5.71	5.50
Na ₂ O	3.42	2.82	2.89	3.03	3.01	2.85	2.84	2.84
K ₂ O	2.79	2.50	2.29	2.24	2.14	2.16	2.10	2.22
P ₂ O ₅	0.12	0.18	0.19	0.18	0.19	0.19	0.19	0.18
LOI	0.71	0.92	1.06	0.66	0.94	0.53	0.57	0.63
Total	99.95	99.93	99.66	99.77	99.99	99.88	99.84	99.84
<i>Trace elements (µg/g)</i>								
Sc	7.83	15.75	18.03	15.28	17.18	17.49	15.47	16.90
V	83.74	110.72	120.54	106.84	131.86	106.44	110.84	102.39
Cr						16.61	17.01	18.76
Co	49.66	63.45	80.42	57.12	68.29	35.55	45.50	39.69
Ni	10.42	10.02	10.62	10.48	12.74	5.17	5.10	5.17
Cu	2.69	5.88	4.79	9.19	8.20	8.21	6.16	7.01
Zn	161.47	176.39	182.33	166.65	174.59	64.78	63.51	71.96
Rb	98.59	88.93	85.10	82.25	81.60	78.01	79.18	85.48
Sr	336.2	323.9	325.2	355.5	387.8	314.8	317.2	298.5
Y	13.19	20.25	22.16	19.15	19.80	22.41	19.20	23.20
Zr	106.33	138.62	137.01	133.24	143.63	129.07	124.80	120.97
Nb	14.23	12.96	13.78	13.80	14.42	12.71	12.54	13.49
Cs	5.81	2.76	3.37	3.63	3.70	2.38	2.33	4.32
Ba	412.3	620.8	500.0	501.4	560.9	468.1	476.9	472.9
La	42.67	40.11	31.25	27.16	25.07	41.20	39.90	52.79
Ce	80.19	74.46	58.65	49.21	46.01	78.40	74.56	97.53
Pr	8.525	7.917	6.573	5.428	5.060	8.342	7.820	9.896
Nd	29.91	28.86	24.97	20.81	19.54	31.10	28.24	35.13
Sm	4.569	4.946	4.760	4.020	3.985	5.590	4.787	5.848
Eu	1.035	1.158	1.221	1.124	1.142	1.230	1.204	1.240
Gd	2.805	4.232	4.129	3.724	3.517	4.700	4.003	4.927
Tb	0.376	0.579	0.626	0.545	0.547	0.640	0.549	0.691
Dy	2.035	3.507	3.964	3.176	3.367	4.141	3.534	4.386
Ho	0.402	0.740	0.766	0.679	0.702	0.817	0.708	0.888
Er	1.216	2.065	2.238	1.923	1.965	2.303	1.922	2.451
Tm	0.206	0.303	0.336	0.289	0.286	0.350	0.288	0.373
Yb	1.623	2.109	2.233	1.927	2.046	2.399	2.133	2.661
Lu	0.262	0.319	0.344	0.307	0.329	0.377	0.309	0.392
Hf	3.271	3.713	3.741	3.474	3.642	3.636	3.485	3.623
Ta	1.906	1.116	1.189	1.105	1.151	1.133	1.120	1.579
Pb	23.03	18.38	14.50	15.97	13.40	16.07	14.78	18.78
Th	22.925	16.863	12.517	11.282	9.421	17.485	15.580	22.003
U	6.847	2.697	3.097	3.181	2.405	4.485	3.764	4.104

(Continued.)

A.1. Supplementary Material to Chapter 2

Sample	CJ4C	CJ10A	CJ10B	CJ17B	CJ26	CJ28	CJ29	CJ32
Rock type	Tonalite							
<i>Major elements (wt.%)</i>								
SiO ₂	63.23	60.34	62.34	63.89	63.11	61.38	61.89	61.80
TiO ₂	0.60	0.69	0.62	0.56	0.61	0.66	0.64	0.61
Al ₂ O ₃	16.63	17.01	17.15	16.76	17.04	17.43	17.22	17.12
Fe ₂ O ₃	5.71	6.37	5.55	5.18	5.35	6.06	5.86	5.72
MnO	0.14	0.14	0.12	0.12	0.12	0.13	0.13	0.14
MgO	2.36	3.12	2.54	2.15	2.24	2.59	2.47	2.59
CaO	5.66	6.69	6.16	5.36	5.55	6.02	5.80	5.98
Na ₂ O	2.83	2.84	2.99	2.82	2.92	2.91	2.83	2.87
K ₂ O	2.06	1.83	1.69	2.10	2.08	1.89	2.21	2.05
P ₂ O ₅	0.19	0.18	0.16	0.19	0.17	0.20	0.20	0.19
LOI	0.55	0.50	0.52	0.83	0.52	0.71	0.60	0.87
Total	99.96	99.70	99.83	99.95	99.70	99.97	99.85	99.93
<i>Trace elements (μg/g)</i>								
Sc	19.19	21.01	15.92	13.92	14.11	19.34	17.66	17.66
V	105.66	144.74	125.16	85.83	96.02	108.66	108.72	116.67
Cr	19.78	16.73	18.54	19.44	16.83	20.28	23.94	13.76
Co	40.95	41.37	40.78	38.43	45.58	40.15	39.65	45.20
Ni	5.49	5.80	7.00	5.60	5.40	5.03	8.72	5.34
Cu	7.85	9.99	5.55	4.27	7.88	9.01	8.08	12.24
Zn	66.63	61.67	57.34	64.26	65.56	68.48	67.09	70.91
Rb	77.47	63.98	62.12	78.07	78.79	71.14	80.91	71.77
Sr	302.9	319.2	331.8	313.6	335.5	348.9	312.6	370.8
Y	24.35	20.67	15.42	18.14	16.20	21.94	21.57	19.71
Zr	130.13	116.29	105.92	135.01	116.45	138.18	126.21	114.87
Nb	13.00	11.23	10.29	12.66	13.51	12.33	12.99	13.06
Cs	3.05	2.36	2.06	2.72	2.70	2.60	2.59	2.58
Ba	452.6	386.3	379.3	483.9	504.6	447.6	467.3	562.4
La	31.87	30.07	23.64	32.55	18.56	20.20	28.49	30.73
Ce	60.87	56.22	42.73	62.25	35.80	40.79	54.38	55.92
Pr	6.696	5.932	4.439	6.788	4.035	4.829	5.971	5.977
Nd	25.91	22.58	16.40	25.42	16.06	19.96	22.77	22.25
Sm	5.062	4.354	3.249	4.636	3.384	4.375	4.579	4.360
Eu	1.244	1.019	0.901	1.097	1.039	1.193	1.174	1.145
Gd	4.721	3.909	2.831	3.777	3.099	4.172	4.104	3.853
Tb	0.671	0.555	0.416	0.534	0.440	0.634	0.613	0.542
Dy	4.513	3.718	2.790	3.334	2.978	3.943	3.936	3.607
Ho	0.897	0.733	0.544	0.631	0.580	0.793	0.763	0.689
Er	2.550	2.127	1.618	1.835	1.641	2.281	2.218	1.986
Tm	0.375	0.308	0.232	0.270	0.237	0.317	0.325	0.306
Yb	2.653	2.183	1.681	1.883	1.739	2.244	2.327	2.091
Lu	0.388	0.342	0.250	0.284	0.260	0.339	0.348	0.306
Hf	3.606	3.113	2.885	3.718	3.113	3.725	3.497	3.079
Ta	1.119	0.957	0.873	1.094	1.105	0.934	1.117	1.027
Pb	15.98	8.74	10.60	16.10	15.09	13.36	15.57	15.33
Th	12.864	11.183	7.335	13.392	7.913	6.339	10.905	10.148
U	2.533	2.951	1.635	2.867	2.924	2.553	2.262	1.968

(Continued.)

A. Supplementary Materials

Sample	CJ34	CJ36	CJ45	CJ46	CJ48	CJ50	WA21-6B	WA21-17
Rock type	Tonalite	Tonalite	Tonalite	Tonalite	Tonalite	Tonalite	Gabbro	Gabbro
<i>Major elements (wt.%)</i>								
SiO ₂	61.47	61.37	63.12	64.13	63.52	66.07	53.24	52.47
TiO ₂	0.63	0.64	0.59	0.58	0.55	0.49	1.46	1.21
Al ₂ O ₃	17.49	17.81	16.93	16.68	17.10	16.24	15.25	14.21
Fe ₂ O ₃	5.81	5.69	5.36	5.16	4.95	4.57	12.14	13.13
MnO	0.13	0.12	0.12	0.12	0.12	0.11	0.28	0.32
MgO	2.57	2.44	2.21	2.09	2.08	1.88	5.15	5.96
CaO	5.93	6.40	5.57	5.14	5.37	4.87	3.16	6.20
Na ₂ O	2.99	2.94	2.83	2.92	3.06	2.85	1.96	2.02
K ₂ O	2.03	1.80	2.11	2.39	2.24	2.19	5.10	2.79
P ₂ O ₅	0.18	0.19	0.17	0.16	0.16	0.16	0.27	0.36
LOI	0.73	0.53	0.72	0.44	0.57	0.52	1.22	1.14
Total	99.95	99.94	99.74	99.82	99.73	99.94	99.21	99.80
<i>Trace elements (µg/g)</i>								
Sc	15.66	15.47	14.09	13.29	14.26	12.75	28.12	74.26
V	119.94	123.45	98.77	93.58	88.24	78.81	233.99	262.96
Cr	19.83	19.33	19.91	20.50	18.27	18.71		
Co	47.36	34.77	45.51	41.24	39.94	38.57	46.62	51.30
Ni	6.42	5.17	5.22	5.00	5.51	5.37	14.26	16.74
Cu	14.93	9.99	3.97	5.92	9.95	5.43	6.20	28.15
Zn	69.96	61.56	63.21	58.23	60.97	57.71	338.11	253.74
Rb	78.86	67.78	78.43	85.78	81.97	78.90	219.38	111.84
Sr	382.6	396.7	301.7	322.8	334.8	286.2	172.7	182.7
Y	18.32	17.43	16.45	17.36	18.65	16.51	31.25	90.76
Zr	123.39	123.72	127.44	128.18	121.31	112.23	203.60	294.37
Nb	13.73	12.41	12.04	13.86	13.33	12.03	32.89	23.02
Cs	3.35	3.30	3.49	4.50	3.25	3.33	9.54	3.79
Ba	563.0	474.9	475.5	534.3	501.6	449.5	1167.4	668.0
La	88.31	41.33	23.42	35.78	34.14	47.20	167.16	62.37
Ce	152.66	74.39	43.86	66.62	63.22	87.69	308.54	134.15
Pr	14.427	7.579	4.727	6.971	6.611	8.968	31.089	17.137
Nd	46.26	27.21	18.06	25.39	24.09	31.18	101.84	73.45
Sm	6.021	4.381	3.625	4.230	4.277	4.915	13.569	17.631
Eu	1.293	1.130	1.061	1.027	1.136	1.094	1.678	2.374
Gd	4.271	3.594	3.297	3.454	3.734	3.787	8.149	16.545
Tb	0.551	0.495	0.467	0.497	0.541	0.490	1.031	2.621
Dy	3.451	3.193	2.976	3.119	3.285	3.042	5.683	16.172
Ho	0.659	0.640	0.609	0.615	0.657	0.570	1.121	3.307
Er	1.820	1.842	1.732	1.741	1.940	1.648	3.067	9.257
Tm	0.275	0.262	0.264	0.280	0.288	0.252	0.441	1.321
Yb	1.908	1.826	1.835	1.935	2.062	1.714	3.250	8.755
Lu	0.291	0.274	0.265	0.284	0.327	0.256	0.480	1.221
Hf	3.335	3.311	3.480	3.640	3.367	3.099	5.735	7.834
Ta	1.094	1.095	1.068	1.192	1.252	1.210	2.249	1.380
Pb	14.72	12.97	14.85	16.48	18.05	17.32	19.07	11.36
Th	34.314	14.292	8.833	16.947	15.309	19.029	74.062	20.245
U	2.794	3.660	2.749	2.831	3.822	3.554	8.423	4.790

(Continued.)

A.1. Supplementary Material to Chapter 2

Sample	WA21-18	WA21-21	WA21-26	CJ1B	CJ2B	CJ4B	CJ8	CJ9
Rock type	Gabbro	Gabbro	Gabbro	Gabbro	Gabbro	Gabbro	Gabbro	Gabbro
<i>Major elements (wt.%)</i>								
SiO ₂	51.76	52.73	51.11	52.56	54.26	50.54	51.85	53.53
TiO ₂	1.32	1.17	1.32	1.01	1.27	1.44	1.19	1.29
Al ₂ O ₃	13.19	12.56	13.04	12.11	17.06	14.45	16.02	15.61
Fe ₂ O ₃	14.38	13.28	14.36	14.24	10.19	14.07	12.04	11.81
MnO	0.36	0.39	0.35	0.44	0.23	0.36	0.32	0.28
MgO	6.60	6.81	7.19	6.75	4.53	6.23	4.96	5.11
CaO	5.75	6.08	7.20	7.15	4.15	5.02	4.14	4.23
Na ₂ O	1.77	1.88	1.70	1.62	2.41	1.74	1.94	2.11
K ₂ O	3.26	3.47	2.27	2.46	4.27	4.30	5.10	4.35
P ₂ O ₅	0.36	0.35	0.38	0.47	0.21	0.39	0.36	0.28
LOI	1.15	1.07	1.05	0.87	0.83	0.88	1.28	0.64
Total	99.90	99.81	99.97	99.68	99.42	99.43	99.21	99.25
<i>Trace elements (µg/g)</i>								
Sc	83.18	70.17	68.47	93.22	21.69	55.60	43.67	36.09
V	280.07	281.26	324.91	281.51	185.16	263.58	203.38	212.19
Cr				33.77	32.77	31.63	36.20	34.31
Co	47.24	50.45	51.63	45.23	39.68	38.62	39.23	40.27
Ni	16.55	20.11	15.24	11.26	9.77	10.29	10.89	9.70
Cu	9.90	12.33	17.28	9.90	5.12	7.77	5.65	4.80
Zn	266.94	259.36	238.54	139.38	121.62	146.74	132.75	132.20
Rb	131.62	131.53	86.99	87.98	179.89	173.12	188.95	175.52
Sr	137.5	118.2	177.5	128.0	232.2	157.5	186.2	178.6
Y	102.19	82.80	72.82	118.67	21.36	66.75	62.16	42.62
Zr	284.55	242.12	303.99	323.10	144.75	252.35	254.46	207.39
Nb	26.53	29.40	21.61	22.12	27.20	28.57	30.17	26.24
Cs	4.80	5.25	3.32	3.06	6.85	6.24	12.01	6.00
Ba	770.7	797.6	565.8	394.7	920.5	947.8	1133.3	960.0
La	42.00	151.60	40.38	40.56	17.23	69.91	274.60	108.66
Ce	100.44	263.36	101.11	113.87	35.55	143.16	523.52	205.96
Pr	14.302	27.387	14.167	17.286	4.236	16.340	51.766	21.247
Nd	67.48	95.43	62.39	84.09	17.71	66.39	175.26	74.47
Sm	18.313	17.430	14.377	22.744	4.106	14.124	24.569	12.166
Eu	2.392	2.772	2.304	2.914	0.898	1.992	2.485	1.531
Gd	18.524	15.109	13.086	22.444	3.789	12.831	15.998	9.295
Tb	3.064	2.389	2.059	3.356	0.573	1.933	2.039	1.297
Dy	18.389	14.229	12.604	22.489	3.658	12.680	12.323	8.174
Ho	3.703	2.974	2.605	4.390	0.727	2.456	2.301	1.531
Er	10.516	8.343	7.542	12.452	2.152	6.832	6.221	4.262
Tm	1.498	1.212	1.035	1.807	0.327	0.996	0.903	0.645
Yb	9.814	8.237	7.267	12.281	2.250	7.000	6.202	4.251
Lu	1.402	1.206	1.050	1.704	0.336	0.998	0.922	0.619
Hf	7.748	6.687	7.780	8.971	3.941	6.945	7.214	5.562
Ta	1.624	2.120	1.329	1.767	1.885	1.923	2.304	1.849
Pb	10.15	15.73	5.67	10.45	15.45	11.87	19.57	13.93
Th	13.768	57.794	10.344	18.107	9.573	30.178	114.274	46.571
U	4.074	5.704	3.065	8.011	5.325	4.555	3.560	3.898

(Continued.)

A. Supplementary Materials

Sample	CJ11A	CJ12B	CJ14	CJ15A	CJ15	CJ17	CJ18	CJ19
Rock type	Gabbro							
<i>Major elements (wt.%)</i>								
SiO ₂	49.93	55.62	53.25	53.42	53.42	52.67	53.75	49.36
TiO ₂	1.36	1.12	1.05	1.06	1.06	1.19	1.49	1.81
Al ₂ O ₃	11.02	11.47	12.78	11.39	11.39	14.25	14.29	14.67
Fe ₂ O ₃	15.75	11.74	12.63	13.61	13.61	12.65	13.02	15.46
MnO	0.41	0.32	0.39	0.41	0.41	0.35	0.27	0.33
MgO	8.50	7.76	6.76	7.50	7.50	5.84	5.64	6.93
CaO	8.04	7.78	6.39	7.16	7.16	5.85	3.21	2.81
Na ₂ O	1.28	1.43	1.88	1.74	1.74	1.91	1.59	1.33
K ₂ O	1.87	1.16	3.34	2.18	2.18	3.54	4.77	5.82
P ₂ O ₅	0.38	0.26	0.30	0.39	0.39	0.35	0.37	0.33
LOI	1.17	1.22	0.94	0.75	0.75	0.86	0.89	0.96
Total	99.72	99.88	99.70	99.61	99.61	99.46	99.29	99.82
<i>Trace elements (µg/g)</i>								
Sc	77.16	64.34	71.85	74.58	74.58	58.68	29.19	38.97
V	384.84	271.49	246.60	284.70	284.70	232.07	220.40	277.29
Cr	35.41	26.73	27.89	30.24	30.24	33.20	43.83	50.29
Co	49.37	51.79	51.24	47.74	47.74	39.86	46.42	41.37
Ni	14.97	15.18	11.61	11.77	11.77	9.84	14.41	16.70
Cu	23.69	17.76	9.90	14.14	14.14	8.31	8.67	5.40
Zn	145.48	114.32	140.03	140.86	140.86	137.86	153.72	181.32
Rb	62.91	36.89	112.11	83.47	83.47	136.10	195.15	244.48
Sr	99.2	143.1	127.1	127.1	127.1	182.0	149.0	107.3
Y	79.75	63.70	84.33	86.15	86.15	72.32	34.40	37.51
Zr	239.90	168.92	188.78	259.49	259.49	255.73	246.20	219.30
Nb	21.29	15.30	28.72	23.13	23.13	27.05	29.49	36.60
Cs	1.97	1.14	4.12	4.42	4.42	3.98	6.62	11.53
Ba	344.2	223.5	818.7	500.4	500.4	799.2	1193.6	1351.5
La	78.36	30.45	40.46	47.09	47.09	101.85	75.77	119.55
Ce	159.56	82.77	89.50	116.47	116.47	195.00	144.06	223.93
Pr	18.249	11.564	11.912	15.916	15.916	20.945	15.189	22.787
Nd	72.82	51.84	54.78	72.04	72.04	78.82	54.75	77.35
Sm	15.378	11.972	14.650	17.121	17.121	15.391	9.313	11.712
Eu	2.655	2.121	2.475	2.741	2.741	2.246	1.206	1.281
Gd	14.573	11.498	15.027	16.075	16.075	14.036	7.605	8.743
Tb	2.167	1.740	2.315	2.408	2.408	2.081	1.057	1.204
Dy	14.558	11.763	15.688	15.859	15.859	13.546	6.624	7.156
Ho	2.972	2.354	3.086	3.166	3.166	2.676	1.244	1.393
Er	8.431	6.670	8.820	9.031	9.031	7.544	3.531	3.775
Tm	1.214	0.999	1.291	1.319	1.319	1.097	0.503	0.554
Yb	8.410	6.791	8.880	8.943	8.943	7.324	3.426	3.748
Lu	1.219	0.962	1.286	1.296	1.296	1.063	0.509	0.538
Hf	6.973	4.858	5.555	7.043	7.043	6.958	6.625	5.828
Ta	1.448	0.967	2.170	1.539	1.539	1.766	1.822	2.393
Pb	5.45	4.06	14.42	8.42	8.42	10.68	10.17	10.35
Th	24.394	5.732	17.096	18.603	18.603	41.420	26.304	46.763
U	2.957	1.383	3.507	3.292	3.292	3.393	3.810	3.622

(Continued.)

A.1. Supplementary Material to Chapter 2

Sample	CJ21	CJ22	CJ23	CJ24	CJ25	CJ27	CJ33	CJ35
Rock type	Gabbro	Gabbro	Gabbro	Gabbro	Gabbro	Gabbro	Gabbro	Gabbro
<i>Major elements (wt.%)</i>								
SiO ₂	50.45	52.73	53.05	58.11	49.06	49.25	54.65	52.81
TiO ₂	1.61	1.30	0.98	0.91	2.01	1.19	1.01	1.16
Al ₂ O ₃	14.60	14.57	13.28	16.00	13.87	12.53	12.73	11.91
Fe ₂ O ₃	15.15	12.64	14.27	8.76	17.40	15.64	12.46	13.51
MnO	0.35	0.33	0.40	0.22	0.34	0.45	0.35	0.40
MgO	5.94	5.84	5.63	3.79	4.72	7.57	6.32	7.30
CaO	2.60	5.31	6.34	5.46	6.06	7.50	6.38	6.97
Na ₂ O	1.26	1.88	1.97	2.49	1.76	1.57	1.99	1.74
K ₂ O	6.18	3.70	2.56	2.76	2.89	2.51	2.60	2.73
P ₂ O ₅	0.29	0.36	0.36	0.26	1.07	0.46	0.37	0.35
LOI	0.91	0.76	0.72	0.70	0.56	0.83	0.97	0.75
Total	99.33	99.41	99.57	99.46	99.77	99.50	99.84	99.63
<i>Trace elements (µg/g)</i>								
Sc	33.90	51.27	75.10	33.07	41.17	91.31	56.03	67.56
V	271.56	231.83	294.90	157.88	478.47	304.43	253.12	279.38
Cr	37.37	29.86	76.98	25.17	80.53	34.22	27.17	24.98
Co	39.87	43.55	46.49	40.37	41.00	44.21	43.79	43.24
Ni	10.55	10.12	11.24	8.02	12.16	11.93	9.60	9.99
Cu	8.03	13.43	8.62	9.74	76.19	18.80	23.21	19.60
Zn	162.71	130.80	135.15	96.59	152.66	144.52	118.27	127.24
Rb	271.56	144.40	96.14	117.14	113.13	92.01	95.00	100.31
Sr	127.1	177.4	157.9	246.2	178.0	126.1	163.8	121.9
Y	41.50	67.46	100.65	43.78	67.96	117.76	68.64	81.97
Zr	200.81	229.88	234.26	172.72	717.94	325.06	266.13	229.18
Nb	34.87	26.35	21.52	19.47	32.70	23.21	22.48	25.49
Cs	34.18	4.30	3.73	5.46	4.38	4.77	3.31	5.34
Ba	1202.4	861.7	477.3	594.0	472.2	473.5	612.5	536.8
La	293.19	58.54	125.65	47.49	32.60	28.48	59.90	74.17
Ce	561.70	122.46	259.69	94.02	88.22	91.62	127.02	157.71
Pr	53.669	14.556	29.963	10.639	12.763	15.039	15.420	19.239
Nd	176.89	60.41	118.02	41.99	60.71	77.19	63.82	79.81
Sm	21.985	13.424	23.578	8.922	14.576	21.716	14.026	17.116
Eu	2.178	1.907	2.893	1.524	2.063	3.013	2.305	2.766
Gd	12.748	12.802	19.955	8.407	13.840	21.345	13.029	15.746
Tb	1.473	1.919	2.984	1.228	1.972	3.339	1.940	2.322
Dy	8.334	12.561	19.185	8.149	12.618	22.075	12.697	15.058
Ho	1.504	2.431	3.692	1.617	2.440	4.336	2.498	2.989
Er	4.161	6.877	10.394	4.560	6.902	12.282	7.071	8.485
Tm	0.599	1.034	1.511	0.656	1.013	1.808	1.049	1.258
Yb	4.260	7.018	10.313	4.497	6.925	12.206	7.071	8.789
Lu	0.641	0.973	1.442	0.671	1.052	1.745	1.061	1.267
Hf	5.562	6.296	6.648	4.723	18.091	9.092	7.189	6.507
Ta	2.852	1.889	1.618	1.556	2.464	1.535	1.653	2.317
Pb	17.98	10.65	12.15	12.55	10.31	7.85	11.80	9.60
Th	130.582	25.043	57.671	19.969	10.705	6.215	23.489	27.580
U	6.599	2.179	3.841	2.097	5.049	4.171	4.829	5.936

(Continued.)

A. Supplementary Materials

Sample	CJ39	CJ41	CJ44	CJ47	CJ49	CJ2A	WA21-16B	WA21-19
Rock type	Gabbro	Gabbro	Gabbro	Gabbro	Gabbro	Leucoto.	Leucoto.	Leucoto.
<i>Major elements (wt.%)</i>								
SiO ₂	54.80	54.40	51.98	48.03	48.59	62.07	66.80	64.23
TiO ₂	1.18	1.07	1.33	1.52	1.51	0.29	0.11	0.09
Al ₂ O ₃	13.47	11.96	13.72	16.53	13.89	20.69	19.26	21.15
Fe ₂ O ₃	11.59	13.05	13.79	14.16	15.95	2.57	1.13	0.97
MnO	0.28	0.39	0.36	0.31	0.43	0.06	0.03	0.03
MgO	6.60	6.65	6.16	5.79	6.71	0.98	0.37	0.24
CaO	7.39	6.27	4.99	5.01	4.01	6.57	6.71	6.70
Na ₂ O	1.65	1.54	1.58	2.13	1.30	3.96	3.86	4.52
K ₂ O	1.64	3.27	3.97	4.76	5.49	1.94	0.80	1.54
P ₂ O ₅	0.29	0.40	0.35	0.35	0.42	0.08	0.05	0.05
LOI	0.95	0.84	0.83	0.70	0.92	0.50	0.76	0.63
Total	99.85	99.84	99.06	99.30	99.24	99.70	99.87	100.12
<i>Trace elements (µg/g)</i>								
Sc	45.65	65.71	63.03	35.37	70.48	7.40	5.90	3.69
V	265.76	264.10	250.06	276.18	293.68	47.02	36.81	31.71
Cr	26.08	25.44	42.09	39.84	50.77	11.83		
Co	46.67	49.59	40.74	35.04	37.33	35.78	93.72	69.43
Ni	11.85	10.67	12.58	11.52	13.88	2.97	12.95	12.23
Cu	24.65	15.62	6.74	14.58	5.94	5.51	6.03	6.12
Zn	103.85	127.95	136.25	142.40	177.44	33.23	139.57	138.60
Rb	59.11	114.82	154.96	186.08	224.97	61.58	25.86	56.48
Sr	203.8	136.1	136.0	209.5	107.8	410.3	430.4	475.9
Y	45.06	81.54	78.89	46.67	96.31	11.23	4.92	8.95
Zr	160.21	260.83	246.65	251.31	297.93	63.55	44.45	46.12
Nb	13.53	26.90	26.51	32.27	35.86	7.79	2.91	9.18
Cs	1.66	5.32	5.08	5.67	9.11	2.51	1.05	2.62
Ba	410.4	668.4	866.6	1119.9	1078.0	322.3	192.3	225.0
La	26.30	72.59	86.18	259.93	470.10	18.09	7.94	9.41
Ce	65.50	150.91	173.80	468.75	872.20	34.95	15.71	19.14
Pr	8.671	17.888	19.696	44.620	84.549	3.778	1.565	1.904
Nd	38.63	73.01	77.31	143.67	280.32	14.32	5.90	6.63
Sm	8.521	16.244	17.046	17.909	37.070	2.670	1.126	1.304
Eu	1.731	2.525	2.000	2.437	3.265	1.102	1.173	1.059
Gd	8.333	14.908	15.451	11.918	24.818	2.120	0.894	1.182
Tb	1.266	2.227	2.329	1.498	3.230	0.316	0.159	0.242
Dy	8.278	14.834	14.916	8.860	19.213	1.953	0.892	1.276
Ho	1.651	2.950	2.906	1.692	3.579	0.378	0.190	0.316
Er	4.801	8.438	8.218	4.676	9.733	1.168	0.508	0.964
Tm	0.705	1.257	1.215	0.692	1.399	0.177	0.099	0.187
Yb	4.719	8.731	8.198	4.696	9.399	1.367	0.834	1.211
Lu	0.677	1.253	1.146	0.679	1.332	0.224	0.091	0.218
Hf	4.246	7.307	6.988	6.799	8.374	1.964	1.236	1.635
Ta	0.790	1.851	1.860	2.004	2.820	1.183	0.402	2.072
Pb	4.19	13.08	9.64	14.53	13.71	24.07	25.34	41.06
Th	4.189	35.121	35.216	109.620	182.065	9.997	1.802	7.310
U	1.221	4.140	3.282	5.301	7.062	9.073	5.489	7.586

(Continued.)

A.1. Supplementary Material to Chapter 2

Sample	WA21-22	WA21-23	WA21-25	LB22-1	LB22-2	WA21-1A	WA21-1B
Rock type	Leucoto.	Leucoto.	Leucoto.	Leucoto.	Leucoto.	Granite	Granite
<i>Major elements (wt.%)</i>							
SiO ₂	72.23	73.34	66.81	61.42	63.59	70.95	71.01
TiO ₂	0.21	0.23	0.19	0.31	0.20	0.19	0.19
Al ₂ O ₃	15.04	14.18	18.90	21.02	20.76	15.33	15.20
Fe ₂ O ₃	1.91	1.91	1.55	2.44	1.39	1.93	1.91
MnO	0.05	0.04	0.03	0.05	0.03	0.04	0.04
MgO	0.65	0.80	0.66	0.97	0.63	0.63	0.64
CaO	4.58	4.26	6.68	7.07	6.27	3.50	3.52
Na ₂ O	3.13	2.65	3.58	4.22	4.64	2.91	2.93
K ₂ O	1.46	1.96	0.90	1.45	1.74	3.64	3.50
P ₂ O ₅	0.07	0.08	0.05	0.12	0.12	0.06	0.07
LOI	0.61	0.54	0.57	0.50	0.47	0.45	0.44
Total	99.93	99.97	99.95	99.56	99.84	99.64	99.44
<i>Trace elements (μg/g)</i>							
Sc	4.58	4.90	5.04	4.16	2.14	7.04	7.04
V	41.39	48.73	40.14	45.17	28.37	47.40	45.26
Cr				6.37	5.37		
Co	87.18	78.51	68.12	56.79	52.40	70.70	66.11
Ni	18.20	15.26	29.55	7.55	6.41	21.27	15.72
Cu	2.92	4.00	4.50	1.99		2.71	3.82
Zn	105.14	114.30	123.82	30.15	20.01	134.60	140.46
Rb	50.43	53.86	26.24	46.40	39.42	81.95	76.52
Sr	358.3	352.4	437.4	622.2	778.0	270.5	263.8
Y	6.66	4.40	4.14	4.88	1.52	10.96	9.86
Zr	62.59	57.91	42.90	67.43	93.68	70.23	66.80
Nb	7.83	6.04	4.58	7.07	2.37	9.35	9.23
Cs	5.15	1.94	1.34	1.02	0.83	3.97	3.70
Ba	270.8	413.2	233.8	404.2	1314.5	532.1	504.8
La	17.43	11.97	6.67	14.83	27.88	9.58	9.53
Ce	32.77	20.61	11.91	25.94	46.41	20.85	20.03
Pr	3.469	2.125	1.386	2.636	4.205	2.574	2.682
Nd	12.34	7.32	4.82	9.14	12.68	11.24	10.98
Sm	2.153	1.120	0.888	1.481	1.190	2.453	2.628
Eu	0.750	0.640	0.868	0.667	0.532	0.884	0.798
Gd	1.308	0.866	0.721	1.049	0.551	2.138	2.226
Tb	0.182	0.129	0.094	0.140	0.058	0.315	0.315
Dy	1.007	0.692	0.605	0.787	0.239	1.888	1.773
Ho	0.208	0.138	0.139	0.160	0.055	0.364	0.331
Er	0.649	0.418	0.455	0.492	0.156	1.111	0.893
Tm	0.103	0.062	0.062	0.068	0.026	0.169	0.130
Yb	0.924	0.394	0.483	0.519	0.212	1.350	1.131
Lu	0.145	0.080	0.083	0.082	0.040	0.221	0.184
Hf	1.965	1.522	1.257	1.639	2.412	2.603	2.577
Ta	1.440	0.642	0.662	0.594	0.196	1.864	1.777
Pb	18.45	12.74	12.48	12.48	13.78	26.82	29.37
Th	11.628	6.260	2.151	6.385	10.101	8.936	9.268
U	5.812	5.066	2.647	2.204	1.416	9.143	8.502

(Continued.)

A. Supplementary Materials

Sample	WA21-2A	WA21-8	WA21-10B	WA21-20	WA22-1	WA22-2A	WA22-4	CJ30
Rock type	Granite	Granite	Granite	Granite	Granite	Granite	Granite	Granite
<i>Major elements (wt.%)</i>								
SiO ₂	76.06	75.94	75.00	75.11	76.51	77.48	70.63	70.26
TiO ₂	0.06	0.05	0.03	0.09	0.05	0.05	0.06	0.16
Al ₂ O ₃	12.84	13.15	13.40	13.78	13.03	12.45	16.77	16.42
Fe ₂ O ₃	0.85	0.67	0.39	0.87	0.69	0.70	0.70	1.51
MnO	0.03	0.02	0.19	0.03	0.03	0.02	0.02	0.04
MgO	0.17	0.12	0.05	0.21	0.04	0.15	0.15	0.47
CaO	1.76	1.63	0.53	2.01	1.21	1.66	3.69	3.83
Na ₂ O	2.91	2.97	3.51	3.12	3.51	2.71	3.62	3.61
K ₂ O	4.28	4.76	5.98	4.43	4.52	4.42	3.79	3.04
P ₂ O ₅	0.03	0.01	0.01	0.02	0.01	0.02	0.05	0.07
LOI	0.37	0.37	0.40	0.41	0.20	0.24	0.30	0.39
Total	99.38	99.70	99.47	100.07	99.80	99.91	99.80	99.80
<i>Trace elements (µg/g)</i>								
Sc	5.27	4.83	8.49	4.19	2.84	3.23	2.25	5.61
V	29.69	21.69	16.61	27.45	6.59	9.98	13.16	23.57
Cr					4.89	5.79	4.19	11.53
Co	114.11	121.32	118.66	120.32	87.57	91.99	80.47	45.32
Ni	27.34	32.04	27.43	26.17	5.18	5.98	5.79	3.43
Cu	6.05	4.12	6.56	5.99				7.36
Zn	171.75	148.90	126.17	187.61	11.78	6.78	9.47	20.73
Rb	145.05	137.10	428.79	128.15	151.81	119.86	78.75	95.01
Sr	154.7	90.4	11.5	206.3	24.1	123.8	323.1	237.2
Y	12.30	18.98	66.81	5.17	18.91	18.63	4.30	20.03
Zr	40.12	47.94	50.08	28.59	74.61	56.79	31.65	60.94
Nb	11.09	16.45	55.40	8.34	10.23	11.95	3.31	12.50
Cs	7.70	4.90	13.53	4.59	3.23	4.81	1.98	3.44
Ba	495.2	111.9	35.5	768.1	9.5	289.8	837.6	342.5
La	5.03	3.53	6.03	5.71	4.46	4.19	2.47	6.74
Ce	14.91	9.31	17.83	15.70	10.83	11.42	5.55	15.16
Pr	1.886	1.270	2.519	1.934	1.494	1.526	0.746	1.968
Nd	7.81	5.18	11.85	7.04	6.45	6.56	2.96	8.94
Sm	2.010	1.859	5.426	1.391	2.061	2.021	0.793	2.628
Eu	0.751	0.446	0.105	0.717	0.412	0.534	0.839	0.704
Gd	1.664	2.043	5.964	0.792	1.912	2.188	0.659	2.572
Tb	0.291	0.414	1.276	0.151	0.359	0.401	0.144	0.403
Dy	1.753	2.648	7.651	0.750	2.612	2.651	0.640	2.705
Ho	0.419	0.637	1.711	0.197	0.678	0.595	0.167	0.580
Er	1.321	2.094	5.454	0.510	2.420	1.857	0.426	1.931
Tm	0.246	0.425	1.062	0.131	0.410	0.358	0.097	0.351
Yb	1.849	2.981	9.126	0.825	3.444	2.524	0.560	2.903
Lu	0.327	0.498	1.508	0.145	0.620	0.418	0.116	0.435
Hf	1.895	2.637	5.030	1.381	3.309	2.033	1.021	2.588
Ta	2.509	2.400	13.735	1.641	1.478	1.822	0.582	3.124
Pb	64.83	67.76	137.37	59.18	59.39	45.49	34.25	39.07
Th	10.342	9.865	12.100	12.501	16.065	8.703	2.780	10.069
U	18.635	29.504	32.566	10.371	43.288	18.721	3.493	16.146

(Continued.)

Sample	WA22-3	WA22-5	CJ31
Rock type	Granite	Granite	Granite
<i>Major elements (wt.%)</i>			
SiO ₂	74.10	77.45	74.19
TiO ₂	0.12	0.07	0.15
Al ₂ O ₃	14.42	12.51	13.96
Fe ₂ O ₃	1.07	0.78	1.46
MnO	0.03	0.02	0.04
MgO	0.34	0.20	0.49
CaO	3.24	2.62	3.36
Na ₂ O	3.09	2.40	2.63
K ₂ O	2.97	3.46	3.01
P ₂ O ₅	0.04	0.03	0.05
LOI	0.40	0.40	0.36
Total	99.80	99.94	99.71
<i>Trace elements (µg/g)</i>			
Sc	2.98	2.80	5.05
V	16.53	14.44	25.14
Cr	5.08	4.18	7.37
Co	80.15	99.66	52.06
Ni	4.82	7.15	3.00
Cu	2.19	1.59	63.28
Zn	14.64	6.77	22.52
Rb	69.09	73.42	76.90
Sr	253.8	214.8	250.2
Y	10.38	7.77	9.06
Zr	39.27	33.14	49.40
Nb	8.06	4.69	8.06
Cs	2.08	1.81	2.53
Ba	424.5	499.1	690.8
La	3.35	3.18	6.49
Ce	6.76	6.86	13.49
Pr	0.838	0.876	1.640
Nd	3.83	3.73	6.61
Sm	1.199	1.069	1.579
Eu	0.707	0.555	0.729
Gd	1.207	0.905	1.390
Tb	0.216	0.299	0.199
Dy	1.524	1.120	1.510
Ho	0.311	0.252	0.310
Er	1.017	0.745	0.941
Tm	0.203	0.193	0.168
Yb	1.464	1.039	1.284
Lu	0.257	0.201	0.217
Hf	1.519	1.295	1.797
Ta	1.557	1.136	1.429
Pb	28.90	29.25	28.35
Th	4.211	3.934	6.012
U	8.058	8.737	11.967

LOI, loss on ignition

Leucoto., leucotonalite

A. Supplementary Materials

Table A1.2. Trace element analyses ($\mu\text{g/g}$, unless stated otherwise) of the secondary standard BCR-2G using LA-ICP-MS.

	BCR-2G							
Li	9.05	8.89	9.12	9.18	9.66	8.74	9.25	8.94
Sc	33.0	33.7	33.1	32.3	33.8	33.8	32.8	32.4
TiO ₂ *	2.51	2.49	2.48	2.47	0.80	2.67	2.72	2.68
V	450	425	437	440	419	467	476	471
Cr								
Ni								
Zn	185	176	176	178	187	168	167	167
Rb	46.5	45.9	47.2	46.7	49.1	46.2	47.7	47.6
Sr	328	326	324	322	333	334	328	332
Y	32.3	32.7	31.9	31.4	33.3	32.7	31.7	31.7
Zr	182	183	174	176	179	179	178	178
Nb								
Cs	1.13	1.03	1.12	1.08	1.19	1.15	1.10	1.11
Ba	710	692	717	682	661	735	757	765
La	24.7	25.2	25.8	23.9	26.6	24.3	24.6	24.6
Ce	53.8	51.7	54.0	52.0	56.2	51.5	52.5	52.3
Pr	6.53	6.43	6.62	6.22	6.84	6.53	6.39	6.40
Nd	28.1	28.6	28.9	27.5	29.9	27.6	27.8	27.9
Sm	6.42	6.61	6.53	6.32	6.77	6.51	6.38	6.36
Eu	1.95	1.94	1.99	1.86	2.04	1.88	1.93	1.86
Gd	6.36	6.50	6.48	6.29	6.74	6.43	6.36	6.32
Tb	0.994	1.011	1.015	0.966	1.046	0.993	0.984	0.995
Dy	6.16	6.26	6.34	5.93	6.50	6.11	5.99	6.06
Ho	1.26	1.26	1.28	1.20	1.30	1.25	1.24	1.25
Er	3.51	3.61	3.61	3.46	3.68	3.56	3.49	3.46
Tm	0.491	0.487	0.500	0.465	0.509	0.492	0.476	0.484
Yb	3.30	3.44	3.43	3.23	3.47	3.34	3.24	3.20
Lu	0.494	0.498	0.490	0.477	0.501	0.494	0.477	0.471
Hf								
Ta								
Pb	11.60	10.81	10.97	11.03	11.77	10.15	10.74	10.68
Th	5.82	5.98	5.96	5.74	6.17	5.82	5.75	5.64
U	1.75	1.68	1.78	1.74	1.85	1.66	1.73	1.73

(Continued.)

A.1. Supplementary Material to Chapter 2

	BCR-2G							
Li	9.14	9.09	9.09	9.12	9.38	9.06	8.93	9.16
Sc	32.5	32.4	32.9	33.5	33.4	33.2	33.0	33.0
TiO ₂ *	2.74	2.78	2.82	2.80	2.89	2.83	2.77	2.84
V	487	488	491	493	509	494	485	492
Cr								
Ni								
Zn	169	170	168	176	163	163	168	163
Rb	47.8	47.5	47.2	48.4	49.8	46.8	47.0	45.9
Sr	327	335	342	342	353	354	343	350
Y	31.3	31.2	33.0	32.2	33.4	32.9	32.8	31.8
Zr	194	181	185	171	185	188	174	172
Nb								
Cs	1.12	1.16	1.17	1.20	1.17	1.11	1.16	1.16
Ba	766	788	770	796	788	787	773	798
La	24.2	24.7	24.5	24.9	24.6	24.9	24.4	24.5
Ce	52.7	53.4	52.3	53.3	53.6	52.6	52.1	51.9
Pr	6.33	6.53	6.50	6.61	6.67	6.66	6.61	6.62
Nd	27.9	28.2	28.0	28.1	28.2	28.5	27.8	27.7
Sm	6.30	6.42	6.50	6.46	6.48	6.56	6.30	6.44
Eu	1.88	1.90	1.91	1.95	1.93	1.99	1.92	1.90
Gd	6.22	6.27	6.40	6.42	6.36	6.51	6.32	6.27
Tb	0.977	0.996	1.009	0.990	1.017	1.015	1.000	0.997
Dy	5.99	6.06	6.20	6.13	6.11	6.17	6.16	6.15
Ho	1.22	1.25	1.26	1.25	1.25	1.28	1.25	1.25
Er	3.41	3.51	3.55	3.52	3.51	3.56	3.53	3.53
Tm	0.476	0.491	0.495	0.487	0.490	0.493	0.491	0.490
Yb	3.18	3.28	3.30	3.36	3.33	3.31	3.31	3.28
Lu	0.465	0.476	0.498	0.499	0.481	0.485	0.484	0.494
Hf								
Ta								
Pb	10.90	11.00	10.77	11.07	11.15	10.58	10.74	10.46
Th	5.67	5.80	5.79	5.85	5.83	5.90	5.80	5.78
U	1.74	1.71	1.72	1.75	1.80	1.73	1.69	1.70

(Continued.)

A. Supplementary Materials

	BCR-2G							
Li	9.08	9.54	9.72	9.56	9.52	9.71	9.57	9.17
Sc	32.4	32.0	32.0	31.6	31.8	31.4	32.5	32.4
TiO ₂ *	2.84	2.41	2.42	2.43	2.42	2.43	2.46	2.45
V	500	448	455	444	438	459	453	429
Cr								
Ni								
Zn	169	180	179	172	171	183	181	169
Rb	46.9	49.1	50.0	49.2	49.0	50.5	49.2	47.0
Sr	353	328	333	328	336	337	338	331
Y	31.8	31.0	31.3	30.5	31.1	30.8	31.9	31.9
Zr	173	163	165	160	165	162	168	168
Nb								
Cs	1.19	1.21	1.25	1.20	1.19	1.25	1.27	1.18
Ba	797	589	617	627	624	626	616	637
La	24.4	23.9	24.2	23.5	24.1	23.6	24.7	24.6
Ce	52.5	52.4	53.7	52.2	52.5	53.0	54.5	52.4
Pr	6.56	6.50	6.57	6.39	6.57	6.51	6.75	6.68
Nd	27.5	26.5	27.1	27.0	27.1	26.8	28.2	27.8
Sm	6.48	6.23	6.29	6.07	6.20	6.16	6.45	6.38
Eu	1.90	1.85	1.90	1.83	1.87	1.87	1.91	1.91
Gd	6.16	6.06	6.13	5.94	6.03	5.94	6.33	6.26
Tb	0.977	0.954	0.968	0.945	0.961	0.941	0.980	0.988
Dy	6.01	5.83	5.84	5.77	5.91	5.80	6.03	5.97
Ho	1.23	1.19	1.20	1.18	1.20	1.19	1.23	1.24
Er	3.40	3.35	3.36	3.27	3.35	3.29	3.45	3.46
Tm	0.474	0.471	0.467	0.462	0.472	0.458	0.487	0.491
Yb	3.26	3.15	3.23	3.11	3.20	3.12	3.23	3.29
Lu	0.487	0.464	0.468	0.466	0.460	0.453	0.481	0.484
Hf								
Ta								
Pb	10.95	11.18	11.33	11.03	10.86	11.68	11.40	11.31
Th	5.74	5.58	5.59	5.56	5.65	5.56	5.75	5.72
U	1.79	1.80	1.84	1.79	1.74	1.80	1.79	1.74

(Continued.)

A.1. Supplementary Material to Chapter 2

	BCR-2G							
Li	9.67	9.09	9.65	9.30	9.56	9.66	9.61	9.72
Sc	32.0	32.4	32.1	32.1	31.8	31.5	31.5	31.8
TiO ₂ *	2.42	2.39	2.48	2.44	2.48	2.46	2.44	2.47
V	448	430	460	447	448	452	443	454
Cr								
Ni								
Zn	180	165	178	180	177	182	175	179
Rb	48.0	46.1	50.0	48.2	48.9	48.4	48.2	49.2
Sr	332	327	343	332	338	326	331	335
Y	31.2	31.7	31.4	30.8	31.0	30.0	30.4	31.3
Zr	166	168	165	162	165	160	162	166
Nb								
Cs	1.20	1.14	1.21	1.18	1.21	1.18	1.20	1.23
Ba	618	620	627	630	627	634	610	652
La	24.4	24.5	24.1	23.5	23.9	23.1	23.7	24.3
Ce	53.2	52.5	53.3	51.5	52.8	51.2	52.0	54.2
Pr	6.59	6.57	6.56	6.40	6.51	6.33	6.40	6.65
Nd	27.7	27.7	27.3	26.4	27.2	26.3	27.0	27.5
Sm	6.23	6.28	6.27	6.19	6.32	6.00	6.18	6.42
Eu	1.87	1.92	1.92	1.85	1.89	1.83	1.87	1.90
Gd	6.21	6.21	6.13	6.07	6.11	5.90	6.02	6.15
Tb	0.970	1.002	0.975	0.947	0.950	0.925	0.959	0.975
Dy	5.94	6.09	5.92	5.83	5.95	5.69	5.83	5.94
Ho	1.22	1.23	1.22	1.18	1.20	1.19	1.18	1.21
Er	3.39	3.47	3.37	3.29	3.38	3.30	3.30	3.40
Tm	0.479	0.487	0.469	0.459	0.475	0.461	0.464	0.470
Yb	3.21	3.23	3.18	3.13	3.15	3.06	3.13	3.17
Lu	0.472	0.478	0.470	0.473	0.467	0.454	0.456	0.471
Hf								
Ta								
Pb	11.35	10.70	11.60	11.35	11.29	11.50	11.14	11.45
Th	5.63	5.76	5.67	5.58	5.63	5.53	5.51	5.64
U	1.78	1.72	1.84	1.76	1.80	1.82	1.75	1.82

(Continued.)

A. Supplementary Materials

	BCR-2G							
Li	9.57	9.55	9.73	9.64	9.54	9.99	9.69	8.76
Sc	31.4	31.7	31.3	31.9	31.6	31.3	31.4	32.1
TiO ₂ *	2.44	2.42	2.46	2.49	2.46	2.54	2.47	
V	454	435	459	451	440	467	451	419
Cr								15.1
Ni								13.3
Zn	179	176	185	182	174	188	183	202
Rb	48.0	48.7	49.6	50.2	48.3	50.0	49.9	46.6
Sr	329	331	335	343	335	339	343	328
Y	30.6	30.0	30.2	31.0	31.0	29.9	30.3	31.2
Zr	163	159	161	163	164	158	161	167
Nb								11.4
Cs	1.20	1.17	1.22	1.23	1.17	1.28	1.22	1.17
Ba	644	642	644	651	641	640	642	708
La	24.1	23.5	23.7	24.0	23.9	23.6	23.8	24.1
Ce	53.8	51.8	53.5	54.2	52.7	55.1	53.3	51.0
Pr	6.64	6.43	6.50	6.53	6.52	6.65	6.52	6.37
Nd	27.5	26.5	26.8	27.2	27.2	26.9	27.1	27.2
Sm	6.24	6.13	6.09	6.21	6.19	6.24	6.23	6.21
Eu	1.85	1.83	1.89	1.90	1.90	1.89	1.85	1.86
Gd	6.02	5.97	6.04	6.10	6.13	5.94	6.09	6.05
Tb	0.951	0.945	0.943	0.953	0.964	0.934	0.940	0.961
Dy	5.84	5.68	5.76	5.90	5.92	5.68	5.75	5.82
Ho	1.19	1.18	1.17	1.19	1.20	1.17	1.17	1.21
Er	3.31	3.24	3.28	3.36	3.34	3.24	3.28	3.37
Tm	0.472	0.453	0.465	0.472	0.465	0.454	0.456	0.480
Yb	3.18	3.12	3.20	3.18	3.17	3.11	3.12	3.20
Lu	0.460	0.459	0.460	0.461	0.462	0.452	0.463	0.460
Hf								4.59
Ta								0.668
Pb	11.37	11.16	11.78	11.59	11.29	11.92	11.36	10.25
Th	5.57	5.49	5.51	5.64	5.63	5.56	5.55	5.60
U	1.81	1.76	1.83	1.82	1.77	1.89	1.82	1.65

(Continued.)

A.1. Supplementary Material to Chapter 2

	BCR-2G							
Li	9.05	9.53	9.18	9.16	8.62	8.80	8.50	8.65
Sc	32.3	32.8	32.0	32.8	33.0	32.9	32.8	33.1
TiO ₂ *								
V	445	460	437	459	454	458	451	459
Cr	15.5	15.5	15.4	15.9	15.1	15.0	14.7	14.9
Ni	13.9	14.0	12.9	13.0	13.0	13.3	12.3	13.3
Zn	238	224	206	265	223	224	226	214
Rb	48.0	49.6	48.2	48.5	47.0	46.7	46.3	45.7
Sr	335	336	329	364	356	366	381	376
Y	30.7	31.2	31.3	31.5	31.8	31.5	32.4	32.1
Zr	165	166	166	169	169	170	170	170
Nb	11.8	11.8	11.4	12.0	11.9	11.9	11.7	11.8
Cs	1.19	1.27	1.21	1.23	1.18	1.19	1.16	1.16
Ba	738	741	673	725	726	744	721	732
La	24.5	24.5	23.7	24.9	24.5	24.8	24.7	24.8
Ce	53.2	53.5	49.9	53.3	52.4	52.4	51.5	51.5
Pr	6.59	6.63	6.33	6.75	6.70	6.72	6.62	6.61
Nd	27.6	27.8	26.7	28.2	28.3	28.1	27.9	28.0
Sm	6.31	6.37	6.15	6.42	6.39	6.48	6.39	6.45
Eu	1.91	1.91	1.83	1.93	1.90	1.90	1.93	1.93
Gd	6.18	6.16	6.04	6.26	6.29	6.27	6.31	6.29
Tb	0.960	0.990	0.955	0.992	0.998	0.992	0.990	1.001
Dy	5.79	5.93	5.81	6.03	6.00	6.01	6.01	6.09
Ho	1.19	1.23	1.18	1.23	1.24	1.25	1.23	1.27
Er	3.36	3.37	3.37	3.46	3.42	3.48	3.43	3.52
Tm	0.472	0.483	0.453	0.495	0.494	0.478	0.484	0.483
Yb	3.18	3.20	3.19	3.29	3.28	3.31	3.24	3.33
Lu	0.464	0.477	0.458	0.476	0.483	0.485	0.473	0.491
Hf	4.58	4.60	4.43	4.66	4.63	4.71	4.70	4.73
Ta	0.697	0.694	0.675	0.707	0.714	0.715	0.714	0.722
Pb	11.02	11.58	10.54	11.25	10.89	10.57	10.20	10.22
Th	5.66	5.61	5.57	5.79	5.82	5.85	5.81	5.86
U	1.73	1.76	1.66	1.74	1.70	1.69	1.65	1.65

(Continued.)

A. Supplementary Materials

	BCR-2G							
Li	8.48	8.44	8.84	8.98	8.81	8.70	8.65	8.47
Sc	32.9	33.9	33.0	32.2	33.0	33.1	33.8	33.4
TiO ₂ *								
V	453	465	491	500	493	488	493	496
Cr	14.2	14.8	15.5	15.4	15.4	14.8	15.2	14.9
Ni	12.5	13.0	14.4	14.9	13.2	13.3	12.9	13.7
Zn	263	206	230	220	240	205	216	212
Rb	45.1	45.9	48.0	48.1	47.5	46.7	46.6	46.2
Sr	376	395	400	399	407	408	413	431
Y	32.1	33.6	31.5	30.8	31.9	32.5	32.7	33.8
Zr	171	181	170	164	171	172	174	176
Nb	11.6	12.1	12.4	12.1	12.2	11.9	12.1	12.0
Cs	1.12	1.15	1.20	1.20	1.20	1.15	1.18	1.12
Ba	693	752	755	721	743	667	681	673
La	24.2	25.3	25.3	24.4	25.1	25.0	25.3	25.2
Ce	50.1	52.5	53.8	53.4	53.1	51.8	52.6	52.2
Pr	6.49	6.78	6.78	6.76	6.82	6.69	6.82	6.74
Nd	27.6	28.4	28.8	27.7	28.3	28.1	28.9	28.4
Sm	6.47	6.60	6.57	6.39	6.55	6.47	6.73	6.53
Eu	1.91	1.98	1.98	1.93	1.97	1.98	1.97	1.99
Gd	6.22	6.43	6.30	6.13	6.40	6.39	6.55	6.63
Tb	0.978	1.031	0.995	0.968	0.996	1.015	1.025	1.034
Dy	6.02	6.30	6.12	5.85	6.15	6.22	6.36	6.25
Ho	1.26	1.29	1.25	1.23	1.26	1.29	1.32	1.32
Er	3.48	3.67	3.49	3.37	3.46	3.61	3.68	3.67
Tm	0.478	0.501	0.484	0.465	0.487	0.512	0.509	0.509
Yb	3.27	3.34	3.28	3.21	3.30	3.35	3.39	3.37
Lu	0.485	0.500	0.474	0.481	0.482	0.502	0.496	0.507
Hf	4.77	4.82	4.67	4.57	4.70	4.77	4.89	4.96
Ta	0.722	0.745	0.741	0.704	0.742	0.743	0.746	0.750
Pb	10.18	10.27	11.16	11.20	10.89	10.65	10.56	10.32
Th	5.86	6.01	5.94	5.69	5.87	6.00	6.04	6.11
U	1.63	1.68	1.77	1.73	1.72	1.70	1.71	1.70

(Continued.)

A.1. Supplementary Material to Chapter 2

	BCR-2G							
Li	8.55	8.49	8.58	8.63	8.70	8.78	8.94	8.94
Sc	33.1	33.7	33.9	33.4	34.0	33.5	33.1	33.0
TiO ₂ *								
V	495	505	513	517	523	522	559	560
Cr	15.5	15.3	15.1	15.2	15.3	14.9	15.4	15.9
Ni	13.3	13.5	13.6	13.3	14.1	13.1	13.9	14.7
Zn	204	208	207	207	206	201	221	229
Rb	46.4	46.4	47.4	47.2	47.4	48.0	48.4	48.6
Sr	431	427	443	445	451	457	470	472
Y	33.6	32.5	33.1	33.0	33.2	32.9	32.7	32.2
Zr	175	173	175	174	176	173	172	171
Nb	11.9	12.0	12.2	12.2	12.3	12.1	12.4	12.4
Cs	1.15	1.16	1.19	1.19	1.21	1.23	1.20	1.25
Ba	667	675	694	682	687	690	702	703
La	24.7	25.1	25.8	25.4	25.8	25.6	25.6	25.4
Ce	51.5	52.3	53.8	53.1	53.5	53.4	54.1	54.7
Pr	6.62	6.76	6.89	6.88	6.93	6.86	6.91	6.84
Nd	28.1	29.0	29.3	28.5	29.3	28.9	28.6	28.8
Sm	6.65	6.55	6.65	6.72	6.90	6.64	6.58	6.52
Eu	1.96	2.01	1.98	1.97	1.98	1.98	2.00	1.96
Gd	6.41	6.56	6.58	6.50	6.47	6.51	6.58	6.41
Tb	1.015	1.035	1.059	1.027	1.043	1.041	1.031	1.013
Dy	6.29	6.20	6.42	6.25	6.40	6.23	6.29	6.21
Ho	1.28	1.30	1.29	1.29	1.29	1.30	1.31	1.28
Er	3.55	3.58	3.68	3.64	3.72	3.61	3.57	3.57
Tm	0.492	0.495	0.511	0.507	0.514	0.513	0.504	0.482
Yb	3.30	3.29	3.47	3.45	3.43	3.39	3.38	3.29
Lu	0.498	0.507	0.500	0.511	0.505	0.497	0.509	0.500
Hf	4.86	4.91	5.04	4.92	4.97	4.91	4.86	4.75
Ta	0.730	0.749	0.751	0.738	0.760	0.748	0.745	0.746
Pb	10.43	10.73	10.90	10.90	10.77	10.66	11.37	11.47
Th	5.97	6.05	6.10	6.08	6.11	6.02	6.12	6.01
U	1.71	1.68	1.75	1.72	1.73	1.72	1.75	1.83

(Continued.)

A. Supplementary Materials

	BCR-2G							
Li	8.83	9.48	9.82	9.41	9.29	9.65	9.22	9.58
Sc	34.3	31.8	31.8	32.3	32.2	31.4	32.1	31.9
TiO ₂ *								
V	557	493	511	495	483	503	492	520
Cr	15.1	15.7	16.6	15.5	15.6	15.8	15.7	16.3
Ni	13.8	14.0	15.1	14.9	13.7	15.8	13.7	15.7
Zn	229	221	231	218	206	221	211	227
Rb	49.1	49.0	51.1	49.0	47.1	47.9	48.8	48.7
Sr	481	366	380	376	369	363	379	375
Y	33.6	30.3	30.8	31.0	30.6	29.3	31.0	30.1
Zr	178	162	164	163	164	156	164	162
Nb	12.5	11.6	12.1	11.6	11.5	11.6	11.7	12.1
Cs	1.28	1.22	1.24	1.17	1.15	1.18	1.20	1.24
Ba	709	729	752	730	718	728	748	767
La	26.0	23.7	24.1	23.8	23.6	22.9	24.0	24.1
Ce	54.9	52.8	53.9	52.1	50.9	52.0	52.4	53.7
Pr	6.99	6.43	6.52	6.40	6.35	6.25	6.48	6.57
Nd	29.4	26.9	27.3	27.0	26.8	26.2	27.2	27.2
Sm	6.81	6.15	6.24	6.17	6.20	5.90	6.28	6.14
Eu	2.06	1.88	1.87	1.87	1.84	1.81	1.87	1.89
Gd	6.66	6.05	6.01	6.08	6.08	5.84	6.08	6.03
Tb	1.043	0.946	0.950	0.945	0.930	0.907	0.949	0.935
Dy	6.33	5.72	5.74	5.82	5.87	5.60	5.90	5.76
Ho	1.32	1.18	1.17	1.19	1.20	1.16	1.19	1.18
Er	3.67	3.33	3.29	3.29	3.40	3.23	3.38	3.32
Tm	0.497	0.467	0.454	0.454	0.459	0.438	0.462	0.462
Yb	3.49	3.12	3.15	3.09	3.15	3.06	3.14	3.10
Lu	0.510	0.459	0.439	0.458	0.457	0.445	0.462	0.463
Hf	4.92	4.48	4.43	4.44	4.51	4.31	4.53	4.46
Ta	0.759	0.688	0.695	0.688	0.689	0.667	0.687	0.678
Pb	11.28	11.58	11.93	11.14	10.55	11.25	11.11	11.65
Th	6.19	5.52	5.65	5.50	5.60	5.43	5.67	5.55
U	1.78	1.78	1.82	1.73	1.73	1.78	1.77	1.83

(Continued.)

A.1. Supplementary Material to Chapter 2

	BCR-2G							
Li	9.03	9.60	9.37	9.28	9.39	9.66	9.40	9.22
Sc	32.2	31.8	32.2	32.2	32.4	32.1	32.4	32.2
TiO ₂ *								
V	496	519	508	508	516	527	516	525
Cr	15.8	16.4	15.6	15.4	15.9	16.0	16.0	16.4
Ni	15.3	15.6	15.3	14.3	15.4	14.7	15.4	14.3
Zn	215	226	224	225	224	222	219	218
Rb	48.9	50.3	50.2	48.8	49.7	50.1	50.3	50.2
Sr	390	388	399	381	399	393	411	408
Y	31.9	31.1	31.8	30.4	31.6	30.2	31.5	31.8
Zr	168	166	167	163	170	163	167	168
Nb	11.8	12.2	12.2	11.7	12.2	12.0	12.1	12.2
Cs	1.20	1.25	1.26	1.20	1.24	1.22	1.21	1.22
Ba	745	786	779	722	791	763	775	767
La	24.4	24.4	24.7	23.8	24.6	23.9	24.5	24.5
Ce	52.8	54.6	54.0	52.2	54.2	53.5	53.9	54.0
Pr	6.53	6.70	6.72	6.44	6.67	6.52	6.63	6.72
Nd	27.5	28.0	27.8	26.9	27.7	27.2	27.6	27.9
Sm	6.33	6.39	6.30	6.12	6.48	6.18	6.34	6.48
Eu	1.90	1.92	1.93	1.88	1.94	1.88	1.95	1.93
Gd	6.13	6.21	6.15	5.97	6.31	6.00	6.16	6.20
Tb	0.974	0.975	0.987	0.947	0.978	0.949	0.972	0.962
Dy	5.89	6.03	5.98	5.81	6.01	5.85	5.97	5.97
Ho	1.22	1.20	1.22	1.20	1.24	1.18	1.21	1.22
Er	3.42	3.37	3.45	3.36	3.43	3.39	3.42	3.39
Tm	0.481	0.470	0.470	0.468	0.479	0.461	0.478	0.471
Yb	3.29	3.26	3.16	3.17	3.26	3.15	3.26	3.22
Lu	0.479	0.458	0.467	0.459	0.466	0.458	0.467	0.475
Hf	4.59	4.60	4.62	4.40	4.66	4.49	4.55	4.59
Ta	0.694	0.700	0.705	0.684	0.705	0.698	0.705	0.692
Pb	11.42	11.77	11.62	11.41	11.80	11.69	11.36	11.44
Th	5.76	5.72	5.70	5.59	5.78	5.63	5.69	5.69
U	1.78	1.86	1.81	1.78	1.81	1.82	1.80	1.81

(Continued.)

A. Supplementary Materials

	BCR-2G	BCR-2G	BCR-2G	BCR-2G	BCR-2G
Li	9.86	9.38	9.35	9.19	9.28
Sc	32.6	32.3	32.3	33.1	31.8
TiO ₂ *					
V	546	517	515	523	527
Cr	16.5	15.5	16.2	16.0	15.9
Ni	16.1	15.2	14.2	13.9	15.5
Zn	228	219	224	217	223
Rb	52.7	49.0	48.5	50.4	49.5
Sr	416	404	398	418	413
Y	31.7	31.2	31.2	31.9	30.9
Zr	168	164	165	170	164
Nb	12.3	11.7	11.9	12.1	11.9
Cs	1.30	1.19	1.20	1.22	1.21
Ba	819	725	724	669	730
La	24.8	23.8	24.2	24.0	23.6
Ce	55.5	52.4	52.4	51.9	52.5
Pr	6.78	6.44	6.54	6.44	6.45
Nd	28.3	27.0	27.5	27.0	27.0
Sm	6.46	6.28	6.26	6.16	6.22
Eu	1.96	1.89	1.88	1.87	1.85
Gd	6.18	5.99	6.26	6.02	6.00
Tb	0.955	0.952	0.963	0.962	0.920
Dy	6.01	5.89	5.87	5.81	5.81
Ho	1.21	1.19	1.22	1.23	1.18
Er	3.43	3.35	3.42	3.35	3.30
Tm	0.473	0.462	0.486	0.489	0.471
Yb	3.29	3.14	3.23	3.29	3.20
Lu	0.460	0.456	0.470	0.467	0.468
Hf	4.60	4.51	4.62	4.61	4.51
Ta	0.702	0.688	0.694	0.713	0.687
Pb	12.38	11.29	11.30	11.39	11.58
Th	5.72	5.65	5.74	5.87	5.58
U	1.91	1.77	1.81	1.77	1.80

*unit = wt.%

Table A1.3. Quartz trace element analyses and thermometry of the different Western Adamello lithologies.

Sample	Rock type	Comment	Ti µg/g	± µg/g	Al µg/g	± µg/g	$a\text{TiO}_2$	Temperature °C
WA21-11	Tonalite	Phenocryst	47.7	0.3	32.0	3.8	0.62	717
WA21-11	Tonalite	Phenocryst	37.0	0.3	53.7	6.4	0.62	689
WA21-11	Tonalite	Phenocryst	52.6	0.4	82.1	9.9	0.62	728
WA21-11	Tonalite	Phenocryst	53.1	0.4	61.9	7.4	0.62	729
WA21-11	Tonalite	Phenocryst	52.4	0.4	100.0	12.0	0.62	728
WA21-11	Tonalite	Phenocryst	53.9	0.4	46.3	5.6	0.62	731
WA21-11	Tonalite	Phenocryst	39.7	0.3	87.9	10.6	0.62	696
WA21-11	Tonalite	Phenocryst	45.1	0.3	103.7	12.4	0.62	710
WA21-11	Tonalite	Interstitial	24.8	0.2	72.0	8.6	0.67	641
WA21-26	Gabbro	Phenocryst	43.6	0.3	59.8	7.2	0.62	707
WA21-26	Gabbro	Phenocryst	47.4	0.3	73.4	8.8	0.62	716
WA21-26	Gabbro	Phenocryst	46.3	0.3	79.7	9.6	0.62	713
CJ2A	Leucoto.	Interstitial	26.7	0.2	60.6	7.3	0.67	648
CJ2A	Leucoto.	Interstitial	25.9	0.2	63.6	7.6	0.67	645
CJ2A	Leucoto.	Interstitial	21.9	0.2	55.3	6.6	0.67	629
CJ2A	Leucoto.	Interstitial	22.4	0.2	67.5	8.1	0.67	631
WA21-20	Granite	Pegmatitic	30.1	0.2	54.9	6.6	0.67	660
WA21-20	Granite	Pegmatitic	22.5	0.2	38.4	4.6	0.67	631
WA21-20	Granite	Pegmatitic	28.5	0.2	42.6	5.1	0.67	654
WA21-20	Granite	Pegmatitic	30.8	0.2	32.2	3.9	0.67	662
WA21-20	Granite	Pegmatitic	21.0	0.1	25.0	3.0	0.67	625
WA21-20	Granite	Pegmatitic	23.4	0.2	64.4	7.7	0.67	635
WA21-20	Granite	Pegmatitic	23.9	0.2	65.0	7.8	0.67	637
WA21-20	Granite	Pegmatitic	25.1	0.2	69.3	8.3	0.67	642
WA21-20	Granite	Pegmatitic	25.7	0.2	60.6	7.3	0.67	644
WA21-20	Granite	Pegmatitic	26.8	0.2	53.5	6.4	0.67	648
WA21-20	Granite	Pegmatitic	26.6	0.2	53.5	6.4	0.67	647
WA21-20	Granite	Pegmatitic	29.1	0.2	71.0	8.5	0.67	656
WA21-20	Granite	Pegmatitic	26.5	0.2	59.8	7.2	0.67	647
WA21-20	Granite	Pegmatitic	26.7	0.2	46.3	5.6	0.67	648
WA21-2B	Granite	Pegmatitic	21.3	0.1	75.9	9.1	0.67	626
WA21-2B	Granite	Pegmatitic	21.2	0.1	90.2	10.8	0.67	625
WA21-2B	Granite	Pegmatitic	19.4	0.1	74.7	9.0	0.67	618
WA21-2B	Granite	Pegmatitic	21.6	0.2	39.1	4.7	0.67	628

Leucoto., leucotonalite

A. Supplementary Materials

Table A1.4. Plagioclase and amphibole major element compositions and thermometry of the different Western Adamello lithologies.

Sample	CJ48	CJ48	CJ48	CJ48	CJ48	CJ4C	CJ4C	CJ4C
Rock type	Tonalite							
<i>Amphibole (wt.%)</i>								
SiO ₂	43.98	44.20	43.71	45.17	43.63	43.24	43.15	43.88
TiO ₂	0.90	0.82	0.91	0.96	0.84	0.89	0.96	0.76
Al ₂ O ₃	8.51	8.51	8.74	7.63	8.72	9.22	9.12	8.81
FeO	18.03	18.27	18.37	17.47	18.58	17.78	18.06	17.90
MnO	0.84	0.83	0.77	0.84	0.82	9.88	9.98	10.16
MgO	10.11	10.05	9.82	10.63	9.85	0.77	0.75	0.82
CaO	11.89	11.92	12.08	11.90	11.95	11.83	11.61	11.90
Na ₂ O	1.08	1.01	0.96	0.95	1.06	0.87	1.08	0.82
K ₂ O	0.78	0.93	0.96	0.63	0.81	0.86	0.74	0.84
Total	96.26	96.66	96.46	96.33	96.39	95.34	95.55	95.98
<i>Plagioclase (mol.%)</i>								
An	46.0	52.5	52.7	62.1	54.3	48.7	55.7	55.7
Ab	52.6	46.6	46.3	37.3	44.4	50.4	43.6	43.6
Or	1.4	0.8	1.0	0.6	1.3	0.9	0.7	0.7
T (°C)	747	764	751	798	779	738	797	767

(Continued.)

Sample	CJ4C							
Rock type	Tonalite							
<i>Amphibole (wt.%)</i>								
SiO ₂	44.20	45.46	45.04	44.99	45.12	45.42	45.02	44.85
TiO ₂	0.87	1.01	1.13	1.02	0.86	0.82	0.95	0.96
Al ₂ O ₃	8.93	8.21	8.51	8.44	8.34	8.22	8.57	8.38
FeO	17.55	16.29	16.71	16.60	16.71	16.59	16.90	16.77
MnO	10.31	11.35	11.07	11.03	11.35	11.30	11.09	11.01
MgO	0.77	0.78	0.73	0.72	0.74	0.71	0.75	0.72
CaO	11.76	10.99	10.79	11.39	11.52	11.47	11.75	11.76
Na ₂ O	0.86	1.16	1.24	1.07	0.99	1.07	1.00	0.96
K ₂ O	0.85	0.40	0.42	0.48	0.59	0.43	0.68	0.71
Total	96.18	95.74	95.68	95.84	96.26	96.17	96.79	96.12
<i>Plagioclase (mol.%)</i>								
An	60.0	60.0	60.0	60.0	60.0	60.0	60.0	60.0
Ab	39.4	39.4	39.4	39.4	39.4	39.4	39.4	39.4
Or	0.6	0.6	0.6	0.6	0.6	0.6	0.6	0.6
T (°C)	783	807	816	801	813	801	800	793

(Continued.)

A.1. Supplementary Material to Chapter 2

Sample	CJ4C	CJ4C	CJ4C	CJ4C	CJ10A	CJ10A	CJ10A	CJ10A
Rock type	Tonalite							
<i>Amphibole (wt.%)</i>								
SiO ₂	44.68	43.67	43.97	42.81	44.91	45.75	44.75	45.71
TiO ₂	0.90	0.95	0.82	0.87	1.10	0.99	1.12	1.01
Al ₂ O ₃	8.45	9.36	9.27	9.49	8.95	8.19	9.06	8.24
FeO	16.92	17.75	18.72	18.41	16.17	15.60	16.29	16.00
MnO	11.02	10.37	9.72	9.48	11.15	11.82	11.26	11.56
MgO	0.69	0.80	0.79	0.78	0.57	0.60	0.57	0.58
CaO	11.74	11.60	11.77	11.71	11.72	11.78	11.75	11.82
Na ₂ O	0.98	1.03	1.04	1.00	0.93	0.89	0.97	0.82
K ₂ O	0.71	0.83	0.88	1.05	1.01	0.86	0.99	0.86
Total	96.14	96.42	97.09	95.65	96.56	96.53	96.79	96.66
<i>Plagioclase (mol.%)</i>								
An	60.0	60.0	62.0	62.0	45.8	51.4	51.4	51.4
Ab	39.4	39.4	36.9	36.9	52.8	47.3	47.3	47.3
Or	0.6	0.6	1.0	1.0	1.4	1.3	1.3	1.3
T (°C)	801	816	802	799	724	747	758	742

(Continued.)

Sample	CJ10A							
Rock type	Tonalite							
<i>Amphibole (wt.%)</i>								
SiO ₂	44.87	46.41	46.74	46.26	46.85	45.12	46.57	46.33
TiO ₂	1.07	1.00	1.05	1.23	1.11	1.30	1.09	1.05
Al ₂ O ₃	8.91	7.93	7.92	7.92	7.71	8.72	7.81	7.56
FeO	16.33	14.46	13.87	14.68	14.20	15.40	14.73	14.73
MnO	11.23	12.82	13.05	12.73	12.89	12.00	12.67	12.51
MgO	0.55	0.57	0.55	0.58	0.60	0.72	0.55	0.65
CaO	11.80	11.51	11.78	11.33	11.17	11.43	11.56	11.62
Na ₂ O	0.94	0.91	0.86	1.06	0.99	1.02	0.96	0.82
K ₂ O	0.97	0.67	0.65	0.60	0.55	0.84	0.59	0.74
Total	96.80	96.32	96.50	96.42	96.12	96.66	96.58	96.02
<i>Plagioclase (mol.%)</i>								
An	48.2	46.4	51.8	52.2	68.9	68.8	51.5	52.2
Ab	50.3	52.3	47.2	46.2	30.3	30.4	47.2	46.3
Or	1.5	1.3	1.0	1.6	0.8	0.8	1.3	1.5
T (°C)	740	733	741	779	817	857	758	750

(Continued.)

A. Supplementary Materials

Sample	CJ10A							
Rock type	Tonalite							
<i>Amphibole (wt.%)</i>								
SiO ₂	46.78	45.81	44.83	44.70	45.22	45.34	45.83	45.56
TiO ₂	0.96	1.04	1.06	1.07	1.15	1.09	1.01	1.04
Al ₂ O ₃	7.46	7.93	9.01	8.91	8.82	8.55	8.26	8.46
FeO	14.90	15.34	15.93	16.32	15.57	15.92	15.47	15.58
MnO	12.67	12.10	11.41	11.56	11.80	11.94	12.41	11.98
MgO	0.68	0.58	0.60	0.64	0.60	0.61	0.60	0.67
CaO	11.58	11.59	11.83	12.02	11.98	12.02	12.03	12.10
Na ₂ O	0.80	0.84	0.86	1.03	0.93	1.01	0.92	0.89
K ₂ O	0.69	0.76	0.95	0.91	0.90	0.85	0.77	0.81
Total	96.58	96.06	96.53	97.21	97.03	97.42	97.36	97.18
<i>Plagioclase (mol.%)</i>								
An	58.3	49.0	47.6	58.7	52.6	48.1	64.8	64.8
Ab	40.7	49.8	51.2	40.3	46.7	51.2	34.5	34.5
Or	1.0	1.2	1.1	1.0	0.7	0.8	0.8	0.8
<i>T</i> (°C)	768	744	734	800	756	759	823	803

(Continued.)

Sample	CJ10A	CJ10A	CJ10A	CJ10A	CJ10A	WA21-11	WA21-11	WA21-11
Rock type	Tonalite							
<i>Amphibole (wt.%)</i>								
SiO ₂	45.20	45.04	45.47	45.35	45.94	43.93	43.90	43.43
TiO ₂	1.04	1.01	1.04	1.02	0.85	0.87	0.92	0.88
Al ₂ O ₃	8.65	8.71	8.49	8.43	8.05	9.06	9.19	9.21
FeO	15.68	15.44	15.52	15.49	15.68	18.42	18.46	18.89
MnO	12.06	12.01	12.18	12.17	12.25	0.76	0.79	0.74
MgO	0.64	0.69	0.59	0.64	0.71	9.89	9.86	9.79
CaO	12.09	12.18	12.09	12.04	12.20	11.20	11.21	11.25
Na ₂ O	0.90	0.85	0.91	0.93	0.78	1.10	1.16	1.13
K ₂ O	0.79	0.79	0.79	0.82	0.78	0.86	0.73	0.99
Total	97.13	96.84	97.12	96.93	97.32	96.10	96.23	96.30
<i>Plagioclase (mol.%)</i>								
An	64.8	64.8	64.8	64.8	64.8	43.8	44.2	44.3
Ab	34.5	34.5	34.5	34.5	34.5	53.8	55.1	54.9
Or	0.8	0.8	0.8	0.8	0.8	2.4	0.7	0.9
<i>T</i> (°C)	817	803	813	818	807	753	758	774

(Continued.)

A.1. Supplementary Material to Chapter 2

Sample	WA21-11	WA21-11	WA21-11	WA21-11	WA21-11	CJ4B	CJ12B	CJ12B
Rock type	Tonalite	Tonalite	Tonalite	Tonalite	Tonalite	Gabbro	Gabbro	Gabbro
<i>Amphibole (wt.%)</i>								
SiO ₂	44.17	44.30	43.75	43.80	44.66	42.88	45.99	45.36
TiO ₂	0.86	0.80	0.85	0.89	0.95	0.97	1.01	1.12
Al ₂ O ₃	9.00	8.87	9.13	9.24	8.82	9.60	8.82	9.04
FeO	18.66	18.55	18.80	18.83	18.02	18.02	15.60	14.87
MnO	0.82	0.70	0.77	0.78	0.73	0.81	0.66	0.63
MgO	10.00	9.99	9.82	9.82	10.47	9.42	12.31	12.49
CaO	11.21	11.60	11.37	11.30	11.27	11.76	11.33	11.25
Na ₂ O	1.11	0.89	1.08	1.10	1.09	1.10	1.11	1.12
K ₂ O	0.71	0.86	0.85	0.95	0.73	0.91	0.49	0.50
Total	96.55	96.56	96.42	96.71	96.74	95.54	97.46	96.46
<i>Plagioclase (mol.%)</i>								
An	46.8	41.0	40.3	47.6	53.8	55.1	49.1	47.5
Ab	52.2	57.8	58.8	51.5	45.3	44.2	50.4	51.9
Or	1.0	1.2	0.9	0.9	1.0	0.7	0.5	0.5
<i>T</i> (°C)	775	729	748	777	796	758	767	765

(Continued.)

Sample	CJ15A	CJ15A	CJ15A	CJ15A	CJ15A	CJ15A	CJ6	CJ6
Rock type	Gabbro							
<i>Amphibole (wt.%)</i>								
SiO ₂	44.60	44.42	44.46	44.65	45.05	44.69	43.53	43.74
TiO ₂	0.93	1.03	0.90	0.98	0.96	0.89	0.86	0.74
Al ₂ O ₃	8.44	8.89	8.56	8.61	8.58	8.73	9.26	8.70
FeO	16.14	16.14	16.10	16.10	16.03	16.87	18.39	18.50
MnO	0.69	0.71	0.67	0.69	0.70	0.78	9.51	9.58
MgO	11.30	11.39	11.14	11.57	11.53	11.24	0.83	0.84
CaO	11.60	11.42	11.68	11.61	11.47	11.57	11.41	11.58
Na ₂ O	1.21	1.29	1.16	1.26	1.26	1.22	1.17	1.02
K ₂ O	0.61	0.72	0.71	0.63	0.58	0.69	0.76	0.92
Total	95.56	96.07	95.49	96.20	96.21	96.74	95.79	95.69
<i>Plagioclase (mol.%)</i>								
An	43.2	43.9	46.8	41.2	49.0	55.5	48.6	48.6
Ab	56.0	54.9	52.5	57.8	49.6	43.9	50.2	50.2
Or	0.8	1.2	0.7	1.0	1.3	0.6	1.2	1.2
<i>T</i> (°C)	743	761	741	751	769	808	754	748

(Continued.)

A. Supplementary Materials

Sample	CJ6	CJ6	CJ35	CJ35	CJ35	CJ35	CJ35	CJ35
Rock type	Gabbro							
<i>Amphibole (wt.%)</i>								
SiO ₂	42.76	42.89	43.68	44.01	43.76	44.05	44.38	43.82
TiO ₂	0.87	0.85	0.94	0.91	0.88	0.91	0.93	0.96
Al ₂ O ₃	9.50	9.48	8.91	8.87	8.54	8.75	8.83	8.69
FeO	18.51	18.44	17.31	16.97	17.00	17.23	16.89	17.04
MnO	9.45	9.35	10.96	11.08	11.02	11.06	11.33	11.09
MgO	0.83	0.82	0.66	0.67	0.67	0.65	0.68	0.68
CaO	11.44	11.48	11.69	11.72	11.69	11.54	11.57	11.39
Na ₂ O	1.05	1.12	1.13	1.23	1.06	1.19	1.29	1.24
K ₂ O	0.96	0.95	0.83	0.73	0.75	0.74	0.60	0.73
Total	95.42	95.39	96.19	96.21	95.51	96.15	96.55	95.68
<i>Plagioclase (mol.%)</i>								
An	41.2	50.6	55.9	55.9	55.9	55.9	55.9	55.9
Ab	57.4	48.6	43.5	43.5	43.5	43.5	43.5	43.5
Or	1.4	0.9	0.6	0.6	0.6	0.6	0.6	0.6
T (°C)	739	761	819	809	808	821	821	829

(Continued.)

Sample	CJ35	CJ35	CJ35	CJ35	CJ35	CJ35	WA21-26	WA21-26
Rock type	Gabbro	Gabbro						
<i>Amphibole (wt.%)</i>								
SiO ₂	44.12	44.22	44.88	43.63	44.05	43.80	44.98	45.23
TiO ₂	1.00	0.83	1.21	0.94	1.05	0.93	0.96	0.91
Al ₂ O ₃	8.94	8.57	7.89	8.80	8.43	8.33	8.80	8.53
FeO	16.97	17.24	16.86	17.24	17.09	16.35	17.54	17.38
MnO	11.23	11.19	11.39	10.68	11.11	11.48	11.30	11.51
MgO	0.68	0.68	0.68	0.70	0.69	0.66	0.68	0.72
CaO	11.43	11.56	11.53	11.45	11.54	11.41	11.54	11.45
Na ₂ O	1.23	1.10	1.12	1.19	1.16	1.19	1.08	1.11
K ₂ O	0.74	0.80	0.49	0.86	0.74	0.72	0.54	0.50
Total	96.48	96.30	96.10	95.56	95.93	94.96	97.41	97.34
<i>Plagioclase (mol.%)</i>								
An	55.9	58.0	49.5	58.0	58.0	58.0	41.4	62.2
Ab	43.5	41.5	49.9	41.5	41.5	41.5	58.1	34.5
Or	0.6	0.5	0.7	0.5	0.5	0.5	0.5	3.4
T (°C)	827	830	800	820	834	838	769	857

(Continued.)

A.1. Supplementary Material to Chapter 2

Sample	WA21-26							
Rock type	Gabbro							
<i>Amphibole (wt.%)</i>								
SiO ₂	44.74	44.67	45.19	44.24	44.35	44.47	44.83	44.74
TiO ₂	0.99	1.04	0.87	0.95	0.96	0.93	0.95	0.96
Al ₂ O ₃	8.76	8.93	8.44	8.75	8.57	8.78	8.56	8.62
FeO	17.82	17.56	17.54	17.38	17.25	17.22	17.38	17.37
MnO	11.24	11.21	11.30	11.06	11.00	11.02	11.32	11.20
MgO	0.64	0.64	0.64	0.63	0.68	0.67	0.63	0.67
CaO	11.63	11.43	11.77	11.21	11.46	11.44	11.10	11.14
Na ₂ O	1.06	1.19	1.07	1.21	1.05	1.13	1.24	1.20
K ₂ O	0.51	0.63	0.55	0.51	0.56	0.52	0.49	0.51
Total	97.40	97.31	97.37	95.94	95.88	96.19	96.50	96.41
<i>Plagioclase (mol.%)</i>								
An	45.8	57.7	50.8	48.0	42.4	44.5	61.4	46.0
Ab	53.8	42.0	48.7	51.5	56.8	54.9	37.9	53.6
Or	0.5	0.3	0.5	0.6	0.8	0.6	0.7	0.4
<i>T</i> (°C)	794	839	792	799	763	768	859	791

(Continued.)

Sample	WA21-26							
Rock type	Gabbro							
<i>Amphibole (wt.%)</i>								
SiO ₂	44.27	44.43	44.44	44.85	44.47	45.02	44.33	45.25
TiO ₂	1.04	1.00	0.95	0.91	0.94	0.97	0.97	0.95
Al ₂ O ₃	9.02	8.89	8.73	8.62	8.83	8.51	9.02	8.62
FeO	17.50	17.41	17.30	17.25	17.49	17.38	17.49	17.16
MnO	10.95	11.07	11.27	11.26	11.08	11.32	11.12	11.37
MgO	0.68	0.63	0.70	0.66	0.66	0.66	0.56	0.60
CaO	11.16	11.21	11.23	11.39	11.29	11.30	11.47	11.21
Na ₂ O	1.30	1.23	1.21	1.10	1.14	1.15	1.16	1.13
K ₂ O	0.56	0.54	0.51	0.52	0.58	0.52	0.48	0.43
Total	96.48	96.41	96.34	96.56	96.48	96.82	96.60	96.71
<i>Plagioclase (mol.%)</i>								
An	46.0	52.1	52.1	47.4	65.1	46.7	45.4	48.9
Ab	53.6	47.1	47.1	52.0	34.6	52.9	54.0	50.6
Or	0.4	0.7	0.7	0.6	0.3	0.4	0.6	0.5
<i>T</i> (°C)	793	813	822	785	865	792	784	783

(Continued.)

A. *Supplementary Materials*

Sample	WA21-26	WA21-26	WA21-26	CJ2A	CJ2A	CJ2A	CJ2A
Rock type	Gabbro	Gabbro	Gabbro	Leucoto.	Leucoto.	Leucoto.	Leucoto.
<i>Amphibole (wt.%)</i>							
SiO ₂	44.64	44.84	44.26	43.92	44.13	44.86	44.11
TiO ₂	0.91	0.93	0.92	0.83	0.81	0.73	0.91
Al ₂ O ₃	8.91	8.68	9.11	9.09	8.96	8.42	9.30
FeO	17.38	17.30	17.72	19.27	19.09	18.87	19.16
MnO	11.25	11.23	10.77	9.28	9.67	9.92	9.55
MgO	0.56	0.54	0.53	0.96	0.95	0.99	0.93
CaO	11.36	11.26	11.41	11.37	11.21	11.24	11.17
Na ₂ O	1.16	1.14	1.15	1.01	1.10	1.01	1.22
K ₂ O	0.49	0.41	0.44	0.80	0.77	0.81	0.80
Total	96.65	96.33	96.31	96.53	96.68	96.85	97.16
<i>Plagioclase (mol.%)</i>							
An	48.4	41.3	53.5	45.2	61.1	61.1	45.2
Ab	51.2	58.3	46.1	53.9	38.4	38.4	53.9
Or	0.4	0.4	0.4	0.9	0.5	0.5	0.9
<i>T</i> (°C)	794	762	801	750	829	816	767

Leucoto., leucotonalite

A.2 Supplementary Material to Chapter 3

A.2.1 Supplementary Figures

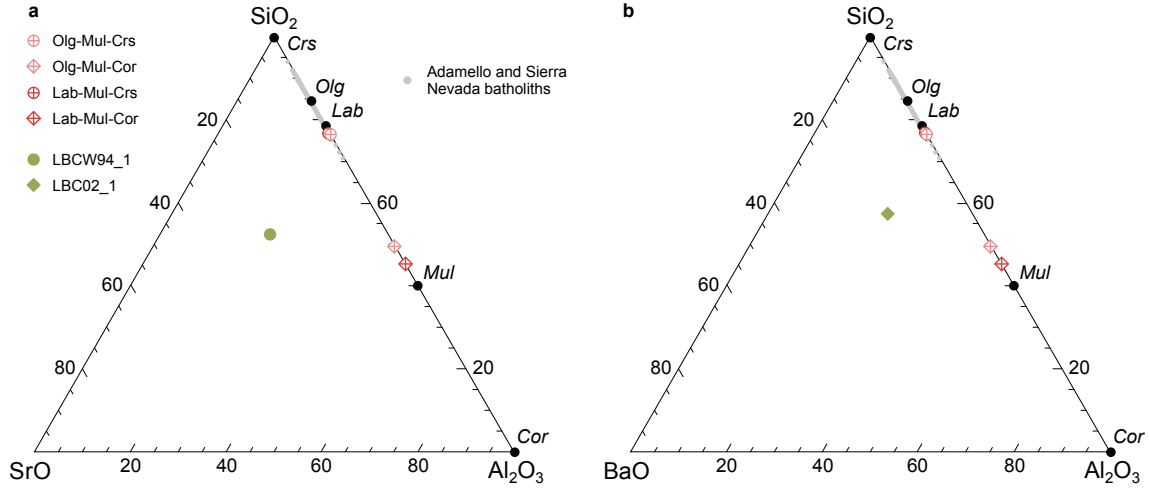


Figure A2.1. Compositions of the source powders used in this study. **a**, SiO₂-Al₂O₃-SrO ternary diagram highlighting the composition of the four source powders synthesised using the sol-gel method and the Sr-enriched source powder synthesised from oxide powders following [Cherniak and Watson \(1992, 1994\)](#). Note the different Sr concentrations between the sol-gel-derived powders and the ones used in the experiments of [Cherniak and Watson \(1992, 1994\)](#). **b**, SiO₂-Al₂O₃-BaO ternary diagram highlighting the composition of the four source powders synthesised using the sol-gel method and the Ba-enriched source powder synthesised from oxide powders following [Cherniak \(2002\)](#). Note the different Ba concentrations between the sol-gel-derived powders and the ones used in the experiments of [Cherniak \(2002\)](#).

A. Supplementary Materials

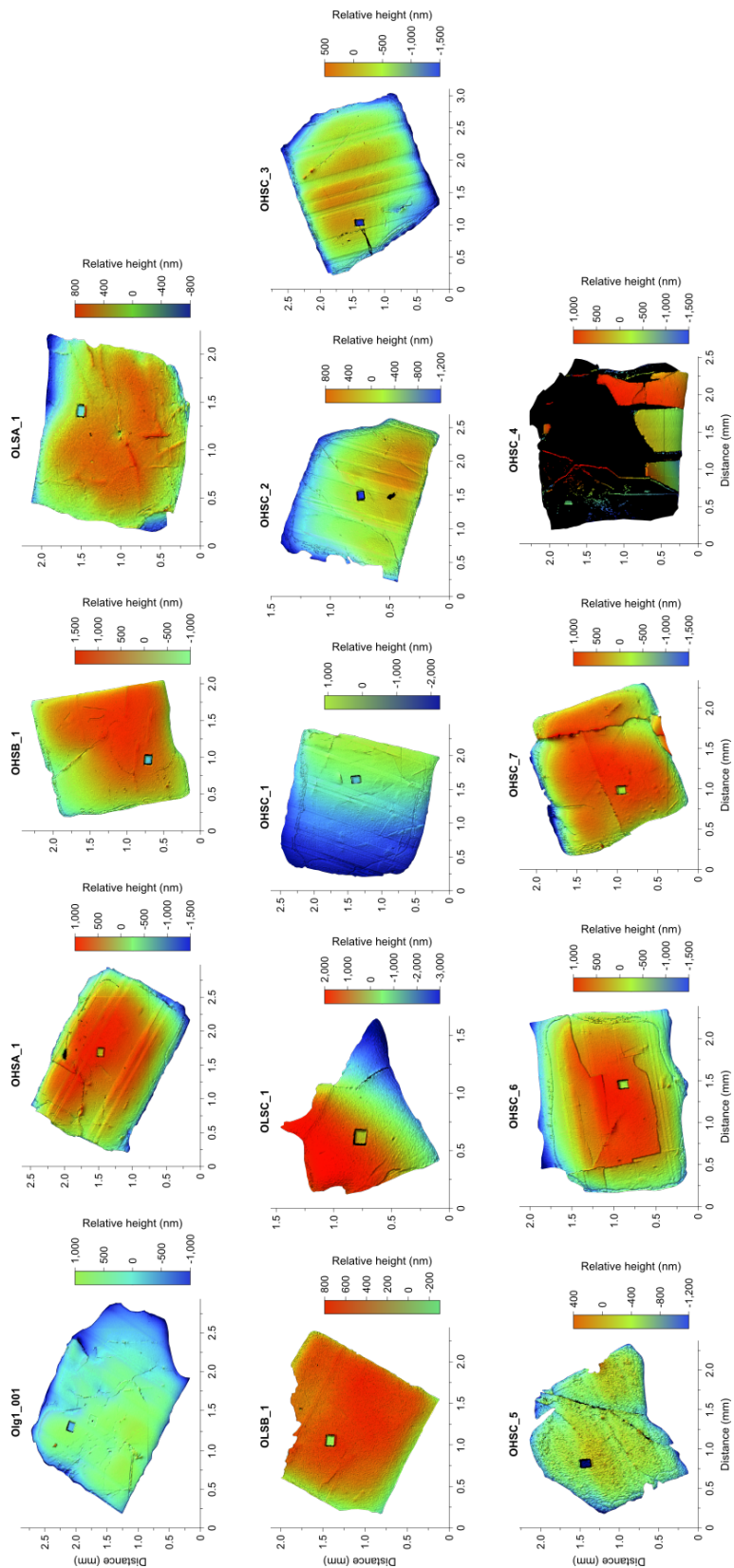


Figure A2.2. Topography variations of the diffusion interface from the experimental runs using oligoclase as starting material.

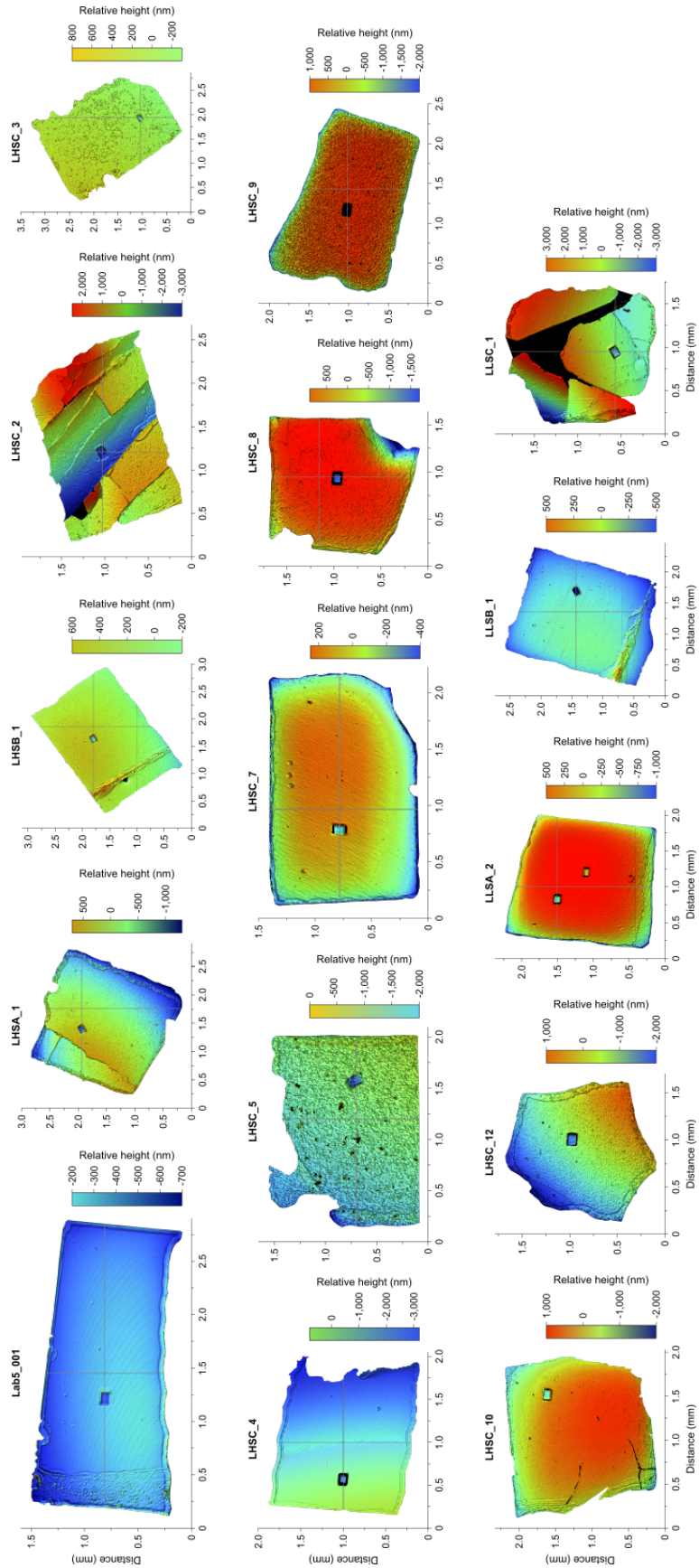


Figure A2.3. Topography variations of the diffusion interface from the experimental runs using labradorite as starting material.

A. Supplementary Materials

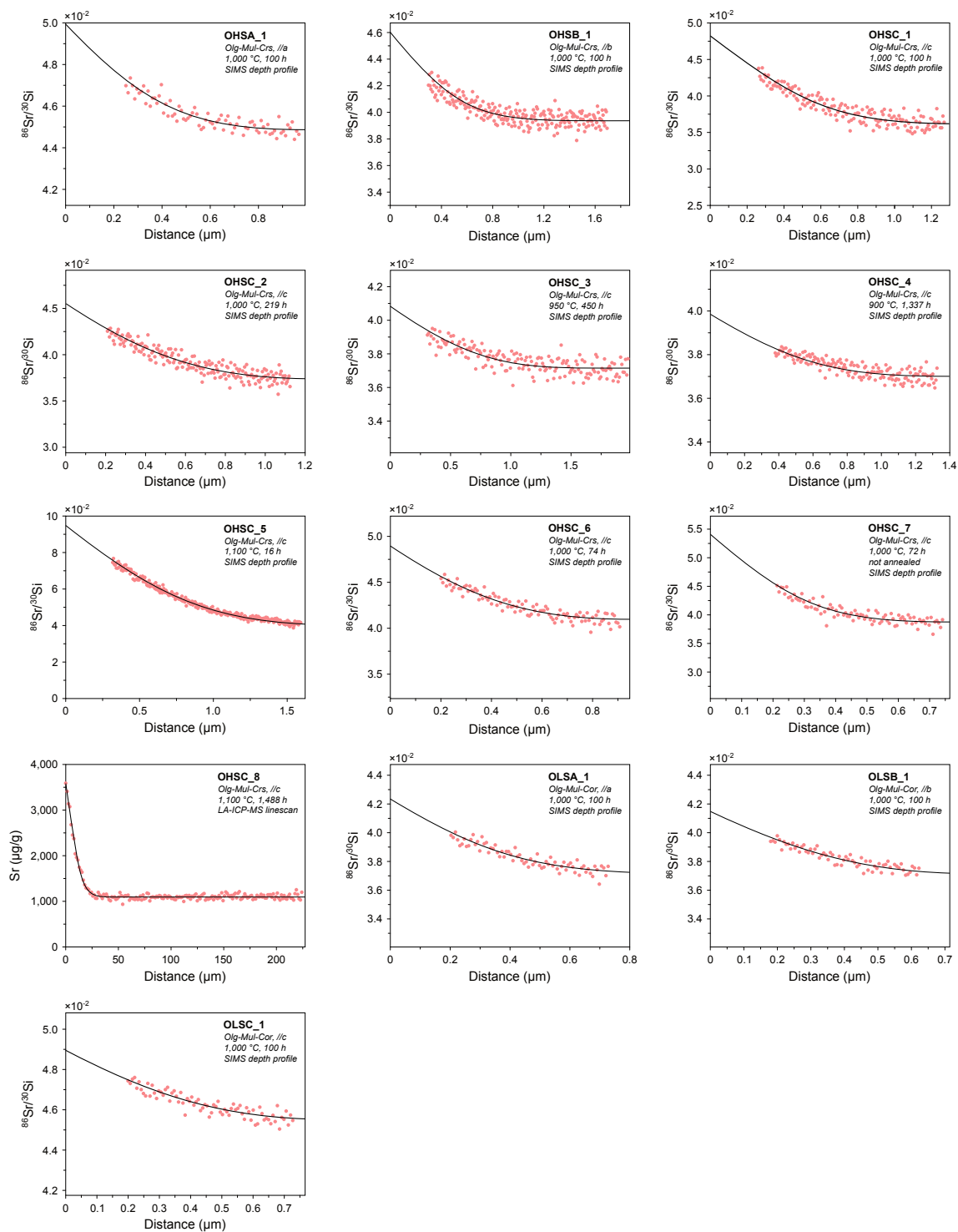


Figure A2.4. Experimental diffusion profiles for Sr in oligoclase measured by SIMS depth profiling or LA-ICP-MS line scanning. The stable phase assemblage of the Sr and Ba source powders and analytical technique used for each experiment are labelled, along with temperature and duration of the experiments. Model fits are solid lines obtained using Eq. 3.1 from the main text.

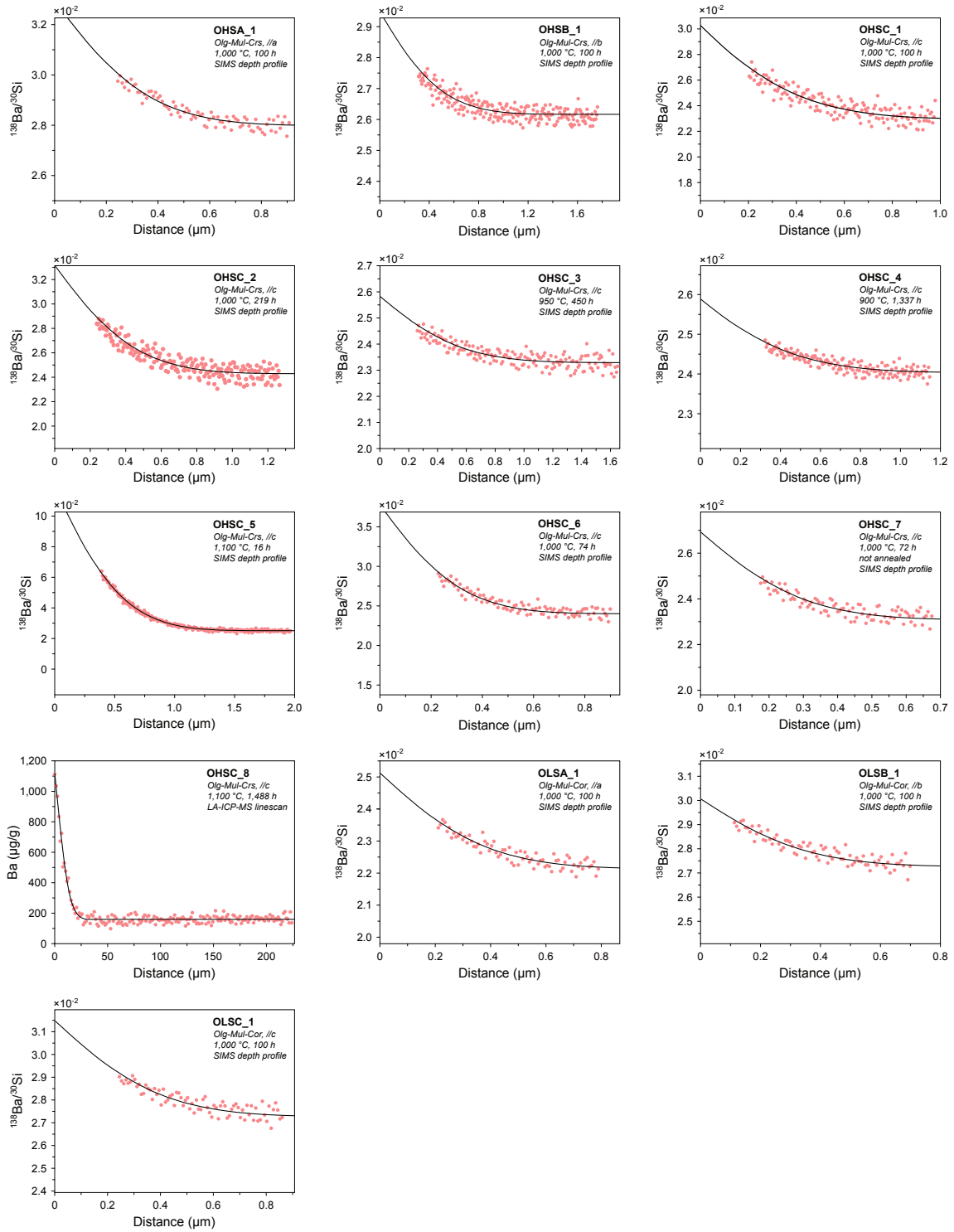


Figure A2.5. Experimental diffusion profiles for Ba in oligoclase measured by SIMS depth profiling or LA-ICP-MS line scanning. The stable phase assemblage of the Sr and Ba source powders and analytical technique used for each experiment are labelled, along with temperature and duration of the experiments. Model fits are solid lines obtained using Eq. 3.1 from the main text.

A. Supplementary Materials

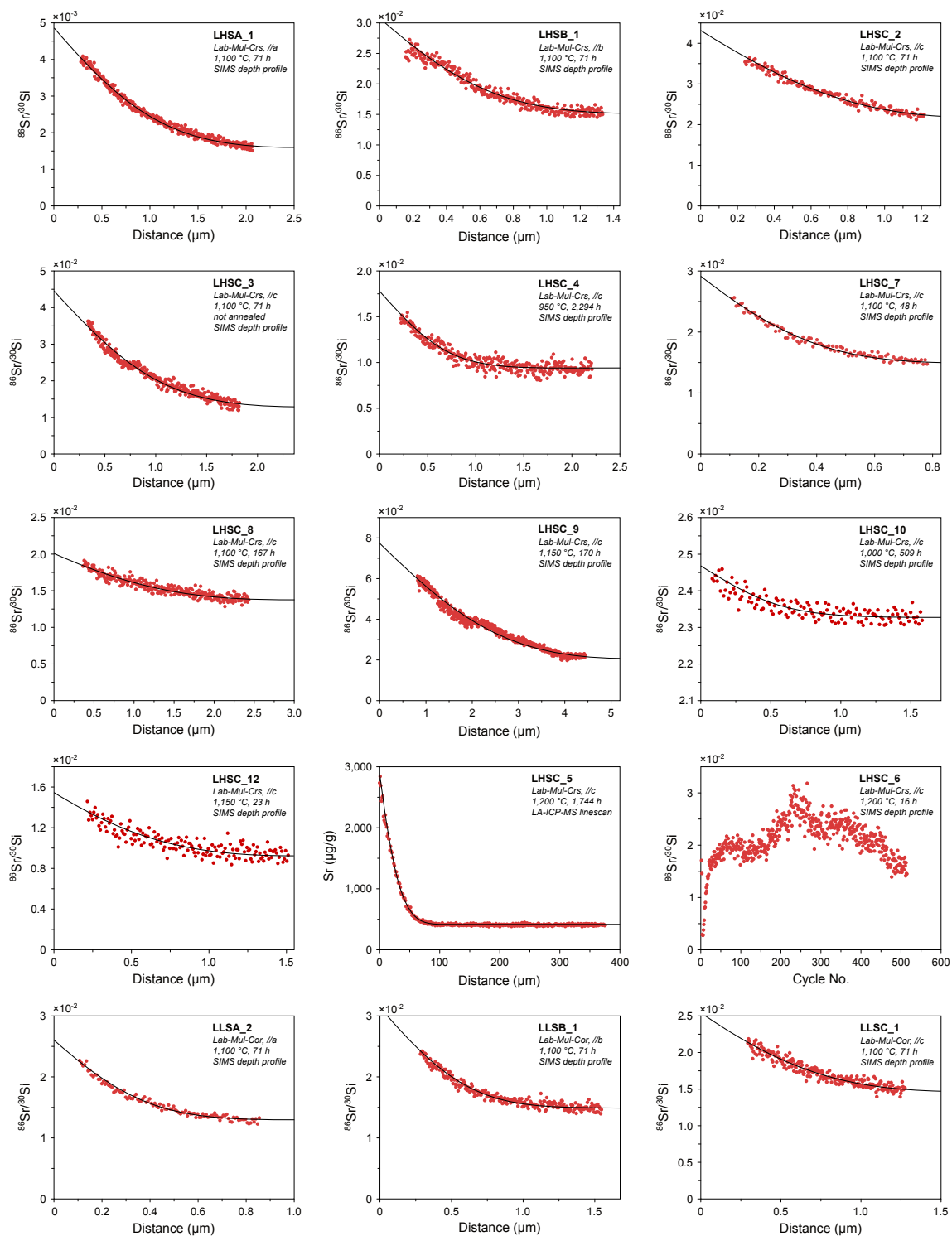


Figure A2.6. Experimental diffusion profiles for Sr in labradorite measured by SIMS depth profiling or LA-ICP-MS line scanning. The stable phase assemblage of the Sr and Ba source powders and analytical technique used for each experiment are labelled, along with temperature and duration of the experiments. Model fits are solid lines obtained using Eq. 3.1 from the main text.

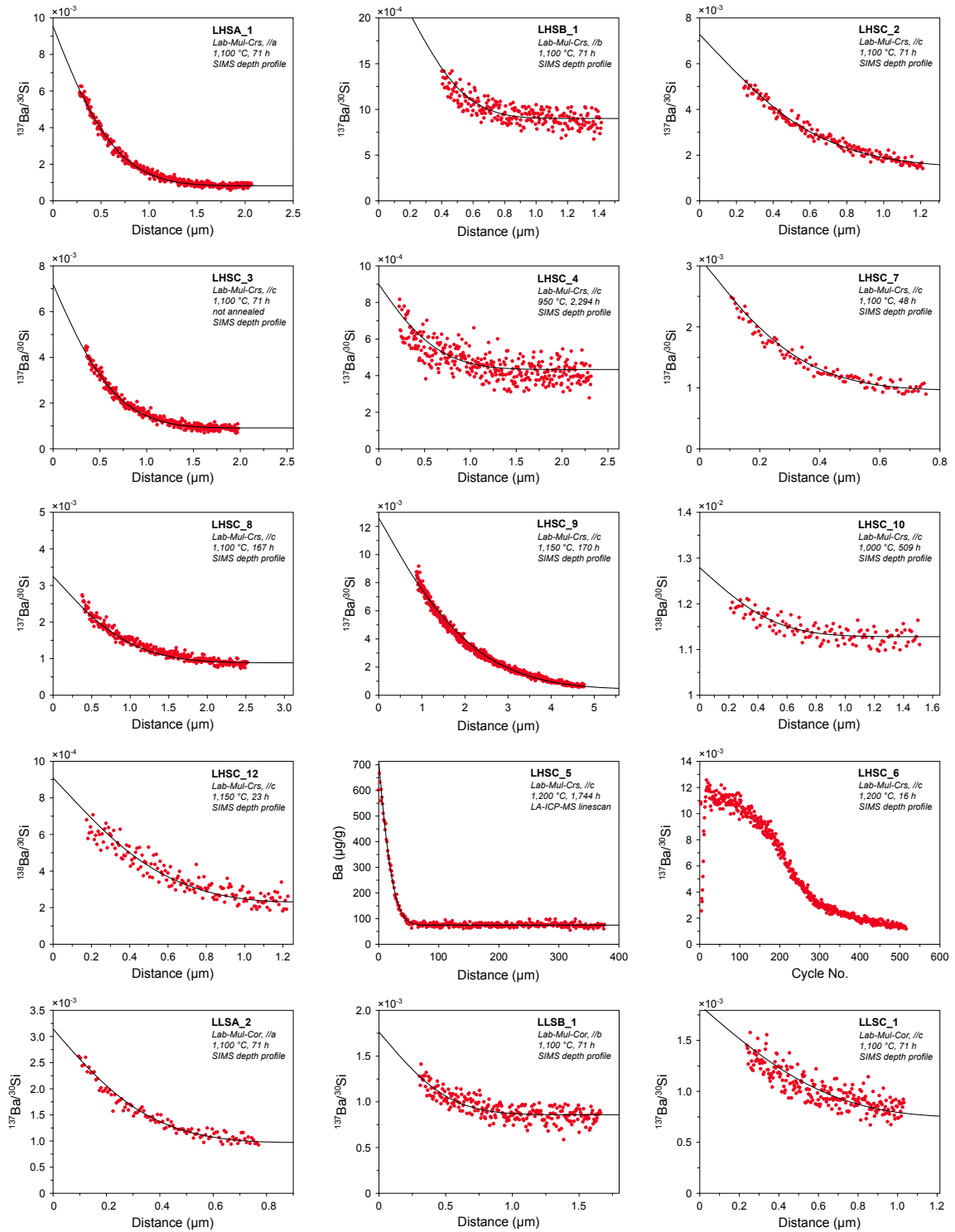


Figure A2.7. Experimental diffusion profiles for Ba in labradorite measured by SIMS depth profiling or LA-ICP-MS line scanning. The stable phase assemblage of the Sr and Ba source powders and analytical technique used for each experiment are labelled, along with temperature and duration of the experiments. Model fits are solid lines obtained using Eq. 3.1 from the main text.

A. Supplementary Materials

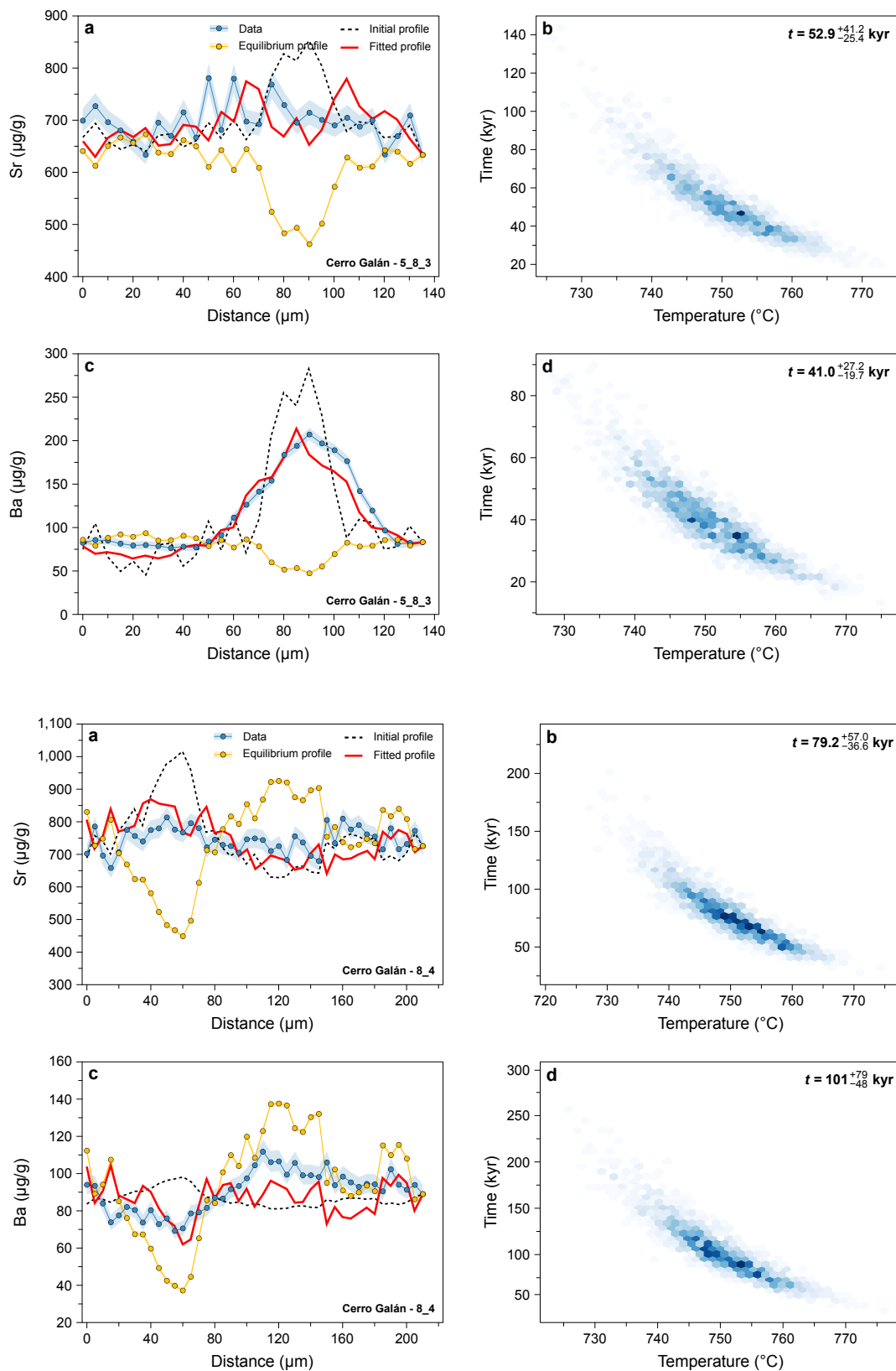


Figure A2.8. (Continued.)

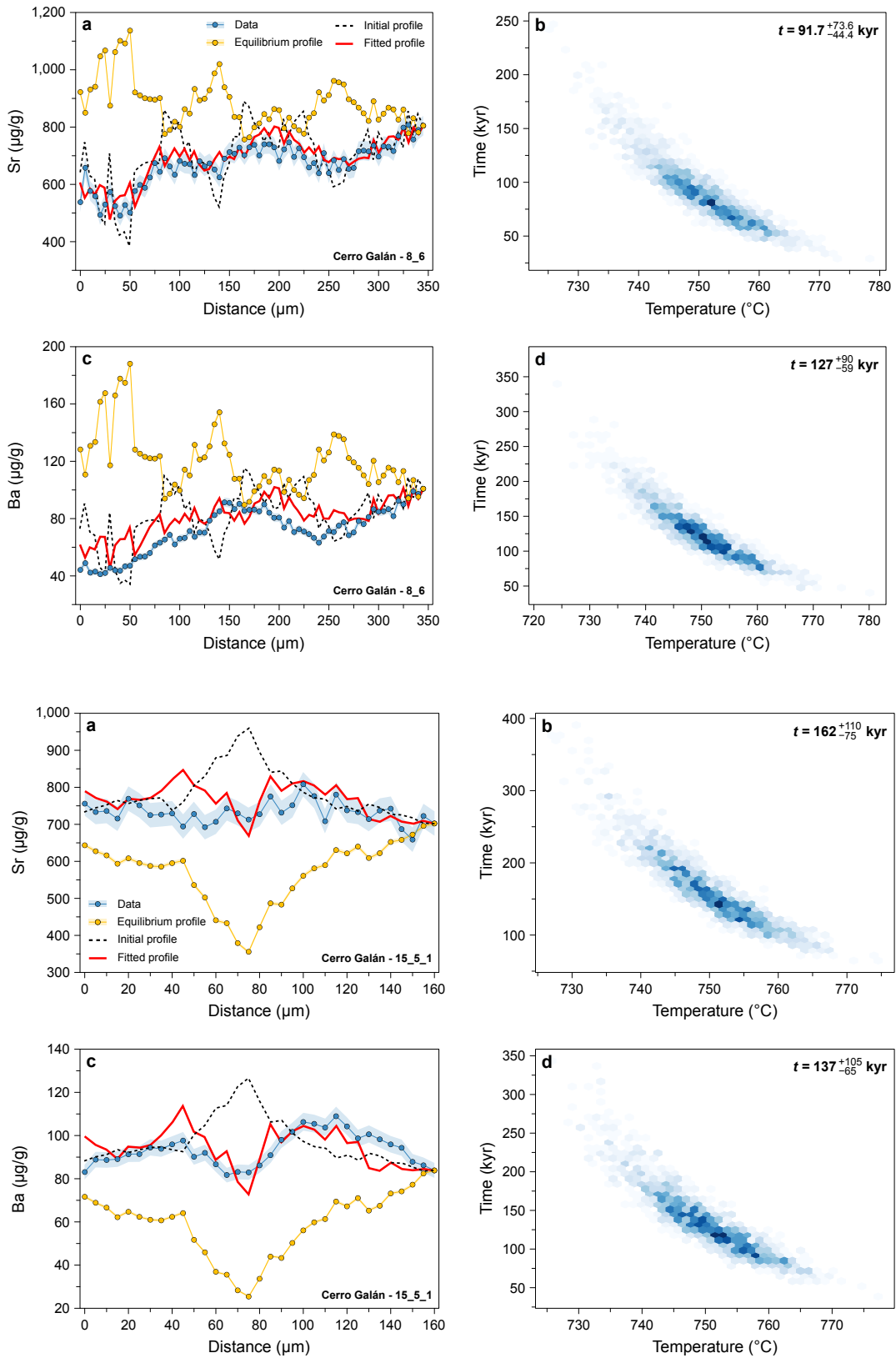


Figure A2.8. (Continued.)

A. Supplementary Materials

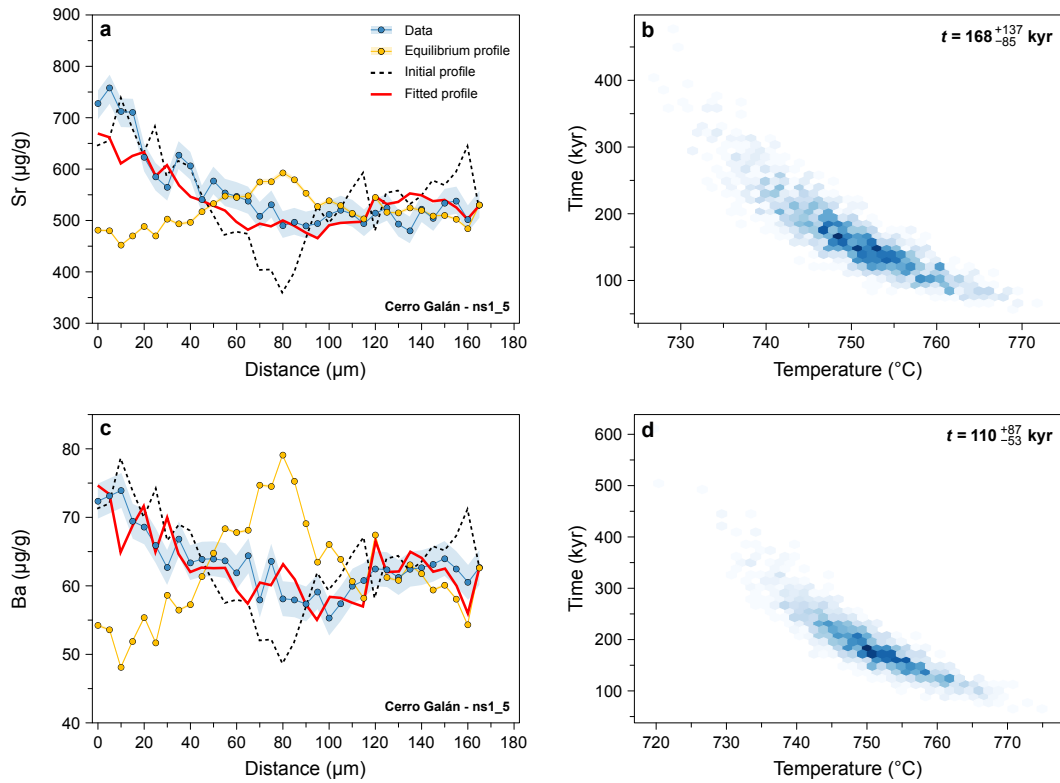


Figure A2.8. Application of the parameterised Sr and Ba diffusion coefficients determined in this study to natural data from the Cerro Galán ignimbrite. (a, c) Plagioclase Sr and Ba diffusion profiles alongside the initial profiles, the equilibrium profiles, and the fitted profiles. (b, d) Results of the Monte Carlo simulation represented as temperature ($^{\circ}\text{C}$) vs. time (kyr). See main text for explanations regarding diffusion modelling and Monte Carlo resampling.

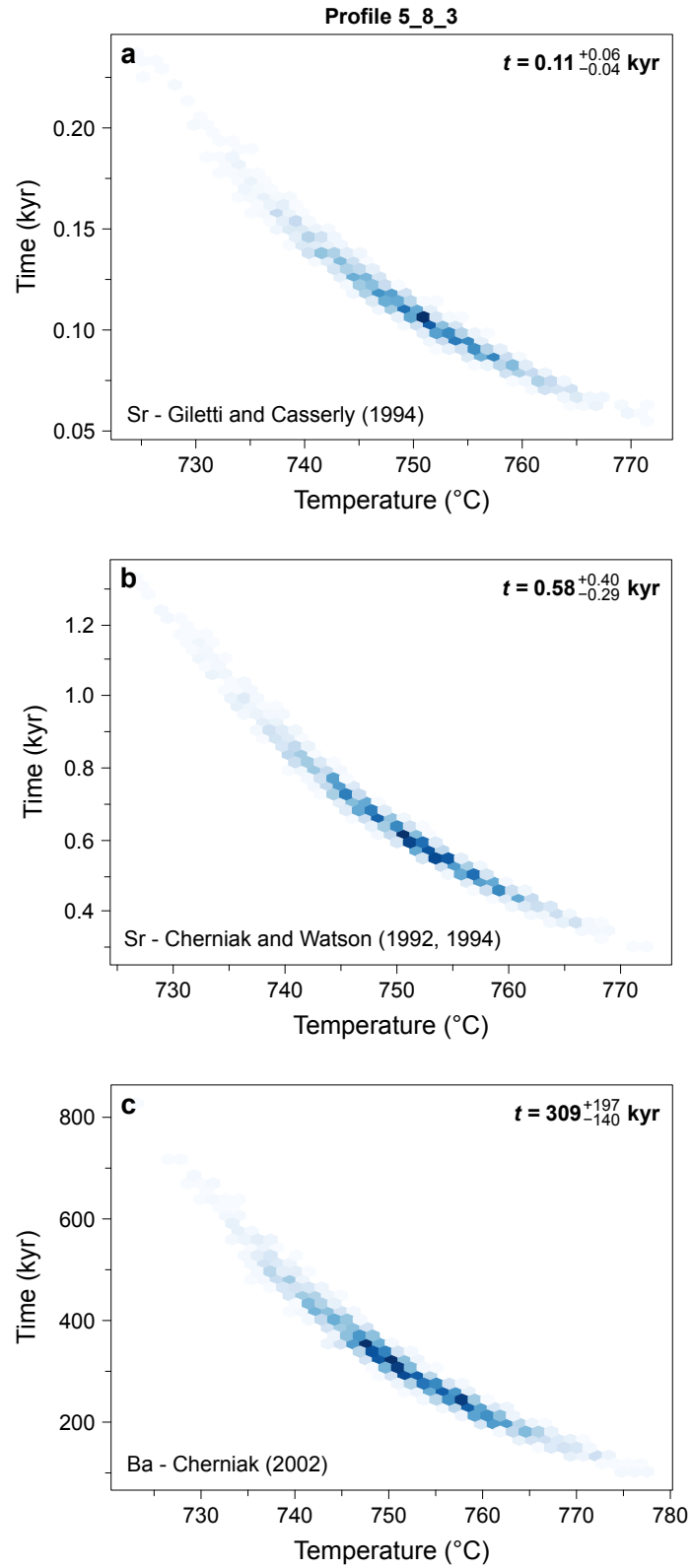


Figure A2.9. (Continued.)

A. Supplementary Materials

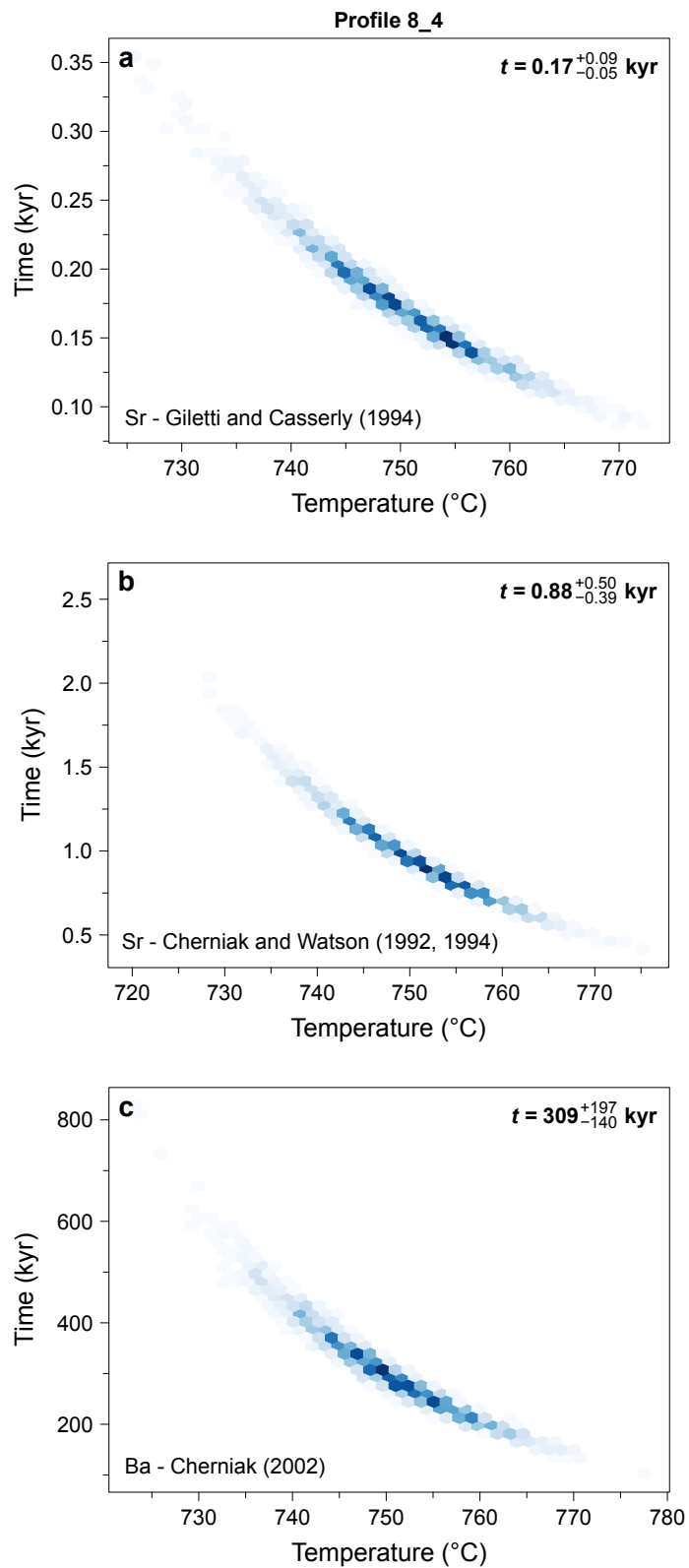


Figure A2.9. (Continued.)

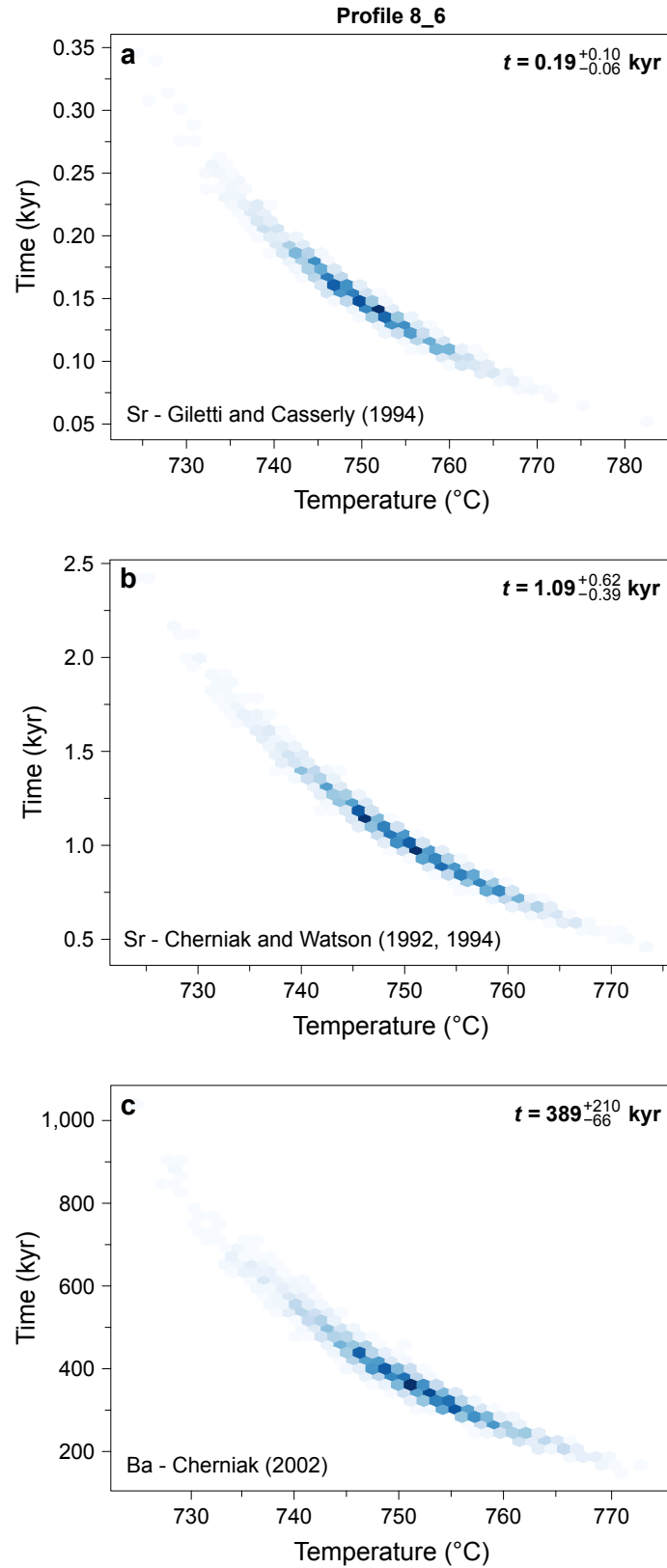


Figure A2.9. (Continued.)

A. Supplementary Materials

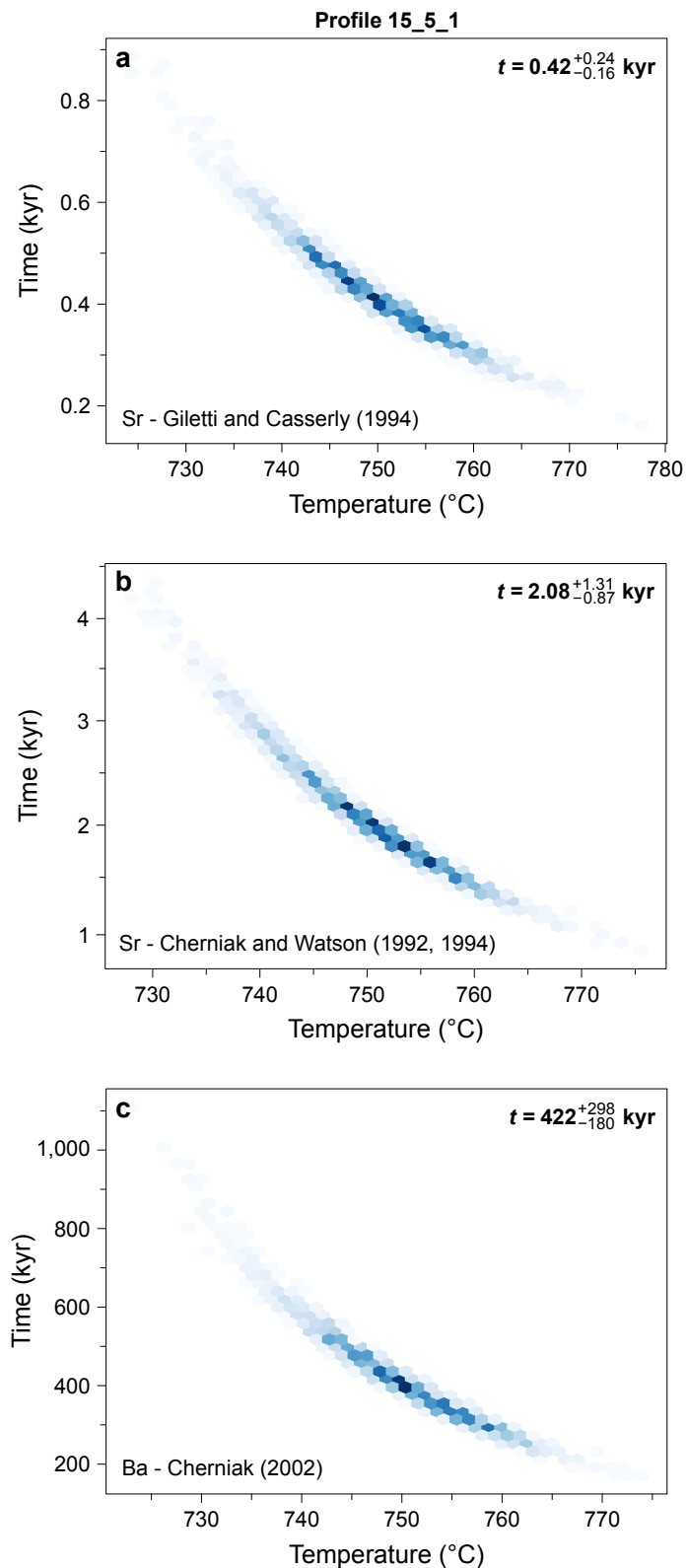


Figure A2.9. (Continued.)

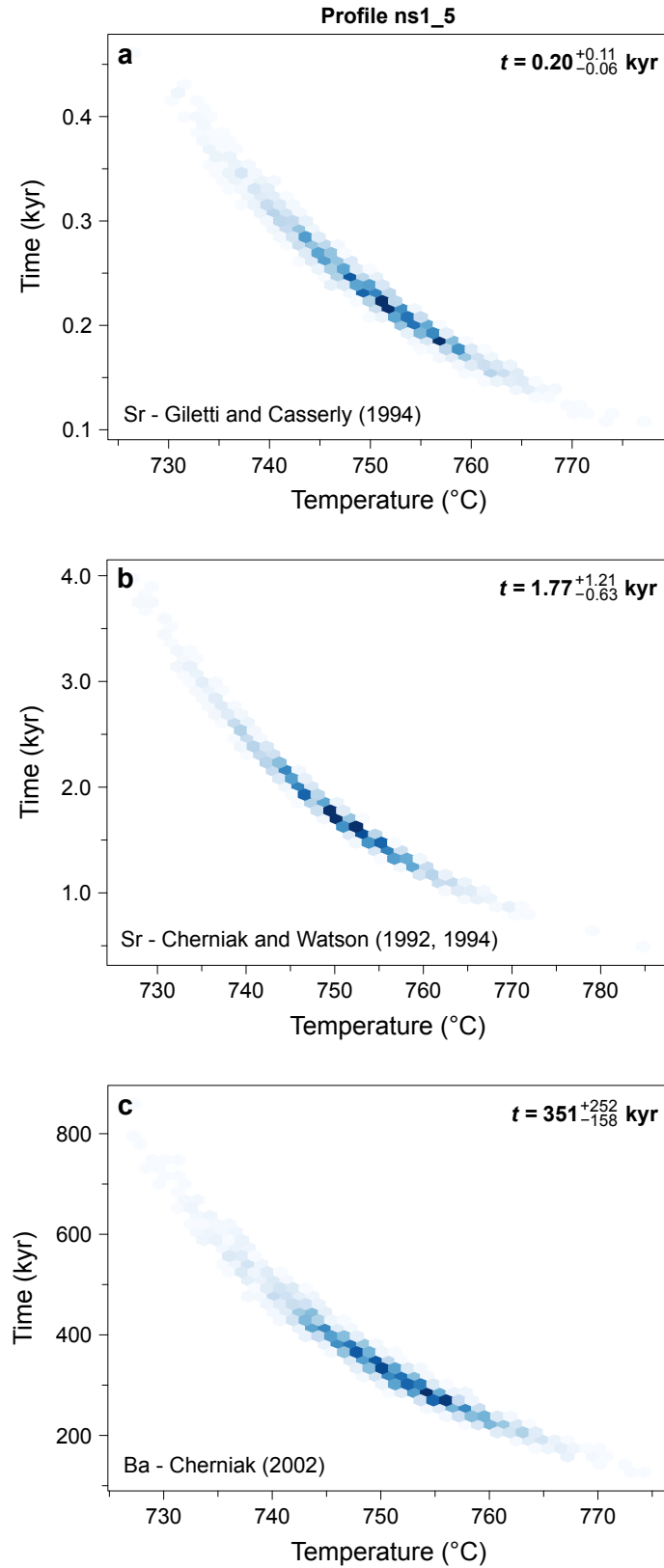


Figure A2.9. (Continued.)

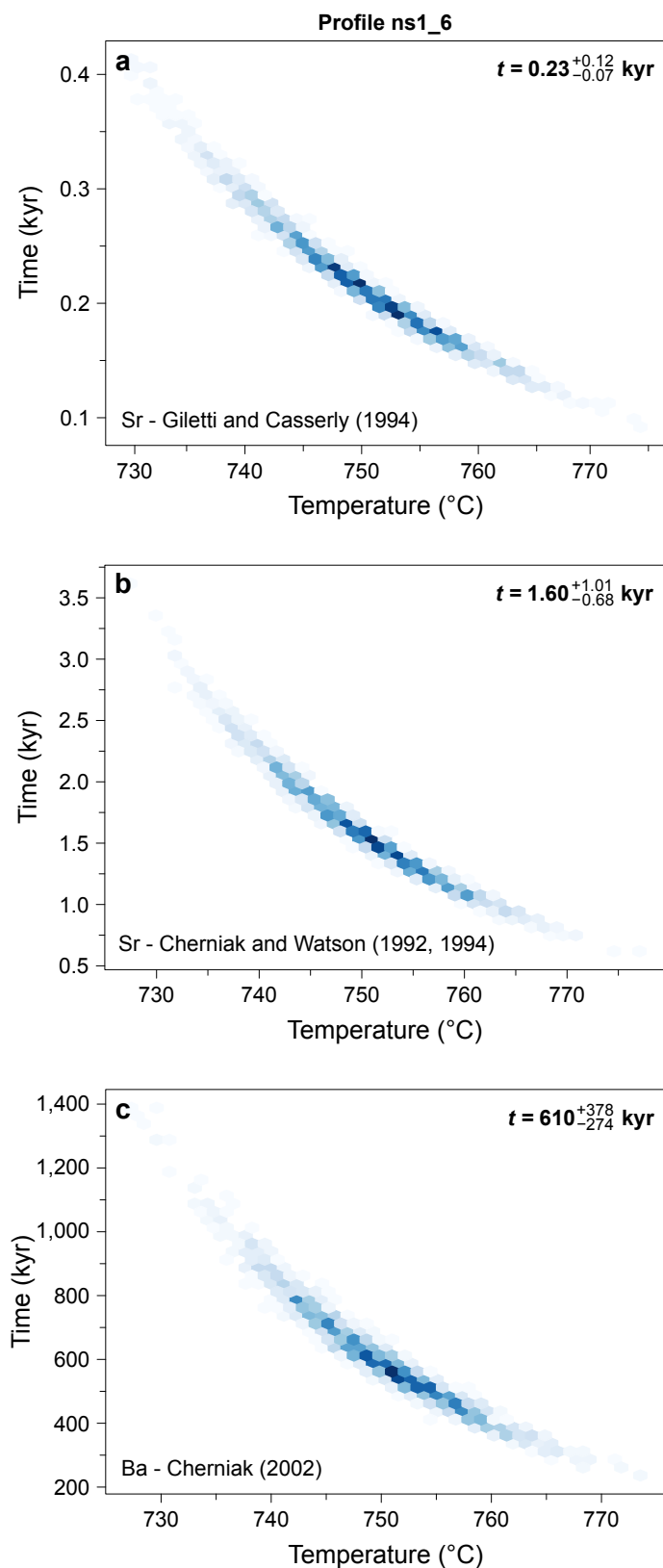


Figure A2.9. Results of the Monte Carlo diffusion modelling using diffusion coefficients from previous studies applied to the same plagioclase crystals from the Cerro Galán ignimbrite (Lubbers et al., 2022) as in Figs. 3.11 and A2.8. **a**, Sr diffusion in plagioclase using the data from Giletti and Casserly (1994). **b**, Sr diffusion in plagioclase using the data from Cherniak and Watson (1992, 1994). **c**, Ba diffusion in plagioclase using the data from Cherniak (2002).

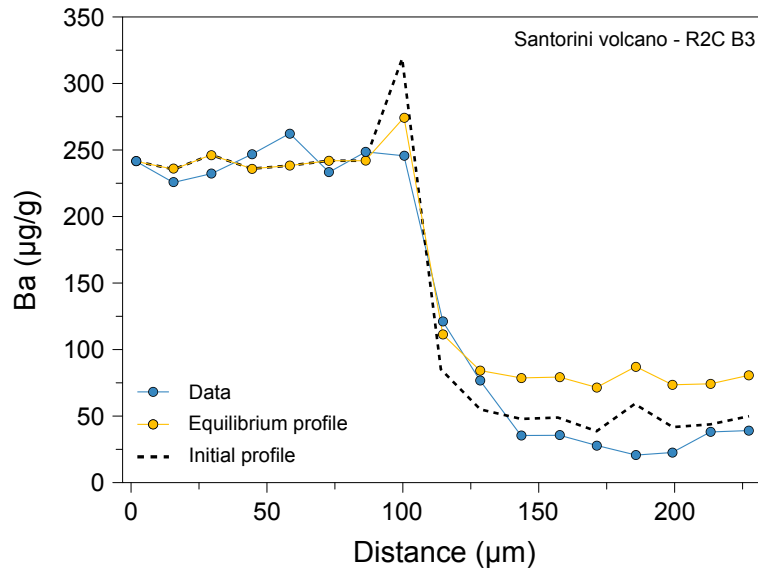


Figure A2.10. Plagioclase Ba diffusion profile from the same plagioclase crystal from the Santorini caldera (Druitt et al., 2012) as in Fig. 3.11 alongside the initial profile and the equilibrium profile. Note the similarity between the three profiles, highlighting that the measured Ba profile reached quasi-steady state.

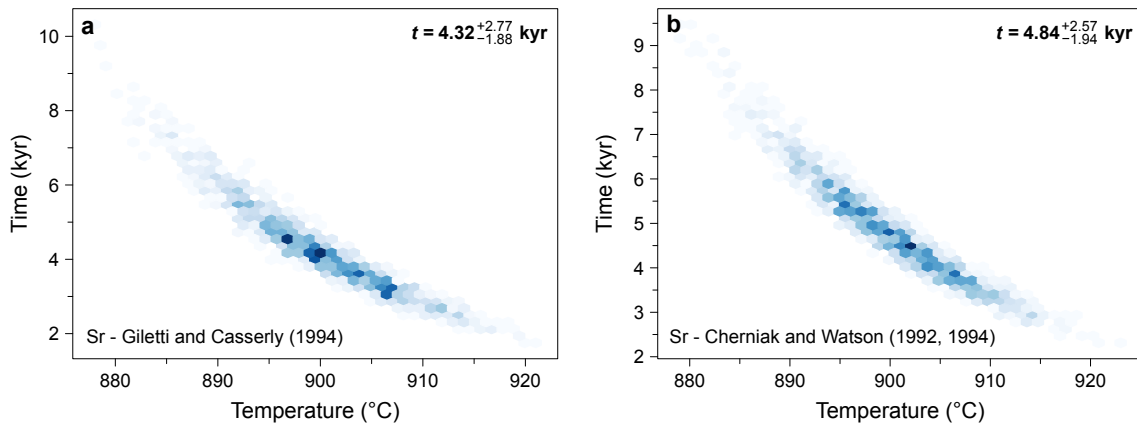


Figure A2.11. Results of the Monte Carlo diffusion modelling using diffusion coefficients from previous studies applied to the same plagioclase crystal from the Santorini caldera (Druitt et al., 2012) as in Fig. 3.11. **a**, Sr diffusion in plagioclase using the data from Giletti and Casserly (1994). **b**, Sr diffusion in plagioclase using the data from Cherniak and Watson (1992, 1994).

A.2.2 Supplementary Tables

Table A2.1. Summary of the experimental designs used for the determination of Sr, Ba and Mg diffusivities in plagioclase.

Reference	Cation	T (°C)	Crystal composition	Crystal orientation	Source	$a\text{SiO}_2$	Analytical technique
Cherniak and Watson (1992)	Sr^{2+}	724-1,076	An_{93}	// b	Oxide powder	n.d.	RBS depth profiling
Cherniak and Watson (1994)	Sr^{2+}	724-1,076	An_{23-67}	// b, c	Oxide powder	n.d.	RBS depth profiling
Cherniak (2002)	Ba^{2+}	775-1,124	An_{23-67}	// b, c	Oxide powder	n.d.	RBS depth profiling
Faak et al. (2013)	Mg^{2+}	1,100-1,200	An_{12-70}	n.d.	Natural powder	0.45-1.00	EPMA
Giletti and Casserly (1994)	Sr^{2+}	550-1,300	An_{2-96}	// a, b, c	Solution	n.d.	SIMS depth profiling
LaTourrette and Wasserburg (1998)	$\text{Sr}^{2+}, \text{Mg}^{2+}$	1,200-1,400	An_{95}	// b, c	Synthetic glass	n.d.	SIMS
Van Orman et al. (2014)	Mg^{2+}	798-1,150	An_{23-93}	// b, c	Oxide powder	1.00	SIMS depth profiling

n.d., not determined

Table A2.2. Starting material used to synthesise the source powders used in this study.

Phase	Mix No.	Tetraethyl orthosilicate (g)	Al-nitrate (g)	Sr-nitrate (g)	Ba-nitrate (g)
Mullite	Mul10	2.0100	7.1000	0.0215	0.0072
Mullite	Mul11	4.7200	14.5873	0.0468	0.0161
Mullite	Mul15	1.4131	5.4600	0.0248	0.0092
Cristobalite	Crs3	10.4500	-	-	-
Cristobalite	Crs8	11.0200	-	-	-
Corundum	Cor3	-	7.9500	-	-
Corundum	Cor5	-	18.4910	-	-

Table A2.3. Mixing proportions of the source powders used in this study.

Powder assemblage	Plagioclase (g)	Mullite (g)	Cristobalite (g)	Corundum (g)
Olg1-Mul15-Crs8	0.60	0.60	0.60	-
Olg1-Mul15-Cor5	0.42	0.42	-	0.35
Lab1-Mul11-Crs3	0.60	0.60	0.60	-
Lab1-Mul10-Cor3	0.30	0.30	-	0.30

Table A2.4. Mixing proportions of the source powders used to recreate the diffusion experiments of Cherniak and Watson (1992, 1994) and Cherniak (2002).

Powder assemblage	SiO ₂ (g)	Al ₂ O ₃ (g)	SrO (g)	BaO (g)	Labradorite (g)
Lab-Si-Al-Sr	0.3136	0.2615	0.3919	-	0.3222
Lab-Si-Al-Ba	0.1503	0.1255	-	0.1884	0.1549

A. Supplementary Materials

Table A2.5. Major and trace element composition of the source powders used in this study.

	Olg-Mul-Crs	2 s.d.	Olg-Mul-Cor	2 s.d.	Lab-Mul-Crs	2 s.d.	Lab-Mul-Cor	2 s.d.
<i>Major elements (wt.%)</i>								
SiO ₂	61.12	0.21	29.95	0.16	60.64	0.14	26.74	0.12
TiO ₂	<0.01	0	<0.01	0	<0.01	0	<0.01	0
Al ₂ O ₃	33.85	0.10	65.31	0.09	33.77	0.09	67.20	0.14
FeO	0.03	0.03	0.03	0.03	0.14	0.02	0.15	0.04
MnO	<0.01	0	0.01	0.01	<0.01	0	0.01	0.01
MgO	<0.01	0	<0.01	0	<0.01	0	<0.01	0
CaO	2.16	0.06	2.04	0.05	4.49	0.04	4.53	0.10
Na ₂ O	2.81	0.07	2.66	0.03	1.25	0.11	1.20	0.09
K ₂ O	0.14	0.02	0.13	0.01	0.03	0.02	0.02	0.01
Total	100.11	0.22	100.12	0.19	100.32	0.28	99.85	0.22
<i>Trace elements (µg/g)</i>								
Sc	1.13	0.22	0.36	0.05	2.21	0.09	0.29	0.08
Rb	2.58	0.34	1.07	0.13	1.01	2.09	0.28	0.04
Sr	3611	30	1725	8	2253	125	1071	36
Y	0.203	0.097	0.162	0.059	0.177	0.084	0.222	0.024
Zr	30.78	2.53	14.96	1.19	5.17	4.27	6.36	1.61
Nb	0.165	0.249	0.036	0.028	0.504	0.876	0.096	0.003
Cs	0.223	0.487	0.258	0.408	0.512	0.384	0.063	0.100
Ba	1611	14	797	10	923	74	437	19
La	1.73	0.10	0.82	0.03	0.20	0.06	0.82	0.05
Ce	2.82	0.15	1.45	0.18	0.81	0.34	1.39	0.09
Pr	0.262	0.043	0.138	0.030	0.158	0.164	0.216	0.131
Nd	0.752	0.035	0.326	0.005	0.200	0.125	0.347	0.073
Sm	0.129	0.041	0.080	0.050	0.083	0.104	0.052	0.030
Eu	0.215	0.044	0.122	0.030	0.134	0.109	0.051	0.028
Gd	0.097	0.138	0.070	0.054	0.086	0.040	0.059	0.012
Tb	0.022	0.015	0.006	0.006	0.096	0.177	0.026	0.042
Dy	0.030	0.022	0.056	0.137	0.127	0.046	0.044	0.032
Ho	0.038	0.072	0.016	0.022	0.043	0.035	0.017	0.021
Er	0.045	0.033	0.011	0	0.112	0.204	0.018	0.017
Tm	0.073	0.160	0.062	0.187	0.049	0.111	0.0430	0.1103
Yb	0.037	0.045	0.009	0.010	0.090	0.121	0.042	0.083
Lu	0.016	0.018	0.006	0.012	0.114	0.147	1.3093	0.0422
Hf	0.735	0.014	5.228	0.065	0.791	1.978	1.826	0.217
Ta	0.052	0.030	0.055	0.039	0.069	0.055	0.013	0.014
Pb	4.51	0.46	2.27	0.46	2.91	1.66	2.29	0.82
Th	0.173	0.027	0.068	0.014	0.174	0.204	0.061	0.014
U	0.399	0.439	0.423	0.604	0.607	0.228	0.167	0.314

Table A2.6. Major and trace element composition of the starting materials used in this study.

	Lab-4	2 s.d.	Lab-5	2 s.d.	Olg-1	2 s.d.	Olg-2	2 s.d.
<i>Major elements (wt.%)</i>								
SiO ₂	51.78	0.48	51.97	0.32	61.86	0.27	61.65	0.35
TiO ₂	<0.01	0.01	0.01	0.01	0.01	0.01	<0.01	0
Al ₂ O ₃	29.62	0.27	29.87	0.26	24.21	0.19	24.12	0.22
FeO	0.45	0.08	0.45	0.011	0.12	0.05	0.09	0.06
MnO	0.02	0.01	0.01	0.01	0.01	0.01	0.02	0.01
MgO	0.01	0.01	0.01	0.01	<0.01	0	<0.01	0
CaO	13.46	0.16	13.46	0.19	6.04	0.09	6.11	0.10
Na ₂ O	3.63	0.08	3.75	0.11	7.99	0.21	7.97	0.28
K ₂ O	0.12	0.03	0.10	0.03	0.40	0.04	0.39	0.06
Total	99.09	0.58	99.63	0.79	100.64	0.57	100.35	0.70
An (mol.%)	66.7	0.5	66.0	0.5	28.8	0.4	29.1	0.6
<i>Trace elements (µg/g)</i>								
Sc	0.37	0.05	0.34	0.04	0.45	0.04	0.46	0.05
V	2.77	0.07	2.67	0.27	0.03	0.01	0.03	0.01
Zn	2.78	1.04	2.43	0.27	0.51	0.09	1.13	2.84
Rb	0.107	0.015	0.115	0.024	0.253	0.039	0.631	0.708
Sr	576	25	596	51	1130	29	757	18
Y	0.249	0.012	0.243	0.022	0.139	0.059	0.132	0.052
Zr	0.013	0.005	0.013	0.003	0.009	0.010	0.007	0.001
Cs	0.006	0	0.008	0	b.d.l.	b.d.l.	0.017	0
Ba	61.3	2.1	66.0	8.3	138.2	1.3	110.6	2.2
La	0.432	0.019	0.440	0.033	2.44	0.07	5.54	0.05
Ce	0.81	0.05	0.82	0.04	3.63	0.10	7.89	0.09
Pr	0.101	0.008	0.101	0.009	0.337	0.017	0.698	0.014
Nd	0.48	0.06	0.49	0.07	1.09	0.04	2.21	0.08
Sm	0.097	0.010	0.096	0.012	0.131	0.012	0.227	0.033
Eu	0.242	0.018	0.249	0.021	0.327	0.017	0.594	0.011
Gd	0.089	0.018	0.087	0.011	0.072	0.006	0.113	0.020
Tb	0.010	0.002	0.010	0.002	0.006	0.001	0.010	0.001
Dy	0.051	0.005	0.053	0.010	0.021	0.005	0.033	0.008
Ho	0.0089	0.0019	0.0087	0.0021	0.0028	0.0008	0.0040	0.0020
Er	0.021	0.002	0.021	0.005	0.0052	0.0008	0.0068	0.0046
Tm	0.0021	0.0007	0.0020	0.0004	0.0010	0.0000	0.0013	0.0010
Yb	0.012	0.004	0.013	0.004	0.0035	0.0010	0.0043	0.0012
Lu	0.0017	0.0007	0.0014	0.0004	0.0010	0	0.0010	0
Pb	0.184	0.029	0.189	0.026	8.00	0.18	7.41	0.68
Th	<0.001	0	<0.001	0	<0.001	0	0.0010	0.0014
U	<0.001	0	<0.001	0.000	<0.001	0	<0.001	0

A.3 Supplementary Material to Chapter 4

A.3.1 Supplementary Text

The temperature evolution of the Western Adamello tonalite was modelled by solving the two-dimensional axisymmetric formulation of the heat equation (Eq. A3.1):

$$\rho c \frac{\partial T}{\partial t} = \frac{1}{r} \frac{\partial}{\partial r} \left(r k \frac{\partial T}{\partial r} \right) + \frac{\partial}{\partial z} \left(k \frac{\partial T}{\partial z} \right) + \rho L \left(\frac{\partial X_c}{\partial t} \right), \quad (\text{A3.1})$$

where T is the temperature ($^{\circ}\text{C}$), t is the time (s), r is the radial coordinate relative to the symmetry axis (m), z is the depth (m), k is the thermal conductivity ($\text{W m}^{-1} \text{K}^{-1}$), L is the latent heat of crystallisation (J kg^{-1}), ρ is the magma density (kg m^{-3}), c is the specific heat ($\text{J kg}^{-1} \text{K}^{-1}$), and X_c is the magma crystallinity. The values associated with these parameters can be found in the Supplementary Material 3. The employed liquidus and solidus temperatures were 950°C and 670°C , respectively, while the magma crystallinity was parameterised based on the experiments of Marxer and Ulmer (2019) and follows Eq. A3.2:

$$X_c = -0.002632 \times T + 2.7105. \quad (\text{A3.2})$$

Calculations were performed based on those of Floess and Baumgartner (2015), whereby a magma reservoir grows by the horizontal stacking of vertical, 20-m-thick dikes with a flow time of 60 yr and a no-flow time of 3,000 yr. These values correspond to an average magma flux of $2 \times 10^{-4} \text{ km}^3 \text{ yr}^{-1}$, assuming a dike length of 3 km and a width of 10 km, which is similar to the flux inferred from high-precision zircon dating (Floess, 2013).

Eq. A3.1 was numerically solved using an explicit finite-difference method. The numerical grid was large enough ($15 \times 15 \text{ km}$) so that the boundary conditions were kept constant. The temperature evolution, as shown on Fig. 4.11 from the main text, was tracked at a point located 3 km away from the southwestern contact, which corresponds to the average of the three investigated leucotonalite samples. Following the high-precision zircon ages (Floess, 2013), the magma flux was stopped after 1.2 Myr of dike injection. Although this ignores the subsequent development of the Central Adamello leucotonalite (CAL), the leucotonalite sample are located $\geq 1 \text{ km}$ away from the contact with the CAL, therefore limiting its thermal impact on the central part of the WAT. The complete temperature evolution of the point of interest can be found in the Supplementary Material 3.

A.3.2 Supplementary Figures

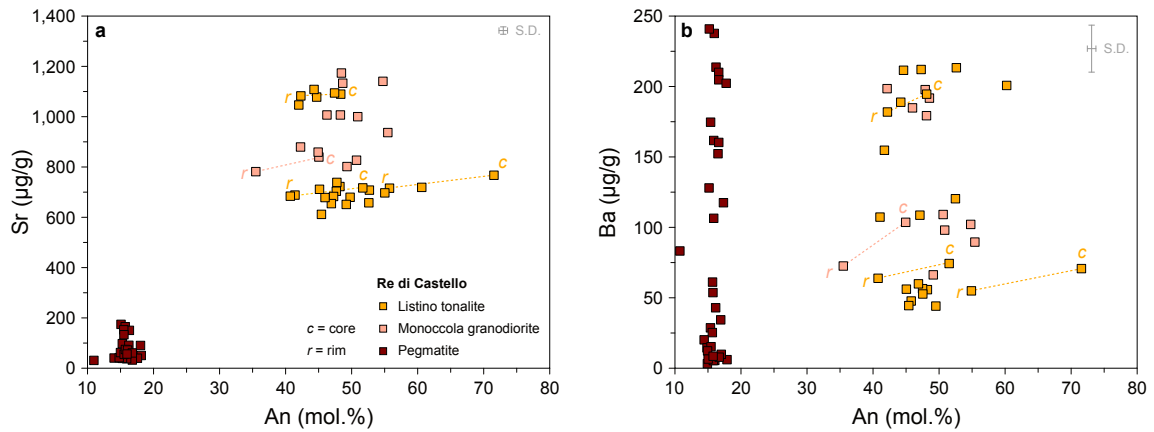


Figure A3.1. Composition of plagioclase from the Listino ring complex measured by LA-ICP-MS spot analysis. **a**, An (mol.%) vs. Sr (µg/g). **b**, An (mol.%) vs. Ba (µg/g). Core-rim pairs are shown to highlight the slope and, therefore, the mechanism controlling trace element diffusion in plagioclase.

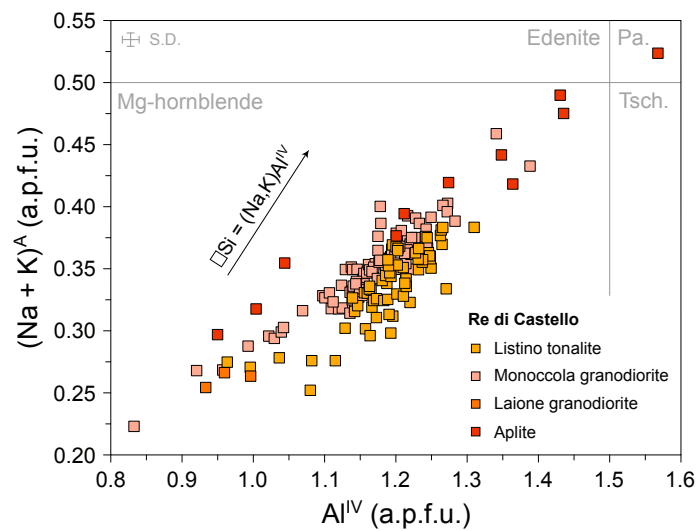


Figure A3.2. Composition of amphibole from the Re di Castello superunit, which comprised the Listino ring complex, plotted as Al^{IV} (a.p.f.u.) vs. $(Na + K)^A$ (a.p.f.u.). The edenite exchange controlling the amphibole chemistry is also represented.

A. Supplementary Materials

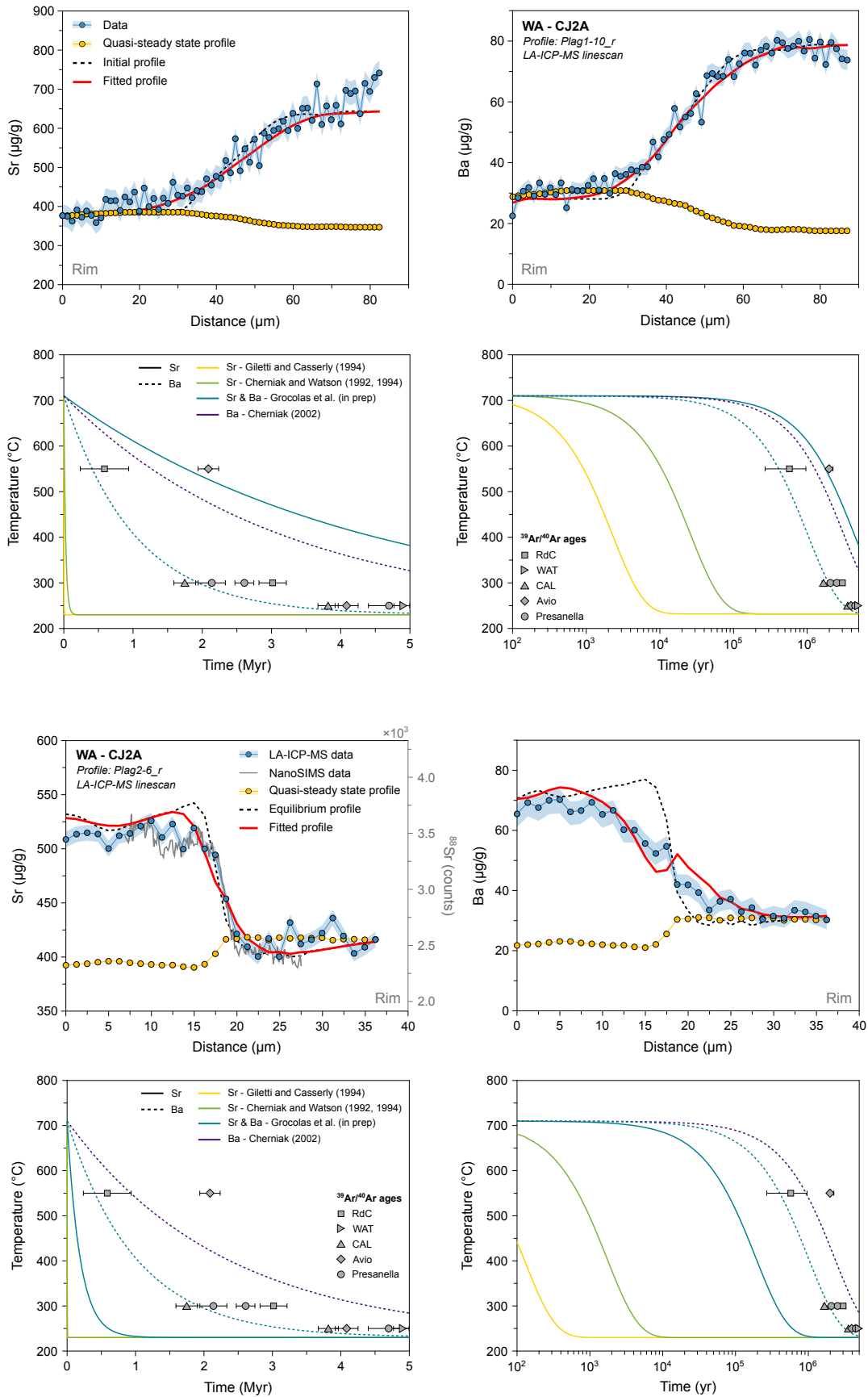


Figure A3.3. (Continued.)

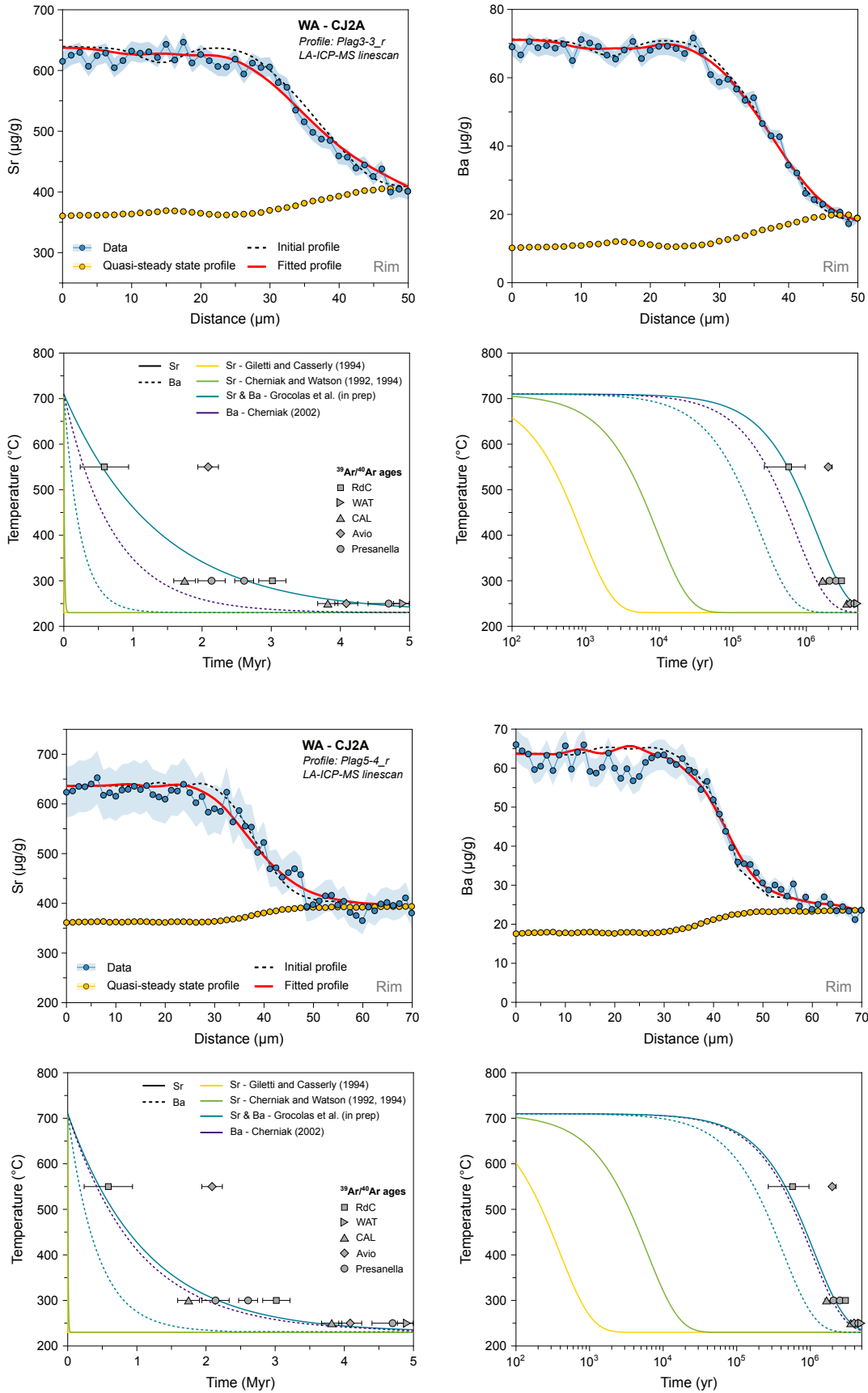


Figure A3.3. (Continued.)

A. Supplementary Materials

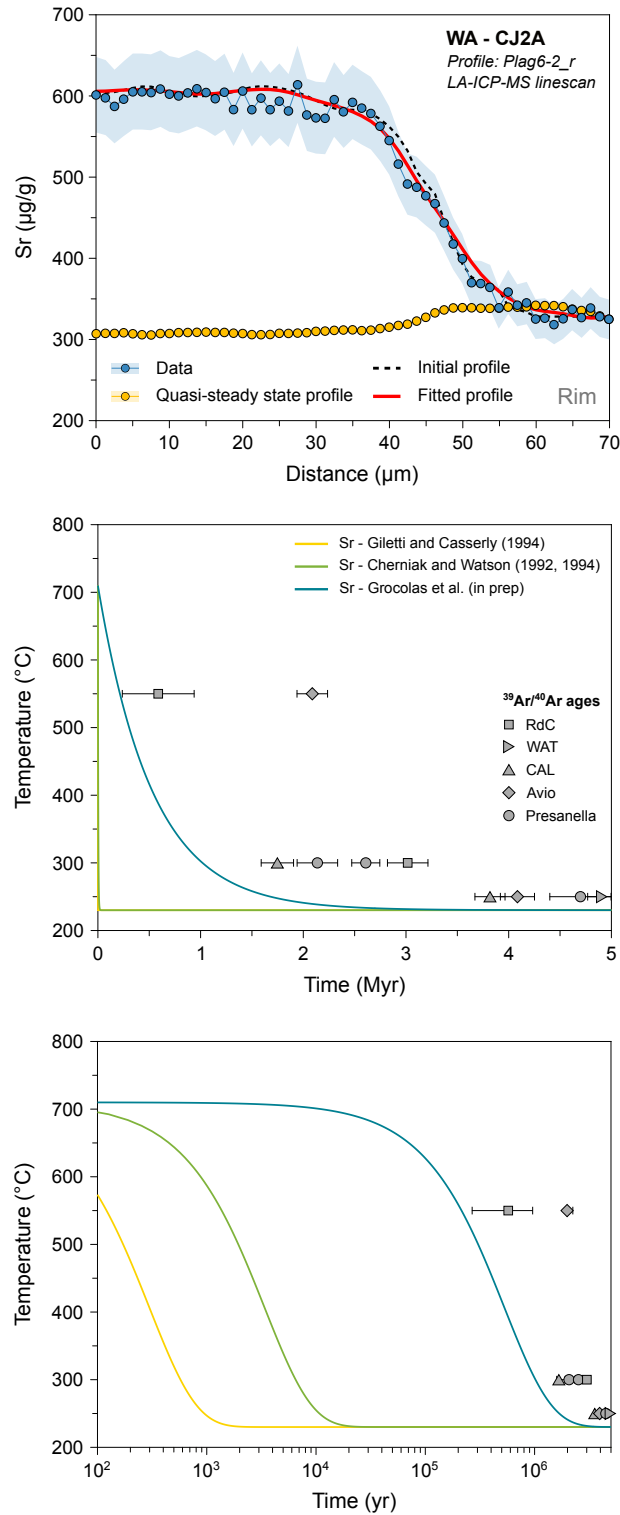


Figure A3.3. (Continued.)

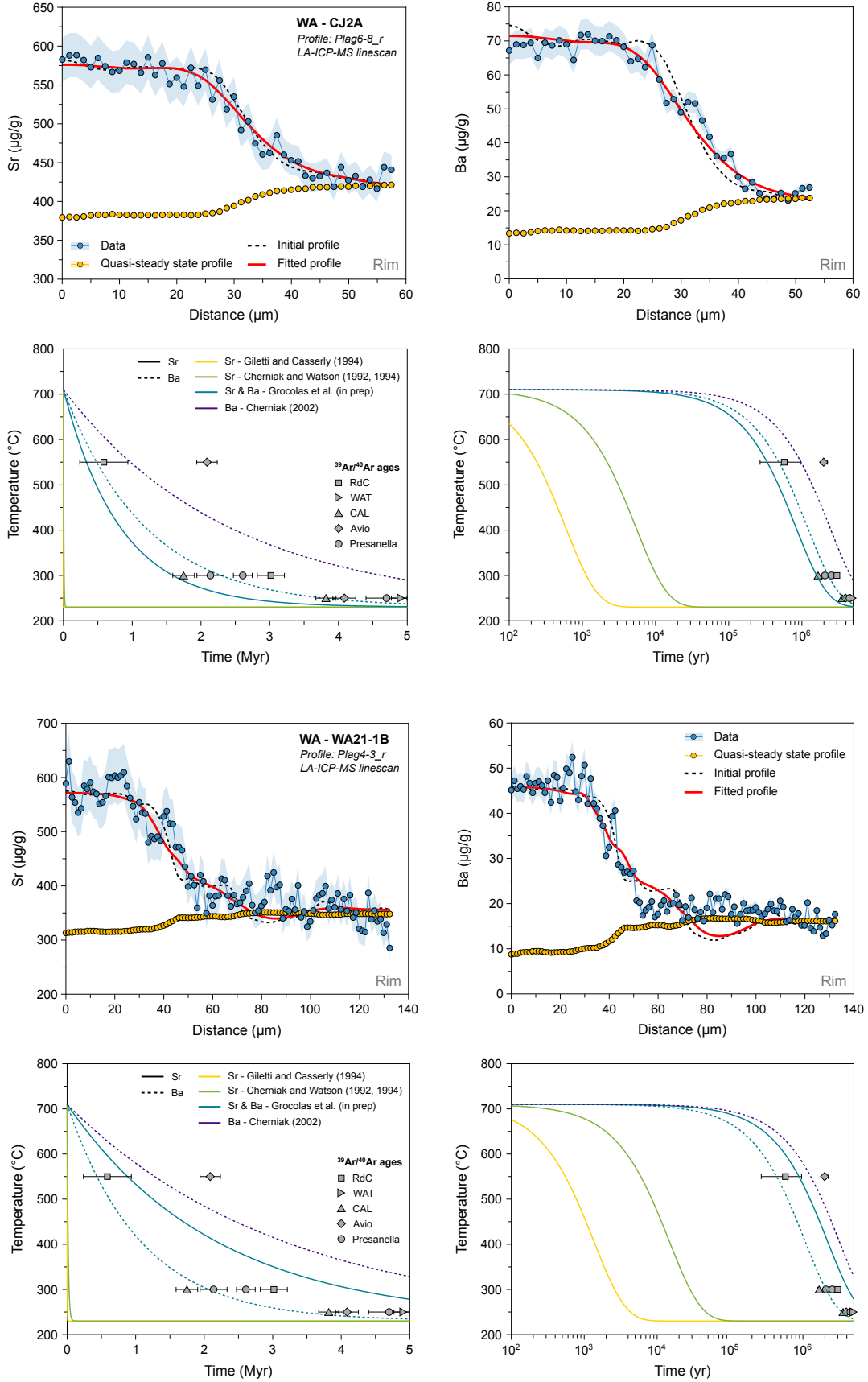


Figure A3.3. (Continued.)

A. Supplementary Materials

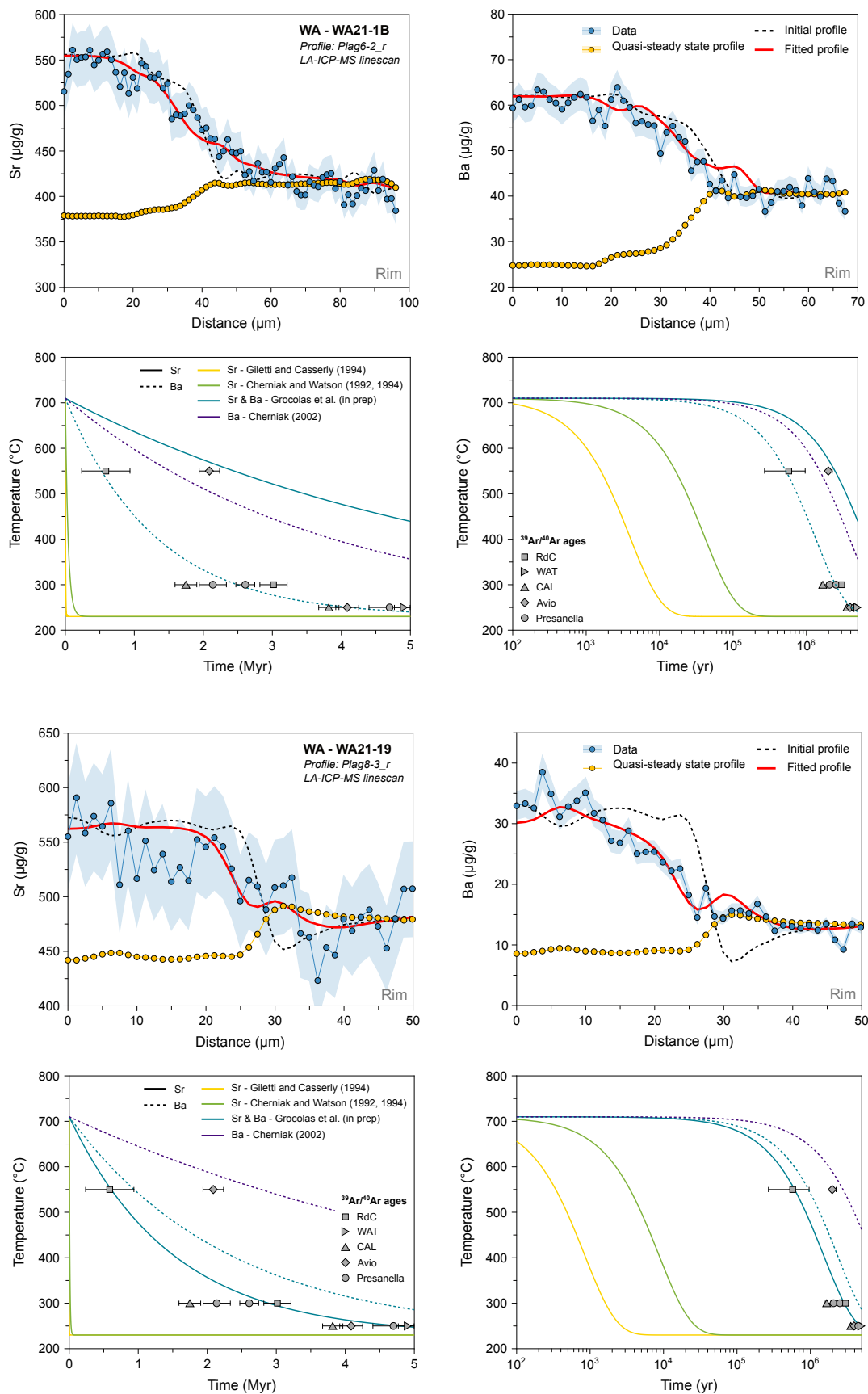


Figure A3.3. (Figure caption on next page.)

Figure A3.3. Measured profiles and results of Sr- and Ba-in-plagioclase diffusion modelling used to infer cooling rates. The black dotted line represents the initial conditions, the red line corresponds to the best fit to the data (blue), and the yellow data points are for the calculated quasi-steady state profile. The diagrams highlighting the temperature (°C) evolution through time (Myr) show the best fits using different diffusion coefficients for Sr and Ba diffusion in plagioclase (Cherniak and Watson, 1992, 1994; Cherniak, 2002; Gilletti and Casserly, 1994; Grocolas et al., in review). The $^{39}\text{Ar}/^{40}\text{Ar}$ ages obtained on minerals with different closure temperatures (Schaltegger et al., 2019) are represented as comparison.

A. Supplementary Materials

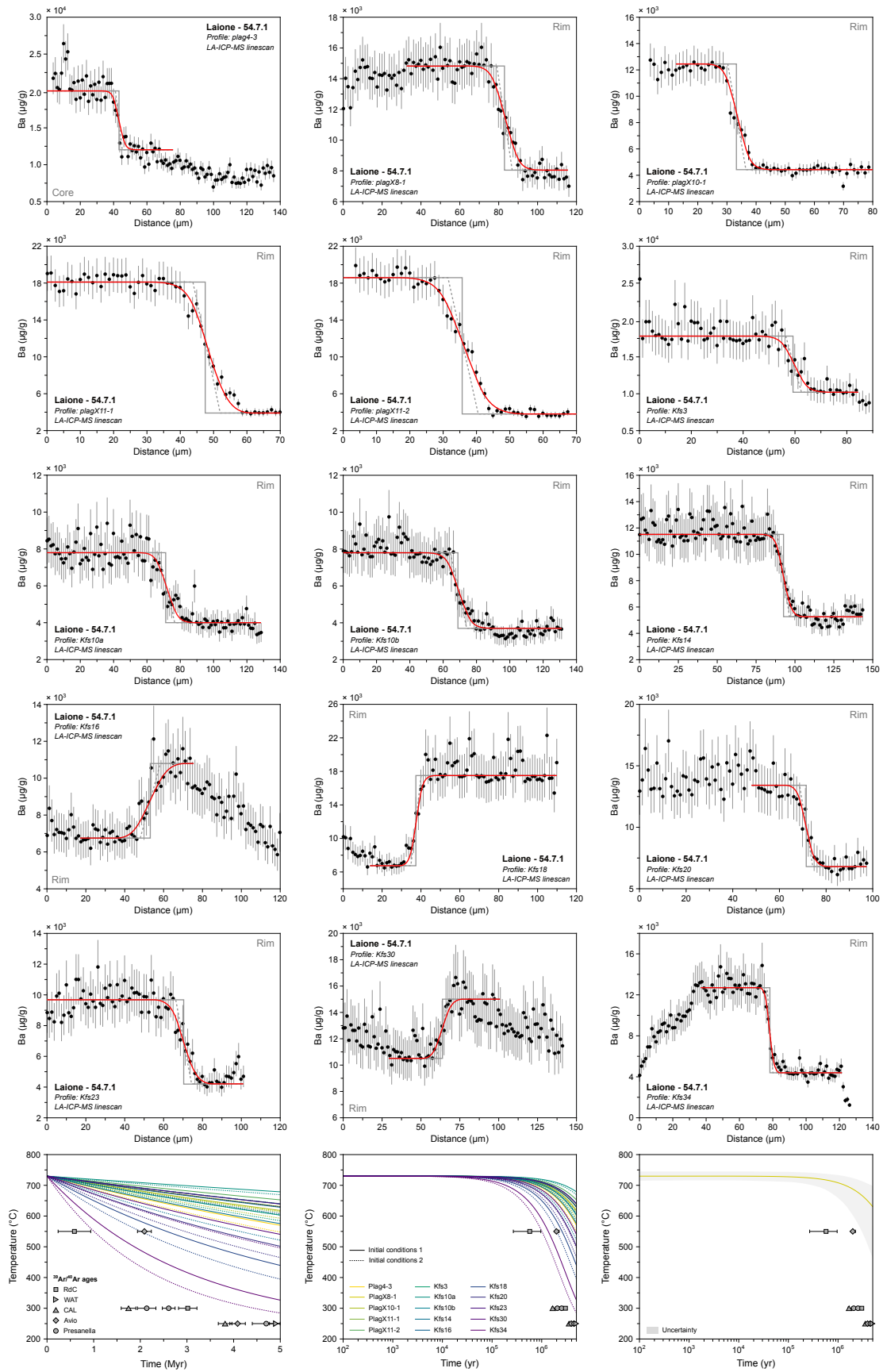


Figure A3.4. (Figure caption on next page.)

Figure A3.4. Measured profiles and results of Ba-in-alkali-feldspar diffusion modelling used to infer cooling rates. The black dotted line and continuous line represent the two initial conditions tested in the model, and the red line corresponds to the best fit to the data (black). The diagrams highlighting the temperature (°C) evolution through time (Myr) show the best fits using the two different initial conditions. The $^{39}\text{Ar}/^{40}\text{Ar}$ ages obtained on minerals with different closure temperatures (Schaltegger et al., 2019) are represented as comparison.

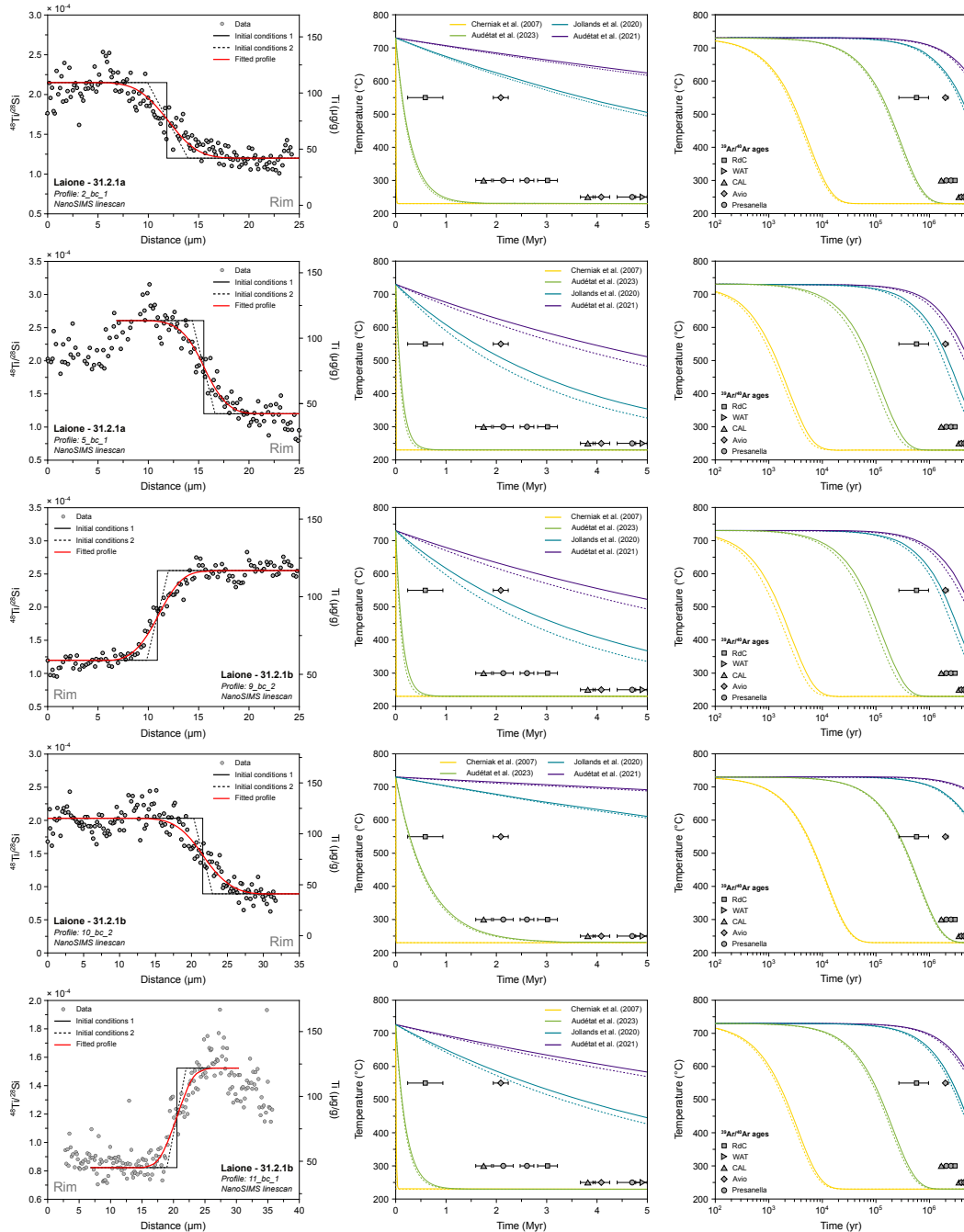


Figure A3.5. Results of Ti-in-quartz diffusion modelling used to infer cooling rates. The black dotted line and continuous line represent the two initial conditions tested in the model, and the red line corresponds to the best fit to the data (grey). The diagrams highlighting the temperature (°C) evolution through time (Myr) show the best fits using the two different initial conditions. The $^{39}\text{Ar}/^{40}\text{Ar}$ ages obtained on minerals with different closure temperatures (Schaltegger et al., 2019) are represented as comparison.

A. Supplementary Materials

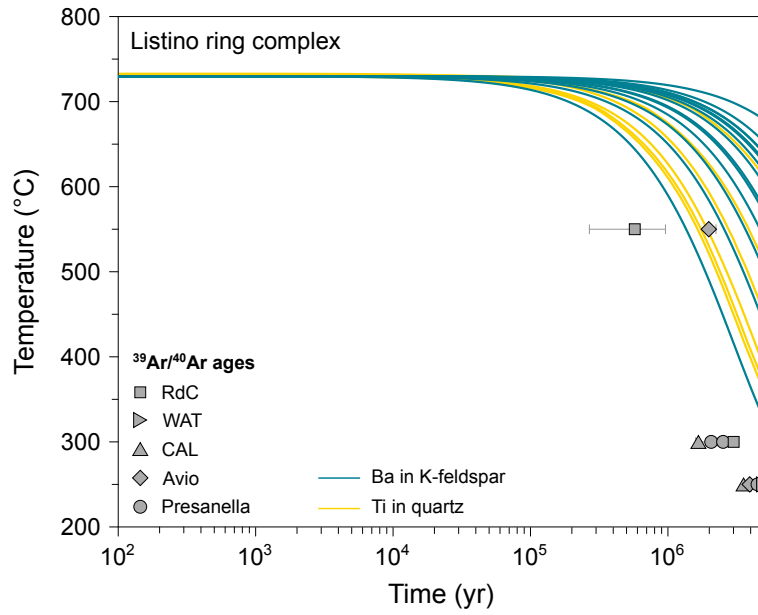


Figure A3.6. Compilation of the cooling rates obtained from Ti-in-quartz and Ba-in-alkali-feldspar diffusion modelling on crystals from the Laione granodiorite compared to cooling rates inferred from mineral $^{39}\text{Ar}/^{40}\text{Ar}$ ages (Schaltegger et al., 2019).

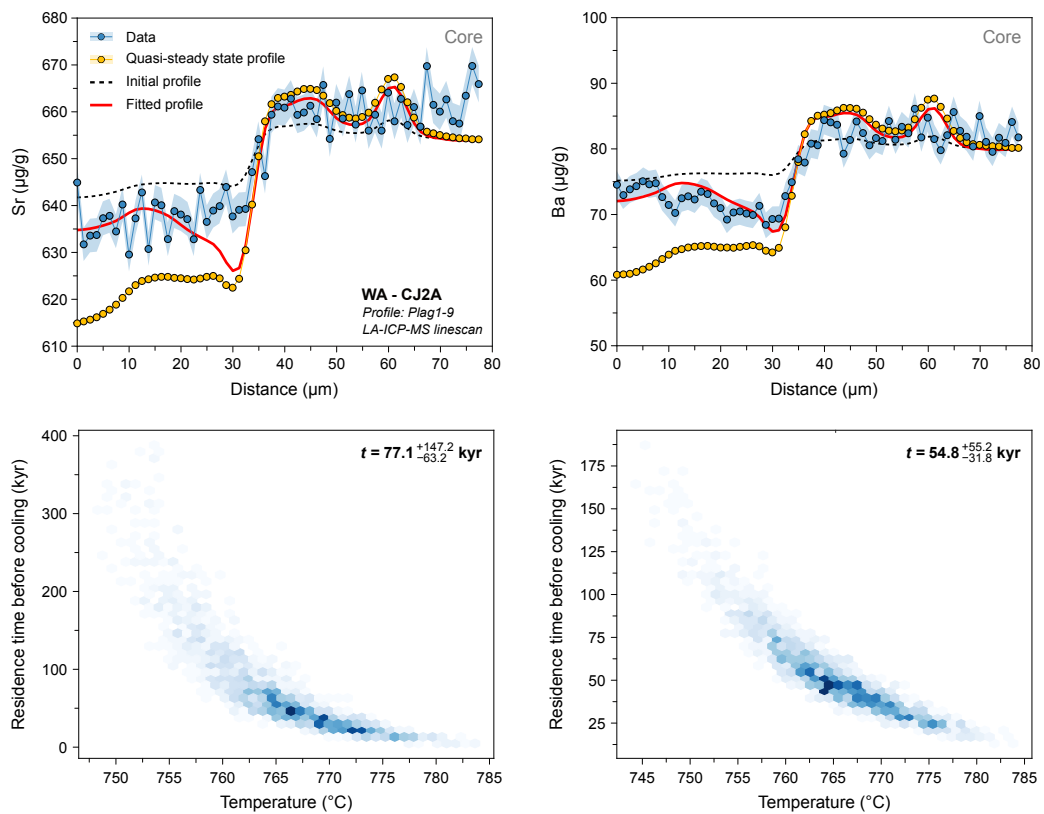


Figure A3.7. (Continued.)

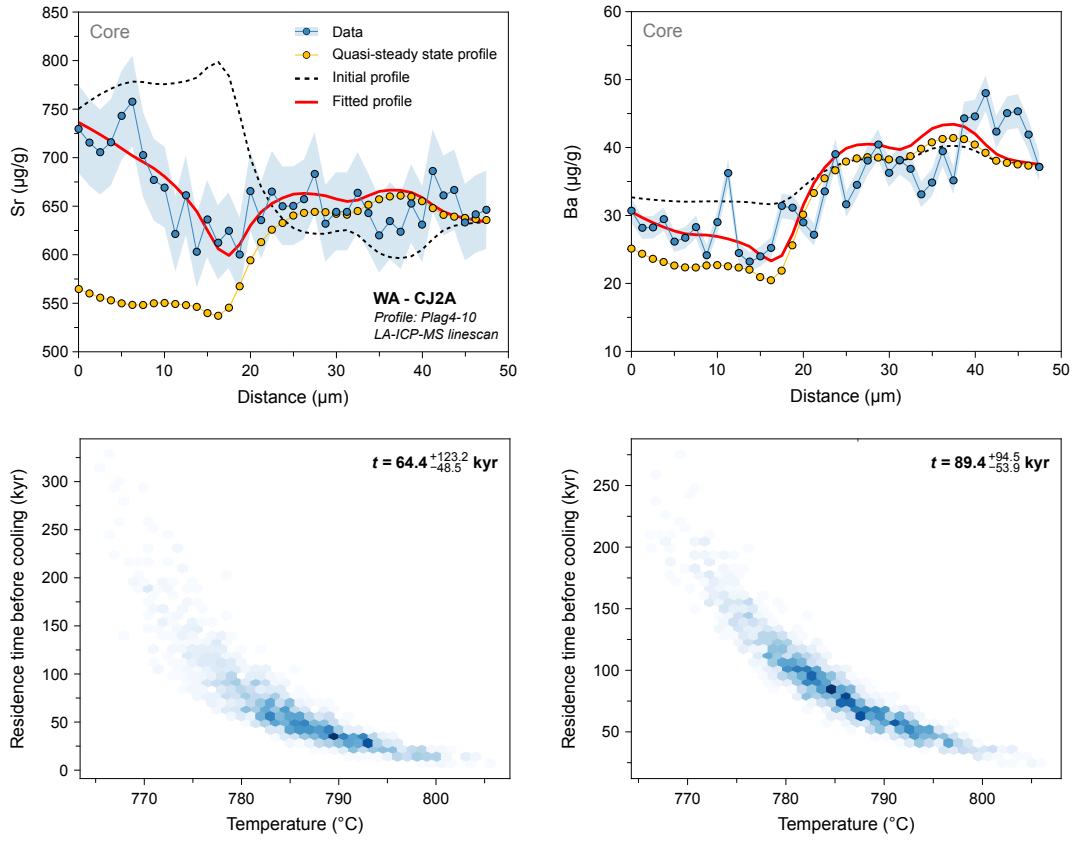


Figure A3.7. (Continued.)

A. Supplementary Materials

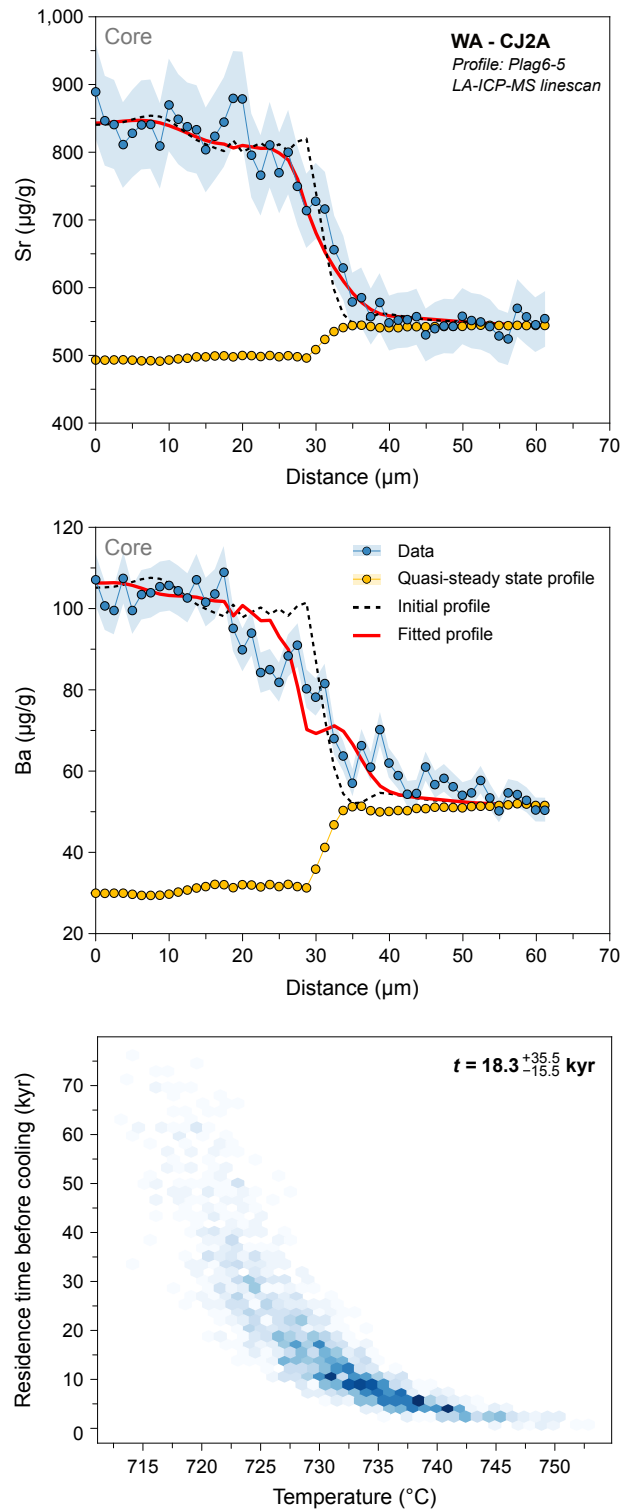


Figure A3.7. (Continued.)

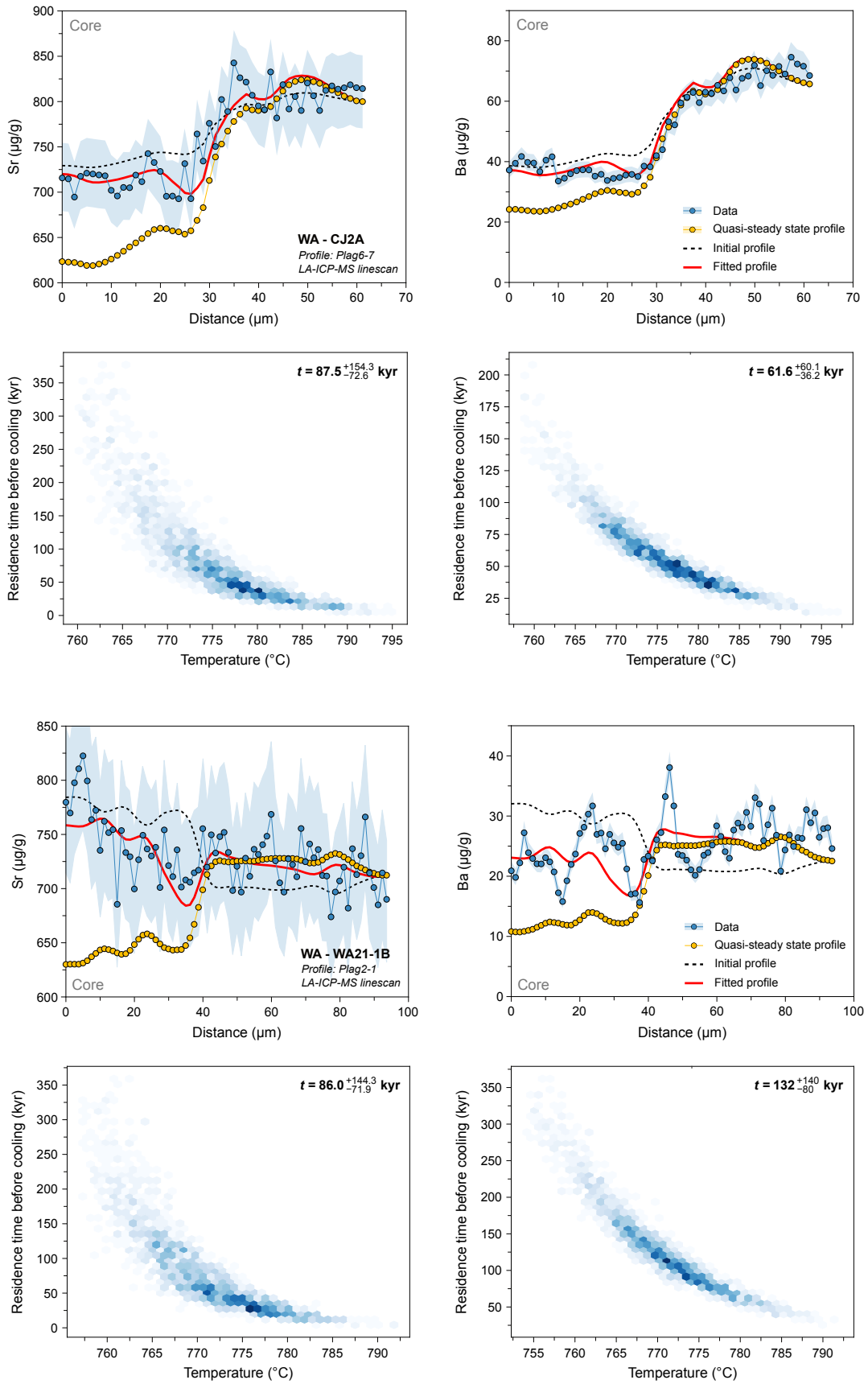


Figure A3.7. (Figure caption on next page.)

Figure A3.7. Results of Sr- and Ba-in-plagioclase diffusion modelling used to infer crystal-melt segregation timescales. The black dotted line represents the initial conditions, the red line corresponds to the best fit to the data (blue), and the yellow data points are for the calculated quasi-steady state profile. The results of the Monte Carlo simulation for Sr and Ba diffusion are represented as temperature (°C) vs. time (kyr). See main text for explanations regarding diffusion modelling and Monte Carlo resampling.

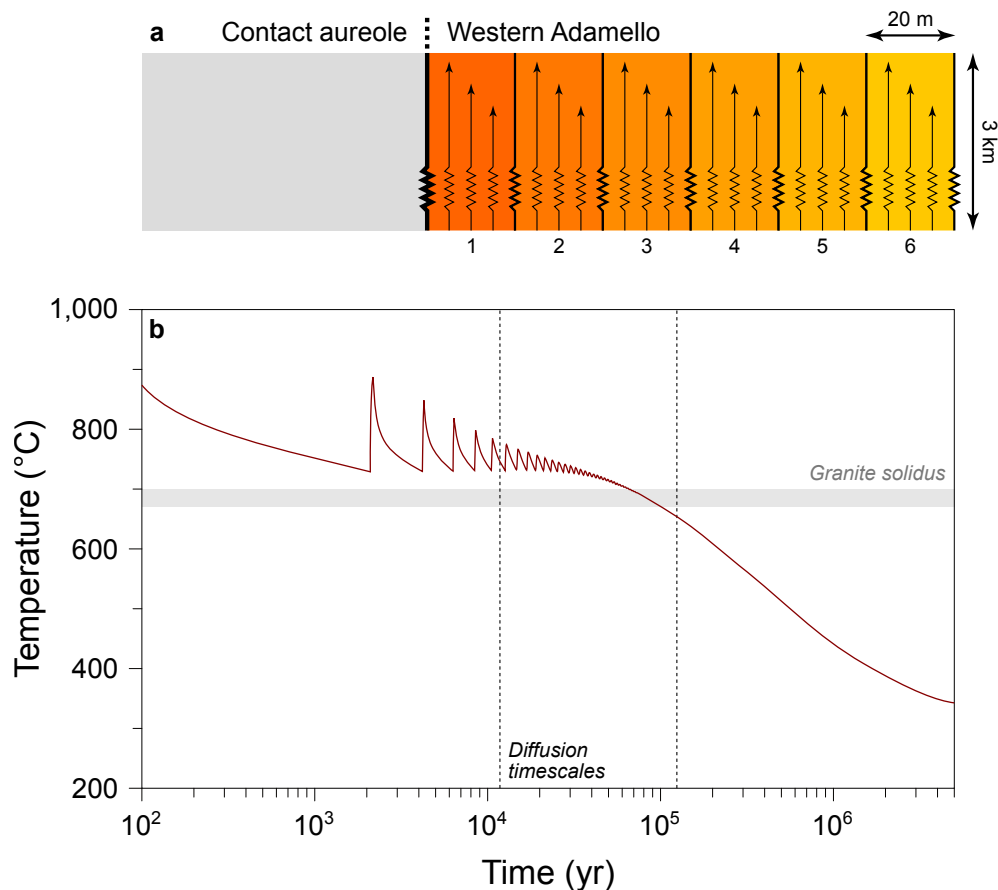


Figure A3.8. Thermal model reproducing the emplacement of the Western Adamello tonalite. **a**, Model setup for the horizontal stacking of 20-m-thick vertical dikes aimed at reproducing the emplacement of the Western Adamello tonalite. The temperature of the emplaced magma (930 °C) is maintained as long as magma is flowing. After a 60-yr flow time, the system cools down for 3,000 yr until the next magma recharge. **b**, Temperature evolution of a point located at 3 km from the first dike (i.e., from the southeastern contact with the sediments) represented as temperature (°C) vs. time (yr). The solidus temperature (Johannes and Holtz, 2012; Piwinski, 1968) and modelled diffusion timescales (Fig. 4.13) are shown for comparison. Note the good agreement between the plagioclase residence times inferred using diffusion modelling and the magma residence time above solidus ($\sim 10^5$ yr) inferred from thermal modelling.

A.3.3 Supplementary Tables

Table A3.1. Bulk rock major and trace element analyses of the Laione granodiorite.

Sample	LR22-1	LR22-2	LR22-4	LR22-8	LR22-9	54.7.1	28.2.1	NHS25
Rock type	Granodi.							
<i>Major elements (wt.%)</i>								
SiO ₂	68.37	68.22	68.89	68.91	69.23	68.94	65.66	69.56
TiO ₂	0.35	0.34	0.33	0.33	0.32	0.35	0.44	0.32
Al ₂ O ₃	15.89	15.83	15.73	15.55	15.55	15.66	16.52	15.82
Fe ₂ O ₃	3.12	3.14	2.95	2.86	2.87	3.26	3.97	2.94
MnO	0.09	0.09	0.10	0.10	0.10	0.07	0.10	0.10
MgO	1.22	1.22	1.14	1.11	1.09	1.20	1.81	1.05
CaO	4.21	4.23	3.99	3.93	3.92	4.15	5.17	3.95
Na ₂ O	3.83	3.79	3.87	3.97	4.01	3.42	3.55	3.66
K ₂ O	2.24	2.27	2.41	2.23	2.32	2.25	1.52	2.26
P ₂ O ₅	0.13	0.13	0.12	0.12	0.12	0.13	0.16	0.12
LOI	0.38	0.45	0.44	0.52	0.34	0.29	0.33	0.27
Total	99.99	99.88	99.99	99.62	99.87	99.72	99.23	100.05
<i>Trace elements (µg/g)</i>								
Sc	7.12	7.32	6.75	6.65	6.46	6	8	6
V	60.37	59.43	54.96	52.92	53.12	78	98	72
Cr	9.66	9.95	9.66	8.16	8.27	55	72	58
Co	65.02	47.10	64.75	45.74	66.89	8	8	9
Ni	8.01	7.03	7.81	7.89	7.84	7	11	15
Cu	3.79	4.58	2.99	2.59	4.88	5	9	8
Zn	32.28	31.66	34.15	36.61	37.17	28	30	34
Rb	47.07	46.10	59.56	62.07	67.09	47.82	39.07	68.03
Sr	433.8	428.9	401.1	394.1	389.5	395	454	375
Y	12.01	11.70	11.06	11.47	11.00	12.42	10.77	10.87
Zr	137.0	142.6	134.4	142.1	135.3	135	160	130
Nb	13.13	12.57	12.38	13.75	13.64	12.54	7.68	12.07
Cs	0.932	0.750	0.881	0.926	1.203	0.920	0.790	1.380
Ba	874.512	859.744	814.411	797.588	813.808	851	630	748
La	44.970	41.814	41.102	40.585	41.404	40.750	45.800	46.270
Ce	68.330	63.780	62.410	61.829	62.751	59.230	66.570	66.300
Pr	6.067	5.744	5.535	5.548	5.682	5.090	5.870	5.660
Nd	19.359	18.281	17.554	17.688	17.539	18.510	18.070	16.900
Sm	2.786	2.665	2.546	2.578	2.552	2.800	2.490	2.640
Eu	0.750	0.744	0.718	0.705	0.667	0.700	0.820	0.740
Gd	2.085	2.063	1.880	2.026	1.984	2.090	2.010	2.560
Tb	0.311	0.293	0.293	0.295	0.286	0.330	0.340	0.300
Dy	1.882	1.845	1.717	1.794	1.740	2.010	1.590	1.810
Ho	0.391	0.384	0.362	0.377	0.380	0.420	0.370	0.390
Er	1.200	1.179	1.103	1.138	1.099	1.230	1.010	1.050
Tm	0.176	0.177	0.171	0.179	0.167	0.170	0.190	0.170
Yb	1.391	1.318	1.249	1.340	1.306	1.470	1.300	1.250
Lu	0.214	0.215	0.209	0.216	0.210	0.220	0.220	0.200
Hf	3.150	3.179	2.990	3.318	3.062	3.130	3.590	3.300
Ta	1.222	1.102	1.118	1.205	1.203	1.040	0.490	0.970
Pb	7.947	7.920	8.438	9.620	9.565	8.560	4.620	11.43
Th	18.66	18.29	19.05	19.65	19.66	19.08	14.27	21.43
U	1.784	2.185	2.635	3.341	3.538	2.390	2.080	4.280

LOI, loss on ignition; *Granodi.*, granodiorite

A. Supplementary Materials

Table A3.2. Amphibole major element analyses of the different Listino ring complex lithologies.

Sample	Rock type	SiO ₂ wt.%	TiO ₂ wt.%	Al ₂ O ₃ wt.%	FeO wt.%	MgO wt.%	MnO wt.%	CaO wt.%	Na ₂ O wt.%	K ₂ O wt.%	Total wt.%
54.7.1	LGD	48.40	0.76	6.58	13.81	13.47	0.93	12.19	0.79	0.49	97.54
54.7.1	LGD	47.48	1.00	6.90	14.83	12.74	0.84	11.70	0.88	0.53	96.95
54.7.1	LGD	47.78	1.00	6.70	14.72	12.92	0.76	11.54	0.89	0.61	97.00
54.7.3	LRT	45.55	0.97	8.10	14.65	13.03	0.46	11.79	0.91	0.66	96.14
54.7.3	LRT	46.61	0.48	7.70	14.53	12.98	0.39	12.15	0.62	0.54	96.09
54.7.3	LRT	45.51	1.02	7.89	14.59	12.94	0.44	11.79	0.97	0.45	95.60
54.7.3	LRT	46.77	0.97	7.34	13.79	13.46	0.53	11.85	0.83	0.35	95.97
54.7.3	LRT	47.00	0.86	6.81	13.87	13.68	0.44	12.06	0.70	0.55	95.99
54.7.3	LRT	45.63	0.93	7.98	14.64	12.79	0.42	11.79	0.94	0.50	95.67
54.7.3	LRT	45.63	0.99	7.97	14.01	13.22	0.44	11.59	1.05	0.39	95.29
54.7.3	LRT	45.71	0.91	7.86	14.88	12.82	0.42	11.85	0.92	0.56	95.93
54.7.3	LRT	46.32	0.96	7.39	14.52	13.14	0.42	11.99	0.71	0.46	95.99
54.7.3	LRT	46.01	1.11	7.65	13.96	13.26	0.57	11.72	0.92	0.51	95.70
54.7.3	LRT	47.26	0.83	6.62	13.21	14.03	0.52	11.83	0.76	0.54	95.65
54.7.3	LRT	45.39	0.89	7.72	14.73	12.83	0.45	11.83	0.84	0.72	95.44
54.7.3	LRT	45.72	0.87	7.24	14.81	12.84	0.43	12.09	0.75	0.45	95.19
54.7.3	LRT	45.52	0.80	7.64	14.15	13.40	0.40	12.25	0.73	0.45	95.34
54.7.3	LRT	44.81	0.97	7.89	14.98	12.89	0.41	11.88	0.92	0.57	95.30
54.7.3	LRT	45.45	1.15	7.75	14.13	13.14	0.48	11.80	0.88	0.30	95.08
54.7.3	LRT	44.58	0.86	7.85	15.23	12.76	0.38	12.13	0.78	0.55	95.12
54.7.3	LRT	47.26	0.72	6.18	13.78	14.01	0.51	11.65	0.78	0.26	95.16
54.7.3	LRT	44.66	0.99	7.91	15.05	12.75	0.45	11.81	0.94	0.57	95.13
51.4.2	LRT	45.56	0.88	8.10	14.38	13.24	0.68	11.81	1.02	0.60	96.31
51.4.2	LRT	45.71	0.82	7.78	14.32	13.31	0.66	11.83	0.95	0.63	96.09
51.4.2	LRT	45.62	0.89	8.00	14.22	13.16	0.73	11.66	1.07	0.35	95.80
51.4.2	LRT	46.19	0.82	7.63	14.02	13.58	0.76	11.61	1.04	0.27	96.00
51.4.2	LRT	45.41	0.79	7.86	15.02	12.81	0.67	11.78	0.98	0.42	95.80
51.4.2	LRT	45.33	0.91	7.82	15.45	12.46	0.62	11.83	0.82	0.59	95.86
51.4.2	LRT	45.69	0.93	7.46	15.55	12.41	0.72	11.71	0.92	0.57	95.96
51.4.2	LRT	45.65	1.02	7.67	15.65	12.21	0.73	11.83	0.88	0.62	96.30
51.4.2	LRT	45.74	0.79	7.66	15.65	12.11	0.66	11.96	0.75	0.62	95.94
51.4.2	LRT	45.61	1.03	7.57	15.67	12.33	0.74	11.84	0.96	0.55	96.31
51.4.2	LRT	45.38	1.05	7.85	15.98	12.23	0.69	11.83	0.94	0.63	96.58
51.4.2	LRT	45.63	0.85	7.36	15.47	12.58	0.67	11.77	0.87	0.54	95.79
51.4.2	LRT	45.62	0.98	7.50	15.70	12.18	0.71	11.74	0.87	0.61	96.00
51.4.2	LRT	46.13	0.92	7.62	14.07	13.50	0.73	11.61	1.04	0.48	96.18
51.4.2	LRT	45.62	0.96	7.83	14.47	13.36	0.69	11.54	1.11	0.51	96.19
51.4.2	LRT	45.38	0.92	7.93	14.66	13.14	0.72	11.68	1.03	0.53	96.04
51.4.2	LRT	45.01	1.01	8.12	15.38	12.40	0.72	11.81	0.99	0.61	96.12
51.4.2	LRT	45.68	0.95	7.69	14.92	12.65	0.67	11.91	0.81	0.59	95.97
51.4.2	LRT	46.06	0.90	7.73	14.54	13.30	0.71	11.89	0.91	0.48	96.55
51.4.2	LRT	45.32	0.95	8.44	14.30	13.00	0.67	11.86	1.05	0.52	96.18
51.4.2	LRT	45.52	0.89	8.31	13.74	13.53	0.69	11.66	1.13	0.39	95.87
51.4.2	LRT	45.71	0.86	8.13	13.66	13.59	0.65	11.62	1.08	0.36	95.74
51.4.2	LRT	46.28	0.88	7.81	13.26	13.95	0.66	11.73	1.05	0.36	96.11
51.4.2	LRT	45.48	1.03	7.95	15.77	12.36	0.78	11.64	1.06	0.52	96.62
51.4.2	LRT	45.47	0.98	7.74	15.81	12.30	0.71	11.65	0.96	0.61	96.30

(Continued.)

A.3. Supplementary Material to Chapter 4

Sample	Rock type	SiO ₂ wt.%	TiO ₂ wt.%	Al ₂ O ₃ wt.%	FeO wt.%	MgO wt.%	MnO wt.%	CaO wt.%	Na ₂ O wt.%	K ₂ O wt.%	Total wt.%
51.4.2	LRT	45.38	0.97	7.68	15.67	12.20	0.73	11.83	0.95	0.61	96.07
51.4.2	LRT	45.38	1.03	7.88	15.51	12.55	0.71	11.61	1.04	0.55	96.30
51.4.2	LRT	45.76	0.95	7.65	15.69	12.73	0.71	11.76	0.95	0.49	96.71
51.4.2	LRT	45.81	0.95	7.70	15.26	12.68	0.64	11.87	0.93	0.56	96.44
51.4.2	LRT	45.77	0.81	7.78	15.51	12.38	0.63	11.93	0.71	0.64	96.23
51.4.2	LRT	45.67	0.92	7.57	15.67	12.25	0.67	11.84	0.86	0.59	96.09
51.4.2	LRT	45.51	0.83	8.33	14.20	13.20	0.68	11.71	0.99	0.66	96.16
51.4.2	LRT	44.77	0.90	8.66	15.40	12.28	0.70	11.77	0.99	0.63	96.10
51.4.2	LRT	46.27	0.60	7.77	14.56	13.25	0.69	11.73	1.00	0.50	96.44
51.4.2	LRT	46.31	0.98	7.55	14.42	13.33	0.71	11.80	1.02	0.49	96.68
51.4.2	LRT	45.52	0.95	8.06	15.05	12.69	0.66	11.80	1.04	0.53	96.32
51.4.2	LRT	46.32	0.91	7.37	14.97	13.02	0.74	11.80	0.94	0.47	96.65
51.4.2	LRT	45.81	0.97	7.81	15.46	12.52	0.64	11.84	0.95	0.57	96.69
51.4.2	LRT	45.50	0.93	7.75	16.08	12.08	0.74	11.75	0.97	0.55	96.35
51.4.2	LRT	45.79	0.91	7.83	16.11	12.23	0.67	12.00	0.89	0.65	97.12
51.4.2	LRT	45.38	1.13	8.02	15.48	12.47	0.74	11.69	1.06	0.51	96.49
51.4.2	LRT	45.80	0.97	7.67	15.79	12.41	0.72	11.88	0.92	0.56	96.83
LR21-2	Tonalite	44.97	0.96	8.40	16.87	12.24	0.54	12.11	1.01	0.81	97.91
LR21-2	Tonalite	43.99	1.16	8.92	17.21	11.55	0.57	12.02	1.12	0.88	97.41
LR21-2	Tonalite	44.44	1.08	8.50	17.11	11.75	0.50	12.12	1.00	0.68	97.18
LR21-2	Tonalite	45.51	0.78	7.29	15.93	12.91	0.55	12.14	0.85	0.68	96.65
LR21-2	Tonalite	44.81	0.81	7.72	16.74	12.26	0.50	12.10	0.97	0.73	96.63
LR21-2	Tonalite	49.87	0.12	4.05	13.92	15.59	0.50	12.12	0.32	0.19	96.68
LR21-2	Tonalite	44.68	1.18	9.64	13.18	13.75	0.34	12.38	1.23	0.67	97.05
LR21-2	Tonalite	43.75	1.37	10.89	13.64	13.02	0.26	12.41	1.38	0.70	97.42
LR21-2	Tonalite	49.15	0.83	6.24	10.68	16.45	0.27	12.63	0.81	0.39	97.46
LR21-2	Tonalite	48.17	1.03	6.98	10.83	15.92	0.21	12.55	0.94	0.50	97.13
LR21-2	Tonalite	55.21	0.09	1.26	6.54	20.34	0.36	13.29	0.11	0.04	97.23
LR21-2	Tonalite	55.22	0.07	1.39	6.97	20.16	0.33	13.43	0.11	0.06	97.73
LR21-2	Tonalite	47.95	0.70	6.34	12.78	15.07	0.32	12.46	0.77	0.54	96.94
LR21-2	Tonalite	46.87	0.88	8.04	11.03	15.81	0.21	12.72	0.95	0.69	97.20
54.5.1	MGD	46.18	0.77	7.47	15.11	12.86	0.84	11.93	0.73	0.61	96.56
54.5.1	MGD	45.65	0.78	7.67	15.25	12.76	0.92	11.93	0.93	0.64	96.58
54.5.1	MGD	45.71	0.83	7.76	15.54	12.62	1.02	11.55	1.12	0.56	96.82
54.5.1	MGD	45.64	0.90	8.15	15.16	12.72	0.92	11.60	1.12	0.55	96.79
54.5.1	MGD	45.76	0.76	7.60	15.38	12.61	0.89	11.53	1.07	0.75	96.46
54.5.1	MGD	48.86	0.51	5.57	13.32	14.36	0.87	12.06	0.60	0.38	96.62
54.5.1	MGD	45.59	0.81	7.86	15.36	12.67	0.92	11.77	0.99	0.62	96.67
54.5.1	MGD	46.13	0.71	7.60	15.23	12.73	0.89	11.69	0.94	0.68	96.66
54.5.1	MGD	46.43	0.68	7.28	14.79	13.02	0.90	11.91	0.80	0.60	96.52
54.5.1	MGD	45.80	0.75	7.41	14.83	12.87	0.89	11.79	0.88	0.61	95.86
54.5.1	MGD	46.14	0.76	7.37	15.05	12.93	0.89	11.63	0.97	0.60	96.38
54.5.1	MGD	46.72	0.72	6.77	14.43	13.12	0.89	11.89	0.83	0.51	95.93
54.5.1	MGD	45.15	0.88	7.99	15.39	12.40	0.90	11.67	1.01	0.61	96.04
54.5.1	MGD	46.12	0.77	7.36	15.27	12.83	0.96	11.59	0.99	0.50	96.45
54.5.1	MGD	45.67	0.82	7.73	14.98	12.81	0.86	11.50	1.14	0.50	96.07
54.5.1	MGD	46.35	0.66	7.13	14.50	13.30	0.84	11.83	0.83	0.64	96.19

(Continued.)

A. Supplementary Materials

Sample	Rock type	SiO ₂ wt.%	TiO ₂ wt.%	Al ₂ O ₃ wt.%	FeO wt.%	MgO wt.%	MnO wt.%	CaO wt.%	Na ₂ O wt.%	K ₂ O wt.%	Total wt.%
54.5.1	MGD	45.67	0.78	7.74	15.20	12.67	0.93	11.61	1.04	0.60	96.30
54.5.1	MGD	46.08	0.79	7.47	15.24	12.73	0.88	11.86	0.88	0.62	96.63
54.5.1	MGD	45.65	0.74	7.49	15.31	12.63	0.83	11.84	0.84	0.66	96.04
54.5.1	MGD	45.68	0.72	7.56	15.25	12.65	0.88	11.83	0.84	0.59	96.03
54.5.1	MGD	45.41	0.78	7.72	15.24	12.60	0.92	11.66	1.02	0.56	95.92
54.5.1	MGD	45.88	0.78	7.53	15.22	12.74	0.89	11.68	0.96	0.60	96.38
54.5.1	MGD	45.96	0.74	7.45	14.97	12.97	0.85	11.67	0.91	0.66	96.25
54.5.1	MGD	46.30	0.70	7.28	14.75	13.00	0.86	11.82	0.80	0.63	96.22
54.5.1	MGD	46.05	0.71	7.27	15.13	12.93	0.90	11.74	0.91	0.62	96.34
54.5.1	MGD	45.59	0.73	7.53	15.64	12.50	0.90	11.45	0.99	0.65	96.05
54.5.1	MGD	45.77	0.79	7.68	15.23	12.82	0.87	11.54	1.06	0.56	96.37
54.5.1	MGD	46.02	0.72	7.51	15.61	12.47	0.85	11.51	0.95	0.61	96.27
54.5.1	MGD	45.63	0.80	7.61	15.30	12.56	0.89	11.75	0.95	0.59	96.10
54.5.1	MGD	46.11	0.79	7.48	15.01	12.73	0.85	11.71	1.03	0.56	96.34
54.5.1	MGD	45.67	0.84	7.85	15.24	12.80	0.86	11.49	1.14	0.52	96.49
54.5.1	MGD	45.61	0.82	7.90	15.50	12.54	0.90	11.59	1.10	0.56	96.61
54.5.1	MGD	46.18	0.80	7.42	14.81	12.94	0.93	11.58	0.95	0.50	96.19
54.5.1	MGD	45.97	0.78	7.58	15.23	12.70	0.97	11.36	1.07	0.54	96.34
51.2.1	MGD	47.20	0.68	6.73	14.53	13.39	0.75	11.86	0.77	0.58	96.60
51.2.1	MGD	46.39	0.83	7.59	15.27	12.90	0.78	11.81	1.00	0.61	97.24
51.2.1	MGD	46.23	0.88	7.63	15.41	12.63	0.78	11.94	0.94	0.61	97.15
51.2.1	MGD	45.94	0.84	7.89	15.43	12.65	0.76	11.85	1.03	0.57	97.02
51.2.1	MGD	45.33	0.92	8.11	15.88	12.61	0.75	11.83	1.02	0.57	97.13
51.2.1	MGD	46.27	0.85	7.68	15.44	12.64	0.73	11.82	1.04	0.51	97.06
51.2.1	MGD	45.86	0.93	7.68	15.32	12.90	0.79	11.80	1.01	0.53	96.91
51.2.1	MGD	45.52	0.89	8.03	15.35	12.56	0.79	11.84	0.99	0.70	96.76
51.2.1	MGD	45.90	0.86	7.96	15.27	12.77	0.79	11.84	0.99	0.54	96.99
51.2.1	MGD	45.77	0.84	7.73	15.57	12.66	0.75	11.80	0.89	0.63	96.65
51.2.1	MGD	45.96	0.84	7.71	15.14	12.89	0.79	11.67	1.01	0.55	96.57
51.2.1	MGD	46.41	0.77	7.33	15.22	13.03	0.78	11.95	0.76	0.65	96.99
51.2.1	MGD	46.11	0.89	7.79	15.44	12.84	0.78	11.82	1.03	0.63	97.39
51.2.1	MGD	45.49	0.93	8.19	15.36	12.48	0.78	11.71	1.10	0.61	96.68
51.2.1	MGD	45.72	0.90	8.16	15.42	12.62	0.80	11.85	1.04	0.55	97.17
51.2.1	MGD	45.78	0.89	8.13	15.20	12.69	0.76	11.77	1.09	0.55	96.92
51.2.1	MGD	46.21	0.73	7.52	15.11	12.95	0.71	12.07	0.74	0.64	96.72
51.2.1	MGD	46.10	0.84	7.82	15.46	13.01	0.78	11.74	1.01	0.51	97.30
51.2.1	MGD	45.26	0.91	7.94	15.34	12.70	0.80	11.49	1.09	0.50	96.08
51.2.1	MGD	47.11	0.71	6.78	14.59	13.31	0.77	11.88	0.77	0.56	96.57
51.2.1	MGD	46.29	0.82	7.75	15.34	12.84	0.75	11.94	0.97	0.59	97.37
51.2.1	MGD	46.62	0.70	7.38	15.20	12.99	0.70	12.11	0.71	0.62	97.07
51.2.1	MGD	46.03	0.88	8.17	15.79	12.56	0.75	11.94	0.96	0.62	97.77
51.2.1	MGD	46.39	0.88	7.84	15.57	12.72	0.76	11.95	0.98	0.63	97.72
51.2.1	MGD	46.29	0.89	7.85	15.36	12.78	0.77	11.77	1.08	0.55	97.46
51.2.1	MGD	45.14	0.82	7.79	15.29	12.50	0.73	11.64	0.92	0.72	95.64
51.2.1	MGD	47.42	0.59	6.24	14.24	13.70	0.70	11.82	0.67	0.48	95.89
51.2.1	MGD	48.00	0.54	5.96	14.17	13.96	0.82	11.81	0.70	0.49	96.48
51.2.1	MGD	46.00	0.76	7.79	15.35	12.75	0.77	11.77	0.94	0.64	96.86

(Continued.)

A.3. Supplementary Material to Chapter 4

Sample	Rock type	SiO ₂ wt.%	TiO ₂ wt.%	Al ₂ O ₃ wt.%	FeO wt.%	MgO wt.%	MnO wt.%	CaO wt.%	Na ₂ O wt.%	K ₂ O wt.%	Total wt.%
51.2.1	MGD	45.99	0.91	8.06	15.24	12.85	0.78	11.69	1.09	0.51	97.14
51.2.1	MGD	45.92	0.88	7.95	15.20	12.78	0.77	11.66	1.05	0.54	96.84
51.2.1	MGD	46.25	0.85	7.65	14.78	12.81	0.77	11.73	0.95	0.60	96.42
51.2.1	MGD	45.93	0.91	7.90	14.85	12.81	0.80	11.82	1.03	0.55	96.67
51.2.1	MGD	47.77	0.65	6.43	14.40	13.88	0.78	11.88	0.77	0.51	97.10
51.2.1	MGD	45.97	0.82	7.87	15.17	12.80	0.72	11.85	0.91	0.70	96.84
51.2.1	MGD	45.82	0.91	7.95	15.44	12.65	0.75	11.87	0.95	0.63	97.06
51.2.1	MGD	45.87	0.91	8.15	15.19	12.63	0.74	11.68	0.98	0.78	97.03
51.2.1	MGD	46.25	0.82	7.55	15.28	12.70	0.73	11.83	0.91	0.64	96.77
51.2.1	MGD	46.49	0.75	7.33	15.51	12.81	0.77	11.80	0.89	0.54	96.94
51.2.1	MGD	44.36	1.04	9.13	16.29	11.75	0.74	11.84	1.07	0.75	97.06
51.2.1	MGD	46.17	0.78	7.43	15.19	12.82	0.72	11.85	0.85	0.66	96.50
51.2.1	MGD	45.26	0.89	8.06	15.54	12.65	0.75	11.85	1.00	0.68	96.78
51.2.1	MGD	46.55	0.70	7.16	14.77	13.38	0.77	11.93	0.86	0.60	96.77
51.2.1	MGD	46.36	0.79	7.31	14.93	13.35	0.74	11.87	0.83	0.58	96.86
51.2.1	MGD	45.85	0.91	7.67	15.43	12.79	0.72	11.86	0.95	0.58	96.80
51.2.1	MGD	46.80	0.56	6.66	15.98	12.73	0.69	11.94	0.69	0.55	96.60
51.2.1	MGD	45.72	0.85	7.69	15.14	12.81	0.73	11.77	0.88	0.65	96.27
51.2.1	MGD	46.85	0.66	6.75	14.79	13.44	0.73	11.93	0.78	0.57	96.63
51.2.1	MGD	45.85	0.88	7.75	15.31	12.77	0.74	11.86	0.93	0.60	96.75
51.2.1	MGD	46.28	0.77	7.26	15.23	13.10	0.78	11.88	0.84	0.60	96.82
51.2.1	MGD	46.06	0.79	7.51	15.21	12.95	0.72	11.91	0.83	0.71	96.75
51.2.1	MGD	46.90	0.75	7.01	15.10	13.32	0.77	11.83	0.87	0.61	97.26
51.2.1	MGD	46.00	0.88	7.83	15.23	12.83	0.76	11.81	1.01	0.55	96.95
51.2.1	MGD	46.17	0.95	7.30	15.08	12.41	0.77	11.79	0.91	0.62	96.09
51.2.1	MGD	45.72	0.96	8.39	15.97	12.33	0.78	12.01	1.07	0.61	97.88
51.2.1	MGD	46.02	0.88	8.00	15.58	12.65	0.83	11.78	1.12	0.55	97.51
51.2.1	MGD	46.22	0.85	7.81	15.64	12.90	0.81	11.86	1.09	0.66	97.94
51.2.1	MGD	47.39	0.82	7.54	15.18	13.37	0.75	11.75	1.17	0.57	98.69
51.2.1	MGD	46.50	0.87	7.74	14.98	13.07	0.79	11.90	1.10	0.62	97.66
51.2.1	MGD	46.91	0.75	7.35	15.43	13.18	0.73	12.08	0.87	0.67	97.98
51.2.1	MGD	46.43	0.87	7.80	15.04	13.09	0.81	11.89	1.03	0.52	97.51
LR21-4	MGD	44.96	0.75	7.45	15.77	12.76	0.81	11.78	0.95	0.59	95.81
LR21-4	MGD	45.17	0.77	7.68	15.77	12.76	0.80	11.85	0.99	0.54	96.33
LR21-4	MGD	45.79	0.82	7.46	15.09	12.85	0.77	11.91	0.88	0.58	96.15
LR21-4	MGD	45.26	0.83	7.95	15.83	12.54	0.76	11.93	1.02	0.56	96.69
LR21-4	MGD	44.76	1.09	8.50	14.24	13.31	0.82	11.32	1.35	0.37	95.75
LR21-4	MGD	45.56	0.74	7.26	15.40	12.96	0.82	11.61	1.03	0.52	95.90
LR21-4	MGD	45.28	0.75	7.36	15.52	12.84	0.75	11.81	0.92	0.58	95.81

LGD, Laione granodiorite

LRT, Listino ring tonalite

MGD, Monoccola granodiorite

A. Supplementary Materials

Table A3.3. Plagioclase major and trace element analyses of the different Listino ring complex lithologies.

Sample	54.7.3	54.7.3	54.7.3	54.7.3	54.7.3	54.7.3	LR21-12A	LR21-12A
Rock type	LRT	LRT						
<i>Major elements (wt.%)</i>								
SiO ₂	55.88	55.64	57.08	57.03	56.53	55.35	55.08	54.58
Al ₂ O ₃	26.65	27.25	26.49	26.55	26.74	27.22	27.02	27.89
FeO	0.19	0.16	0.15	0.19	0.18	0.16	0.17	0.13
MgO	0.00	0.00	0.01	0.00	0.00	0.00	0.00	0.00
CaO	9.10	9.66	8.46	8.72	9.04	9.83	9.02	9.88
SrO	0.05	0.05	0.01	0.00	0.06	0.12	0.04	0.04
BaO	0.05	0.01	0.03	0.04	0.03	0.04	0.04	0.01
Na ₂ O	6.06	5.80	6.27	6.45	6.06	5.65	5.90	5.43
K ₂ O	0.24	0.21	0.31	0.18	0.30	0.27	0.22	0.13
Total	98.22	98.78	98.80	99.16	98.93	98.64	97.50	98.09
<i>Trace elements (µg/g)</i>								
Li	0.33	0.603	n.d.	0.306	n.d.	0.153	1.63	0.683
Sc	1.545	2.501	1.37	1.868	0.958	0.578	1.098	1.039
V	8.652	14.145	7.768	10.94	4.466	1.385	2.869	1.908
Zn	7.699	8.507	5.251	5.635	4.513	3.091	4.821	4.679
Rb	0.211	0.363	0.237	0.73	0.412	0.382	0.226	0.923
Sr	1075	1094	1042	1079	1109	1088	708.5	676.4
Y	0.686	1.074	0.573	0.749	0.365	0.197	0.509	0.553
Zr	0.266	0.492	0.194	0.264	0.123	0.046	0.156	0.158
Cs	0.017	0.011	0.014	0.229	0.017	0.034	0.003	0.004
Ba	210.7	211.5	153.9	181.5	188.2	194.5	56.18	43.82
La	15.24	14.56	14.22	15.17	16.83	15.73	7.69	12.74
Ce	15.91	16.25	14.60	15.38	17.03	15.01	9.08	14.25
Pr	1.123	1.25	0.953	1.005	1.08	0.903	0.718	1.065
Nd	2.883	3.44	2.26	2.425	2.395	2.03	1.972	2.911
Sm	0.328	0.425	0.24	0.276	0.147	0.152	0.182	0.259
Eu	0.728	0.697	0.574	0.646	0.598	0.636	0.736	0.826
Gd	0.163	0.262	0.138	0.185	0.119	0.074	0.146	0.15
Tb	0.027	0.038	0.016	0.023	0.015	0.005	0.017	0.016
Dy	0.137	0.209	0.107	0.135	0.068	0.036	0.085	0.12
Ho	0.027	0.042	0.02	0.027	0.012	0.006	0.022	0.016
Er	0.076	0.095	0.048	0.062	0.028	0.012	0.041	0.05
Tm	0.01	0.016	0.007	0.009	0.004	0.002	0.007	0.009
Yb	0.074	0.119	0.052	0.055	0.022	0.016	0.058	0.058
Lu	0.007	0.011	0.007	0.009	0.003	0.002	0.007	0.007
Pb	8.48	6.92	7.19	8.13	6.80	8.46	17.36	15.52
Th	0.05	0.106	0.027	0.046	0.024	0.069	0.009	0.065
U	0.018	0.055	0.01	0.021	0.007	0.01	0.007	0.138

(Continued.)

A.3. Supplementary Material to Chapter 4

Sample	LR21-12A						
Rock type	LRT						
<i>Major elements (wt.%)</i>							
SiO ₂	55.30	52.50	57.09	57.37	55.58	55.26	55.15
Al ₂ O ₃	27.08	28.77	26.45	26.70	27.80	27.11	27.23
FeO	0.11	0.11	0.11	0.22	0.13	0.23	0.13
MgO	0.00	0.00	0.00	0.00	0.01	0.00	0.00
CaO	9.20	10.96	8.31	8.37	9.67	9.72	9.85
SrO	0.05	0.08	0.05	0.02	0.08	0.09	0.07
BaO	0.00	0.00	0.05	0.03	0.00	0.01	0.00
Na ₂ O	5.96	4.88	6.48	6.55	5.71	5.76	5.71
K ₂ O	0.15	0.10	0.12	0.23	0.23	0.20	0.22
Total	97.86	97.40	98.66	99.48	99.20	98.38	98.35
<i>Trace elements (µg/g)</i>							
Li	1.786	0.318	2.503	1.767	2.752	2.508	2.776
Sc	13.42	1.27	10.984	6.006	0.794	1.105	0.536
V	60.562	4.103	70.492	27.73	2.353	3.914	0.374
Zn	41.105	6.609	52.504	22.849	5.78	6.346	3.934
Rb	2.128	6.274	11.259	1.381	0.267	0.387	0.191
Sr	604.8	691.2	684.3	682.8	738.1	694.8	722.3
Y	7.967	0.826	7.747	4.304	0.514	0.835	0.223
Zr	2.456	0.249	2.454	1.412	0.127	0.166	0.033
Cs	0.16	0.283	0.123	0.029	0.006	0.015	0.015
Ba	43.51	54.71	107.2	63.57	56.24	52.13	55.42
La	6.75	4.37	3.43	12.58	16.67	11.35	13.30
Ce	13.13	5.24	10.07	17.13	18.37	12.29	14.17
Pr	1.766	0.408	1.364	1.619	1.372	0.909	1.016
Nd	6.919	1.277	6.257	5.8	3.61	2.524	2.574
Sm	1.692	0.181	1.715	1.181	0.27	0.294	0.199
Eu	0.798	0.336	0.611	0.858	0.908	0.69	0.835
Gd	1.422	0.172	1.297	0.798	0.143	0.207	0.083
Tb	0.243	0.023	0.204	0.134	0.019	0.023	0.008
Dy	1.442	0.121	1.425	0.848	0.085	0.133	0.04
Ho	0.292	0.023	0.27	0.158	0.014	0.022	0.006
Er	0.802	0.082	0.737	0.451	0.043	0.055	0.01
Tm	0.114	0.01	0.114	0.065	0.005	0.006	0.001
Yb	0.935	0.079	0.844	0.5	0.037	0.062	0.013
Lu	0.119	0.008	0.113	0.062	0.007	0.007	0.002
Pb	15.20	17.93	19.47	17.89	18.36	17.12	17.49
Th	0.016	0.022	0.106	0.014	0.001	0.002	0.007
U	0.046	0.156	0.123	0.021	0.007	0.007	0.009

(Continued.)

A. Supplementary Materials

Sample	LR21-12A						
Rock type	LRT						
<i>Major elements (wt.%)</i>							
SiO ₂	55.34	55.12	54.22	50.06	56.52	55.66	52.62
Al ₂ O ₃	26.90	28.79	29.21	31.69	27.57	28.10	29.97
FeO	0.17	0.13	0.16	0.18	0.14	0.17	0.13
MgO	0.00	0.00	0.00	0.00	0.00	0.00	0.00
CaO	9.33	10.92	11.49	14.64	9.63	10.08	12.40
SrO	0.02	0.05	0.09	0.07	0.02	0.00	0.00
BaO	0.03	0.01	0.00	0.02	0.00	0.01	0.01
Na ₂ O	5.98	5.30	4.95	3.15	5.91	5.65	4.39
K ₂ O	0.12	0.16	0.16	0.08	0.16	0.19	0.12
Total	97.89	100.48	100.27	99.88	99.94	99.86	99.65
<i>Trace elements (µg/g)</i>							
Li	n.d.	15.743	18.274	2.884	3.325	2.276	2.103
Sc	1.34	3.15	3.765	19.867	11.808	10.807	3.959
V	4.608	78.25	85.028	67.293	36.62	46.664	14.915
Zn	6.504	51.051	72.126	46.609	30.695	33.026	18.124
Rb	2.564	54.307	54.12	4.32	1.909	17.618	6.99
Sr	675.7	651.2	710.1	763.2	649.1	643.4	717.5
Y	0.779	0.946	1.424	15.313	9.37	8.998	2.764
Zr	0.132	0.456	9.372	1.96	1.359	2.406	0.737
Cs	0.034	1.178	0.86	0.054	0.046	0.1	0.037
Ba	46.90	212.2	361.0	70.37	59.64	629.2	200.3
La	1.90	9.32	4.13	14.58	8.54	13.00	13.82
Ce	2.24	11.33	6.27	26.09	13.74	22.13	18.54
Pr	0.262	0.846	0.564	3.031	1.682	2.506	1.613
Nd	0.954	2.337	1.928	14.415	7.126	9.478	4.935
Sm	0.189	0.315	0.385	4.004	1.945	2.148	0.842
Eu	0.285	0.517	0.377	1.567	0.895	1.14	0.95
Gd	0.172	0.195	0.26	3.073	1.688	1.842	0.581
Tb	0.013	0.031	0.042	0.429	0.267	0.263	0.084
Dy	0.133	0.138	0.245	2.934	1.616	1.796	0.541
Ho	0.025	0.032	0.057	0.577	0.345	0.338	0.095
Er	0.072	0.078	0.158	1.581	0.956	0.952	0.287
Tm	0.006	0.012	0.026	0.236	0.12	0.139	0.033
Yb	0.091	0.082	0.187	1.742	1.081	1.081	0.363
Lu	0.01	0.01	0.026	0.225	0.131	0.121	0.03
Pb	17.32	17.28	19.87	19.26	17.78	20.20	20.66
Th	0.002	0.014	0.067	0.176	0.348	0.039	0.011
U	0.014	0.062	0.22	0.258	0.309	0.074	0.031

(Continued.)

A.3. Supplementary Material to Chapter 4

Sample	LR21-12A	LR21-12A	LR21-12A	51.2.1	51.2.1	51.2.1	51.2.1	51.2.1
Rock type	LRT	LRT	LRT	MGD	MGD	MGD	MGD	MGD
<i>Major elements (wt.%)</i>								
SiO ₂	55.22	56.07	54.59	56.14	56.13	56.26	57.76	57.24
Al ₂ O ₃	28.11	27.61	28.31	27.73	27.91	27.72	26.70	27.80
FeO	0.17	0.16	0.14	0.14	0.15	0.17	0.17	0.14
MgO	0.00	0.01	0.00	0.00	0.00	0.00	0.00	0.00
CaO	10.66	9.78	10.87	9.95	10.04	9.92	8.71	9.50
SrO	0.05	0.00	0.06	0.08	0.00	0.05	0.00	0.06
BaO	0.00	0.00	0.01	0.01	0.06	0.07	0.03	0.00
Na ₂ O	5.38	5.93	5.26	5.65	5.65	5.70	6.45	6.26
K ₂ O	0.19	0.15	0.21	0.27	0.27	0.29	0.27	0.22
Total	99.78	99.71	99.45	99.97	100.22	100.19	100.08	101.22
<i>Trace elements (µg/g)</i>								
Li	1.263	2.596	15.263	n.d.	0.34	0.594	0.29	1.201
Sc	5.095	5.494	3.098	1.222	0.936	0.92	0.869	10.924
V	17.786	18.009	14.328	2.115	0.407	0.296	0.311	56.306
Zn	13.369	13.611	15.742	4.244	3.825	4.026	3.834	39.622
Rb	0.949	11.269	23.463	1.954	2.966	3.546	2.259	2.014
Sr	712.2	675.2	707.7	1173	1132	1006	876.6	837.0
Y	3.824	3.899	3.219	0.591	0.248	0.216	0.258	6.769
Zr	0.771	0.813	2.278	0.079	0.024	0.011	n.d.	1.523
Cs	0.01	0.049	0.433	0.014	0.025	0.023	0.017	0.017
Ba	74.51	108.0	120.6	178.1	190.5	196.0	198.8	103.0
La	3.48	9.90	13.99	12.98	12.89	12.81	5.31	10.00
Ce	5.09	12.49	16.82	14.49	14.82	15.21	7.85	17.91
Pr	0.652	1.198	1.346	1.033	0.993	0.977	0.565	2.249
Nd	3.136	4.475	4.272	2.501	2.272	2.44	1.431	9.012
Sm	0.955	0.963	0.597	0.212	0.17	0.173	0.134	2.257
Eu	0.547	0.789	1.025	0.67	0.667	0.799	0.732	1.182
Gd	0.848	0.725	0.495	0.11	0.057	0.087	0.058	1.342
Tb	0.121	0.126	0.069	0.02	0.005	0.006	0.007	0.231
Dy	0.766	0.741	0.483	0.099	0.025	0.023	0.027	1.43
Ho	0.159	0.147	0.103	0.014	0.005	0.006	0.004	0.269
Er	0.388	0.392	0.251	0.045	0.005	0.012	0.007	0.677
Tm	0.052	0.06	0.048	0.006	0.002	0.001	0.001	0.111
Yb	0.484	0.472	0.343	0.045	0.006	0.007	0.006	0.851
Lu	0.055	0.055	0.043	0.006	0.001	0.001	0	0.095
Pb	18.60	15.87	25.88	11.64	13.04	16.46	17.55	17.58
Th	0.034	0.007	0.327	0.008	0.008	0.007	0.002	0.017
U	0.03	0.053	0.457	0.014	0.014	0.005	0.003	0.056

(Continued.)

A. *Supplementary Materials*

Sample	51.2.1	51.2.1	51.2.1	51.2.1	51.2.1	51.2.1	51.2.1	51.2.1	54.2.1
Rock type	MGD	Pegm.							
<i>Major elements (wt.%)</i>									
SiO ₂	57.15	55.87	55.94	53.94	55.36	56.45	53.76	58.99	64.53
Al ₂ O ₃	27.03	28.24	28.31	28.94	27.92	27.55	28.88	25.43	22.35
FeO	0.14	0.14	0.19	0.15	0.21	0.17	0.18	0.17	0.12
MgO	0.00	0.00	0.00	0.00	0.00	0.00	0.01	0.00	0.00
CaO	9.22	10.45	10.51	11.34	10.20	9.64	11.51	7.39	3.38
SrO	0.01	0.03	0.06	0.12	0.00	0.08	0.06	0.03	0.00
BaO	0.04	0.01	0.04	0.06	0.04	0.02	0.02	0.00	0.00
Na ₂ O	6.02	5.46	5.45	5.01	5.70	6.00	4.97	7.20	9.38
K ₂ O	0.26	0.20	0.21	0.19	0.16	0.24	0.17	0.34	0.56
Total	99.87	100.40	100.72	99.75	99.59	100.15	99.56	99.55	100.32
<i>Trace elements (µg/g)</i>									
Li	1.793	0.273	n.d.	0.323	0.432	n.d.	0.628	0.856	6.344
Sc	0.929	0.703	0.672	1.232	5.615	1.628	15.781	7.756	0.646
V	1.823	0.303	0.168	2.604	23.625	3.134	69.316	29.467	1.496
Zn	3.787	3.119	3.275	4.093	16.858	4.767	52.97	23.278	4.822
Rb	3.806	4.234	0.677	0.397	1.058	5.187	1.125	2.197	5.715
Sr	853.4	820.6	998.8	1137	798	1005	937	780	35.19
Y	0.377	0.242	0.242	0.639	2.905	0.665	7.258	4.264	0.205
Zr	0.049	0.021	0.074	0.135	0.744	0.137	1.227	0.59	1.476
Cs	0.139	0.042	0.005	0.006	0.015	0.029	0.013	0.043	0.155
Ba	103.3	108.6	97.87	101.7	65.17	184.3	89.76	72.14	5.455
La	7.51	6.35	16.59	14.18	10.56	13.82	12.71	2.83	3.76
Ce	8.26	6.28	17.35	15.23	13.43	15.32	18.65	5.60	4.87
Pr	0.621	0.457	1.23	1.092	1.284	1.084	2.076	0.68	0.335
Nd	1.649	1.133	3.243	2.685	4.291	2.753	7.77	2.927	0.689
Sm	0.184	0.109	0.225	0.282	0.927	0.261	2.214	1.007	0.141
Eu	0.724	0.643	0.869	0.756	0.852	0.737	1.293	0.803	0.246
Gd	0.093	0.065	0.108	0.148	0.638	0.163	1.508	0.668	n.d.
Tb	0.011	0.006	0.008	0.02	0.092	0.018	0.264	0.107	0.011
Dy	0.057	0.023	0.037	0.112	0.604	0.11	1.587	0.715	0.044
Ho	0.011	0.005	0.009	0.019	0.118	0.022	0.324	0.132	0.004
Er	0.031	0.015	0.023	0.068	0.331	0.073	0.862	0.392	0.01
Tm	0.005	0.001	0.002	0.009	0.042	0.008	0.124	0.058	0.007
Yb	0.029	0.006	0.022	0.065	0.374	0.079	1.195	0.543	n.d.
Lu	0.005	0.001	0.003	0.008	0.05	0.01	0.11	0.058	0.005
Pb	17.38	17.01	16.42	15.56	16.29	15.59	16.48	16.29	31.61
Th	0.19	0.074	0.027	0.025	0.017	0.024	0.052	0.208	20.608
U	0.03	0.016	0.067	0.041	0.017	0.1	0.033	0.019	4.53

(Continued.)

A.3. Supplementary Material to Chapter 4

Sample	54.2.1	54.2.1	54.2.1	54.2.1	54.2.1	54.2.1	54.2.1	54.2.1	54.2.1
Rock type	Pegm.								
<i>Major elements (wt.%)</i>									
SiO ₂	64.25	63.75	64.12	64.15	64.64	64.61	64.19	64.53	64.28
Al ₂ O ₃	22.48	22.52	22.47	22.40	22.15	22.28	22.63	22.26	22.40
FeO	0.11	0.12	0.08	0.07	0.10	0.07	0.01	0.12	0.09
MgO	0.00	0.00	0.00	0.00	0.00	0.00	0.00	0.01	0.00
CaO	3.49	3.65	3.30	3.26	3.17	3.33	3.63	3.25	3.45
SrO	0.00	0.00	0.00	0.00	0.00	0.00	0.00	0.00	0.00
BaO	0.00	0.00	0.03	0.00	0.00	0.00	0.00	0.00	0.00
Na ₂ O	9.20	9.31	9.53	9.54	9.55	9.57	9.60	9.54	9.47
K ₂ O	0.62	0.43	0.35	0.34	0.49	0.37	0.16	0.47	0.37
Total	100.14	99.78	99.88	99.76	100.11	100.24	100.22	100.18	100.06
<i>Trace elements (µg/g)</i>									
Li	48.352	69.58	9.615	4.319	16.744	22.897	8.915	3.845	2.495
Sc	2.083	6.399	0.894	0.522	1.013	1.36	1.18	0.941	1.436
V	2.494	8.327	0.579	0.526	2.287	1.465	0.898	0.519	0.502
Zn	29.848	87.894	7.495	5.113	19.311	12.332	7.057	4.774	4.121
Rb	10.3	83.11	3.556	5.876	26.163	42.364	45.965	9.259	11.497
Sr	27.58	31.91	35.69	41.59	39.90	43.87	45.57	45.51	44.04
Y	0.782	0.256	0.242	0.225	0.158	1.25	0.417	0.286	0.256
Zr	0.287	1.182	1.882	3.699	1.649	3.226	5.333	5.024	7.962
Cs	0.324	3.16	0.093	0.065	0.56	1.432	1.354	0.181	0.269
Ba	7.023	9.452	4.654	14.59	13.44	24.24	33.44	27.51	41.27
La	0.97	3.50	3.94	4.02	5.14	4.58	4.66	5.30	4.84
Ce	3.66	3.75	4.75	4.49	5.60	5.52	5.85	6.48	6.39
Pr	0.216	0.195	0.359	0.285	0.404	0.375	0.372	0.401	0.431
Nd	0.469	1.381	0.969	0.856	1.065	1.04	0.969	1.106	1.232
Sm	n.d.	0.103	0.072	0.128	0.121	0.176	0.137	0.246	0.142
Eu	0.043	0.343	0.207	0.216	0.239	0.224	0.285	0.315	0.272
Gd	n.d.	n.d.	0.093	n.d.	0.078	0.114	0.083	0.08	0.088
Tb	0.012	n.d.	0.011	n.d.	0.006	0.028	0.018	0.018	0.008
Dy	0.144	0.064	0.015	0.06	0.04	0.158	0.083	0.082	0.052
Ho	0.025	0.016	0.008	n.d.	0.006	0.031	0.018	0.017	0.015
Er	0.034	n.d.	0.023	0.015	0.017	0.142	0.037	0.033	0.009
Tm	0.012	n.d.	0.011	n.d.	0.007	0.019	0.019	0.005	0.008
Yb	0.116	0.072	n.d.	0.048	0.017	0.221	0.141	0.067	0.077
Lu	n.d.	0.011	0.003	n.d.	0.003	0.038	0.017	0.007	0.005
Pb	23.44	83.04	30.01	28.50	32.35	35.60	40.31	39.33	32.90
Th	7.015	13.098	11.39	9.626	16.774	26.451	43.228	32.857	26.894
U	19.791	20.377	4.081	12.39	2.342	5.723	8.923	9.951	4.677

(Continued.)

A. Supplementary Materials

Sample	54.2.1	54.2.1	54.2.1	54.2.1	54.2.1	54.2.1	54.2.1	54.2.1	54.2.1
Rock type	Pegm.	Pegm.	Pegm.	Pegm.	Pegm.	Pegm.	Pegm.	Pegm.	Pegm.
<i>Major elements (wt.%)</i>									
SiO ₂	64.56	64.32	64.06	64.00	64.37	64.42	63.76	64.44	64.80
Al ₂ O ₃	22.33	22.33	22.25	22.56	22.25	22.17	22.10	22.30	22.32
FeO	0.10	0.14	0.09	0.10	0.11	0.14	0.10	0.08	0.14
MgO	0.00	0.00	0.00	0.00	0.00	0.00	0.00	0.00	0.00
CaO	3.30	3.36	3.49	3.70	3.32	3.33	3.39	3.19	3.14
SrO	0.00	0.00	0.00	0.00	0.00	0.00	0.00	0.00	0.00
BaO	0.02	0.02	0.00	0.02	0.00	0.06	0.02	0.04	0.00
Na ₂ O	9.35	9.37	9.38	9.36	9.55	9.35	9.32	9.61	9.56
K ₂ O	0.50	0.60	0.46	0.29	0.39	0.57	0.47	0.37	0.45
Total	100.17	100.14	99.73	100.03	99.99	100.04	99.16	100.04	100.42
<i>Trace elements (µg/g)</i>									
Li	5.708	10.098	23.826	29.788	65.695	25.81	6.537	13.018	7.795
Sc	1.151	2.639	4.974	3.141	2.652	4.793	0.806	0.596	0.746
V	0.739	1.466	3	5.036	2.631	2.023	1.133	2.494	1.414
Zn	5.692	10.496	26.034	62.791	59.863	30.098	3.668	5.32	5.321
Rb	14.953	35.588	42.589	64.644	61.16	29.919	3.42	2.838	3.783
Sr	50.66	70.15	62.12	49.51	31.43	34.43	45.72	35.98	34.55
Y	0.626	1.503	0.744	0.637	0.27	0.47	0.141	0.174	0.109
Zr	42.129	110.599	26.709	29.388	17.973	13.769	0.262	3.31	0.436
Cs	0.204	0.413	1.38	0.849	1.098	1.789	0.162	0.022	n.d.
Ba	104.3	237.4	151.4	116.7	60.88	160.3	4.652	6.171	3.117
La	5.45	5.41	3.61	2.33	1.94	2.04	4.15	2.41	2.77
Ce	6.68	7.67	8.91	5.29	3.26	4.01	4.51	4.47	3.45
Pr	0.538	0.656	0.371	0.368	0.174	0.235	0.319	0.219	0.238
Nd	1.495	2.065	1.053	0.983	0.344	0.89	0.941	0.685	0.083
Sm	0.2	0.386	0.359	0.052	n.d.	n.d.	0.103	n.d.	0.222
Eu	0.306	0.399	0.219	0.148	0.128	0.088	0.22	0.037	0.157
Gd	0.082	0.228	0.05	0.164	0.144	n.d.	n.d.	0.063	0.22
Tb	0.017	0.041	0.008	n.d.	n.d.	0.034	0.004	n.d.	n.d.
Dy	0.092	0.232	0.223	0.034	n.d.	0.046	n.d.	n.d.	n.d.
Ho	0.025	0.06	0.024	0.009	0.046	0.035	0.008	0.03	n.d.
Er	0.06	0.182	0.049	n.d.	n.d.	0.105	0.012	0.029	0.107
Tm	0.015	0.025	0.056	n.d.	n.d.	0.023	n.d.	n.d.	n.d.
Yb	0.081	0.234	0.153	0.119	n.d.	0.221	0.038	0.047	0.056
Lu	0.008	0.039	0.024	0.006	n.d.	n.d.	0.003	0.015	n.d.
Pb	38.45	42.44	39.50	27.49	13.06	22.34	46.83	23.03	28.51
Th	2.366	4.657	18.649	4.324	12.138	39.431	12.29	22.663	32.678
U	2.366	2.301	15.883	7.286	9.371	11.263	6.439	12.661	14.007

(Continued.)

A.3. Supplementary Material to Chapter 4

Sample	54.2.1	54.2.1	54.2.1	54.2.1	54.2.1	54.2.1	54.2.1	54.2.1	54.2.1
Rock type	Pegm.	Pegm.	Pegm.	Pegm.	Pegm.	Pegm.	Pegm.	Pegm.	Pegm.
<i>Major elements (wt.%)</i>									
SiO ₂	63.82	64.80	64.42	64.29	64.62	66.43	64.85	64.75	63.96
Al ₂ O ₃	22.64	22.47	22.37	22.29	22.39	21.74	22.14	22.20	22.60
FeO	0.14	0.07	0.11	0.12	0.12	0.01	0.13	0.12	0.15
MgO	0.00	0.00	0.00	0.00	0.00	0.00	0.00	0.00	0.00
CaO	3.80	3.17	3.44	3.49	3.31	2.30	3.17	3.30	3.76
SrO	0.00	0.00	0.00	0.00	0.00	0.00	0.00	0.00	0.00
BaO	0.04	0.00	0.01	0.03	0.04	0.00	0.00	0.00	0.04
Na ₂ O	9.30	9.77	9.32	9.30	9.37	10.38	9.40	9.27	9.12
K ₂ O	0.24	0.15	0.47	0.50	0.55	0.07	0.56	0.65	0.51
Total	99.98	100.43	100.15	100.02	100.40	100.93	100.26	100.29	100.13
<i>Trace elements (μg/g)</i>									
Li	7.018	6.425	16.889	13.407	7.411	28.141	31.957	52.796	10.692
Sc	0.909	0.776	1.99	4.425	0.832	2.117	7.566	7.666	3.017
V	0.683	1.568	4.75	3.425	0.539	5.37	7.046	11.513	1.812
Zn	3.88	13.283	15.853	18.948	7.841	21.681	75.198	136.135	26.818
Rb	3.668	87.275	72.1	63.654	15.603	56.691	100.101	151.037	42.437
Sr	50.48	56.35	83.34	53.20	61.24	24.39	167.6	161.9	85.1
Y	0.532	1.126	1.796	0.87	0.268	0.916	2.855	3.351	1.322
Zr	2.868	20.017	79.256	47.6	11.507	17.878	115.285	209.279	72.92
Cs	0.112	2.599	1.604	0.554	0.167	2.799	1.988	2.689	0.6
Ba	5.954	126.7	211.3	202.9	59.63	83.11	240.6	382.5	200.9
La	6.10	3.43	3.51	2.90	5.11	1.33	11.77	12.94	6.68
Ce	7.08	4.66	7.25	5.96	6.35	5.70	16.09	17.86	9.89
Pr	0.693	0.274	0.587	0.289	0.426	0.267	1.29	1.99	0.807
Nd	1.157	1.175	0.884	0.903	1.151	n.d.	2.972	5.409	2.011
Sm	0.335	0.146	n.d.	0.161	0.032	n.d.	0.759	1.118	0.252
Eu	0.555	0.267	0.676	0.124	0.352	n.d.	0.592	1.028	0.412
Gd	0.193	0.298	0.28	0.341	0.044	0.191	0.3	0.379	0.171
Tb	0.03	0.03	0.043	0.039	0.003	0.096	0.128	0.151	0.01
Dy	0.149	0.241	0.171	0.102	0.027	0.126	0.328	0.465	0.118
Ho	0.069	0.055	0.163	n.d.	0.007	n.d.	0.037	0.108	0.061
Er	0.205	0.161	0.174	0.038	0.041	n.d.	0.306	0.212	0.12
Tm	0.022	0.038	0.057	0.013	0.007	0.031	0.046	0.046	0.023
Yb	0.107	0.365	0.137	n.d.	0.049	n.d.	0.481	0.163	0.285
Lu	0.028	0.023	0.043	0.01	0.005	0.024	0.098	0.009	0.02
Pb	72.94	42.53	59.31	17.84	38.52	28.27	114.6	152.2	88.81
Th	153.485	107.801	88.65	31.503	9.349	66.018	140.846	109.189	74.669
U	197.881	22.619	32.328	26.744	2.355	25.968	114.51	78.801	22.78

(Continued.)

A. Supplementary Materials

Sample	54.2.1	54.2.1	54.2.1	54.2.1	54.2.1	54.2.1	54.2.1	54.2.1
Rock type	Pegm.	Pegm.	Pegm.	Pegm.	Pegm.	Pegm.	Pegm.	Pegm.
<i>Major elements (wt.%)</i>								
SiO ₂	62.78	64.55	64.91	64.74	64.56	64.51	64.34	64.69
Al ₂ O ₃	22.01	22.33	22.18	22.41	22.32	22.17	22.48	22.23
FeO	0.11	0.13	0.10	0.07	0.09	0.08	0.11	0.10
MgO	0.00	0.00	0.00	0.00	0.00	0.00	0.00	0.00
CaO	3.38	3.46	3.01	3.31	3.35	3.24	3.51	3.15
SrO	0.00	0.00	0.00	0.01	0.00	0.00	0.00	0.00
BaO	0.04	0.00	0.00	0.00	0.00	0.00	0.01	0.00
Na ₂ O	8.94	9.35	9.65	9.53	9.55	9.62	9.30	9.63
K ₂ O	0.47	0.54	0.39	0.40	0.47	0.31	0.41	0.33
Total	97.73	100.35	100.24	100.48	100.35	99.93	100.16	100.13
<i>Trace elements (µg/g)</i>								
Li	37.016	19.601	17.633	n.d.	2.733	8.441	8.171	5.892
Sc	2.138	2.265	1.26	6.104	0.562	4.263	1.554	0.475
V	4.459	19.603	1.402	3.703	0.793	5.203	2.625	n.d.
Zn	23.858	29.873	12.982	55.984	5.855	47.036	11.893	1.981
Rb	28.392	98.707	4.512	6.673	2.548	67	25.502	3.415
Sr	41.63	144.2	38.75	128.7	50.76	141.1	59.87	41.56
Y	0.952	5.172	0.311	5.961	0.343	2.428	1.22	0.117
Zr	24.684	401.054	6.899	1.918	2.566	140.361	73.876	1.445
Cs	0.499	1.793	0.038	0.319	0.017	0.818	0.343	0.093
Ba	208.2	846.6	19.49	53.13	7.86	283.2	159.6	10.50
La	3.93	9.72	2.81	14.31	5.14	7.92	6.22	4.50
Ce	5.73	13.51	3.32	17.99	5.95	13.27	7.80	5.16
Pr	0.252	1.538	0.236	1.217	0.452	0.83	0.678	0.398
Nd	0.934	4.425	0.884	0.881	0.74	3.451	2.681	1.189
Sm	n.d.	0.877	n.d.	0.181	0.236	0.259	0.328	0.046
Eu	0.174	0.898	0.248	0.547	0.303	0.558	0.411	0.278
Gd	n.d.	0.652	0.162	0.171	0.095	0.128	0.207	0.058
Tb	0.015	0.137	0.025	0.113	0.015	0.081	0.024	0.024
Dy	0.058	0.746	n.d.	1.022	0.029	0.081	0.189	0.01
Ho	n.d.	0.256	0.026	0.116	0.008	0.042	0.028	0.01
Er	0.136	0.528	0.116	0.346	0.112	0.03	0.071	0.007
Tm	n.d.	0.111	0.038	0.085	0.007	0.06	0.024	0.005
Yb	n.d.	1.373	0.121	0.684	0.034	0.145	0.131	n.d.
Lu	0.058	0.172	0.068	0.174	0.022	0.023	0.039	0.002
Pb	32.83	75.11	43.14	127.9	59.28	110.0	50.24	29.49
Th	30.259	15.576	17.464	66.365	24.304	31.885	2.107	0.337
U	13.073	17.709	5.448	68.01	8.879	46.873	2.963	0.399

LRT, Listino ring tonalite

MGD, Monoccola granodiorite

Pegm., pegmatite

n.d., not detected

Table A3.4. Quartz trace element analyses and thermometry of the Laione granodiorite.

Sample	Rock type	Comment	Al μg/g	± μg/g	Ti μg/g	± μg/g	$a\text{TiO}_2$	Temperature °C
31.2.1a	LGD	Rim	34.52	3.09	44.94	1.06	0.57	720
31.2.1a	LGD	Core	30.66	2.61	83.90	2.42	0.57	796
31.2.1a	LGD	Rim	33.43	2.83	42.44	0.97	0.57	713
31.2.1a	LGD	Rim	38.63	3.26	43.97	1.13	0.57	717
31.2.1a	LGD	Rim	26.59	2.26	33.13	0.74	0.57	686
31.2.1a	LGD	Core	55.13	4.75	105.45	2.51	0.57	827
31.2.1a	LGD	Rim	56.22	4.80	47.34	1.10	0.57	726
31.2.1a	LGD	Rim	35.39	3.00	46.93	1.18	0.57	724
31.2.1a	LGD	Core	29.18	2.48	78.63	1.86	0.57	787
31.2.1a	LGD	Rim	45.56	3.91	45.17	1.08	0.57	720
31.2.1b	LGD	Rim	38.82	3.27	32.82	0.92	0.57	685
31.2.1b	LGD	Rim	39.15	3.58	44.74	1.12	0.57	719
31.2.1b	LGD	Core	46.59	8.07	111.34	3.03	0.57	835
31.2.1b	LGD	Rim	34.63	2.92	48.77	1.09	0.57	729
31.2.1b	LGD	Core	55.56	4.67	105.20	2.76	0.57	827
31.2.1b	LGD	Rim	48.87	4.11	51.40	1.16	0.57	735
31.2.1b	LGD	Rim	51.72	4.39	49.60	1.22	0.57	731
54.7.1	LGD	Core	29.06	2.45	68.15	2.00	0.57	769
54.7.1	LGD	Rim	26.52	2.24	44.84	1.05	0.57	719
54.7.1	LGD	Core	26.50	2.24	76.69	2.59	0.57	784
54.7.1	LGD	Core	26.46	2.24	82.41	2.03	0.57	794
54.7.1	LGD	Rim	23.46	1.99	40.79	0.93	0.57	709
54.7.1	LGD	Core	24.70	2.10	68.66	1.64	0.57	770
54.7.1	LGD	Rim	25.78	2.18	45.33	1.04	0.57	721
54.7.1	LGD	Rim	32.21	2.72	45.49	1.03	0.57	721
54.7.1	LGD	Rim	32.74	2.94	27.04	0.66	0.57	665
54.7.1	LGD	Core	26.87	2.28	69.85	2.80	0.57	772
54.7.1	LGD	Rim	20.70	1.77	42.91	1.25	0.57	714
54.7.1	LGD	Rim	28.07	2.38	45.35	1.17	0.57	721
54.7.1	LGD	Rim	41.13	3.47	44.56	1.05	0.57	719
54.7.1	LGD	Rim	29.37	2.49	46.62	1.91	0.57	724
54.7.1	LGD	Core	44.62	5.45	89.97	2.07	0.57	805
54.7.1	LGD	Rim	32.31	2.77	58.37	1.34	0.57	750

LGD, Laione granodiorite

Table A3.5. Zircon trace element ($\mu\text{g/g}$) analyses and thermometry for the different Western Adamello lithologies.

Sample	CJ48												
Rock type	Tonalite												
Comment	Core	Rim	Core	Rim	Core	Rim	Core	Rim	Rim	Core	Rim	Core	Rim
Ti	3.42	2.76	2.94	2.76	3.42	4.44	6.00	2.64	2.52	2.28	3.42	2.88	4.14
Sr	0.204	0.176	0.189	0.204	0.238	0.24	0.246	0.176	0.234	0.148	0.208	0.235	0.204
Y	764	505	524	645	798	779	1263	500	675	355	680	638	464
Nb	1.589	1.732	1.831	3.01	3.968	2.559	1.064	1.986	2.634	1.032	2.675	1.458	2.065
La	0.0015	0.0012	0.0024	0.002	0.0041	0.0022	0.0062	0.0013	0.0015	0.0008	0.0037	0.002	0.0025
Ce	8.42	8.99	11.16	12.33	13.41	10.32	9.67	10.08	10.39	6.28	14.92	11.86	14.18
Pr	0.026	0.022	0.024	0.025	0.034	0.024	0.145	0.028	0.034	0.015	0.037	0.036	0.036
Nd	0.61	0.482	0.574	0.545	0.636	0.536	2.669	0.5	0.569	0.29	0.666	0.752	0.696
Sm	1.714	1.157	1.302	1.488	1.645	1.337	5.401	1.348	1.45	0.75	1.674	1.505	1.36
Eu	0.449	0.339	0.402	0.4	0.427	0.466	1.175	0.342	0.394	0.225	0.476	0.536	0.439
Gd	11.49	7.65	7.45	9.08	11.83	10.69	28.85	7.99	9.76	5.25	11.04	9.62	7.22
Tb	4.445	2.843	2.794	3.457	4.755	4.242	9.838	2.936	3.728	1.931	4.132	3.656	2.696
Dy	60.04	37.71	37.29	45.87	64.40	58.07	119.54	38.10	50.41	26.60	54.02	46.91	34.74
Ho	24.73	15.64	16.14	19.81	27.07	24.34	45.13	15.52	21.65	11.48	21.92	20.08	14.47
Er	127.2	82.7	87.4	104.6	142.4	130.7	210.4	83.4	116.1	61.5	113.6	106.4	77.1
Tm	28.26	19.08	21.32	25.70	31.96	29.46	42.46	19.23	27.21	14.68	25.26	25.00	18.44
Yb	288	198	235	270	321	305	385	206	292	157	257	271	199
Lu	63.64	44.79	57.33	63.22	71.98	68.73	77.48	47.47	68.57	37.50	58.04	63.73	47.02
Hf	9755	10,488	10,232	11,573	9,954	11,414	9,180	11,066	10,644	10,678	11,306	10,807	11,052
Ta	0.745	1.027	0.977	1.729	1.908	1.395	0.58	1.226	1.517	0.642	1.357	0.878	1.249
Pb	n.d.	1.529	n.d.	n.d.	n.d.								
Th	137	142	175	177	218	133	172	197	154	77	361	196	270
U	338	402	450	472	613	368	263	521	466	243	651	483	622
T ($^{\circ}\text{C}$)	693	675	680	675	693	715	743	671	668	660	693	679	709

(Continued.)

Sample	CJ48												
Rock type	Tonalite												
Comment	Core	Rim	Core										
Ti	2.94	1.32	3.30	3.90	2.94	1.80	4.14	4.38	5.88	4.92	4.20	5.82	2.64
Sr	0.237	0.199	0.21	0.173	0.226	0.221	0.221	0.23	0.188	0.221	0.201	0.271	0.165
Y	965	434	601	594	583	586	493	671	673	707	644	1225	262
Nb	1.725	2.198	1.889	1.912	2.046	2.545	1.662	3.896	1.005	2.373	1.28	4.673	0.957
La	0.0077	0.002	0.0043	0.0014	0.0135	0.0014	0.002	0.003	0.0071	0.0017	0.0018	0.0028	0.0008
Ce	17.78	6.20	11.80	8.52	12.06	9.65	10.99	17.25	8.37	11.43	6.93	18.38	6.85
Pr	0.119	0.011	0.031	0.021	0.033	0.02	0.029	0.032	0.095	0.032	0.024	0.061	0.011
Nd	2.202	0.214	0.518	0.463	0.501	0.466	0.538	0.66	1.459	0.673	0.521	1.223	0.195
Sm	3.834	0.713	1.296	1.245	1.175	1.217	1.406	1.439	2.578	1.45	1.384	2.703	0.525
Eu	1.154	0.234	0.434	0.294	0.404	0.359	0.518	0.497	1.08	0.592	0.33	0.663	0.192
Gd	19.31	5.05	8.28	8.16	7.56	7.69	6.89	8.39	12.59	9.57	9.67	17.85	3.39
Tb	6.517	2.065	3.067	3.266	2.929	3.053	2.713	3.226	4.35	3.734	3.813	7.089	1.284
Dy	77.66	28.07	41.66	44.12	39.56	40.36	36.26	44.08	52.68	51.25	52.18	95.24	18.19
Ho	30.30	12.70	17.92	18.60	17.12	17.51	15.42	19.56	21.07	21.80	21.56	39.99	7.97
Er	150.4	70.7	96.7	100.1	94.7	94.5	81.7	109.0	106.6	116.9	108.6	202.6	44.4
Tm	32.87	17.58	22.93	22.71	23.01	22.87	19.25	26.78	24.42	27.19	24.19	44.46	10.83
Yb	340	197	255	238	258	251	217	297	261	293	238	435	123
Lu	75.78	47.25	60.73	52.93	61.60	59.41	50.58	72.65	60.08	68.69	51.98	93.57	29.85
Hf	10,246	12,561	10,351	10,294	10,589	11,323	11,747	10,488	8,761	9,513	10,086	9,308	10,869
Ta	0.99	1.584	0.945	1.000	1.004	1.677	0.804	1.919	0.439	1.05	0.718	1.83	0.675
Pb	n.d.	0.981	n.d.	0.828	n.d.								
Th	368	156	191	107	195	171	148	264	106	135	92	296	71
U	630	796	475	293	498	540	362	631	181	318	248	584	214
T (°C)	680	619	690	704	680	642	709	714	741	725	711	740	671

(Continued.)

Sample	CJ48												
Rock type	Tonalite												
Comment	Rim	Core	Rim	Core	Rim	Core	Rim	Tonalite	Tonalite	Tonalite	Tonalite	Tonalite	Tonalite
Ti	3.36	3.06	3.42	3.06	3.72	3.30	3.30	3.54	3.24	9.71	3.18	4.62	29.20
Sr	0.257	0.175	0.198	0.183	0.194	0.214	0.218	0.247	0.211	0.611	0.219	0.25	0.222
Y	923	513	732	561	516	692	683	817	704	3880	831	1083	1216
Nb	3.921	1.63	3.352	2.514	2.183	1.886	3.172	2.696	1.51	6.244	1.967	3.689	2.087
La	0.0035	0.0026	0.0021	0.0038	0.0015	0.0043	0.0022	0.0065	0.005	0.1593	0.0127	0.0066	0.0317
Ce	16.73	11.42	12.42	13.57	13.03	13.79	14.47	17.97	12.12	53.65	16.29	18.42	27.45
Pr	0.076	0.027	0.028	0.042	0.032	0.076	0.034	0.093	0.057	1.448	0.114	0.106	0.304
Nd	1.324	0.518	0.617	0.642	0.625	1.233	0.673	1.459	1.026	20.286	2.012	1.848	4.715
Sm	2.681	1.292	1.477	1.584	1.487	2.298	1.535	2.768	2.164	27.614	3.447	3.737	7.393
Eu	0.697	0.45	0.414	0.477	0.374	0.726	0.476	0.9	0.665	10.071	1.031	0.906	2.528
Gd	15.19	7.51	10.18	8.62	7.83	11.81	9.96	14.24	12.09	103.87	15.98	21.20	33.56
Tb	5.339	2.79	3.961	3.169	2.924	4.077	3.755	4.842	4.39	31.188	5.455	7.374	10.725
Dy	68.81	36.75	52.79	41.37	38.22	52.74	52.02	60.95	55.00	343.83	66.96	90.95	121.55
Ho	28.33	16.04	22.56	17.31	15.89	21.35	21.32	25.38	22.71	125.76	26.98	35.96	42.76
Er	144.3	86.9	122.0	91.3	83.1	109.6	114.7	131.6	117.4	602.3	136.7	175.8	190.9
Tm	33.42	21.32	28.47	21.60	19.28	25.73	26.36	30.10	26.72	131.46	30.92	38.23	37.64
Yb	343	234	298	229	203	273	277	321	283	1314	319	381	337
Lu	81.39	57.29	68.51	54.65	46.79	64.12	63.99	75.42	65.45	290.8	73.69	83.77	65.40
Hf	10,305	10,606	10,677	10,327	10,750	10,322	10,391	10,322	9,953	7,529	10,346	9,626	7,679
Ta	2.758	1.004	1.603	1.284	1.252	0.948	1.54	1.292	0.833	1.566	0.959	1.339	0.676
Pb	n.d.	n.d.	n.d.	n.d.	n.d.	n.d.	0.931	n.d.	n.d.	n.d.	n.d.	1.143	n.d.
Th	305	179	200	206	229	258	304	356	212	1541	339	350	38
U	749	462	572	478	525	523	662	707	455	1214	583	639	50
T (°C)	691	684	693	684	700	690	690	696	688	790	687	719	916

(Continued.)

Sample	CJ48	CJ26	CJ26	CJ26	CJ26	CJ26							
Rock type	Tonalite												
Comment									Core	Rim	Rim	Core	Rim
Ti	5.46	2.94	4.80	5.52	7.19	5.22	3.66	5.82	10.01	3.90	3.78	3.06	2.76
Sr	0.411	0.224	0.194	0.289	0.445	0.297	0.22	0.518	0.737	0.195	0.27	0.167	0.214
Y	2278	847	773	1357	3701	1236	1409	3679	3936	695	915	390	560
Nb	4.674	2.009	1.312	6.224	8.325	3.094	2.141	4.393	7.727	2.261	4.707	1.657	2.499
La	0.0438	0.0164	0.0051	0.0574	0.1508	0.0084	0.0047	0.0494	0.0119	0.0015	0.0025	0.0028	0.0021
Ce	43.30	18.52	13.40	23.12	65.03	16.80	8.59	34.98	55.65	12.91	16.45	10.11	11.05
Pr	0.443	0.144	0.072	0.151	1.277	0.065	0.101	0.583	0.239	0.042	0.042	0.03	0.029
Nd	6.77	1.843	1.263	2.045	17.749	1.389	1.995	9.413	4.395	0.744	0.763	0.402	0.548
Sm	11.56	3.644	2.312	4.081	27.129	3.421	5.434	17.166	10.12	1.867	1.92	0.924	1.278
Eu	3.343	1.124	0.923	0.771	5.478	1.011	0.89	3.815	5.126	0.479	0.527	0.312	0.383
Gd	53.57	17.14	13.53	22.74	113.34	21.03	36.03	85.95	60.28	11.50	11.58	5.46	7.86
Tb	17.084	5.818	4.713	8.547	34.006	7.665	12.235	28.964	22.512	4.158	4.666	2.162	3.039
Dy	203.18	71.86	60.01	108.98	365.60	105.25	141.29	339.41	294.20	54.49	64.04	28.26	40.55
Ho	76.06	27.55	24.21	43.90	124.18	41.87	49.24	126.67	123.03	22.50	27.77	12.34	17.19
Er	361.9	141.2	126.2	221.1	537.7	210.3	210.4	586.7	646.4	114.1	153.0	65.3	92.3
Tm	77.32	32.23	29.18	48.26	104.18	46.90	39.96	119.64	149.13	25.51	37.31	15.44	22.59
Yb	750	325	304	460	921	492	357	1098	1598	254	395	169	237
Lu	159.25	75.61	68.20	98.13	174.2	104.7	69.37	218.6	365.6	55.36	93.06	40.76	56.82
Hf	8,933	9,618	9,590	9,017	7,855	9,381	10,042	9,214	7,426	10,004	11,190	9,973	11,038
Ta	1.64	1.108	0.572	2.149	1.648	1.106	0.964	1.62	1.598	1.129	2.179	0.936	1.433
Pb	n.d.	1.812	n.d.	n.d.	5.646	n.d.							
Th	909	411	227	429	1571	345	232	1035	734	245	267	155	203
U	1021	643	419	717	1441	558	525	1191	763	530	775	387	568
T (°C)	734	680	722	735	760	730	699	740	793	704	701	684	675

(Continued.)

Sample	CJ26												
Rock type	Tonalite												
Comment	Rim	Core	Rim										
Ti	2.40	4.20	2.82	3.18	2.94	2.46	2.52	3.12	4.56	3.96	2.52	3.66	3.00
Sr	0.2	0.297	0.179	0.286	0.203	0.21	0.19	0.184	0.194	0.226	0.177	0.14	0.198
Y	546	1003	503	884	397	622	549	493	681	680	379	275	507
Nb	2.578	4.113	1.833	1.956	2.206	1.493	2.294	1.611	2.451	2.081	1.72	1.651	2.559
La	0.0019	0.1636	0.0012	0.0101	0.0011	0.0025	0.0015	0.0017	0.0008	0.0027	0.0017	0.0263	0.003
Ce	11.75	18.44	9.10	11.92	11.71	9.27	12.22	10.24	11.99	12.91	7.95	16.46	13.04
Pr	0.025	0.103	0.022	0.056	0.022	0.026	0.034	0.03	0.034	0.036	0.015	0.04	0.029
Nd	0.472	1.242	0.473	1.018	0.399	0.527	0.622	0.477	0.56	0.653	0.301	0.533	0.59
Sm	1.065	2.475	1.283	2.63	0.934	1.346	1.475	1.198	1.478	1.54	0.907	1.061	1.166
Eu	0.36	0.58	0.333	0.609	0.319	0.419	0.374	0.439	0.406	0.567	0.249	0.289	0.441
Gd	6.95	14.55	7.42	13.98	5.37	8.86	8.41	6.92	10.11	9.82	5.20	4.81	6.91
Tb	2.668	5.758	2.833	4.962	2.034	3.358	3.142	2.597	3.869	3.745	2.06	1.734	2.623
Dy	36.93	76.81	38.29	63.24	27.50	45.70	41.74	35.06	49.85	48.87	27.08	22.09	35.00
Ho	15.95	32.43	15.73	26.10	11.69	19.50	17.40	14.71	20.84	20.58	11.68	8.94	15.20
Er	88.6	166.5	82.9	140.4	65.0	101.5	89.3	79.9	106.8	109.6	62.3	48.4	84.0
Tm	21.58	37.60	19.72	31.83	16.11	23.71	20.63	19.46	24.06	25.90	14.53	10.79	20.29
Yb	236	379	208	328	177	250	218	215	240	277	156	116	224
Lu	56.86	83.70	49.77	75.13	43.70	58.38	50.32	52.66	53.77	65.78	36.79	25.94	54.27
Hf	10,946	10,489	11,018	12,294	11,130	10,227	10,859	10,261	10,233	10,237	11,356	9,551	10,803
Ta	1.344	1.655	1.17	0.922	1.372	0.816	1.254	0.856	1.196	0.984	1.092	0.691	1.508
Pb	n.d.	0.983	n.d.	n.d.	n.d.								
Th	172	299	160	217	190	151	220	153	207	208	146	66	203
U	453	626	437	528	496	404	551	414	456	500	477	120	534
T (°C)	664	711	677	687	680	666	668	685	718	705	668	699	682

(Continued.)

Sample	CJ26												
Rock type	Tonalite												
Comment	Core	Rim	Core										
Ti	2.64	3.24	2.82	3.60	3.48	3.84	4.44	2.52	2.64	3.60	3.00	3.90	4.08
Sr	0.187	0.211	0.254	0.263	0.206	0.238	0.251	0.239	0.183	0.233	0.236	0.237	0.236
Y	413	553	838	784	646	915	1184	927	575	862	857	950	1127
Nb	1.296	2.426	2.917	3.079	2.362	4.079	1.726	1.682	1.272	3.899	2.183	3.415	4.443
La	0.0178	0.0016	0.0037	0.003	0.0115	0.0455	0.0181	0.0052	0.0043	0.0166	0.0051	0.0012	0.0196
Ce	7.88	12.59	16.31	13.76	12.73	15.51	16.80	17.72	10.59	16.10	17.51	13.45	28.33
Pr	0.029	0.021	0.039	0.034	0.035	0.055	0.21	0.096	0.071	0.05	0.114	0.039	0.197
Nd	0.369	0.53	0.786	0.705	0.539	0.778	3.138	1.804	1.044	0.872	1.744	0.706	3.507
Sm	0.827	1.211	1.91	1.758	1.438	1.78	5.461	3.553	2.15	1.915	3.224	2.032	5.096
Eu	0.316	0.416	0.634	0.434	0.454	0.519	1.665	1.049	0.576	0.501	0.982	0.506	1.456
Gd	5.62	7.77	11.47	10.77	8.75	12.60	24.07	17.43	10.45	12.94	16.19	13.49	24.19
Tb	2.067	3.152	4.529	4.208	3.402	4.983	8.009	5.849	3.662	4.989	5.523	5.206	8.342
Dy	27.54	40.43	61.12	58.56	45.51	67.26	93.99	71.53	45.90	64.58	68.98	69.98	100.21
Ho	12.07	16.87	26.04	25.19	19.71	28.80	37.18	28.05	18.60	26.21	27.59	30.36	38.19
Er	67.2	90.8	139.6	130.3	106.9	151.9	183.2	139.8	93.5	133.5	137.9	159.7	185.7
Tm	16.28	21.44	32.82	29.84	25.67	34.81	41.00	31.82	21.61	30.21	31.06	36.71	41.65
Yb	183	229	364	309	282	359	416	326	224	307	319	377	406
Lu	44.74	54.72	85.79	69.31	67.72	82.05	94.68	75.13	52.28	69.82	73.64	85.31	86.73
Hf	11,054	10,804	10,841	11,707	10,974	10,410	9,146	10,620	10,503	10,390	10,593	10,435	9,699
Ta	0.774	1.335	1.36	1.446	1.159	1.625	0.775	0.901	0.754	1.581	1.052	1.468	1.233
Pb	n.d.	0.894	n.d.	n.d.	n.d.	n.d.	n.d.	0.797	1.302	n.d.	n.d.	n.d.	n.d.
Th	104	178	309	180	188	224	405	365	204	298	344	203	563
U	323	426	772	465	509	545	615	641	404	630	596	534	873
T (°C)	671	688	677	697	694	703	715	668	671	697	682	704	708

(Continued.)

Sample	CJ26												
Rock type	Tonalite												
Comment	Rim												
Ti	2.64	2.94	3.12	9.35	3.36	2.04	3.18	8.57	3.96	2.82	5.88	6.41	4.38
Sr	0.181	0.194	0.192	0.358	0.207	0.261	0.208	0.169	0.354	0.223	0.278	0.573	0.2
Y	370	677	618	2208	721	1096	629	465	998	827	1859	1804	806
Nb	1.309	1.514	1.919	1.591	2.662	2.269	2.177	1.331	4.446	1.85	4.548	2.083	1.009
La	0.0006	0.0016	0.0076	0.0298	0.0173	0.0067	0.0491	0.0045	0.2135	0.0228	0.0501	0.0215	0.0111
Ce	7.10	9.99	14.78	8.66	13.79	17.11	15.30	15.90	6.53	11.97	36.23	15.37	17.27
Pr	0.011	0.042	0.058	0.372	0.074	0.109	0.121	0.063	0.146	0.082	0.401	0.207	0.09
Nd	0.245	0.821	0.998	5.624	1.137	1.712	1.786	1.156	1.748	1.235	5.892	3.709	1.527
Sm	0.652	1.728	1.862	10.295	2.054	3.761	2.914	2.052	3.303	2.528	9.42	7.149	2.715
Eu	0.206	0.452	0.637	2.145	0.624	0.956	0.663	0.41	0.289	0.541	2.984	1.826	1.324
Gd	4.88	10.63	9.98	53.55	11.83	20.88	14.44	10.01	19.47	15.19	41.14	43.61	16.89
Tb	2.004	4.027	3.522	17.669	4.131	7.175	4.64	3.262	7.041	5.595	13.343	14.918	5.576
Dy	27.15	51.42	45.55	209.33	51.97	89.74	53.65	37.89	85.84	69.76	159.20	178.55	67.68
Ho	11.76	21.36	19.18	77.29	21.40	36.44	20.30	15.08	33.68	27.77	59.51	66.67	26.81
Er	61.7	112.1	103.8	355.9	109.2	178.8	102.5	73.7	162.6	137.2	287.7	309.4	131.7
Tm	14.86	26.40	24.60	71.86	25.39	40.44	23.22	16.04	34.85	30.03	62.25	62.84	29.54
Yb	157	270	270	656	263	413	242	156	345	298	621	577	302
Lu	36.68	62.87	64.22	129.2	60.14	91.05	55.69	32.42	69.49	65.08	136.4	112.3	65.63
Hf	11,249	11,133	9,846	7,795	10,457	10,932	11,958	10,027	9,893	10,674	8,296	9,874	10,251
Ta	0.866	0.786	0.994	0.579	1.193	1.275	1.057	1.225	3.667	1.058	1.563	0.955	0.294
Pb	n.d.												
Th	78	159	273	252	267	383	331	48	270	270	890	364	98
U	249	374	544	318	539	725	476	63	1741	481	970	536	285
T (°C)	671	680	685	786	691	651	687	777	705	677	741	749	714

(Continued.)

Sample	CJ26	CJ26	CJ26	CJ26	CJ10A								
Rock type	Tonalite												
Comment					Core	Rim	Core	Rim	Core				
Ti	2.64	5.22	3.66	4.14	5.16	3.72	3.72	4.26	4.56	3.60	6.00	6.00	6.00
Sr	0.189	0.3	0.273	0.24	0.245	0.232	0.18	0.188	0.153	0.238	0.279	0.161	0.142
Y	596	1394	896	1090	896	815	614	470	339	891	1284	403	264
Nb	3.152	3.204	1.879	2.094	1.198	1.308	1.105	1.72	1.001	1.42	2.684	0.912	0.758
La	0.0038	0.0385	0.0134	0.0119	0.0037	0.007	0.0022	0.001	0.0007	0.0104	0.017	0.001	0.02
Ce	19.24	37.42	18.92	17.51	11.73	13.81	8.84	8.13	6.31	12.37	18.70	7.23	5.81
Pr	0.039	0.294	0.188	0.166	0.074	0.134	0.032	0.025	0.02	0.151	0.151	0.034	0.042
Nd	0.81	4.429	2.657	2.899	1.306	2.098	0.455	0.439	0.386	2.449	2.558	0.532	0.662
Sm	1.645	7.323	4.491	4.845	2.795	3.26	1.119	0.977	0.708	3.997	4.97	1.08	0.923
Eu	0.519	1.719	1.318	1.309	0.937	1.124	0.463	0.408	0.376	1.352	1.473	0.398	0.394
Gd	9.65	36.65	20.29	22.18	14.66	15.32	8.13	5.92	4.42	18.56	26.42	6.25	4.13
Tb	3.444	11.523	6.37	7.844	5.016	5.245	3.279	2.392	1.797	6.265	9.213	2.269	1.586
Dy	43.53	129.32	78.19	92.14	62.76	63.04	43.27	31.41	24.18	75.21	111.74	30.63	20.09
Ho	17.91	47.84	30.03	35.35	24.50	25.40	18.79	14.17	10.54	29.05	42.04	13.01	7.98
Er	92.1	224.0	149.6	171.1	126.3	130.1	100.6	79.0	57.5	143.2	200.4	67.9	42.7
Tm	21.45	46.61	33.69	36.36	28.31	30.48	24.68	19.43	14.20	33.34	44.76	16.54	10.58
Yb	230	435	347	368	293	321	267	216	154	345	441	183	122
Lu	52.99	86.10	77.51	76.63	65.59	75.11	65.77	53.83	37.99	71.08	84.49	41.23	28.07
Hf	10,701	10,518	11,113	10,712	11,138	10,255	10,452	10,083	9,382	8,984	9,367	9,377	10,461
Ta	1.649	1.48	0.911	1.025	0.713	0.95	0.782	1.17	0.562	0.777	0.889	0.512	0.503
Pb	n.d.	1.149	n.d.	n.d.	n.d.	n.d.	n.d.						
Th	635	337	410	256	219	294	130	107	96	295	348	100	82
U	942	411	619	389	440	555	354	322	249	544	438	246	221
T (°C)	671	730	699	709	729	700	700	712	718	697	743	743	743

(Continued.)

Sample	CJ10A	CJ10A	CJ10A	CJ10A	CJ10A	CJ10A	CJ35						
Rock type	Tonalite	Tonalite	Tonalite	Tonalite	Tonalite	Tonalite	Gabbro						
Comment							Core	Rim	Core	Rim	Core	Rim	Core
Ti	6.00	6.00	6.00	4.44	8.09	3.66	3.12	2.40	4.62	2.52	4.44	3.48	3.72
Sr	0.167	0.23	0.183	0.248	0.355	0.144	0.191	0.16	0.155	0.181	0.173	0.208	0.251
Y	427	878	670	756	2444	423	384	269	381	405	379	648	937
Nb	0.779	1.929	0.908	1.733	1.43	1.791	0.943	1.029	0.916	1.562	1.061	1.191	1.218
La	0.003	0.008	0.008	0.004	0.0437	0.0024	0.0011	0.001	0.0029	0.0012	0.0012	0.0061	0.0071
Ce	7.16	11.97	9.14	10.63	9.12	8.99	6.12	7.71	6.37	8.22	7.73	9.70	12.43
Pr	0.045	0.099	0.087	0.065	0.369	0.024	0.02	0.016	0.018	0.017	0.019	0.078	0.132
Nd	0.732	1.649	1.327	0.912	6.338	0.5	0.369	0.273	0.34	0.332	0.361	1.056	2.238
Sm	1.356	3.031	2.534	2.456	11.956	0.994	0.898	0.674	0.959	0.937	0.844	2.154	3.748
Eu	0.482	1.052	0.875	0.725	0.776	0.345	0.279	0.216	0.275	0.286	0.304	0.669	1.12
Gd	7.29	15.56	12.19	11.97	63.68	5.82	5.30	3.92	5.56	5.45	5.13	10.95	17.75
Tb	2.701	5.33	4.2	4.268	20.339	2.232	2.042	1.466	2.004	2.082	1.972	3.819	5.926
Dy	33.04	66.65	52.75	56.87	231.78	30.58	26.90	19.75	28.50	28.24	26.03	48.23	71.99
Ho	13.39	26.36	20.43	22.67	84.95	13.16	11.84	8.47	12.03	12.28	11.35	19.85	28.48
Er	71.5	135.3	104.1	122.4	386.4	73.2	64.0	45.7	67.0	68.4	61.1	101.2	142.6
Tm	16.75	31.18	23.88	28.69	76.84	17.58	15.33	11.03	15.42	17.20	14.49	22.91	32.09
Yb	180	330	251	312	696	192	171	121	174	192	159	241	338
Lu	41.07	71.37	55.96	68.94	127.7	45.07	41.10	29.34	41.30	47.42	37.89	56.09	77.36
Hf	9,816	9,532	9,492	9,759	10,231	10,017	10,704	11,492	11,808	10,987	10,215	9,681	10,421
Ta	0.515	0.801	0.569	0.857	0.698	0.861	0.566	0.716	0.526	1.204	0.614	0.633	0.726
Pb	n.d.	n.d.	n.d.	n.d.	n.d.	n.d.	n.d.	n.d.	n.d.	n.d.	n.d.	1.39	n.d.
Th	102	251	181	220	296	140	85	107	84	113	102	178	295
U	230	421	348	429	452	366	252	307	243	360	267	353	530
T ($^{\circ}\text{C}$)	743	743	743	715	772	699	685	664	719	668	715	694	700

(Continued.)

Sample	CJ35												
Rock type	Gabbro												
Comment	Rim	Core	Core										
Ti	4.08	2.64	2.52	6.17	2.76	5.58	3.72	3.72	4.08	2.82	3.18	4.38	3.30
Sr	0.204	0.194	0.219	0.258	0.15	0.192	0.195	0.237	0.233	0.192	0.219	0.151	0.168
Y	592	590	739	856	238	650	477	870	847	486	558	473	381
Nb	2.107	1.121	1.489	2.825	0.894	1.5	1.713	1.706	3.652	1.157	2.288	0.773	0.904
La	0.002	0.0023	0.004	0.0042	0.0025	0.0375	0.0015	0.002	0.0033	0.0009	0.0022	0.0168	0.001
Ce	10.27	9.51	13.32	13.30	5.91	11.52	8.80	10.35	16.55	7.62	12.12	7.12	5.82
Pr	0.029	0.048	0.066	0.047	0.01	0.083	0.027	0.036	0.041	0.022	0.028	0.053	0.019
Nd	0.534	0.898	1.261	0.728	0.185	1.042	0.381	0.665	0.813	0.412	0.556	0.719	0.281
Sm	1.176	1.926	2.694	1.598	0.515	2.004	0.972	1.848	1.875	1.098	1.216	1.521	0.817
Eu	0.425	0.612	0.73	0.683	0.174	0.746	0.348	0.497	0.522	0.336	0.372	0.447	0.28
Gd	7.87	10.10	13.58	9.60	3.41	11.11	6.45	12.33	12.12	6.59	7.44	8.04	5.09
Tb	3.002	3.666	4.753	4.003	1.293	3.643	2.443	4.863	4.549	2.555	2.862	2.812	2.123
Dy	40.86	45.72	59.02	54.68	17.44	49.34	32.73	63.31	61.27	34.34	39.36	36.09	28.50
Ho	18.10	18.69	23.84	25.27	7.57	21.02	14.32	26.62	26.29	15.04	16.96	14.20	12.20
Er	99.1	95.0	118.6	137.9	40.7	110.5	80.5	137.3	140.6	79.7	92.7	72.8	65.6
Tm	24.17	21.91	26.91	31.45	9.91	26.12	19.73	31.54	32.87	19.55	22.54	17.37	15.47
Yb	264	233	277	344	108	279	220	324	346	212	248	185	168
Lu	62.69	54.37	62.74	78.81	25.69	66.16	53.02	72.22	79.62	51.00	59.91	42.54	38.97
Hf	10,468	11,109	10,690	9,823	10,879	10,570	10,183	10,045	11,099	10,651	10,671	11,495	10,384
Ta	1.105	0.706	0.948	1.077	0.613	0.797	1.03	0.848	1.6	0.669	1.246	0.437	0.522
Pb	n.d.	1.675	n.d.	n.d.	n.d.	n.d.							
Th	153	168	243	222	85	169	121	159	233	123	190	121	74
U	439	364	499	492	262	322	330	411	575	357	485	220	208
<i>T</i> (°C)	708	671	668	746	675	736	700	700	708	677	687	714	690

(Continued.)

Sample	CJ35												
Rock type	Gabbro												
Comment	Rim		Core	Rim	Core	Rim	Core	Rim	Core	Rim			Rim
Ti	4.50	4.14	3.30	3.00	3.36	2.70	5.58	3.78	11.57	3.66	3.06	3.96	4.26
Sr	0.169	0.215	0.202	0.235	0.177	0.168	0.475	0.25	0.39	0.176	0.182	0.203	0.203
Y	436	635	799	416	475	352	698	964	1924	490	461	818	676
Nb	1.48	2.422	1.163	1.108	1.697	1.637	2.616	4.069	3.822	1.416	0.93	1.092	2.296
La	0.0014	0.0032	0.0057	0.038	0.0126	0.001	0.0247	0.0114	0.0112	0.0023	0.0006	0.0067	0.0081
Ce	7.86	11.42	10.29	9.97	8.64	10.13	13.01	17.49	20.69	8.23	6.77	10.99	11.38
Pr	0.02	0.038	0.085	0.035	0.029	0.023	0.046	0.05	0.117	0.027	0.019	0.123	0.03
Nd	0.432	0.596	1.608	0.417	0.487	0.352	0.729	0.814	2.083	0.418	0.42	1.851	0.562
Sm	0.929	1.449	2.817	1.458	1.054	0.868	1.542	1.871	4.573	1.012	0.997	3.093	1.584
Eu	0.334	0.527	0.871	0.342	0.329	0.318	0.478	0.564	1.725	0.373	0.335	1.029	0.433
Gd	5.63	8.20	14.13	6.75	6.18	4.96	9.46	12.61	30.31	6.60	6.08	15.22	9.60
Tb	2.234	3.105	4.844	2.543	2.408	1.861	3.738	5.131	11.526	2.456	2.293	4.962	3.731
Dy	31.06	42.44	61.80	29.62	32.70	25.16	51.07	68.61	148.12	34.67	31.44	63.24	49.55
Ho	13.48	18.83	24.98	13.21	14.98	10.90	22.05	29.48	59.82	15.05	13.70	25.14	20.79
Er	72.0	102.0	125.1	72.6	80.9	59.7	115.8	153.6	300.2	81.4	74.0	127.1	108.5
Tm	17.28	24.83	28.26	16.96	19.75	14.83	27.61	35.42	66.03	19.42	17.70	29.09	24.95
Yb	186	272	293	179	224	165	297	373	659	208	196	305	258
Lu	43.86	65.76	67.15	40.56	54.89	39.58	69.09	83.77	139.8	48.45	47.57	69.73	58.50
Hf	9,825	10,441	9,361	12,339	10,453	11,021	9,263	9,914	8,712	10,112	10,154	9,966	10,517
Ta	0.738	1.278	0.628	0.689	0.971	1.191	1.202	1.731	1.132	0.671	0.547	0.616	1.177
Pb	n.d.	1.099											
Th	98	203	201	209	129	182	218	258	420	106	100	229	176
U	249	544	357	387	362	608	483	607	609	264	290	404	419
<i>T</i> (°C)	717	709	690	682	691	673	736	701	808	699	684	705	712

(Continued.)

Sample	CJ35	CJ12B	CJ12B	CJ12B									
Rock type	Gabbro												
Comment	Core	Rim	Core										
Ti	4.92	2.70	3.00	3.90	5.52	3.36	5.76	3.06	7.97	3.42	4.68	4.68	3.60
Sr	0.197	0.15	0.143	0.192	0.341	0.18	0.375	0.221	0.415	0.221	0.19	0.195	0.18
Y	799	370	322	537	1355	415	1092	639	2431	573	583	323	383
Nb	1.016	1.406	0.849	1.583	1.824	0.895	4.449	3.075	11.5	1.901	1.18	1.201	0.674
La	0.0046	n.d.	0.0012	0.001	0.0167	0.0017	0.0431	0.0016	0.0144	0.0015	0.0006	0.0134	n.d.
Ce	8.37	11.09	5.08	8.13	18.29	6.09	24.94	13.24	42.89	9.84	9.04	9.38	6.65
Pr	0.06	0.024	0.012	0.027	0.177	0.019	0.098	0.032	0.148	0.023	0.028	0.025	0.026
Nd	1.208	0.53	0.231	0.442	2.813	0.344	1.404	0.582	2.428	0.525	0.527	0.426	0.436
Sm	2.486	0.998	0.536	1.062	5.411	0.86	2.734	1.345	6.467	1.167	1.261	0.769	0.99
Eu	0.626	0.297	0.179	0.318	1.454	0.306	0.972	0.5	2.891	0.396	0.464	0.352	0.385
Gd	14.82	5.69	4.12	7.00	27.27	5.46	16.56	8.07	43.92	7.43	8.33	4.50	6.13
Tb	5.331	2.121	1.626	2.716	9.505	2.119	6.246	3.214	16.768	2.95	3.11	1.721	2.215
Dy	68.27	28.18	23.47	37.80	117.34	29.20	82.92	42.93	206.40	40.04	41.29	22.97	28.68
Ho	27.04	11.36	10.06	16.18	45.87	12.57	35.02	18.84	79.15	17.66	18.14	10.11	11.89
Er	131.4	61.9	55.4	89.0	221.6	69.0	180.4	104.9	368.8	95.0	98.8	54.9	62.9
Tm	28.28	14.66	13.51	21.23	48.12	16.55	42.19	25.55	77.50	22.50	22.89	13.45	14.69
Yb	271	157	146	231	469	181	438	284	747	246	255	153	158
Lu	58.00	37.10	34.15	54.28	100.4	43.98	102.0	69.38	153.3	59.03	61.06	37.94	37.43
Hf	8,787	9,985	11,748	10,905	9,479	9,727	10,442	10,419	9,143	9,823	9,418	10,363	10,264
Ta	0.515	1.018	0.55	0.901	0.751	0.513	1.743	1.576	1.931	0.901	0.625	0.79	0.444
Pb	n.d.												
Th	118	203	55	104	356	83	630	211	646	146	116	130	83
U	215	527	193	312	476	245	818	583	1010	395	267	319	200
<i>T</i> (°C)	725	673	682	704	735	691	739	684	770	693	720	720	697

(Continued.)

Sample	CJ12B												
Rock type	Gabbro												
Comment	Rim	Core	Rim										
Ti	5.28	3.90	4.44	4.74	6.12	5.70	5.70	3.48	4.14	4.02	3.84	9.29	6.89
Sr	0.15	0.131	0.219	0.182	0.353	0.26	0.223	0.241	0.148	0.15	0.194	0.164	0.152
Y	339	319	467	494	759	1075	565	1008	399	285	386	701	531
Nb	1.066	0.726	1.471	0.919	2.949	1.391	1.848	1.14	1.358	0.621	1.588	1.579	1.377
La	0.0018	0.0059	0.0026	0.0033	0.0023	0.0051	0.0052	0.0107	0.0031	0.0007	0.0021	0.0065	0.0019
Ce	6.55	5.56	10.70	7.33	17.29	12.54	9.65	11.09	8.62	5.86	9.00	10.31	7.57
Pr	0.018	0.023	0.025	0.033	0.037	0.097	0.028	0.123	0.019	0.014	0.017	0.048	0.029
Nd	0.327	0.316	0.788	0.674	0.812	1.838	0.524	2.193	0.427	0.283	0.359	0.767	0.496
Sm	0.715	0.857	1.119	1.177	1.632	3.589	1.164	4.129	1.002	0.755	0.787	1.472	0.934
Eu	0.284	0.319	0.357	0.46	0.619	0.941	0.603	1.047	0.336	0.276	0.339	0.671	0.478
Gd	4.78	4.00	6.35	7.52	8.65	19.18	6.91	22.05	4.67	3.99	4.77	9.09	6.65
Tb	1.784	1.691	2.4	2.866	3.756	7.042	2.722	7.079	1.808	1.613	1.789	3.569	2.746
Dy	24.41	22.43	33.17	37.12	50.43	88.74	36.04	89.26	26.24	21.52	25.03	48.06	36.84
Ho	10.46	9.79	14.47	15.84	23.58	34.83	15.70	34.46	11.58	9.24	11.63	21.24	16.69
Er	56.5	54.0	79.9	83.2	130.2	170.9	85.8	166.2	67.0	50.2	65.7	114.5	90.4
Tm	13.35	13.02	19.23	19.60	32.74	37.62	20.76	34.71	16.81	11.77	16.39	27.13	21.21
Yb	145	142	215	215	372	375	230	356	201	129	193	299	233
Lu	34.87	33.95	52.25	51.09	89.54	80.99	56.58	76.21	51.70	31.16	49.31	72.83	55.34
Hf	10,094	9,248	9,791	10,009	11,388	10,273	9,704	9,522	8,949	10,105	10,645	7,974	8,665
Ta	0.571	0.436	0.876	0.519	1.403	0.735	0.625	0.608	0.863	0.445	0.966	0.614	0.66
Pb	n.d.	3.762	n.d.	0.969	n.d.	n.d.							
Th	90	61	107	104	228	220	97	221	128	52	122	151	138
U	224	172	256	247	500	393	216	353	337	137	318	246	315
T (°C)	731	704	715	721	745	738	738	694	709	707	703	785	756

(Continued.)

Sample	CJ12B												
Rock type	Gabbro												
Comment	Core	Rim	Core										
Ti	3.84	6.41	6.00	4.20	4.32	5.64	4.26	3.78	4.02	4.50	3.78	5.82	7.19
Sr	0.19	0.199	0.284	0.189	0.177	0.197	0.224	0.142	0.17	0.154	0.193	0.173	0.214
Y	449	788	1077	388	522	515	990	228	526	398	573	429	849
Nb	0.848	3.578	0.589	1.022	1.067	1.674	1.373	0.915	0.976	1.364	0.855	1.417	0.887
La	0.0013	0.0036	0.0145	0.0007	0.0021	0.0035	0.0063	0.0085	0.0038	0.0014	0.0029	0.0014	0.0174
Ce	7.15	17.38	3.85	6.42	7.39	9.61	11.43	6.60	9.20	7.99	9.20	8.88	9.44
Pr	0.024	0.05	0.075	0.019	0.03	0.028	0.108	0.013	0.067	0.021	0.042	0.025	0.179
Nd	0.425	0.938	1.802	0.378	0.521	0.529	1.838	0.225	1.209	0.345	0.736	0.397	2.594
Sm	1.009	1.66	4.255	0.816	1.07	1.094	3.147	0.466	2.224	0.89	1.807	1.097	3.657
Eu	0.438	0.62	0.876	0.333	0.426	0.442	0.831	0.191	0.76	0.298	0.642	0.347	1.456
Gd	6.09	9.76	22.34	4.93	6.67	7.20	17.09	3.02	10.82	5.53	10.29	5.83	17.64
Tb	2.382	3.817	7.932	1.985	2.455	2.718	6.193	1.185	3.639	2.126	3.621	2.293	5.858
Dy	31.37	51.15	97.41	25.55	33.63	34.33	78.38	16.24	43.72	28.78	45.88	30.26	71.38
Ho	13.97	22.98	37.42	11.60	14.94	15.52	31.74	7.00	17.27	12.45	18.37	13.21	27.81
Er	73.9	125.6	170.3	62.6	78.4	85.4	159.4	38.9	86.4	68.7	95.3	73.0	136.8
Tm	17.97	30.31	35.84	15.74	19.51	20.33	35.41	9.64	19.47	16.17	21.04	17.35	30.49
Yb	197	335	321	173	214	227	347	107	199	175	218	187	307
Lu	47.05	79.93	64.06	42.99	51.19	55.04	75.84	26.00	44.55	41.07	49.19	44.59	69.58
Hf	9,477	9,678	8,434	9,965	9,408	9,471	9,449	10,172	9,307	9,925	10,415	9,508	8,039
Ta	0.487	1.484	0.289	0.532	0.51	0.858	0.72	0.505	0.641	0.789	0.417	0.777	0.46
Pb	n.d.	1.526	n.d.	1.446	n.d.	n.d.	n.d.						
Th	91	333	65	77	97	128	208	68	108	88	130	95	182
U	215	597	112	222	228	288	376	184	310	241	254	234	276
<i>T</i> (°C)	703	749	743	711	713	737	712	701	707	717	701	740	760

(Continued.)

Sample	CJ12B												
Rock type	Gabbro												
Comment	Rim	Core	Rim	Core	Rim								
Ti	3.12	4.08	5.22	4.26	2.40	4.98	4.50	4.08	5.70	5.70	4.08	6.89	4.50
Sr	0.16	0.181	0.157	0.174	0.148	0.242	0.221	0.287	0.274	0.155	0.169	0.171	0.214
Y	312	539	441	430	346	1174	545	1344	917	405	433	654	476
Nb	1.007	0.978	1.526	0.813	1.338	1.898	0.955	3.46	1.437	0.847	1.447	2.239	1.339
La	0.0009	0.003	0.0016	0.0077	0.0012	0.0183	0.0232	0.0138	0.0149	0.0021	0.0038	0.0028	0.0649
Ce	6.73	8.16	8.80	8.09	7.86	15.38	8.99	7.45	13.41	6.35	9.82	14.74	9.86
Pr	0.018	0.039	0.025	0.04	0.015	0.211	0.068	0.056	0.13	0.029	0.027	0.045	0.046
Nd	0.294	0.694	0.468	0.654	0.246	2.888	1.088	1.092	2.249	0.459	0.519	0.739	0.577
Sm	0.687	1.378	0.877	1.269	0.692	4.924	1.917	3.51	3.947	0.87	0.998	1.47	1.096
Eu	0.256	0.624	0.37	0.465	0.267	1.921	0.581	0.617	1.132	0.489	0.373	0.696	0.421
Gd	4.08	7.92	6.06	6.55	4.37	23.73	9.14	23.26	18.03	5.80	6.25	9.40	6.20
Tb	1.59	2.899	2.278	2.354	1.698	7.737	3.381	8.947	6.265	2.081	2.352	3.522	2.491
Dy	21.50	39.45	31.36	31.93	23.52	92.29	41.49	116.47	77.60	28.32	31.89	47.32	33.62
Ho	9.51	16.88	13.67	13.47	10.58	36.55	17.26	45.10	30.58	12.44	13.49	20.45	14.65
Er	54.3	91.4	75.9	71.4	60.6	179.7	88.7	213.9	149.8	71.1	73.0	106.1	79.7
Tm	13.55	22.26	18.60	16.96	15.44	40.57	20.69	43.76	34.40	17.89	17.47	24.76	19.04
Yb	155	245	207	186	180	434	219	413	352	211	188	262	210
Lu	38.76	59.55	50.06	44.82	45.74	102.3	51.31	82.14	79.20	54.02	45.29	61.52	50.37
Hf	10,114	8,580	9,079	9,493	10,923	7,926	9,984	10,712	10,118	8,411	9,995	9,030	9,644
Ta	0.703	0.467	0.708	0.514	0.966	0.683	0.604	1.343	0.827	0.434	0.845	0.769	0.725
Pb	n.d.												
Th	82	111	104	104	110	357	155	161	252	100	176	187	118
U	232	250	253	212	357	481	300	384	433	225	387	243	254
T (°C)	685	708	730	712	664	726	717	708	738	738	708	756	717

(Continued.)

Sample	CJ12B	CJ2A	CJ2A	CJ2A	CJ2A	CJ2A	CJ2A						
Rock type	Gabbro	Leucoto.	Leucoto.	Leucoto.	Leucoto.	Leucoto.	Leucoto.						
Comment								Core	Rim	Core	Rim	Core	Rim
Ti	3.24	4.80	6.35	6.41	5.28	6.65	5.46	3.18	3.90	3.78	2.34	5.22	3.06
Sr	0.183	0.209	0.242	0.305	0.232	0.189	0.184	0.194	0.208	0.223	0.201	0.248	0.194
Y	599	939	935	1314	780	573	569	506	667	775	521	1176	589
Nb	1.234	1.228	2.001	2.947	1.064	0.932	1.751	1.779	3.312	1.338	2.368	1.829	2.195
La	0.0027	0.004	0.0297	0.0068	0.0068	0.0008	0.0096	0.0017	0.0021	0.0114	0.0018	0.0042	0.0011
Ce	7.74	11.56	14.32	16.43	10.26	8.11	11.48	12.11	14.59	13.38	9.93	10.98	9.89
Pr	0.039	0.103	0.274	0.106	0.136	0.035	0.042	0.025	0.038	0.046	0.024	0.086	0.028
Nd	0.655	1.63	3.382	1.694	1.851	0.709	0.709	0.578	0.567	1.129	0.372	1.42	0.519
Sm	1.371	3.589	4.774	3.504	3.009	1.506	1.45	1.161	1.581	2.512	1.164	3.643	1.296
Eu	0.515	0.936	1.999	1.136	0.962	0.522	0.512	0.426	0.438	0.696	0.31	0.949	0.324
Gd	8.77	19.24	19.67	21.34	14.54	8.67	8.34	6.93	9.31	14.32	7.46	20.53	8.63
Tb	3.187	6.654	6.112	7.966	5.001	3.372	3.069	2.78	3.606	5.184	2.845	7.736	3.39
Dy	45.42	81.41	71.50	101.70	62.59	44.29	41.24	37.23	49.06	63.03	38.15	99.11	46.19
Ho	18.58	31.63	27.84	41.52	24.29	18.50	17.66	15.90	21.10	24.83	16.35	39.33	19.14
Er	98.9	153.5	140.0	211.7	125.2	98.3	94.2	86.8	112.9	123.6	86.3	195.7	98.2
Tm	24.51	32.99	33.16	47.07	28.38	21.69	22.54	21.41	26.47	26.59	20.16	41.93	22.16
Yb	262	320	360	475	297	226	236	235	280	267	217	412	227
Lu	62.77	69.07	84.72	105.07	67.50	51.62	57.09	57.29	65.51	58.42	50.58	85.37	50.64
Hf	10,528	10,244	8,593	9,729	9,234	10,468	9,412	10,690	10,450	11,077	11,721	9,735	11,105
Ta	0.69	0.709	0.677	1.1	0.673	0.616	0.92	0.962	1.414	0.876	1.491	0.759	1.337
Pb	n.d.	n.d.	n.d.	n.d.	n.d.	n.d.							
Th	137	201	257	317	211	89	203	200	204	222	159	176	150
U	377	336	336	569	395	198	423	465	477	403	559	350	428
<i>T</i> (°C)	688	722	748	749	731	753	734	687	704	701	662	730	684

(Continued.)

Sample	CJ2A												
Rock type	Leucoto.												
Comment	Core	Rim	Core										
Ti	4.86	3.12	2.04	3.30	3.78	3.84	2.58	3.48	1.74	4.56	4.68	3.42	3.24
Sr	0.242	0.232	0.177	0.205	0.259	0.171	0.187	0.176	0.24	0.268	0.226	0.192	0.225
Y	849	791	503	611	1316	466	557	518	652	1099	818	674	793
Nb	2.212	3.551	1.847	2.096	2.115	2.069	1.06	1.839	2.499	2.005	2.326	1.597	2.723
La	0.0086	0.0009	0.0079	0.0017	0.0094	0.0017	0.0016	0.0308	0.0013	0.0178	0.0056	0.0022	0.0025
Ce	9.56	10.38	7.69	8.16	13.69	13.09	10.07	8.25	6.11	17.17	12.94	8.80	10.27
Pr	0.035	0.027	0.024	0.023	0.102	0.029	0.028	0.029	0.012	0.142	0.059	0.024	0.024
Nd	0.707	0.497	0.38	0.432	1.893	0.574	0.637	0.506	0.309	2.345	0.84	0.468	0.531
Sm	1.943	1.607	1.111	1.271	4.726	1.133	1.554	1.157	1.071	4.087	1.983	1.439	1.553
Eu	0.516	0.356	0.336	0.324	0.971	0.378	0.463	0.366	0.277	1.324	0.557	0.375	0.365
Gd	13.11	10.88	7.34	8.58	28.86	6.88	9.40	7.47	7.91	20.51	12.17	9.22	10.54
Tb	5.069	4.394	2.726	3.34	10.26	2.555	3.397	2.971	3.386	7.271	4.547	3.591	4.122
Dy	68.84	59.82	38.85	45.99	122.30	33.91	42.70	39.93	46.92	90.76	60.61	48.74	55.72
Ho	28.83	25.38	16.82	19.34	45.39	14.28	17.49	16.83	20.08	35.83	25.71	20.47	23.41
Er	145.7	131.6	87.7	102.6	204.6	77.1	88.0	88.4	107.0	178.0	128.0	108.1	125.7
Tm	32.72	29.89	20.79	24.08	41.25	17.77	19.96	20.95	25.58	39.72	29.08	25.05	28.43
Yb	332	307	219	253	376	190	206	222	267	400	283	265	301
Lu	71.79	68.42	50.95	57.80	76.04	44.22	47.01	50.76	60.93	89.02	63.08	59.22	67.90
Hf	9,813	11,459	9,606	10,919	10,009	10,609	10,693	11,923	12,399	10,342	10,710	10,058	10,939
Ta	1.042	1.869	1.137	1.266	0.915	1.099	0.656	0.965	1.935	0.983	1.208	0.803	1.456
Pb	n.d.												
Th	142	177	101	116	288	216	148	114	135	346	204	127	150
U	374	547	297	377	470	472	322	302	712	555	477	342	447
T ($^{\circ}\text{C}$)	723	685	651	690	701	703	670	694	639	718	720	693	688

(Continued.)

Sample	CJ2A												
Rock type	Leucoto.												
Comment	Core	Rim	Core	Core	Rim								
Ti	2.70	2.70	2.46	3.54	3.42	3.60	3.54	2.64	2.10	2.22	3.12	3.06	5.64
Sr	0.161	0.252	0.205	0.226	0.218	0.189	0.228	0.234	0.231	0.159	0.217	0.169	0.141
Y	408	783	579	637	721	622	937	468	600	372	795	456	463
Nb	1.102	3.336	1.761	1.869	2.833	1.547	3.864	1.82	4.043	1.136	1.959	1.237	1.259
La	0.0018	0.0012	0.0019	0.0025	0.0018	0.0136	0.0027	0.0218	0.0007	0.0015	n.d.	0.0027	0.0019
Ce	6.67	10.19	8.94	12.85	10.73	8.17	13.52	9.94	7.10	7.77	10.53	7.90	7.12
Pr	0.018	0.025	0.027	0.036	0.033	0.027	0.036	0.031	0.014	0.021	0.04	0.022	0.027
Nd	0.359	0.532	0.474	0.581	0.558	0.518	0.681	0.466	0.299	0.366	0.683	0.435	0.403
Sm	0.976	1.543	1.23	1.501	1.551	1.288	2.004	1.015	0.866	0.936	2.176	0.922	1.103
Eu	0.292	0.338	0.319	0.491	0.423	0.393	0.482	0.344	0.351	0.283	0.504	0.29	0.319
Gd	5.85	10.35	7.73	9.15	10.13	8.48	13.47	6.30	6.38	5.24	11.93	6.16	7.21
Tb	2.336	4.182	3.09	3.393	3.925	3.405	5.244	2.33	2.677	2.047	4.32	2.485	2.734
Dy	30.01	56.74	40.31	46.39	52.45	45.64	70.38	31.88	38.74	27.94	58.30	33.61	36.37
Ho	12.55	24.48	17.50	19.81	23.03	19.17	29.96	13.97	17.46	11.72	24.82	13.95	15.21
Er	66.4	129.2	95.0	107.2	124.2	101.6	153.9	76.5	96.2	62.0	124.7	76.8	79.2
Tm	15.59	29.50	22.18	25.86	29.08	23.12	34.77	18.47	23.74	14.83	27.90	18.25	17.46
Yb	168	304	242	282	308	240	354	203	265	160	279	195	179
Lu	39.73	68.58	57.45	68.17	71.33	54.49	79.32	49.47	64.88	38.21	61.37	47.13	40.03
Hf	11,013	11,364	10,937	10,668	10,333	10,249	10,797	10,605	12,062	10,820	12,281	10,920	9,555
Ta	0.635	1.669	0.907	1.073	1.421	0.801	1.787	0.93	2.223	0.691	1.276	0.657	0.652
Pb	n.d.	0.925	n.d.	n.d.	n.d.	n.d.	n.d.	0.906	n.d.	n.d.	n.d.	1.037	n.d.
Th	86	160	146	232	157	127	205	143	138	100	156	110	69
U	254	503	440	552	486	325	585	381	747	272	436	325	174
<i>T</i> (°C)	673	673	666	696	693	697	696	671	653	658	685	684	737

(Continued.)

Sample	CJ2A												
Rock type	Leucoto.												
Comment													
Ti	2.52	3.18	3.18	2.40	3.90	3.72	6.77	3.78	7.37	5.28	3.60	4.56	5.76
Sr	0.402	0.281	0.202	0.315	0.24	0.224	0.373	0.205	0.316	0.186	0.225	0.223	0.253
Y	1666	1448	657	899	908	909	2211	872	1621	1415	870	1255	1236
Nb	4.563	2.812	1.516	2.366	4.106	2.688	9.24	1.681	5.976	1.552	3.33	2.755	1.999
La	0.1841	0.0198	0.0046	0.288	0.0036	n.d.	0.0064	0.0035	0.0044	0.011	0.0042	0.056	0.0157
Ce	13.38	22.92	10.69	20.81	19.66	12.48	11.41	12.71	20.65	11.56	13.33	18.59	14.88
Pr	0.122	0.212	0.038	0.242	0.063	0.045	0.122	0.049	0.072	0.173	0.047	0.258	0.168
Nd	1.406	3.733	0.768	2.897	1.103	0.827	2.352	0.913	1.376	2.557	0.836	3.638	2.777
Sm	3.332	7.145	1.975	4.246	2.18	1.978	5.718	2.172	3.684	6.112	2.022	4.733	5.385
Eu	0.633	1.426	0.505	1.328	0.704	0.477	1.147	0.722	1.084	1.042	0.544	1.613	1.355
Gd	21.79	35.34	11.29	19.78	12.76	13.34	35.98	13.37	23.54	31.78	13.11	24.01	27.25
Tb	9.462	11.967	4.179	6.319	4.566	5.387	14.15	4.933	9.253	10.614	5.067	7.22	9.199
Dy	130.87	137.23	52.93	77.23	61.30	69.33	186.21	64.86	125.11	130.09	65.85	89.69	109.75
Ho	53.29	51.81	21.17	30.03	26.36	28.97	75.46	27.31	52.15	49.50	27.53	33.09	41.24
Er	274.5	240.5	105.7	146.4	140.0	148.0	362.3	141.3	265.5	220.6	145.9	165.8	193.0
Tm	60.35	49.82	23.74	33.18	33.35	32.91	75.98	32.47	59.30	43.58	34.34	39.80	40.35
Yb	599	471	242	337	361	341	711	352	585	404	358	405	385
Lu	125.3	96.52	52.74	75.63	83.74	71.70	141.2	81.08	126.3	79.50	82.94	93.24	78.82
Hf	12,201	10,511	10,520	9,034	10,186	11,383	8,730	10,547	9,423	9,268	11,430	8,300	8,869
Ta	1.992	1.177	0.918	0.889	1.693	1.393	1.839	0.887	1.806	0.737	1.769	1.081	0.638
Pb	1.949	n.d.	1.084										
Th	277	559	162	410	320	183	325	192	275	242	235	558	321
U	932	750	365	505	761	469	697	419	550	320	678	740	348
T (°C)	668	687	687	664	704	700	754	701	762	731	697	718	739

(Continued.)

Sample	CJ2A	CJ31											
Rock type	Leucoto.	Granite											
Comment		Core	Rim										
Ti	4.50	2.46	1.98	3.12	3.48	2.46	4.14	2.16	3.24	2.10	3.54	2.52	2.04
Sr	0.213	0.209	0.211	0.232	0.222	0.189	0.211	0.253	0.224	0.248	0.249	0.146	0.298
Y	1071	577	559	667	686	657	632	709	796	728	972	393	802
Nb	1.787	2.022	2.928	1.726	1.901	1.894	2.351	2.783	2.052	2.942	3.386	1.62	2.099
La	0.009	0.0012	0.0016	0.0035	0.0015	0.0029	0.0013	0.0012	0.0025	0.0017	0.0216	0.0011	0.0025
Ce	13.91	8.12	8.56	9.27	9.60	12.62	11.73	8.49	8.64	9.16	11.39	8.70	10.62
Pr	0.151	0.019	0.02	0.025	0.03	0.036	0.029	0.02	0.029	0.021	0.048	0.014	0.037
Nd	2.48	0.386	0.364	0.49	0.646	0.606	0.565	0.452	0.538	0.448	0.829	0.338	0.619
Sm	4.336	1.225	0.951	1.399	1.229	1.46	1.504	1.189	1.619	1.296	2.135	0.869	1.645
Eu	1.162	0.301	0.322	0.353	0.448	0.507	0.392	0.343	0.359	0.288	0.487	0.233	0.571
Gd	21.00	7.40	7.14	9.42	9.95	9.12	9.58	8.66	10.69	9.02	13.50	6.04	10.72
Tb	7.367	2.84	2.829	3.521	3.637	3.439	3.615	3.578	4.257	3.687	5.012	2.187	4.19
Dy	89.22	40.09	39.13	47.77	50.22	47.37	47.47	49.65	57.67	50.88	67.80	29.61	56.56
Ho	34.59	17.29	16.73	20.00	21.09	19.87	19.62	22.14	24.04	21.26	28.37	12.29	23.39
Er	167.6	93.3	93.4	106.6	109.5	103.8	100.3	124.3	129.2	115.3	146.8	66.0	129.8
Tm	36.71	22.71	23.12	25.25	26.62	24.75	22.84	31.03	29.67	27.15	32.24	15.26	30.69
Yb	366	249	255	267	287	274	233	345	305	291	324	161	342
Lu	79.46	56.69	59.53	59.98	63.35	64.13	52.35	82.95	69.60	66.91	71.23	37.27	79.93
Hf	9,679	10,884	11,118	10,963	11,707	10,695	10,801	12,488	11,705	12,260	9,481	11,138	13,105
Ta	0.868	1.173	1.98	0.964	1.355	0.91	1.175	1.774	1.266	2.187	1.344	1.117	1.74
Pb	n.d.	n.d.	n.d.	n.d.	n.d.	n.d.	n.d.	n.d.	n.d.	n.d.	n.d.	n.d.	n.d.
Th	291	132	135	141	144	196	185	177	130	143	168	131	212
U	500	511	594	434	470	503	438	1118	490	662	383	442	811
<i>T</i> (°C)	717	666	649	685	694	666	709	656	688	653	696	668	651

(Continued.)

Sample	CJ31	CJ30	CJ30							
Rock type	Granite									
Comment										
Ti	2.88	1.86	3.24	5.64	3.96	1.98	2.10	3.36	3.30	2.64
Sr	0.175	0.197	0.247	0.267	0.168	0.211	0.191	0.226	0.2	0.292
Y	403	537	1002	1155	579	474	731	692	651	1097
Nb	1.561	2.184	1.84	1.96	1.373	1.976	2.767	2.042	1.91	2.378
La	0.0104	0.0017	0.0053	0.0188	0.0008	0.004	0.0032	0.0026	0.0021	0.004
Ce	9.10	6.55	13.38	11.47	6.23	7.16	11.96	10.17	10.01	13.80
Pr	0.049	0.018	0.103	0.125	0.023	0.019	0.023	0.026	0.027	0.082
Nd	0.783	0.292	1.828	1.828	0.456	0.275	0.612	0.61	0.564	1.488
Sm	1.276	0.948	3.591	3.801	1.228	0.865	1.514	1.471	1.504	3.619
Eu	0.413	0.25	0.902	0.823	0.268	0.339	0.367	0.36	0.425	0.73
Gd	6.71	6.69	19.05	22.59	8.87	5.44	9.92	10.05	9.52	19.22
Tb	2.445	2.702	6.621	7.698	3.461	2.269	3.883	3.727	3.461	7.051
Dy	31.15	37.54	81.81	99.98	46.21	32.47	52.56	51.32	47.56	88.44
Ho	12.24	16.56	32.28	38.79	19.16	14.93	22.66	21.21	21.03	34.87
Er	65.1	92.1	157.9	190.1	98.1	82.6	119.5	114.2	110.8	176.7
Tm	15.22	22.67	35.28	40.54	21.82	21.29	28.49	27.45	26.65	39.32
Yb	165	254	356	396	219	248	310	299	290	394
Lu	38.94	60.26	78.55	84.88	47.92	61.67	73.96	70.24	70.00	86.85
Hf	11,195	13,137	10,251	10,036	10,965	13,075	12,421	11,879	11,534	10,977
Ta	0.998	2.267	0.978	0.906	0.871	1.519	1.891	1.153	1.246	1.375
Pb	n.d.									
Th	219	111	271	191	80	117	183	175	169	292
U	332	747	543	328	253	652	554	559	550	696
T (°C)	679	644	688	737	705	649	653	691	690	671

Leucoto., leucotonalite

n.d., not detected

Table A3.6. Trace element analyses ($\mu\text{g/g}$) of the primary standard NIST SRM-612 used to determine zircon trace element concentrations and to calculate uncertainties on Ti concentrations.

	SRM-612							
Ti	43.5	44.4	43.3	44.7	42.9	45.1	44.8	43.2
Sr	79.1	77.7	76.9	79.9	78.3	78.5	78.4	78.4
Y	38.4	38.2	36.6	40.0	38.9	37.7	38.4	38.2
Nb	39.6	38.2	37.1	40.7	39.0	38.8	38.7	39.1
La	36.0	36.0	35.8	36.2	36.2	35.8	35.9	36.1
Ce	38.4	38.4	38.5	38.4	38.7	38.1	38.3	38.5
Pr	37.8	38.0	37.8	38.0	38.1	37.7	37.8	38.0
Nd	35.5	35.5	35.2	35.8	35.7	35.3	35.5	35.5
Sm	37.9	37.5	37.6	37.8	38.1	37.3	37.6	37.8
Eu	35.4	35.8	35.3	35.9	35.6	35.6	35.5	35.7
Gd	37.1	37.5	37.1	37.5	37.7	36.9	37.5	37.1
Tb	37.7	37.5	37.5	37.7	37.7	37.5	37.7	37.5
Dy	35.4	35.6	35.6	35.4	35.8	35.2	35.5	35.5
Ho	38.4	38.2	38.2	38.4	38.8	37.8	38.3	38.3
Er	38.0	38.0	37.9	38.1	37.9	38.1	37.9	38.1
Tm	36.7	36.9	36.7	36.9	37.0	36.6	36.7	36.9
Yb	39.2	39.2	39.0	39.4	39.3	39.1	39.1	39.3
Lu	37.0	37.0	36.6	37.4	37.1	36.9	37.2	36.8
Hf	37.2	36.3	36.6	36.8	36.8	36.6	36.5	36.9
Ta	37.5	37.7	37.3	37.9	37.9	37.3	37.4	37.8
Pb	39.5	37.7	38.3	38.9	38.6	38.6	38.2	39.0
Th	37.9	37.7	37.6	38.0	37.9	37.7	37.7	37.9
U	37.2	37.5	36.9	37.9	37.6	37.2	37.1	37.6

(Continued.)

A. Supplementary Materials

	SRM-612							
Ti	43.8	44.2	43.8	44.2	43.5	44.5	43.3	44.7
Sr	79.4	77.4	77.1	79.7	76.5	80.3	78.0	78.8
Y	38.5	38.1	37.5	39.1	37.2	39.4	38.1	38.5
Nb	39.5	38.3	38.3	39.5	38.1	39.7	38.6	39.2
La	36.1	35.9	36.0	36.0	36.0	36.0	35.7	36.3
Ce	38.6	38.2	38.5	38.3	38.5	38.3	38.0	38.8
Pr	38.1	37.7	37.9	37.9	37.8	38.0	37.6	38.2
Nd	35.5	35.5	35.7	35.3	35.3	35.7	35.2	35.8
Sm	37.8	37.6	37.7	37.7	37.7	37.7	37.3	38.1
Eu	35.9	35.3	35.7	35.5	35.6	35.6	35.2	36.0
Gd	37.5	37.2	37.2	37.4	37.2	37.4	37.1	37.5
Tb	37.9	37.3	37.6	37.6	37.5	37.7	37.4	37.8
Dy	35.9	35.1	35.5	35.5	35.3	35.7	35.3	35.7
Ho	38.6	38.0	38.3	38.3	38.3	38.3	38.0	38.6
Er	38.3	37.7	37.9	38.1	37.8	38.2	37.3	38.7
Tm	37.0	36.6	36.7	36.9	36.6	37.0	36.6	37.0
Yb	39.5	38.9	39.1	39.3	39.0	39.4	39.2	39.2
Lu	37.3	36.7	36.9	37.1	36.8	37.2	36.8	37.2
Hf	36.9	36.5	36.3	37.1	36.6	36.8	36.3	37.1
Ta	37.8	37.4	37.7	37.5	37.7	37.5	37.4	37.8
Pb	39.3	37.8	38.0	39.1	38.9	38.2	38.2	38.9
Th	37.8	37.8	37.6	38.0	37.5	38.0	37.7	37.9
U	37.6	37.2	37.4	37.4	37.3	37.5	37.0	37.8

(Continued.)

A.3. Supplementary Material to Chapter 4

	SRM-612							
Ti	45.0	43.0	44.0	43.9	43.6	44.4	43.5	44.5
Sr	79.9	76.9	77.7	79.1	79.4	77.4	79.2	77.6
Y	39.0	37.6	38.4	38.2	39.0	37.6	38.8	37.8
Nb	39.9	37.9	38.9	38.9	39.2	38.6	39.3	38.5
La	36.5	35.5	35.9	36.1	36.2	35.8	36.3	35.7
Ce	38.6	38.2	38.1	38.7	38.4	38.4	38.8	38.0
Pr	38.3	37.5	37.7	38.1	38.1	37.7	38.2	37.6
Nd	35.7	35.3	35.3	35.7	35.6	35.4	35.9	35.1
Sm	38.2	37.2	37.6	37.8	37.7	37.7	38.5	36.9
Eu	35.8	35.4	35.3	35.9	35.7	35.5	35.7	35.5
Gd	38.0	36.6	37.1	37.5	37.2	37.4	37.4	37.2
Tb	38.0	37.2	37.5	37.7	37.7	37.5	38.0	37.2
Dy	35.5	35.5	35.5	35.5	35.6	35.4	35.6	35.4
Ho	38.9	37.7	38.2	38.4	38.4	38.2	38.8	37.8
Er	38.3	37.7	37.7	38.3	38.0	38.0	38.5	37.5
Tm	37.1	36.5	36.6	37.0	37.0	36.6	37.2	36.4
Yb	39.6	38.8	39.0	39.4	39.4	39.0	39.4	39.0
Lu	37.4	36.6	36.9	37.1	37.2	36.8	37.2	36.8
Hf	37.2	36.2	36.6	36.8	36.9	36.5	37.1	36.3
Ta	37.9	37.3	37.6	37.6	37.6	37.6	37.8	37.4
Pb	39.5	37.7	38.1	39.0	39.8	37.4	38.1	39.1
Th	38.3	37.3	37.7	37.8	38.1	37.4	38.2	37.3
U	37.6	37.2	37.3	37.4	37.5	37.2	37.8	37.0

(Continued.)

A. Supplementary Materials

	SRM-612							
Ti	44.0	44.0	44.3	43.6	45.4	42.6	43.5	44.5
Sr	79.9	76.9	78.3	78.5	77.7	79.1	78.0	78.8
Y	39.2	37.4	38.0	38.6	38.0	38.6	38.1	38.5
Nb	39.5	38.3	38.9	38.9	39.1	38.7	38.4	39.4
La	36.3	35.7	36.1	35.9	36.0	36.0	35.8	36.2
Ce	38.9	37.9	38.7	38.1	38.3	38.5	38.1	38.7
Pr	38.2	37.6	38.2	37.6	37.9	37.9	37.7	38.1
Nd	35.9	35.1	36.0	35.0	35.5	35.5	35.5	35.5
Sm	38.3	37.1	38.0	37.4	37.8	37.6	37.6	37.8
Eu	35.8	35.4	35.9	35.3	35.6	35.6	35.5	35.7
Gd	37.4	37.2	37.5	37.1	37.6	37.0	37.1	37.5
Tb	37.9	37.3	37.8	37.4	37.6	37.6	37.4	37.8
Dy	35.9	35.1	35.9	35.1	35.5	35.5	35.4	35.6
Ho	38.8	37.8	38.6	38.0	38.3	38.3	38.1	38.5
Er	38.2	37.8	38.2	37.9	38.0	38.0	37.9	38.1
Tm	37.4	36.2	37.2	36.4	36.8	36.9	36.7	36.9
Yb	39.5	38.9	39.6	38.8	39.1	39.3	39.0	39.4
Lu	37.4	36.6	37.1	36.9	37.0	37.0	36.8	37.2
Hf	37.2	36.2	37.0	36.4	36.7	36.7	36.5	36.9
Ta	38.1	37.1	37.9	37.3	37.6	37.6	37.4	37.8
Pb	38.7	38.5	39.4	37.8	39.3	37.8	38.4	38.7
Th	38.2	37.4	38.2	37.4	37.7	37.8	37.7	37.8
U	37.8	37.0	37.8	37.0	37.3	37.5	37.1	37.7

(Continued.)

A.3. Supplementary Material to Chapter 4

	SRM-612							
Ti	44.2	43.8	43.2	44.7	43.6	44.3	43.5	44.5
Sr	75.8	81.0	76.9	79.9	79.3	77.5	78.7	78.1
Y	36.7	39.9	37.6	39.0	39.0	37.6	39.0	37.6
Nb	37.5	40.3	38.5	39.3	39.4	38.4	39.6	38.2
La	35.7	36.3	36.0	36.0	36.0	36.0	36.2	35.8
Ce	38.2	38.6	38.5	38.3	38.4	38.4	38.6	38.2
Pr	37.5	38.3	38.0	37.8	37.9	37.9	38.1	37.7
Nd	35.3	35.7	35.5	35.5	35.5	35.5	35.7	35.3
Sm	37.4	38.0	38.0	37.4	37.9	37.5	37.9	37.5
Eu	35.3	35.9	35.8	35.4	35.5	35.7	35.7	35.5
Gd	37.0	37.7	37.5	37.2	37.1	37.5	37.8	36.8
Tb	37.4	37.8	37.7	37.5	37.6	37.6	37.8	37.4
Dy	35.3	35.7	35.6	35.4	35.6	35.4	35.6	35.4
Ho	38.0	38.6	38.5	38.1	38.3	38.3	38.4	38.2
Er	37.6	38.4	38.2	37.8	38.0	38.0	38.1	37.9
Tm	36.4	37.2	36.9	36.7	36.8	36.8	36.8	36.8
Yb	38.7	39.7	39.9	38.5	39.5	38.9	39.4	39.0
Lu	36.9	37.1	37.1	36.9	37.0	37.0	37.2	36.8
Hf	36.4	37.0	36.9	36.5	36.6	36.8	36.9	36.5
Ta	37.5	37.7	37.7	37.5	37.5	37.7	37.8	37.4
Pb	38.5	38.6	39.5	37.6	38.8	38.4	39.6	37.6
Th	37.5	38.1	37.8	37.8	37.9	37.7	38.1	37.5
U	37.1	37.7	37.4	37.3	37.4	37.4	37.6	37.2

(Continued.)

A. Supplementary Materials

	SRM-612							
Ti	44.6	43.4	43.8	44.2	44.7	43.3	44.7	43.3
Sr	78.4	78.4	79.1	77.7	78.5	78.3	78.5	78.3
Y	38.0	38.6	38.6	38.0	38.6	38.0	38.0	38.6
Nb	38.4	39.4	38.6	39.2	39.2	38.6	38.6	39.2
La	36.3	35.7	36.0	36.0	35.9	36.1	35.8	36.2
Ce	38.9	37.9	38.3	38.5	38.2	38.6	38.4	38.5
Pr	38.2	37.6	37.9	37.9	37.8	38.0	37.9	37.9
Nd	35.8	35.2	35.7	35.3	35.4	35.6	35.5	35.5
Sm	38.0	37.4	37.9	37.5	37.7	37.7	37.6	37.8
Eu	36.0	35.2	35.4	35.8	35.5	35.7	35.7	35.5
Gd	37.4	37.2	37.2	37.4	37.1	37.5	37.3	37.3
Tb	37.9	37.3	37.7	37.6	37.3	37.9	37.5	37.7
Dy	35.9	35.1	35.2	35.8	35.3	35.7	35.6	35.4
Ho	38.7	37.9	38.3	38.3	38.3	38.3	38.2	38.4
Er	38.4	37.6	37.9	38.1	37.9	38.1	38.0	38.0
Tm	37.2	36.4	36.7	36.9	36.6	37.0	36.7	36.9
Yb	39.5	38.9	39.5	38.9	39.0	39.4	39.5	38.9
Lu	37.3	36.7	37.0	37.0	36.8	37.2	36.8	37.2
Hf	37.0	36.4	36.8	36.6	36.7	36.7	36.7	36.7
Ta	37.8	37.4	37.3	37.9	37.4	37.8	37.8	37.4
Pb	38.6	38.5	38.7	38.4	37.9	39.2	38.5	38.6
Th	38.1	37.4	37.8	37.8	37.7	37.8	38.0	37.6
U	37.7	37.0	37.3	37.4	37.3	37.4	37.6	37.2

(Continued.)

A.3. Supplementary Material to Chapter 4

	SRM-612							
Ti	44.8	43.2	43.6	44.4	43.7	44.2	44.2	43.7
Sr	78.4	78.4	79.9	76.9	77.8	79.0	79.7	77.1
Y	38.4	38.2	39.1	37.5	37.6	39.0	38.8	37.8
Nb	39.0	38.8	39.5	38.3	38.4	39.4	39.5	38.3
La	36.1	35.9	36.1	35.9	35.7	36.3	36.2	35.8
Ce	38.6	38.2	38.5	38.3	38.4	38.4	38.7	38.1
Pr	38.0	37.8	38.1	37.7	37.9	37.9	38.2	37.6
Nd	35.6	35.4	35.7	35.3	35.4	35.6	35.6	35.4
Sm	37.8	37.6	37.9	37.5	37.7	37.7	38.1	37.3
Eu	35.6	35.6	35.8	35.4	35.7	35.5	35.8	35.4
Gd	37.4	37.2	37.5	37.1	37.3	37.3	37.3	37.3
Tb	37.8	37.4	37.9	37.3	37.6	37.6	37.7	37.5
Dy	35.9	35.1	35.4	35.6	35.6	35.4	35.8	35.2
Ho	38.3	38.3	38.7	37.9	38.2	38.4	38.5	38.1
Er	38.3	37.7	38.3	37.7	38.1	37.9	38.4	37.6
Tm	36.9	36.7	36.9	36.7	36.8	36.8	36.9	36.7
Yb	39.7	38.7	39.3	39.1	39.3	39.1	39.0	39.4
Lu	37.2	36.8	37.2	36.8	36.9	37.1	37.3	36.7
Hf	36.9	36.5	36.9	36.5	36.6	36.8	36.8	36.6
Ta	37.7	37.5	37.7	37.5	37.5	37.7	37.7	37.5
Pb	38.8	38.3	39.1	38.1	38.6	38.5	38.4	38.8
Th	37.7	37.9	37.9	37.7	37.7	37.9	38.0	37.6
U	37.6	37.1	37.7	37.1	37.5	37.3	37.8	37.0

(Continued.)

A. Supplementary Materials

	SRM-612	SRM-612	SRM-612	SRM-612
Ti	43.1	44.9	44.2	43.8
Sr	79.3	77.5	78.5	78.3
Y	38.8	37.8	38.2	38.4
Nb	39.4	38.4	38.9	38.9
La	36.4	35.6	36.2	35.8
Ce	38.6	38.2	38.6	38.2
Pr	38.3	37.5	38.0	37.8
Nd	36.0	35.0	35.7	35.3
Sm	38.2	37.2	38.2	37.2
Eu	35.9	35.3	35.7	35.5
Gd	37.9	36.7	37.3	37.3
Tb	38.1	37.1	37.7	37.5
Dy	35.9	35.1	35.6	35.4
Ho	38.7	37.9	38.4	38.2
Er	38.5	37.5	38.5	37.5
Tm	37.2	36.4	36.8	36.8
Yb	39.4	39.0	39.1	39.3
Lu	37.4	36.6	37.0	37.0
Hf	37.1	36.3	37.0	36.4
Ta	37.8	37.4	37.7	37.5
Pb	39.3	37.8	37.9	39.2
Th	38.4	37.2	37.9	37.7
U	37.8	37.0	37.7	37.1

Table A3.7. Plagioclase and amphibole major element compositions and thermometry of different Listino ring complex lithologies.

Sample	LR21-12A						
Rock type	LRT						
<i>Amphibole (wt.%)</i>							
SiO ₂	44.39	44.94	45.74	44.88	44.12	44.61	44.12
TiO ₂	1.11	1.36	1.11	1.27	0.95	1.15	0.95
Al ₂ O ₃	9.07	8.39	7.38	8.23	8.72	8.84	8.72
FeO	16.68	15.99	15.57	15.87	16.25	15.96	16.25
MnO	11.79	12.17	12.56	12.35	11.85	12.13	11.85
MgO	0.66	0.63	0.64	0.65	0.62	0.68	0.62
CaO	12.21	12.05	11.99	11.95	11.93	11.84	11.93
Na ₂ O	0.92	0.89	0.79	0.91	0.92	1.06	0.92
K ₂ O	0.95	0.78	0.78	0.73	0.85	0.74	0.85
Total	97.78	97.20	96.56	96.84	96.21	97.01	96.21
<i>Plagioclase (mol.%)</i>							
An	45.6	55.0	45.6	41.2	40.8	47.7	47.7
Ab	53.5	44.3	53.6	58.1	57.8	51.0	51.1
Or	0.9	0.6	0.7	0.7	1.3	1.3	1.2
<i>T</i> (°C)	775	814	771	774	759	795	783

(Continued.)

Sample	LR21-12A						
Rock type	LRT						
<i>Amphibole (wt.%)</i>							
SiO ₂	44.53	44.61	44.72	44.36	45.28	44.16	46.70
TiO ₂	1.15	1.15	1.04	1.07	0.92	0.86	0.76
Al ₂ O ₃	9.03	8.84	8.78	9.15	8.15	8.99	7.10
FeO	15.88	15.96	16.39	16.44	16.18	16.92	15.10
MnO	12.11	12.13	11.91	11.62	12.30	11.66	13.22
MgO	0.65	0.68	0.72	0.66	0.66	0.64	0.64
CaO	11.77	11.84	12.05	11.97	12.13	11.96	12.04
Na ₂ O	1.03	1.06	1.06	1.09	0.85	0.92	0.77
K ₂ O	0.83	0.74	0.69	0.84	0.75	0.93	0.61
Total	96.98	97.01	97.36	97.20	97.21	97.04	96.95
<i>Plagioclase (mol.%)</i>							
An	46.9	48.2	46.0	39.8	51.2	55.7	40.6
Ab	52.0	50.6	53.3	59.0	47.7	43.4	58.2
Or	1.1	1.3	0.7	1.2	1.1	0.9	1.2
<i>T</i> (°C)	788	796	779	750	792	818	746

(Continued.)

A. Supplementary Materials

Sample	LR21-12A						
Rock type	LRT						
<i>Amphibole (wt.%)</i>							
SiO ₂	44.37	44.40	44.38	43.98	44.00	44.23	44.29
TiO ₂	1.02	0.98	1.01	0.99	1.11	1.05	1.00
Al ₂ O ₃	9.01	8.95	8.83	8.75	8.67	8.76	8.45
FeO	16.78	16.62	16.27	15.81	16.66	16.66	16.08
MnO	11.58	11.49	11.87	11.95	11.69	11.79	11.88
MgO	0.64	0.67	0.68	0.65	0.62	0.67	0.63
CaO	12.12	11.93	12.00	11.93	12.00	12.01	12.01
Na ₂ O	0.95	1.02	0.98	0.99	0.89	0.87	0.90
K ₂ O	0.92	0.78	0.78	0.77	0.90	0.91	0.84
Total	97.39	96.84	96.79	95.82	96.53	96.95	96.07
<i>Plagioclase (mol.%)</i>							
An	71.6	46.9	49.1	60.5	51.7	40.7	47.3
Ab	27.9	52.1	49.8	38.8	47.2	57.8	51.9
Or	0.5	0.9	1.1	0.7	1.1	1.5	0.9
<i>T</i> (°C)	871	770	787	828	805	766	773

(Continued.)

Sample	LR21-12A	LR21-12A	LR21-4	LR21-4	LR21-2	LR21-2	LR21-2
Rock type	LRT	LRT	MGD	MGD	Tonalite	Tonalite	Tonalite
<i>Amphibole (wt.%)</i>							
SiO ₂	44.55	44.00	45.79	45.48	44.44	43.99	44.81
TiO ₂	1.05	1.11	0.82	0.74	1.08	1.16	0.81
Al ₂ O ₃	8.46	8.67	7.46	7.46	8.50	8.92	7.72
FeO	16.31	16.66	15.09	15.32	17.11	17.21	16.74
MnO	11.89	11.69	12.85	12.63	11.75	11.55	12.26
MgO	0.63	0.62	0.77	0.73	0.50	0.57	0.50
CaO	11.96	12.00	11.91	12.10	12.12	12.02	12.10
Na ₂ O	0.85	0.89	0.88	0.84	1.00	1.12	0.97
K ₂ O	0.79	0.90	0.58	0.64	0.68	0.88	0.73
Total	96.49	96.53	96.15	95.94	97.18	97.41	96.63
<i>Plagioclase (mol.%)</i>							
An	62.9	52.7	49.7	51.0	49.0	36.4	42.4
Ab	36.5	46.1	49.6	48.1	49.6	62.3	56.2
Or	0.6	1.2	0.7	0.9	1.4	1.4	1.4
<i>T</i> (°C)	839	809	787	779	800	765	758

LRT, Listino ring tonalite

MGD, Monoccola granodiorite

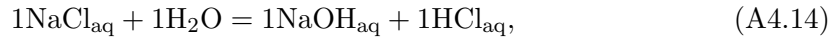
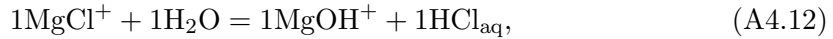
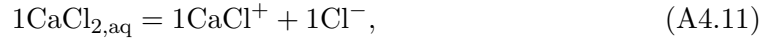
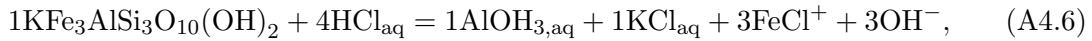
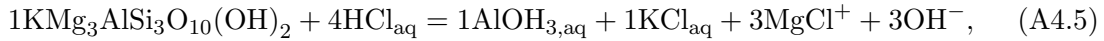
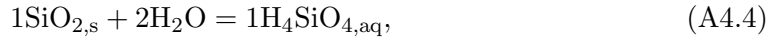
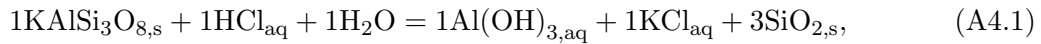
Table A3.8. List of parameters used for thermal modelling.

Symbol	Definition	Value	Unit	Reference
c	Specific heat	1,000	$\text{J kg}^{-1} \text{K}^{-1}$	Annen et al. (2006)
k	Thermal conductivity	2.7	$\text{W m}^{-1} \text{K}^{-1}$	Whittington et al. (2009)
L	Latent heat	3.13×10^5	J kg^{-1}	Blundy and Annen (2016)
ρ	Density	2,700	kg m^{-3}	Blundy and Annen (2016)
$\partial T/\partial z$	Initial geothermal gradient	35	$^{\circ}\text{C km}^{-1}$	-
T_{liq}	Liquidus temperature	930	$^{\circ}\text{C}$	Caricchi and Blundy (2015)
T_{sol}	Solidus temperature	670	$^{\circ}\text{C}$	Caricchi and Blundy (2015)
T_{sur}	Surface temperature	8	$^{\circ}\text{C}$	-
z	Intrusion depth	6.5-9.5	km	Floess and Baumgartner (2013)

A.4 Supplementary Material to Chapter 5

A.4.1 Supplementary Text

The composition of the fluid in equilibrium with apatite was modelled based on dissolution and dissociation reactions in the system $\text{SiO}_2\text{-Al}_2\text{O}_3\text{-FeO-MgO-CaO-Na}_2\text{O-K}_2\text{O-H}_2\text{O-Cl}$ following a similar method as [Hauzenberger et al. \(2001\)](#) and [Pak et al. \(2003\)](#). First, dissolution reaction involving silicate phases were written to define each element, and then dissociation reactions were used to add the aqueous species of interest:



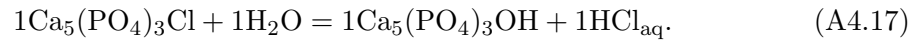
Equilibrium constants for each reaction were calculated from the thermodynamic database SUPCRTBL ([Zimmer et al., 2016](#)), which is an extended database of SUPCRT92 ([Johnson et al., 1992](#)). Activity coefficients for charged aqueous species were calculated using the extended Debye-Hückel equation ([Helgeson et al., 1981](#); [Hückel, 1925](#)):

$$\log\gamma_i = \frac{-(A_\gamma Z_i^2 \sqrt{I})}{(1 + aB_\gamma \sqrt{I})} \Gamma_\gamma + bI, \quad (\text{A4.16})$$

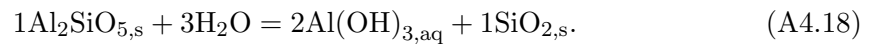
where A_γ and B_γ are the temperature- and pressure-dependent Debye-Hückel coefficients, respectively, Z_i is the charge of ion i , I is the ionic strength, a is the ion size parameter, b is the extended term parameter for ion i , and Γ_γ is the mole fraction to molality conversion factor. The mixing behaviour for mineral phases was assumed to be ideal, which is

reasonable given the temperatures of interest (700-900 °C) and the plagioclase (An_{40–60}) and biotite (Mg# = 45-65 mol.%) compositions. This resulted in the following activities: $a_{\text{An}} = 0.49$; $a_{\text{Ab}} = 0.51$; $a_{\text{Kfs}} = 0.75$; $a_{\text{Phl}} = 0.58$; $a_{\text{Ann}} = 0.42$; $a_{\text{Qz}} = 0.95$.

To obtain the total Cl content of the fluid in equilibrium with the measured apatite compositions, the total Al content and a Cl-bearing specie must be constrained. The fluid HCl_{aq} is determined based on the measured apatite compositions and the equilibrium constant following Eq. A4.17:



As for the total Al concentration of the fluid, a similar approach was employed whereby the equilibrium reaction of Eq. A4.18 was inferred from SUPCRTBL and a sillimanite activity of 0.5 was assumed:



Finally, the total Cl concentration of the fluid in equilibrium with apatite was calculated by summing all the Cl species considered in our calculations. This operation was done for a temperature step of 50 °C from 700 to 900 °C, and for each measured apatite composition.

A.4.2 Supplementary Figures

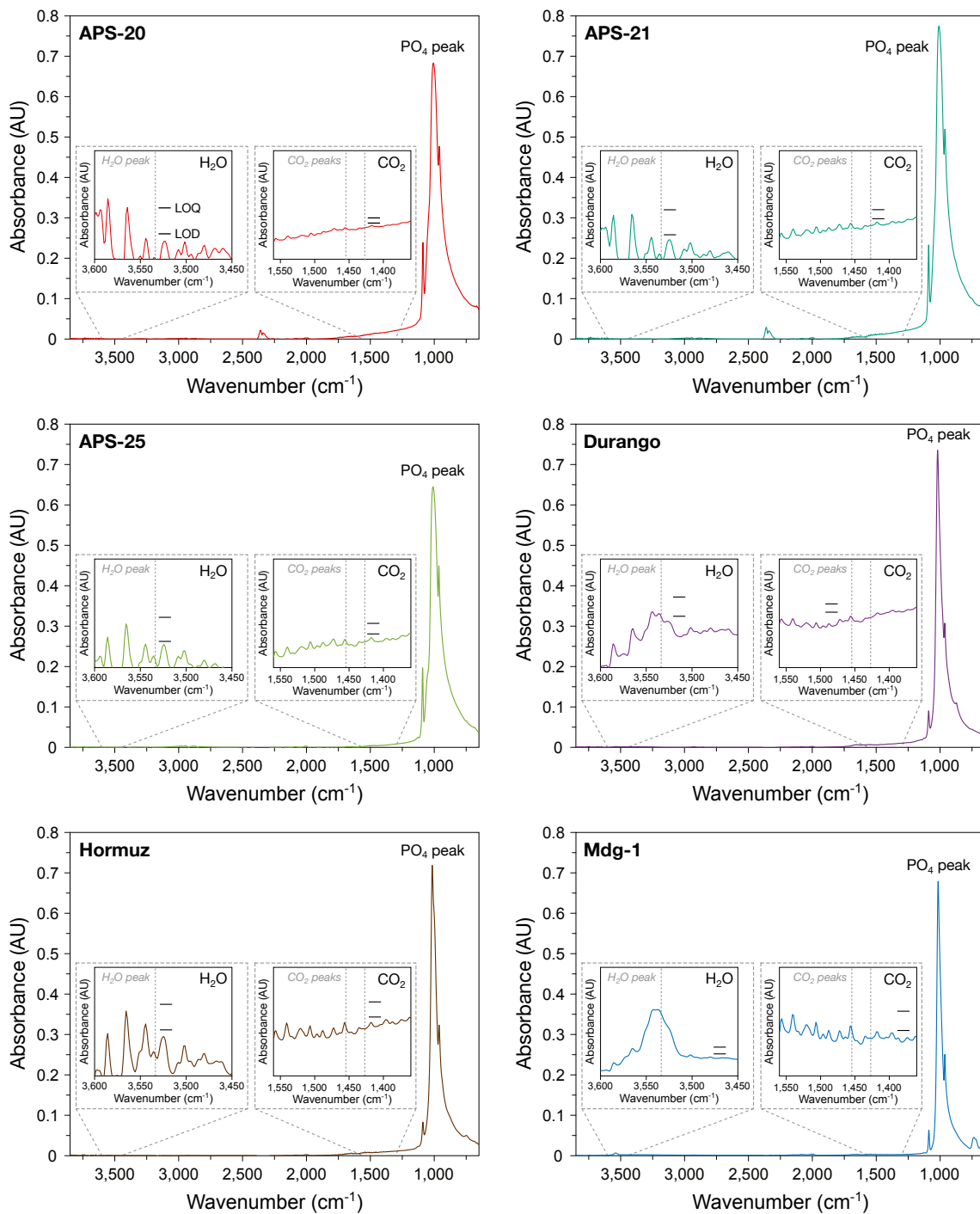


Figure A4.1. (Continued.)

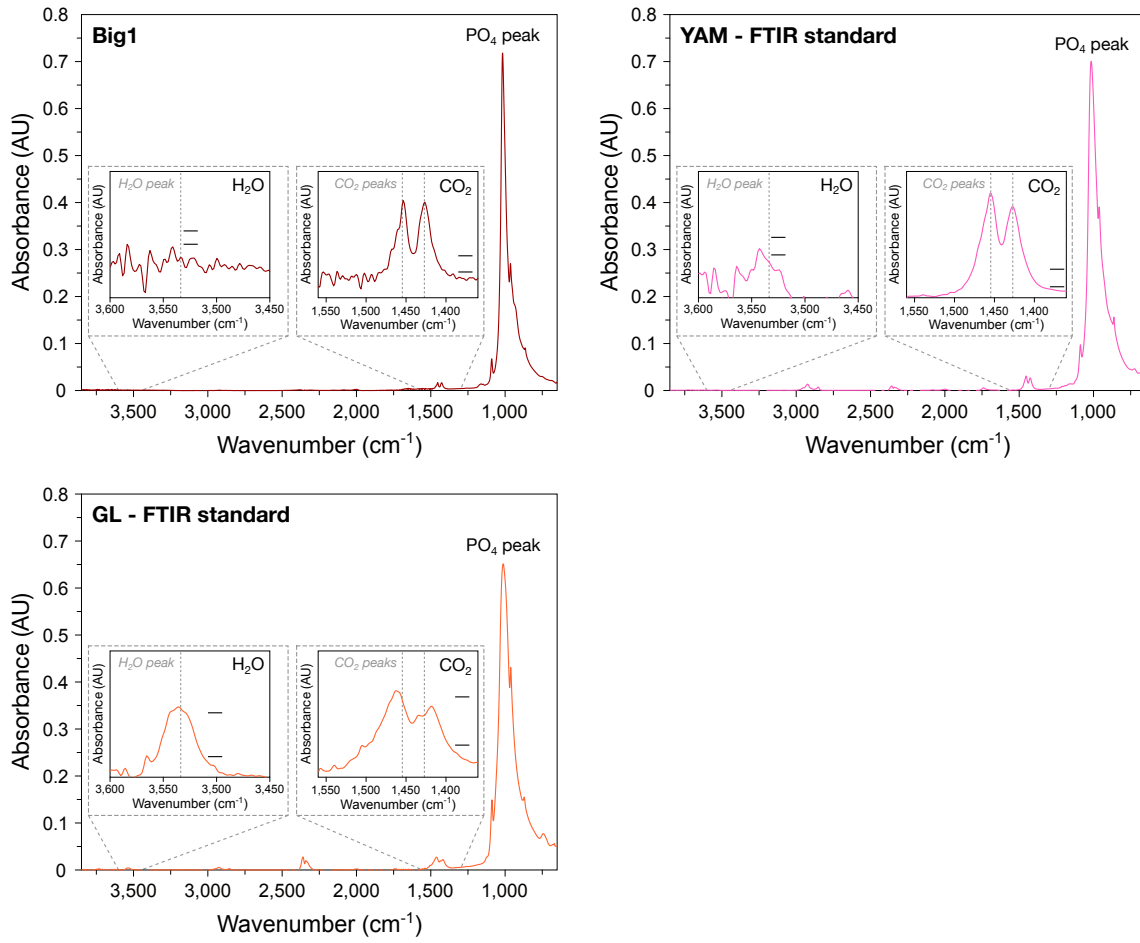


Figure A4.1. Measured ATR-FTIR profiles used to quantify the H₂O and CO₂ contents of the apatite standards used for the SIMS analysis. In each panel, the insets represent the detailed H₂O and CO₂ profiles. The location of the main H₂O and CO₂ peaks is highlighted by the vertical grey dashed lines. The quantification was done following [Hammerli et al. \(2021b\)](#). *LOD*, limit of detection; *LOQ*, limit of quantification.

A. Supplementary Materials

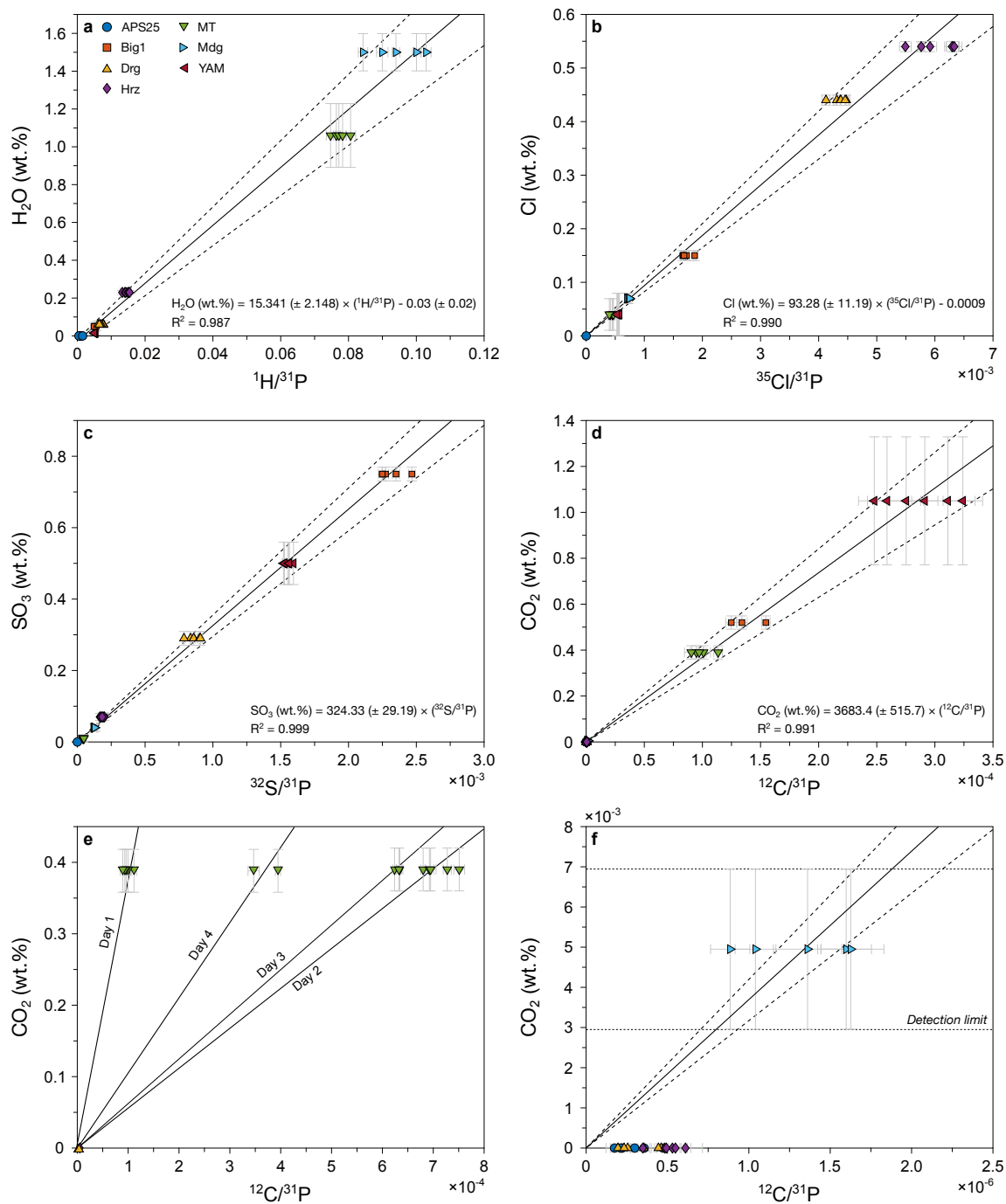


Figure A4.2. Calibration curves used to quantify the counts per second measured by SIMS, and define the limit of detection. **a**, $^1\text{H}/^{31}\text{P}$ vs. H_2O (wt.%). **b**, $^{35}\text{Cl}/^{31}\text{P}$ vs. Cl (wt.%). **c**, $^{32}\text{S}/^{31}\text{P}$ vs. SO_3 (wt.%). **d**, $^{12}\text{C}/^{31}\text{P}$ vs. CO_2 (wt.%). **e**, $^{12}\text{C}/^{31}\text{P}$ vs. CO_2 (wt.%) highlighting the daily shift in the CO_2 calibration. **f**, $^{12}\text{C}/^{31}\text{P}$ vs. CO_2 (wt.%) showing the method to define the limit of detection for CO_2 .

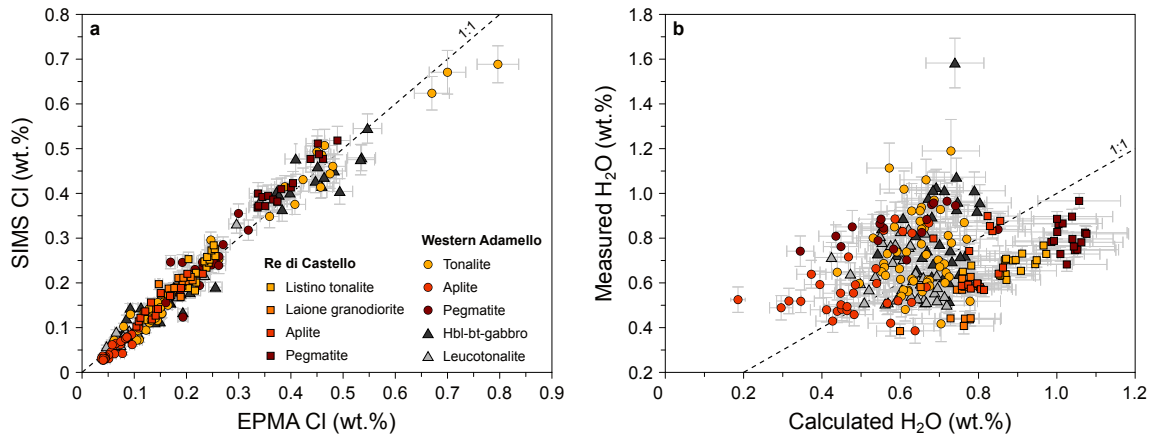


Figure A4.3. Comparison between the volatile contents measured (and calculated) by EPMA and by SIMS. **a**, EPMA Cl (wt.%) vs. SIMS Cl (wt.%). The data points follow the 1:1 line, with a deviation below 15 %. **b**, EPMA H₂O (wt.%) vs. SIMS H₂O (wt.%). This diagram highlights the necessity of quantifying H₂O instead of assuming a perfect stoichiometry.

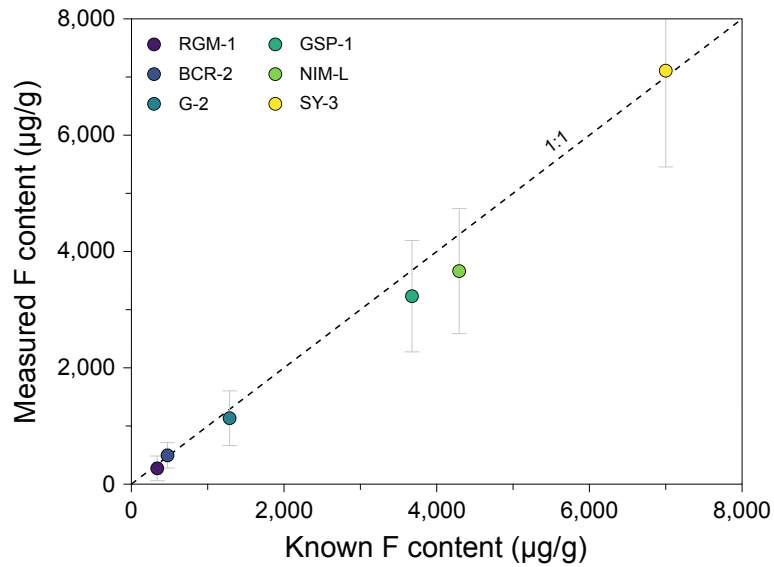


Figure A4.4. EPMA analysis of the bulk F content of the standards plotted as known F (µg/g) vs. measured F (µg/g). This confirms that the employed method allows a reasonable quantification of the bulk F content.

A. Supplementary Materials

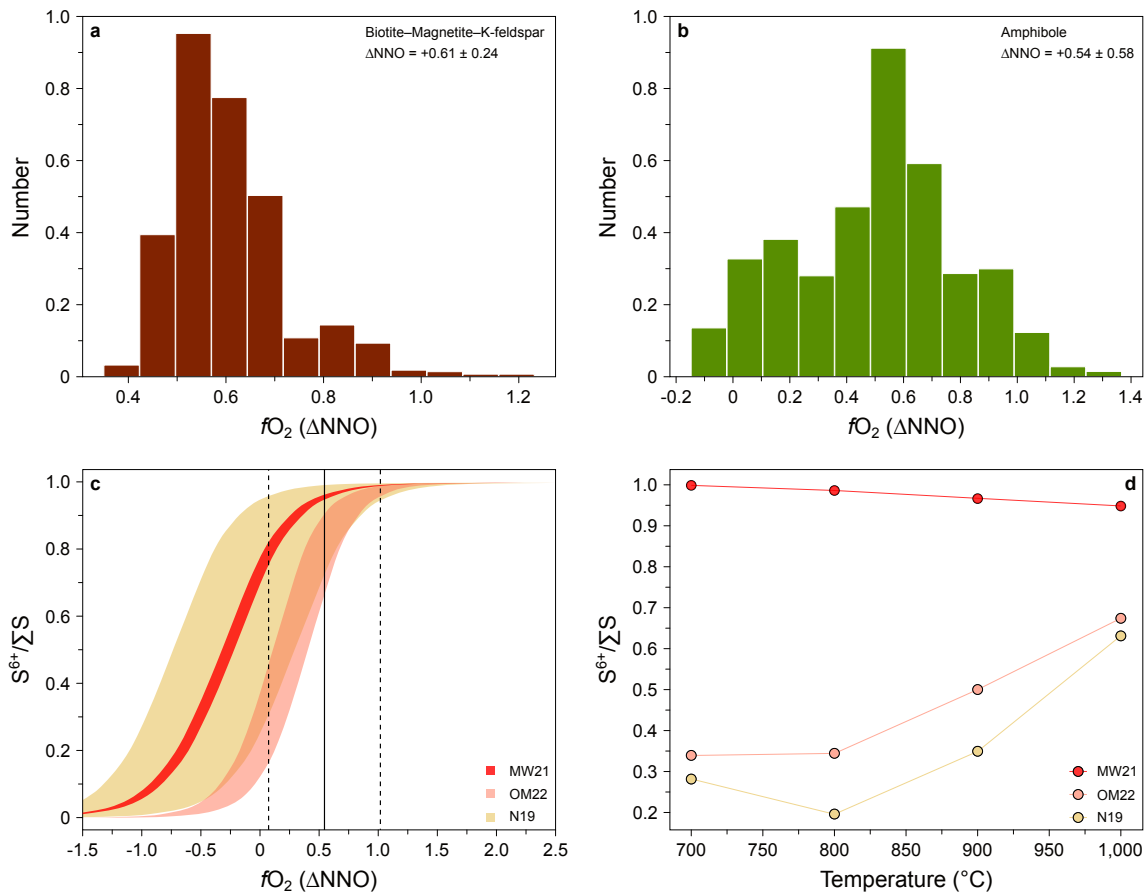


Figure A4.5. Determination of fO_2 and the sulphur budget of the studied lithologies. **a**, Histogram representing the results of the biotite-feldspar-magnetite oxybarometer of [Wones \(1972\)](#). **b**, Histogram representing the results of the amphibole-only oxybarometer of [Ridolfi et al. \(2010\)](#). **c**, $S^{6+}/\Sigma S$ vs. fO_2 (ΔNNO). Diagram modified after [Ding et al. \(2023\)](#). The average results of the two oxybarometers are also represented. **d**, Sulphur budget evolution with differentiation plotted as temperature ($^{\circ}C$) vs. $S^{6+}/\Sigma S$. This was modelled using Sulfur_X ([Ding et al., 2023](#)) at $NNO+0.55$. *MW21*, [Muth and Wallace \(2021\)](#); *N19*, [Nash et al. \(2019\)](#); *OM22*, [O'Neill and Mavrogenes \(2022\)](#).

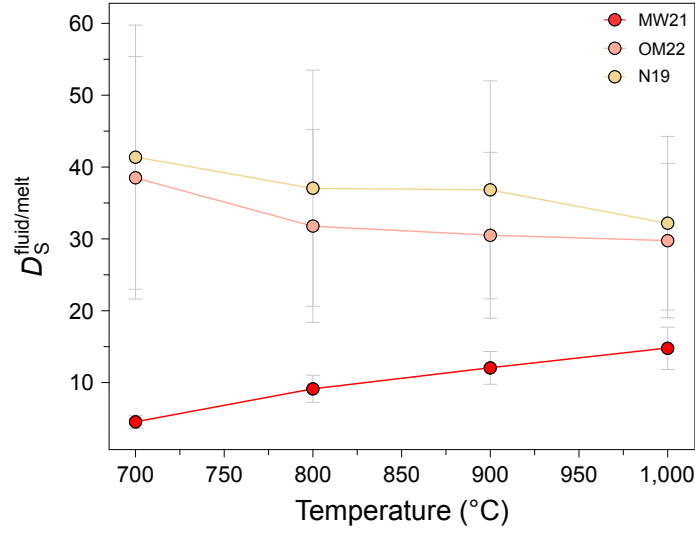


Figure A4.6. Determination of the S partitioning between fluid and melt plotted as temperature ($^{\circ}\text{C}$) vs. $D_S^{\text{fluid/melt}}$. This was modelled using Sulfur_X (Ding et al., 2023) at NNO+0.55 and for different $\text{S}^{6+}/\Sigma\text{S}$ parameterisations.

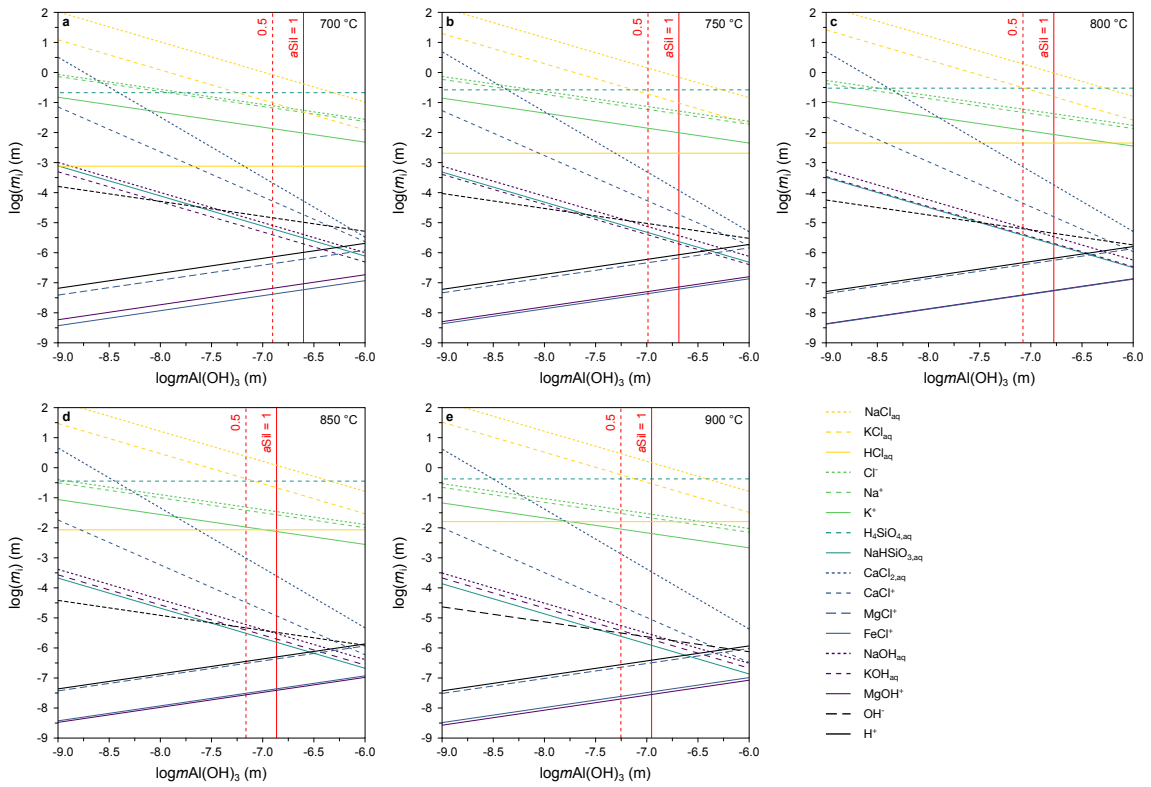


Figure A4.7. Modelling of the fluid composition in equilibrium with the observed assemblage forming the Western Adamello and Listino tonalites, plotted as $\log m_i$ (m) vs. $\log m\text{Al}(\text{OH})_3$ (m) at (a) 700 $^{\circ}\text{C}$, (b) 750 $^{\circ}\text{C}$, (c) 800 $^{\circ}\text{C}$, (d) 850 $^{\circ}\text{C}$, and (e) 900 $^{\circ}\text{C}$. The $\log m\text{Al}(\text{OH})_3$ values corresponding to $a\text{Sil} = 1$ and 0.5 are also represented.

A. Supplementary Materials

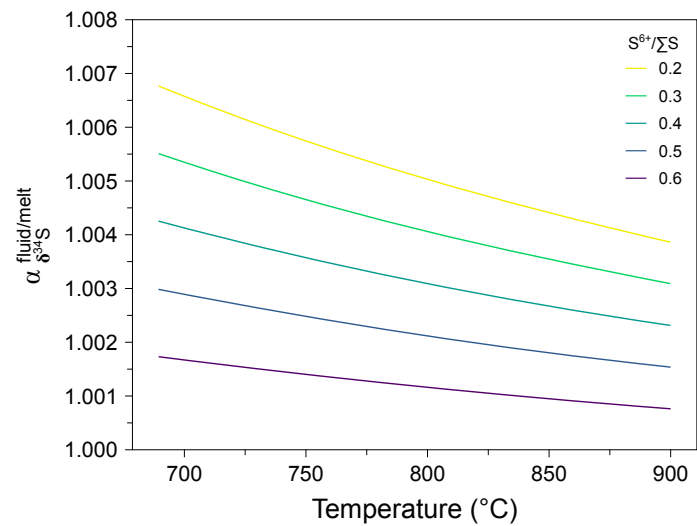


Figure A4.8. Examples of the evolution of the $\delta^{34}\text{S}$ fractionation factor (α) between fluid and melt as a function of temperature (°C) and $f\text{O}_2$, here represented as $\text{S}^{6+}/\Sigma\text{S}$. Note the increase of the fractionation factor at lower temperatures and $f\text{O}_2$.

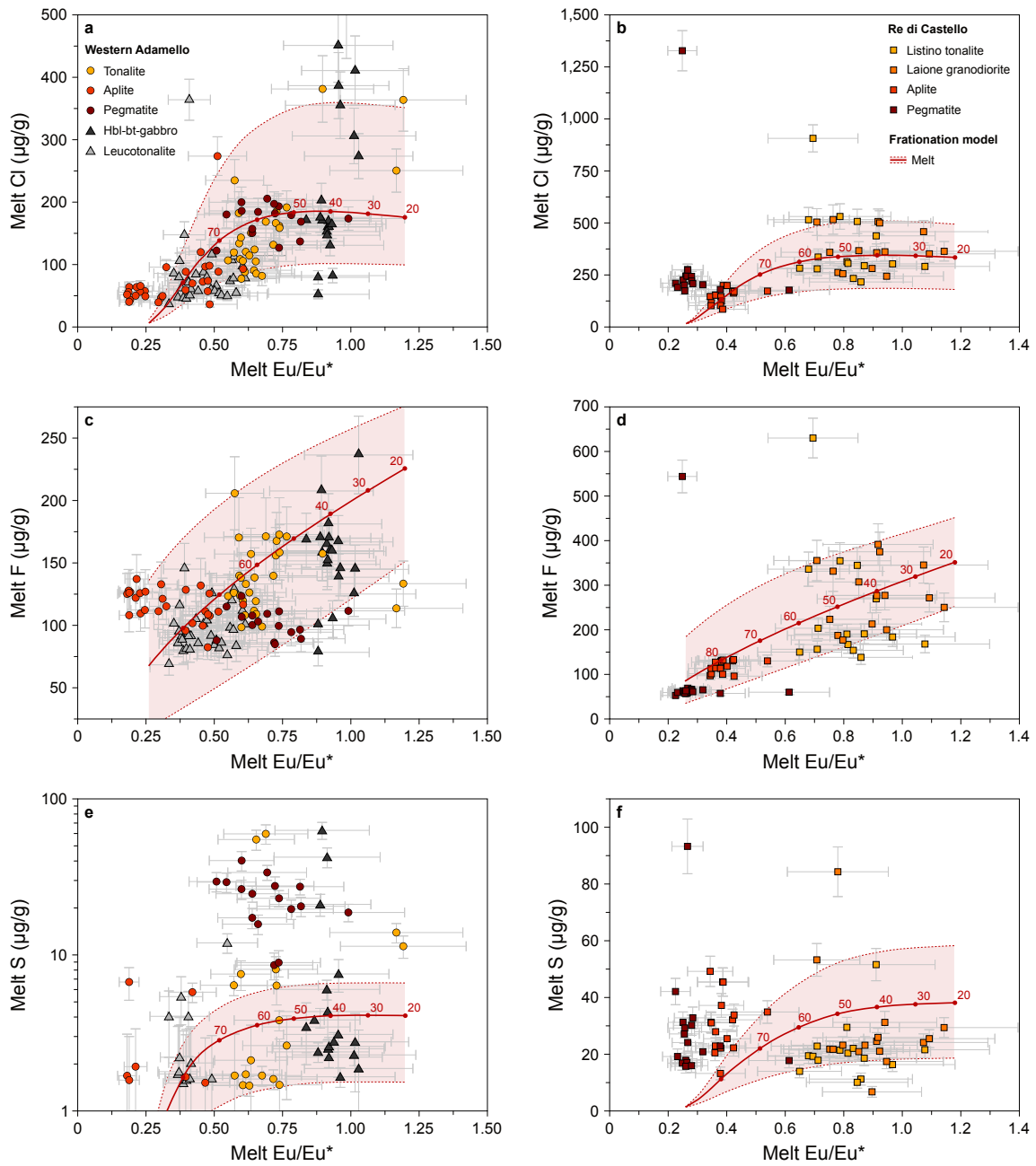


Figure A4.9. Modelling of the melt volatile evolution in the Western Adamello (a, c, e) and Listino ring complex (b, d, f). a, b, Melt Eu/Eu^* vs. melt Cl ($\mu\text{g/g}$). c, d, Melt Eu/Eu^* vs. melt F ($\mu\text{g/g}$). e, f, Melt Eu/Eu^* vs. melt S ($\mu\text{g/g}$). The measured data are also represented. The modelling was done using the fractional crystallisation equation. The error envelopes account for different starting Cl, F and S contents, and the numbers correspond to the crystal fraction in the magma. Note that the model starts at 20 % crystallinity, which approximately corresponds to the magma crystallinity at the onset of apatite crystallisation. Most of the data are relatively well-reproduced by the melt evolution.

A. Supplementary Materials

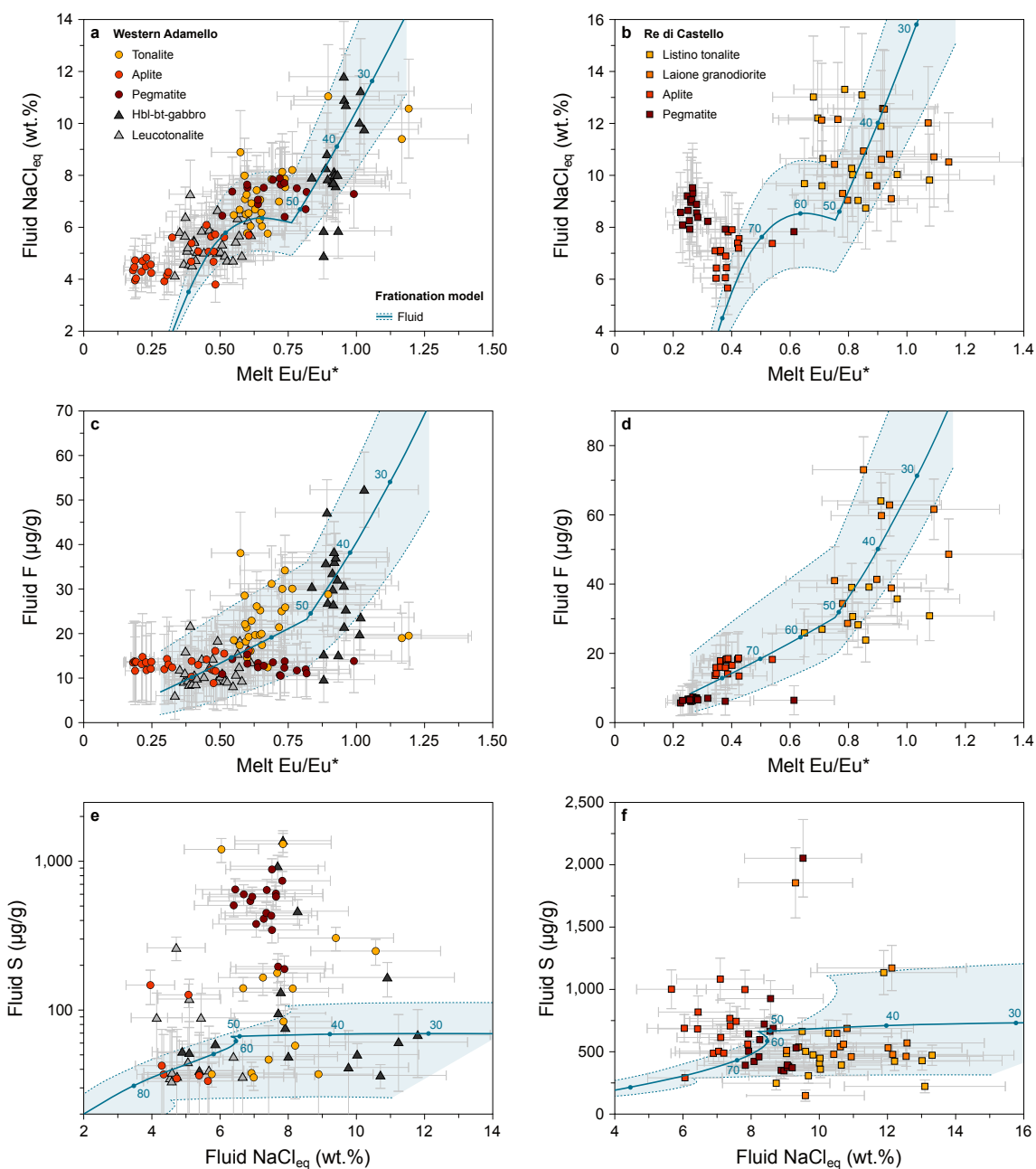


Figure A4.10. Modelling of the fluid (and melt) volatile evolution in the Western Adamello (a, c, e) and Listino ring complex (b, d, f). a, b, Melt Eu/Eu* vs. fluid NaCl_{eq} (wt.%). c, d, Melt Eu/Eu* vs. fluid F (μg/g). e, f, Melt Eu/Eu* vs. fluid S (μg/g). The measured data are also represented. The modelling was done using the fractional crystallisation equation. The error envelopes account for different starting Cl, F and S contents, and the numbers correspond to the crystal fraction in the magma. Note that the model starts at 20 % crystallinity, which approximately corresponds to the magma crystallinity at the onset of apatite crystallisation. Most of the data are relatively well-reproduced by the fluid evolution.

A.4.3 Supplementary Tables

Table A4.1. Compositions of the apatite standards used during SIMS sessions.

Apatite	P ₂ O ₅ wt.%	Na ₂ O wt.%	CaO wt.%	SiO ₂ wt.%	MgO wt.%	FeO wt.%	F wt.%	Cl wt.%	SO ₃ wt.%	Total wt.%	δ ³⁴ S ‰	± ‰	H ₂ O wt.%	± wt.%	CO ₂ wt.%	± wt.%
APS-20	41.99		55.02				2.97	1.33		101.31			<0.01		<0.004	
APS-21	42.15		54.92				3.38	0.75		101.20			<0.01		<0.004	
APS-25	42.3		55.24				3.8	<0.01		101.34			<0.01		<0.004	
Madagascar	42.38	0.02	56.13	0.02	0.02	0.05	1.98	0.07	0.04	100.71	1.42	0.60	1.70	0.09	0.005	0.005
DurangoB	41.71	0.19	55.52	0.34	0.02	0.03	3.46	0.44	0.29	102.00	-1.39	0.50	0.06	0.05	0.005	0.005
Big1	40.05	0.05	55.8	0.83	0.01	0.01	3.86	0.15	0.75	101.51	14.02	0.22	0.05	0.04	0.52	0.06
Hormuz	40.67	0.55	52.93	0.40	0.04	0.04	3.22	0.54	0.07	98.46	25.78	0.60	0.23	0.01	<0.002	
Mud Tank	42.12	0.19	55.71	<0.01	0.06	0.08	1.81	0.04	0.01	100.02			1.06	0.17	0.39	0.03
YAM	39.3	0.07	54.87	0.91	0.01	0.02	3.94	0.04	0.50	99.66			0.01	0.01	1.05	0.28
SAP1	40.47	0.07	55.63	0.62	0.01	0.02	3.89	0.26	0.55	101.52	-1.39	0.48				

A. Supplementary Materials

Table A4.2. Measured apatite major, trace and volatile element compositions from the Western Adamello and Re di Castello units.

Sample	CJ38	CJ38	CJ38	CJ38	CJ38	CJ38	CJ38	CJ38	CJ38
Rock type	Pegm.	Pegm.	Pegm.	Pegm.	Pegm.	Pegm.	Pegm.	Pegm.	Pegm.
<i>Major elements (wt.%)</i>									
SiO ₂	0.20	0.20	0.20	0.17	0.22	0.14	0.24	0.12	0.16
FeO	0.01	0.01	0.02	0.02	0.02	0.00	0.02	0.03	0.03
CaO	55.57	55.56	55.49	55.76	55.80	55.68	49.48	55.57	56.15
Na ₂ O	0.06	0.02	0.03	0.05	0.02	0.04	0.05	0.05	0.06
P ₂ O ₅	41.73	41.91	41.88	41.74	41.47	41.77	40.75	41.03	41.41
F	2.39	2.24	2.20	2.51	2.74	2.35	2.28	1.98	2.16
Cl	0.25	0.26	0.23	0.19	0.16	0.19	0.19	0.32	0.27
Total	100.30	100.37	100.22	100.54	100.50	100.25	93.26	99.41	100.42
<i>Trace elements (µg/g)</i>									
Rb	0.297	0.348		0.856	0.394	0.329			0.15
Sr	190	178		189	158	181	208	185	249
Y	2060	1546		2100	2244	1404	1045	917	1222
Zr	0.582	0.237		0.735	0.359	0.391	0.551	0.225	0.715
Nb	0.011	0.077		0.038	0.061	0.019	0.039	0.019	0.018
Ba	0.21	0.31		0.839	0.092	0.447	0.108	0.083	0.154
La	136	174		137	78.0	38.9	559.0	487.6	646.3
Ce	452	653		490	349	181	1772	1655	1722
Pr	78.6	111		88.8	73.2	38.3	223	219	229
Nd	444	589		500	449	248	1004	966	989
Sm	158	178		181	181	109	207	208	212
Eu	22.3	24.5		23.0	27.2	22.4	28.1	24.6	29.0
Gd	226	216		248	261	162	199	195	205
Tb	42.3	36.6		44.3	48.3	30.7	30.3	28.9	31.4
Dy	297	239		297	329	218	181	174	192
Ho	65.6	51.0		64.0	72.8	49.0	36.5	34.1	39.4
Er	197	145		187	214	147	103	90	113
Tm	28.8	20.8		26.4	30.6	20.9	14.0	11.7	16.0
Yb	193	136		175	199	138	86	70	104
Lu	25.9	19.5		24.7	28.3	20.3	12.1	9.5	13.7
Hf	0.063	0.021		0.017	0.028	0.017	0.02	0.007	0.023
Ta		0.007		0.008	0.011	0.004	0.005		0.005
Pb	2.301	1.76		2.90	2.07	2.24	2.08	2.16	2.52
Th	69.0	22.2		47.5	40.2	18.4	94.4	19.1	74.7
U	57.5	48.6		47.3	59.8	56.3	57.6	42.2	59.6
<i>Volatile elements and isotopes</i>									
H ₂ O (wt.%)	0.751	0.825	0.949	0.788	0.809	0.702	0.864	0.945	0.957
±	0.050	0.054	0.050	0.051	0.051	0.051	0.051	0.051	0.082
CO ₂ (µg/g)	35.6	1042.0	33.0	443.5	36.7	69.1	35.2	34.1	<30
±	30.1	207.5	30.1	43.1	30.1	30.5	30.1	30.1	
S (µg/g)	573.2	161.4	456.0	428.5	402.3	329.9	472.4	155.6	359.8
±	26.3	26.3	26.4	26.4	27.1	26.6	26.4	26.1	36.4
δ ³⁴ S (‰)	9.35		13.53	13.85	12.88	13.10	13.50		12.62
±	1.08		0.73	0.64	0.81	0.71	0.66		0.78

(Continued.)

A.4. Supplementary Material to Chapter 5

Sample	CJ38	CJ38	CJ30						
Rock type	Pegm.	Pegm.	Aplite						
<i>Major elements (wt.%)</i>									
SiO ₂	0.12	0.17	0.16	0.22	0.11	0.12	0.12	0.16	0.14
FeO	0.01	0.01	0.03	0.01	0.01	0.00	0.03	0.01	0.00
CaO	56.42	56.56	56.48	56.69	56.93	56.92	56.42	55.28	55.84
Na ₂ O	0.04	0.04	0.03	0.08	0.04	0.04	0.03	0.04	0.08
P ₂ O ₅	41.31	41.40	41.31	41.28	41.45	41.51	41.20	40.10	42.14
F	2.20	2.45	2.47	2.62	2.92	1.89	2.68	1.98	3.02
Cl	0.26	0.25	0.23	0.25	0.23	0.17	0.22	0.30	0.06
Total	100.51	101.11	100.82	101.44	101.86	100.82	100.73	98.21	101.39
<i>Trace elements (µg/g)</i>									
Rb	0.284	0.266	0.262	0.285	0.303	0.331	0.336	0.169	0.677
Sr	223	197	205	195	193	191	184	208	105
Y	1399	1485	1357	1670	1784	1724	1720	990	3355
Zr	0.633	0.71	0.482	0.653	0.691	0.754	0.647	0.78	0.504
Nb	0.033	0.019	0.009	0.013	0.038	0.031	0.035	0.025	0.01
Ba	0.145	0.093	0.35	0.22	0.292	0.246	0.267	0.203	0.018
La	457.2	431.2	242.3	409.1	375.9	293.7	205.0	658.7	134.7
Ce	1267	1451	840	1370	1298	1179	922	1844	551
Pr	171	217	126	211	202	191	156	248	124
Nd	787	1010	628	996	996	972	829	1047	859
Sm	188	240	170	256	265	262	237	218	473
Eu	26.0	26.8	19.7	26.8	27.9	23.3	23.2	25.8	16.2
Gd	204	237	193	268	283	278	264	202	542
Tb	33.7	38.1	32.6	43.8	46.4	45.5	43.9	30.3	90.5
Dy	216	237	210	274	291	283	279	177	526
Ho	45.4	48.4	43.9	56.5	60.3	58.3	58.1	34.8	96.9
Er	133	139	129	159	172	168	166	94	270
Tm	18.8	19.8	18.1	22.3	24.0	23.0	23.0	12.1	41.5
Yb	121	133	120	149	160	152	150	76	309
Lu	16.5	18.2	16.7	20.5	22.3	20.8	20.8	10.0	45.4
Hf	0.023	0.029	0.026	0.033	0.028	0.034	0.026	0.022	0.023
Ta	0.008	0.008	0.007	0.008	0.012	0.014	0.011	0.006	0.01
Pb	2.05	2.38	3.31	2.86	2.63	3.24	2.87	2.35	8.39
Th	68.1	92.4	38.5	59.6	69.5	78.9	67.1	50.3	46.8
U	51.7	61.1	39.6	65.8	66.6	72.4	66.3	54.4	25.5
<i>Volatile elements and isotopes</i>									
H ₂ O (wt.%)	0.883	0.845	0.885	0.850	0.742	0.839	0.762	0.965	0.518
±	0.075	0.074	0.083	0.073	0.068	0.073	0.068	0.079	0.050
CO ₂ (µg/g)	<30	<30	1269.4	41.9	<30	<30	<30	<30	<30
±			139.5	4.4					
S (µg/g)	346.0	279.8	306.1	672.2	456.7	506.7	502.7	477.0	29.0
±	34.9	28.7	33.4	67.8	45.9	50.9	50.6	48.7	26.0
δ ³⁴ S (‰)	13.39	13.36	12.67	14.61	13.23	13.77		11.00	
±	0.63	0.79	0.94	0.66	0.77	0.65		1.18	

(Continued.)

A. *Supplementary Materials*

Sample	CJ30								
Rock type	Aplite								
<i>Major elements (wt.%)</i>									
SiO ₂	0.15	0.12	0.11	0.14	0.02	0.11	0.07	0.12	0.14
FeO	0.03	0.01	0.03	0.03	0.03	0.00	0.02	0.04	0.02
CaO	55.21	55.37	55.53	55.68	55.77	55.33	55.63	55.40	56.06
Na ₂ O	0.10	0.08	0.07	0.07	0.08	0.07	0.08	0.10	0.07
P ₂ O ₅	41.90	42.23	42.07	42.11	42.59	42.00	42.24	42.06	41.24
F	2.75	2.82	2.84	2.77	2.75	3.07	2.73	2.79	2.93
Cl	0.04	0.04	0.05	0.04	0.05	0.04	0.04	0.04	0.04
Total	100.30	100.73	100.76	100.88	101.31	100.69	100.89	100.65	100.62
<i>Trace elements (µg/g)</i>									
Rb	0.544	0.476	0.644	0.542		0.592	0.373	0.523	0.235
Sr	84	96	94	96		98	89	89	187
Y	3060	3304	3574	3435		3588	2892	3141	1907
Zr	0.361	0.368	0.642	0.462		0.704	0.48	0.446	0.693
Nb		0.033					0.012		0.01
Ba	0.066			0.032		0.025	0.058	0.035	0.083
La	36.9	60.2	51.4	36.6		88.9	93.6	102.0	467.4
Ce	194	276	218	151		370	399	437	1332
Pr	56.0	73.9	54.8	39.2		89.0	97.6	105	187
Nd	473	600	450	339		680	717	767	945
Sm	368	410	352	295		436	421	448	294
Eu	15.3	14.6	15.5	14.3		15.8	14.1	14.5	23.1
Gd	490	522	507	459		541	462	494	268
Tb	83.4	86.7	86.0	80.3		91.1	75.6	83.0	42.8
Dy	493	506	505	477		529	437	479	247
Ho	91.3	92.9	96.3	92.0		99.1	80.4	89.9	47.0
Er	254	262	276	260		281	227	254	132
Tm	38.3	39.6	42.2	39.9		43.3	34.0	38.9	20.5
Yb	284	295	319	302		326	256	285	155
Lu	41.6	44.7	48.5	45.8		48.4	38.2	42.2	22.1
Hf	0.063	0.022	0.051	0.045		0.039	0.043	0.04	0.024
Ta	0.002	0.017	0.008	0.007		0.018	0.008	0.01	0.007
Pb	6.45	5.65	5.80	5.85		7.80	8.18	7.75	8.38
Th	37.9	44.0	54.1	43.3		55.0	31.7	42.4	60.1
U	25.4	24.3	26.5	27.7		27.0	16.9	21.8	21.1
<i>Volatile elements and isotopes</i>									
H ₂ O (wt.%)	0.494	0.473	0.429	0.476	0.458	0.519	0.591	0.482	0.639
±	0.050	0.051	0.051	0.051	0.050	0.057	0.055	0.050	0.062
CO ₂ (µg/g)	223.4	<30	61.7	<30	<30	2524.9	2471.6	189.8	<30
±	50.5		30.2			101.2	437.5	35.0	
S (µg/g)	35.4	<30	<30	<30	<30	<30	121.9	31.0	<30
±	26.2						26.1	26.0	
δ ³⁴ S (‰)							9.17		
±							1.16		

(Continued.)

A.4. Supplementary Material to Chapter 5

Sample	CJ30	CJ31							
Rock type	Aplite								
<i>Major elements (wt.%)</i>									
SiO ₂	0.10	0.09	0.17	0.43	0.15	0.13	0.16	0.17	0.00
FeO	0.04	0.01	0.00	0.05	0.02	0.01	0.03	0.02	0.02
CaO	56.01	56.21	55.90	55.66	56.07	55.82	55.27	55.28	56.02
Na ₂ O	0.07	0.07	0.08	0.09	0.08	0.07	0.07	0.08	0.06
P ₂ O ₅	40.89	41.52	41.38	40.98	41.12	41.40	39.73	39.87	42.40
F	2.69	2.89	3.33	2.84	3.08	2.77	2.59	2.68	2.55
Cl	0.07	0.06	0.04	0.04	0.05	0.04	0.06	0.04	0.08
Total	100.05	100.95	101.09	100.27	100.64	100.33	98.09	98.23	101.20
<i>Trace elements (µg/g)</i>									
Rb	0.773	0.427	0.365	0.563		0.361	0.425	0.349	0.471
Sr	160	117	131	105		125	119	134	129
Y	2341	2980	2823	3529		2551	2997	2518	3514
Zr	0.619	0.585	0.429	1.115		0.229	0.699	0.642	0.824
Nb	0.012		0.007	0.012		0.009	0.006	0.007	
Ba	2.734	0.043		0.035		0.011	0.039	0.089	0.033
La	219.5	123.0	246.3	136.3		165.5	148.8	207.9	46.4
Ce	806	522	913	557		669	533	739	194
Pr	135	102	151	110		119	94.9	122	48.1
Nd	793	700	899	752		740	624	731	397
Sm	314	386	378	430		339	360	333	233
Eu	21.3	17.5	20.0	19.5		18.4	15.4	17.1	15.9
Gd	321	454	392	498		359	433	346	355
Tb	54.0	76.4	66.3	84.7		60.5	73.5	59.6	64.8
Dy	323	448	390	496		354	430	348	437
Ho	62.2	85.5	75.1	94.1		67.5	81.2	66.4	95.6
Er	177	241	214	270		192	230	189	302
Tm	27.5	36.6	33.6	42.1		29.7	36.0	29.7	47.7
Yb	203	272	256	319		224	270	226	359
Lu	29.6	39.8	38.2	48.2		33.1	40.6	33.1	56.2
Hf	0.03	0.045	0.043	0.065		0.039	0.031	0.03	0.046
Ta	0.013	0.007	0.008	0.017		0.01	0.013	0.011	0.01
Pb	9.54	8.01	6.06	7.51		6.49	7.29	7.97	5.29
Th	37.5	37.6	42.8	73.7		27.8	46.5	37.4	61.0
U	19.1	22.5	21.3	30.6		17.7	24.5	18.9	30.2
<i>Volatile elements and isotopes</i>									
H ₂ O (wt.%)	0.716	0.592	0.525	0.480	0.489	0.502	0.555	0.554	0.509
±	0.066	0.060	0.057	0.055	0.055	0.056	0.058	0.058	0.050
CO ₂ (µg/g)	<30	<30	<30	47.5	<30	<30	<30	<30	<30
±				4.7					
S (µg/g)	<30	<30	<30	<30	<30	<30	<30	<30	<30
±									
δ ³⁴ S (‰)									
±									

(Continued.)

A. Supplementary Materials

Sample	CJ31								
Rock type	Aplite								
<i>Major elements (wt.%)</i>									
SiO ₂	0.11	0.16	0.12	0.13	0.15	0.12	0.11	0.11	0.15
FeO	0.03	0.02	0.04	0.02	0.02	0.01	0.03	0.03	0.03
CaO	55.44	55.88	56.31	55.77	56.28	56.28	56.21	56.20	55.90
Na ₂ O	0.06	0.05	0.08	0.04	0.06	0.04	0.06	0.05	0.07
P ₂ O ₅	42.02	41.96	41.66	41.13	41.52	41.38	41.17	41.35	41.34
F	2.46	2.59	2.32	2.36	2.37	2.50	2.41	2.56	2.45
Cl	0.09	0.08	0.07	0.06	0.08	0.06	0.09	0.10	0.10
Total	100.28	100.80	100.64	99.61	100.51	100.40	100.12	100.56	100.13
<i>Trace elements (µg/g)</i>									
Rb	0.427		0.5	0.363	0.472	0.569	0.443	0.258	0.559
Sr	136		125	136	115	124	137	133	138
Y	3087		3473	2828	2609	3131	2966	2148	2868
Zr	0.596		0.638	0.642	0.035	0.387	0.687	0.153	0.776
Nb			0.013		0.205		0.004	0.007	0.052
Ba	0.073		0.16	0.053	0.058	0.124	0.122	0.052	0.16
La	83.1		38.8	50.3	24.6	32.7	90.0	81.1	205.7
Ce	270		127	176	77	104	320	236	666
Pr	49.4		25.5	35.8	16.8	21.7	55.5	38.6	95.5
Nd	320		190	253	141	173	355	226	542
Sm	164		137	142	110	132	167	113	208
Eu	16.8		15.5	15.5	12.4	12.8	17.1	12.1	17.3
Gd	273		289	257	240	274	267	194	281
Tb	53.1		58.3	49.7	46.4	53.9	50.8	36.8	50.8
Dy	370		419	343	337	381	348	252	340
Ho	82.7		95.4	77.6	73.8	87.4	78.0	57.0	73.6
Er	257		303	244	231	274	244	177	230
Tm	40.0		47.1	38.0	33.2	40.8	38.6	27.2	37.0
Yb	302		350	278	223	290	283	198	280
Lu	46.7		55.2	44.6	36.7	46.0	44.6	33.1	44.3
Hf	0.033		0.032	0.042	0.089	0.036	0.033	0.021	0.035
Ta	0.008		0.009	0.003	0.04	0.013	0.01	0.008	0.009
Pb	6.23		5.54	5.59	3.44	5.26	6.08	5.27	5.28
Th	44.2		57.4	43.6	4.9	40.3	46.4	14.3	51.1
U	22.4		30.7	20.8	11.5	27.8	23.1	13.5	24.3
<i>Volatile elements and isotopes</i>									
H ₂ O (wt.%)	0.520	0.598	0.581	0.513	0.386	0.420	0.830	0.664	0.886
±	0.052	0.050	0.053	0.056	0.056	0.058	0.073	0.064	0.075
CO ₂ (µg/g)	56.4	<30	<30	<30	163.1	2601.0	<30	<30	54.3
±	32.0				31.8	134.7			5.4
S (µg/g)	30.1	<30	<30	<30	<30	30.5	<30	<30	105.2
±	26.0					26.1			10.7
δ ³⁴ S (‰)									
±									

(Continued.)

A.4. Supplementary Material to Chapter 5

Sample	CJ31	CJ31	CJ35	CJ35	CJ35	CJ35	CJ35	CJ35
Rock type	Aplite	Aplite	Gabbro	Gabbro	Gabbro	Gabbro	Gabbro	Gabbro
<i>Major elements (wt.%)</i>								
SiO ₂	0.15	0.20	0.19	0.14	0.24	0.17	0.11	0.05
FeO	0.04	0.03	0.02	0.01	0.01	0.03	0.02	0.02
CaO	55.48	55.08	55.97	56.20	55.91	55.66	56.12	56.43
Na ₂ O	0.04	0.05	0.00	0.00	0.00	0.03	0.02	0.01
P ₂ O ₅	40.37	40.18	42.02	42.39	41.72	42.05	41.13	41.29
F	2.29	2.18	2.48	2.61	2.30	2.06	2.11	2.17
Cl	0.11	0.11	0.09	0.09	0.15	0.18	0.14	0.14
Total	98.67	98.00	100.83	101.49	100.56	100.54	99.86	100.25
<i>Trace elements (µg/g)</i>								
Rb	0.225	0.309					0.11	0.142
Sr	173	156			148	264	167	163
Y	1757	2080			907	536	452	542
Zr	0.686	0.742			0.439		0.379	0.478
Nb	0.008	0.003			0.087	1.994		0.034
Ba	0.095	0.105			0.066		0.086	0.441
La	330.3	278.7			115.0	360.6	384.7	297.5
Ce	1029	917			646	1116	1375	1147
Pr	146	133			133	166	180	160
Nd	766	719			750	808	802	759
Sm	227	237			201	153	142	157
Eu	23.3	21.8			28.4	23.6	19.6	21.5
Gd	225	260			198	119	112	127
Tb	35.9	42.9			28.1	17.6	14.5	16.6
Dy	216	261			161	86	80	92
Ho	42.6	53.7			31.6	21.3	15.6	17.8
Er	126	160			90	45	42	49
Tm	19.7	25.1			11.8	5.8	5.6	6.8
Yb	149	189			76.3	49.9	37.1	43.8
Lu	22.5	28.8			12.1	4.7	5.5	6.7
Hf	0.033	0.022			0.031		0.011	0.014
Ta	0.004	0.008			0.01		0.007	0.005
Pb	5.89	5.65			4.31	81.76	6.08	12.24
Th	39.3	45.1			37.6	29.1	36.3	39.1
U	17.4	19.5			44.5	15.1	21.4	22.8
<i>Volatile elements and isotopes</i>								
H ₂ O (wt.%)	0.822	0.867	0.722	0.729	0.713	0.719	0.694	0.622
±	0.072	0.074	0.052	0.051	0.051	0.054	0.058	0.053
CO ₂ (µg/g)	<30	<30	<30	<30	<30	<30	40.1	78.5
±							30.2	30.3
S (µg/g)	<30	<30	32.7	43.1	63.3	34.5	79.3	992.3
±			26.1	26.1	26.3	26.0	26.1	73.9
δ ³⁴ S (‰)							1.61	
±							3.02	

(Continued.)

A. Supplementary Materials

Sample	CJ35							
Rock type	Gabbro							
<i>Major elements (wt.%)</i>								
SiO ₂	0.12	0.09	0.09	0.07	0.09	0.09	0.08	0.00
FeO	0.02	0.03	0.01	0.02	0.03	0.03	0.02	0.04
CaO	56.05	56.45	56.39	56.44	56.35	56.16	56.27	55.55
Na ₂ O	0.02	0.02	0.02	0.03	0.03	0.02	0.03	0.03
P ₂ O ₅	41.36	41.19	41.19	41.61	41.25	41.09	41.73	40.45
F	2.08	2.26	2.41	2.16	2.08	2.18	2.23	1.92
Cl	0.18	0.12	0.09	0.19	0.19	0.17	0.18	0.17
Total	100.10	100.34	100.31	100.78	100.26	99.99	100.76	98.35
<i>Trace elements (µg/g)</i>								
Rb		0.112	0.143	0.101	0.079	0.081	0.057	0.104
Sr	237	229	150	204	335	237	274	268
Y	536	740	987	465	505	485	408	532
Zr	0.623	0.693	0.278	0.511	0.544	0.557	0.423	0.57
Nb	0.006	0.02	0.052		0.006	0.025		0.009
Ba	0.216	0.25	0.131	0.142	0.239	0.21	0.14	0.258
La	591.0	450.5	99.2	463.3	646.7	520.9	578.5	485.8
Ce	1681	1398	587	1369	1716	1501	1558	1372
Pr	213	192	115	179	228	210	205	194
Nd	925	910	689	803	966	917	874	879
Sm	175	196	200	152	175	169	154	171
Eu	24.0	26.6	29.0	20.4	23.9	23.1	21.0	23.8
Gd	135	161	188	119	132	131	117	138
Tb	17.4	21.8	26.7	15.4	17.2	16.7	14.7	17.7
Dy	92	121	152	81	93	89	78	96
Ho	17.6	24.0	30.9	15.6	17.9	17.0	14.8	18.5
Er	47	66	87	42	48	46	38	49
Tm	6.1	8.9	11.6	5.6	6.3	6.0	4.9	6.4
Yb	38.9	58.0	77.3	35.7	40.9	39.3	30.5	40.8
Lu	5.7	8.4	11.7	5.3	6.1	5.9	4.4	6.0
Hf	0.019	0.018	0.015	0.009	0.009		0.003	0.011
Ta	0.005	0.007	0.004	0.002	0.002			0.002
Pb	6.46	6.22	4.85	6.08	7.09	6.98	6.42	6.58
Th	44.7	48.0	26.7	34.5	43.2	47.5	34.5	38.9
U	19.2	26.9	59.2	18.0	21.1	24.2	18.8	16.4
<i>Volatile elements and isotopes</i>								
H ₂ O (wt.%)	1.072	0.978	0.888	1.012	1.582	1.026	1.014	1.012
±	0.085	0.080	0.077	0.082	0.111	0.082	0.081	0.084
CO ₂ (µg/g)	92.3	<30	<30	57.6	<30	38.6	<30	182.3
±	9.3			6.0		4.3		16.9
S (µg/g)	40.7	<30	43.9	<30	<30	109.5	<30	703.5
±	4.2		4.5			11.5		73.9
δ ³⁴ S (‰)			5.66			8.87		
±			1.79			2.35		

(Continued.)

A.4. Supplementary Material to Chapter 5

Sample	CJ35	CJ35	CJ35	CJ12B	CJ12B	CJ12B	CJ12B	CJ12B
Rock type	Gabbro							
<i>Major elements (wt.%)</i>								
SiO ₂	0.09	0.10	0.10	0.13	0.11	0.11	0.12	0.07
FeO	0.02	0.05	0.03	0.03	0.07	0.06	0.10	0.09
CaO	55.65	55.57	56.38	55.57	55.61	55.64	56.17	56.20
Na ₂ O	0.04	0.04	0.01	0.02	0.02	0.03	0.04	0.01
P ₂ O ₅	40.58	40.92	40.57	41.06	41.87	41.46	41.03	41.30
F	1.92	1.92	2.48	2.08	1.97	1.93	2.13	2.19
Cl	0.17	0.18	0.11	0.37	0.38	0.41	0.40	0.38
Total	98.71	99.16	99.81	99.53	100.28	99.95	100.30	100.42
<i>Trace elements (µg/g)</i>								
Rb	0.091		0.092			0.187	0.149	0.073
Sr	333	340	174	242	247	237	248	237
Y	376	323	458	474	384	368	569	404
Zr	0.39	0.518	0.384	0.329	0.53	0.408	0.624	0.32
Nb	0.012	0.011	0.009	0.014		0.026		0.011
Ba	0.399	0.365	0.09	0.27	0.397	0.204	0.285	0.349
La	523.5	753.9	345.6	459.2	393.3	608.6	415.5	392.5
Ce	1340	1794	1140	1684	1398	1937	1425	1234
Pr	174	218	168	214	174	217	203	164
Nd	737	850	769	896	730	843	889	694
Sm	131	135	150	160	124	132	173	126
Eu	18.2	17.5	21.5	23.3	19.3	19.0	26.0	19.7
Gd	101	100	122	128	101	103	146	103
Tb	12.9	12.0	15.7	16.5	13.1	13.0	19.2	13.6
Dy	69	62	83	88	71	68	104	73
Ho	13.2	11.6	16.2	17.6	13.6	13.1	20.5	14.3
Er	36	30	43	46	38	35	55	38
Tm	4.7	3.8	5.6	5.9	4.7	4.5	7.1	5.0
Yb	30.5	23.3	36.3	36.2	28.8	28.6	44.3	31.7
Lu	4.6	3.3	5.3	5.3	4.4	4.2	6.7	4.9
Hf	0.007	0.005	0.004		0.009	0.005	0.013	0.004
Ta	0.002		0.002			0.002	0.004	0.002
Pb	6.38	6.39	5.81	2.89	3.41	3.19	3.57	3.53
Th	27.2	37.3	33.8	45.5	32.2	39.5	48.6	28.5
U	14.9	16.0	20.2	62.3	38.7	28.5	42.1	49.2
<i>Volatile elements and isotopes</i>								
H ₂ O (wt.%)	0.920	0.958	0.842	0.627	0.638	0.717	0.830	0.811
±	0.081	0.081	0.075	0.053	0.052	0.051	0.088	0.080
CO ₂ (µg/g)	<30	81.8	<30	33.8	<30	<30	<30	<30
±		7.9		30.2				
S (µg/g)	<30	369.5	49.3	137.0	50.9	56.8	30.5	42.0
±		46.5	5.1	29.3	26.0	26.0	3.2	4.5
δ ³⁴ S (‰)		4.51	9.86	7.14	4.18			5.33
±		1.67	0.85	1.60	2.05			1.73

(Continued.)

A. Supplementary Materials

Sample	CJ10A	CJ10A	CJ10A	CJ26	CJ26	CJ26	CJ26	CJ26
Rock type	Tonalite							
<i>Major elements (wt.%)</i>								
SiO ₂	0.05	0.01	0.11	0.19	0.12	0.08	0.11	0.09
FeO	0.02	0.01	0.04	0.01	0.03	0.03	0.03	0.00
CaO	56.06	56.49	55.85	56.25	55.64	55.41	55.97	55.96
Na ₂ O	0.00	0.02	0.00	0.01	0.02	0.02	0.03	0.03
P ₂ O ₅	42.14	41.21	41.28	41.87	40.98	41.56	41.45	41.20
F	2.25	2.14	2.12	2.44	2.12	2.28	2.16	2.40
Cl	0.36	0.41	0.39	0.13	0.15	0.13	0.14	0.15
Total	101.01	100.41	100.03	101.11	99.30	99.69	100.04	99.90
<i>Trace elements (µg/g)</i>								
Rb			0.052		0.126	0.245	0.206	0.067
Sr	196	211	208	207	279	283	199	221
Y	518	216	289	965	726	725	1078	630
Zr	0.25	0.028	0.27	0.663	0.466	0.436	0.683	0.564
Nb	0.027		0.011	0.048	0.01	0.024	0.013	0.011
Ba	0.162	0.21	0.233	2.299	0.532	0.431	0.177	0.176
La	153.8	99.2	319.3	282.4	309.3	286.6	162.3	229.2
Ce	545	355	835	1064	1142	1040	621	808
Pr	91.8	55.0	105	173	170	159	120	130
Nd	468	264	440	940	841	801	694	662
Sm	115	57	84	233	201	196	218	167
Eu	22.6	8.3	15.7	28.2	23.3	22.9	28.6	18.5
Gd	109	52	75	216	176	175	221	149
Tb	15.6	6.9	9.6	29.0	24.1	24.0	32.4	20.3
Dy	89	38	52	169	132	133	187	112
Ho	18.1	7.6	10.4	33.0	25.9	25.8	36.9	21.7
Er	49	20	28	93	70	70	103	59
Tm	6.4	2.6	3.6	12.3	9.0	9.0	14.0	7.6
Yb	41.8	16.2	23.2	83	59	58	94	48
Lu	6.3	2.4	3.7	11.8	8.3	8.5	13.7	6.9
Hf	0.016	0.003	0.004			0.012	0.008	0.004
Ta	0.006	0.001	0.002	0.008	0.002			0.001
Pb	2.31	2.64	2.91	5.11	6.13	6.34	4.79	4.42
Th	14.2	3.2	30.3	52.7	40.3	37.4	42.8	39.8
U	70.3	13.9	44.6	35.1	29.6	37.1	28.7	18.5
<i>Volatile elements and isotopes</i>								
H ₂ O (wt.%)	0.608	0.840	1.060	0.616	0.646	0.561	0.600	0.739
±	0.052	0.076	0.092	0.056	0.054	0.054	0.053	0.107
CO ₂ (µg/g)	<30	<30	65.1	<30	50.9	45.6	49.0	113.4
±			6.3		30.2	30.1	30.1	10.7
S (µg/g)	204.2	<30	248.3	<30	115.8	146.4	48.2	949.8
±	26.3		25.1		26.3	26.2	26.0	95.7
δ ³⁴ S (‰)	8.09				7.27		3.60	
±	1.26				1.58		3.00	

(Continued.)

A.4. Supplementary Material to Chapter 5

Sample	CJ26	CJ26	CJ26	CJ26	CJ26	CJ26	CJ48	CJ48
Rock type	Tonalite							
<i>Major elements (wt.%)</i>								
SiO ₂	0.13	0.14	0.14	0.15	0.10	0.15	0.13	0.09
FeO	0.03	0.01	0.03	0.03	0.03	0.01	0.01	0.03
CaO	56.20	56.09	55.25	55.11	55.84	55.25	56.06	55.60
Na ₂ O	0.02	0.01	0.02	0.02	0.03	0.02	0.03	0.04
P ₂ O ₅	41.15	40.98	41.60	41.36	41.57	41.86	41.93	41.01
F	2.32	2.47	2.18	2.34	2.13	2.22	2.52	2.32
Cl	0.16	0.12	0.14	0.09	0.14	0.15	0.14	0.15
Total	100.18	99.92	99.61	99.26	99.99	99.88	100.94	99.35
<i>Trace elements (µg/g)</i>								
Rb	0.124	0.117	0.064	0.185	0.118	0.147	0.309	0.175
Sr	214	225	258	244	237	265	190	203
Y	981	935	659	1038	771	813	1323	1085
Zr	0.634	0.43	0.432	0.74	0.384	0.894	0.566	0.27
Nb		0.006	0.007	0.011		0.029		
Ba	0.128	0.167	0.493	0.709	0.331	0.422	0.087	0.036
La	180.9	200.2	386.7	376.8	251.2	471.8	160.5	170.9
Ce	693	741	1193	1203	856	1407	609	792
Pr	122	125	177	186	134	206	120	137
Nd	671	683	859	951	701	1003	723	780
Sm	203	196	195	242	183	229	239	228
Eu	25.6	23.7	19.9	26.6	19.2	23.4	26.5	22.9
Gd	204	193	166	222	167	197	253	240
Tb	29.5	27.3	21.9	30.6	23.1	26.2	38.3	33.5
Dy	170	157	120	173	130	143	227	194
Ho	33.9	31.1	22.9	33.8	25.5	27.8	44.9	38.6
Er	94	86	61	93	69	74	130	105
Tm	13.0	11.6	7.8	12.4	9.1	9.8	18.0	13.6
Yb	82	76	49	82	60	61	118	89
Lu	12.3	11.3	7.1	12.1	8.7	8.8	17.7	12.8
Hf	0.024	0.017	0.016	0.023	0.007	0.014	0.007	
Ta	0.005	0.004	0.003	0.003	0.003	0.007	0.009	0.013
Pb	5.41	4.78	5.26	5.35	4.92	5.59	4.52	3.65
Th	45.0	39.0	32.7	45.8	29.6	40.5	53.1	31.7
U	30.3	33.1	20.2	32.7	24.5	17.8	42.3	66.4
<i>Volatile elements and isotopes</i>								
H ₂ O (wt.%)	0.921	0.633	0.928	0.618	1.189	0.970	0.669	0.561
±	0.123	0.099	0.127	0.099	0.141	0.130	0.050	0.052
CO ₂ (µg/g)	44.7	<30	34.5	35.7	<30	<30	<30	<30
±	4.7		3.6	3.7				
S (µg/g)	69.9	29.5	<30	31.1	<30	<30	38.9	31.1
±	7.4	3.1		3.2			26.1	26.0
δ ³⁴ S (‰)		1.21						
±		2.22						

(Continued.)

A. Supplementary Materials

Sample	CJ48							
Rock type	Tonalite							
<i>Major elements (wt.%)</i>								
SiO ₂	0.17	0.23	0.10	0.13	0.06	0.13	0.10	0.12
FeO	0.04	0.04	0.03	0.01	0.00	0.02	0.02	0.03
CaO	55.86	55.41	56.29	56.05	55.99	56.08	56.27	56.03
Na ₂ O	0.02	0.02	0.03	0.01	0.04	0.02	0.02	0.01
P ₂ O ₅	41.00	40.79	41.24	41.14	41.22	41.37	41.14	41.10
F	2.39	2.21	2.36	2.49	2.40	2.30	2.38	2.36
Cl	0.13	0.12	0.14	0.12	0.11	0.12	0.13	0.12
Total	99.71	99.05	100.23	100.02	99.90	100.15	100.22	99.85
<i>Trace elements (µg/g)</i>								
Rb	0.148	0.263	0.529	0.206	0.258	0.139	0.172	0.228
Sr	204	204	210	196	184	219	243	213
Y	1173	1118	1251	1255	1415	1290	948	1317
Zr	0.52	0.547	0.634	0.36	0.379	0.615	0.516	0.672
Nb		0.017	0.033	0.004	0.008	0.009	0.044	0.009
Ba	0.213	0.268	0.735	0.093	0.087	0.225	0.637	0.229
La	163.6	198.7	238.2	160.9	123.1	293.4	372.7	308.1
Ce	582	743	878	642	539	991	1110	1011
Pr	111	129	147	114	105	163	165	161
Nd	657	731	818	677	653	877	821	866
Sm	213	222	242	220	229	251	206	248
Eu	22.2	22.9	24.3	22.7	23.2	25.3	21.8	26.4
Gd	229	228	242	228	248	244	186	246
Tb	33.9	33.1	35.1	34.2	37.3	35.5	26.6	35.7
Dy	200	193	204	197	222	206	151	207
Ho	39.9	38.3	40.5	40.2	45.4	40.9	29.4	41.2
Er	113	107	111	113	130	114	80	115
Tm	15.6	14.3	15.1	15.4	18.1	15.3	11.0	15.7
Yb	105	94	98	104	126	100	73	103
Lu	15.3	13.5	14.2	15.3	18.9	14.5	10.3	14.9
Hf	0.009	0.013	0.025	0.019	0.019	0.014	0.011	0.019
Ta	0.01	0.004	0.019	0.005	0.007	0.005	0.005	0.006
Pb	5.57	5.30	4.34	4.06	4.04	5.67	8.39	5.68
Th	35.0	48.4	47.0	36.5	43.3	43.9	42.7	51.6
U	30.7	24.8	25.9	32.2	46.1	20.9	17.8	21.3
<i>Volatile elements and isotopes</i>								
H ₂ O (wt.%)	0.663	0.586	0.567	0.686	0.540	0.938	1.019	0.738
±	0.052	0.052	0.087	0.083	0.092	0.135	0.081	0.067
CO ₂ (µg/g)	<30	38.7	<30	<30	78.0	<30	133.5	<30
±		30.1			7.5		13.0	
S (µg/g)	<30	136.8	<30	<30	116.3	<30	884.4	<30
±		26.1			11.8		95.0	
δ ³⁴ S (‰)		9.02			4.33			5.63
±		0.83			4.24			1.58

(Continued.)

A.4. Supplementary Material to Chapter 5

Sample	CJ48	CJ48	CJ48	CJ48	CJ2A	CJ2A	CJ2A	CJ2A
Rock type	Tonalite	Tonalite	Tonalite	Tonalite	Leucoto.	Leucoto.	Leucoto.	Leucoto.
<i>Major elements (wt.%)</i>								
SiO ₂	0.13	0.37	0.13	0.00	0.19	0.12	0.15	0.05
FeO	0.03	0.32	0.03	0.00	0.00	0.04	0.04	0.01
CaO	56.20	55.52	56.12	56.45	55.70	55.55	55.26	55.67
Na ₂ O	0.02	0.01	0.02	0.02	0.03	0.04	0.05	0.04
P ₂ O ₅	40.96	40.26	40.87	41.64	41.88	41.96	42.02	42.32
F	2.26	2.39	2.27	2.50	2.73	2.35	2.37	2.59
Cl	0.13	0.12	0.14	0.12	0.07	0.12	0.12	0.11
Total	99.92	99.17	99.72	100.78	100.76	100.30	100.17	101.03
<i>Trace elements (µg/g)</i>								
Rb	0.218	0.215	0.213	0.06	0.252	0.316	0.279	0.139
Sr	194	186	193	179	179	173	154	230
Y	1366	1352	1514	578	1435	1957	1956	903
Zr	0.583	0.471	0.797	0.041	0.658	0.582	0.535	0.422
Nb	0.01	0.005	0.013	0.025	0.018			
Ba	0.122	0.067	0.186	0.093	0.066	0.067	0.063	0.083
La	192.1	139.7	194.5	49.7	302.1	199.4	154.1	464.5
Ce	737	560	769	210	1043	794	605	1471
Pr	131	105	140	45.8	155	143	117	198
Nd	763	641	828	298	825	831	705	947
Sm	241	220	261	104	242	291	266	208
Eu	25.4	23.8	27.9	10.2	22.0	25.1	18.8	19.0
Gd	253	238	272	115	250	311	302	183
Tb	37.4	36.0	41.0	16.7	37.2	47.8	46.7	25.4
Dy	218	211	239	97	218	284	279	142
Ho	44.0	43.2	48.4	19.4	43.5	57.0	56.6	27.1
Er	122	121	136	54	126	161	160	76
Tm	16.4	16.8	19.0	7.2	18.2	22.8	23.0	10.9
Yb	111	114	128	47	129	158	156	74
Lu	16.0	17.0	18.9	6.8	19.5	23.2	22.8	10.7
Hf	0.033	0.015	0.028	0.011		0.03	0.036	0.019
Ta	0.005	0.007	0.006	0.004	0.003	0.004	0.009	0.006
Pb	4.74	4.40	5.03	3.53	5.76	6.17	5.71	7.30
Th	49.7	36.9	54.2	5.2	38.3	51.9	40.1	30.5
U	29.4	41.2	30.2	16.6	20.2	36.0	31.2	15.0
<i>Volatile elements and isotopes</i>								
H ₂ O (wt.%)	0.845	0.850	0.875	0.730	0.639	0.644	0.540	0.629
±	0.073	0.073	0.074	0.067	0.050	0.050	0.051	0.052
CO ₂ (µg/g)	<30	<30	42.9	38.3	31.8	<30	<30	<30
±			4.4	4.2	30.1			
S (µg/g)	<30	<30	31.6	<30	<30	30.3	<30	<30
±			3.3			26.0		
δ ³⁴ S (‰)	1.93				0.55			
±	2.04				2.34			

(Continued.)

A. Supplementary Materials

Sample	CJ2A							
Rock type	Leucoto.							
<i>Major elements (wt.%)</i>								
SiO ₂	0.00	0.16	0.13	0.14	0.13	0.15	0.13	0.12
FeO	0.02	0.02	0.04	0.02	0.01	0.04	0.05	0.03
CaO	56.06	55.92	55.99	56.12	56.32	56.26	56.15	56.23
Na ₂ O	0.05	0.02	0.04	0.05	0.06	0.03	0.04	0.05
P ₂ O ₅	42.19	41.83	41.20	41.71	41.62	41.12	41.56	41.47
F	2.69	2.47	2.52	2.45	2.55	2.48	2.44	2.46
Cl	0.07	0.10	0.11	0.09	0.09	0.08	0.11	0.10
Total	101.17	100.73	100.31	100.86	100.93	100.43	100.77	100.71
<i>Trace elements (µg/g)</i>								
Rb		0.193	0.3	0.243	0.256	0.235	0.288	0.212
Sr	155	198	191	198	187	193	177	194
Y	687	1319	1559	1530	1697	1663	1856	1561
Zr		0.642	0.598	0.798	0.57	0.851	0.882	0.929
Nb	0.06	0.015	0.012			0.005	0.008	0.007
Ba	1.045	0.179	0.263	0.102	0.125	0.183	0.132	0.215
La	56.6	370.0	382.1	425.5	304.8	408.7	340.4	482.4
Ce	228	1304	1153	1267	933	1276	1034	1437
Pr	47.6	195	170	186	140	196	157	214
Nd	302	1005	883	912	745	1006	837	1004
Sm	111	271	246	242	225	285	264	249
Eu	8.4	25.5	19.7	20.3	17.4	24.9	20.1	25.0
Gd	129	259	243	234	240	280	284	231
Tb	19.2	38.1	37.1	35.1	37.9	41.9	44.3	34.7
Dy	107	217	220	207	230	244	263	203
Ho	21.5	42.0	45.0	42.2	48.4	48.8	54.2	41.0
Er	57	116	133	124	145	139	155	122
Tm	7.9	16.0	20.7	19.0	22.4	20.4	22.4	18.8
Yb	52	108	156	143	164	144	154	142
Lu	7.5	15.0	24.7	21.8	25.2	21.2	22.8	21.5
Hf		0.034	0.034	0.024	0.03	0.025	0.034	0.025
Ta	0.008	0.003	0.007	0.005	0.006	0.007	0.008	0.005
Pb	4.94	6.57	6.26	5.90	5.78	6.05	6.29	6.48
Th	6.1	46.6	36.5	34.0	28.2	51.1	47.0	61.3
U	6.9	24.5	19.2	18.3	17.3	26.7	24.1	27.3
<i>Volatile elements and isotopes</i>								
H ₂ O (wt.%)	0.596	0.524	0.808	0.829	0.780	0.766	0.738	0.772
±	0.052	0.052	0.071	0.072	0.070	0.069	0.068	0.070
CO ₂ (µg/g)	89.4	39.7	40.1	<30	<30	<30	<30	256.8
±	30.6	30.1	4.0					53.2
S (µg/g)	37.4	<30	<30	<30	<30	<30	<30	<30
±	26.1							
δ ³⁴ S (‰)								
±								

(Continued.)

A.4. Supplementary Material to Chapter 5

Sample	CJ2A	CJ2A	CJ2A	CJ2A	CJ2A	WA21-19	WA21-19	WA21-19
Rock type	Leucoto.							
<i>Major elements (wt.%)</i>								
SiO ₂	0.12	0.13	0.18	0.15	0.08	0.16	0.00	0.16
FeO	0.06	0.04	0.05	0.06	0.03	0.00	0.02	0.02
CaO	50.88	55.54	55.30	55.75	55.76	54.81	54.34	54.95
Na ₂ O	0.04	0.04	0.07	0.04	0.05	0.05	0.04	0.07
P ₂ O ₅	39.38	39.40	39.77	39.27	40.18	41.83	42.64	42.57
F	2.56	2.36	2.27	2.29	2.30	2.30	2.65	2.29
Cl	0.08	0.07	0.12	0.10	0.09	0.08	0.07	0.05
Total	93.31	97.71	98.15	97.88	98.71	99.38	99.80	100.23
<i>Trace elements (µg/g)</i>								
Rb	0.238	0.161	0.167	0.146	0.183	0.369	0.166	0.497
Sr	260	199	250	239	209	184	186	162
Y	1015	857	865	1146	1531	2262	1798	2723
Zr	0.687	0.204	0.729	0.692	0.38	0.62	0.642	0.894
Nb	0.01	0.02	0.013	0.012	0.024	0.01		
Ba	0.61	0.037	0.436	0.379	0.12	0.093	0.122	
La	639.6	318.6	816.8	574.9	339.7	299.1	182.1	223.5
Ce	1697	1021	2140	1581	1039	955	636	691
Pr	228	148	289	220	151	138	111	117
Nd	1017	736	1207	1024	779	723	637	643
Sm	222	180	239	235	212	233	229	244
Eu	20.3	15.8	22.1	21.5	18.3	16.9	20.3	15.4
Gd	190	160	194	209	211	261	261	303
Tb	26.1	22.8	25.6	29.4	32.9	44.0	42.9	52.6
Dy	145	128	137	168	196	275	261	335
Ho	28.5	25.0	26.0	33.5	41.0	56.3	53.1	67.9
Er	78	69	70	97	123	170	151	203
Tm	11.3	9.9	9.6	14.5	19.3	27.3	21.9	32.3
Yb	76	70	65	109	145	215	158	248
Lu	10.9	10.2	9.5	16.7	22.1	33.9	23.2	38.7
Hf	0.02	0.022	0.019	0.013	0.031	0.035	0.046	
Ta	0.002	0.004	0.005	0.006	0.01	0.006	0.005	0.015
Pb	6.44	2.72	6.63	6.39	6.51	5.40	5.65	4.54
Th	40.2	17.5	51.4	39.0	31.1	39.0	40.7	55.5
U	17.8	12.9	21.3	18.0	17.2	16.7	23.0	22.9
<i>Volatile elements and isotopes</i>								
H ₂ O (wt.%)	0.713	0.691	0.758	0.705	0.769	0.527	0.511	0.520
±	0.067	0.065	0.068	0.065	0.069	0.031	0.031	0.031
CO ₂ (µg/g)	31.0	66.7	35.1	<30	<30	38.8	41.0	70.9
±	3.4	6.5	3.6			4.8	5.4	14.8
S (µg/g)	<30	214.4	<30	<30	<30	<30	<30	74.0
±		21.8						32.7
δ ³⁴ S (‰)		9.44	10.92					
±		1.52	0.77					

(Continued.)

A. Supplementary Materials

Sample Rock type	WA21-19 Leucoto.						
<i>Major elements (wt.%)</i>							
SiO ₂	0.00	0.10	0.15	0.12	0.13	0.21	0.02
FeO	0.05	0.02	0.02	0.02	0.00	0.02	0.03
CaO	54.70	54.84	54.86	55.09	55.00	54.83	55.23
Na ₂ O	0.06	0.08	0.06	0.10	0.07	0.09	0.03
P ₂ O ₅	42.32	42.96	42.23	41.55	41.47	42.08	41.74
F	2.30	2.36	2.21	2.33	2.30	2.33	2.51
Cl	0.08	0.07	0.08	0.07	0.08	0.06	0.08
Total	99.60	100.49	99.78	99.37	99.13	99.72	99.73
<i>Trace elements (µg/g)</i>							
Rb	0.309	0.318	0.349	0.31	0.319	0.389	0.068
Sr	169	166	163	173	170	162	210
Y	2620	2653	2544	2360	2485	3045	734
Zr	0.795	0.678	0.79	0.413	0.501	0.441	0.086
Nb	0.016			0.006	0.007	0.01	
Ba				0.04	0.016	0.031	0.058
La	226.0	208.3	250.7	225.8	160.6	141.2	186.2
Ce	764	631	855	714	540	456	607
Pr	126	101	133	108	87.9	74.7	92.3
Nd	714	556	725	572	507	439	482
Sm	262	203	251	193	196	187	135
Eu	17.1	14.9	17.2	14.4	15.4	15.1	12.7
Gd	311	263	296	252	255	280	134
Tb	52.7	46.2	50.2	43.4	45.0	52.0	19.5
Dy	332	300	315	281	287	345	114
Ho	69.4	63.7	64.3	61.3	60.4	75.8	22.9
Er	210	196	193	189	188	239	65
Tm	33.2	32.4	30.6	30.6	30.8	40.0	9.4
Yb	254	254	234	239	248	316	68
Lu	40.1	40.9	36.8	38.3	39.3	50.4	10.4
Hf	0.021	0.033	0.043	0.031	0.039	0.018	0.011
Ta	0.012	0.008	0.007	0.01	0.01	0.008	
Pb	5.57	5.39	4.96	5.65	4.88	5.27	4.83
Th	53.5	37.5	50.3	39.3	48.3	53.0	8.8
U	25.8	14.9	21.7	23.9	21.8	27.1	7.1
<i>Volatile elements and isotopes</i>							
H ₂ O (wt.%)	0.512	0.510	0.539	0.529	0.594	0.623	0.506
±	0.030	0.031	0.031	0.031	0.032	0.032	0.031
CO ₂ (µg/g)	30.9	74.3	275.6	68.9	39.4	42.1	<30
±	3.3	6.9	28.4	6.8	4.2	5.5	
S (µg/g)	<30	98.6	32.9	<30	74.0	<30	<30
±		32.1	32.0		32.2		
δ ³⁴ S (‰)					7.05		
±					1.92		

(Continued.)

A.4. Supplementary Material to Chapter 5

Sample	WA21-19	WA21-19	WA21-19	WA21-19	WA21-19	LR22-9	LR22-9
Rock type	Leucoto.	Leucoto.	Leucoto.	Leucoto.	Leucoto.	LGD	LGD
<i>Major elements (wt.%)</i>							
SiO ₂	0.14	0.11	0.18	0.14	0.07	0.16	0.14
FeO	0.74	0.02	0.00	0.00	0.02	0.03	0.00
CaO	54.38	54.82	54.93	55.07	54.92	54.43	54.58
Na ₂ O	0.06	0.08	0.07	0.07	0.08	0.18	0.10
P ₂ O ₅	41.11	41.91	41.67	41.53	42.06	41.28	42.37
F	2.31	2.24	2.33	2.42	2.30	2.01	2.04
Cl	0.11	0.09	0.07	0.06	0.06	0.18	0.15
Total	99.08	99.50	99.33	99.38	99.68	98.71	99.80
<i>Trace elements (µg/g)</i>							
Rb	0.234	0.301	0.455	0.386	0.322	n.d.	n.d.
Sr	182	211	174	160	192	164	177
Y	1970	1703	2540	2715	2304	321	391
Zr	0.548	0.638	0.61	0.308	0.431	1.515	1.382
Nb	0.011		0.013	0.04	0.022	0.01	n.d.
Ba	0.12	0.182	0.031	0.046	0.11	0.049	0.194
La	320.4	438.3	223.2	156.2	158.3	1170.2	1409.3
Ce	962	1208	721	543	456	2429	2875
Pr	134	162	110	91.2	69.9	236	281
Nd	670	774	605	538	390	859	1019
Sm	206	205	206	206	146	123	146
Eu	14.3	16.5	16.1	15.0	11.7	14.4	17.4
Gd	246	217	257	279	204	96	113
Tb	40.7	34.8	44.6	49.0	37.3	11.5	13.8
Dy	254	212	288	318	249	61	72
Ho	52.9	44.1	60.8	68.2	54.8	11.6	14.0
Er	161	132	193	215	177	30.1	37.7
Tm	25.5	21.2	33.1	35.5	30.2	3.9	4.7
Yb	193	164	271	285	245	24	31
Lu	30.1	25.4	44.3	46.0	40.3	3.5	4.7
Hf	0.035	0.021	0.024	0.042	0.034	0.011	0.011
Ta	0.004	0.006	0.007	0.011	0.006	n.d.	n.d.
Pb	5.60	5.78	5.23	3.28	5.55	3.59	3.52
Th	34.9	34.4	46.7	36.2	19.4	35.7	60.8
U	18.1	14.7	20.7	17.9	10.9	10.5	13.7
<i>Volatile elements and isotopes</i>							
H ₂ O (wt.%)	0.610	0.555	0.610	0.570	0.594	0.569	0.437
±	0.031	0.030	0.031	0.032	0.034	0.031	0.030
CO ₂ (µg/g)	50.8	<30	42.0	37.7	88.4	95.5	<30
±	5.4		4.4	4.7	8.0	8.8	
S (µg/g)	40.6	<30	29.9	31.8	29.2	1263.2	404.8
±	32.0		32.0	32.1	32.1	35.3	32.3
δ ³⁴ S (‰)						7.08	
±						0.46	

(Continued.)

A. *Supplementary Materials*

Sample	LR22-9							
Rock type	LGD							
<i>Major elements (wt.%)</i>								
SiO ₂	0.15	0.07	0.16	0.10	0.20	0.11	0.09	0.03
FeO	0.01	0.02	0.01	0.02	0.00	0.00	0.02	0.02
CaO	54.76	54.86	54.76	54.75	54.95	55.43	54.75	54.99
Na ₂ O	0.04	0.09	0.07	0.08	0.21	0.09	0.17	0.06
P ₂ O ₅	41.86	42.52	42.68	41.95	41.46	41.18	41.23	41.60
F	2.03	2.03	2.44	2.03	2.09	2.24	1.91	2.06
Cl	0.17	0.18	0.15	0.19	0.19	0.19	0.21	0.17
Total	99.21	100.13	100.63	99.45	99.40	99.58	98.92	99.22
<i>Trace elements (µg/g)</i>								
Rb	n.d.	n.d.		n.d.	n.d.	n.d.	n.d.	n.d.
Sr	151	163		157	144	249	281	167
Y	292	299		303	340	251	308	225
Zr	0.389	0.64		0.613	0.391	0.526	0.684	0.793
Nb	n.d.	n.d.		n.d.	n.d.	n.d.	n.d.	0.016
Ba	0.224	0.138		0.101	0.123	0.146	0.026	0.085
La	809.1	1143.0		1084.1	812.4	1270.2	1545.5	1138.5
Ce	1485	2320		2188	1765	2392	2946	2200
Pr	135	226		212	179	227	280	208
Nd	515	807		777	687	788	953	738
Sm	81	116		112	108	106	129	96
Eu	14.5	12.8		12.9	11.7	14.1	17.4	12.7
Gd	69	86		88	88	78	96	72
Tb	9.0	10.4		10.7	11.1	9.2	11.1	8.3
Dy	48	55		56	60	48	58	43
Ho	10.4	10.5		10.9	12.1	9.1	11.2	8.3
Er	28.2	27.7		28.8	31.5	23.7	28.0	21.7
Tm	3.7	3.5		3.5	4.0	2.9	3.5	2.7
Yb	28	23		22	29	19	22	17
Lu	5.1	3.5		3.5	4.8	2.8	3.1	2.5
Hf	n.d.	n.d.		0.018	n.d.	0.007	0.011	0.016
Ta	0.008	n.d.		0.003	n.d.	0.001	n.d.	0.002
Pb	2.83	3.11		3.00	2.64	3.69	3.57	3.26
Th	38.6	44.5		42.4	43.8	39.7	49.0	35.6
U	26.4	11.5		12.1	15.5	10.5	13.1	12.4
<i>Volatile elements and isotopes</i>								
H ₂ O (wt.%)	0.440	0.442	0.385	0.407	0.441	0.581	0.595	0.569
±	0.033	0.034	0.031	0.035	0.032	0.031	0.031	0.031
CO ₂ (µg/g)	149.6	<30	<30	<30	3732.0	35.7	34.8	<30
±	71.4				942.1	3.7	3.7	
S (µg/g)	505.2	381.9	425.6	380.9	862.4	427.0	369.5	122.6
±	32.8	32.3	32.4	32.4	35.6	32.2	32.3	32.1
δ ³⁴ S (‰)		5.20		5.07	5.42	5.09	5.17	5.14
±		0.87		0.70	0.56	0.73	0.66	0.68

(Continued.)

A.4. Supplementary Material to Chapter 5

Sample	LR22-9	LR22-9	LR22-9	LR22-9	LR22-9	LR22-9	LR22-3	LR22-3
Rock type	LGD	LGD	LGD	LGD	LGD	LGD	LRT	LRT
<i>Major elements (wt.%)</i>								
SiO ₂	0.10	0.12	0.10	0.14	0.04	0.06	0.11	0.17
FeO	0.00	0.01	0.02	0.03	0.00	0.02	0.03	0.01
CaO	54.90	55.04	54.99	54.85	55.02	54.95	55.43	55.08
Na ₂ O	0.09	0.13	0.10	0.09	0.11	0.11	0.05	0.04
P ₂ O ₅	41.43	41.54	41.53	41.42	41.58	41.50	42.10	42.12
F	1.94	1.98	1.94	2.02	2.04	2.00	1.75	1.57
Cl	0.19	0.19	0.20	0.18	0.17	0.21	0.23	0.25
Total	99.15	99.36	99.22	99.11	99.35	99.29	99.75	99.29
<i>Trace elements (µg/g)</i>								
Rb	0.1	n.d.	n.d.	0.077	0.119	0.128	n.d.	0.203
Sr	155	209	240	142	261	154	222	264
Y	275	347	292	280	233	199	354	647
Zr	0.453	0.686	0.52	0.421	0.383	0.306	0.275	0.249
Nb	0.008	0.012	n.d.	0.012	n.d.	n.d.	0.023	0.033
Ba	0.093	0.221	0.166	0.071	0.156	0.644	0.118	n.d.
La	1076.7	935.0	930.8	1056.8	1252.4	742.5	94.0	94.6
Ce	2196	1958	1899	2326	2354	1524	302	446
Pr	213	206	194	232	220	151	52.6	85.7
Nd	737	781	726	835	760	552	295	484
Sm	98	130	113	114	101	79	82	136
Eu	13.6	21.5	18.0	14.1	13.9	10.7	11.7	18.6
Gd	74	103	86	83	74	60	88	142
Tb	8.7	12.6	10.5	10.0	8.8	7.3	11.8	20.2
Dy	46	66	55	52	45	38	66	112
Ho	9.2	12.6	10.4	9.9	8.5	7.2	13.3	22.1
Er	25.4	33.1	27.3	26.1	22.2	19.6	35.0	61.8
Tm	3.4	4.1	3.5	3.3	2.6	2.4	4.3	8.0
Yb	23	26	21	21	16	15	25	52
Lu	3.7	3.8	3.2	3.1	2.3	2.3	3.8	7.6
Hf	0.008	0.004	0.011	0.003	0.004	0.005	0.016	0.018
Ta	0.002	n.d.	n.d.	n.d.	0.003	0.001	0.002	0.002
Pb	2.83	3.59	3.78	2.78	3.58	3.58	2.52	2.20
Th	43.1	41.5	30.4	33.0	24.2	31.6	25.4	26.8
U	17.0	16.5	13.0	13.6	8.2	12.2	22.2	25.8
<i>Volatile elements and isotopes</i>								
H ₂ O (wt.%)	0.595	0.627	0.587	0.618	0.620	0.582	0.703	0.729
±	0.031	0.032	0.031	0.032	0.033	0.031	0.034	0.033
CO ₂ (µg/g)	33.2	40.0	30.8	31.7	35.1	35.3	40.3	43.2
±	3.5	4.2	3.7	3.4	3.7	3.7	4.1	4.7
S (µg/g)	534.2	442.3	420.4	367.2	308.9	449.5	506.5	376.0
±	39.6	32.6	32.3	32.3	32.3	32.6	32.8	32.5
δ ³⁴ S (‰)	5.58	6.44		5.70	7.87	6.17	5.78	
±	0.65	0.99		0.71	0.70	0.62	0.62	

(Continued.)

A. Supplementary Materials

Sample	LR22-3							
Rock type	LRT							
<i>Major elements (wt.%)</i>								
SiO ₂	0.05	0.06	0.09	0.19	0.13	0.13	0.10	0.14
FeO	0.03	0.04	0.01	0.02	0.01	0.02	0.02	0.02
CaO	55.19	55.25	55.05	55.00	55.20	55.41	55.56	55.31
Na ₂ O	0.02	0.03	0.06	0.09	0.04	0.02	0.02	0.02
P ₂ O ₅	42.14	42.02	42.26	41.89	42.43	41.87	41.91	41.81
F	1.97	1.80	2.03	1.70	1.65	1.82	1.81	1.79
Cl	0.26	0.22	0.24	0.24	0.25	0.24	0.20	0.22
Total	99.69	99.47	99.84	99.23	99.79	99.64	99.67	99.36
<i>Trace elements (µg/g)</i>								
Rb	0.236	0.152	0.116	n.d.	n.d.	0.094	n.d.	n.d.
Sr	228	231	227	236	216	243	224	214
Y	456	424	520	517	598	490	524	340
Zr	0.171	0.198	0.346	0.442	0.219	0.397	0.344	0.165
Nb	0.014	0.032	n.d.	0.022	0.103	0.015	0.035	0.052
Ba	0.085	0.284	0.157	0.325	0.093	0.173	0.159	0.154
La	212.7	90.1	237.4	192.6	101.4	278.5	115.2	79.9
Ce	644	329	795	604	425	942	497	255
Pr	97.4	58.3	116	92.3	79.3	132	90.2	43.2
Nd	480	324	563	465	448	625	495	243
Sm	116	92	134	115	128	136	126	69
Eu	12.5	15.8	16.1	17.5	15.5	17.6	17.6	13.4
Gd	111	100	132	111	134	119	123	77
Tb	15.1	13.6	17.8	15.9	18.6	16.1	17.0	10.6
Dy	85	77	98	90	108	88	95	60
Ho	16.8	15.5	19.1	17.9	21.4	17.3	19.0	12.3
Er	43.7	41.5	50.2	49.7	57.9	46.2	50.5	33.9
Tm	5.8	5.4	6.3	6.6	7.2	5.9	6.4	4.4
Yb	34	34	38	43	46	37	41	28
Lu	5.0	5.2	5.5	6.4	6.9	5.3	5.9	4.7
Hf	0.006	n.d.	0.016	0.012	0.014	0.005	0.013	0.009
Ta	0.006	n.d.	0.004	n.d.	0.006	0.001	0.002	0.001
Pb	2.96	2.64	2.52	2.63	2.45	2.97	2.59	2.37
Th	18.2	29.9	33.5	34.9	31.1	32.1	31.6	20.0
U	15.2	30.9	22.3	17.8	39.9	15.4	21.2	38.4
<i>Volatile elements and isotopes</i>								
H ₂ O (wt.%)	0.677	0.638	0.650	0.654	0.684	0.634	0.708	0.613
±	0.033	0.032	0.034	0.031	0.031	0.032	0.031	0.031
CO ₂ (µg/g)	31.3	41.7	35.3	38.6	762.0	41.1	41.3	41.9
±	3.7	4.6	4.2	4.0	66.0	4.2	4.2	4.2
S (µg/g)	249.7	290.3	399.3	838.8	339.8	358.1	386.4	378.3
±	32.2	32.2	32.3	38.7	32.2	32.2	32.6	32.2
δ ³⁴ S (‰)	3.89	5.74	5.56	5.16	4.54	5.96	4.60	4.92
±	1.05	0.98	0.84	0.77	0.89	0.92	0.72	0.57

(Continued.)

A.4. Supplementary Material to Chapter 5

Sample	LR22-3	LR22-3	LR22-3	LR22-3	LR22-3	LR22-3	LR22-6	LR22-6
Rock type	LRT	LRT	LRT	LRT	LRT	LRT	Pegm.	Pegm.
<i>Major elements (wt.%)</i>								
SiO ₂	0.12	0.04	0.15	0.11	0.05	0.11	0.16	0.12
FeO	0.03	0.01	0.00	0.03	0.03	0.00	0.01	0.01
CaO	55.29	55.35	55.42	55.36	55.48	55.55	54.84	55.13
Na ₂ O	0.01	0.00	0.02	0.03	0.04	0.01	0.15	0.06
P ₂ O ₅	41.83	41.95	41.90	41.89	41.94	41.98	42.04	41.99
F	1.61	1.81	1.70	1.76	1.58	1.83	1.45	1.46
Cl	0.25	0.20	0.24	0.22	0.25	0.22	0.34	0.34
Total	99.22	99.37	99.52	99.46	99.53	99.74	99.08	99.22
<i>Trace elements (µg/g)</i>								
Rb	0.103	n.d.	0.118	0.141	n.d.		0.502	0.341
Sr	217	217	216	221	275		115	104
Y	586	266	577	589	408		2557	1100
Zr	0.154	0.123	0.309	0.34	0.362		0.285	0.296
Nb	0.047	0.013	0.041	0.063	n.d.		n.d.	0.055
Ba	0.094	0.207	0.096	0.299	0.277		0.019	n.d.
La	93.9	58.4	161.5	119.2	351.4		62.9	156.7
Ce	434	181	659	563	978		264	611
Pr	80.9	32.1	106	99.0	122		52.6	101
Nd	463	194	559	547	540		326	528
Sm	131	59	143	141	109		164	167
Eu	15.4	9.0	17.0	20.7	14.6		9.2	18.5
Gd	135	65	138	138	95		270	187
Tb	19.1	8.8	19.0	18.7	13.0		49.6	28.7
Dy	107	49	106	105	73		335	175
Ho	21.6	9.7	20.7	20.6	14.3		76.5	37.0
Er	58.3	25.6	56.0	56.8	39.0		232	105
Tm	7.4	3.1	7.0	7.3	5.1		33.8	15.2
Yb	46	19	43	46	32		232	101
Lu	6.8	3.0	6.2	6.8	4.7		35.4	15.8
Hf	0.014	0.006	0.006	0.006	0.003		0.031	0.024
Ta	0.006	0.002	0.004	0.005	0.002		0.012	n.d.
Pb	2.61	2.39	2.53	2.48	2.91		2.98	2.73
Th	26.2	11.4	31.9	39.2	25.8		39.2	41.5
U	35.2	26.2	28.3	32.2	8.3		39.4	81.0
<i>Volatile elements and isotopes</i>								
H ₂ O (wt.%)	0.701	0.701	0.731	0.700	0.767	0.631	0.863	0.886
±	0.031	0.031	0.033	0.034	0.035	0.033	0.032	0.033
CO ₂ (µg/g)	61.8	42.8	44.4	43.4	35.4	54.5	40.3	36.1
±	5.9	4.3	4.5	5.2	4.2	5.3	4.7	4.3
S (µg/g)	342.8	202.2	316.2	328.6	182.1	517.3	502.8	314.5
±	32.2	32.3	32.4	32.4	32.2	33.5	32.6	32.6
δ ³⁴ S (‰)	4.20	3.21	4.48	6.05	5.72		2.60	1.86
±	0.98	0.98	0.86	0.70	1.29		0.64	0.77

(Continued.)

A. *Supplementary Materials*

Sample Rock type	LR22-6 Pegm.							
<i>Major elements (wt.%)</i>								
SiO ₂	0.12	0.24	0.16	0.12	0.19	0.25	0.15	0.21
FeO	0.04	0.03	0.03	0.03	0.03	0.05	0.04	0.01
CaO	54.77	54.36	54.95	54.63	54.39	54.75	55.09	55.10
Na ₂ O	0.11	0.19	0.12	0.13	0.12	0.25	0.11	0.05
P ₂ O ₅	41.93	41.56	41.53	41.66	41.18	40.91	41.79	41.43
F	1.36	1.24	1.43	1.39	1.38	1.19	1.48	1.39
Cl	0.35	0.46	0.37	0.36	0.37	0.49	0.34	0.38
Total	98.77	98.25	98.65	98.42	97.73	97.95	98.99	98.61
<i>Trace elements (µg/g)</i>								
Rb	n.d.	0.49	0.434	0.549	0.544	0.321	0.349	0.529
Sr	111	114	117	118	114	103	119	132
Y	1841	3545	2010	2624	2457	2295	2054	3087
Zr	0.341	0.569	0.392	0.307	0.317	0.662	0.181	0.193
Nb	0.152	0.022	n.d.	0.022	n.d.	0.018	0.058	0.034
Ba	n.d.	0.066	n.d.	0.062	0.061	n.d.	0.051	0.078
La	75.3	204.1	103.9	173.0	105.3	229.8	44.0	23.0
Ce	243	651	332	508	349	708	188	152
Pr	48.0	105	56.7	82.7	61.8	99.4	39.4	39.0
Nd	261	567	318	444	357	501	260	288
Sm	129	248	142	189	163	192	133	169
Eu	10.6	11.7	8.4	9.1	10.0	10.2	9.3	10.7
Gd	210	373	218	284	262	265	220	300
Tb	36.6	67.0	39.8	51.9	48.0	46.3	40.3	56.3
Dy	247	448	270	341	318	303	276	384
Ho	59.2	100.6	61.8	77.6	73.4	66.3	62.2	88.4
Er	180	308	189	238	225	201	192	273
Tm	26.4	46.2	26.6	34.4	32.1	29.3	27.8	39.9
Yb	168	328	187	236	210	206	192	281
Lu	25.7	50.8	29.0	36.4	34.0	32.0	31.0	44.3
Hf	n.d.	0.058	0.018	0.023	0.059	0.031	0.035	0.045
Ta	0.034	0.014	n.d.	0.007	0.013	0.012	0.009	0.012
Pb	2.83	3.13	2.62	2.96	2.96	2.49	2.78	2.33
Th	21.4	67.2	29.4	41.9	38.4	41.5	25.0	31.5
U	34.3	24.3	22.3	38.4	54.0	14.6	48.5	66.5
<i>Volatile elements and isotopes</i>								
H ₂ O (wt.%)	0.896	0.966	0.788	0.865	0.827	0.781	0.783	0.729
±	0.033	0.033	0.032	0.033	0.032	0.031	0.031	0.031
CO ₂ (µg/g)	34.4	43.6	46.6	39.0	41.7	61.5	40.3	35.5
±	3.6	4.3	4.9	4.1	4.4	5.9	4.4	3.7
S (µg/g)	400.2	701.0	518.0	338.3	559.4	1366.4	366.5	283.8
±	32.4	32.4	32.6	32.3	32.5	36.1	32.2	32.3
δ ³⁴ S (‰)	7.94	7.49		6.58		9.41	6.24	4.12
±	0.77	0.49		1.00		0.42	0.91	0.95

(Continued.)

A.4. Supplementary Material to Chapter 5

Sample Rock type	LR22-6 Pegm.	LR21-1 Aplite						
<i>Major elements (wt.%)</i>								
SiO ₂	0.25	0.25	0.11	0.05	0.14	0.37	0.22	0.16
FeO	0.02	0.01	0.02	0.03	0.03	0.03	0.05	0.01
CaO	55.03	54.71	55.01	55.09	55.05	54.72	54.99	54.78
Na ₂ O	0.17	0.12	0.14	0.09	0.11	0.10	0.11	0.11
P ₂ O ₅	41.42	41.57	41.80	41.59	41.79	40.79	41.19	41.50
F	1.31	1.29	1.36	1.22	1.36	1.18	1.29	2.21
Cl	0.37	0.44	0.35	0.45	0.40	0.45	0.40	0.12
Total	98.63	98.56	98.88	98.60	98.96	97.89	98.35	99.00
<i>Trace elements (µg/g)</i>								
Rb	0.473	0.596	0.358	0.219	0.365	0.783	0.621	0.258
Sr	113	107	107	125	125	127	123	114
Y	3284	3533	2040	1718	2232	4715	3369	1882
Zr	0.459	0.887	0.297	0.18	0.3	0.794	0.487	0.318
Nb	0.035	0.173	0.008	0.015	0.025	0.058	0.055	0.019
Ba	0.063	0.214	0.059	0.119	0.032	0.061	0.042	0.189
La	84.6	241.7	147.2	132.1	138.8	456.2	222.6	197.4
Ce	316	824	489	403	419	1336	707	585
Pr	60.7	124	76.9	62.4	66.9	187	106	82.2
Nd	382	656	413	340	364	958	570	439
Sm	201	276	162	135	155	378	236	186
Eu	11.1	13.9	8.5	7.3	8.8	20.2	12.8	13.2
Gd	337	390	234	196	240	555	352	268
Tb	63.3	66.8	41.3	34.7	43.5	100.7	64.4	46.2
Dy	434	433	280	227	297	663	438	286
Ho	96.4	94.5	62.4	49.8	66.1	145.4	99.5	58.0
Er	294	286	187	149	203	427	307	165
Tm	43.2	43.5	27.2	21.2	29.8	59.4	45.9	24.5
Yb	302	327	188	148	207	398	325	187
Lu	46.9	52.2	28.6	22.8	32.1	57.9	50.9	32.7
Hf	0.024	0.054	0.028	0.036	0.03	0.068	0.045	0.027
Ta	0.01	0.039	0.007	0.014	0.004	0.024	0.013	0.005
Pb	2.87	3.90	2.39	2.35	2.92	3.48	2.86	3.07
Th	60.0	114.6	24.9	13.1	27.5	76.5	49.2	55.7
U	45.0	107.3	23.0	8.0	22.2	144.3	120.7	46.0
<i>Volatile elements and isotopes</i>								
H ₂ O (wt.%)	0.748	0.762	0.796	0.824	0.682	0.819	0.746	0.798
±	0.032	0.031	0.031	0.031	0.031	0.033	0.032	0.031
CO ₂ (µg/g)	40.1	252.2	31.3	32.1	<30	33.2	40.2	546.5
±	4.1	21.8	3.6	3.5		3.6	4.1	158.4
S (µg/g)	534.5	299.3	469.3	302.5	420.1	316.1	280.4	535.0
±	32.7	32.4	32.3	32.2	32.4	32.3	32.3	32.4
δ ³⁴ S (‰)	4.86	4.28	8.57	7.27	7.57		2.42	5.41
±	0.68	0.87	0.74	0.69	0.87		0.94	0.77

(Continued.)

A. *Supplementary Materials*

Sample	LR21-1							
Rock type	Aplite							
<i>Major elements (wt.%)</i>								
SiO ₂	0.32	0.20	0.20	0.14	0.16	0.13	0.19	0.14
FeO	0.05	0.04	0.05	0.01	0.03	0.03	0.02	0.03
CaO	54.32	54.90	54.88	54.79	54.71	55.23	54.96	55.16
Na ₂ O	0.28	0.16	0.10	0.09	0.13	0.09	0.09	0.08
P ₂ O ₅	40.91	41.39	41.55	42.08	41.25	42.24	41.53	41.54
F	1.76	1.88	1.92	2.05	1.86	2.08	1.83	1.83
Cl	0.23	0.15	0.11	0.11	0.20	0.10	0.19	0.15
Total	98.07	98.91	98.99	99.31	98.48	99.98	99.03	99.12
<i>Trace elements (µg/g)</i>								
Rb	0.272	0.301	0.292	0.234	0.323	0.53	0.105	0.285
Sr	121	118	127	117	123	115	120	125
Y	1295	1745	1718	2021	1681	2145	1271	1471
Zr	0.662	0.544	0.773	0.151	0.448	0.734	0.48	0.688
Nb	0.018	0.015	0.01	0.015	n.d.	0.014	0.011	0.009
Ba	0.04	0.064	0.036	n.d.	n.d.	0.031	0.06	0.056
La	497.5	333.5	367.6	102.3	311.0	298.6	406.6	569.8
Ce	1058	819	891	334	760	792	991	1233
Pr	120	99.1	108	54.0	96.0	98.6	112	135
Nd	554	484	522	313	470	494	507	600
Sm	179	183	194	152	178	186	157	173
Eu	14.5	12.9	15.1	12.6	12.3	14.6	12.1	11.9
Gd	225	261	271	252	251	270	200	214
Tb	36.1	44.4	45.3	44.8	42.3	47.4	32.9	35.2
Dy	214	274	278	286	264	303	201	218
Ho	42.1	55.6	57.0	61.5	55.1	65.5	41.2	45.6
Er	111	154	157	175	152	187	114	130
Tm	14.4	21.2	21.6	25.7	21.8	28.1	15.3	18.0
Yb	97	148	153	191	159	218	106	131
Lu	15.7	24.4	25.1	32.7	27.3	38.3	17.2	21.9
Hf	0.021	0.012	0.027	0.006	0.012	0.02	0.024	0.028
Ta	0.006	0.015	0.003	0.007	0.004	0.009	0.006	0.006
Pb	2.97	2.67	2.86	2.55	2.71	2.98	2.69	3.04
Th	54.9	53.3	57.9	19.0	44.7	64.5	38.2	61.9
U	24.4	40.4	38.0	41.1	34.4	50.4	23.4	21.2
<i>Volatile elements and isotopes</i>								
H ₂ O (wt.%)	0.877	0.831	0.854	0.742	0.898	0.592	0.641	0.668
±	0.032	0.031	0.031	0.031	0.034	0.030	0.031	0.031
CO ₂ (µg/g)	33.7	<30	34.6	32.3	35.5	36.9	32.3	48.5
±	3.6		3.6	3.4	3.7	5.3	3.8	6.7
S (µg/g)	574.9	531.5	751.3	236.7	804.9	627.0	442.3	481.9
±	32.6	32.3	32.9	32.1	34.0	32.4	32.5	32.8
δ ³⁴ S (‰)				6.23	7.10		5.95	7.66
±				0.78	0.77		0.58	0.70

(Continued.)

A.4. Supplementary Material to Chapter 5

Sample	LR21-1	LR21-1	LR21-1	LR21-1	LR21-1	LR21-1
Rock type	Aplite	Aplite	Aplite	Aplite	Aplite	Aplite
<i>Major elements (wt.%)</i>						
SiO ₂	0.09	0.20	0.15	0.17	0.15	0.13
FeO	0.00	0.02	0.02	0.01	0.02	0.03
CaO	55.54	55.04	55.07	54.97	54.82	55.09
Na ₂ O	0.06	0.11	0.09	0.09	0.14	0.09
P ₂ O ₅	41.96	41.59	41.61	41.53	41.47	41.58
F	2.04	1.94	1.98	1.95	2.03	1.97
Cl	0.13	0.14	0.13	0.14	0.17	0.12
Total	99.87	99.17	99.15	99.07	98.89	99.16
<i>Trace elements (µg/g)</i>						
Rb	0.304	0.269	0.234	0.4	0.305	0.306
Sr	119	115	119	115	118	114
Y	1526	1630	1578	1708	1805	1461
Zr	0.366	0.315	0.34	0.479	0.305	0.27
Nb	0.025	0.038	0.041	0.04	0.023	0.023
Ba	n.d.	0.067	0.021	0.023	0.04	0.115
La	231.3	147.3	323.7	328.1	277.3	302.8
Ce	683	417	898	872	705	792
Pr	90.1	61.9	111	106	88.8	96.8
Nd	456	335	533	513	443	465
Sm	172	143	190	184	170	164
Eu	14.7	16.2	13.4	15.3	13.5	12.4
Gd	241	217	249	248	245	223
Tb	40.6	37.1	41.5	42.3	42.8	37.4
Dy	251	232	253	259	268	228
Ho	50.9	48.8	50.7	52.8	55.6	46.8
Er	137	140	140	149	158	129
Tm	18.5	19.9	18.9	20.7	22.6	17.7
Yb	127	153	136	151	168	127
Lu	20.7	28.1	21.7	25.0	28.2	20.8
Hf	0.014	0.024	0.023	0.02	0.035	0.026
Ta	0.004	0.006	0.008	0.007	0.009	0.008
Pb	2.70	2.91	2.70	3.11	2.90	3.05
Th	45.0	37.8	36.2	53.0	36.9	37.7
U	36.5	60.9	57.0	34.3	47.7	38.9
<i>Volatile elements and isotopes</i>						
H ₂ O (wt.%)	0.575	0.568	0.598	0.571	0.586	0.581
±	0.030	0.031	0.030	0.030	0.030	0.031
CO ₂ (µg/g)	33.5	87.9	35.9	111.3	107.9	38.5
±	3.6	22.6	3.8	25.2	15.2	4.2
S (µg/g)	389.1	591.4	400.1	548.5	749.7	388.0
±	32.2	32.3	32.2	33.1	32.4	32.5
δ ³⁴ S (‰)	6.19	5.66	5.86		5.91	
±	0.70	0.71	0.89		0.50	

Leucoto., leucotonalite; *LGD*, Laione granodiorite; *LRT*, Listino ring tonalite; *Pegm.*, pegmatite; *n.d.*, not detected

A. *Supplementary Materials*

Table A4.3. Volatile element analyses (wt.%) of apatite standards during a 3-day SIMS session.

Grain	Durango	Mud Tank	Durango	Mud Tank	Durango	Mud Tank	Durango
H ₂ O _{corr}	0.055	1.065	0.054	1.072	0.057	1.041	0.070
CO ₂	0.001	0.416	0.001	0.403	0.001	0.408	0.001
SO ₃	0.260	0.015	0.237	0.014	0.340	0.014	0.299
Cl	0.422	0.045	0.396	0.044	0.418	0.042	0.477

(Continued.)

Grain	Mud Tank	Durango	Mud Tank	Durango	Mud Tank	Durango	Mud Tank
H ₂ O _{corr}	0.975	0.058	0.989	0.049	1.022	0.055	1.104
CO ₂	0.372	0.001	0.404	0.001	0.383	0.001	0.394
SO ₃	0.011	0.278	0.013	0.264	0.013	0.268	0.013
Cl	0.041	0.464	0.044	0.437	0.041	0.430	0.042

(Continued.)

Grain	Durango	Mud Tank	Durango	Mud Tank	Durango	Mud Tank	Mud Tank
H ₂ O _{corr}	0.049	1.062	0.045	1.032	0.067	0.960	1.049
CO ₂	0.001	0.361	0.001	0.376	0.001	0.371	0.364
SO ₃	0.286	0.010	0.284	0.013	0.283	0.013	0.011
Cl	0.464	0.038	0.460	0.042	0.456	0.043	0.042

(Continued.)

Grain	Durango	Mud Tank	Durango	Mud Tank	Durango	Mud Tank	Durango
H ₂ O _{corr}	0.058	1.076	0.089	0.978	0.068	0.995	0.081
CO ₂	0.001	0.406	0.002	0.404	0.002	0.423	0.002
SO ₃	0.328	0.020	0.310	0.020	0.263	0.020	0.307
Cl	0.392	0.038	0.501	0.038	0.418	0.041	0.488

(Continued.)

Grain	Mud Tank	Durango	Mud Tank	Durango	Mud Tank	Durango	Mud Tank
H ₂ O _{corr}	0.987	0.090	1.047	0.068	1.091	0.090	1.050
CO ₂	0.407	0.003	0.389	0.002	0.380	0.002	0.421
SO ₃	0.019	0.301	0.019	0.274	0.018	0.302	0.019
Cl	0.039	0.506	0.036	0.457	0.036	0.462	0.039

(Continued.)

Grain	Mud Tank	Durango	Mud Tank	Durango	Mud Tank	Durango	Mud Tank
H ₂ O _{corr}	0.997	0.112	1.037	0.101	0.966	0.102	1.034
CO ₂	0.399	0.003	0.386	0.002	0.646	0.002	0.672
SO ₃	0.016	0.306	0.022	0.287	0.023	0.298	0.021
Cl	0.040	0.432	0.050	0.421	0.058	0.421	0.059

(Continued.)

Grain	Durango	Mud Tank	Durango	Mud Tank	Durango	Mud Tank	Durango
H ₂ O _{corr}	0.100	0.991	0.097	1.012	0.101	1.017	0.090
CO ₂	0.002	0.645	0.002	0.722	0.002	0.697	0.002
SO ₃	0.280	0.021	0.287	0.024	0.302	0.022	0.295
Cl	0.390	0.057	0.412	0.062	0.429	0.061	0.418

(Continued.)

Grain	Mud Tank	Durango	Mud Tank	Mud Tank	Durango	Mud Tank	Mud Tank
H ₂ O _{corr}	1.037	0.112	0.980	0.983	0.105	0.981	0.954
CO ₂	0.680	0.003	0.391	0.682	0.002	0.683	0.723
SO ₃	0.022	0.308	0.021	0.023	0.305	0.023	0.024
Cl	0.063	0.436	0.054	0.060	0.429	0.062	0.058

H₂O_{corr} corresponds to drift-corrected H₂O contents

Table A4.4. Sulphur isotope analyses (‰) of the Durango apatite standard during a 3-day SIMS session.

Grain	Durango							
δ ³⁴ S	-34.59	-33.70	-33.07	-32.89	-32.42	-32.35	-32.63	-32.66
1 s.e.	0.21	0.17	0.21	0.20	0.17	0.19	0.18	0.17
IMF	-33.20	-32.31	-31.68	-31.50	-31.03	-30.96	-31.24	-31.27

(Continued.)

Grain	Durango							
δ ³⁴ S	-32.43	-32.86	-33.05	-33.17	-33.79	-33.00	-33.32	-33.23
1 s.e.	0.21	0.20	0.23	0.21	0.19	0.19	0.22	0.19
IMF	-31.04	-31.47	-31.66	-31.78	-32.40	-31.61	-31.93	-31.84

(Continued.)

Grain	Durango							
δ ³⁴ S	-33.35	-33.05	-32.48	-34.14	-34.38	-34.61	-34.21	-34.13
1 s.e.	0.21	0.21	0.17	0.19	0.25	0.16	0.24	0.19
IMF	-31.96	-31.66	-31.09	-32.75	-32.99	-33.22	-32.82	-32.74

(Continued.)

A. Supplementary Materials

Grain	Durango							
$\delta^{34}\text{S}$	-33.83	-34.03	-33.73	-34.77	-35.06	-34.87	-35.46	-34.96
1 s.e.	0.25	0.17	0.19	0.20	0.22	0.21	0.19	0.18
IMF	-32.44	-32.64	-32.34	-33.38	-33.67	-33.48	-34.07	-33.57

(Continued.)

Grain	Durango							
$\delta^{34}\text{S}$	-34.61	-35.19	-35.51	-34.99	-35.28	-35.24	-34.68	-36.72
1 s.e.	0.21	0.24	0.21	0.21	0.22	0.25	0.27	0.18
IMF	-33.22	-33.80	-34.12	-33.60	-33.89	-33.85	-33.29	-35.33

(Continued.)

Grain	Durango							
$\delta^{34}\text{S}$	-36.14	-36.07	-35.66	-36.07	-36.46	-36.73	-35.80	-36.56
1 s.e.	0.24	0.22	0.22	0.19	0.17	0.20	0.18	0.23
IMF	-34.75	-34.68	-34.27	-34.68	-35.07	-35.34	-34.41	-35.17

(Continued.)

Grain	Durango	Durango	Durango	Durango
$\delta^{34}\text{S}$	-35.98	-36.21	-35.92	-35.73
1 s.e.	0.23	0.22	0.24	0.18
IMF	-34.59	-34.82	-34.53	-34.34

IMF, instrumental mass fractionation; s.e., standard error

Table A4.5. Trace element analyses ($\mu\text{g/g}$, unless stated otherwise) of the secondary standard BCR-2G.

	BCR-2G						
Na ₂ O*	3.35	3.36	3.37	3.36	3.43	3.44	3.47
MgO*	4.11	4.08	4.11	4.10	4.18	4.14	4.10
Sc	33.4	33.3	32.8	32.7	32.9	33.0	32.8
TiO ₂ *	2.44	2.56	2.48	2.47	2.48	2.55	2.50
V	442	448	443	443	450	460	462
Cr	15.63	16.23	16.20	16.13	17.38	18.77	15.02
MnO*	0.215	0.218	0.217	0.217	0.215	0.217	0.218
FeO*	11.0	10.8	11.6	11.7	11.2	10.9	11.8
Ni	12.5	12.2	12.6	12.6	12.6	12.8	12.8
Cu	16.7	17.0	17.0	16.9	17.2	17.1	16.9
Zn	177	183	179	178	191	190	191
Rb	50.1	49.7	49.9	49.8	51.9	51.8	52.3
Sr	336	342	335	335	343	339	337
Y	31.8	31.8	31.1	31.0	31.1	30.8	30.6
Zr	170	169	166	166	166	167	164
Nb	12.0	12.2	11.9	11.9	12.3	12.2	12.2
Ba	688	686	686	687	698	692	697
La	24.3	24.5	23.8	23.8	24.5	24.2	24.0
Ce	52.7	53.0	52.0	52.1	53.3	53.4	53.6
Pr	6.50	6.57	6.48	6.49	6.60	6.48	6.48
Nd	27.8	28.0	27.1	27.1	27.7	27.0	27.3
Sm	6.53	6.58	6.26	6.27	6.35	6.22	6.11
Eu	1.89	1.92	1.95	1.95	1.91	1.87	1.95
Gd	6.15	6.02	6.01	6.01	5.95	6.11	5.90
Tb	0.960	0.977	0.970	0.971	0.934	0.920	0.914
Dy	5.99	6.05	6.03	6.03	5.89	5.82	5.74
Ho	1.22	1.20	1.19	1.19	1.20	1.14	1.20
Er	3.49	3.42	3.27	3.28	3.45	3.42	3.24
Tm	0.472	0.476	0.448	0.449	0.463	0.457	0.453
Yb	3.24	3.20	3.03	3.03	3.22	3.19	3.17
Lu	0.498	0.457	0.474	0.475	0.447	0.458	0.453
Hf	4.55	4.63	4.47	4.47	4.43	4.56	4.40
Ta	0.717	0.747	0.699	0.699	0.694	0.701	0.698
Pb	11.2	11.3	11.2	11.2	11.6	12.6	11.8
Th	5.74	5.75	5.62	5.62	5.58	5.48	5.34
U	1.77	1.75	1.73	1.73	1.74	1.77	1.79

(Continued.)

A. Supplementary Materials

	BCR-2G						
Na ₂ O	3.43	3.43	3.39	3.39	3.58	3.55	3.49
MgO	4.18	4.16	4.13	4.12	4.25	4.19	4.24
Sc	32.0	32.5	32.6	33.1	32.6	32.2	32.6
TiO ₂	2.47	2.51	2.46	2.44	2.50	2.62	2.53
V	454	457	452	448	464	477	463
Cr	15.33	16.08	15.40	13.95	15.32	17.01	15.73
MnO	0.218	0.218	0.216	0.218	0.223	0.226	0.223
FeO	11.2	10.9	10.7	10.5	11.9	11.7	11.5
Ni	12.9	12.7	12.8	13.1	13.0	14.3	12.5
Cu	17.2	17.3	17.4	16.7	17.6	17.9	17.8
Zn	191	200	193	188	190	203	193
Rb	51.2	51.2	51.5	50.5	52.4	53.1	52.9
Sr	337	340	333	339	338	338	338
Y	30.9	30.8	30.7	31.6	30.9	30.6	31.5
Zr	166	164	165	167	167	165	169
Nb	12.1	12.2	12.1	12.1	12.4	12.4	12.1
Ba	694	688	688	675	702	710	697
La	24.1	23.9	23.9	24.2	24.2	24.1	24.2
Ce	53.1	53.0	52.7	52.6	53.6	54.2	53.6
Pr	6.55	6.49	6.45	6.64	6.55	6.58	6.67
Nd	27.9	27.0	27.3	27.8	27.5	26.9	27.8
Sm	6.09	6.39	6.20	6.30	6.17	6.12	6.27
Eu	1.87	1.93	1.92	1.93	1.83	1.91	1.92
Gd	6.13	6.28	6.11	6.12	5.98	5.95	6.04
Tb	0.943	0.945	0.932	0.941	0.927	0.951	0.925
Dy	5.69	5.80	5.62	5.89	5.92	5.79	5.96
Ho	1.21	1.16	1.17	1.21	1.18	1.23	1.20
Er	3.28	3.27	3.32	3.38	3.31	3.32	3.36
Tm	0.454	0.475	0.470	0.467	0.464	0.480	0.453
Yb	3.29	3.21	3.10	3.13	3.11	3.14	3.29
Lu	0.469	0.450	0.473	0.474	0.496	0.468	0.473
Hf	4.60	4.44	4.45	4.64	4.55	4.48	4.37
Ta	0.737	0.702	0.703	0.724	0.676	0.720	0.718
Pb	11.4	11.7	11.4	11.4	12.0	11.8	12.1
Th	5.46	5.70	5.50	5.61	5.58	5.61	5.59
U	1.68	1.73	1.72	1.82	1.88	1.88	1.87

(Continued.)

	BCR-2G	BCR-2G	BCR-2G	BCR-2G	BCR-2G
Na ₂ O*	3.40	3.37	3.43	3.40	3.44
MgO*	4.19	4.20	4.19	4.17	4.25
Sc	32.6	33.2	33.3	32.4	32.4
TiO ₂ *	2.40	2.52	2.54	2.44	2.50
V	458	451	445	442	452
Cr	16.26	15.83	14.38	14.56	17.97
MnO*	0.221	0.222	0.221	0.217	0.225
FeO*	10.7	11.1	11.2	10.9	12.2
Ni	12.9	13.4	13.0	12.1	13.5
Cu	17.2	16.7	16.8	16.6	17.2
Zn	191	191	187	176	185
Rb	51.3	50.2	51.5	50.5	51.5
Sr	337	337	342	340	338
Y	30.9	31.8	32.1	31.4	30.7
Zr	166	168	169	169	167
Nb	12.2	12.0	12.3	12.0	12.1
Ba	689	686	690	688	695
La	24.1	24.0	24.7	24.3	24.2
Ce	53.5	52.9	52.8	52.6	53.5
Pr	6.57	6.49	6.64	6.61	6.66
Nd	27.0	28.1	28.0	27.9	27.4
Sm	6.34	6.40	6.57	6.28	6.41
Eu	1.87	1.88	1.86	1.90	1.94
Gd	6.24	6.28	6.28	6.02	6.34
Tb	0.948	0.960	0.993	0.978	0.920
Dy	5.92	5.89	5.98	5.78	5.70
Ho	1.19	1.19	1.24	1.19	1.18
Er	3.37	3.40	3.31	3.43	3.34
Tm	0.472	0.478	0.476	0.477	0.447
Yb	3.08	3.14	3.19	3.22	3.11
Lu	0.477	0.467	0.477	0.466	0.442
Hf	4.50	4.69	4.61	4.61	4.55
Ta	0.698	0.736	0.712	0.700	0.714
Pb	11.5	11.3	11.1	11.0	11.4
Th	5.51	5.63	5.61	5.51	5.56
U	1.83	1.73	1.73	1.70	1.78

*unit = wt.%

Bibliography

- Acosta, M. D., Watkins, J. M., Reed, M. H., Donovan, J. J. and DePaolo, D. J. (2020). Ti-in-quartz: Evaluating the role of kinetics in high temperature crystal growth experiments. *Geochimica et Cosmochimica Acta* 281, 149–167.
- Aiuppa, A., Bertagnini, A., Métrich, N., Moretti, R., Di Muro, A., Liuzzo, M. and Tamburello, G. (2010). A model of degassing for Stromboli volcano. *Earth and Planetary Science Letters* 295(1-2), 195–204.
- Aiuppa, A., Giudice, G., Gurrieri, S., Liuzzo, M., Burton, M., Caltabiano, T., McGonigle, A., Salerno, G., Shinohara, H. and Valenza, M. (2008). Total volatile flux from Mount Etna. *Geophysical Research Letters* 35(24).
- Albert, H., Costa, F., Di Muro, A., Herrin, J., Métrich, N. and Deloule, E. (2019). Magma interactions, crystal mush formation, timescales, and unrest during caldera collapse and lateral eruption at ocean island basaltic volcanoes (Piton de la Fournaise, La Réunion). *Earth and Planetary Science Letters* 515, 187–199.
- Allibon, J., Bussy, F., Lewin, E. and Darbellay, B. (2011). The tectonically controlled emplacement of a vertically sheeted gabbro-pyroxenite intrusion: Feeder-zone of an ocean-island volcano (Fuerteventura, Canary Islands). *Tectonophysics* 500(1-4), 78–97.
- Alonso-Perez, R., Müntener, O. and Ulmer, P. (2009). Igneous garnet and amphibole fractionation in the roots of island arcs: experimental constraints on andesitic liquids. *Contributions to Mineralogy and Petrology* 157(4), 541–558.
- Anderson, E. M. (1951). *The dynamics of faulting and dyke formation with applications to Britain*. Oliver and Boyd.
- Angel, R. J., Carpenter, M. and Finger, L. (1990). Structural variation associated with compositional variation and order-disorder behavior in anorthite-rich feldspars. *American Mineralogist* 75(1-2), 150–162.
- Annen, C. (2009). From plutons to magma chambers: Thermal constraints on the accumulation of eruptible silicic magma in the upper crust. *Earth and Planetary Science Letters* 284(3-4), 409–416.
- Annen, C., Blundy, J. and Sparks, R. (2006). The genesis of intermediate and silicic magmas in deep crustal hot zones. *Journal of Petrology* 47(3), 505–539.
- Ardill, K. E., Paterson, S. R., Stanback, J., Alasino, P. H., King, J. J. and Crosbie, S. E. (2020). Schlieren-bound magmatic structures record crystal flow-sorting in dynamic upper-crustal magma-mush chambers. *Frontiers in Earth Science* 8, 540100.
- Armstrong, J. T. (1995). Citzaf—A package of correction programs for the quantitative Electron Microbeam X-Ray-Analysis of thick polished materials, thin-films, and particles. *Microbeam Analysis* 4, 177–200.
- Audétat, A. (2019). The metal content of magmatic-hydrothermal fluids and its relationship to mineralization potential. *Economic Geology* 114(6), 1033–1056.
- Audétat, A., Garbe-Schönberg, D., Kronz, A., Pettke, T., Rusk, B., Donovan, J. J. and Lowers, H. A. (2015). Characterisation of a natural quartz crystal as a reference material for micro-analytical determination of Ti, Al, Li, Fe, Mn, Ga and Ge. *Geostandards and Geoanalytical Research* 39(2), 171–184.
- Audétat, A., Gunther, D. and Heinrich, C. A. (1998). Formation of a magmatic-hydrothermal ore deposit: Insights with LA-ICP-MS analysis of fluid inclusions. *Science* 279(5359), 2091–2094.
- Audétat, A., Miyajima, N., Wiesner, D. and Audinot, J.-N. (2021). Confirmation of slow Ti

- diffusion in quartz by diffusion couple experiments and evidence from natural samples. *Geology* 49(8), 963–967.
- Audéat, A. and Pettke, T. (2003). The magmatic-hydrothermal evolution of two barren granites: A melt and fluid inclusion study of the Rito del Medio and Canada Pinabete plutons in northern New Mexico (USA). *Geochimica et Cosmochimica Acta* 67(1), 97–121.
- Audéat, A., Pettke, T., Heinrich, C. A. and Bodnar, R. J. (2008). Special paper: the composition of magmatic-hydrothermal fluids in barren and mineralized intrusions. *Economic Geology* 103(5), 877–908.
- Audéat, A., Schmitt, A. K., Njul, R., Saalfeld, M., Borisova, A. and Lu, Y. (2023). New constraints on Ti diffusion in quartz and the priming of silicic volcanic eruptions. *Nature Communications* 14(1), 4277.
- Bachl, C. A., Miller, C. F., Miller, J. S. and Faulds, J. E. (2001). Construction of a pluton: Evidence from an exposed cross section of the Searchlight pluton, Eldorado Mountains, Nevada. *Geological Society of America Bulletin* 113(9), 1213–1228.
- Bachmann, O., Dungan, M. A. and Lipman, P. W. (2002). The Fish Canyon magma body, San Juan volcanic field, Colorado: rejuvenation and eruption of an upper-crustal batholith. *Journal of Petrology* 43(8), 1469–1503.
- Bachmann, O. and Huber, C. (2016). Silicic magma reservoirs in the Earth’s crust. *American Mineralogist* 101(11), 2377–2404.
- Bachmann, O. and Huber, C. (2019). The inner workings of crustal distillation columns; the physical mechanisms and rates controlling phase separation in silicic magma reservoirs. *Journal of Petrology* 60(1), 3–18.
- Baker, D. R. and Alletti, M. (2012). Fluid saturation and volatile partitioning between melts and hydrous fluids in crustal magmatic systems: The contribution of experimental measurements and solubility models. *Earth-Science Reviews* 114(3-4), 298–324.
- Baker, M. B., Grove, T. L. and Price, R. (1994). Primitive basalts and andesites from the Mt. Shasta region, N. California: products of varying melt fraction and water content. *Contributions to Mineralogy and Petrology* 118, 111–129.
- Balcone-Boissard, H., Villemant, B. and Boudon, G. (2010). Behavior of halogens during the degassing of felsic magmas. *Geochemistry, Geophysics, Geosystems* 11(9), Q09005.
- Ballhaus, C. and Frost, B. R. (1994). The generation of oxidized CO₂-bearing basaltic melts from reduced CH₄-bearing upper mantle sources. *Geochimica et Cosmochimica Acta* 58(22), 4931–4940.
- Barboni, M., Boehnke, P., Schmitt, A. K., Harrison, T. M., Shane, P., Bouvier, A.-S. and Baumgartner, L. P. (2016). Warm storage for arc magmas. *Proceedings of the National Academy of Sciences* 113(49), 13959–13964.
- Barboni, M. and Schoene, B. (2014). Short eruption window revealed by absolute crystal growth rates in a granitic magma. *Nature Geoscience* 7(7), 524–528.
- Barker, F. (1979). Trondhjemite: definition, environment and hypotheses of origin. In: *Developments in Petrology*, volume 6. Elsevier, pp. 1–12.
- Barnes, C. G., Burton, B. R., Burling, T. C., Wright, J. E. and Karlsson, H. R. (2001). Petrology and geochemistry of the late Eocene Harrison Pass pluton, Ruby Mountains core complex, northeastern Nevada. *Journal of Petrology* 42(5), 901–929.
- Barnes, C. G., Coint, N. and Yoshinobu, A. (2016a). Crystal accumulation in a tilted arc batholith. *American Mineralogist* 101(8), 1719–1734.
- Barnes, C. G., Memeti, V. and Coint, N. (2016b). Deciphering magmatic processes in calc-alkaline plutons using trace element zoning in hornblende. *American Mineralogist* 101, 328–342.
- Barnes, C. G., Werts, K., Memeti, V. and Ardill, K. (2019). Most granitoid rocks are cumulates: deductions from hornblende compositions and zircon saturation. *Journal of Petrology* 60(11), 2227–2240.
- Barrett, T. and Spooner, E. (1977). Ophiolitic breccias associated with allochthonous oceanic crustal rocks in the East Ligurian Apennines, Italy—a comparison with observations from rifted oceanic ridges. *Earth and Planetary Science Letters* 35(1), 79–91.
- Bartels, K. S., Kinzler, R. J. and Grove, T. L. (1991). High pressure phase relations of primitive high-alumina basalts from Medicine Lake volcano, northern California. *Contributions to Mineralogy and Petrology* 108, 253–270.

Bibliography

- Bateman, P. C. and Chappell, B. W. (1979). Crystallization, fractionation, and solidification of the Tuolumne intrusive series, Yosemite National Park, California. *Geological Society of America Bulletin* 90(5), 465–482.
- Bateman, P. C., Dodge, F. and Bruggman, P. E. (1984). Major oxide analyses, CIPW norms, modes, and bulk specific gravities of plutonic rocks from the Mariposa 1° × 2° sheet, central Sierra Nevada, California. Technical report, U.S. Geological Survey.
- Bateman, R. (1985). Aureole deformation by flattening around a diapir during *in situ* ballooning: the Cannibal Creek granite. *The Journal of Geology* 93(3), 293–310.
- Behrens, H. (1995). Determination of water solubilities in high-viscosity melts; an experimental study on NaAlSi₃O₈ and KAlSi₃O₈ melts. *European Journal of Mineralogy* 7(4), 905–920.
- Behrens, H., Johannes, W. and Schmalzried, H. (1990). On the mechanisms of cation diffusion processes in ternary feldspars. *Physics and Chemistry of Minerals* 17, 62–78.
- Behrens, H. and Zhang, Y. (2009). H₂O diffusion in peralkaline to peraluminous rhyolitic melts. *Contributions to Mineralogy and Petrology* 157(6), 765–780.
- Béjina, F., Raterron, P., Zhang, J., Jaoul, O. and Liebermann, R. (1997). Activation volume of silicon diffusion in San Carlos olivine. *Geophysical research letters* 24(21), 2597–2600.
- Belousova, E., Griffin, W., O'Reilly, S. Y. and Fisher, N. (2002). Apatite as an indicator mineral for mineral exploration: trace-element compositions and their relationship to host rock type. *Journal of Geochemical Exploration* 76(1), 45–69.
- Bénard, A., Le Losq, C., Nebel, O. and Arculus, R. J. (2018). Low-Ca boninite formation by second-stage melting of spinel harzburgite residues at mature subduction zones: new evidence from veined mantle xenoliths from the West Bismarck Arc. *Contributions to Mineralogy and Petrology* 173(12), 105.
- Bergantz, G., Schleicher, J. and Burgisser, A. (2015). Open-system dynamics and mixing in magma mushes. *Nature Geoscience* 8(10), 793–796.
- Bianchi, A., Callegari, E., Jobstraibizer, P. and nazionale delle ricerche (Italia). Centro di studio per la geologia e la petrografia delle formazioni cristalline, C. (1970). *I tipi petrografici fondamentali del plutone dell'Adamello: tonaliti, quarzodioriti, granodioriti e loro varietà leucocrate*. Società cooperativa tipografica.
- Bigazzi, G., Del Moro, A. and Macera, P. (1986). A quantitative approach to trace element and Sr isotope evolution in the Adamello batholith (northern Italy). *Contributions to Mineralogy and Petrology* 94(1), 46–53.
- Bindeman, I. N. (2003). Crystal sizes in evolving silicic magma chambers. *Geology* 31(4), 367–370.
- Bindeman, I. N., Davis, A. M. and Drake, M. J. (1998). Ion microprobe study of plagioclase-basalt partition experiments at natural concentration levels of trace elements. *Geochimica et Cosmochimica Acta* 62(7), 1175–1193.
- Bini, G., Chiodini, G., Caliro, S., Tassi, F., Vaselli, O., Rizzo, A. L., Mollo, S., Vougioukalakis, G. E. and Bachmann, O. (2022). Nitrogen, helium, and argon reveal the magmatic signature of fumarole gases and episodes of outgassing from upper-crustal magma reservoirs: The case of the Nisyros caldera (Aegean Arc, Greece). *Geochimica et Cosmochimica Acta* 335, 68–84.
- Blatter, D. L., Sisson, T. W. and Hankins, W. B. (2013). Crystallization of oxidized, moderately hydrous arc basalt at mid-to lower-crustal pressures: implications for andesite genesis. *Contributions to Mineralogy and Petrology* 166, 861–886.
- Blatter, D. L., Sisson, T. W. and Hankins, W. B. (2017). Voluminous arc dacites as amphibole reaction-boundary liquids. *Contributions to Mineralogy and Petrology* 172, 1–37.
- Blatter, D. L., Sisson, T. W. and Hankins, W. B. (2023). Garnet stability in arc basalt, andesite, and dacite—an experimental study. *Contributions to Mineralogy and Petrology* 178(6), 33.
- Bloch, E. M., Ganguly, J., Hervig, R. and Cheng, W. (2015). ¹⁷⁶Lu–¹⁷⁶Hf geochronology of garnet I: Experimental determination of the diffusion kinetics of Lu³⁺ and Hf⁴⁺ in garnet, closure temperatures and geochronological implications. *Contributions to Mineralogy and Petrology* 169, 1–18.
- Bloch, E. M., Jollands, M. C., Gerstl, S. S., Bouvier, A.-S., Plane, F. and Baumgartner, L. P. (2019). Diffusion of calcium in forsterite and ultra-high resolution of experimental diffusion profiles in minerals using local electrode atom probe tomography. *Geochimica et Cosmochimica Acta* 265, 85–95.

- Bloch, E. M., Jollands, M. C., Tollan, P., Plane, F., Bouvier, A.-S., Hervig, R., Berry, A. J., Zaubitzer, C., Escrig, S., Müntener, O., Ibañez-Mejia, M., Alleon, J., Meibom, A., Baumgartner, L. P., Marin-Carbonne, J. and Newville, M. (2022). Diffusion anisotropy of Ti in zircon and implications for Ti-in-zircon thermometry. *Earth and Planetary Science Letters* 578, 117317.
- Blundy, J. D. and Annen, C. J. (2016). Crustal magmatic systems from the perspective of heat transfer. *Elements* 12(2), 115–120.
- Blundy, J. D. and Cashman, K. (2001). Ascent-driven crystallisation of dacite magmas at Mount St Helens, 1980–1986. *Contributions to Mineralogy and Petrology* 140, 631–650.
- Blundy, J. D. and Cashman, K. (2005). Rapid decompression-driven crystallization recorded by melt inclusions from Mount St. Helens volcano. *Geology* 33(10), 793–796.
- Blundy, J. D., Mavrogenes, J., Tattitch, B., Sparks, R. and Gilmer, A. (2015). Generation of porphyry copper deposits by gas–brine reaction in volcanic arcs. *Nature Geoscience* 8(3), 235–240.
- Blundy, J. D. and Shimizu, N. (1991). Trace element evidence for plagioclase recycling in calc-alkaline magmas. *Earth and Planetary Science Letters* 102(2), 178–197.
- Blundy, J. D. and Sparks, R. S. J. (1992). Petrogenesis of mafic inclusions in granitoids of the Adamello Massif, Italy. *Journal of Petrology* 33(5), 1039–1104.
- Blundy, J. D. and Wood, B. (1994). Prediction of crystal–melt partition coefficients from elastic moduli. *Nature* 372(6505), 452–454.
- Bluth, G., Schnetzler, C., Krueger, A. and Walter, L. (1993). The contribution of explosive volcanism to global atmospheric sulphur dioxide concentrations. *Nature* 366(6453), 327–329.
- Bodnar, R. (1995). Fluid-inclusion evidence for a magmatic source for metals in porphyry copper deposits. In: *Magma, fluid and ore deposit*, volume 23. Mineralogical Association of Canada, Ottawa, pp. 139–152.
- Boro, J. R., Wolff, J. A., Neill, O. K., Steiner, A. R. and Ramos, F. C. (2021). Titanium diffusion profiles and melt inclusion chemistry and morphology in quartz from the Tshirege Member of the Bandelier Tuf. *American Mineralogist* 106(4), 620–632.
- Botcharnikov, R., Behrens, H. and Holtz, F. (2006). Solubility and speciation of C–O–H fluids in andesitic melt at T = 1100–1300 °C and P = 200 and 500 MPa. *Chemical Geology* 229(1-3), 125–143.
- Botcharnikov, R., Behrens, H., Holtz, F., Koepke, J. and Sato, H. (2004). Sulfur and chlorine solubility in Mt. Unzen rhyodacitic melt at 850 °C and 200 MPa. *Chemical Geology* 213(1-3), 207–225.
- Botcharnikov, R., Holtz, F. and Behrens, H. (2015). Solubility and fluid–melt partitioning of H₂O and Cl in andesitic magmas as a function of pressure between 50 and 500 MPa. *Chemical Geology* 418, 117–131.
- Boudreau, A. E. and McBirney, A. R. (1997). The Skaergaard layered series. Part III. Non-dynamic layering. *Journal of Petrology* 38(8), 1003–1020.
- Bouilhol, P., Burg, J.-P., Bodinier, J.-L., Schmidt, M. W., Dawood, H. and Hussain, S. (2009). Magma and fluid percolation in arc to forearc mantle: evidence from Sapat (Kohistan, Northern Pakistan). *Lithos* 107(1-2), 17–37.
- Bouilhol, P., Schmidt, M. W. and Burg, J.-P. (2015). Magma transfer and evolution in channels within the arc crust: the pyroxenitic feeder pipes of Sapat (Kohistan, Pakistan). *Journal of Petrology* 56(7), 1309–1342.
- Bourdon, B., Turner, S., Henderson, G. M. and Lundstrom, C. C. (2003). Introduction to U-series geochemistry. *Reviews in Mineralogy and Geochemistry* 52(1), 1–21.
- Bowen, N. L. (1928). *The evolution of the igneous rocks*. Princeton University Press.
- Brack, P. (1985). Multiple intrusions: Examples from the Adamello batholith (Italy) and their significance for the mechanisms of intrusion. *Memorie della Societa Geologica Italiana* 26, 145–157.
- Broderick, C., Wotzlaw, J., Frick, D. A., Gerdes, A., Ulianov, A., Günther, D. and Schaltegger, U. (2015). Linking the thermal evolution and emplacement history of an upper-crustal pluton to its lower-crustal roots using zircon geochronology and geochemistry (southern Adamello batholith, N. Italy). *Contributions to Mineralogy and Petrology* 170, 1–17.
- Brophy, J. G., Ota, T., Kunihiro, T., Tsujimori, T. and Nakamura, E. (2011). In situ ion-microprobe determination of trace element partition coefficients for hornblende, plagioclase, orthopyroxene,

Bibliography

- and apatite in equilibrium with natural rhyolitic glass, Little Glass Mountain Rhyolite, California. *American Mineralogist* 96(11-12), 1838–1850.
- Brown, M. and Solar, G. S. (1998). Shear-zone systems and melts: feedback relations and self-organization in orogenic belts. *Journal of Structural Geology* 20(2-3), 211–227.
- Brückel, K., Lundstrom, C. C., Ackerson, M. and Campe, C. (2023). Testing the limits of Ti-in-quartz thermometry and diffusion modelling to determine the thermal history of the Fish Canyon Tuff. *Journal of Petrology* 64(12), egad082.
- Bucholz, C. E., Gaetani, G. A., Behn, M. D. and Shimizu, N. (2013). Post-entrapment modification of volatiles and oxygen fugacity in olivine-hosted melt inclusions. *Earth and Planetary Science Letters* 374, 145–155.
- Buck, W. R., Einarsson, P. and Brandsdóttir, B. (2006). Tectonic stress and magma chamber size as controls on dike propagation: Constraints from the 1975–1984 Krafla rifting episode. *Journal of Geophysical Research: Solid Earth* 111(B12), B12404.
- Burg, J.-P. (2011). The Asia–Kohistan–India collision: Review and discussion. In: *Arc-Continent Collision*. Springer, pp. 279–309.
- Burg, J.-P., Bodinier, J.-L., Chaudhry, S., Hussain, S. and Dawood, H. (1998). Infra-arc mantle–crust transition and intra-arc mantle diapirs in the Kohistan Complex (Pakistani Himalaya): petro-structural evidence. *Terra Nova* 10(2), 74–80.
- Burg, J.-P., Jagoutz, O., Dawood, H. and Hussain, S. S. (2006). Precollision tilt of crustal blocks in rifted island arcs: Structural evidence from the Kohistan Arc. *Tectonics* 25(5), TC5005.
- Burgess, S. and Miller, J. (2008). Construction, solidification and internal differentiation of a large felsic arc pluton: Cathedral Peak granodiorite, Sierra Nevada Batholith. *Geological Society, London, Special Publications* 304(1), 203–233.
- Burgisser, A., Alletti, M. and Scaillet, B. (2015). Simulating the behavior of volatiles belonging to the C–O–H–S system in silicate melts under magmatic conditions with the software D-Compress. *Computers & Geosciences* 79, 1–14.
- Burgisser, A., Scaillet, B. and Harshvardhan (2008). Chemical patterns of erupting silicic magmas and their influence on the amount of degassing during ascent. *Journal of Geophysical Research: Solid Earth* 113(B12).
- Callegari, E. and Brack, P. (2002). Geological map of the Tertiary Adamello batholith (northern Italy): Explanatory notes and legend. *Memorie di Scienze Geologiche* 54, 19–49.
- Callegari, E. and Dal Piaz, G. (1973). Field relationships between the main igneous masses of the Adamello intrusive massif (northern Italy). *Memorie degli Istituti di Geologia e Mineralogia dell'Università di Padova* 29, 1–39.
- Callegaro, S., Geraki, K., Marzoli, A., De Min, A., Maneta, V. and Baker, D. R. (2020). The quintet completed: The partitioning of sulfur between nominally volatile-free minerals and silicate melts. *American Mineralogist: Journal of Earth and Planetary Materials* 105(5), 697–707.
- Candela, P. A. (1997). A review of shallow, ore-related granites: textures, volatiles, and ore metals. *Journal of Petrology* 38(12), 1619–1633.
- Caricchi, L., Annen, C., Blundy, J. D., Simpson, G. and Pinel, V. (2014a). Frequency and magnitude of volcanic eruptions controlled by magma injection and buoyancy. *Nature Geoscience* 7(2), 126–130.
- Caricchi, L. and Blundy, J. D. (2015). The temporal evolution of chemical and physical properties of magmatic systems. *Geological Society, London, Special Publications* 422(1), 1–15.
- Caricchi, L., Burlini, L., Ulmer, P., Gerya, T., Vassalli, M. and Papale, P. (2007). Non-Newtonian rheology of crystal-bearing magmas and implications for magma ascent dynamics. *Earth and Planetary Science Letters* 264(3-4), 402–419.
- Caricchi, L., Simpson, G. and Schaltegger, U. (2014b). Zircons reveal magma fluxes in the Earth's crust. *Nature* 511(7510), 457–461.
- Caricchi, L., Townsend, M., Rivalta, E. and Namiki, A. (2021). The build-up and triggers of volcanic eruptions. *Nature Reviews Earth & Environment* 2(7), 458–476.
- Carley, T. L., Miller, C. F., Wooden, J. L., Bindeman, I. N. and Barth, A. P. (2011). Zircon from historic eruptions in Iceland: reconstructing storage and evolution of silicic magmas. *Mineralogy and Petrology* 102, 135–161.
- Carn, S., Clarisse, L. and Prata, A. J. (2016). Multi-decadal satellite measurements of global volcanic degassing. *Journal of Volcanology and Geothermal Research* 311, 99–134.

- Carn, S., Fioletov, V., McLinden, C., Li, C. and Krotkov, N. (2017). A decade of global volcanic SO₂ emissions measured from space. *Scientific reports* 7(1), 44095.
- Carpenter, M. A. and McConnell, J. D. C. (1984). Experimental delineation of the $\text{C}\bar{1} \rightleftharpoons \text{I}\bar{1}$ transformation in intermediate plagioclase feldspars. *American Mineralogist* 69(1-2), 112–121.
- Carroll, M. R. and Webster, J. D. (1994). Solubilities of sulfur, noble gases, nitrogen, chlorine, and fluorine in magmas. In: M. R. Carroll and J. R. Holloway, eds., *Reviews in Mineralogy*, volume 30. Mineralogical Society of America, pp. 231–231.
- Cashman, K. V. (2004). Volatile controls on magma ascent and eruption. *Geophysical Monograph Series* 150, 109–124.
- Cashman, K. V., Sparks, R. S. J. and Blundy, J. D. (2017). Vertically extensive and unstable magmatic systems: a unified view of igneous processes. *Science* 355(6331), eaag3055.
- Cassidy, M., Manga, M., Cashman, K. and Bachmann, O. (2018). Controls on explosive-effusive volcanic eruption styles. *Nature Communications* 9(1), 2839.
- Catchpole, H., Kouzmanov, K., Putlitz, B., Seo, J. H. and Fontboté, L. (2015). Zoned base metal mineralization in a porphyry system: Origin and evolution of mineralizing fluids in the Morococha district, Peru. *Economic Geology* 110(1), 39–71.
- Cawood, P. A., Hawkesworth, C. and Dhuime, B. (2012). Detrital zircon record and tectonic setting. *Geology* 40(10), 875–878.
- Ceriani, S., Fügenschuh, B. and Schmid, S. M. (2001). Multi-stage thrusting at the "Penninic Front" in the Western Alps between Mont Blanc and Pelvoux massifs. *International Journal of Earth Sciences* 90(3), 685–702.
- Chakraborty, S. (2010). Diffusion coefficients in olivine, wadsleyite and ringwoodite. *Reviews in Mineralogy and Geochemistry* 72(1), 603–639.
- Chakraborty, S., Knoche, R., Schulze, H., Rubie, D., Dobson, D., Ross, N. and Angel, R. (1999). Enhancement of cation diffusion rates across the 410-kilometer discontinuity in Earth's mantle. *Science* 283(5400), 362–365.
- Chamberlain, K. J., Morgan, D. J. and Wilson, C. J. (2014a). Timescales of mixing and mobilisation in the Bishop Tuff magma body: perspectives from diffusion chronometry. *Contributions to Mineralogy and Petrology* 168, 1–24.
- Chamberlain, K. J., Wilson, C. J., Wooden, J. L., Charlier, B. L. and Ireland, T. R. (2014b). New perspectives on the Bishop Tuff from zircon textures, ages and trace elements. *Journal of Petrology* 55(2), 395–426.
- Chambers, M., Memeti, V., Eddy, M. P. and Schoene, B. (2020). Half a million years of magmatic history recorded in a K-feldspar megacryst of the Tuolumne Intrusive Complex, California, USA. *Geology* 48(4), 400–404.
- Cherniak, D. J. (1995). Diffusion of lead in plagioclase and K-feldspar: an investigation using Rutherford backscattering and resonant nuclear reaction analysis. *Contributions to Mineralogy and Petrology* 120, 358–371.
- Cherniak, D. J. (2002). Ba diffusion in feldspar. *Geochimica et Cosmochimica Acta* 66(9), 1641–1650.
- Cherniak, D. J. (2003). REE diffusion in feldspar. *Chemical Geology* 193(1-2), 25–41.
- Cherniak, D. J. and Watson, E. B. (1992). A study of strontium diffusion in K-feldspar, Na-K feldspar and anorthite using Rutherford Backscattering Spectroscopy. *Earth and Planetary Science Letters* 113(3), 411–425.
- Cherniak, D. J. and Watson, E. B. (1994). A study of strontium diffusion in plagioclase using Rutherford backscattering spectroscopy. *Geochimica et Cosmochimica Acta* 58(23), 5179–5190.
- Cherniak, D. J. and Watson, E. B. (2007). Ti diffusion in zircon. *Chemical Geology* 242(3-4), 473–483.
- Cherniak, D. J., Watson, E. B. and Wark, D. A. (2007). Ti diffusion in quartz. *Chemical Geology* 236(1-2), 65–74.
- Christensen, J. N. and DePaolo, D. J. (1993). Time scales of large volume silicic magma systems: Sr isotopic systematics of phenocrysts and glass from the Bishop Tuff, Long Valley, California. *Contributions to Mineralogy and Petrology* 113, 100–114.
- Claiborne, L. L., Miller, C. F., Flanagan, D. M., Clynne, M. A. and Wooden, J. L. (2010). Zircon reveals protracted magma storage and recycling beneath Mount St. Helens. *Geology* 38(11), 1011–1014.

- Clarke, D. B., Renno, A. D., Hamilton, D. C., Gilbricht, S. and Bachmann, K. (2022). The spatial association of accessory minerals with biotite in granitic rocks from the South Mountain Batholith, Nova Scotia, Canada. *Geosphere* 18(1), 1–18.
- Clemens, J. and Mawer, C. (1992). Granitic magma transport by fracture propagation. *Tectonophysics* 204(3-4), 339–360.
- Clemens, J. D., Mawer, C. and Petford, N. (1997). Ascent mechanisms of granitic magmas: causes and consequences. In: M. B. Holness, ed., *Deformation-enhanced fluid transport in the Earth's crust and mantle*. Chapman & Hall, pp. 145–172.
- Clemens, J. D. and Vielzeuf, D. (1987). Constraints on melting and magma production in the crust. *Earth and Planetary Science Letters* 86(2-4), 287–306.
- Cline, J. S. and Bodnar, R. J. (1991). Can economic porphyry copper mineralization be generated by a typical calc-alkaline melt? *Journal of Geophysical Research: Solid Earth* 96(B5), 8113–8126.
- Cofrade, G., Závada, P., Krýza, O., Cantarero, I., Gratacós, Ò., Ferrer, O., Adineh, S., Ramirez-Perez, P., Roca, E. and Travé, A. (2023). The kinematics of a salt sheet recorded in an array of distorted intrasalt stringers (Les Avellanes Diapir–South-Central Pyrenees). *Journal of Structural Geology* 176, 104963.
- Colbertaldo, D. (1940). Petrografia del Monte Blumone (Adamello meridionale); con 3 tavole, una cartina e 9 figure nel testo. *Memorie degli Istituti di Geologia e Mineralogia dell'Università di Padova* 14.
- Coleman, D. S., Bartley, J. M., Glazner, A. F. and Pardue, M. J. (2012). Is chemical zonation in plutonic rocks driven by changes in source magma composition or shallow-crustal differentiation? *Geosphere* 8(6), 1568–1587.
- Coleman, D. S., Gray, W. and Glazner, A. F. (2004). Rethinking the emplacement and evolution of zoned plutons: Geochronologic evidence for incremental assembly of the Tuolumne Intrusive Suite, California. *Geology* 32(5), 433–436.
- Colin, A., Schmidt, C., Pokrovski, G. S., Wilke, M., y Borisova, A. and Toplis, M. (2020). In situ determination of sulfur speciation and partitioning in aqueous fluid-silicate melt systems. *Geochemical Perspectives Letters* 14, 31–35.
- Collins, W. J., Murphy, J. B., Johnson, T. E. and Huang, H.-Q. (2020). Critical role of water in the formation of continental crust. *Nature Geoscience* 13(5), 331–338.
- Condie, K. C. and Aster, R. C. (2009). Zircon age episodicity and growth of continental crust. *EOS, Transactions American Geophysical Union* 90(41), 364–364.
- Condomines, M., Gauthier, P.-J. and Sigmarrsson, O. (2003). Timescales of magma chamber processes and dating of young volcanic rocks. *Reviews in Mineralogy and Geochemistry* 52(1), 125–174.
- Connolly, J. A. D. (2005). Computation of phase equilibria by linear programming: a tool for geodynamic modeling and its application to subduction zone decarbonation. *Earth and Planetary Science Letters* 236(1-2), 524–541.
- Connolly, J. A. D. (2009). The geodynamic equation of state: what and how. *Geochemistry, Geophysics, Geosystems* 10(10).
- Cooper, K. M. (2015). Timescales of crustal magma reservoir processes: insights from U-series crystal ages. *Geological Society, London, Special Publications* 422(1), 141–174.
- Cooper, K. M. (2019). Time scales and temperatures of crystal storage in magma reservoirs: implications for magma reservoir dynamics. *Philosophical Transactions of the Royal Society A* 377(2139), 20180009.
- Cooper, K. M. and Kent, A. J. (2014). Rapid remobilization of magmatic crystals kept in cold storage. *Nature* 506(7489), 480–483.
- Cooper, K. M. and Reid, M. R. (2003). Re-examination of crystal ages in recent Mount St. Helens lavas: implications for magma reservoir processes. *Earth and Planetary Science Letters* 213(1-2), 149–167.
- Cooper, K. M. and Reid, M. R. (2008). Uranium-series crystal ages. *Reviews in Mineralogy and Geochemistry* 69(1), 479–544.
- Cooper, K. M., Reid, M. R., Murrell, M. T. and Clague, D. A. (2001). Crystal and magma residence at Kilauea Volcano, Hawaii: ^{230}Th – ^{226}Ra dating of the 1955 east rift eruption. *Earth and Planetary Science Letters* 184(3-4), 703–718.

- Coplen, T. B. and Krouse, H. R. (1998). Sulphur isotope data consistency improved. *Nature* 392(6671), 32–32.
- Corry, C. E. (1988). *Laccoliths: mechanics of emplacement and growth*, volume 220. Geological Society of America.
- Costa, F. (2008). Residence times of silicic magmas associated with calderas. In: J. Gottsmann and J. Martì, eds., *Developments in Volcanology*, volume 10. Elsevier, Amsterdam, pp. 1–55.
- Costa, F. and Chakraborty, S. (2008). The effect of water on Si and O diffusion rates in olivine and implications for transport properties and processes in the upper mantle. *Physics of the Earth and Planetary Interiors* 166(1-2), 11–29.
- Costa, F., Chakraborty, S. and Dohmen, R. (2003). Diffusion coupling between trace and major elements and a model for calculation of magma residence times using plagioclase. *Geochimica et Cosmochimica Acta* 67(12), 2189–2200.
- Costa, F., Coogan, L. A. and Chakraborty, S. (2010). The time scales of magma mixing and mingling involving primitive melts and melt–mush interaction at mid-ocean ridges. *Contributions to Mineralogy and Petrology* 159, 371–387.
- Costa, F., Dohmen, R. and Chakraborty, S. (2008). Time scales of magmatic processes from modeling the zoning patterns of crystals. *Reviews in Mineralogy and Geochemistry* 69(1), 545–594.
- Costa, F. and Dungan, M. (2005). Short time scales of magmatic assimilation from diffusion modeling of multiple elements in olivine. *Geology* 33(10), 837–840.
- Costa, F. and Morgan, D. (2010). Time constraints from chemical equilibration in magmatic crystals. In: A. Dosseto, S. Turner and J. Van Orman, eds., *Timescales of magmatic processes: from core to atmosphere*. Wiley, pp. 125–159.
- Costa, F., Shea, T. and Ubide, T. (2020). Diffusion chronometry and the timescales of magmatic processes. *Nature Reviews Earth & Environment* 1(4), 201–214.
- Cottrell, E., Birner, S. K., Brounce, M., Davis, F. A., Waters, L. E. and Kelley, K. A. (2021). Oxygen fugacity across tectonic settings. *Magma redox geochemistry*, 33–61.
- Couch, S., Sparks, R. and Carroll, M. (2001). Mineral disequilibrium in lavas explained by convective self-mixing in open magma chambers. *Nature* 411(6841), 1037–1039.
- Courrioux, G. (1987). Oblique diapirism: the Criffel granodiorite/granite zoned pluton (southwest Scotland). *Journal of Structural Geology* 9(3), 313–330.
- Crank, J. (1975). *The mathematics of diffusion*. Oxford university press.
- Cruden, A. R. (1990). Flow and fabric development during the diapiric rise of magma. *The Journal of Geology* 98(5), 681–698.
- Curry, A., Gaynor, S. P., Davies, J., Ovtcharova, M., Simpson, G. and Caricchi, L. (2021). Timescales and thermal evolution of large silicic magma reservoirs during an ignimbrite flare-up: perspectives from zircon. *Contributions to Mineralogy and Petrology* 176, 1–27.
- Daczko, N. R., Piazzolo, S., Meek, U., Stuart, C. A. and Elliott, V. (2016). Hornblende delineates zones of mass transfer through the lower crust. *Scientific Reports* 6(1), 31369.
- Dalou, C., Koga, K. T., Shimizu, N., Boulon, J. and Devidal, J.-L. (2012). Experimental determination of F and Cl partitioning between ilmenite and basaltic melt. *Contributions to Mineralogy and Petrology* 163, 591–609.
- Danyushevsky, L. V., McNeill, A. W. and Sobolev, A. V. (2002). Experimental and petrological studies of melt inclusions in phenocrysts from mantle-derived magmas: an overview of techniques, advantages and complications. *Chemical Geology* 183(1-4), 5–24.
- Davidson, J., Morgan, D., Charlier, B., Harlou, R. and Hora, J. (2007). Microsampling and isotopic analysis of igneous rocks: implications for the study of magmatic systems. *Annual Review in Earth and Planetary Sciences* 35, 273–311.
- Dawson, P., Evans, J. and Iyer, H. (1990). Teleseismic tomography of the compressional wave velocity structure beneath the Long Valley region, California. *Journal of Geophysical Research: Solid Earth* 95(B7), 11021–11050.
- de Maisonneuve, C. B., Costa, F., Huber, C., Vonlanthen, P., Bachmann, O. and Dungan, M. A. (2016). How do olivines record magmatic events? Insights from major and trace element zoning. *Contributions to Mineralogy and Petrology* 171, 1–20.
- de Moor, J. M., Aiuppa, A., Avard, G., Wehrmann, H., Dunbar, N., Muller, C., Tamburello, G., Giudice, G., Liuzzo, M., Moretti, R. et al. (2016). Turmoil at Turrialba Volcano (Costa

- Rica): Degassing and eruptive processes inferred from high-frequency gas monitoring. *Journal of Geophysical Research: Solid Earth* 121(8), 5761–5775.
- de Saint-Blanquat, M., Habert, G., Horsman, E., Morgan, S. S., Tikoff, B., Launeau, P. and Gleizes, G. (2006). Mechanisms and duration of non-tectonically assisted magma emplacement in the upper crust: The Black Mesa pluton, Henry Mountains, Utah. *Tectonophysics* 428(1-4), 1–31.
- de Saint Blanquat, M., Horsman, E., Habert, G., Morgan, S., Vanderhaeghe, O., Law, R. and Tikoff, B. (2011). Multiscale magmatic cyclicality, duration of pluton construction, and the paradoxical relationship between tectonism and plutonism in continental arcs. *Tectonophysics* 500(1-4), 20–33.
- de Silva, S. L. and Gosnold, W. D. (2007). Episodic construction of batholiths: Insights from the spatiotemporal development of an ignimbrite flare-up. *Journal of Volcanology and Geothermal Research* 167(1-4), 320–335.
- DeBari, S. M. and Coleman, R. (1989). Examination of the deep levels of an island arc: Evidence from the Tonsina ultramafic-mafic assemblage, Tonsina, Alaska. *Journal of Geophysical Research: Solid Earth* 94(B4), 4373–4391.
- Deering, C. and Bachmann, O. (2010). Trace element indicators of crystal accumulation in silicic igneous rocks. *Earth and Planetary Science Letters* 297(1-2), 324–331.
- Degruyter, W. and Huber, C. (2014). A model for eruption frequency of upper crustal silicic magma chambers. *Earth and Planetary Science Letters* 403, 117–130.
- Degruyter, W., Huber, C., Bachmann, O., Cooper, K. M. and Kent, A. J. (2017). Influence of exsolved volatiles on reheating silicic magmas by recharge and consequences for eruptive style at Volcán Quizapu (Chile). *Geochemistry, Geophysics, Geosystems* 18(11), 4123–4135.
- Del Moro, A., Ferrara, G., Pescia, A. and Callegari, E. (1985). A geochemical study on the acid and basic rocks of the Adamello batholith. *Memorie della Società Geologica Italiana* 26.
- Del Moro, A., Pardini, G., Quercioli, C., Villa, I. and Callegari, E. (1983). Rb/Sr and K/Ar chronology of Adamello granitoids, southern Alps. *Memorie della Società Geologica Italiana* 26(1), 285–299.
- Demers-Roberge, A., Jollands, M. C., Tollan, P. and Müntener, O. (2021). H diffusion in orthopyroxene and the retention of mantle water signatures. *Geochimica et Cosmochimica Acta* 305, 263–281.
- Devineau, K., Champallier, R. and Pichavant, M. (2020). Dynamic crystallization of a haplogranitic melt: application to pegmatites. *Journal of Petrology* 61(5), ega054.
- Devoir, A., Bloch, E. and Müntener, O. (2021). Residence time of igneous garnet in Si-rich magmatic systems: Insights from diffusion modeling of major and trace elements. *Earth and Planetary Science Letters* 560, 116771.
- Dewey, J. F., Pitman III, W. C., Ryan, W. B. and Bonnin, J. (1973). Plate tectonics and the evolution of the Alpine system. *Geological society of America bulletin* 84(10), 3137–3180.
- Diella, V., Spalla, M. and Tunesi, A. (1992). Contrasting thermomechanical evolutions in the Southalpine metamorphic basement of the Orobic Alps (Central Alps, Italy). *Journal of Metamorphic Geology* 10(2), 203–219.
- Ding, S., Plank, T., Wallace, P. J. and Rasmussen, D. J. (2023). Sulfur_X: A model of sulfur degassing during magma ascent. *Geochemistry, Geophysics, Geosystems* 24(4), e2022GC010552.
- Ding, T., Valkiers, S., Kipphardt, H., De Bievre, P., Taylor, P., Gonfiantini, R. and Krouse, R. (2001). Calibrated sulfur isotope abundance ratios of three IAEA sulfur isotope reference materials and V-CDT with a reassessment of the atomic weight of sulfur. *Geochimica et Cosmochimica Acta* 65(15), 2433–2437.
- Doherty, A. L., Webster, J. D., Goldoff, B. A. and Piccoli, P. M. (2014). Partitioning behavior of chlorine and fluorine in felsic melt–fluid(s)–apatite systems at 50 MPa and 850–950 °C. *Chemical Geology* 384, 94–111.
- Dohmen, R. and Blundy, J. D. (2014). A predictive thermodynamic model for element partitioning between plagioclase and melt as a function of pressure, temperature and composition. *American Journal of Science* 314(9), 1319–1372.
- Dohmen, R., Faak, K. and Blundy, J. D. (2017). Chronometry and speedometry of magmatic processes using chemical diffusion in olivine, plagioclase and pyroxenes. *Reviews in Mineralogy and Geochemistry* 83(1), 535–575.

- Dohmen, R., Ter Heege, J. H., Becker, H.-W. and Chakraborty, S. (2016). Fe-Mg interdiffusion in orthopyroxene. *American Mineralogist* 101(10), 2210–2221.
- Donev, A., Cisse, I., Sachs, D., Variano, E. A., Stillinger, F. H., Connelly, R., Torquato, S. and Chaikin, P. M. (2004). Improving the density of jammed disordered packings using ellipsoids. *Science* 303(5660), 990–993.
- Driesner, T. and Heinrich, C. A. (2007). The system H₂O–NaCl. Part I: Correlation formulae for phase relations in temperature–pressure–composition space from 0 to 1000 °C, 0 to 5000 bar, and 0 to 1 X_{NaCl}. *Geochimica et Cosmochimica Acta* 71(20), 4880–4901.
- Druitt, T. H., Costa, F., Deloule, E., Dungan, M. and Scaillet, B. (2012). Decadal to monthly timescales of magma transfer and reservoir growth at a caldera volcano. *Nature* 482(7383), 77–80.
- Dufek, J. and Bergantz, G. (2005). Lower crustal magma genesis and preservation: a stochastic framework for the evaluation of basalt–crust interaction. *Journal of Petrology* 46(11), 2167–2195.
- Dupuy, C., Dostal, J. and Fratta, M. (1982). Geochemistry of the Adamello massif (northern Italy). *Contributions to Mineralogy and Petrology* 80, 41–48.
- Economos, R., Boehnke, P. and Burgisser, A. (2017). Sulfur isotopic zoning in apatite crystals: A new record of dynamic sulfur behavior in magmas. *Geochimica et Cosmochimica Acta* 215, 387–403.
- Edmonds, M. (2008). New geochemical insights into volcanic degassing. *Philosophical Transactions of the Royal Society A: Mathematical, Physical and Engineering Sciences* 366(1885), 4559–4579.
- Elter, P. and Pertusati, P. (1973). Considerazioni sul limite Alpi-Appennino e sulle sue relazioni con l'arc delle Alpi occidentali. *Memorie della Società Geologica Italiana* 12, 359–375.
- Faak, K., Chakraborty, S. and Coogan, L. A. (2013). Mg in plagioclase: Experimental calibration of a new geothermometer and diffusion coefficients. *Geochimica et Cosmochimica Acta* 123, 195–217.
- Faroughi, S. A. and Huber, C. (2015). Unifying the relative hindered velocity in suspensions and emulsions of nondeformable particles. *Geophysical Research Letters* 42(1), 53–59.
- Farver, J. R. and Yund, R. (1991). Oxygen diffusion in quartz: dependence on temperature and water fugacity. *Chemical Geology* 90(1-2), 55–70.
- Faure, F., Schiano, P., Trolliard, G., Nicollet, C. and Soulestin, B. (2007). Textural evolution of polyhedral olivine experiencing rapid cooling rates. *Contributions to Mineralogy and Petrology* 153, 405–416.
- Faure, F., Trolliard, G., Nicollet, C. and Montel, J.-M. (2003). A developmental model of olivine morphology as a function of the cooling rate and the degree of undercooling. *Contributions to Mineralogy and Petrology* 145, 251–263.
- Ferguson, D. J., Gonnermann, H. M., Ruprecht, P., Plank, T., Hauri, E. H., Houghton, B. F. and Swanson, D. A. (2016). Magma decompression rates during explosive eruptions of Kīlauea volcano, Hawaii, recorded by melt embayments. *Bulletin of Volcanology* 78, 1–12.
- Fick, A. (1855). Ueber diffusion. *Annalen der physik* 170(1), 59–86.
- Fiege, A., Holtz, F., Behrens, H., Mandeville, C. W., Shimizu, N., Crede, L. S. and Göttlicher, J. (2015). Experimental investigation of the S and S-isotope distribution between H₂O–S±Cl fluids and basaltic melts during decompression. *Chemical Geology* 393, 36–54.
- Fiege, A., Holtz, F., Shimizu, N., Mandeville, C. W., Behrens, H. and Knipping, J. L. (2014). Sulfur isotope fractionation between fluid and andesitic melt: An experimental study. *Geochimica et Cosmochimica Acta* 142, 501–521.
- Fischer, T. P., Arellano, S., Carn, S., Aiuppa, A., Galle, B., Allard, P., Lopez, T., Shinohara, H., Kelly, P., Werner, C., Cardellini, C. and Chiodini, G. (2019). The emissions of CO₂ and other volatiles from the world's subaerial volcanoes. *Scientific reports* 9(1), 18716.
- Fitz Gerald, J. D., Parise, J. B. and Mackinnon, I. D. (1986). Average structure of an An₄₈ plagioclase from the Hogarth Ranges. *American Mineralogist* 71(11-12), 1399–1408.
- Flaherty, T., Druitt, T., Tuffen, H., Higgins, M. D., Costa, F. and Cadoux, A. (2018). Multiple timescale constraints for high-flux magma chamber assembly prior to the Late Bronze Age eruption of Santorini (Greece). *Contributions to Mineralogy and Petrology* 173, 1–21.
- Floess, D. (2013). *Contact metamorphism and emplacement of the Western Adamello tonalite*. Ph.D. thesis, University of Lausanne.

Bibliography

- Floess, D. and Baumgartner, L. P. (2013). Formation of garnet clusters during polyphase metamorphism. *Terra Nova* 25(2), 144–150.
- Floess, D. and Baumgartner, L. P. (2015). Constraining magmatic fluxes through thermal modelling of contact metamorphism. *Geological Society, London, Special Publications* 422(1), 41–56.
- Foden, J. and Green, D. (1992). Possible role of amphibole in the origin of andesite: some experimental and natural evidence. *Contributions to Mineralogy and Petrology* 109(4), 479–493.
- Fogel, R. A. and Rutherford, M. J. (1990). The solubility of carbon dioxide in rhyolitic melts; a quantitative FTIR study. *American Mineralogist* 75(11-12), 1311–1326.
- Fossen, H. and Cavalcante, G. C. G. (2017). Shear zones—A review. *Earth-Science Reviews* 171, 434–455.
- France-Lanord, C. and Le Fort, P. (1988). Crustal melting and granite genesis during the Himalayan collision orogenesis. *Earth and Environmental Science Transactions of The Royal Society of Edinburgh* 79(2-3), 183–195.
- Fuhrman, M. L. and Lindsley, D. H. (1988). Ternary-feldspar modeling and thermometry. *American Mineralogist* 73(3-4), 201–215.
- Gaetani, G. A., O’Leary, J. A., Shimizu, N., Bucholz, C. E. and Newville, M. (2012). Rapid reequilibration of H₂O and oxygen fugacity in olivine-hosted melt inclusions. *Geology* 40(10), 915–918.
- Ganguly, J., Tirone, M. and Hervig, R. (1998). Diffusion kinetics of samarium and neodymium in garnet, and a method for determining cooling rates of rocks. *Science* 281(5378), 805–807.
- Gardien, V., Thompson, A. B., Grujic, D. and Ulmer, P. (1995). Experimental melting of biotite + plagioclase + quartz ± muscovite assemblages and implications for crustal melting. *Journal of Geophysical Research: Solid Earth* 100(B8), 15581–15591.
- Gardner, J. E. (2009). The impact of pre-existing gas on the ascent of explosively erupted magma. *Bulletin of Volcanology* 71, 835–844.
- Gaynor, S. P., Ruiz, M. and Schaltegger, U. (2022). The importance of high precision in the evaluation of U-Pb zircon age spectra. *Chemical Geology* 603, 120913.
- Ghiorso, M. S. (1984). Activity/composition relations in the ternary feldspars. *Contributions to Mineralogy and Petrology* 87(3), 282–296.
- Ghiorso, M. S. and Gualda, G. A. (2013). A method for estimating the activity of titania in magmatic liquids from the compositions of coexisting rhombohedral and cubic iron–titanium oxides. *Contributions to Mineralogy and Petrology* 165, 73–81.
- Ghiorso, M. S. and Sack, O. (1991). Fe-Ti oxide geothermometry: thermodynamic formulation and the estimation of intensive variables in silicic magmas. *Contributions to Mineralogy and Petrology* 108, 485–510.
- Giesting, P. A. and Filiberto, J. (2014). Quantitative models linking igneous amphibole composition with magma Cl and OH content. *American Mineralogist* 99(4), 852–865.
- Giletti, B. and Casserly, J. (1994). Strontium diffusion kinetics in plagioclase feldspars. *Geochimica et Cosmochimica Acta* 58(18), 3785–3793.
- Giletti, B. J. and Shanahan, T. M. (1997). Alkali diffusion in plagioclase feldspar. *Chemical Geology* 139(1-4), 3–20.
- Ginibre, C., Wörner, G. and Kronz, A. (2002). Minor-and trace-element zoning in plagioclase: implications for magma chamber processes at Parínacota volcano, northern Chile. *Contributions to Mineralogy and Petrology* 143(3), 300–315.
- Ginibre, C., Wörner, G. and Kronz, A. (2007). Crystal zoning as an archive for magma evolution. *Elements* 3(4), 261–266.
- Glazner, A. F., Bartley, J. M., Coleman, D. S., Gray, W. and Taylor, R. Z. (2004). Are plutons assembled over millions of years by amalgamation from small magma chambers? *GSA today* 14(5-Apr), 4–11.
- Glazner, A. F., Bartley, J. M., Coleman, D. S. and Lindgren, K. (2020). Aplite diking and infiltration: A differentiation mechanism restricted to plutonic rocks. *Contributions to Mineralogy and Petrology* 175, 1–17.
- Glazner, A. F., Bartley, J. M. and Law, B. S. (2021). Immiscibility and the origin of ladder structures, mafic layering, and schlieren in plutons. *Geology* 49(1), 86–90.

- Gordeychik, B., Churikova, T., Shea, T., Kronz, A., Simakin, A. and Wörner, G. (2020). Fo and Ni relations in olivine differentiate between crystallization and diffusion trends. *Journal of Petrology* 61(9), egaa083.
- Götze, J., Plötze, M. and Habermann, D. (2001). Origin, spectral characteristics and practical applications of the cathodoluminescence (CL) of quartz—a review. *Mineralogy and petrology* 71, 225–250.
- Gray, W., Glazner, A. F., Coleman, D. S. and Bartley, J. M. (2008). Long-term geochemical variability of the Late Cretaceous Tuolumne intrusive suite, central Sierra Nevada, California. *Geological Society, London, Special Publications* 304(1), 183–201.
- Green, D. and Ringwood, A. (1970). Mineralogy of peridotitic compositions under upper mantle conditions. *Physics of the Earth and Planetary Interiors* 3, 359–371.
- Green, E., White, R., Diener, J., Powell, R., Holland, T. and Palin, R. (2016). Activity–composition relations for the calculation of partial melting equilibria in metabasic rocks. *Journal of Metamorphic Geology* 34(9), 845–869.
- Greene, A. R., DeBari, S. M., Kelemen, P. B., Blusztajn, J. and Clift, P. D. (2006). A detailed geochemical study of island arc crust: the Talkeetna arc section, south-central Alaska. *Journal of Petrology* 47(6), 1051–1093.
- Grocolas, T., Bloch, E. M., Bouvier, A.-S. and Müntener, O. (in review). Diffusion of Sr and Ba in plagioclase: Composition and silica activity dependencies, and application to volcanic rocks. *Earth and Planetary Science Letters* .
- Grocolas, T. and Müntener, O. (2024). The role of peritectic biotite for the chemical and mechanical differentiation of felsic plutonic rocks (Western Adamello, Italy). *Journal of Petrology* 65(3), egae009.
- Grocott, J., Brown, M., Dallmeyer, R. D., Taylor, G. K. and Treloar, P. J. (1994). Mechanisms of continental growth in extensional arcs: An example from the Andean plate-boundary zone. *Geology* 22(5), 391–394.
- Grove, T. L. (1993). Corrections to expressions for calculating mineral components in “Origin of calc-alkaline series lavas at medicine lake volcano by fractionation, assimilation and mixing” and “Experimental petrology of normal MORB near the Kane fracture zone: 22-25°N, mid-Atlantic ridge”. *Contributions to Mineralogy and Petrology* 114(3), 422–424.
- Grove, T. L., Baker, M. B. and Kinzler, R. J. (1984). Coupled CaAl-NaSi diffusion in plagioclase feldspar: experiments and applications to cooling rate speedometry. *Geochimica et Cosmochimica Acta* 48(10), 2113–2121.
- Grove, T. L., Elkins-Tanton, L. T., Parman, S. W., Chatterjee, N., Müntener, O. and Gaetani, G. A. (2003). Fractional crystallization and mantle-melting controls on calc-alkaline differentiation trends. *Contributions to Mineralogy and Petrology* 145, 515–533.
- Grujic, D., Stipp, M. and Wooden, J. L. (2011). Thermometry of quartz mylonites: Importance of dynamic recrystallization on Ti-in-quartz reequilibration. *Geochemistry, Geophysics, Geosystems* 12(6).
- Gualda, G. A., Pamukcu, A. S., Ghiorso, M. S., Anderson Jr, A. T., Sutton, S. R. and Rivers, M. L. (2012). Timescales of quartz crystallization and the longevity of the Bishop giant magma body. *PloS one* 7(5), e37492.
- Guggino, S. (2012). *Fluorine partitioning between nominally anhydrous minerals (olivine, clinopyroxene, and plagioclase) and silicate melt using secondary ion mass spectrometry and newly synthesized basaltic fluorine microanalytical glass standards*. Ph.D. thesis, Arizona State University.
- Hacker, B. R., Mehl, L., Kelemen, P. B., Rioux, M., Behn, M. D. and Luffi, P. (2008). Reconstruction of the Talkeetna intraoceanic arc of Alaska through thermobarometry. *Journal of Geophysical Research: Solid Earth* 113(B3), B03204.
- Hamilton, D., Burnham, C. W. and Osborn, E. (1964). The solubility of water and effects of oxygen fugacity and water content on crystallization in mafic magmas. *Journal of Petrology* 5(1), 21–39.
- Hammarstrom, J. M. and Zen, E. (1986). Aluminum in hornblende: an empirical igneous geobarometer. *American Mineralogist* 71(11-12), 1297–1313.

Bibliography

- Hammerli, J., Greber, N. D., Martin, L., Bouvier, A.-S., Kemp, A. I., Fiorentini, M. L., Spangenberg, J. E., Ueno, Y. and Schaltegger, U. (2021a). Tracing sulfur sources in the crust via SIMS measurements of sulfur isotopes in apatite. *Chemical Geology* 579, 120242.
- Hammerli, J., Hermann, J., Tollan, P. and Naab, F. (2021b). Measuring in situ CO₂ and H₂O in apatite via ATR-FTIR. *Contributions to Mineralogy and Petrology* 176, 1–20.
- Handy, M., Schmid, S., Paffrath, M. and Friederich, W. (2021). European tectosphere and slabs beneath the greater Alpine area—Interpretation of mantle structure in the Alps–Apennines–Pannonian region from teleseismic V_p studies. *Solid Earth Discussions* 2021, 1–61.
- Handy, M. R., Schmid, S. M., Bousquet, R., Kissling, E. and Bernoulli, D. (2010). Reconciling plate-tectonic reconstructions of Alpine Tethys with the geological–geophysical record of spreading and subduction in the Alps. *Earth-Science Reviews* 102(3-4), 121–158.
- Hansmann, W. and Oberli, F. (1991). Zircon inheritance in an igneous rock suite from the southern Adamello batholith (Italian Alps) Implications for petrogenesis. *Contributions to Mineralogy and Petrology* 107(4), 501–518.
- Harris, A. C. and Golding, S. D. (2002). New evidence of magmatic-fluid-related phyllic alteration: Implications for the genesis of porphyry Cu deposits. *Geology* 30(4), 335–338.
- Hartley, M. E., Morgan, D. J., MacLennan, J., Edmonds, M. and Thordarson, T. (2016). Tracking timescales of short-term precursors to large basaltic fissure eruptions through Fe–Mg diffusion in olivine. *Earth and Planetary Science Letters* 439, 58–70.
- Hauri, E. H., Gaetani, G. A. and Green, T. H. (2006). Partitioning of water during melting of the Earth’s upper mantle at H₂O-undersaturated conditions. *Earth and Planetary Science Letters* 248(3-4), 715–734.
- Hauzenberger, C. A., Baumgartner, L. P. and Pak, T. M. (2001). Experimental study on the solubility of the “model”-pelite mineral assemblage albite + K-feldspar + andalusite + quartz in supercritical chloride-rich aqueous solutions at 0.2 GPa and 600 °C. *Geochimica et Cosmochimica Acta* 65(24), 4493–4507.
- Hawkesworth, C., George, R., Turner, S. and Zellmer, G. (2004). Time scales of magmatic processes. *Earth and Planetary Science Letters* 218(1-2), 1–16.
- Hawkesworth, C. J., Dhuime, B., Pietranik, A., Cawood, P. A., Kemp, A. I. and Storey, C. (2010). The generation and evolution of the continental crust. *Journal of the Geological Society* 167(2), 229–248.
- Hawkesworth, C. J. and Kemp, A. (2006). Evolution of the continental crust. *Nature* 443(7113), 811–817.
- Hedenquist, J. W. and Lowenstern, J. B. (1994). The role of magmas in the formation of hydrothermal ore deposits. *Nature* 370(6490), 519–527.
- Helgeson, H. C. and Kirkham, D. H. (1974). Theoretical prediction of the thermodynamic behavior of aqueous electrolytes at high pressures and temperatures; II, Debye-Huckel parameters for activity coefficients and relative partial molal properties. *American Journal of Science* 274(10), 1199–1261.
- Helgeson, H. C., Kirkham, D. H. and Flowers, G. C. (1981). Theoretical prediction of the thermodynamic behavior of aqueous electrolytes by high pressures and temperatures; IV, Calculation of activity coefficients, osmotic coefficients, and apparent molal and standard and relative partial molal properties to 600 °C and 5 kb. *American Journal of Science* 281(10), 1249–1516.
- Hennings, S. K., Wagner, T., Ulmer, P. and Heinrich, C. A. (2017). Fluid evolution of the Monte Mattoni mafic complex, Adamello batholith, northern Italy: insights from fluid inclusion analysis and thermodynamic modeling. *Journal of Petrology* 58(8), 1645–1670.
- Higgins, M. D. (2006). Verification of ideal semi-logarithmic, lognormal or fractal crystal size distributions from 2D datasets. *Journal of Volcanology and Geothermal Research* 154(1-2), 8–16.
- Hill, G. J., Caldwell, T. G., Heise, W., Chertkoff, D. G., Bibby, H. M., Burgess, M. K., Cull, J. P. and Cas, R. A. (2009). Distribution of melt beneath Mount St Helens and Mount Adams inferred from magnetotelluric data. *Nature Geoscience* 2(11), 785–789.
- Holland, T. and Powell, R. (2011). An improved and extended internally consistent thermodynamic dataset for phases of petrological interest, involving a new equation of state for solids. *Journal of Metamorphic Geology* 29(3), 333–383.

- Holland, T. J. B. and Blundy, J. D. (1994). Non-ideal interactions in calcic amphiboles and their bearing on amphibole-plagioclase thermometry. *Contributions to Mineralogy and Petrology* 116, 433–447.
- Holland, T. J. B., Green, E. C. and Powell, R. (2018). Melting of peridotites through to granites: a simple thermodynamic model in the system KNCFMASHTOCr. *Journal of Petrology* 59(5), 881–900.
- Holland, T. J. B. and Powell, R. (1990). An enlarged and updated internally consistent thermodynamic dataset with uncertainties and correlations: the system K_2O – Na_2O – CaO – MgO – MnO – FeO – Fe_2O_3 – Al_2O_3 – TiO_2 – SiO_2 – C – H_2 – O_2 . *Journal of metamorphic Geology* 8(1), 89–124.
- Holland, T. J. B. and Powell, R. (2003). Activity–composition relations for phases in petrological calculations: an asymmetric multicomponent formulation. *Contributions to Mineralogy and Petrology* 145, 492–501.
- Holness, M. B. (2018). Melt segregation from silicic crystal mushes: a critical appraisal of possible mechanisms and their microstructural record. *Contributions to Mineralogy and Petrology* 173(6), 48.
- Holness, M. B., Clemens, J. D. and Vernon, R. H. (2018). How deceptive are microstructures in granitic rocks? Answers from integrated physical theory, phase equilibrium, and direct observations. *Contributions to Mineralogy and Petrology* 173, 1–18.
- Holness, M. B., Vukmanovic, Z. and Mariani, E. (2017). Assessing the role of compaction in the formation of adcumulates: a microstructural perspective. *Journal of Petrology* 58(4), 643–673.
- Holtz, F., Behrens, H., Dingwell, D. B. and Johannes, W. (1995). H_2O solubility in haplogranitic melts: compositional, pressure, and temperature dependence. *American Mineralogist* 80(1-2), 94–108.
- Holycross, M. E. and Watson, E. B. (2018). Trace element diffusion and kinetic fractionation in wet rhyolitic melt. *Geochimica et Cosmochimica Acta* 232, 14–29.
- Holzappel, C., Chakraborty, S., Rubie, D. and Frost, D. (2009). Fe–Mg interdiffusion in wadsleyite: the role of pressure, temperature and composition and the magnitude of jump in diffusion rates at the 410 km discontinuity. *Physics of the Earth and Planetary Interiors* 172(1-2), 28–33.
- Huang, R. and Audétat, A. (2012). The titanium-in-quartz (TitaniQ) thermobarometer: A critical examination and re-calibration. *Geochimica et Cosmochimica Acta* 84, 75–89.
- Huang, W., Stock, M. J., Guyett, P. C., Xia, X.-P., Liang, H., Sun, W. and Lai, C.-k. (2024). Reconstructing volatile exsolution in a porphyry ore-forming magma chamber: Perspectives from apatite inclusions. *American Mineralogist* 109(8), 1406–1418.
- Hückel, E. (1925). Zur theorie konzentrierterer wässriger Lösungen starker elektrolyte. *Phys Z* 26, 93–147.
- Humphreys, M. C., Smith, V. C., Coumans, J. P., Riker, J. M., Stock, M. J., de Hoog, J. and Brooker, R. A. (2021). Rapid pre-eruptive mush reorganisation and atmospheric volatile emissions from the 12.9 ka Laacher See eruption, determined using apatite. *Earth and Planetary Science Letters* 576, 117198.
- Hürlimann, N., Müntener, O., Ulmer, P., Nandedkar, R., Chiaradia, M. and Ovtcharova, M. (2016). Primary magmas in continental arcs and their differentiated products: petrology of a post-plutonic dyke suite in the Tertiary Adamello batholith (Alps). *Journal of Petrology* 57(3), 495–534.
- Hutton, D. H. (1982). A tectonic model for the emplacement of the Main Donegal Granite, NW Ireland. *Journal of the Geological Society* 139(5), 615–631.
- Hutton, D. H. (1988). Granite emplacement mechanisms and tectonic controls: inferences from deformation studies. *Earth and Environmental Science Transactions of the Royal Society of Edinburgh* 79(2-3), 245–255.
- Hutton, D. H., Dempster, T., Brown, P. and Becker, S. (1990). A new mechanism of granite emplacement: intrusion in active extensional shear zones. *Nature* 343(6257), 452–455.
- Iacono-Marziano, G., Morizet, Y., Le Trong, E. and Gaillard, F. (2012). New experimental data and semi-empirical parameterization of H_2O – CO_2 solubility in mafic melts. *Geochimica et Cosmochimica Acta* 97, 1–23.
- Icenhower, J. P. and London, D. (1997). Partitioning of fluorine and chlorine between biotite and granitic melt: experimental calibration at 200 MPa H_2O . *Contributions to Mineralogy and Petrology* 127(1), 17–29.

Bibliography

- Irvine, T. (1982). Terminology for layered intrusions. *Journal of Petrology* 23(2), 127–162.
- Iveson, A. A., Rowe, M. C., Webster, J. D. and Neill, O. K. (2018). Amphibole-, clinopyroxene- and plagioclase-melt partitioning of trace and economic metals in halogen-bearing rhyodacitic melts. *Journal of Petrology* 59(8), 1579–1604.
- Jackson, S. E. (2008). LAMTRACE data reduction software for LA-ICP-MS. *Laser ablation ICP-MS in the Earth sciences: Current practices and outstanding issues* 40, 305–307.
- Jagoutz, O. E. (2010). Construction of the granitoid crust of an island arc. Part II: a quantitative petrogenetic model. *Contributions to Mineralogy and Petrology* 160, 359–381.
- Jagoutz, O. E., Burg, J.-P., Hussain, S., Dawood, H., Pettke, T., Iizuka, T. and Maruyama, S. (2009). Construction of the granitoid crust of an island arc part I: geochronological and geochemical constraints from the plutonic Kohistan (NW Pakistan). *Contributions to Mineralogy and Petrology* 158, 739–755.
- Jagoutz, O. E. and Klein, B. Z. (2018). On the importance of crystallization-differentiation for the generation of SiO₂-rich melts and the compositional build-up of arc (and continental) crust. *American Journal of Science* 318(1), 29–63.
- Jagoutz, O. E., Müntener, O., Schmidt, M. W. and Burg, J.-P. (2011). The roles of flux- and decompression melting and their respective fractionation lines for continental crust formation: Evidence from the Kohistan arc. *Earth and Planetary Science Letters* 303(1-2), 25–36.
- Jagoutz, O. E., Müntener, O., Ulmer, P., Pettke, T., Burg, J.-P., Dawood, H. and Hussain, S. (2007). Petrology and mineral chemistry of lower crustal intrusions: the Chilas Complex, Kohistan (NW Pakistan). *Journal of Petrology* 48(10), 1895–1953.
- Jégo, S. and Dasgupta, R. (2013). Fluid-present melting of sulfide-bearing ocean-crust: Experimental constraints on the transport of sulfur from subducting slab to mantle wedge. *Geochimica et Cosmochimica Acta* 110, 106–134.
- Jégo, S. and Dasgupta, R. (2014). The fate of sulfur during fluid-present melting of subducting basaltic crust at variable oxygen fugacity. *Journal of Petrology* 55(6), 1019–1050.
- Jensen, B. B. (1973). Patterns of trace element partitioning. *Geochimica et Cosmochimica Acta* 37(10), 2227–2242.
- Ji, W.-Q., Malusà, M. G., Tiepolo, M., Langone, A., Zhao, L. and Wu, F.-Y. (2019). Synchronous Periadriatic magmatism in the Western and Central Alps in the absence of slab breakoff. *Terra Nova* 31(2), 120–128.
- Jiang, H. and Lee, C.-T. A. (2017). Coupled magmatism–erosion in continental arcs: Reconstructing the history of the Cretaceous Peninsular Ranges batholith, southern California through detrital hornblende barometry in forearc sediments. *Earth and Planetary Science Letters* 472, 69–81.
- Jin, S., Wang, X. and Xu, H. (2018). Revisiting the IĪ structures of high-temperature Ca-rich plagioclase feldspar—a single-crystal neutron and X-ray diffraction study. *Acta Crystallographica Section B: Structural Science, Crystal Engineering and Materials* 74(2), 152–164.
- Jin, S. and Xu, H. (2017). Solved: The enigma of labradorite feldspar with incommensurately modulated structure. *American Mineralogist* 102(1), 21–32.
- Johannes, W. and Holtz, F. (2012). *Petrogenesis and experimental petrology of granitic rocks*, volume 22. Springer Science & Business Media.
- John, B. E. and Blundy, J. D. (1993). Emplacement-related deformation of granitoid magmas, southern Adamello Massif, Italy. *Geological Society of America Bulletin* 105(12), 1517–1541.
- Johnson, E. A. and Rossman, G. R. (2013). The diffusion behavior of hydrogen in plagioclase feldspar at 800–1000 °C: Implications for re-equilibration of hydroxyl in volcanic phenocrysts. *American Mineralogist* 98(10), 1779–1787.
- Johnson, J. W., Oelkers, E. H. and Helgeson, H. C. (1992). SUPCRT92: A software package for calculating the standard molal thermodynamic properties of minerals, gases, aqueous species, and reactions from 1 to 5000 bar and 0 to 1000 °C. *Computers & Geosciences* 18(7), 899–947.
- Johnson, M. C. and Rutherford, M. J. (1989). Experimentally determined conditions in the Fish Canyon Tuff, Colorado, magma chamber. *Journal of Petrology* 30(3), 711–737.
- Jollands, M., Hermann, J., O'Neill, H. S. C., Spandler, C. and Padrón-Navarta, J. (2016a). Diffusion of Ti and some divalent cations in olivine as a function of temperature, oxygen fugacity, chemical potentials and crystal orientation. *Journal of Petrology* 57(10), 1983–2010.

- Jollands, M. C., Bloch, E. M. and Müntener, O. (2020). New Ti-in-quartz diffusivities reconcile natural Ti zoning with time scales and temperatures of upper crustal magma reservoirs. *Geology* 48(7), 654–657.
- Jollands, M. C., Bloch, E. M., Van Orman, J. A., Hermann, J. and O'Neill, H. S. C. (2023). Scandium diffusion in forsterite: concentration dependence, inter-site reactions and the effect of trivalent cations on Fe diffusion. *Physics of the Earth and Planetary Interiors* 334, 106954.
- Jollands, M. C., Burnham, A. D., O'Neill, H. S. C., Hermann, J. and Qian, Q. (2016b). Beryllium diffusion in olivine: A new tool to investigate timescales of magmatic processes. *Earth and Planetary Science Letters* 450, 71–82.
- Jossevel, C. (2018). *Mineral segregation process within the Western Adamello Tonalite (Italy)*. Master's thesis, University of Lausanne.
- Jugo, P. J., Luth, R. W. and Richards, J. P. (2005). An experimental study of the sulfur content in basaltic melts saturated with immiscible sulfide or sulfate liquids at 1300 °C and 1.0 GPa. *Journal of Petrology* 46(4), 783–798.
- Kagami, H., Ulmer, P., Hansmann, W., Dietrich, V. and Steiger, R. H. (1991). Nd-Sr isotopic and geochemical characteristics of the southern Adamello (northern Italy) intrusives: Implications for crustal versus mantle origin. *Journal of Geophysical Research: Solid Earth* 96(B9), 14331–14346.
- Kahl, M., Chakraborty, S., Costa, F. and Pompilio, M. (2011). Dynamic plumbing system beneath volcanoes revealed by kinetic modeling, and the connection to monitoring data: An example from Mt. Etna. *Earth and Planetary Science Letters* 308(1-2), 11–22.
- Kahl, M., Mutch, E., MacLennan, J., Morgan, D., Couperthwaite, F., Bali, E., Thordarson, T., Gudfinnsson, G., Walshaw, R., Buisman, I., Buhre, S., van der Meer, Q., Caracciolo, A., Marshall, E., Rasmussen, M., Gallagher, C., Moreland, W., Höskuldsson, Á. and Askew, R. (2023). Deep magma mobilization years before the 2021 CE Fagradalsfjall eruption, Iceland. *Geology* 51(2), 184–188.
- Karakas, O., Degruyter, W., Bachmann, O. and Dufek, J. (2017). Lifetime and size of shallow magma bodies controlled by crustal-scale magmatism. *Nature Geoscience* 10(6), 446–450.
- Karakas, O., Wotzlaw, J.-F., Guillong, M., Ulmer, P., Brack, P., Economos, R., Bergantz, G. W., Sinigoi, S. and Bachmann, O. (2019). The pace of crustal-scale magma accretion and differentiation beneath silicic caldera volcanoes. *Geology* 47(8), 719–723.
- Kelemen, P. B. (1995). Genesis of high Mg# andesites and the continental crust. *Contributions to Mineralogy and Petrology* 120(1), 1–19.
- Kelemen, P. B., Dick, H. J. and Quick, J. E. (1992). Formation of harzburgite by pervasive melt/rock reaction in the upper mantle. *Nature* 358(6388), 635–641.
- Kelemen, P. B., Hanghøj, K. and Greene, A. (2003). One view of the geochemistry of subduction-related magmatic arcs, with an emphasis on primitive andesite and lower crust. *Treatise on geochemistry* 3, 659.
- Kelemen, P. B., Koga, K. and Shimizu, N. (1997). Geochemistry of gabbro sills in the crust-mantle transition zone of the Oman ophiolite: Implications for the origin of the oceanic lower crust. *Earth and Planetary Science Letters* 146(3-4), 475–488.
- Kelemen, P. B., Shimizu, N. and Salters, V. J. (1995). Extraction of mid-ocean-ridge basalt from the upwelling mantle by focused flow of melt in dunite channels. *Nature* 375(6534), 747–753.
- Keller, F., Popa, R.-G., Allaz, J., Bovay, T., Bouvier, A.-S., Geshi, N., Miyakawa, A. and Bachmann, O. (2023). Variations in water saturation states and their impact on eruption size and frequency at the Aso supervolcano, Japan. *Earth and Planetary Science Letters* 622, 118400.
- Kendall-Langley, L. A., Kemp, A. I., Hawkesworth, C. J., EIMF and Roberts, M. P. (2021). Quantifying F and Cl concentrations in granitic melts from apatite inclusions in zircon. *Contributions to Mineralogy and Petrology* 176, 1–19.
- Kepler, H. (2010). The distribution of sulfur between haplogranitic melts and aqueous fluids. *Geochimica et Cosmochimica Acta* 74(2), 645–660.
- Khitarov, N., Kadik, A. and Lebedev, E. (1968). Solubility of water in a basalt melt. *Geochemistry International* 5, 667–674.
- Kidder, S., Ducea, M., Gehrels, G., Patchett, P. J. and Vervoort, J. (2003). Tectonic and magmatic development of the Salinian Coast Ridge belt, California. *Tectonics* 22(5), 1058.

- Kieffer, M. A., Dare, S. A. and Namur, O. (2023). The use of trace elements in apatite to trace differentiation of a ferrobasaltic melt in the Sept-Iles Intrusive Suite, Québec, Canada: Implications for provenance discrimination. *Geochimica et Cosmochimica Acta* 342, 169–197.
- Kim, Y., Konecke, B., Fiege, A., Simon, A. and Becker, U. (2017). An ab-initio study of the energetics and geometry of sulfide, sulfite, and sulfate incorporation into apatite: The thermodynamic basis for using this system as an oxybarometer. *American Mineralogist* 102(8), 1646–1656.
- Kistler, R. W., Wooden, J. L. and Morton, D. M. (2003). Isotopes and ages in the northern Peninsular Ranges batholith, southern California. Technical report, U.S. Geological Survey.
- Klein, B. Z. and Eddy, M. P. (2023). What’s in an age? Calculation and interpretation of ages and durations from U-Pb zircon geochronology of igneous rocks. *Bulletin* 136(1-2), 93–109.
- Klein, B. Z. and Jagoutz, O. (2021). Construction of a trans-crustal magma system: building the Bear Valley Intrusive Suite, southern Sierra Nevada, California. *Earth and Planetary Science Letters* 553, 116624.
- Klein, B. Z. and Müntener, O. (2023). MnO/MgO ratios of arc basalts highlight the role of early garnet fractionation. *Geochemical Perspectives Letters* 25, 18–24.
- Kleinsasser, J. M., Simon, A. C., Konecke, B. A., Kleinsasser, M. J., Beckmann, P. and Holtz, F. (2022). Sulfide and sulfate saturation of dacitic melts as a function of oxygen fugacity. *Geochimica et Cosmochimica Acta* 326, 1–16.
- Kohlstedt, D. L. and Holtzman, B. K. (2009). Shearing melt out of the Earth: An experimentalist’s perspective on the influence of deformation on melt extraction. *Annual Review of Earth and Planetary Sciences* 37, 561–593.
- Konecke, B. A., Fiege, A., Simon, A. C., Linsler, S. and Holtz, F. (2019). An experimental calibration of a sulfur-in-apatite oxybarometer for mafic systems. *Geochimica et Cosmochimica Acta* 265, 242–258.
- Konecke, B. A., Fiege, A., Simon, A. C., Parat, F. and Stechern, A. (2017). Co-variability of S^{6+} , S^{4+} , and S^{2-} in apatite as a function of oxidation state: Implications for a new oxybarometer. *American Mineralogist* 102(3), 548–557.
- Krawczynski, M. J., Grove, T. L. and Behrens, H. (2012). Amphibole stability in primitive arc magmas: effects of temperature, H_2O content, and oxygen fugacity. *Contributions to Mineralogy and Petrology* 164(2), 317–339.
- Kröger, F. and Vink, H. (1956). Relations between the concentrations of imperfections in crystalline solids. In: *Solid State Physics*, volume 3. Elsevier, pp. 307–435.
- Krueger, A. J. (1983). Sighting of El Chichon sulfur dioxide clouds with the Nimbus 7 total ozone mapping spectrometer. *Science* 220(4604), 1377–1379.
- Kubo, T., Shimojuku, A. and Ohtani, E. (2004). Mg–Fe interdiffusion rates in wadsleyite and the diffusivity jump at the 410-km discontinuity. *Physics and Chemistry of Minerals* 31, 456–464.
- Lagabrielle, Y. and Cannat, M. (1990). Alpine Jurassic ophiolites resemble the modern central Atlantic basement. *Geology* 18(4), 319–322.
- Lagabrielle, Y. and Lemoine, M. (1997). Alpine, Corsican and Apennine ophiolites: the slow-spreading ridge model. *Comptes Rendus de l’Académie des Sciences-Series IIA-Earth and Planetary Science* 325(12), 909–920.
- Lahondère, D. and Guerrot, C. (1997). Datation Sm-Nd du métamorphisme éclogitique en Corse alpine: un argument pour l’existence au Crétacé supérieur d’une zone de subduction active localisée sous le bloc corso-sarde. *Géologie de la France* 3, 3–11.
- Lanari, P., Vidal, O., De Andrade, V., Dubacq, B., Lewin, E., Grosch, E. G. and Schwartz, S. (2014). XMapTools: A MATLAB[®]-based program for electron microprobe X-ray image processing and geothermobarometry. *Computers & Geosciences* 62, 227–240.
- Lange, R. and Carmichael, I. S. (1990). Thermodynamic properties of silicate liquids with emphasis on density, thermal expansion and compressibility. *Reviews in Mineralogy and Geochemistry* 24(1), 25–64.
- Lange, R. A. (1994). The Effect of H_2O , CO_2 and F on the Density and Viscosity of Silicate Melts. In: M. R. Carroll and J. Holloway, eds., *Reviews in Mineralogy*, volume 30. Mineralogical Society of America, pp. 331–370.

- Lange, R. A., Cashman, K. V. and Navrotsky, A. (1994). Direct measurements of latent heat during crystallization and melting of a ugandite and an olivine basalt. *Contributions to Mineralogy and Petrology* 118, 169–181.
- Lange, R. A., De Yoreo, J. J. and Navrotsky, A. (1991). Scanning calorimetric measurement of heat capacity during incongruent melting of diopside. *American Mineralogist* 76(5-6), 904–912.
- LaTourrette, T. and Wasserburg, G. (1998). Mg diffusion in anorthite: implications for the formation of early solar system planetesimals. *Earth and Planetary Science Letters* 158(3-4), 91–108.
- Laubscher, H. (1985). Large-scale, thin-skinned thrusting in the southern Alps: Kinematic models. *Geological Society of America Bulletin* 96(6), 710–718.
- Laubscher, H. and Bernoulli, D. (1977). Mediterranean and Tethys. In: *The Ocean Basins and Margins: Volume 4A The Eastern Mediterranean*. Springer, pp. 1–28.
- Le Bas, M., Maitre, R. L., Streckeisen, A., Zanettin, B. and the Systematics of Igneous Rocks, I. S. (1986). A chemical classification of volcanic rocks based on the total alkali-silica diagram. *Journal of Petrology* 27(3), 745–750.
- Le Breton, N. and Thompson, A. B. (1988). Fluid-absent (dehydration) melting of biotite in metapelites in the early stages of crustal anatexis. *Contributions to Mineralogy and Petrology* 99, 226–237.
- Leake, B. E. (1978). Nomenclature of amphiboles. *American Mineralogist* 63(11-12), 1023–1052.
- Leake, B. E., Woolley, A. R., Arps, C. E., Birch, W. D., Gilbert, M. C., Grice, J. D., Hawthorne, F. C., Kato, A., Kisch, H. J., Krivovichev, V. G., Linthout, K., Laird, J., Mandarino, J. A., Maresch, W. V., Nickel, E. H., Rock, N. M., Schumacher, J. C., Smith, D. C., Stephenson, N. C., Ungaretti, L., Whittaker, E. J. and Youzhi, G. (1997). Nomenclature of amphiboles; report of the Subcommittee on Amphiboles of the International Mineralogical Association Commission on new minerals and mineral names. *Mineralogical magazine* 61(405), 295–310.
- Ledru, P., Courrioux, G., Dallain, C., Lardeaux, J., Montel, J., Vanderhaeghe, O. and Vitel, G. (2001). The Velay dome (French Massif Central): melt generation and granite emplacement during orogenic evolution. *Tectonophysics* 342(3-4), 207–237.
- Lee, C.-T. A., Cheng, X. and Horodyskyj, U. (2006). The development and refinement of continental arcs by primary basaltic magmatism, garnet pyroxenite accumulation, basaltic recharge and delamination: insights from the Sierra Nevada, California. *Contributions to Mineralogy and Petrology* 151, 222–242.
- Lee, C.-T. A. and Morton, D. M. (2015). High silica granites: Terminal porosity and crystal settling in shallow magma chambers. *Earth and Planetary Science Letters* 409, 23–31.
- Lee, C.-T. A., Morton, D. M., Farner, M. J. and Moitra, P. (2015). Field and model constraints on silicic melt segregation by compaction/hindered settling: The role of water and its effect on latent heat release. *American Mineralogist* 100(8-9), 1762–1777.
- Lee, C.-T. A., Morton, D. M., Kistler, R. W. and Baird, A. K. (2007). Petrology and tectonics of Phanerozoic continent formation: From island arcs to accretion and continental arc magmatism. *Earth and Planetary Science Letters* 263(3-4), 370–387.
- Lesne, P., Kohn, S. C., Blundy, J. D., Witham, F., Botcharnikov, R. E. and Behrens, H. (2011). Experimental simulation of closed-system degassing in the system basalt–H₂O–CO₂–S–Cl. *Journal of Petrology* 52(9), 1737–1762.
- Leuthold, J., Müntener, O., Baumgartner, L. P. and Putlitz, B. (2014). Petrological constraints on the recycling of mafic crystal mushes and intrusion of braided sills in the Torres del Paine mafic complex (Patagonia). *Journal of Petrology* 55(5), 917–949.
- Leuthold, J., Müntener, O., Baumgartner, L. P., Putlitz, B., Ovtcharova, M. and Schaltegger, U. (2012). Time resolved construction of a bimodal laccolith (Torres del Paine, Patagonia). *Earth and Planetary Science Letters* 325, 85–92.
- Li, H. and Hermann, J. (2015). Apatite as an indicator of fluid salinity: An experimental study of chlorine and fluorine partitioning in subducted sediments. *Geochimica et Cosmochimica Acta* 166, 267–297.
- Li, H. and Hermann, J. (2017). Chlorine and fluorine partitioning between apatite and sediment melt at 2.5 GPa, 800 °C: A new experimentally derived thermodynamic model. *American Mineralogist* 102(3), 580–594.

Bibliography

- Li, W., Chakraborty, S., Nagashima, K. and Costa, F. (2020). Multicomponent diffusion of F, Cl and OH in apatite with application to magma ascent rates. *Earth and Planetary Science Letters* 550, 116545.
- Li, W., Cheng, Y. and Yang, Z. (2019). Geo- fO_2 : Integrated software for analysis of magmatic oxygen fugacity. *Geochemistry, Geophysics, Geosystems* 20(5), 2542–2555.
- Li, W. and Costa, F. (2020). A thermodynamic model for F-Cl-OH partitioning between silicate melts and apatite including non-ideal mixing with application to constraining melt volatile budgets. *Geochimica et Cosmochimica Acta* 269, 203–222.
- Li, W., Costa, F. and Nagashima, K. (2021). Apatite crystals reveal melt volatile budgets and magma storage depths at Merapi volcano, Indonesia. *Journal of Petrology* 62(4), egaa100.
- Li, W., Costa, F., Oppenheimer, C. and Nagashima, K. (2023). Volatile and trace element partitioning between apatite and alkaline melts. *Contributions to Mineralogy and Petrology* 178(2), 9.
- Liebscher, A. and Heinrich, C. A. (2007). Fluid–fluid interactions in the Earth’s lithosphere. *Reviews in Mineralogy and Geochemistry* 65(1), 1–13.
- Lin, H. and Foster, W. (1968). Studies in the system BaO-Al₂O₃-SiO₂ I. The polymorphism of celsian. *American Mineralogist: Journal of Earth and Planetary Materials* 53(1-2), 134–144.
- Liu, M. and Yund, R. A. (1992). NaSi-CaAl interdiffusion in plagioclase. *American Mineralogist* 77(3-4), 275–283.
- Liu, Y., Zhang, Y. and Behrens, H. (2005). Solubility of H₂O in rhyolitic melts at low pressures and a new empirical model for mixed H₂O–CO₂ solubility in rhyolitic melts. *Journal of Volcanology and Geothermal Research* 143(1-3), 219–235.
- London, D. (2014). A petrologic assessment of internal zonation in granitic pegmatites. *Lithos* 184, 74–104.
- London, D., Morgan, G. B. and Hervig, R. L. (1989). Vapor-undersaturated experiments with Macusani glass + H₂O at 200 MPa, and the internal differentiation of granitic pegmatites. *Contributions to Mineralogy and Petrology* 102, 1–17.
- Long, L. E., Castellana, C. H. and Sial, A. N. (2005). Age, origin and cooling history of the Coronel João Sá pluton, Bahia, Brazil. *Journal of Petrology* 46(2), 255–273.
- Longhi, J., Walker, D. and Hays, J. F. (1976). Fe and Mg in plagioclase. In: *Lunar Science Conference, 7th, Houston, Texas*, volume 7. pp. 1281–1300.
- Lormand, C., Humphreys, M. C., Colby, D. J., Coumans, J. P., Chelle-Michou, C. and Li, W. (2024). Volatile budgets and evolution in porphyry-related magma systems, determined using apatite. *Lithos* 480, 107623.
- Lowenstern, J. B. (1995). Applications of silicate-melt inclusions to the study of magmatic volatiles. *Mineralogical Association of Canada Short Course* 23, 71–99.
- Lu, G., Winkler, W., Rahn, M., von Quadt, A. and Willett, S. D. (2018). Evaluating igneous sources of the Taveyannaz formation in the Central Alps by detrital zircon U–Pb age dating and geochemistry. *Swiss Journal of Geosciences* 111, 399–416.
- Lubbers, J., Kent, A. J. and de Silva, S. (2022). Thermal budgets of magma storage constrained by diffusion chronometry: the Cerro Galán ignimbrite. *Journal of Petrology* 63(7), egac048.
- Lynn, K. J., Garcia, M. O., Shea, T., Costa, F. and Swanson, D. A. (2017). Timescales of mixing and storage for Keanakāko ‘i Tephra magmas (1500–1820 CE), Kīlauea Volcano, Hawai‘i. *Contributions to Mineralogy and Petrology* 172(9), 76.
- Macera, P., Ferrara, G., Pescia, A., Callegari, E. et al. (1983). A geochemical study on the acid and basic rocks of the Adamello batholith. *Memorie di Scienze Geologiche* 26, 223–259.
- Mackwell, S. J. and Kohlstedt, D. L. (1990). Diffusion of hydrogen in olivine: implications for water in the mantle. *Journal of Geophysical Research: Solid Earth* 95(B4), 5079–5088.
- Marsh, B. D. (1981). On the crystallinity, probability of occurrence, and rheology of lava and magma. *Contributions to Mineralogy and Petrology* 78, 85–98.
- Marsh, B. D. (1988). Crystal size distribution (CSD) in rocks and the kinetics and dynamics of crystallization: I. Theory. *Contributions to Mineralogy and Petrology* 99, 277–291.
- Marsh, B. D. (1989). Magma chambers. *Annual Review of Earth and Planetary Sciences* 17(1), 439–472.
- Martin, D., Griffiths, R. W. and Campbell, I. H. (1987). Compositional and thermal convection in magma chambers. *Contributions to Mineralogy and Petrology* 96, 465–475.

- Martin, D. and Nokes, R. (1989). A fluid-dynamical study of crystal settling in convecting magmas. *Journal of Petrology* 30(6), 1471–1500.
- Marxer, F. and Ulmer, P. (2019). Crystallisation and zircon saturation of calc-alkaline tonalite from the Adamello Batholith at upper crustal conditions: an experimental study. *Contributions to Mineralogy and Petrology* 174(10), 84.
- Marxer, F., Ulmer, P. and Müntener, O. (2022). Polybaric fractional crystallisation of arc magmas: an experimental study simulating trans-crustal magmatic systems. *Contributions to Mineralogy and Petrology* 177(1), 3.
- Marxer, F., Ulmer, P. and Müntener, O. (2023). Ascent-driven differentiation: a mechanism to keep arc magmas metaluminous? *Contributions to Mineralogy and Petrology* 178(8), 51.
- Mathez, E. A. and Webster, J. D. (2005). Partitioning behavior of chlorine and fluorine in the system apatite-silicate melt-fluid. *Geochimica et Cosmochimica Acta* 69(5), 1275–1286.
- Matile, L. (1996). *Aufstieg und Platznahme von kalk-alkalinen Magmen—der Adamello-Batholith als Beispiel*. Ph.D. thesis, ETH Zürich.
- Matthews, N., Huber, C., Pyle, D. and Smith, V. (2012). Timescales of magma recharge and reactivation of large silicic systems from Ti diffusion in quartz. *Journal of Petrology* 53(7), 1385–1416.
- Mayer, A., Cortiana, G., Dal Piaz, G., Deloule, E., De Pieri, R. and Jobstraibizer, P. (2003). U-Pb single zircon ages of the Adamello batholith, Southern Alps. *Memorie di Scienze Geologiche* 55, 151–167.
- McCarthy, A., Chelle-Michou, C., Müntener, O., Arculus, R. and Blundy, J. D. (2018). Subduction initiation without magmatism: The case of the missing Alpine magmatic arc. *Geology* 46(12), 1059–1062.
- McCubbin, F. M., Vander Kaaden, K. E., Tartèse, R., Boyce, J. W., Mikhail, S., Whitson, E. S., Bell, A. S., Anand, M., Franchi, I. A., Wang, J. and Hauri, E. H. (2015). Experimental investigation of F, Cl, and OH partitioning between apatite and Fe-rich basaltic melt at 1.0–1.2 GPa and 950–1000 °C. *American Mineralogist* 100(8-9), 1790–1802.
- McFadden, R., Siddoway, C. S., Teyssier, C. and Fanning, C. (2010). Cretaceous oblique extensional deformation and magma accumulation in the Fosdick Mountains migmatite-cored gneiss dome, West Antarctica. *Tectonics* 29(4), TC4022.
- McKenzie, D. (1985). The extraction of magma from the crust and mantle. *Earth and Planetary Science Letters* 74(1), 81–91.
- Melekhova, E., Blundy, J. D., Robertson, R. and Humphreys, M. C. (2015). Experimental evidence for polybaric differentiation of primitive arc basalt beneath St. Vincent, Lesser Antilles. *Journal of Petrology* 56(1), 161–192.
- Menand, T. (2011). Physical controls and depth of emplacement of igneous bodies: A review. *Tectonophysics* 500(1-4), 11–19.
- Métrich, N. and Wallace, P. J. (2008). Volatile abundances in basaltic magmas and their degassing paths tracked by melt inclusions. *Reviews in Mineralogy and Geochemistry* 69(1), 363–402.
- Michard, A., Chalouan, A., Feinberg, H., Goffé, B. and Montigny, R. (2002). How does the Alpine belt end between Spain and Morocco? *Bulletin de la Société Géologique de France* 173(1), 3–15.
- Michel, J., Baumgartner, L. P., Putlitz, B., Schaltegger, U. and Ovtcharova, M. (2008). Incremental growth of the Patagonian Torres del Paine laccolith over 90 ky. *Geology* 36(6), 459–462.
- Middlemost, E. A. (1994). Naming materials in the magma/igneous rock system. *Earth-Science Reviews* 37(3-4), 215–224.
- Miller, C. F. and Miller, J. S. (2002). Contrasting stratified plutons exposed in tilt blocks, Eldorado Mountains, Colorado River Rift, NV, USA. *Lithos* 61(3-4), 209–224.
- Miller, J. S., Matzel, J. E., Miller, C. F., Burgess, S. D. and Miller, R. B. (2007). Zircon growth and recycling during the assembly of large, composite arc plutons. *Journal of Volcanology and Geothermal Research* 167(1-4), 282–299.
- Mitchell, A. L., Gaetani, G. A., O’Leary, J. A. and Hauri, E. H. (2017). H₂O solubility in basalt at upper mantle conditions. *Contributions to Mineralogy and Petrology* 172, 1–16.
- Mitchell, A. L. and Grove, T. L. (2016). Experiments on melt–rock reaction in the shallow mantle wedge. *Contributions to Mineralogy and Petrology* 171, 1–21.
- Miyoshi, T., Sakai, H. and Chiba, H. (1984). Experimental study of sulfur isotope fractionation factors between sulfate and sulfide in high temperature melts. *Geochemical Journal* 18(2), 75–84.

- Momma, K. and Izumi, F. (2011). VESTA 3 for three-dimensional visualization of crystal, volumetric and morphology data. *Journal of Applied Crystallography* 44(6), 1272–1276.
- Moore, A., Coogan, L., Costa, F. and Perfit, M. (2014). Primitive melt replenishment and crystal-mush disaggregation in the weeks preceding the 2005–2006 eruption 9°50' N, EPR. *Earth and Planetary Science Letters* 403, 15–26.
- Moore, J. G. and Sisson, T. W. (2008). Igneous phenocrystic origin of K-feldspar megacrysts in granitic rocks from the Sierra Nevada batholith. *Geosphere* 4(2), 387–400.
- Morgan, D., Blake, S., Rogers, N., De Vivo, B., Rolandi, G. and Davidson, J. (2006). Magma chamber recharge at Vesuvius in the century prior to the eruption of AD 79. *Geology* 34(10), 845–848.
- Morton, D. (1969). The Lakeview Mountains pluton, southern California batholith part I: petrology and structure. *Geological Society of America Bulletin* 80(8), 1539–1552.
- Morton, D., Miller, F., Kistler, R., Premo, W., Lee, C. A., Langenheim, V., Wooden, J., Snee, L., Clausen, B. and Cossette, P. (2014). Framework and petrogenesis of the northern Peninsular Ranges batholith, southern California. *Geological Society of America Memoirs* 211, 61–143.
- Mottana, A., Nicoletti, M., Petrucciani, C., Liborio, G., De Capitani, L. and Bocchio, R. (1985). Pre-alpine and alpine evolution of the South-alpine basement of the Orobic Alps. *Geologische Rundschau* 74, 353–366.
- Mourey, A. J., Shea, T., Costa, F., Shiro, B. and Longman, R. J. (2023). Years of magma intrusion primed Kilauea Volcano (Hawai'i) for the 2018 eruption: evidence from olivine diffusion chronometry and monitoring data. *Bulletin of Volcanology* 85(3), 18.
- Moyen, J.-F., Janoušek, V., Laurent, O., Bachmann, O., Jacob, J.-B., Farina, F., Fiannacca, P. and Villaros, A. (2021). Crustal melting vs. fractionation of basaltic magmas: Part 1, granites and paradigms. *Lithos* 402, 106291.
- Müntener, O., Kelemen, P. B. and Grove, T. L. (2001). The role of H₂O during crystallization of primitive arc magmas under uppermost mantle conditions and genesis of igneous pyroxenites: an experimental study. *Contributions to Mineralogy and Petrology* 141, 643–658.
- Müntener, O. and McCarthy, A. (2024). One view on the petrology and geochemistry of the mantle and oceanic crustal remnants in the Alps, reconciling rifts and ultra-slow seafloor spreading. In: *Geodynamics of the Alps 2: Pre-collisional Processes*. Wiley Online Library, pp. 157–203.
- Müntener, O., McCarthy, A., Hauser, A.-C. and Mohn, G. (in prep). Jurassic ages for the Valais and Piemonte Liguria basins indicate simultaneous, short-lived magmatism around the Briançonnais microplate. *Geology*.
- Müntener, O. and Ulmer, P. (2006). Experimentally derived high-pressure cumulates from hydrous arc magmas and consequences for the seismic velocity structure of lower arc crust. *Geophysical Research Letters* 33(21).
- Müntener, O. and Ulmer, P. (2018). Arc crust formation and differentiation constrained by experimental petrology. *American Journal of Science* 318(1), 64–89.
- Müntener, O., Ulmer, P. and Blundy, J. D. (2021). Superhydrous arc magmas in the Alpine context. *Elements* 17(1), 35–40.
- Murphy, M., Sparks, R. S. J., Barclay, J., Carroll, M. R. and Brewer, T. (2000). Remobilization of andesite magma by intrusion of mafic magma at the Soufriere Hills Volcano, Montserrat, West Indies. *Journal of petrology* 41(1), 21–42.
- Mutch, E. J., Blundy, J. D., Tattitch, B., Cooper, F. and Brooker, R. (2016). An experimental study of amphibole stability in low-pressure granitic magmas and a revised Al-in-hornblende geobarometer. *Contributions to Mineralogy and Petrology* 171, 1–27.
- Mutch, E. J., MacLennan, J., Holland, T. J. and Buisman, I. (2019). Millennial storage of near-Moho magma. *Science* 365(6450), 260–264.
- Mutch, E. J., MacLennan, J. and Madden-Nadeau, A. L. (2022). The dichotomous nature of Mg partitioning between plagioclase and melt: Implications for diffusion chronometry. *Geochimica et Cosmochimica Acta* 339, 173–189.
- Mutch, E. J., MacLennan, J., Shorttle, O., Rudge, J. F. and Neave, D. A. (2021). DFENS: diffusion chronometry using finite elements and nested sampling. *Geochemistry, Geophysics, Geosystems* 22(4), e2020GC009303.
- Muth, M. J. and Wallace, P. J. (2021). Slab-derived sulfate generates oxidized basaltic magmas in the southern Cascade arc (California, USA). *Geology* 49(10), 1177–1181.

- Nagasawa, H. (1970). Rare earth concentrations in zircons and apatites and their host dacites and granites. *Earth and Planetary Science Letters* 9(4), 359–364.
- Nandedkar, R. H., Hürlimann, N., Ulmer, P. and Müntener, O. (2016). Amphibole–melt trace element partitioning of fractionating calc-alkaline magmas in the lower crust: an experimental study. *Contributions to Mineralogy and Petrology* 171, 1–25.
- Nandedkar, R. H., Ulmer, P. and Müntener, O. (2014). Fractional crystallization of primitive, hydrous arc magmas: an experimental study at 0.7 GPa. *Contributions to Mineralogy and Petrology* 167(6), 1015.
- Nash, W. M., Smythe, D. J. and Wood, B. J. (2019). Compositional and temperature effects on sulfur speciation and solubility in silicate melts. *Earth and Planetary Science Letters* 507, 187–198.
- Nicolas, A. (1986). Structure and petrology of peridotites: clues to their geodynamic environment. *Reviews of Geophysics* 24(4), 875–895.
- Nield, D. A. and Bejan, A. (2006). *Convection in porous media*, volume 3. Springer.
- Nielsen, R. L., Ustunisik, G., Weinstieger, A. B., Tepley III, F. J., Johnston, A. D. and Kent, A. J. (2017). Trace element partitioning between plagioclase and melt: An investigation of the impact of experimental and analytical procedures. *Geochemistry, Geophysics, Geosystems* 18(9), 3359–3384.
- Nimis, P. and Ulmer, P. (1998). Clinopyroxene geobarometry of magmatic rocks Part 1: An expanded structural geobarometer for anhydrous and hydrous, basic and ultrabasic systems. *Contributions to Mineralogy and Petrology* 133(1), 122–135.
- O'Neill, H. S. C. and Mavrogenes, J. A. (2022). The sulfate capacities of silicate melts. *Geochimica et Cosmochimica Acta* 334, 368–382.
- Oppenheim, L. F., Memeti, V., Barnes, C. G., Chambers, M., Krause, J. and Esposito, R. (2021). Feldspar recycling across magma mush bodies during the voluminous Half Dome and Cathedral Peak stages of the Tuolumne intrusive complex, Yosemite National Park, California, USA. *Geosphere* 17(2), 322–351.
- Oppenheimer, C. (2003). Climatic, environmental and human consequences of the largest known historic eruption: Tambora volcano (Indonesia) 1815. *Progress in Physical Geography* 27(2), 230–259.
- Oppenheimer, C., Scaillet, B. and Martin, R. S. (2011). Sulfur degassing from volcanoes: source conditions, surveillance, plume chemistry and earth system impacts. *Reviews in Mineralogy and Geochemistry* 73(1), 363–421.
- Otamendi, J. E., Vujovich, G. I., de la Rosa, J. D., Tibaldi, A. M., Castro, A., Martino, R. D. and Pinotti, L. P. (2009). Geology and petrology of a deep crustal zone from the Famatinian paleo-arc, Sierras de Valle Fértil and La Huerta, San Juan, Argentina. *Journal of South American Earth Sciences* 27(4), 258–279.
- O'Connor, J. (1965). A classification for quartz-rich igneous rocks based on feldspar ratios. *US Geological Survey Professional Paper* 525, 79–84.
- Pak, T. M., Hauzenberger, C. A. and Baumgartner, L. P. (2003). Solubility of the assemblage albite + K-feldspar + andalusite + quartz in supercritical aqueous chloride solutions at 650 °C and 2 kbar. *Chemical Geology* 200(3-4), 377–393.
- Pamukçu, A. S., Ghiorso, M. S. and Gualda, G. A. (2016). High-Ti, bright-CL rims in volcanic quartz: a result of very rapid growth. *Contributions to Mineralogy and Petrology* 171, 1–9.
- Pan, Y. and Batiza, R. (2002). Mid-ocean ridge magma chamber processes: Constraints from olivine zonation in lavas from the East Pacific Rise at 9°30'N and 10°30'N. *Journal of Geophysical Research: Solid Earth* 107(B1), ECV–9.
- Pankhurst, M. J., Morgan, D. J., Thordarson, T. and Loughlin, S. C. (2018). Magmatic crystal records in time, space, and process, causatively linked with volcanic unrest. *Earth and Planetary Science Letters* 493, 231–241.
- Papale, P., Moretti, R. and Barbato, D. (2006). The compositional dependence of the saturation surface of H₂O + CO₂ fluids in silicate melts. *Chemical Geology* 229(1-3), 78–95.
- Parat, F. and Holtz, F. (2004). Sulfur partitioning between apatite and melt and effect of sulfur on apatite solubility at oxidizing conditions. *Contributions to Mineralogy and Petrology* 147, 201–212.

Bibliography

- Parat, F. and Holtz, F. (2005). Sulfur partition coefficient between apatite and rhyolite: the role of bulk S content. *Contributions to Mineralogy and Petrology* 150(6), 643–651.
- Parmigiani, A., Faroughi, S., Huber, C., Bachmann, O. and Su, Y. (2016). Bubble accumulation and its role in the evolution of magma reservoirs in the upper crust. *Nature* 532(7600), 492–495.
- Parsons, T., Sleep, N. H. and Thompson, G. A. (1992). Host rock rheology controls on the emplacement of tabular intrusions: Implications for underplating of extending crust. *Tectonics* 11(6), 1348–1356.
- Paterson, S. R. (2009). Magmatic tubes, pipes, troughs, diapirs, and plumes: Late-stage convective instabilities resulting in compositional diversity and permeable networks in crystal-rich magmas of the Tuolumne batholith, Sierra Nevada, California. *Geosphere* 5(6), 496–527.
- Paterson, S. R. and Fowler Jr, T. K. (1993). Re-examining pluton emplacement processes. *Journal of Structural Geology* 15(2), 191–206.
- Paterson, S. R. and Vernon, R. H. (1995). Bursting the bubble of ballooning plutons: a return to nested diapirs emplaced by multiple processes. *Geological Society of America Bulletin* 107(11), 1356–1380.
- Paterson, S. R., Žák, J. and Janoušek, V. (2008). Growth of complex sheeted zones during recycling of older magmatic units into younger: Sawmill Canyon area, Tuolumne batholith, Sierra Nevada, California. *Journal of Volcanology and Geothermal Research* 177(2), 457–484.
- Patiño Douce, A. E. and Harris, N. (1998). Experimental constraints on Himalayan anatexis. *Journal of Petrology* 39(4), 689–710.
- Paton, C., Hellstrom, J., Paul, B., Woodhead, J. and Hergt, J. (2011). Iolite: Freeware for the visualisation and processing of mass spectrometric data. *Journal of Analytical Atomic Spectrometry* 26(12), 2508–2518.
- Pearce, N. J., Perkins, W. T., Westgate, J. A., Gorton, M. P., Jackson, S. E., Neal, C. R. and Chenery, S. P. (1997). A compilation of new and published major and trace element data for NIST SRM 610 and NIST SRM 612 glass reference materials. *Geostandards newsletter* 21(1), 115–144.
- Pearce, T. (1987). The theory of zoning patterns in magmatic minerals using olivine as an example. *Contributions to Mineralogy and Petrology* 97(4), 451–459.
- Peters, M. T., Shaffer, E. E., Burnett, D. S. and Kim, S. S. (1995). Magnesium and titanium partitioning between anorthite and Type B CAI liquid: Dependence on oxygen fugacity and liquid composition. *Geochimica et Cosmochimica Acta* 59(13), 2785–2796.
- Petford, N., Cruden, A., McCaffrey, K. and Vigneresse, J.-L. (2000). Granite magma formation, transport and emplacement in the Earth's crust. *Nature* 408(6813), 669–673.
- Petford, N., Kerr, R. C. and Lister, J. R. (1993). Dike transport of granitoid magmas. *Geology* 21(9), 845–848.
- Petrone, C. M., Braschi, E., Francalanci, L., Casalini, M. and Tommasini, S. (2018). Rapid mixing and short storage timescale in the magma dynamics of a steady-state volcano. *Earth and Planetary Science Letters* 492, 206–221.
- Philpotts, A. (1981). Liquid immiscibility in silicate melt inclusion in plagioclase phenocrysts. *Bulletin de Minéralogie* 104(4), 317–324.
- Philpotts, A. R. and Ague, J. J. (2009). *Principles of igneous and metamorphic petrology*. Cambridge University Press.
- Philpotts, A. R., Shi, J. and Brustman, C. (1998). Role of plagioclase crystal chains in the differentiation of partly crystallized basaltic magma. *Nature* 395(6700), 343–346.
- Piccoli, P. and Candela, P. (1994). Apatite in felsic rocks; a model for the estimation of initial halogen concentrations in the Bishop Tuff (Long Valley) and Tuolumne Intrusive Suite (Sierra Nevada Batholith) magmas. *American Journal of Science* 294(1), 92–135.
- Piccoli, P. M. and Candela, P. A. (2002). Apatite in igneous systems. *Reviews in Mineralogy and Geochemistry* 48(1), 255–292.
- Pimenta Silva, M., Giuliani, A., Schaltegger, U., Chiaradia, M., Nowak, A., Schoene, B., Ulmer, P. and Müntener, O. (2024). Tracing Lower Crustal Contamination in Continental Arc Magmas Using Sr–Nd–Hf Isotopes: A Combined In Situ and Bulk Rock Approach Applied to the Adamello Batholith. *Journal of Petrology* 65(8), egae084.
- Pimenta Silva, M., Marxer, F., Keller, T., Giuliani, A., Ulmer, P. and Müntener, O. (2023). Alkaline magmas in shallow arc plutonic roots: a field and experimental investigation of hydrous cumulate

- melting in the southern Adamello batholith. *Contributions to Mineralogy and Petrology* 178(9), 64.
- Piromallo, C. and Faccenna, C. (2004). How deep can we find the traces of Alpine subduction? *Geophysical Research Letters* 31(6).
- Pistone, M., Arzilli, F., Dobson, K. J., Cordonnier, B., Reusser, E., Ulmer, P., Marone, F., Whittington, A. G., Mancini, L., Fife, J. L. and Blundy, J. D. (2015). Gas-driven filter pressing in magmas: Insights into in-situ melt segregation from crystal mushes. *Geology* 43(8), 699–702.
- Pistone, M., Caricchi, L., Ulmer, P., Reusser, E. and Ardia, P. (2013). Rheology of volatile-bearing crystal mushes: mobilization vs. viscous death. *Chemical Geology* 345, 16–39.
- Piwinskii, A. J. (1968). Experimental studies of igneous rock series central Sierra Nevada batholith, California. *The Journal of Geology* 76(5), 548–570.
- Plank, T. and Langmuir, C. H. (1993). Tracing trace elements from sediment input to volcanic output at subduction zones. *Nature* 362(6422), 739–743.
- Poli, S. (2015). Carbon mobilized at shallow depths in subduction zones by carbonatitic liquids. *Nature Geoscience* 8(8), 633–636.
- Popa, R.-G., Tollan, P., Bachmann, O., Schenker, V., Ellis, B. and Allaz, J. M. (2021). Water exsolution in the magma chamber favors effusive eruptions: application of Cl-F partitioning behavior at the Nisyros-Yali volcanic area. *Chemical Geology* 570, 120170.
- Powell, R. (1983). Fluids and melting under upper amphibolite facies conditions. *Journal of the Geological Society* 140(4), 629–633.
- Ptáček, P., Šoukal, F., Opravil, T., Bartoníčková, E. and Wasserbauer, J. (2016). The formation of feldspar strontian ($\text{SrAl}_2\text{Si}_2\text{O}_8$) via ceramic route: Reaction mechanism, kinetics and thermodynamics of the process. *Ceramics International* 42(7), 8170–8178.
- Puga, E., Fanning, M., de Federico, A. D., Nieto, J. M., Beccaluva, L., Bianchini, G. and Puga, M. A. D. (2011). Petrology, geochemistry and U–Pb geochronology of the Betic Ophiolites: inferences for Pangaea break-up and birth of the westernmost Tethys Ocean. *Lithos* 124(3–4), 255–272.
- Putirka, K. D. (2005). Igneous thermometers and barometers based on plagioclase + liquid equilibria: Tests of some existing models and new calibrations. *American Mineralogist* 90(2–3), 336–346.
- Putirka, K. D. (2008). Thermometers and barometers for volcanic systems. *Reviews in Mineralogy and Geochemistry* 69(1), 61–120.
- Putirka, K. D., Johnson, M., Kinzler, R., Longhi, J. and Walker, D. (1996). Thermobarometry of mafic igneous rocks based on clinopyroxene-liquid equilibria, 0–30 kbar. *Contributions to Mineralogy and Petrology* 123, 92–108.
- Rabinowicz, M. and Vigneresse, J.-L. (2004). Melt segregation under compaction and shear channeling: Application to granitic magma segregation in a continental crust. *Journal of Geophysical Research: Solid Earth* 109(B4).
- Rae, A. S., Edmonds, M., MacLennan, J., Morgan, D., Houghton, B., Hartley, M. E. and Sides, I. (2016). Time scales of magma transport and mixing at Kīlauea Volcano, Hawai‘i. *Geology* 44(6), 463–466.
- Randolf, A. and Larson, M. (1971). The Theory of Particulate Processes, Chapter I.
- Rapp, R. P. and Watson, E. B. (1995). Dehydration melting of metabasalt at 8–32 kbar: implications for continental growth and crust-mantle recycling. *Journal of Petrology* 36(4), 891–931.
- Rapp, R. P., Watson, E. B. and Miller, C. F. (1991). Partial melting of amphibolite/eclogite and the origin of Archean trondhjemites and tonalites. *Precambrian Research* 51(1–4), 1–25.
- Rasmussen, D. J., Plank, T. A., Roman, D. C., Power, J. A., Bodnar, R. J. and Hauri, E. H. (2018). When does eruption run-up begin? Multidisciplinary insight from the 1999 eruption of Shishaldin volcano. *Earth and Planetary Science Letters* 486, 1–14.
- Reid, M. (2003). Timescales of Magma Transfer. In: R. Rudnick, ed., *The Crust*, volume 3. Elsevier, pp. 167–193.
- Reid, M. R., Coath, C. D., Harrison, T. M. and McKeegan, K. D. (1997). Prolonged residence times for the youngest rhyolites associated with Long Valley Caldera: ^{230}Th – ^{238}U ion microprobe dating of young zircons. *Earth and Planetary Science Letters* 150(1–2), 27–39.

Bibliography

- Reid, M. R. and Vazquez, J. A. (2017). Fitful and protracted magma assembly leading to a giant eruption, Youngest Toba Tuff, Indonesia. *Geochemistry, Geophysics, Geosystems* 18(1), 156–177.
- Reubi, O. and Müntener, O. (2022). Making andesites and the continental crust: Mind the step when wet. *Journal of Petrology* 63(6), egac044.
- Reynolds, T. J. and Beane, R. E. (1985). Evolution of hydrothermal fluid characteristics at the Santa Rita, New Mexico, porphyry copper deposit. *Economic Geology* 80(5), 1328–1347.
- Ribes, C., Petri, B., Ghienne, J.-F., Manatschal, G., Galster, F., Karner, G. D., Figueredo, P. H., Johnson, C. A. and Karpoff, A.-M. (2020). Tectono-sedimentary evolution of a fossil ocean-continent transition: Tasna nappe, central Alps (SE Switzerland). *GSA Bulletin* 132(7-8), 1427–1446.
- Richards, J. P. (2011). Magmatic to hydrothermal metal fluxes in convergent and collided margins. *Ore Geology Reviews* 40(1), 1–26.
- Ridolfi, F., Renzulli, A. and Puerini, M. (2010). Stability and chemical equilibrium of amphibole in calc-alkaline magmas: an overview, new thermobarometric formulations and application to subduction-related volcanoes. *Contributions to Mineralogy and Petrology* 160, 45–66.
- Riker, J., Humphreys, M. C., Brooker, R. A., De Hoog, J. C. and EIMF (2018). First measurements of OH-C exchange and temperature-dependent partitioning of OH and halogens in the system apatite–silicate melt. *American Mineralogist* 103(2), 260–270.
- Riklin, K. (1983). Contact metamorphism of the permian "Red Sandstone" in the Adamello area. *Memorie della Societa Geologica Italiana* 26(1), 159–169.
- Ringwood, A. E. (1974). The petrological evolution of island arc systems: Twenty-seventh William Smith Lecture. *Journal of the Geological Society* 130(3), 183–204.
- Roedder, E. (1971). Fluid inclusion studies on the porphyry-type ore deposits at Bingham, Utah, Butte, Montana, and Climax, Colorado. *Economic Geology* 66(1), 98–118.
- Roeder, P. L., MacArthur, D., Ma, X.-P., Palmer, G. R. and Mariano, A. N. (1987). Cathodoluminescence and microprobe study of rare-earth elements in apatite. *American Mineralogist* 72(7-8), 801–811.
- Rose-Koga, E., Bouvier, A.-S., Gaetani, G., Wallace, P., Allison, C., Andrys, J., De La Torre, C. A., Barth, A., Bodnar, R., Gartner, A. B. et al. (2021). Silicate melt inclusions in the new millennium: A review of recommended practices for preparation, analysis, and data presentation. *Chemical Geology* 570, 120145.
- Rout, S. S., Blum-Oeste, M. and Wörner, G. (2021). Long-term temperature cycling in a shallow magma reservoir: insights from sanidine megacrysts at Taápaca volcano, Central Andes. *Journal of Petrology* 62(9), egab010.
- Rout, S. S. and Wörner, G. (2018). Zoning and exsolution in alkali feldspars from Laacher See volcano (Western Germany): constraints on temperature history prior to eruption. *Contributions to Mineralogy and Petrology* 173(11), 95.
- Rubin, A. E., Cooper, K. M., Till, C. B., Kent, A. J., Costa, F., Bose, M., Gravley, D., Deering, C. and Cole, J. (2017). Rapid cooling and cold storage in a silicic magma reservoir recorded in individual crystals. *Science* 356(6343), 1154–1156.
- Rudnick, R. L. and Fountain, D. M. (1995). Nature and composition of the continental crust: a lower crustal perspective. *Reviews of Geophysics* 33(3), 267–309.
- Ruffini, R., Polino, R., Callegari, E., Hunziker, J. and Pfeifer, H. (1997). Volcanic clast-rich turbidites of the Taveyanne sandstones from the Thônes syncline (Savoie, France): records for a Tertiary postcollisional volcanism. *Schweizerische mineralogische und petrographische Mitteilungen* 77, 161–174.
- Ruprecht, P. and Plank, T. (2013). Feeding andesitic eruptions with a high-speed connection from the mantle. *Nature* 500(7460), 68–72.
- Rusk, B. G., Reed, M. H. and Dilles, J. H. (2008). Fluid inclusion evidence for magmatic-hydrothermal fluid evolution in the porphyry copper-molybdenum deposit at Butte, Montana. *Economic Geology* 103(2), 307–334.
- Rutherford, M. J. and Hill, P. M. (1993). Magma ascent rates from amphibole breakdown: an experimental study applied to the 1980–1986 Mount St. Helens eruptions. *Journal of Geophysical Research: Solid Earth* 98(B11), 19667–19685.

- Rybacki, E. and Dresen, G. (2004). Deformation mechanism maps for feldspar rocks. *Tectonophysics* 382(3-4), 173–187.
- Saleeby, J. B. (1990). Progress in tectonic and petrogenetic studies in an exposed cross-section of young (~100 Ma) continental crust, southern Sierra Nevada, California. In: *Exposed cross-sections of the continental crust*. Springer, pp. 137–158.
- Samperton, K. M., Schoene, B., Cottle, J. M., Keller, C. B., Crowley, J. L. and Schmitz, M. D. (2015). Magma emplacement, differentiation and cooling in the middle crust: Integrated zircon geochronological–geochemical constraints from the Bergell Intrusion, Central Alps. *Chemical Geology* 417, 322–340.
- Saunders, K., Blundy, J. D., Dohmen, R. and Cashman, K. (2012). Linking petrology and seismology at an active volcano. *Science* 336(6084), 1023–1027.
- Schaen, A. J., Cottle, J. M., Singer, B. S., Keller, C. B., Garibaldi, N. and Schoene, B. (2017). Complementary crystal accumulation and rhyolite melt segregation in a late Miocene Andean pluton. *Geology* 45(9), 835–838.
- Schaen, A. J., Schoene, B., Dufek, J., Singer, B. S., Eddy, M. P., Jicha, B. R. and Cottle, J. M. (2021). Transient rhyolite melt extraction to produce a shallow granitic pluton. *Science Advances* 7(21), eabf0604.
- Schaen, A. J., Singer, B. S., Cottle, J. M., Garibaldi, N., Schoene, B., Satkoski, A. M. and Fournelle, J. (2018). Textural and mineralogical record of low-pressure melt extraction and silicic cumulate formation in the late Miocene Risco Bayo–Huemul plutonic complex, southern Andes. *Journal of Petrology* 59(10), 1991–2016.
- Schaltegger, U., Brack, P., Ovtcharova, M., Peytcheva, I., Schoene, B., Stracke, A., Marocchi, M. and Bargossi, G. M. (2009). Zircon and titanite recording 1.5 million years of magma accretion, crystallization and initial cooling in a composite pluton (southern Adamello batholith, northern Italy). *Earth and Planetary Science Letters* 286(1-2), 208–218.
- Schaltegger, U., Nowak, A., Ulianov, A., Fisher, C. M., Gerdes, A., Spikings, R., Whitehouse, M. J., Bindeman, I., Hanchar, J. M., Duff, J., Vervoort, J. D., Sheldrake, T., Caricchi, L., Brack, P. and Müntener, O. (2019). Zircon petrochronology and $^{40}\text{Ar}/^{39}\text{Ar}$ thermochronology of the Adamello Intrusive Suite, N. Italy: Monitoring the growth and decay of an incrementally assembled magmatic system. *Journal of Petrology* 60(4), 701–722.
- Schettler, G., Gottschalk, M. and Harlov, D. E. (2011). A new semi-micro wet chemical method for apatite analysis and its application to the crystal chemistry of fluorapatite-chlorapatite solid solutions. *American Mineralogist* 96(1), 138–152.
- Schmid, S. M., Fügenschuh, B., Kissling, E. and Schuster, R. (2004). Tectonic map and overall architecture of the Alpine orogen. *Eclogae Geologicae Helvetiae* 97, 93–117.
- Schmid, S. M. and Kissling, E. (2000). The arc of the western Alps in the light of geophysical data on deep crustal structure. *Tectonics* 19(1), 62–85.
- Schmidt, M. W. (1992). Amphibole composition in tonalite as a function of pressure: an experimental calibration of the Al-in-hornblende barometer. *Contributions to Mineralogy and Petrology* 110(2), 304–310.
- Schmidt, M. W., Forien, M., Solferino, G. and Bagdassarov, N. (2012). Settling and compaction of olivine in basaltic magmas: an experimental study on the time scales of cumulate formation. *Contributions to Mineralogy and Petrology* 164, 959–976.
- Schmidt, M. W. and Poli, S. (1998). Experimentally based water budgets for dehydrating slabs and consequences for arc magma generation. *Earth and Planetary Science Letters* 163(1-4), 361–379.
- Schmitt, A. K., Wetzell, F., Cooper, K. M., Zou, H. and Wörner, G. (2010). Magmatic longevity of Laacher See volcano (Eifel, Germany) indicated by U–Th dating of intrusive carbonatites. *Journal of Petrology* 51(5), 1053–1085.
- Schmitz, M. D. and Bowring, S. A. (2001). U–Pb zircon and titanite systematics of the Fish Canyon Tuff: an assessment of high-precision U–Pb geochronology and its application to young volcanic rocks. *Geochimica et Cosmochimica Acta* 65(15), 2571–2587.
- Schoene, B., Eddy, M. P., Samperton, K. M., Keller, C. B., Keller, G., Adatte, T. and Khadri, S. F. (2019). U–Pb constraints on pulsed eruption of the Deccan Traps across the end-Cretaceous mass extinction. *Science* 363(6429), 862–866.

- Schoene, B., Guex, J., Bartolini, A., Schaltegger, U. and Blackburn, T. J. (2010). Correlating the end-Triassic mass extinction and flood basalt volcanism at the 100 ka level. *Geology* 38(5), 387–390.
- Schoene, B., Schaltegger, U., Brack, P., Latkoczy, C., Stracke, A. and Günther, D. (2012). Rates of magma differentiation and emplacement in a ballooning pluton recorded by U–Pb TIMS-TEA, Adamello batholith, Italy. *Earth and Planetary Science Letters* 355, 162–173.
- Sclar, C. and Benimoff, A. (1980). Magnesium in anorthite: synthesis and petrological significance of the CaMgSi₃O₈ series. *EOS American Geophysical Union* 61, 392.
- Searle, M., Cottle, J., Streule, M. and Waters, D. (2009). Crustal melt granites and migmatites along the Himalaya: melt source, segregation, transport and granite emplacement mechanisms. *Earth and Environmental Science Transactions of the Royal Society of Edinburgh* 100(1-2), 219–233.
- Seitz, S., Putlitz, B., Baumgartner, L. P., Meibom, A., Escrig, S. and Bouvier, A.-S. (2018). A NanoSIMS investigation on timescales recorded in volcanic quartz from the silicic Chon Aike Province (Patagonia). *Frontiers in Earth Science* 6, 95.
- Self, S. (2006). The effects and consequences of very large explosive volcanic eruptions. *Philosophical Transactions of the Royal Society A: Mathematical, Physical and Engineering Sciences* 364(1845), 2073–2097.
- Shamloo, H. I. and Till, C. B. (2019). Decadal transition from quiescence to supereruption: petrologic investigation of the Lava Creek Tuff, Yellowstone Caldera, WY. *Contributions to Mineralogy and Petrology* 174(4), 32.
- Shane, P., Storm, S., Schmitt, A. K. and Lindsay, J. M. (2012). Timing and conditions of formation of granitoid clasts erupted in recent pyroclastic deposits from Tarawera Volcano (New Zealand). *Lithos* 140, 1–10.
- Shannon, R. D. (1976). Revised effective ionic radii and systematic studies of interatomic distances in halides and chalcogenides. *Foundations of Crystallography* 32(5), 751–767.
- Sharpe, M. S., Barker, S. J., Rooyakkers, S. M., Wilson, C. J., Chambefort, I., Rowe, M. C., Schipper, C. I. and Charlier, B. L. (2022). A sulfur and halogen budget for the large magmatic system beneath Taupō volcano. *Contributions to Mineralogy and Petrology* 177(10), 95.
- Shaw, D. M. (1970). Trace element fractionation during anatexis. *Geochimica et Cosmochimica Acta* 34(2), 237–243.
- Shaw, H. R. (1965). Comments on viscosity, crystal settling, and convection in granitic magmas. *American Journal of Science* 263(2), 120–152.
- Shaw, H. R. (1972). Viscosities of magmatic silicate liquids; an empirical method of prediction. *American Journal of Science* 272(9), 870–893.
- Shea, T., Lynn, K. J. and Garcia, M. O. (2015). Cracking the olivine zoning code: Distinguishing between crystal growth and diffusion. *Geology* 43(10), 935–938.
- Shelton, K. L. (1983). Composition and origin of ore-forming fluids in a carbonate-hosted porphyry copper and skarn deposit; a fluid inclusion and stable isotope study of Mines Gaspé, Québec. *Economic Geology* 78(3), 387–421.
- Shinohara, H. (1994). Exsolution of immiscible vapor and liquid phases from a crystallizing silicate melt: Implications for chlorine and metal transport. *Geochimica et Cosmochimica Acta* 58(23), 5215–5221.
- Shinohara, H. (2013). Composition of volcanic gases emitted during repeating Vulcanian eruption stage of Shinmoedake, Kirishima volcano, Japan. *Earth, Planets and Space* 65, 667–675.
- Shishkina, T. A., Botcharnikov, R. E., Holtz, F., Almeev, R. R., Jazwa, A. M. and Jakubiak, A. A. (2014). Compositional and pressure effects on the solubility of H₂O and CO₂ in mafic melts. *Chemical Geology* 388, 112–129.
- Sigl, M., Winstrup, M., McConnell, J. R., Welten, K. C., Plunkett, G., Ludlow, F., Büntgen, U., Caffee, M., Chellman, N., Dahl-Jensen, D., Fischer, H., Kipfstuhl, S., Kostick, C., Maselli, O., Mekhaldi, F., Mulvaney, R., Muscheler, R., Pasteris, D., Pilcher, J., Salzer, M., Schüpbach, S., Steffensen, J., Vinther, B. and Woodruff, T. (2015). Timing and climate forcing of volcanic eruptions for the past 2,500 years. *Nature* 523(7562), 543–549.
- Sillitoe, R. H. (2010). Porphyry copper systems. *Economic geology* 105(1), 3–41.
- Sims, K. W., Pichat, S., Reagan, M. K., Kyle, P. R., Dulaiova, H., Dunbar, N. W., Prytulak, J., Sawyer, G., Layne, G. D., Blichert-Toft, J., Gauthier, P. J., Charette, M. A. and Elliott, T. R.

- (2013). On the time scales of magma genesis, melt evolution, crystal growth rates and magma degassing in the Erebus volcano magmatic system using the ^{238}U , ^{235}U and ^{232}Th decay series. *Journal of Petrology* 54(2), 235–271.
- Sinclair, H. (1997). Tectonostratigraphic model for underfilled peripheral foreland basins: An Alpine perspective. *Geological Society of America Bulletin* 109(3), 324–346.
- Sisson, T. W. (1994). Hornblende-melt trace-element partitioning measured by ion microprobe. *Chemical Geology* 117(1-4), 331–344.
- Sisson, T. W. and Bacon, C. R. (1999). Gas-driven filter pressing in magmas. *Geology* 27(7), 613–616.
- Sisson, T. W. and Grove, T. L. (1993). Experimental investigations of the role of H_2O in calc-alkaline differentiation and subduction zone magmatism. *Contributions to mineralogy and petrology* 113, 143–166.
- Sisson, T. W., Ratajeski, K., Hankins, W. and Glazner, A. F. (2005). Voluminous granitic magmas from common basaltic sources. *Contributions to Mineralogy and Petrology* 148, 635–661.
- Solar, G. S. and Brown, M. (2001). Petrogenesis of migmatites in Maine, USA: possible source of peraluminous leucogranite in plutons? *Journal of Petrology* 42(4), 789–823.
- Solgadi, F. and Sawyer, E. (2008). Formation of igneous layering in granodiorite by gravity flow: A field, microstructure and geochemical study of the Tuolumne Intrusive Suite at Sawmill Canyon, California. *Journal of Petrology* 49(11), 2009–2042.
- Sparks, R. S. J. (1978). The dynamics of bubble formation and growth in magmas: a review and analysis. *Journal of Volcanology and Geothermal Research* 3(1-2), 1–37.
- Sparks, R. S. J., Annen, C., Blundy, J. D., Cashman, K., Rust, A. and Jackson, M. (2019). Formation and dynamics of magma reservoirs. *Philosophical Transactions of the Royal Society A* 377(2139), 20180019.
- Sparks, R. S. J. and Huppert, H. E. (1984). Density changes during the fractional crystallization of basaltic magmas: fluid dynamic implications. *Contributions to Mineralogy and Petrology* 85, 300–309.
- Sparks, R. S. J., Sigurdsson, H. and Wilson, L. (1977). Magma mixing: a mechanism for triggering acid explosive eruptions. *Nature* 267(5609), 315–318.
- Spear, F. S. and Parrish, R. R. (1996). Petrology and cooling rates of the Valhalla complex, British Columbia, Canada. *Journal of Petrology* 37(4), 733–765.
- Spear, F. S. and Wark, D. A. (2009). Cathodoluminescence imaging and titanium thermometry in metamorphic quartz. *Journal of Metamorphic Geology* 27(3), 187–205.
- Stampfli, G., Mosar, J., Marquer, D., Marchant, R., Baudin, T. and Borel, G. (1998). Subduction and obduction processes in the Swiss Alps. *Tectonophysics* 296(1-2), 159–204.
- Stelling, J., Botcharnikov, R. E., Beermann, O. and Nowak, M. (2008). Solubility of H_2O - and chlorine-bearing fluids in basaltic melt of Mount Etna at $T = 1050\text{--}1250\text{ }^\circ\text{C}$ and $P = 200\text{ MPa}$. *Chemical Geology* 256(3-4), 102–110.
- Stipp, M., Fügenschuh, B., Gromet, L., Stünitz, H. and Schmid, S. (2004). Contemporaneous plutonism and strike-slip faulting along the easternmost segment of the Insubric line: The Tonale fault zone north of the Adamello pluton (Italian Alps). *Tectonics* 23, TC3004.
- Stipp, M., Stünitz, H., Heilbronner, R. and Schmid, S. M. (2002). The eastern Tonale fault zone: a ‘natural laboratory’ for crystal plastic deformation of quartz over a temperature range from 250 to 700 $^\circ\text{C}$. *Journal of structural geology* 24(12), 1861–1884.
- Stock, M. J., Humphreys, M. C., Smith, V. C., Isaia, R., Brooker, R. A. and Pyle, D. M. (2018). Tracking volatile behaviour in sub-volcanic plumbing systems using apatite and glass: insights into pre-eruptive processes at Campi Flegrei, Italy. *Journal of Petrology* 59(12), 2463–2492.
- Stock, M. J., Humphreys, M. C., Smith, V. C., Isaia, R. and Pyle, D. M. (2016). Late-stage volatile saturation as a potential trigger for explosive volcanic eruptions. *Nature Geoscience* 9(3), 249–254.
- Sun, C., Graff, M. and Liang, Y. (2017). Trace element partitioning between plagioclase and silicate melt: The importance of temperature and plagioclase composition, with implications for terrestrial and lunar magmatism. *Geochimica et Cosmochimica Acta* 206, 273–295.
- Sun, S.-S. and McDonough, W. F. (1989). Chemical and isotopic systematics of oceanic basalts: implications for mantle composition and processes. *Geological Society, London, Special Publications* 42(1), 313–345.

Bibliography

- Sverjensky, D., Shock, E. and Helgeson, H. (1997). Prediction of the thermodynamic properties of aqueous metal complexes to 1000 °C and 5 kb. *Geochimica et Cosmochimica Acta* 61(7), 1359–1412.
- Swanson, S. E. (1977). Relation of nucleation and crystal-growth rate to the development of granitic textures. *American Mineralogist* 62(9-10), 966–978.
- Syracuse, E. M., van Keken, P. E. and Abers, G. A. (2010). The global range of subduction zone thermal models. *Physics of the Earth and Planetary Interiors* 183(1-2), 73–90.
- Szymanowski, D., Forni, F., Phua, M., Jicha, B., Lee, D. W., Hsu, Y.-J., Rifai, H., Schoene, B. and de Maisonville, C. B. (2023). A shifty Toba magma reservoir: Improved eruption chronology and petrochronological evidence for lateral growth of a giant magma body. *Earth and Planetary Science Letters* 622, 118408.
- Szymanowski, D., Wotzlaw, J.-F., Ellis, B. S., Bachmann, O., Guillong, M. and von Quadt, A. (2017). Protracted near-solidus storage and pre-eruptive rejuvenation of large magma reservoirs. *Nature Geoscience* 10(10), 777–782.
- Tait, S. and Jaupart, C. (1992). Compositional convection in a reactive crystalline mush and melt differentiation. *Journal of Geophysical Research: Solid Earth* 97(B5), 6735–6756.
- Tait, S., Jaupart, C. and Vergnolle, S. (1989). Pressure, gas content and eruption periodicity of a shallow, crystallising magma chamber. *Earth and Planetary Science Letters* 92(1), 107–123.
- Tatsumi, Y., Furukawa, Y. and Yamashita, S. (1994). Thermal and geochemical evolution of the mantle wedge in the northeast Japan arc: 1. Contribution from experimental petrology. *Journal of Geophysical Research: Solid Earth* 99(B11), 22275–22283.
- Tattitch, B. C., Candela, P. A., Piccoli, P. M. and Bodnar, R. J. (2015). Copper partitioning between felsic melt and H₂O–CO₂ bearing saline fluids. *Geochimica et Cosmochimica Acta* 148, 81–99.
- Tavazzani, L., Peres, S., Sinigoi, S., Demarchi, G., Economos, R. and Quick, J. (2020). Timescales and mechanisms of crystal-mush rejuvenation and melt extraction recorded in Permian plutonic and volcanic rocks of the Sesia Magmatic System (southern Alps, Italy). *Journal of Petrology* 61(5), egaa049.
- Tavazzani, L., Wotzlaw, J.-F., Economos, R., Sinigoi, S., Demarchi, G., Szymanowski, D., Laurent, O., Bachmann, O. and Chelle-Michou, C. (2023). High-precision zircon age spectra record the dynamics and evolution of large open-system silicic magma reservoirs. *Earth and Planetary Science Letters* 623, 118432.
- Taylor, B. E. (1986). Magmatic volatiles; isotopic variation of C, H, and S. *Reviews in Mineralogy and Geochemistry* 16(1), 185–225.
- Taylor, S. R. (1967). The origin and growth of continents. *Tectonophysics* 4(1), 17–34.
- Taylor, S. R. and McLennan, S. M. (1985). *The continental crust: its composition and evolution*. Blackwell Scientific Pub., Palo Alto, CA.
- Taylor, S. R. and McLennan, S. M. (1995). The geochemical evolution of the continental crust. *Reviews of Geophysics* 33(2), 241–265.
- Taylor Jr, H. P. (1980). The effects of assimilation of country rocks by magmas on ¹⁸O/¹⁶O and ⁸⁷Sr/⁸⁶Sr systematics in igneous rocks. *Earth and Planetary Science Letters* 47(2), 243–254.
- Thomas, J. B., Bruce Watson, E., Spear, F. S., Shemella, P. T., Nayak, S. K. and Lanzirrotti, A. (2010). TitaniQ under pressure: the effect of pressure and temperature on the solubility of Ti in quartz. *Contributions to Mineralogy and Petrology* 160(5), 743–759.
- Thomas, J. B., Watson, E. B., Spear, F. S. and Wark, D. A. (2015). TitaniQ recrystallized: experimental confirmation of the original Ti-in-quartz calibrations. *Contributions to Mineralogy and Petrology* 169, 1–16.
- Thompson, A. (1983). Fluid-absent metamorphism. *Journal of the Geological Society* 140(4), 533–547.
- Thompson, A. B. and Connolly, J. A. D. (1995). Melting of the continental crust: some thermal and petrological constraints on anatexis in continental collision zones and other tectonic settings. *Journal of Geophysical Research: Solid Earth* 100(B8), 15565–15579.
- Thompson, A. B., Matile, L. and Ulmer, P. (2002). Some thermal constraints on crustal assimilation during fractionation of hydrous, mantle-derived magmas with examples from central Alpine batholiths. *Journal of Petrology* 43(3), 403–422.

- Till, C. B., Vazquez, J. A. and Boyce, J. W. (2015). Months between rejuvenation and volcanic eruption at Yellowstone caldera, Wyoming. *Geology* 43(8), 695–698.
- Torquato, S., Truskett, T. M. and Debenedetti, P. G. (2000). Is random close packing of spheres well defined? *Physical Review Letters* 84(10), 2064.
- Turnbull, R., Weaver, S., Tulloch, A., Cole, J., Handler, M. and Ireland, T. (2010). Field and geochemical constraints on mafic–felsic interactions, and processes in high-level arc magma chambers: an example from the Halfmoon Pluton, New Zealand. *Journal of Petrology* 51(7), 1477–1505.
- Turner, S., George, R., Jerram, D. A., Carpenter, N. and Hawkesworth, C. (2003). Case studies of plagioclase growth and residence times in island arc lavas from Tonga and the Lesser Antilles, and a model to reconcile discordant age information. *Earth and Planetary Science Letters* 214(1-2), 279–294.
- Ubide, T. and Kamber, B. S. (2018). Volcanic crystals as time capsules of eruption history. *Nature communications* 9(1), 326.
- Ulmer, P. (1982). Monticellite-clintonite bearing assemblages at the southern of the Adamello massif. *Società Italiana di Mineralogia e Petrologia* 38(2), 617–628.
- Ulmer, P. (1988). High-pressure phase equilibria of a calc-alkaline picro-basalt: implications for the genesis of calc-alkaline magmas. *Carnegie Institute Washington Yearbook* 87, 28–35.
- Ulmer, P., Callegari, E. and Sonderegger, U. (1983). Genesis of the mafic and ultramafic rocks and their genetical relations to the tonalitic-trondhjemitic granitoids of the southern part of the Adamello batholith (Northern Italy). *Memorie della Società Geologica Italiana* 26(1), 171–222.
- Ulmer, P., Kaegi, R. and Müntener, O. (2018). Experimentally derived intermediate to silica-rich arc magmas by fractional and equilibrium crystallization at 1.0 GPa: an evaluation of phase relationships, compositions, liquid lines of descent and oxygen fugacity. *Journal of Petrology* 59(1), 11–58.
- Urann, B., Le Roux, V., Jagoutz, O., Müntener, O., Behn, M. and Chin, E. (2022). High water content of arc magmas recorded in cumulates from subduction zone lower crust. *Nature Geoscience* 15(6), 501–508.
- Ussler III, W. and Glazner, A. F. (1992). Graphical analysis of enthalpy-composition relationships in mixed magmas. *Journal of Volcanology and Geothermal Research* 51(1-2), 23–40.
- Van Orman, J. A., Cherniak, D. J. and Kita, N. T. (2014). Magnesium diffusion in plagioclase: Dependence on composition, and implications for thermal resetting of the ^{26}Al – ^{26}Mg early solar system chronometer. *Earth and Planetary Science Letters* 385, 79–88.
- Van Orman, J. A., Grove, T. L. and Shimizu, N. (2001). Rare earth element diffusion in diopside: influence of temperature, pressure, and ionic radius, and an elastic model for diffusion in silicates. *Contributions to Mineralogy and Petrology* 141, 687–703.
- Vance, J. A. (1969). On synneusis. *Contributions to Mineralogy and Petrology* 24(1), 7–29.
- Vazquez, J. A. and Reid, M. R. (2002). Time scales of magma storage and differentiation of voluminous high-silica rhyolites at Yellowstone caldera, Wyoming. *Contributions to Mineralogy and Petrology* 144(3), 274–285.
- Vazquez, J. A. and Reid, M. R. (2004). Probing the accumulation history of the voluminous Toba magma. *Science* 305(5686), 991–994.
- Verberne, R. (2013). *The role of magma rheology during emplacement of the Listino Suite, Adamello Massif, Italy*. Ph.D. thesis, University of Lausanne.
- Vernon, R. and Paterson, S. (2006). Mesoscopic structures resulting from crystal accumulation and melt movement in granites. *Earth and Environmental Science Transactions of the Royal Society of Edinburgh* 97(4), 369–381.
- Vernon, R. and Paterson, S. (2008). How late are K-feldspar megacrysts in granites? *Lithos* 104(1-4), 327–336.
- Vernon, R. H. (2004). *A practical guide to rock microstructure*. Cambridge university press.
- Vielzeuf, D. and Holloway, J. R. (1988). Experimental determination of the fluid-absent melting relations in the pelitic system: consequences for crustal differentiation. *Contributions to Mineralogy and Petrology* 98, 257–276.
- Vigneresse, J.-L. (1995). Control of granite emplacement by regional deformation. *Tectonophysics* 249(3-4), 173–186.

Bibliography

- Villiger, S., Ulmer, P. and Müntener, O. (2007). Equilibrium and fractional crystallization experiments at 0.7 GPa; the effect of pressure on phase relations and liquid compositions of tholeiitic magmas. *Journal of Petrology* 48(1), 159–184.
- Viola, G. (2000). *Kinematics and timing of the Periadriatic fault system in the Giudicarie region (central-eastern Alps)*. Ph.D. thesis, ETH Zürich.
- Viola, G., Mancktelow, N. S. and Seward, D. (2001). Late Oligocene-Neogene evolution of Europe-Adria collision: New structural and geochronological evidence from the Giudicarie fault system (Italian Eastern Alps). *Tectonics* 20(6), 999–1020.
- Vogt, P. R. (1972). Evidence for global synchronism in mantle plume convection, and possible significance for geology. *Nature* 240(5380), 338–342.
- Volpe, A. M. and Hammond, P. E. (1991). ^{238}U - ^{230}Th - ^{226}Ra disequilibria in young Mount St. Helens rocks: time constraint for magma formation and crystallization. *Earth and Planetary Science Letters* 107(3-4), 475–486.
- von Blanckenburg, F. and Davies, J. H. (1995). Slab breakoff: a model for syncollisional magmatism and tectonics in the Alps. *Tectonics* 14(1), 120–131.
- Wade, J. A., Plank, T., Hauri, E. H., Kelley, K. A., Roggensack, K. and Zimmer, M. (2008). Prediction of magmatic water contents via measurement of H_2O in clinopyroxene phenocrysts. *Geology* 36(10), 799–802.
- Walker Jr, B. A., Miller, C., Claiborne, L. L., Wooden, J. and Miller, J. (2007). Geology and geochronology of the Spirit Mountain batholith, southern Nevada: implications for timescales and physical processes of batholith construction. *Journal of Volcanology and Geothermal Research* 167(1-4), 239–262.
- Wang, D.-B., Liu, P.-P., Gao, M.-H., Zhang, D., Xu, C. and Caricchi, L. (2023). Prolonged near-solidus and steady-state magma storage for the Youngest Toba Tuff: Evidence from TitaniQ thermometry and diffusion chronometry. *Earth and Planetary Science Letters* 619, 118326.
- Wark, D. A., Hildreth, W., Spear, F., Cherniak, D. J. and Watson, E. B. (2007). Pre-eruption recharge of the Bishop magma system. *Geology* 35(3), 235–238.
- Wark, D. A. and Spear, F. S. (2005). Ti in quartz: Cathodoluminescence and thermometry. *Geochimica et Cosmochimica Acta Supplement* 69(10), A592.
- Wark, D. A. and Watson, E. B. (2006). TitaniQ: a titanium-in-quartz geothermometer. *Contributions to Mineralogy and Petrology* 152(6), 743–754.
- Waters, L. E. and Lange, R. A. (2015). An updated calibration of the plagioclase-liquid hygrometer-thermometer applicable to basalts through rhyolites. *American Mineralogist* 100(10), 2172–2184.
- Watson, E. B., Cherniak, D. J. and Holycross, M. E. (2015). Diffusion of phosphorus in olivine and molten basalt. *American Mineralogist* 100(10), 2053–2065.
- Watson, E. B. and Green, T. H. (1981). Apatite/liquid partition coefficients for the rare earth elements and strontium. *Earth and Planetary Science Letters* 56, 405–421.
- Watson, E. B. and Harrison, T. M. (1983). Zircon saturation revisited: temperature and composition effects in a variety of crustal magma types. *Earth and Planetary Science Letters* 64(2), 295–304.
- Webber, J. R., Klepeis, K. A., Webb, L. E., Cembrano, J., Morata, D., Mora-Klepeis, G. and Arancibia, G. (2015). Deformation and magma transport in a crystallizing plutonic complex, Coastal Batholith, central Chile. *Geosphere* 11(5), 1401–1426.
- Weber, G., Caricchi, L., Arce, J. L. and Schmitt, A. K. (2020). Determining the current size and state of subvolcanic magma reservoirs. *Nature communications* 11(1), 5477.
- Webster, J., Kinzler, R. and Mathez, E. (1999). Chloride and water solubility in basalt and andesite melts and implications for magmatic degassing. *Geochimica et Cosmochimica Acta* 63(5), 729–738.
- Webster, J. D. (1990). Partitioning of F between H_2O and CO_2 fluids and topaz rhyolite melt: Implications for mineralizing magmatic-hydrothermal fluids in F-rich granitic systems. *Contributions to Mineralogy and Petrology* 104(4), 424–438.
- Webster, J. D. (1992). Water solubility and chlorine partitioning in Cl-rich granitic systems: Effects of melt composition at 2 kbar and 800 °C. *Geochimica et Cosmochimica Acta* 56(2), 679–687.
- Webster, J. D. (1997). Chloride solubility in felsic melts and the role of chloride in magmatic degassing. *Journal of petrology* 38(12), 1793–1807.

- Webster, J. D. and Botcharnikov, R. E. (2011). Distribution of sulfur between melt and fluid in SOHC-Cl-bearing magmatic systems at shallow crustal pressures and temperatures. *Reviews in Mineralogy and Geochemistry* 73(1), 247–283.
- Webster, J. D., Goldoff, B. A., Flesch, R. N., Nadeau, P. A. and Silbert, Z. W. (2017). Hydroxyl, Cl, and F partitioning between high-silica rhyolitic melts-apatite-fluid (s) at 50–200 MPa and 700–1000 °C. *American Mineralogist* 102(1), 61–74.
- Webster, J. D. and Holloway, J. R. (1990). Partitioning of F and Cl between magmatic hydrothermal fluids and highly evolved granitic magmas. *Geological Society of America Special Papers* 246, 21–34.
- Webster, J. D. and Piccoli, P. M. (2015). Magmatic apatite: A powerful, yet deceptive, mineral. *Elements* 11(3), 177–182.
- Webster, J. D., Tappen, C. M. and Mandeville, C. W. (2009). Partitioning behavior of chlorine and fluorine in the system apatite–melt–fluid. II: Felsic silicate systems at 200 MPa. *Geochimica et Cosmochimica Acta* 73(3), 559–581.
- Weinberg, R. F., Mark, G. and Reichardt, H. (2009). Magma ponding in the Karakoram shear zone, Ladakh, NW India. *Geological Society of America Bulletin* 121(1-2), 278–285.
- Weinberg, R. F. and Podladchikov, Y. (1994). Diapiric ascent of magmas through power law crust and mantle. *Journal of Geophysical Research: Solid Earth* 99(B5), 9543–9559.
- Weinberg, R. F., Sial, A. and Mariano, G. (2004). Close spatial relationship between plutons and shear zones. *Geology* 32(5), 377–380.
- Welsch, B., Hammer, J. and Hellebrand, E. (2014). Phosphorus zoning reveals dendritic architecture of olivine. *Geology* 42(10), 867–870.
- Wenk, H., Joswig, W., Tagai, T., Korekawa, M. and Smith, B. K. (1980). The average structure of An_{62–66} labradorite. *American Mineralogist* 65(1-2), 81–95.
- Wenk, H.-R. and Kroll, H. (1984). Analysis of P $\bar{1}$, I $\bar{1}$ and C $\bar{1}$ plagioclase structures. *Bulletin de Minéralogie* 107(3), 467–487.
- Werner, C. A., Doukas, M. P. and Kelly, P. J. (2011). Gas emissions from failed and actual eruptions from Cook Inlet Volcanoes, Alaska, 1989–2006. *Bulletin of Volcanology* 73, 155–173.
- Werts, K., Barnes, C. G., Memeti, V., Ratschbacher, B., Williams, D. and Paterson, S. R. (2020). Hornblende as a tool for assessing mineral-melt equilibrium and recognition of crystal accumulation. *American Mineralogist* 105(1), 77–91.
- White, R., Powell, R., Holland, T. and Worley, B. (2000). The effect of TiO₂ and Fe₂O₃ on metapelitic assemblages at greenschist and amphibolite facies conditions: mineral equilibria calculations in the system K₂O–FeO–MgO–Al₂O₃–SiO₂–H₂O–TiO₂–Fe₂O₃. *Journal of Metamorphic Geology* 18(5), 497–511.
- White, R. W., Powell, R., Holland, T., Johnson, T. and Green, E. (2014). New mineral activity–composition relations for thermodynamic calculations in metapelitic systems. *Journal of Metamorphic Geology* 32(3), 261–286.
- Whittington, A. G., Hofmeister, A. M. and Nabelek, P. I. (2009). Temperature-dependent thermal diffusivity of the Earth’s crust and implications for magmatism. *Nature* 458(7236), 319–321.
- Williams, P. and Baker, J. E. (1981). Implantation and ion beam mixing in thin film analysis. *Nuclear Instruments and Methods* 182, 15–24.
- Wones, D. R. (1972). Stability of biotite: a reply. *American Mineralogist: Journal of Earth and Planetary Materials* 57(1-2), 316–317.
- Woods, S. C., Mackwell, S. and Dyar, D. (2000). Hydrogen in diopside: Diffusion profiles. *American Mineralogist* 85(3-4), 480–487.
- Wotzlaw, J.-F., Bindeman, I. N., Watts, K. E., Schmitt, A. K., Caricchi, L. and Schaltegger, U. (2014). Linking rapid magma reservoir assembly and eruption trigger mechanisms at evolved Yellowstone-type supervolcanoes. *Geology* 42(9), 807–810.
- Wright, H. M., Folkes, C. B., Cas, R. A. and Cashman, K. V. (2011). Heterogeneous pumice populations in the 2.08-Ma Cerro Galán Ignimbrite: implications for magma recharge and ascent preceding a large-volume silicic eruption. *Bulletin of Volcanology* 73, 1513–1533.
- Wu, L.-G., Li, Y., Jollands, M. C., Vermeesch, P. and Li, X.-H. (2022). Diffuser: A user-friendly program for diffusion chronometry with robust uncertainty estimation. *Computers & Geosciences* 163, 105108.

Bibliography

- Yardley, B. W. and Valley, J. W. (1997). The petrologic case for a dry lower crust. *Journal of Geophysical Research: Solid Earth* 102(B6), 12173–12185.
- Yoder, H. (1969). Experimental studies bearing on the origin of anorthosite, Origin of anorthosite and related rocks. *New York State Mus Sci Serv Mem* 18, 13–22.
- Yund, R. A. (1986). Interdiffusion of NaSi–CaAl in peristerite. *Physics and Chemistry of Minerals* 13(1), 11–16.
- Yund, R. A. and Snow, E. (1989). Effects of hydrogen fugacity and confining pressure on the interdiffusion rate of NaSi–CaAl in plagioclase. *Journal of Geophysical Research: Solid Earth* 94(B8), 10662–10668.
- Zajacz, Z., Candela, P. A., Piccoli, P. M. and Sanchez-Valle, C. (2012). The partitioning of sulfur and chlorine between andesite melts and magmatic volatiles and the exchange coefficients of major cations. *Geochimica et Cosmochimica Acta* 89, 81–101.
- Zajacz, Z., Candela, P. A., Piccoli, P. M., Sanchez-Valle, C. and Wälle, M. (2013). Solubility and partitioning behavior of Au, Cu, Ag and reduced S in magmas. *Geochimica et Cosmochimica Acta* 112, 288–304.
- Zajacz, Z. and Halter, W. (2009). Copper transport by high temperature, sulfur-rich magmatic vapor: Evidence from silicate melt and vapor inclusions in a basaltic andesite from the Villarrica volcano (Chile). *Earth and Planetary Science Letters* 282(1-4), 115–121.
- Zajacz, Z., Halter, W. E., Pettke, T. and Guillong, M. (2008). Determination of fluid/melt partition coefficients by LA-ICPMS analysis of co-existing fluid and silicate melt inclusions: Controls on element partitioning. *Geochimica et Cosmochimica Acta* 72(8), 2169–2197.
- Žák, J., Paterson, S. R. and Memeti, V. (2007). Four magmatic fabrics in the Tuolumne batholith, central Sierra Nevada, California (USA): implications for interpreting fabric patterns in plutons and evolution of magma chambers in the upper crust. *Geological Society of America Bulletin* 119(1-2), 184–201.
- Zanettin, B. (1956). Il Gruppo del Marser (Adamello occidentale). Studio geologico-petrografico, con carta geologica 1:25000. *Memorie degli Istituti di Geologia e Mineralogia dell'Università di Padova* 19, 1–86.
- Zantedeschi, P., Bellieni, G., Cavazzini, G. et al. (1989). Microgranular mafic enclaves in the Re di Castello tonalite (Upper Daone Valley, Southern Adamello Batholith): Petrological, geochemical and Sr isotope data. *Periodico di Mineralogia* 58, 153–165.
- Zellmer, G. F., Blake, S., Vance, D., Hawkesworth, C. and Turner, S. (1999). Plagioclase residence times at two island arc volcanoes (Kameni Islands, Santorini, and Soufriere, St. Vincent) determined by Sr diffusion systematics. *Contributions to Mineralogy and Petrology* 136, 345–357.
- Zellmer, G. F., Rubin, K. H., Dulski, P., Iizuka, Y., Goldstein, S. L. and Perfit, M. R. (2011). Crystal growth during dike injection of MOR basaltic melts: evidence from preservation of local Sr disequilibria in plagioclase. *Contributions to Mineralogy and Petrology* 161, 153–173.
- Zhang, H., Harris, N., Parrish, R., Kelley, S., Zhang, L., Rogers, N., Argles, T. and King, J. (2004). Causes and consequences of protracted melting of the mid-crust exposed in the North Himalayan antiform. *Earth and Planetary Science Letters* 228(1-2), 195–212.
- Zhang, Y. and Stolper, E. M. (1991). Water diffusion in a basaltic melt. *Nature* 351(6324), 306–309.
- Zhukova, I., O'Neill, H. S. C., Cambell, I. H. and Kilburn, M. R. (2014). The effect of silica activity on the diffusion of Ni and Co in olivine. *Contributions to Mineralogy and Petrology* 168, 1–15.
- Zimmer, K., Zhang, Y., Lu, P., Chen, Y., Zhang, G., Dalkilic, M. and Zhu, C. (2016). SUPCRTBL: A revised and extended thermodynamic dataset and software package of SUPCRT92. *Computers & geosciences* 90, 97–111.
- Zimmer, M. M., Plank, T., Hauri, E. H., Yogodzinski, G. M., Stelling, P., Larsen, J., Singer, B., Jicha, B., Mandeville, C. and Nye, C. J. (2010). The role of water in generating the calc-alkaline trend: new volatile data for Aleutian magmas and a new tholeiitic index. *Journal of Petrology* 51(12), 2411–2444.